ISBN 978-82-326-6739-0 (printed ver.)
ISBN 978-82-326-6153-4 (electronic ver.)
ISSN 1503-8181 (printed ver.)
ISSN 2703-8084 (electronic ver.)

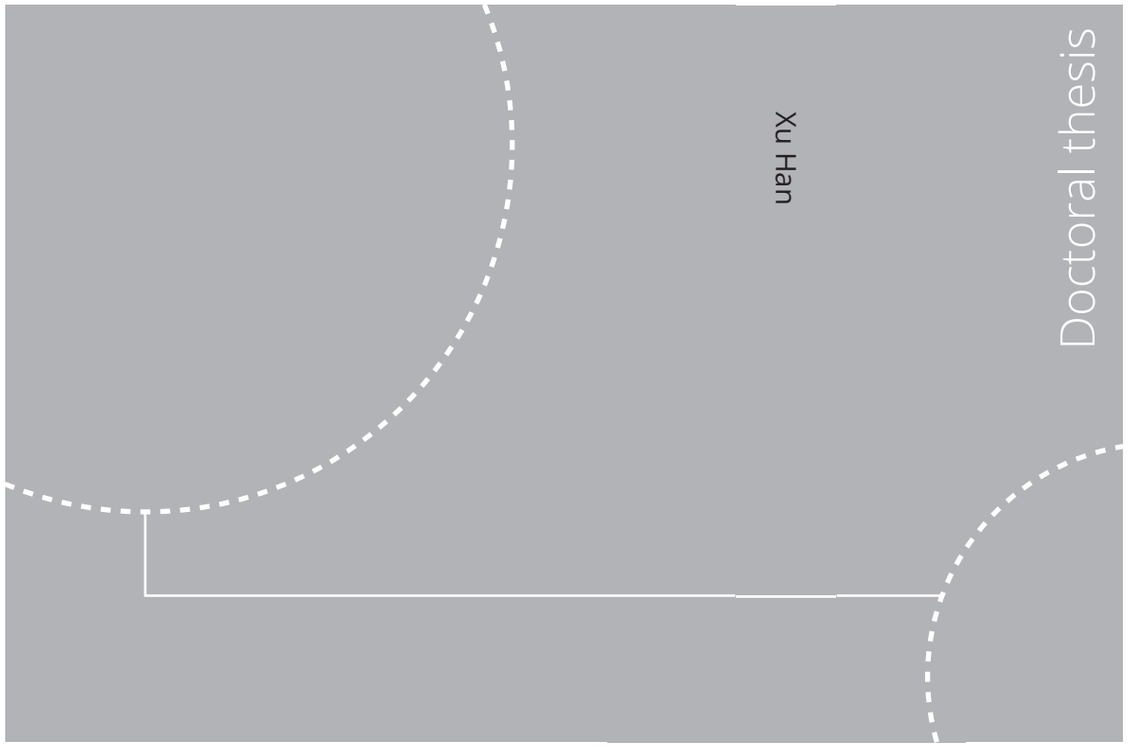

Doctoral theses at NTNU, 2021:356

Xu Han

Onboard Tuning and Uncertainty Estimation of Vessel Seakeeping Model Parameters

Doctoral theses at NTNU, 2021:356

NTNU
Norwegian University of Science and Technology

NTNU
Norwegian University of Science and Technology
Thesis for the degree of Philosophiae Doctor
Faculty of Engineering
Department of Marine Technology

NTNU
Norwegian University of Science and Technology

Xu Han

Onboard Tuning and Uncertainty Estimation of Vessel Seakeeping Model Parameters

Thesis for the degree of Philosophiae Doctor

Trondheim, November 2021

Norwegian University of Science and Technology
Faculty of Engineering
Department of Marine Technology

NTNU
Norwegian University of
Science and Technology

NTNU
Norwegian University of Science and Technology

Thesis for the degree of Philosophiae Doctor

Faculty of Engineering
Department of Marine Technology

ISBN 978-82-326-6739-0 (printed ver.)
ISBN 978-82-326-6153-4 (electronic ver.)
ISSN 1503-8181 (printed ver.)
ISSN 2703-8084 (electronic ver.)

Doctoral theses at NTNU, 2021:356

PRINTED IN NORWAY
NO - 1598

NORDIC SWAN ECOLABEL
Printed matter
2041 0731

Printed by Skipnes Kommunikasjon AS

Abstract

The accurate prediction of critical vessel motions is essential for safe and cost-efficient marine operations. Compared with the difference-frequency responses that can be compensated by mooring and dynamic positioning systems, first-order wave-induced responses are very challenging to control and therefore become increasingly important to accurately predict. Marine operations are usually executed at moderate seas where the rigid body dynamics of conventional vessels can be well represented by linear transfer functions in 6 degrees of freedom, also called response amplitude operators (RAOs). The accuracy of these RAOs depends on the confidence in the vessel loading condition at operation. During the design of marine operations, vessel loading conditions are normally specified according to the best available information on operational arrangement and planning. However, the real condition on board can be different from the planned condition. Therefore, improving knowledge about onboard vessel conditions can increase the motion prediction accuracy, reduce conservatism, and consequently increase cost efficiency. Unfortunately, some critical vessel parameters describing the loading condition and dynamics (e.g., related to inertia distribution and viscous damping) are difficult to measure directly.

The present PhD thesis therefore focuses on how to improve the knowledge about onboard vessel conditions by tuning important vessel parameters and estimating their uncertainties based on available vessel response measurements and wave information for a very limited number of sea states. Consequently, the tuned vessel parameters can improve the accuracy of the corresponding RAOs and the motion prediction for unobserved future sea states, and the quantified uncertainties can be applied to quantitative reliability and risk assessment for real-time onboard applications.

First, the important vessel parameters mostly affecting the critical vessel responses are identified by parametric sensitivity studies. The sensitivity varies with the quantities and locations of the interesting responses, vessel loading conditions, and wave conditions in terms of wave direction and period. Then, an algorithm based on discrete Bayesian inference (DBI) is proposed for tuning these important vessel parameters. Likelihood functions are estimated based on inverse distance weighting. The DBI-based tuning can fully capture the nonlinear and multimodal behavior within the entire predefined parametric uncertainty domain. Sensitivities of the hyperparameters of this DBI-based model are also studied.

The tuning results are influenced by the quality of lowpass filtering of signal noise. A novel algorithm is thus developed to find the sea state dependent optimal cutoff frequency without the need to know sea state information. The optimal cutoff frequency can be found based on the criteria of two newly introduced parameters θ and γ, which describe the relationship of cutoff frequency with the energy and zero-upcrossing period of filtered vessel response signals. An improved tuning of vessel parameters is also demonstrated by applying this adaptive lowpass filter.

Due to linearization, some important hydrodynamic parameters become sea state dependent, such as the linearized viscous damping coefficient. Those tuned parameters and the associated RAOs at the present sea state cannot be applied directly for motion prediction at other sea states. Therefore, a predictive model is required to be implemented in the tuning loop so that the tuned parameter can improve the accuracy of the predictive model, and in return, this model can provide improved prior information for prediction or tuning in the next sea states. Consistent with uncertainty updating in the tuning process, the predictive model should also be able to carry and update the associated uncertainties. To address this challenge, a model based on Gaussian process regression is proposed and applied to tune and predict sea state dependent parameters as part of the DBI-based tuning process. The feasibility of the modified tuning algorithm is demonstrated by numerical simulations. With doubled computational cost, the 2-step tuning algorithm is found to be more promising as a compromise between the different preferred tuning rates for sea state dependent and independent parameters.

For the DBI-based tuning algorithm, the computational cost increases exponentially with the number of considered uncertain vessel parameters. Therefore, a new algorithm inspired by unscented Kalman filter (UKF) is proposed to solve this curse of dimensionality. Only the mean and covariance of the joint probability distribution of uncertain vessel parameters are accounted for in the tuning process. The computational cost of the UKF-based algorithm increases linearly with the number of uncertain parameters and is thus preferred for real applications. The UKF-based tuning algorithm becomes even more attractive because it is also

proven to be able to simultaneously reduce uncertainties of the corresponding sea state characteristics. Numerical simulations are first performed to demonstrate the algorithm.

Furthermore, the UKF-based tuning algorithm is tested based on seakeeping model tests for an offshore construction vessel with open moonpools. Coupling and nonlinear effects from moonpool resonance on vessel motions are significant. Consequently, simplifications of the applied numerical seakeeping simulation introduce significant systematic errors of the estimated RAOs around those resonance frequencies. Unbiased tuning is achieved by carefully designing the measurement space of the UKF model, accounting for such systematic errors.

Preface

This thesis is submitted to the Norwegian University of Science and Technology (NTNU) for partial fulfillment of the requirements for the degree of philosophiae doctor.

This doctoral work was carried out at the Department of Marine Technology at NTNU under the supervision of Professor Bernt Johan Leira as the main supervisor and Professor Svein Sævik, Dr. Stian Skjong, and Dr. Lars Tandle Kyllingstad as the co-supervisors.

This work was financially supported by the Research Council of Norway through the Centre for Research-based Innovation (SFI) MOVE, NFR project No. 237929.

Acknowledgment

Being a PhD student is a special and unique life experience. After several years of engineering work, studying again at NTNU within SFI MOVE offered me a great opportunity to systematically learn new knowledge and challenge myself for interesting topics.

First, I would like to sincerely thank Professor Bernt Johan Leira and Professor Svein Sævik for all their affirmation, support, guidance, trust, encouragement, and advice. It has been my great honor to learn so much from both of you, not only the knowledge but also the attitudes towards life and research. As my main supervisor, Professor Leira has offered me the greatest flexibility of working to balance my own family duties. As one of my co-supervisors, Professor Sævik has given his unreserved trust and provided wide opportunities to me as a junior researcher.

I would also like to thank Dr. Karl Erik Kaasen and two of my co-supervisors, Dr. Stian Skjong and Dr. Lars Tandle Kyllingstad, from SINTEF Ocean for timely support, valuable discussions and advice on my research work.

I am very pleased to have Professor Mogens Blanke (Technical University of Denmark), Professor Emeritus Ove Tobias Gudmestad (University of Stavanger), and Associate Professor Karl Henning Halse (administrator, NTNU) as the doctoral committee. Their valuable editorial comments are highly appreciated for improving this thesis.

DNV is also highly acknowledged for allowing me to take long-term educational leave, providing an office at Høvik in 2019, and providing numerical seakeeping models, powerful simulation tools and timely technical support from many experts. In particular, Dr. Olav Rognebakke, Jens Bloch Helmers, Håvard Nordtveit Austefjord and Dr. Hui Sun in the Section of Hydrodynamics & Stability provided

great technical support for my initial research. Thanks are due to Andreas B. Aardal, Oddrun Steinkjer, Dr. Nils Sødahl, and Torfinn Hørte in the Section of Riser Technology, who encouraged me and gave me valuable suggestions when I decided to take the PhD position.

The PhD project has gone quite smoothly, also partly due to the interest and timely support from NTNU, SINTEF Ocean, DNV, Ocean Installer (now Havfram), Salt Ship Design, Rolls-Royce Marine, and VARD Design. Thanks should also be given to Dr. Zhengru Ren and Gowtham Radhakrishnan for valuable assistance, discussion, and cooperation within the same SFI MOVE project.

I am very grateful for my friends who encouraged and supported me throughout the last few years. Great thanks are also given to my parents, who provided incredible support and patience at a very difficult time in 2020. Finally, I would deeply and sincerely thank my family for being supportive, cooperative, and believing in me throughout my PhD work and being patient with my absence. Your accompanying has been so important, especially during the special and strange years of 2020 and 2021.

Xu Han
October 2021
Trondheim, Norway

List of Publications

Paper A1:
X. Han, S. Sævik, and B. J. Leira, 2020. A sensitivity study of vessel hydrodynamic model parameters. In: *Proceedings of the ASME 2020 39th International Conference on Ocean, Offshore and Arctic Engineering*, volume 1, Virtual, Online.

Paper A2:
X. Han, B. J. Leira, and S. Sævik, 2021. Vessel hydrodynamic model tuning by discrete Bayesian updating using simulated onboard sensor data. *Ocean Engineering* 220.

Paper A3:
X. Han, Z. Ren, B. J. Leira, and S. Sævik, 2021. Adaptive identification of lowpass filter cutoff frequency for online vessel model tuning. *Ocean Engineering* 236.

Paper A4:
X. Han, S. Sævik, and B. J. Leira, 2021. Tuning of vessel parameters including sea state dependent roll damping. *Ocean Engineering* 233.

Paper A5:
X. Han, B. J. Leira, S. Sævik, G. Radhakrishnan, S. Skjong, and L. T. Kyllingstad, 2021. A framework for condition monitoring and risk-based decision support involving a vessel state observer. In: *Proceedings of the ASME 2021 40th International Conference on Ocean, Offshore and Arctic Engineering*, volume 2, Virtual,

Online.

Paper A6:
X. Han, B. J. Leira, S. Sævik, and Z. Ren, 2021. Onboard tuning of vessel seakeeping model parameters and sea state characteristics. *Marine Structures* 78.

Paper A7:
X. Han, B. J. Leira, S. Sævik, and K. E. Kaasen, 2021. Validation of vessel seakeeping model tuning algorithm based on measurements at model scale. *Marine Structures* 80.

This PhD work also resulted in the following co-authored papers within the same project which are not regarded as part of the thesis:

Paper B1:
Z. Ren, X. Han, A. S. Verma, J. A. Dirdal, and R. Skjetne, 2021. Sea state estimation based on vessel motion responses: improved smoothness and robustness using Bézier surface and L1 optimization. *Marine Structures* 76.

Paper B2:
Z. Ren, X. Han, X. Yu, R. Skjetne, B. J. Leira, S. Sævik, and M. Zhu, 2021. Data-driven identification of 6DOF dynamic model and wave load estimation for a ship in waves. *Mechanical Systems and Signal Processing*. Revision under review.

Paper B3:
G. Radhakrishnan, X. Han, S. Sævik, Z. Gao, and B. J. Leira, 2021. System uncertainty effects on wave frequency response of floating vessels based on polynomial chaos expansion. In: *Proceedings of the ASME 2021 40th International Conference on Ocean, Offshore and Arctic Engineering*, volume 2, Virtual, Online.

Contents

List of Tables

List of Figures

Glossary

Abbreviations

AI	Artificial intelligence
CDKF	Central differential Kalman filter
CFD	Computational fluid dynamics
COG	Center of gravity
DBI	Discrete Bayesian inference
DOF	Degree of freedom
DP	Dynamic positioning
EKF	Extended Kalman filter
FFT	Fast Fourier transform
GPR	Gaussian process regression
MRU	Motion reference unit
ODSS	Onboard decision support system
PM	Pierson-Moskowitz spectrum

RAO	Response amplitude operator
RBF	Radial-basis function
SNR	Signal-to-noise ratio
SPKF	Sigma-point Kalman filter
SS	Sea state
SSR	Sensor screening ratio
STD	Standard deviation
UKF	Unscented Kalman filter
VCRP	Vessel condition-related parameter
VMS	Vessel measured state
WN	White noise

Commonly applied symbols

β'_{44}	Difference of the linearized additional roll damping ratio between VERES estimated and its true value
β_{dd}	The ratio between the linearized additional damping and critical damping at mode d, $d = 1, 2, 3, 4, 5, 6$
β_W	Wave direction w.r.t. vessel coordinate system
$\boldsymbol{\phi}$	The random variable vector representing uncertain VCRPs
$\boldsymbol{\theta}$	The random variable vector representing uncertain wave data
$\eta_d, \dot{\eta}_d, \ddot{\eta}_d$	Displacement, velocity, acceleration of response for mode d
γ	Normalized slopes of the $\hat{T}_z$-f_{lp} curve
$\hat{\sigma}$	STD of filtered signal

$\hat{T}_z$	Zero-upcrossing period of the filtered vessel motion signal
$\hat{x}(t)$	Filtered time series of $x(t)$
ω	Wave or response frequency
ω_p	Spectral peak frequency, $\omega_P = 2\pi/T_p$
ϕ_m	The m^{th} VCRP variable in the vector $\boldsymbol{\phi}$, $m \in \{1, 2, ..., M\}$
ψ	RAO phase angle between vessel response and wave elevation
σ	STD of a random variable
σ^2	Variance
θ	Normalized slopes of the $\hat{\sigma}_X$-f_{lp} curve
θ_n	The n^{th} variable in the vector $\boldsymbol{\theta}$
φ	Random phase angle between wave components
ζ	Wave elevation
A^*	True value of A. A can be H_s, T_p, β_W, $x(t)$, n_s, $H(\omega, \beta_W)$, $S(\omega, \beta_W)$, f_{lp}, etc.
B	Vessel breadth
$B_{a,dd}$	Linearized additional damping for mode d
$B_{cr,dd}$	Critical damping for mode d
D	Vessel draft
d	Index of vessel rigid body modes. $d = 1$: surge, $d = 2$: sway, $d = 3$: heave, $d = 4$: roll, $d = 5$: pitch, $d = 6$: yaw
f^*_{lp}	Optimal lowpass filter cutoff frequency
f_{lp,i^*}	Estimated optimal cutoff frequency among the discrete frequencies

f_{lp}	Lowpass filter cutoff frequency [Hz]
$H(\omega, \beta_W)$	Vessel motion RAO
H_s	Significant wave height
J	Total number of sensors
j	Sensor ID, the j^{th} sensor, representing different quantities (displacement, velocity, acceleration) and locations
k	Index of updating times
l	Length-scale of GPR model
L_{PP}	Length between perpendiculars
M	Number of considered variables for tuning, i.e., dimension of $\boldsymbol{\phi}$
m_n	nth order spectral moment
n_s	Spreading parameter for short-crested waves
N_t	Number of discrete time steps
N_{β_W}	Number of discrete wave directions
N_ω	Number of discrete frequencies
N_θ	Number of considered variables in $\boldsymbol{\theta}$
r_{dd}	Radius of gyration for vessel motion in mode d, $d = 4, 5, 6$
$S(\omega, \beta_W)$	Single-sided spectrum
T_p	Spectral peak period
T_z	zero-upcrossing period
u	Vessel forward speed
X	Vessel response

$X(\omega)$	Vessel response in the frequency domain
$x(t)$	Vessel response in the time domain
GML	Free surface correction to the longitudinal metacentric height
GMT	Free surface correction to the transverse metacentric height
PDF	Probability density function
PMF	Probability mass function
PSD	Power spectral density
WD	Water depth
XCG	Longitudinal coordinate of vessel COG
YCG	Transverse coordinate of vessel COG
ZCG	Vertical coordinate of vessel COG

Symbols for algorithm based on discrete Bayesian inference

α	Sensor screening ratio (SSR)
$\boldsymbol{\phi}_r$	The r^{th} point of the discrete distribution of $\boldsymbol{\phi}$, $r \in [1, R]$
$\boldsymbol{\theta}_s$	The s^{th} point of the discrete distribution of $\boldsymbol{\theta}$, $s \in [1, S]$
$\overline{\overline{W}}$	Weight matrix (likelihood function)
ϕ_{im}	The im^{th} discrete value of the vessel parameter ϕ_m in the RAO database
Im	Number of discrete values of ϕ_m used for the RAO database
im	Index of the discrete value of ϕ_m
p	Power parameter

R	Number of possible vessel parameter combinations to build the RAO database, $R = \prod_{m=1}^{M}(Im)$
S	Number of points over the discrete joint probability distribution of $\boldsymbol{\theta}$
w	Weight factor calculated by inverse distance weighting

Symbols for algorithm based on unscented Kalman filter

$\%\Delta\sigma_A^2$	Variance reduction for parameter A due to tuning. A can be H_s, T_p, β_W, etc.
α	Scaling factor for the UKF model
β	Hyperparameter in the UKF model to partially account for higher-order statistical properties
$\bar{\boldsymbol{P}}_k$	State covariance matrix for $\bar{\boldsymbol{x}}_k$
$\bar{\boldsymbol{x}}_k$	Predicted system state for the k^{th} update after system propagation
$\boldsymbol{\mathcal{X}}_{k,i}^{\boldsymbol{\phi}}$	The vessel state for the sigma point $\boldsymbol{\mathcal{X}}_{k,i}$
$\boldsymbol{\mathcal{X}}_{k,i}^{\boldsymbol{\theta}}$	Sea state for the sigma point $\boldsymbol{\mathcal{X}}_{k,i}$
$\boldsymbol{\mathcal{X}}_{k,i}$	The i^{th} sigma point for the system state $\boldsymbol{x}_k$, i.e., the i^{th} column of $\boldsymbol{\mathcal{X}}_k$
$\boldsymbol{\mathcal{X}}_k$	Sigma points for the system state $\boldsymbol{x}_k$
$\boldsymbol{\mathcal{Z}}_k$	Predicted measurement vector estimated based on all sigma points $\boldsymbol{\mathcal{X}}_k$ for the k^{th} update
$\boldsymbol{\theta}_k^{'}$	The acquired sea state information for the k^{th} update
$\boldsymbol{K}$	Kalman gain
$\boldsymbol{P}_k^w$	Covariance matrix for $\boldsymbol{x}_k^w$
$\boldsymbol{P}_{\boldsymbol{\theta}_k}^{'}$	The prior uncertainty of $\boldsymbol{\theta}_k^{'}$

$\boldsymbol{P}_k$	System state covariance matrix for $\boldsymbol{x}_k$
$\boldsymbol{P}_{\boldsymbol{\phi}_k}$	Covariance matrix for $\boldsymbol{\phi}_k$
$\boldsymbol{P}_{\boldsymbol{\theta}_k}$	Covariance matrix for $\boldsymbol{\theta}_k$
$\boldsymbol{P}_{\boldsymbol{x}\boldsymbol{z}_k}$	Cross covariance matrix for the system state in state space and measurement space at the k^{th} measurement update step
$\boldsymbol{P}_{\boldsymbol{z}_k}$	Covariance matrix for the system state in measurement space at the k^{th} measurement update step
$\boldsymbol{Q}$	Process uncertainty covariance matrix
$\boldsymbol{R}$	Measurement uncertainty covariance matrix
$\boldsymbol{v}$	Process disturbance
$\boldsymbol{x}_k^w$	The system state after the weather update step for the k^{th} sea state
$\boldsymbol{x}_k$	System state after the k^{th} update
$\boldsymbol{y}_k$	Residual at the k^{th} measurement update step
$\boldsymbol{Z}_{k,i}$	Predicted measurement vector at $\boldsymbol{\mathcal{X}}_{k,i}$
$\boldsymbol{z}_k$	Observed measurement vector containing the measured response characteristics at the k^{th} update step
$\Delta\hat{A}$	Error between the true and tuned values for parameter A. A can be H_s, T_p, β_W, etc.
$\Delta\overline{A}$	Error between the true and acquired values for parameter A. A can be H_s, T_p, β_W, etc.
$\hat{\sigma}_A$	STD of the tuned parameter A. A can be H_s, T_p, β_W, etc.
$\hat{A}$	Tuned value of parameter A. A can be H_s, T_p, β_W, etc.
κ	Hyperparameter in the UKF model
$\overline{\sigma}_A$	STD of the acquired parameter A. A can be H_s, T_p, β_W, etc.

$\overline{A}$	Acquired value of parameter A. A can be H_s, T_p, β_W, etc.
G	Total number of considered measured response characteristics in the measurement space for one sea state
g	Index of the considered measured response characteristics in measurement space
N	Dimension of the system state
w^c	Weight factor for state mean calculation
w^m	Weight factor for state covariance calculation
z_g	The considered g^{th} quantity from measurements in the measurement space

Chapter 1

Introduction

1.1 Background and motivation

Motion prediction is essential for the design and execution of marine operations involving floating structures such as vessels [1, 2]. Before execution, marine operations are usually designed onshore based on technical specifications and rules [1] so that operational limiting criteria are determined. Compared with second-order difference-frequency motions, which could be well controlled and compensated by mooring and dynamic positioning (DP) systems, the wave-induced motions within wave frequencies (i.e., first-order motions) are more challenging to control due to their high-frequency dynamics. Marine operations can usually be executed during moderate seas, where the first-order wave-induced vessel motions can be estimated with sufficient accuracy by the linearized modeling of vessel dynamics in the frequency domain [1, 3, 4]. Such vessel dynamics as a rigid body are represented by linear transfer functions describing the relations between wave elevation and rigid body motions in 6 degrees of freedom (DOFs). These complex-valued linear transfer functions, also known as response amplitude operators (RAOs), can be calculated by seakeeping simulations based on 3D panel methods [5] or 2D strip theory [6].

In many cases, these first-order wave-induced motions play an important role in determining the operational limiting criteria with respect to environmental conditions [1, 7, 8]. Improving prediction accuracy of the first-order wave-induced vessel motions can potentially lead to a broader operational weather window and increase operational safety and cost efficiency.

Many pure data-driven algorithms for very short-term vessel motion prediction

(e.g., less than 1 minute) have been proposed in the literature in recent years [9, 10, 11, 12, 13, 14, 15]. These algorithms did not consider wave conditions as inputs and can be grouped as time series extrapolation. A series of competitions with respect to general time series extrapolation initiated by Makridakis et al. [16, 17, 18, 19] indicated that simple statistical-based methods (e.g., exponential smoothing) and their equivalent algorithms (e.g., the theta model [20, 21]) can usually outperform other methods based on the application of sophisticated statistical approaches or machine learning. However, all of these pure data-driven methods face difficulty in being practically accepted for safety-critical applications in the energy and maritime industries due to a lack of physical reasoning and documented reliability. In addition, most of these methods can be too computationally expensive for on-site vessel motion predictions in real time with online model training. In the present thesis, "real time" means a sufficiently short time frame within which the assessment must be completed so that the users (operators) can have sufficient time to take necessary actions.

The present thesis focuses on vessel motion predictions that explicitly consider waves and vessel mechanical dynamics as inputs. The prediction accuracy can be improved by 1) modifying the theories with respect to wave-vessel hydrodynamics; 2) reducing on-site wave forecast uncertainties; and 3) improving the knowledge about on-site real-time vessel conditions.

The applications of very high fidelity hydrodynamic models help reducing uncertainties in vessel seakeeping simulations by including nonlinear effects in terms of wave kinematics [22, 23, 24] and vessel hydrodynamics [24, 25, 26, 27, 28, 29, 30]. Furthermore, in the case of safety-critical operations with small operational windows determined by regular seakeeping simulations, computational fluid dynamics (CFD) were applied in [31, 32] to reduce uncertainty and conservatism. However, such seakeeping simulations with high fidelity models are highly computationally demanding and cannot be used for on-site real-time applications.

Instead of putting excessive efforts into improving the seakeeping modeling accuracy with very high fidelity models, many researchers have focused on reducing on-site wave forecast uncertainties to improve vessel motion prediction in real time. Except for the continuous development of third-generation wave models (e.g., WAM [33, 34] and WaveWatch III [35]) to improve the reliability of conventional wave forecast hours and days ahead, many algorithms have been proposed by applying classic or advanced instruments to estimate and forecast wave conditions encountered at the vessel within a short-term time horizon (in magnitudes of seconds up to a few hours). Many onboard decision support systems (ODSSs) have been correspondingly developed. Examples include: 1) The SeaSense [36] was developed based on sea state estimation by the "ship as a wave

buoy" analogy [37, 38, 39, 40, 41, 42] and sea state forecast by extrapolation; 2) The CASH system [43] and the ODSSs in the OWME project (Onboard Wave and Motion Estimator) [44, 45, 46] were developed based on spatiotemporal wave estimation in front of the vessel through onboard noncoherent nautical radar systems [47, 48, 49, 50, 51] and forecasting of encountered waves at the vessel [52]; 3) Similarly, the ODSSs in the ESMF project (Environment and Ship Motion Forecasting) were developed based on estimation of the wave field and prediction of the encountered waves through advanced coherent Doppler marine radar systems [53, 54, 55]; 4) In addition, Chan et al. [56] demonstrated that the well-known alpha factor [1] representing wave forecast uncertainties may be modified locally based on wave measurements near the operating site before the operation starts.

The aforementioned ODSSs mostly predict vessel motions based on predetermined RAOs for real-time purposes based on the presumed vessel condition (named the vessel state). Determining a vessel's on-site loading condition is a challenge. It can shift quite often for some marine operations, such as in pipe laying and heavy lifting. Furthermore, the true on-site vessel state (e.g., related to inertia distribution) during the operation may significantly deviate from the one specified and applied at the design phase. These deviations can be caused by mutual misunderstanding, misinterpretation, engineering defects, and unplanned arrangements due to emergent or urgent issues. These inherited uncertainties render the usage of very high fidelity models less valuable at the design phase. In practice, conservative assumptions about the vessel state during these operations are used in simulations. The motion prediction accuracy is significantly influenced by the uncertainties of the vessel loading condition and consequently applied RAOs [2, 57, 58]. The aforementioned onboard wave estimation algorithms based on the "ship as a wave buoy" analogy and noncoherent nautical radar are also influenced by uncertainties of vessel motion estimation and hence vessel loading conditions (e.g., [47, 50, 59]).

It is therefore important for safe and cost-efficient marine operations to improve the accuracy of RAOs reflecting the true vessel dynamics on board. With so many vessel data from onboard systems and with the corresponding synchronous historical wave data, three main different research approaches on improving the accuracy of RAOs have been considered, i.e.,

1) direct estimation or optimization of the RAOs;

2) estimation of the hydrodynamic coefficients which determine the RAOs (i.e., added mass, damping, and stiffness coefficients);

3) estimation of the important parameters representing the vessel state which determine the hydrodynamic coefficients and the consequent RAOs.

Direct calculation of RAOs based on measurements of vessel motions and waves represents the inverted problem of vessel motion estimation (also referred to as system identification), which typically has no unique solution, especially when considering wave spreading in real applications. RAOs are direction and frequency dependent, containing both amplitude and phase information. Solving such an inversion problem will have to face highly ill-conditioned equations due to significantly more unknown parameters than the number of available equations. Alford et al. [60] tried to solve the ill-conditioned equation system by applying the singular value decomposition (SVD) technique. Consequently, the directional dependency of the dynamic system disappears, and the calculated transfer functions are also sea state dependent. Recently, Nielsen et al. [61] proposed an optimization algorithm for a direct tuning of RAOs based on vessel response measurements and ERA5 2D wave spectra. This algorithm, however, is only able to tune RAOs at the observed wave directions and frequencies without quantifying the tuning uncertainties.

Studies have also been conducted on estimating hydrodynamic coefficients for DP [62, 63] and maneuvering [64, 65] systems based on relevant vessel data, where the wave-induced response is simply considered as a disturbance. Focusing on first-order wave-induced motions, Ren et al. [66] proposed an algorithm to estimate hydrodynamic coefficients based on vessel motion measurements, assuming constant added mass and damping coefficients for a given sea state. However, the algorithm cannot estimate these coefficients for unobserved frequencies and directions.

To improve vessel motion prediction for unobserved wave conditions, the RAOs and the relevant hydrodynamic coefficients must be estimated or updated for all directions and frequencies based on a very limited number of available observations. Therefore, it is more rational to tune the important input parameters of the numerical seakeeping model (e.g., COG, inertia terms, etc.) according to available wave and vessel data. The resulting modified seakeeping model can be used to recalculate the vessel motion RAOs for motion predictions. Such parameters representing the vessel state are usually constant for a vessel loading condition that can be stationary for a relatively long time (in terms of hours or days). Therefore, reliable motion prediction with increased accuracy can be achieved as long as the assumption of stationarity holds. Kaasen et al. [67] proposed a procedure for automatic tuning of a seakeeping simulation model based on output error minimization, which was tested by applying model test data, using precise measurement data and assuming the applied seakeeping theory to be accurate.

The vessel state can be represented by a set of variables (system states) which can either be measured or unmeasurable. Those can be measured are referred to as vessel measured states (VMSs) while those unmeasurable variables are referred to

as vessel condition-related parameters (VCRPs). VMSs consist of system states such as vessel speed, heading, draft, trim, heel, and rigid body motions measured by the inertial navigation system, speed and distance log device, and global positioning system, etc. VCRPs include damping terms and inertia distribution related terms such as mass and radii of gyration (i.e., r_{44}, r_{55}, r_{66}), center of gravity (COG), and transverse metacentric height, which are usually subject to significant uncertainties since they cannot be measured or since they are difficult to determine from available measurements. In the thesis, the terminology *vessel state* is used in equivalence to VCRPs without further explanation.

For real applications, it is essential to consider the uncertainties of wave information and vessel motion measurements when tuning the important vessel seakeeping parameters. The acquired on-site wave information, in the form of wave elevation time series, 2D wave spectrum [68] or its characteristics (e.g., significant wave height H_s, wave spectral peak period T_p, direction β_W, etc.), is always subject to uncertainties due to its random nature as well as systematic and measurement errors. Wave forecast uncertainties, mostly in terms of ensemble spreading [69, 70], significantly influence the accuracy of critical response prediction and hence the efficiency of marine operations [71, 72, 73]. Wave data from hindcast and measurements [74] are preferred for seakeeping model tuning due to an inherently smaller uncertainty than that associated with forecasts. Hindcast accuracy depends on geographical location, season, and uncertainties of the wind data and wave analysis model used, whereas the measured wave data accuracy may depend on the type and installation of instruments, sensor quality, sampling, and temporal and spatial variability [75, 76, 77]. Furthermore, the accuracy of wave information can be improved by combining wave hindcasts with possibly available data from satellites and in situ wave buoys [71]. Similarly, measurements of VMSs can never be exact [78]. In addition, vessel response measurements are influenced by other environmental loads, such as currents and winds, which are also subject to high uncertainties (e.g., [79]).

It is therefore of significant academic and industrial interest to take advantage of the available on-site vessel and wave data in combination with widely acknowledged theoretical models associated with seakeeping to improve knowledge about onboard vessel conditions (i.e., VCRPs), also accounting for the uncertainties associated with the various input parameters in a quantitative manner. This is considered to be the main research objective of the PhD project. Tuning of VCRPs and updating their uncertainties based on available vessel and wave data will be the main contributions of this PhD research work. Actively improving the knowledge about onboard vessel conditions is important in relation to the concepts of digital twins and autonomous ships. Furthermore, quantitative uncertainty estima-

tion of tuned VCRPs can be even more attractive and promising for many advanced applications, such as probabilistic digital twins [80] and reliability-based marine operations [81].

1.2 Objectives

This work was funded by the Research Council of Norway through the Centre for Research-based Innovation MOVE, NFR project number 237929 and the consortium partners, http://www.ntnu.edu/move. The PhD project belongs to Project 6 - Onboard decision tool. The main objectives of the PhD project are as follows:

1. Develop a seakeeping model tuning algorithm by using collected measurement data of vessel motions and environmental information, considering the relevant embedded uncertainties.
2. Modify the important vessel parameters based on on-site data for a limited number of sea states, in order to improve the accuracy of the calculated linear transfer functions across the whole range of wave frequencies and directions, particularly at critical frequencies (e.g., around resonance) that may not have been observed.
3. Contribute to the conceptual development of digital twins, marine operations, and onboard decision support systems based on probabilistic, reliability, or risk assessments. The developed algorithm should preferably be able to quantitatively estimate and update the uncertainties of the tuned vessel seakeeping model parameters.
4. The algorithm should be feasible for real applications, 1) capable of dealing with multiple vessel parameters (preferably large dimensional) simultaneously, and 2) requiring small computational costs in relation to online tuning.
5. The algorithm should be robust, stable, reliable, and supported by physical reasoning.

The project is limited to tuning physically representative seakeeping models with respect to the first-order wave-induced vessel motions. The following research questions will be answered in the thesis:

Q1. Which parameters are influential to the system dynamics and vessel motions and therefore important to include in the tuning process?

Q2. How can those parameters be tuned?

Q3. How can measurements be used?

Q4. How should the uncertainties associated with environmental conditions, the numerical vessel hydrodynamic model, and the measurement data be represented, quantified, and considered through the tuning process, such that the uncertainties of the tuned parameters can be estimated?

Q5. How can such a tuning algorithm be applied to relevant applications?

1.3 Thesis Scope and Organization

The thesis is written in the form of a collection of five journal papers and two conference papers, which are given in the List of Publications, referred to as Papers A1 to A7, and provided in Appendix A. Figure 1.1 illustrates the relations among the appended papers and how they are related to the research questions raised in Section 1.2 for the PhD project. The frame with dotted lines and a heading "Algorithm modifications" indicates that all those three papers (i.e., Papers A3 to A5) in the frame are contributed by modifying the tuning algorithm proposed in Paper A2.

This thesis is composed of 5 chapters. The content of each chapter is briefly described below.

Chapter 1 introduces the project background, motivation, and objectives as well as the thesis structure.

Chapter 2 provides the basis of the case studies that were used in the research, including the models and data available for the two vessels used (i.e., Vessel A and Vessel B) and the procedure of generating synthetic noisy measurement data. In addition, key findings in Paper A1 on identifying the important vessel parameters for vessel motion estimations are also summarized in Chapter 2.

Chapter 3 introduces the concept of tuning seakeeping model parameters based on discrete Bayesian inference (DBI). The overview of Chapter 3 is supplemented by detailed scientific presentation of this DBI-based tuning algorithm proposed in Paper A2, its modifications with respect to optimizing signal noise filtering (Paper A3), tuning and predicting the sea state dependent VCRPs (Paper A4), and accounting for wave data uncertainties (Paper A5). Chapter 3 also describes an application of such DBI-based tuning algorithm in an ODSS that is able to optimize marine operations based on quantitative risk assessment accounting for the estimated vessel state uncertainties (Paper A5).

Chapter 4 investigates seakeeping model tuning by Kalman type of nonlinear filters to increase the computational efficiency compared with the DBI-based tuning. The

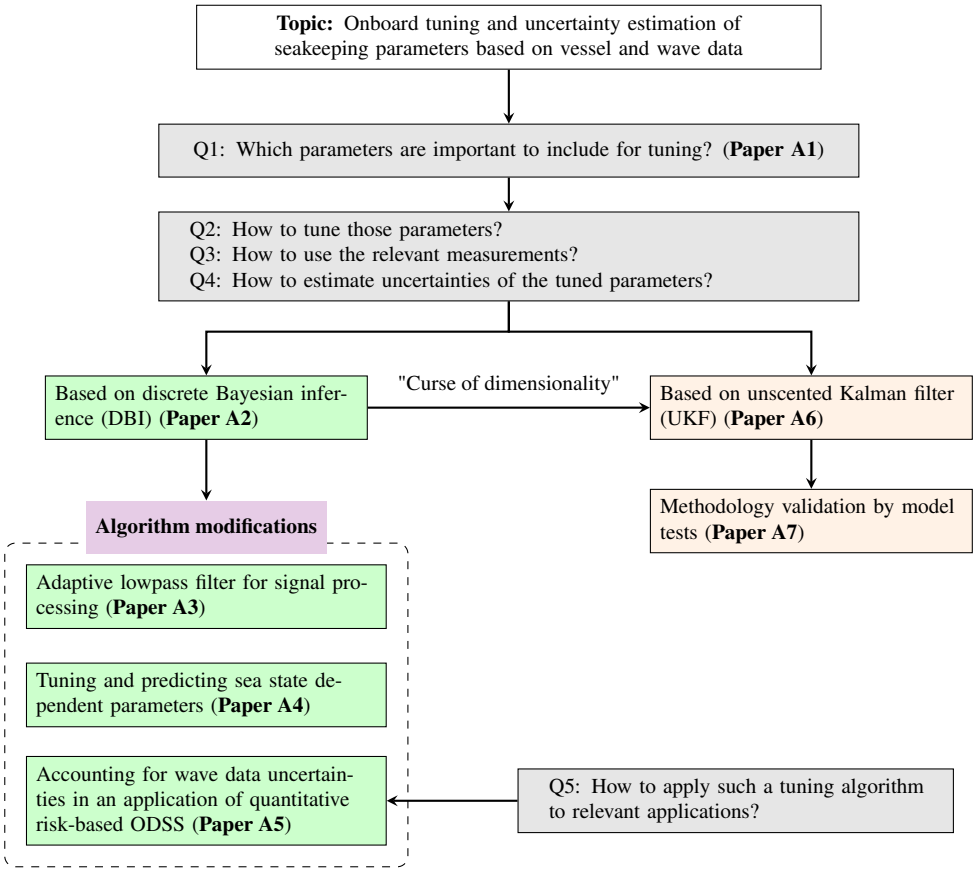

Figure 1.1: Relations among appended papers in response to the five research questions in Section 1.2. Blocks in gray represent the research questions, blocks in green represent the papers in relation to the development of the DBI-based algorithm, and blocks in light orange represent the papers related to the UKF-based algorithm.

overview of Chapter 4 is supported by Papers A6 and A7, where a new tuning algorithm based on the unscented Kalman filter (UKF) [82] was developed in Paper A6 and validated by seakeeping model tests in Paper A7.

Chapter 5 concludes the present thesis work, summarizes the contributions with respect to answering the research questions specified in Section 1.2, and points out related important future work.

Chapter 2

Basis of case studies

Based on the scope and objectives of the present PhD project described in Chapter 1, research has been conducted through various case studies to answer the aforementioned research questions and develop, implement, modify, demonstrate, and validate tuning algorithms.

Numerical seakeeping models for two vessels are used in this research, i.e., Vessel A and Vessel B. Vessel A is used for the research documented in Papers A1 to A4 and Paper A6, while Vessel B together with its associated model tests are used in Paper A7. The tuning algorithms were original and therefore should be first tested by numerical case studies where both inputs and outputs can be fully controlled. Noisy signals were simulated and used in case studies involving the Vessel A model. Measurements from Vessel B seakeeping tests at the model scale were used in Paper A7 for methodology validation purposes.

Therefore, several papers share the same case study basis in terms of the applied vessel and numerical simulation process. This chapter hence summarizes the basis of case studies, including information about the two vessels used, their numerical seakeeping models, the process of synthetic signal generation, the model test setup, etc. This chapter forms the input basis of the demonstrated case studies to be described in Chapters 3 and 4.

2.1 Vessel A

2.1.1 Basis

Vessel A is a typical offshore supply vessel. Its primary dimensions are summarized in Table 2.1. The reference coordinate system of Vessel A, as illustrated in

Figure 2.1, is defined as moving steadily at the vessel forward speed. The origin is at the keel elevation of the stern within the longitudinal symmetric plane. The positive X-axis points towards the bow, the positive Y-axis points towards the port, and the positive Z-axis points vertically upwards. In all case studies using Vessel A, the wave direction β_W follows the going-to convention, as also illustrated in Figure 2.1, i.e., $\beta_W = 0°$ corresponding to a following sea condition.

Table 2.1: Main dimensions of Vessel A

Parameters	**Description**	**Value**	**Unit**
L_{PP}	Length between perpendiculars	∼120	m
B	Breadth	∼27	m
D (Ballast)	Draft	∼5.1	m
D (Full)	Draft	∼6.8	m

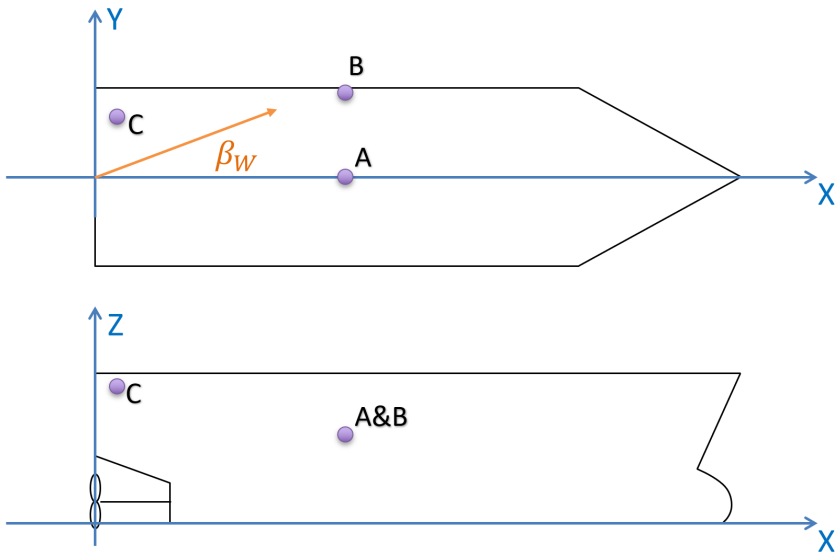

Figure 2.1: Illustration of the coordinate system and locations of considered interesting points for Vessel A.

The numerical seakeeping model of Vessel A was provided by DNV, with quality control for commercial application purposes. Seakeeping analyses were performed by 3D time-domain software Wasim [83] based on the Rankine panel method [5].

2.1.2 Important uncertain vessel parameters

Hundreds of vessel parameters can influence seakeeping performance (i.e., the wave-induced vessel rigid body motions). It is therefore important to find and document the most sensitive parameters to limit the research scope. Therefore, a sensitivity study of hydrodynamic model parameters based on Vessel A was carried out, as documented in Paper A1 [84].

The parametric sensitivities were first compared by visual inspection of RAOs and then further detailed by quantitative assessment. Ballast and fully loaded conditions at infinite water depth were selected as the base cases. All 6 DOF vessel motions except yaw were investigated. The studied parameters and their considered uncertainty ranges are summarized in Table 2.2, where WD is the water depth, u is the vessel forward speed, and XCG, YCG, and ZCG represent the coordinates of COG in the X-, Y-, and Z-axes. r_{dd} represents the radius of gyration for rotational rigid-body mode $d \in 4, 5, 6$. There are 6 rigid-body response modes, i.e., $d = 1, 2, 3, 4, 5, 6$ corresponding to surge, sway, heave, roll, pitch, and yaw, respectively. GMT and GML represent the metacentric height corrections due to the free surface effect in the transverse and longitudinal directions, respectively. β_{dd} represents the ratio of the linearized additional damping (e.g., due to viscous effects) and the critical damping $B_{cr,dd}$ for the motion mode d.

$$\beta_{dd} = \frac{B_{a,dd}}{B_{cr,dd}} \times 100\ [\%] \tag{2.1a}$$

$$B_{cr,dd} = 2\sqrt{(M_{dd} + A_{dd}(\infty))C_{dd}} \tag{2.1b}$$

where M_{dd}, A_{dd}, and C_{dd} are the inertia, added mass, and restoring stiffness for the dth DOF, respectively. The vessel added mass is frequency dependent. For simplicity, a constant value of A_{dd} at infinite frequency $\omega \to \infty$ is considered in Equation (2.1b). $B_{a,dd}$ is the linearized additional damping, and $B_{cr,dd}$ is the critical damping for the dth DOF.

Their effects on the resulting vessel motion RAOs were explained in detail in Paper A1 [84]. The selection of the uncertainty ranges was purely based on engineering judgment after consulting seakeeping experts. Note that WD and u are very important parameters for seakeeping assessment, but due to the relevant available monitoring systems, the consequent variation of vessel response estimation caused by measurement uncertainties of WD and u are very limited and therefore not included in the quantitative comparison.

Quantitative parametric sensitivity studies were carried out in the frequency domain to compare the 90-percentile extreme values of heave velocity at three interesting locations onboard for extensive wave conditions by varying zero-upcrossing

Table 2.2: Parameters considered in sensitivity studies for Vessel A.

Parameter	Uncertainty range - RAO visual inspection	Uncertainty range - quantitative comparison
WD	20 - 2000 m	N/A
u	0 - 20 knots	N/A
XCG	± 4 m	± 4 m
YCG	± 1 m	± 1 m
ZCG	± 1 m	± 1 m
Mass	± 10 %	± 10 %
r_{44}	$\pm 10\%$	$\pm 10\%$
r_{55}	$\pm 10\%$	$\pm 10\%$
r_{66}	$\pm 10\%$	$\pm 10\%$
GMT	± 1.5 m	± 0.5 m
GML	± 10 m	N/A
β_{11}	$0 - 16$ %	N/A
β_{22}	$0 - 16$ %	N/A
β_{33}	$0 - 16$ %	$2 - 14\%$
β_{44}	$2 - 16$ %	$2 - 14\%$
β_{55}	$0 - 16$ %	N/A

period T_z and β_W, with unit H_s, assuming long-crested Pierson Moskowitz (PM) wave spectra. Base cases of ballast and fully loaded conditions at 10 knots and infinite water depth were considered. Each considered vessel parameter is denoted by ϕ_m, where $m \in \{1, 2, \ldots, M\}$ and M is the total number of studied vessel parameters. Each variable ϕ_m was evenly discretized within the specified uncertainty range in Table 2.2, and each discrete value is denoted by ϕ_{im}, where $im \in \{1, 2, \ldots, Im\}$ and Im is the total number of discrete values for ϕ_m. The 90-percentile heave velocity at a specific location due to varying one specific value of a considered vessel parameter ϕ_{im} for a specific sea state (SS) is denoted by $V_{P90}^{loc}(\phi_{im}|SS)$. The parametric sensitivity was compared with respect to the following criterion $Diff_V^{loc}(\phi_m|SS)$:

$$Diff_V^{loc}(\phi_m|SS) = \max V_{P90}^{loc}(\phi_m|SS) - \min V_{P90}^{loc}(\phi_m|SS) \tag{2.2}$$

where $\max V_{P90}^{loc}(\phi_m|SS)$ and $\min V_{P90}^{loc}(\phi_m|SS)$ are the max and min values of $V_{P90}^{loc}(\phi_{im}|SS)$ within the uncertainty range of ϕ_m.

The sensitivity studies were carried out by varying only one parameter at each time around the predefined two base cases. Therefore, this does not strictly investigate the global parametric sensitivities for all the parameters within their uncertainty

ranges [85]. In addition, $Diff_V^{loc}(\phi_m|SS)$ does not capture the local sensitivity of a parameter near ϕ_{im}. The scope may be modified to vary all the considered vessel parameters simultaneously to investigate their global sensitivity to the extreme heave velocity and to more accurately capture the local sensitivity by replacing the criterion as follows:

$$Diff_V^{loc}(\phi_{im}|SS) = \frac{|V_{P90}^{loc}(\phi_{im+1}|SS) - V_{P90}^{loc}(\phi_{im}|SS)|}{V_{P90}^{loc}(\phi_{im}|SS)} \tag{2.3}$$

However, Paper A1 applied the criterion $Diff_V^{loc}(\phi_m|SS)$ in Equation (2.2). The three considered locations are at the MRU location ($loc = MRU$), at the crane tip ($loc = tip$) for lift operations, and at the stern ($loc = pip$) for pipe laying operations. The most important parameters were summarized, as shown in Table 2.3, and their relative importance is illustrated by jittered polar plots (e.g., Figure 2.2) in Paper A1 [84]. One of the key conclusions is that the importance of vessel parameters varies with T_z, β_W, location, and quantity of the interesting vessel response, vessel state, and considered parametric uncertainty range. Note that mass was also found to be important for the heave response at the pip and tip locations, as mentioned in Paper A1.

Table 2.3: Important vessel parameters for first-order wave-induced motions

$\boldsymbol{\beta_W}$	$\boldsymbol{loc = MRU}$	$\boldsymbol{loc = tip}$	$\boldsymbol{loc = pip}$
90°	β_{33}, XCG	β_{33}, β_{44}, YCG, GMT	β_{33}
120°	β_{33}, XCG	β_{33}, β_{44}, XCG, YCG, GMT	r_{55}, XCG
150°	β_{33}, XCG	β_{33}, XCG, YCG	r_{55}, XCG
180°	β_{33}, XCG	β_{33}, XCG, YCG	r_{55}, XCG

In addition, Paper A1 [84] also conducted an initial study on identifying and tuning important vessel parameters assuming precise motion measurements and wave information, with only one vessel parameter to be tuned. The key findings are that

1. the tuning of vessel parameters is a nonlinear problem with respect to the relationship between the vessel parameters and the interesting vessel response quantities;
2. the tuning of vessel parameters is a multimodal problem, meaning that usually there is no unique solution;
3. it can be helpful to consider multiple measurement quantities (e.g., different DOFs, locations, and signal derivatives) for correct tuning results;

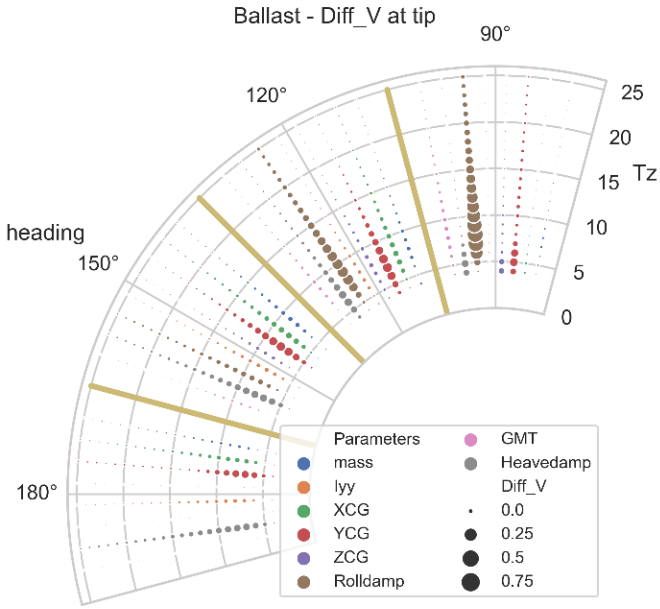

Figure 2.2: Jittered polar plots of $Diff_V^{tip}(\phi_m|SS)$ around ballast condition of Vessel A, for $\beta_W = 90°, 120°, 150°, 180°$, $T_z \in [4, 25]$ s.

4. it is important to simultaneously tune all the important parameters; consequently, such tuning is a multidimensional problem.

2.1.3 RAO database

Inspired by the findings from Paper A1, it is strongly believed that a mindset of identifying the correct RAO set within an RAO database limited by predefined uncertainty ranges of the important vessel parameters could be the key to solving the seakeeping model tuning problem with nonlinear, multimodal, and multidimensional characteristics. Heave responses at various locations on board can be critical for typical marine operations (e.g., lifting) and therefore are focused on for algorithm development (Papers A2, A3, A4, and A6). Based on the aforementioned findings from Paper A1 [84], an RAO database was established considering five important uncertain vessel parameters at the combinations of their discrete values around the ballast condition, i.e.,

$$\begin{aligned} \boldsymbol{\phi} &= [\phi_1 \quad \phi_2 \quad \dots \quad \phi_5]^\top \\ &= [\text{mass} \quad \text{XCG} \quad r_{55} \quad \text{GMT} \quad \beta_{44}]^\top \end{aligned} \tag{2.4}$$

The considered uncertainty ranges and the number of their discretized values (i.e., Im) are summarized in Table 2.4, which can practically be determined based on useful prior information (e.g., available project reports, accuracy of onboard monitoring data, and engineering judgment). In real applications, such an RAO database should ensure sufficiently large parametric uncertainty ranges to cover all possibilities, while the spacing between the discrete values should be sufficiently small to capture any potentially critical nonlinear behavior. RAOs representing the heave displacements, velocities, and accelerations at three locations (i.e., A, B, and C) on board are included in the RAO database, as summarized in Table 2.5 and illustrated in Figure 2.1. Zero forward speed was considered for the RAO database and the case studies of tuning to avoid dealing with the 3-to-1 mapping problem between the absolute and encountered wave frequencies at following sea conditions [86]. Seakeeping simulations by Wasim were extensively carried out to establish this RAO database. In total, 24 wave headings between 0° and 330° with 15° interval were included in the database.

Table 2.4: Parametric range for the considered variables

ϕ_m	**Variation range**	Im
Mass	[-6%, +6%]	7
XCG	[-4 m, +4 m]	5
r_{55}	[-9%, +9%]	7
GMT*	[0, 1 m]	6
β_{44}	[2%, 14%]	7

* "GMT" represents the free surface correction to the transverse metacentric height. GMT= 0.5 m here means that the transverse metacentric height is corrected with -0.5 m due to free surface effects. This is not the value of the transverse metacentric height.

2.2 Vessel B

Vessel B and its associated seakeeping model tests (zero forward speed) were used for algorithm validation purposes, as documented in Paper A7 [87]. Vessel B is a state-of-the-art offshore construction vessel with one main work moonpool and two ROV moonpools and is approximately 150 m long. For convenience of reporting, a reference coordinate system was defined for Vessel B. The origin is at the baseline of the midship ($L_{pp}/2$) along the centerline. The positive X-axis points towards the bow, the positive Y-axis points towards the port, and the positive Z-axis

Table 2.5: Description of sensor measurements of Vessel A.

Sensor ID	Location	Coordinate (x,y,z) [m]	Signal / measurements
Disp_A	A	(60.0, 0.0, 10.0)	$\eta_3(t)$ at location A
Disp_B	B	(60.0, 13.0, 10.0)	$\eta_3(t)$ at location B
Disp_C	C	(0.0, 10.0, 14.0)	$\eta_3(t)$ at location C
Vel_A	A	(60.0, 0.0, 10.0)	$\dot{\eta}_3(t)$ at location A
Vel_B	B	(60.0, 13.0, 10.0)	$\dot{\eta}_3(t)$ at location B
Vel_C	C	(0.0, 10.0, 14.0)	$\dot{\eta}_3(t)$ at location C
Acc_A	A	(60.0, 0.0, 10.0)	$\ddot{\eta}_3(t)$ at location A
Acc_B	B	(60.0, 13.0, 10.0)	$\ddot{\eta}_3(t)$ at location B
Acc_C	C	(0.0, 10.0, 14.0)	$\ddot{\eta}_3(t)$ at location C

$\eta_3(t)$, $\dot{\eta}_3(t)$, $\ddot{\eta}_3(t)$: time series of heave displacement, velocity, and acceleration

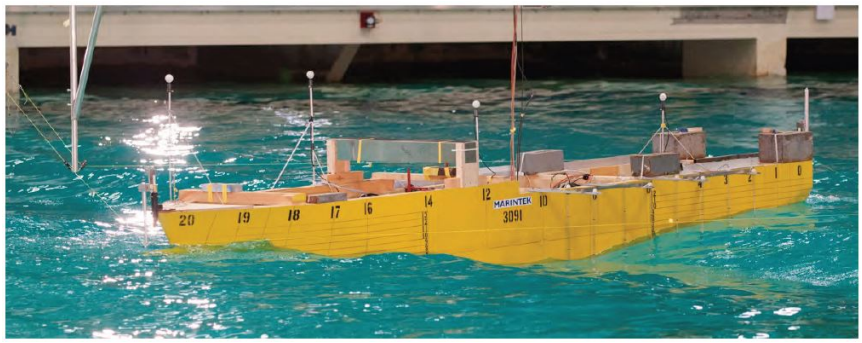

Figure 2.3: Illustration of the Vessel B seakeeping test.

points upwards vertically. β_W was defined following a coming-from convention for case studies of Vessel B. $\beta_W = 0°$ means a head sea condition.

The considered loading condition in the model tests (illustrated in Figure 2.3) corresponds to a displacement of approximately 20000 m^3, with all three moonpools open and roll reduction tanks deactivated. The model at test was weighed and balanced according to the specified loading condition, with high accuracy.

Model tests were performed with only long-crested irregular waves. The considered test cases are summarized in Table 2.6. Tests with narrowband JONSWAP wave spectra with $Tp = 8$ and 10 s and a peak enhancement factor of 3.3 were performed for all wave directions with an interval of 15°. In addition, a test with

a broadband rectangular wave spectrum ("RECT") was also conducted for each wave direction. Vessel motions in 6 DOFs and wave elevations were measured with high accuracy in the form of time series and transferred to full scale according to Froude scaling laws [88]. The details about the test setup, measurement instruments, measured quantities and locations are described in Paper A7 [87].

Table 2.6: Seakeeping model tests performed for irregular waves.

k	Test No.	Spectral type	H_s [m]	T_p [s]	β_W [°]
1	4000	JONSWAP	3	8	0
2	4010	JONSWAP	3	10	0
3	4020	JONSWAP	5	10	0
4	4030	RECT	3	5-16	0
5	4100	JONSWAP	3	8	15
6	4110	JONSWAP	3	10	15
7	4120	JONSWAP	5	10	15
8	4130	RECT	3	5-16	15
9	4200	JONSWAP	3	8	30
10	4210	JONSWAP	3	10	30
11	4220	RECT	3	5-16	30
12	4300	JONSWAP	3	8	45
13	4310	JONSWAP	3	10	45
14	4320	RECT	3	5-16	45
15	4401	JONSWAP	3	8	90
16	4410	JONSWAP	3	10	90
17	4420	RECT	3	5-16	90
18	4500	JONSWAP	3	8	150
19	4510	JONSWAP	3	10	150
20	4600	JONSWAP	3	8	165
21	4610	JONSWAP	3	10	165
22	4700	JONSWAP	3	8	180
23	4710	JONSWAP	3	10	180
24	4720	RECT	3	5-16	180

The corresponding numerical seakeeping model (illustrated in Figure 2.4) of Vessel B, as illustrated in Figure 2.4, was provided by SINTEF Ocean based on commercial seakeeping software ShipX (VERES module) [89]. VERES is based on 2D strip theory [6].

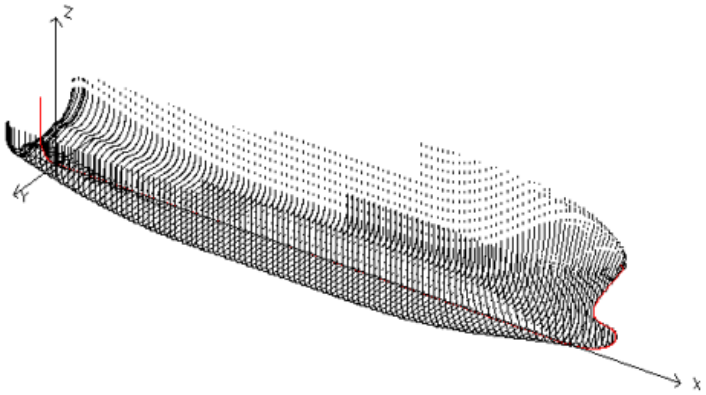

Figure 2.4: Screenshot of the Vessel B ShipX strip model.

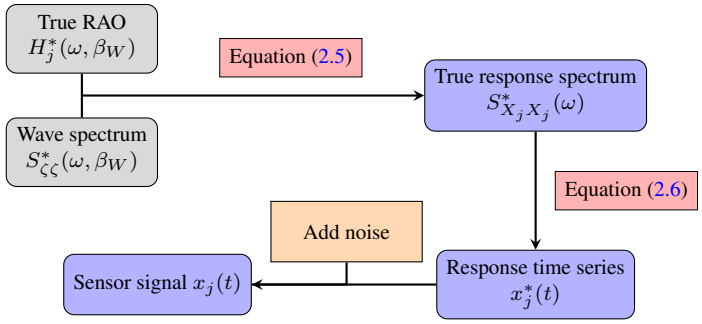

Figure 2.5: Process of generating virtual sensor signal $x_j(t)$ for the interesting response quantity indexed by j.

2.3 Generation and analysis of vessel motion signals

Initially, to better control the inputs and outputs of case studies and investigate algorithm performance, numerically simulated synthetic signals (also called virtual sensor signals) were extensively used in Papers A2, A3, A4, and A6. Figure 2.5 illustrates how the synthetic signal $x_j(t)$ is generated based on predefined true RAO ($H_j^*(\omega, \beta_W)$) corresponding to the predefined true combination of uncertain parameters $\boldsymbol{\phi}^* = [\phi_1^*, \phi_2^*, \ldots, \phi_M^*]^\top$, and the true wave spectrum $S^*_{\zeta\zeta}(\omega, \beta_W)$. ω is the wave or response frequency in rad/s. The synthetic signal $x_j(t)$ corresponds to a specific interesting response indexed by $j \in \{1, 2, \ldots, J\}$ (i.e., displacement, velocity, or acceleration of dth mode vessel motion at any specific location).

Assuming long-crested wave conditions, the true response spectrum for the inter-

esting response X_j, i.e., $S^*_{X_jX_j}(\omega)$, is calculated:

$$S^*_{X_jX_j}(\omega) = |H^*_j(\omega, \beta_W)|^2 S^*_{\zeta\zeta}(\omega, \beta_W) \tag{2.5}$$

The response X_j can be expressed as $X_j(\omega)$ in the frequency domain and $x_j(t)$ in the time domain.

Then a realization $x^*_j(t)$ can be generated by:

$$x^*_j(t) = \sum_{n=1}^{N_\omega} C_n(\omega_n) \cos(\omega_n t + \varphi_n + \psi_{j,n}) \tag{2.6a}$$

$$C_n(\omega_n) = \sqrt{2 S^*_{X_jX_j}(\omega_n) \cdot \Delta\omega_n} \tag{2.6b}$$

where N_ω is the total number of discrete frequencies, ω_n is the nth discrete frequency, and $\Delta\omega_n$ is its interval. $\Delta\omega_n$ is different for each ω_n so as to avoid time record repetition. $\varphi_n \in [0, 2\pi)$ is a random phase angle for the wave component at ω_n, which is considered to be continuously and uniformly distributed. $\psi_{j,n} \in [-\pi, \pi)$ is the phase angle between the vessel response and wave elevation at ω_n for response X_j, determined by $H^*_j(\omega, \beta_W)$. Note that Papers A2, A3, and A4 [90, 91, 92] implicitly considered the term $\psi_{j,n}$ in the process of virtual sensor signal generation, which to some degree lacks physical reasoning. However, this does not influence any tuning results because all the tuning was performed in the frequency domain by mainly considering the response standard deviations (STDs), which are not influenced by the relative phases $\psi_{j,n}$.

Afterwards, the synthetic signal $x_j(t)$ was generated by independently adding Gaussian distributed white noise to each time step of $x^*_j(t)$. The variance of white noise was specified by the signal-to-noise ratio (SNR), defined by

$$SNR = \frac{\sigma^2_{X_j}}{\sigma^2_N} \tag{2.7}$$

where $\sigma^2_{X_j}$ is the variance of $x^*_j(t)$ and σ^2_N is the noise variance.

Considering a 2D wave spectrum with directional spreading, $x^*_j(t)$ can be generated by [93]:

$$x^*_j(t) = \sum_{u=1}^{N_{\beta_W}} \sum_{v=1}^{N_\omega} C_{u,v} \cos(\omega_{u,v} t + \varphi_{u,v} + \psi_{j,u,v}) \tag{2.8a}$$

$$C_{u,v} = \sqrt{2 S^*_{X_jX_j}(\omega_{u,v}, \beta_{W_u}) \Delta\omega_{u,v} \Delta\beta_W} \tag{2.8b}$$

$$S^*_{X_jX_j}(\omega_{u,v},\beta_{W_u}) = |H^*_j(\omega_{u,v},\beta_{W_u})|^2 S_{\zeta\zeta}(\omega_{u,v},\beta_{W_u}) \tag{2.8c}$$

where β_{W_u} is the uth discrete wave direction, $\omega_{u,v}$ is the vth discrete frequency at β_{W_u}, and N_ω is the number of discrete frequencies for each wave direction. The subscript of $\omega_{u,v}$ means that the values of the discrete frequencies depend on the wave direction. In relevant simulations, 800 discrete frequencies ($N_\omega = 800$) were randomly generated for each β_{W_u}, assuming uniform distribution in the wave frequency region, in order to avoid nonergodic wave realizations [94]. $\Delta\beta_W$ is the interval of the discrete wave directions. Similar to φ_n and $\psi_{j,n}$ in Equation (2.6a), $\varphi_{u,v} \in [0, 2\pi)$ is the random phase angle for the wave component at $(\omega_{u,v}, \beta_{W_u})$, and $\psi_{j,u,v} \in [-\pi, \pi)$ is the phase angle of $H^*_j(\omega_{u,v}, \beta_{W_u})$. $S_{\zeta\zeta}(\omega_{u,v}, \beta_{W_u})$ is the 2D wave spectrum.

In addition, time series analysis was also widely applied in the research. Considering the noisy time series $x_j(t)$, a lowpass filter [95] was applied based on fast Fourier transform (FFT) [96] to remove the signal noise. The consequent filtered time series $\hat{x}_j(t)$ containing response within the wave frequency region were further used in the tuning process. For examples, the response STD can be calculated by

$$\hat{\sigma}_j = \sqrt{\frac{\sum_{t=1}^{N_t}(\hat{x}_j(t) - \bar{x}_j)^2}{(N_t - 1)}} \tag{2.9a}$$

$$\bar{x}_j = \frac{\sum_{t=1}^{N_t}\hat{x}_j(t)}{N_t} \tag{2.9b}$$

where N_t is the total number of time steps of $\hat{x}_j(t)$, and $\bar{x}_j$ is the filtered signal mean value.

An IMU measures directly the linear accelerations and rotational velocities of the vessel, with errors [97]. Sensor data fusion and filtering techniques are applied to prevent integration drift for a minimum variance estimate [98, 99, 100, 101]. In reality, the response quantities associated with the available signals vary from project to project. In many cases, only signals of the translational and angular displacements are available whereas information on the associated velocities and accelerations are also of high interest. For example, in the seakeeping model tests of Vessel B, only the angles were recorded for pitch mode while the pitch velocities and accelerations were also required for the case studies of tuning [87].

In order to obtain the derivative information about the available signals, it might be intuitive to apply numerical differentiation of the discrete signals. However, such numerical differentiation is well known to generate very high noise. Instead, the derivative information can be better obtained in the frequency domain from the estimated spectrum of the available response signals. For example, if characteristics

for the derivative of the measured time series $x_j(t)$ (denoted by $\dot{x}_j(t) = \frac{d\,x(t)}{d\,t}$) are wanted, such as the STD $\sigma_{\dot{X}_j}$ and zero-upcrossing period $T_{z(\dot{X}_j)}$, they can be calculated through the response spectrum of $x_j(t)$, i.e., $S_{X_jX_j}(\omega)$, which is obtained by FFT.

$$S_{\dot{X}_j\dot{X}_j}(\omega) = \omega^2 S_{X_jX_j}(\omega) \tag{2.10a}$$

$$m_0 = \sum_{\omega}^{\omega_1 \leq \omega \leq \omega_2} S_{\dot{X}_j\dot{X}_j}(\omega)\Delta\omega \tag{2.10b}$$

$$m_2 = \sum_{\omega}^{\omega_1 \leq \omega \leq \omega_2} \omega^2 S_{\dot{X}_j\dot{X}_j}(\omega)\Delta\omega \tag{2.10c}$$

$$\sigma_{\dot{X}_j} = \sqrt{m_0} \tag{2.10d}$$

$$T_{z(\dot{X}_j)} = 2\pi\sqrt{\frac{m_0}{m_2}} \tag{2.10e}$$

where m_0 and m_2 are the zeroth- and second-order moments of the response spectrum $S_{\dot{X}_j\dot{X}_j}(\omega)$, respectively, within the wave frequency range of interest $\omega_1 \leq \omega \leq \omega_2$. The summations in Equations (2.10b) and (2.10c) only include the frequencies of the considered sea state. Consequently, this calculation (in Equation (2.10)) of signal characteristics based on the raw measurements $x_j(t)$ in the frequency domain is equivalent to applying an FFT bandpass filter and thus avoids numerical noise due to numerical differentiation.

Chapter 3

Model Tuning by Discrete Bayesian Inference

3.1 Algorithm description

Revisiting the main research objectives described in Section 1.2, any tuning algorithm candidates should be capable to 1) tune seakeeping model parameters based on available observations and 2) update the uncertainties of those tuned parameters. These naturally lead to the intuition of applying Bayesian inference according to Bayes' theorem which derives the posterior probability of a hypothesis based on its prior probability and the likelihood [102]:

$$posterior = \frac{prior \cdot likelihood}{normalization} \tag{3.1}$$

where $likelihood$ is the probability of having such an observation with the given hypothesis. The hypothesis in the study is the values of the considered uncertain vessel parameters and the considered wave information being true, while the vessel motion measurements are considered as the observations.

With this intuitive thought, a seakeeping model tuning algorithm based on discrete Bayesian inference (DBI) [102] was first developed and proposed, which requires the preparation of an RAO database for all interesting vessel responses ($j = 1, 2, \ldots, J$) covering the whole uncertainty domain of the considered vessel parameters $\boldsymbol{\phi}$. As stated in Chapter 1, vessel data are categorized into VMSs and VCRPs. The measurement uncertainties of VMSs, such as draft, heading, and forward speed, are much less influential on the vessel RAOs and therefore considered deterministically in case studies (except that noise from motion signals is con-

sidered). In contrast, the uncertainties of VCRPs play critical roles in the resulting simulated RAOs.

The considered uncertain vessel parameters (VCRPs) can be formed as a random vector, denoted by $\boldsymbol{\phi}$, e.g.,

$$\begin{aligned}\boldsymbol{\phi} &= [\text{mass} \quad r_{44} \quad r_{55} \quad \text{XCG} \quad \text{ZCG} \quad \beta_{33} \quad \beta_{44} \quad \text{GMT} \ldots]^\top \\ &= [\phi_1 \quad \phi_2 \quad \ldots \quad \phi_m \quad \ldots \quad \phi_M]^\top\end{aligned} \tag{3.2}$$

The uncertainty domain of $\boldsymbol{\phi}$ is discretized into R points representing the considered possible combinations of those uncertain parameters, where $R = \prod_{m=1}^{M} Im$. Each discrete point is denoted by $\boldsymbol{\phi}_r$, $r = 1, 2, \ldots, R$.

A sea state may be presented by its characteristics, such as H_s, T_p, β_W, directional spreading parameter n_s, etc., which are denoted by a state vector $\boldsymbol{\theta}$, e.g.,

$$\begin{aligned}\boldsymbol{\theta} &= [H_{s,1} \quad T_{p,1} \quad \beta_{W,1} \quad n_{s,1} \quad H_{s,2} \quad T_{p,2} \quad \beta_{W,2} \quad n_{s,2}]^\top \\ &= [\theta_1 \quad \theta_2 \quad \ldots \quad \theta_n \quad \ldots \quad \theta_N]^\top\end{aligned} \tag{3.3}$$

where θ_n represents a wave characteristic, $n \in \{1, 2, \ldots, N_\theta\}$, and N_θ is the number of considered wave characteristics in $\boldsymbol{\theta}$. Equation (3.3) may present a double-peaked sea state, one from the wind sea and the other from the swell. The wave spectrum can be estimated based on the presumed spectral type and spreading function at each discrete point $\boldsymbol{\theta}_s$, where $s = 1, 2, \ldots, S$ and S is the number of discrete points representing the random vector $\boldsymbol{\theta}$. Its uncertainty is expressed by a joint probability distribution $P(\boldsymbol{\theta})$. Due to the discretization of $\boldsymbol{\theta}$, the joint probability distribution is also discretized and becomes a joint probability mass function (PMF). The PMF at each discrete point $\boldsymbol{\theta}_s$ is denoted by $PMF(\boldsymbol{\theta}_s)$.

First, the uncertain parameters $\boldsymbol{\phi}$ and the associated probability distribution $P(\boldsymbol{\phi})$ should be initialized based on the available engineering knowledge from the design of the operation, engineering confidence, and expert opinion. The uncertainty ranges may preferably be initiated larger than the actual ranges to ensure that the corresponding RAO database sufficiently covers the uncertainty ranges. $P(\boldsymbol{\phi})$ may be, for example, initialized as a multivariate Gaussian distribution assuming independent VCRPs. The correlations among parameters can be found automatically through the tuning procedure.

Based on a measurement signal of an interesting vessel response $x_j(t)$ at a specific sea state (i.e., $\boldsymbol{\theta}$ and $P(\boldsymbol{\theta})$), the procedure of tuning the joint probability distribution of the uncertain vessel parameters $P(\boldsymbol{\phi})$ is briefly described in this section and illustrated in Figure 3.1. In the figure, gray blocks represent the inputs, blocks in purple cyan are the intermediate results by processing signals, purple blocks represent the intermediate results derived from the discrete points of VCRPs and wave

data within their uncertainty domains, blocks in light blue represent the likelihood functions, and the white block represents the output of the tuning process. The diamond shape in green indicates a decision-making point. Blocks in orange and red, respectively, represent some important steps and equations for the DBI-based tuning.

Note that the algorithm was initially proposed in Paper A2 [90] without considering the uncertainties of wave conditions. Paper A5 [103] modified the algorithm by taking into account the uncertainties of $\boldsymbol{\theta}$. Figure 3.1 is based on the modified algorithm in Paper A5. For the case studies considering perfect knowledge about the sea state, $S = 1$ and $\boldsymbol{\theta}$ become a deterministic vector.

The STD of the interesting vessel motion signal after filtering, i.e., $\hat{\sigma}_j$, is calculated according to Equation (2.9) or Equation (2.10). Then, the corresponding possible STD, $\sigma_{r,j,s}$, estimated based on each possible combination of $\boldsymbol{\phi}_r$ and $\boldsymbol{\theta}_s$ is calculated:

$$S_{r,j,s}(\omega) = \sum_{\beta_W} |H_{r,j}(\omega, \beta_W)|^2 S_{\zeta\zeta,s}(\omega, \beta_W) \Delta\beta_W \tag{3.4a}$$

$$\sigma_{r,j,s} = \sqrt{\sum_{n=1}^{N_\omega} S_{r,j,s}(\omega_n) \cdot \Delta\omega_n} \tag{3.4b}$$

where $H_{r,j}(\omega, \beta_W)$ is the RAO candidate corresponding to $\boldsymbol{\phi}_r$ and $S_{\zeta\zeta,s}(\omega, \beta_W)$ is the possible wave spectrum according to $\boldsymbol{\theta}_s$.

Then, the prior knowledge about VCRPs obtained after the $(k-1)$th updating, i.e., $P_{k-1}(\boldsymbol{\phi})$, can be further updated according to the Bayesian inference according to Equation (3.1). The $likelihood$ in Equation (3.1) corresponds to the possibility of obtaining such a measurement quantity (e.g., $\hat{\sigma}_j$) resulting from a particular combination of $\boldsymbol{\phi}_r$ and $\boldsymbol{\theta}_s$. Even though the theorem is so simple, in practice, it is usually difficult to find or express such $likelihood$. A weight factor $w_{r,j,s}$, describing the closeness between $\hat{\sigma}_j$ and $\sigma_{r,j,s}$, was introduced to describe $likelihood$ based on the inverse distance weighting [104]:

$$w_{r,j,s} = \frac{1}{|\sigma_{r,j,s} - \hat{\sigma}_j|^p} \tag{3.5}$$

where $p \in \mathbb{R}^+$ is called the power parameter. Selection of the p value shall depend on 1) the uncertainties of the vessel motion measurements, 2) the uncertainties of the applied linear potential theory, 3) the dimension of $\boldsymbol{\phi}$ and the associated uncertainty ranges, and 4) the sensitivity of $\boldsymbol{\phi}$ to the considered vessel motions. The effect of selecting p on the tuning results was studied in Paper A2 [90]. The

introduction of Equation (3.5) is the key to updating our belief in VCRPs after receiving the sensor data.

An initial study of the proposed likelihood function found that Equation (3.5) may lead to unrealistic likelihood estimation across the points $\boldsymbol{\phi}_r$ over the entire uncertainty domain, especially when $\sigma_{r,j,s} - \hat{\sigma}_j$ approaches zero for all $r \in [1, R]$. This means that the considered measurement quantity corresponding to the signal $x_j(t)$ is not sensitive to all the considered VCRPs within the whole uncertainty ranges for $\boldsymbol{\theta}_s$. Therefore, a screening process was introduced before calculating the likelihood functions, as shown in Figure 3.1. A factor named the sensor screening ratio (SSR), denoted by α, was introduced as a criterion for the screening process:

$$\alpha_{j,s} = \frac{\sigma_{j,s}}{\hat{\sigma}_j} \tag{3.6a}$$

$$\sigma_{j,s} = \sqrt{\frac{\sum_{r=1}^{R} (\sigma_{r,j,s} - \overline{\sigma}_{j,s})^2}{R-1}} \tag{3.6b}$$

$$\overline{\sigma}_{j,s} = \frac{\sum_{r=1}^{R} \sigma_{r,j,s}}{R} \tag{3.6c}$$

where $\sigma_{j,s}$ is the STD of $\sigma_{r,j,s}$, for $r = 1, 2, ..., R$. A criterion, e.g., $\alpha_0 = 0.05$, can be set. If $\alpha_{j,s} < \alpha_0$, the likelihood $w_{r,j,s} = \frac{1}{R}$ applies for $\boldsymbol{\theta}_s$ indicating equal likelihood over the whole uncertainty domain to avoid numerical singularities. Otherwise, $w_{r,j,s}$ is calculated according to Equation (3.5) and then applied to build the likelihood function $\overline{\overline{W}}_{j,s}$. Note that much more refined discretization resolution should be applied to the present $PMF(\boldsymbol{\phi})$ compared with that used to establish the RAO database. Therefore, interpolation is required when building $\overline{\overline{W}}_{j,s}$ from $w_{r,j,s}$ for $r = 1, 2, \ldots, R$. In addition, $\overline{\overline{W}}_{j,s}$ should be normalized so that the sum of elements equals 1.0. This normalization is necessary to ensure a fair calculation of the likelihood function over the uncertainty domain of $\boldsymbol{\theta}$, i.e.,

$$\overline{\overline{W}}_j = \sum_{s=1}^{S} \overline{\overline{W}}_{j,s} PMF(\boldsymbol{\theta}_s) \tag{3.7}$$

where $\overline{\overline{W}}_j$ is the likelihood function to be applied for the Bayesian updating:

$$PMF_k(\boldsymbol{\phi}) = \mathcal{NO}(PMF_{k-1}(\boldsymbol{\phi}) \odot \overline{\overline{W}}_j) \tag{3.8}$$

where the $\odot$ operator means the elementwise multiplication of the two matrices of the same dimension, i.e., a Hadamard product [105]. In addition, normalization $\mathcal{NO}(\cdot)$ is again required to ensure that the sum of $PMF(\boldsymbol{\phi})$ over the entire uncertainty domain remains 1.0. $k \in \mathbb{Z}^+$ indicates the tuning step.

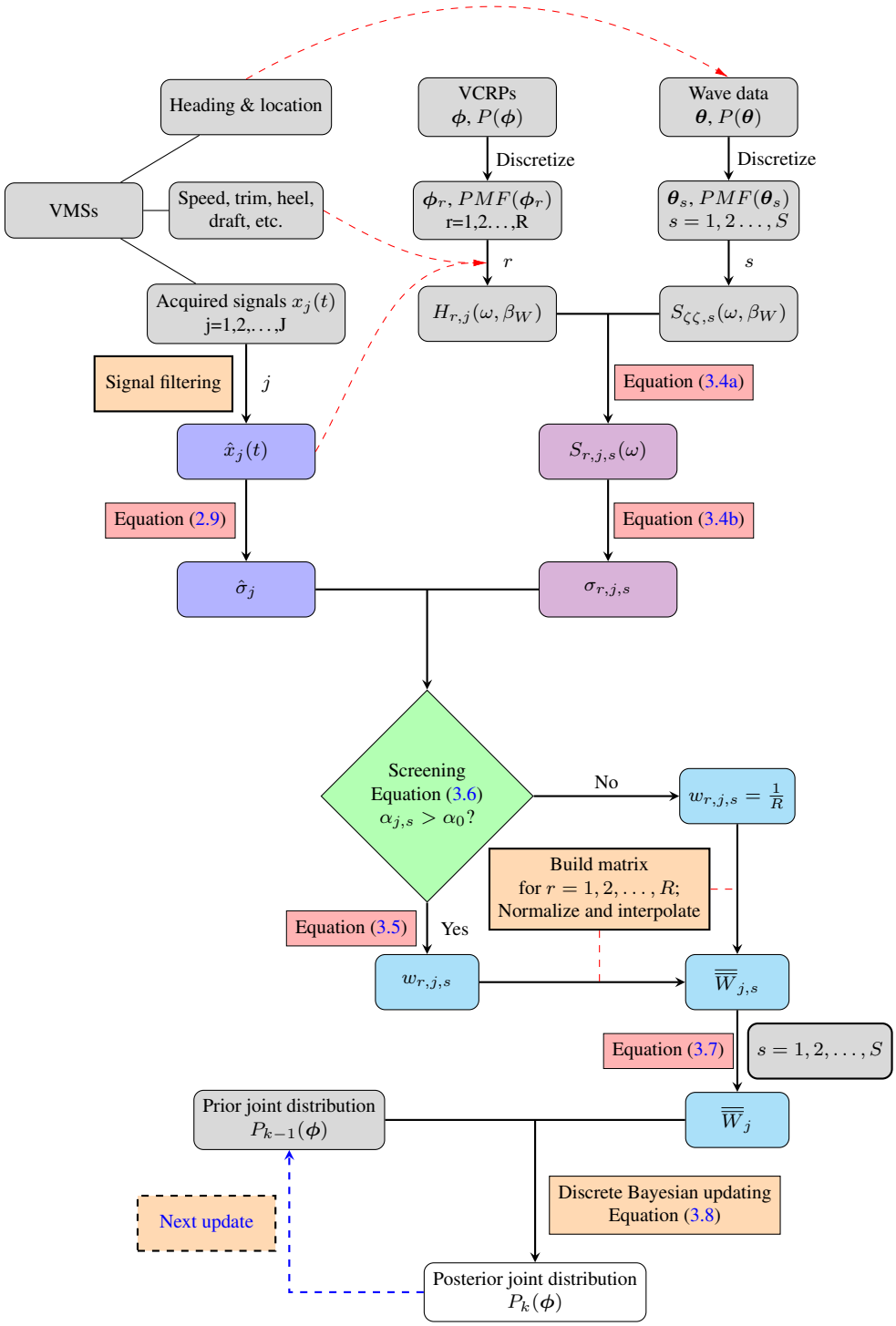

Figure 3.1: Procedure of tuning VCRPs based on discrete Bayesian inference, using wave and vessel data.

3.2 Algorithm demonstration

The DBI-based tuning algorithm was first proposed and demonstrated in Paper A2 [90] considering precise wave information. Case studies with detailed intermediate tuning results and likelihood functions were documented. For example, Figure 3.2 illustrates intermediate tuning results for tuning GMT and β_{44} based on 5 sea states (i.e., SS1 to SS5). Details about the sea states and applied parameters (e.g., α_0 and p for model tuning, SNR for signal generation, and f_{lp} for signal filtering) are described in Paper A2 [90]. Figure 3.2 shows how the joint distribution of GMT and β_{44} changes based on signals of the 9 interesting vessel motion quantities described in Table 2.5. The green stars in the subplots of Figure 3.2 represent the true values of GMT and β_{44}. The uncertainty distribution becomes narrower, and the tuned expected value gets closer to the true value, particularly for β_{44}.

The algorithm was validated by running 120 independent tuning simulations, considering tuning of 4 vessel parameters simultaneously, i.e. GMT, r_{55}, XCG and β_{44}. Each tuning case considered sensor signals from 6 sea states. The sea state characteristics were randomly generated. The expected and variance of those uncertain parameters after tuning are shown in Figures 3.3–3.6. For illustration purposes, each figure only contains tuning results for two parameters. Better tuning results were generally observed for the more sensitive parameters (i.e. β_{44} and XCG), in terms of expected value closer to the truth and more significantly reduced variance after tuning. It is also worth mentioning that the computational time increases exponentially with the number of considered uncertain parameters. It took 90 s to tune 4 vessel parameters simultaneously for one sea state considering 9 sensors but only 10 s to tune 2 parameters. In addition, the linear interpolation of $\overline{\overline{W_j}}$ can require considerably large computational capacity. Therefore, this proposed algorithm may face a commonly recognized computational challenge for large-dimensional problems, i.e., the "curse of dimensionality" [106].

The proposed algorithm involves several hyperparameters, such as p, α_0, and a lowpass filter considering a cutoff frequency f_{lp}. Sensitivity studies of those parameters on the tuning results were also studied. It was found that:

1. A larger p value leads to a shorter forgetting factor in the tuning system, meaning that $P(\boldsymbol{\phi})$ changes more abruptly and variance can be reduced more quickly, similar to an overfitting and overconfident system.

2. A larger α_0 leads to less valuable measurements to be considered in the tuning process. However, an excessively small α_0 amplifies the negative influence of numerical errors on the tuning results for insensitive sensors and sea states. The selection of α_0 should depend on the uncertainties of

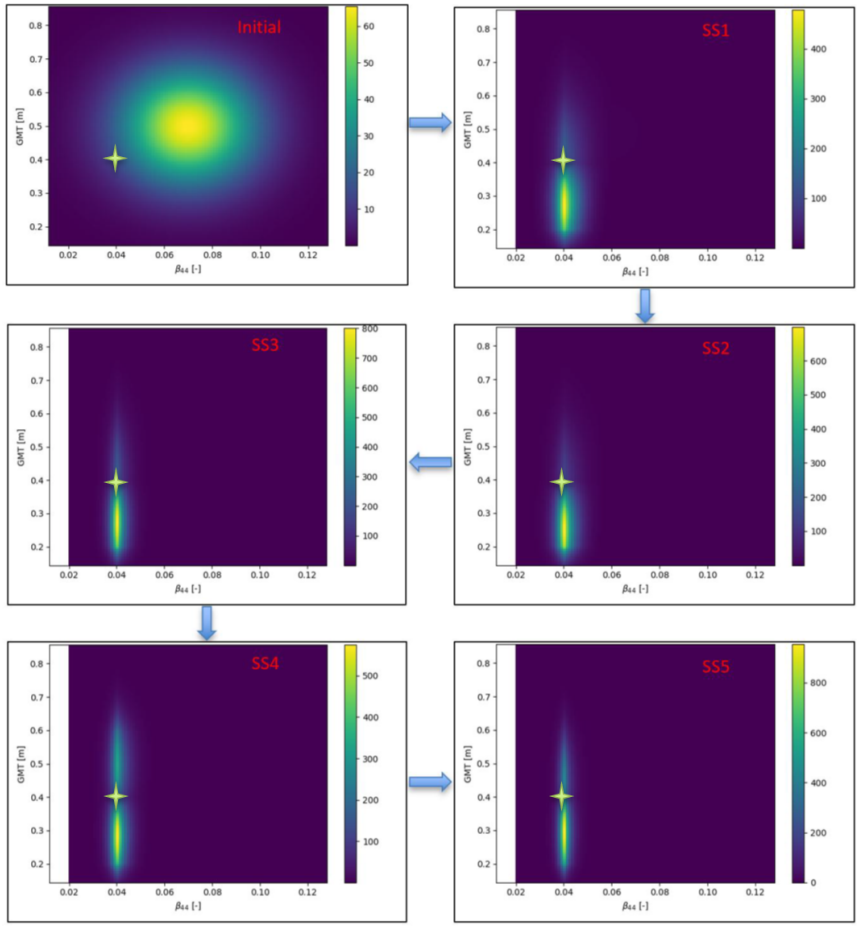

Figure 3.2: Intermediate tuning results of the joint distribution of GMT and β_{44}.

the filtered signals and the systematic errors (such as from simplifications of seakeeping modeling and applied potential theory). A larger α_0 should be applied when, e.g., it is difficult to filter out higher-order wave-induced motions and noise from signals due to frequency overlapping for first-order and higher-order motions or a poorly designed signal filter model.

3. Selection of f_{lp} can be critical for unbiased tuning results, especially for the less sensitive vessel parameters at some frequencies. It is therefore important to design a reliable and more accurate signal filtering model, e.g., considering sea state and vessel condition dependent cutoff frequencies.

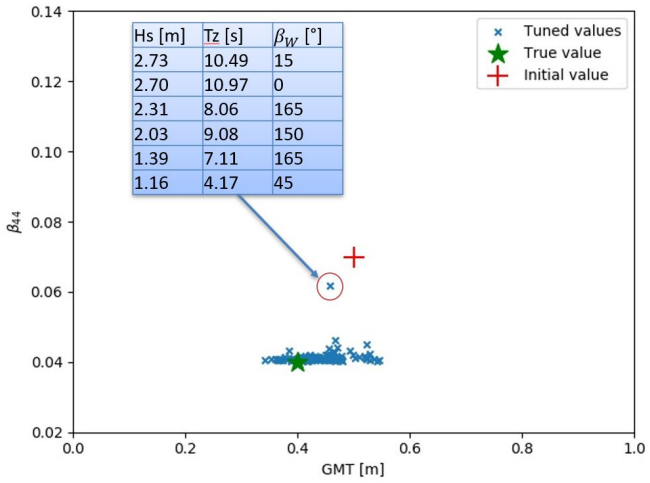

Figure 3.3: Tuning results for validation analyses, expected values of GMT and β_{44}

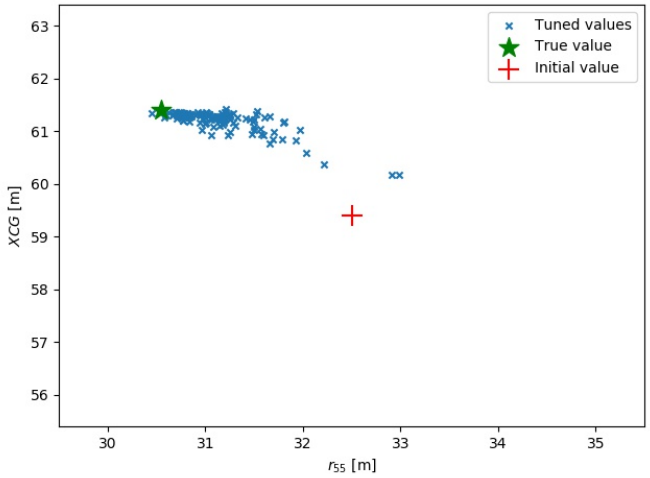

Figure 3.4: Tuning results for validation analyses, expected values of r_{55} and XCG

3.3 Algorithm modification with an adaptive lowpass filter

Tuning results rely on the estimation accuracy of the first-order wave-induced motion STDs from corresponding signals that contain noise and higher-order motions. It is therefore important to design and modify the signal filter. The generated synthetic signals only contained white noise; therefore, only a lowpass filter was considered. The optimal lowpass filter cutoff frequency ideally depends on the sea state and vessel condition [107]. Intuition about dealing with such a sea state and

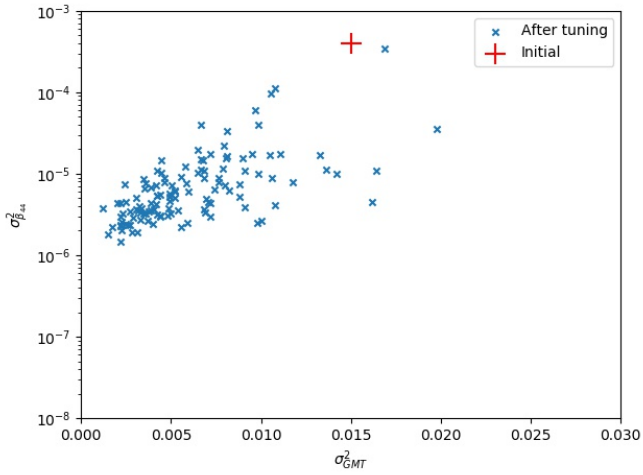

Figure 3.5: Tuning results for validation analyses, variance of GMT and β_{44}

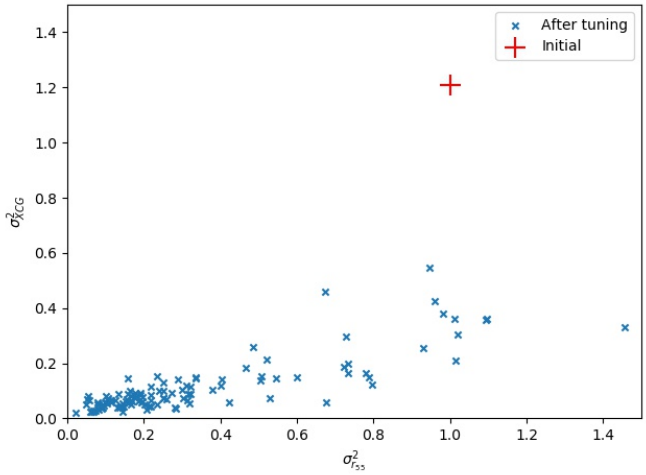

Figure 3.6: Tuning results for validation analyses, variance of r_{55} and XCG

vessel dependent signal lowpass filtering may be to establish a function between the "optimal" cutoff frequency and characteristics representing the sea state and vessel condition. This was proved to be extremely difficult because the fitted function depends on so many parameters, such as T_p, β_W, spectral type, SNR, and the measuring quantity (which DOF, where to measure, velocity or acceleration, etc.); and some factors are not quantitative (e.g., spectral type, measured quantity).

Through deep investigation, a novel algorithm was proposed in Paper A3 [91] to

find the optimal cutoff frequency among selected discrete values of cutoff frequency $f_{lp,i}$ ($i = 1, 2, \dots$) by introducing only two parameters, i.e., θ and γ:

$$\theta(f_{lp,i}) = \frac{\hat{\sigma}_X(f_{lp,i}) - \hat{\sigma}_X(f_{lp,i-1})}{\hat{\sigma}_X(f_{lp,i}) \cdot (f_{lp,i} - f_{lp,i-1})} \tag{3.9a}$$

$$\gamma(f_{lp,i}) = \frac{\hat{T}_z(f_{lp,i-1}) - \hat{T}_z(f_{lp,i})}{\hat{T}_z(f_{lp,i}) \cdot (f_{lp,i} - f_{lp,i-1})} \tag{3.9b}$$

where $\hat{\sigma}_X(f_{lp,i})$ and $\hat{T}_z(f_{lp,i})$ represent the STD and zero-upcrossing period of the filtered signal by application of the cutoff frequency $f_{lp,i}$. $\theta(f_{lp,i})$ and $\gamma(f_{lp,i})$ numerically represent the normalized slopes of the $\hat{\sigma}_X$-f_{lp} and $\hat{T}_z$-f_{lp} curves at $f_{lp,i}$ in absolute values.

For example, as shown in Figure 3.7, the optimal cutoff frequency f_{lp}^* always stays at or near the turning point of the $\hat{\sigma}_X$-f_{lp} curve and sits on the "platea" of the $\hat{T}_z$-f_{lp} curve. The location of f_{lp}^* along $\hat{\sigma}_X$-f_{lp} and $\hat{T}_z$-f_{lp} indicates relatively small values of $\theta(f_{lp}^*)$ and $\gamma(f_{lp}^*)$ compared with values of θ and γ at frequencies of the main vessel motion energy. The proposed algorithm of finding f_{lp}^* based on θ and γ is summarized in Algorithm 1.

The examined $f_{lp,i}$ should have sufficient resolution so that the found optimal cutoff frequency among those values ($f_{lp,i}$ for $i = 1, 2, \dots$), denoted by f_{lp,i^*}, is sufficiently close to the true optimal cutoff frequency, denoted by f_{lp}^*. Similar to a procedure of solving equations numerically, the procedure of finding the optimal cutoff frequency may be numerically optimized and automated by only setting the range of possible optimal cutoff frequencies and numerical tolerance of the change of θ and γ due to the change of f_{lp}.

In fact, the dependency on T_p, β_W, spectral type, and the measurement quantity are all linked to the influence on the resulting response energy spreading. By introducing θ and γ, the relationship between the cutoff frequency and the sea state and vessel condition is, to a very large extent, simplified, which can be quite beneficial for real applications. The algorithm is fundamentally based on the fact that 1) the vessel acts as a lowpass filter of wave energy in the high-frequency region where insignificant vessel motion energy is usually experienced; 2) the energy of signal noise is significantly less than that of wave-induced vessel motions; and 3) the signal noise takes the most energy in the high-frequency region.

$\theta = 0.05$ and $\gamma = 0.9$ were set as the criteria. The sensitivity of the θ and γ criteria to the resulting $\hat{\sigma}_X(f_{lp,i^*})$ was studied in Paper A3 [91]. Generally, slightly stricter criteria can lead to slight underfiltering but do not significantly influence the calculated $\hat{\sigma}_X(f_{lp,i^*})$. However, overly "relaxed" criteria (i.e., a too

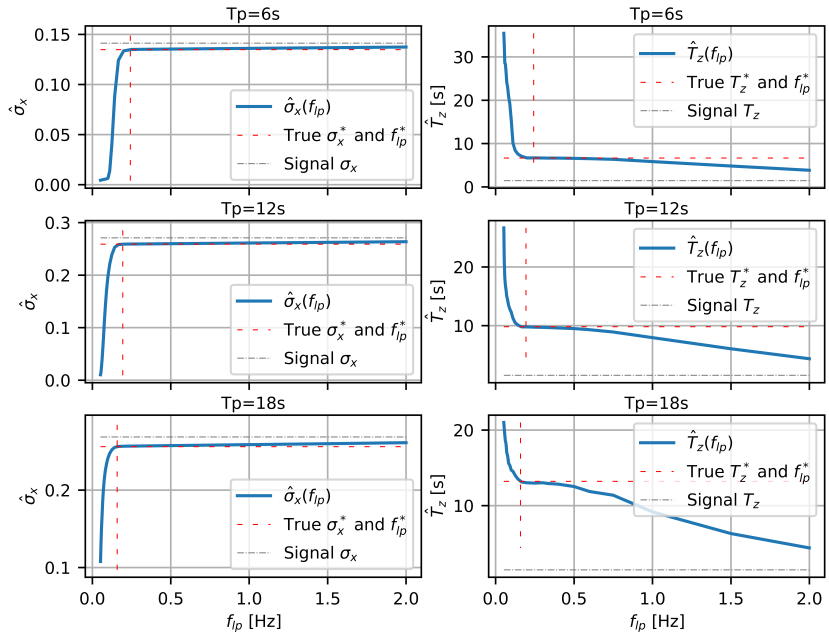

Figure 3.7: $\hat{\sigma}_X$-f_{lp} and $\hat{T}_z$-f_{lp} curves for the Disp_A sensor, SNR=10, $\beta_W = 90°$, $T_p = 6$ s, 12 s, and 18 s.

large value of θ criteria) is risky and can easily lead to significantly overfiltered signals and estimates that are too small for $\hat{\sigma}_X(f_{lp,i^*})$. γ is mainly introduced as a supplementary metric, whereas selection of the θ criterion usually dominates the quality of such an adaptive lowpass filter.

The proposed adaptive lowpass filter was then applied to the proposed DBI-based tuning algorithm and tested for 200 independent tuning simulations. Compared with the same cases with a constant $f_{lp} = 1$ Hz, the adaptive filter statistically improves the tuning of vessel parameters, with more cases having smaller variance and the expected values closer to the truth after tuning, as shown in Figures 3.8 and 3.9. The parameters with subscripts of 0 in the legends refer to the initial values.

3.4 Tuning and predicting sea state dependent parameters

So far, all the considered uncertain vessel parameters are assumed to be constant across different sea states. However, the linearized additional damping terms β_{dd}, which cannot be estimated under linear potential theory, are actually sea state dependent. Consequently, a tuned β_{dd} based on the current sea state might not be

Algorithm 1: Recursive searching of optimal cutoff frequency.

Initialize: i=0, $\theta = 1.0$, $\gamma = 10.0$;
Input: Predefined f_{lp} values in ascending order and the signal $x(t)$;
while $\theta \geq 0.05$ *and* $\gamma \geq 0.9$ **do**
  $i = i + 1$;
  Obtain $\hat{x}(t)$ by filtering $x(t)$ at a cutoff frequency of $f_{lp,i}$;
  Calculate $\hat{\sigma}_X(f_{lp,i})$ and $\hat{T}_z(f_{lp,i})$;
  if $i > 1$ **then**
    Calculate $\theta(f_{lp,i})$ by Equation (3.9a) and $\gamma(f_{lp,i})$ by Equation (3.9b);
    $\theta = \theta(f_{lp,i})$;
    $\gamma = \gamma(f_{lp,i})$;
  end
end
$\tilde{f}^*_{lp} = f_{lp,i}$;
if $\tilde{f}^*_{lp} < 0.1$ *Hz* **then**
  $f^*_{lp} = 0.1Hz$;
else if $\tilde{f}^*_{lp} > 0.9$ *Hz* **then**
  $f^*_{lp} = 0.9$ Hz;
else
  $f^*_{lp} = \tilde{f}^*_{lp}$;
end
return f^*_{lp};

appropriate for estimating vessel motion at mode d for other sea states.

Therefore, modification of the tuning procedure is required such that prediction of those sea state dependent parameters at unobserved wave conditions should be possible based on the available tuning results at the already observed wave conditions. Consequently, the expression of those parameters as functions of sea state characteristics is required. In addition, such a model is preferably able to estimate and update its prediction uncertainty by benefiting from the DBI-based tuning procedure, which estimates the tuning uncertainties. Improving the knowledge about sea state dependent β_{dd} over the whole wave frequency region is critical for accurate vessel response prediction and for potential motion control applications such as ship roll damping control [108].

Paper A4 [92] modified the DBI-based tuning algorithm, considering tuning and predicting sea state dependent parameters (β_{44} as the example) together with other

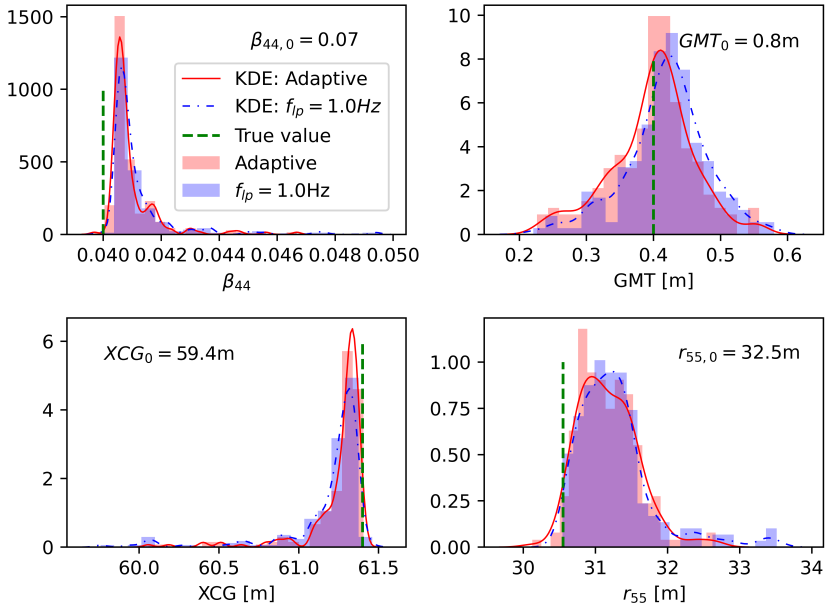

Figure 3.8: Normalized histograms (vertical axes) of the expected values for the tuned vessel parameters, comparing the adaptive filter approach with the use of a fixed cutoff frequency $f_{lp} = 1.0$ Hz. KDE: kernel density estimation.

sea state independent parameters (e.g., GMT and XCG). Tuning of the linearized additional roll damping was selected as the basis for the case study due to its critical and highly nonlinear influence on the vessel roll motions [109, 110, 111, 112, 113]. The nonlinear roll damping due to viscous effects requires linearization (usually by stochastic linearization [114]) to calculate the roll RAOs in the frequency domain.

The Gaussian process regression (GPR) [115] model was introduced to present and update the knowledge (mean and variance) about β_{44} as a function of H_s, T_p, and β_W. Consequently, such a model can be applied to predict β_{44} at other sea states. The GPR model is fundamentally based on the conditional distribution of multivariate Gaussian vectors [116], assuming values of β_{44} over the whole input space are correlated Gaussian variables. Their covariance can be modeled by various kernels. In the case studies, a kernel based on radial-basis function (RBF) was applied, which expresses the correlation of two data points as a function of their distance. The variance of the tuned β_{44} is considered as the sample uncertainties in the GPR model (stochastic kriging algorithm [115]). The Python package scikit-learn [117] was used in the case studies to establish and train the β_{44} GPR model and predict β_{44}.

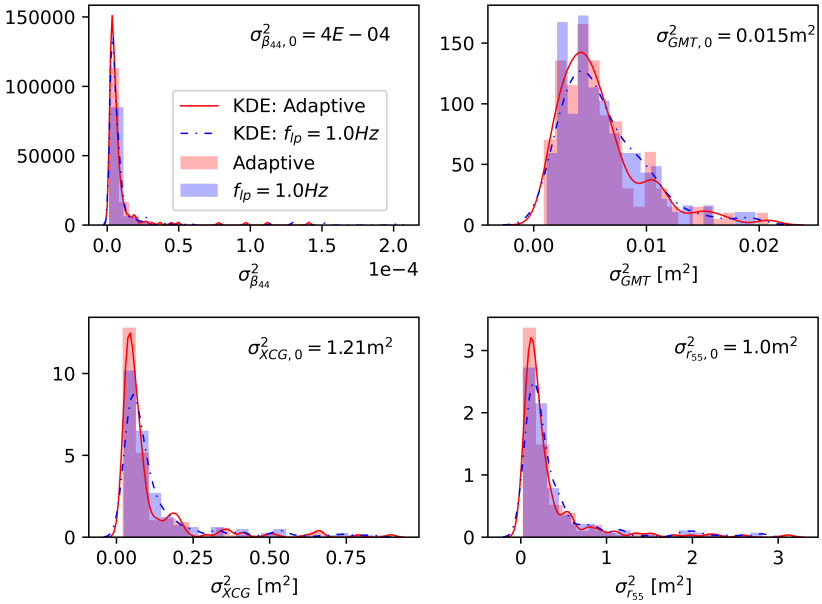

Figure 3.9: Normalized histograms (vertical axes) of the variances for the tuned vessel parameters, comparing the adaptive filter approach with the use of a fixed cutoff frequency $f_{lp} = 1.0$ Hz.

This β_{44} GPR model was implemented into the tuning loop so that the newly tuned β_{44}, as a new sample, can improve the GPR model, which in return improves the prior knowledge about β_{44} at the next sea state for tuning. The 1-step and 2-step tuning processes were proposed in Paper A4, where the 2-step tuning process illustrated in Figure 3.10 is more promising. The 2-step tuning process uses two different power parameters p_1 and p_2 ($p_1 < p_2$) to tune the joint distribution of vessel parameters $P(\boldsymbol{\phi})$. A smaller power parameter p_1 is mainly used to tune the sea state independent parameters to avoid abrupt and overconfident tuning. However, a larger power parameter p_2 is used to tune the sea state dependent parameters due to the significantly fewer available measurements for a particular sea state. Even though two power parameters were introduced, it must be emphasized that all variables in $\boldsymbol{\phi}$ have to be updated together, as shown in Figure 3.10.

The proposed 1-step and 2-step tuning algorithms were demonstrated by randomly simulated case studies. The prior knowledge about β_{44} assumed that $\beta_{44,0} \sim \mathcal{N}(0.07, 0.02^2)$ over the entire input domain described by $H_s \sin\beta_W$ and ω_p, where $\omega_p = 2\pi/T_p$. The true function of β_{44} over $H_s \sin\beta_W$ and ω_p was assumed and illustrated in Figure 3.11. A case study (Case_GMT Seed128) of tuning β_{44} and XCG based on the 2-step tuning process is briefly presented here, which considers

72 randomly simulated sea states and the associated vessel motion measurements. Figure 3.11 indicates a significantly improved β_{44} GPR model. In particular, the updated mean values of β_{44} become closer to the assumed true function with significantly reduced variance, especially at the input subspace with more observed samples. The detailed simulation procedure and results are described in Paper A4 [92].

In addition to β_{44}, the results for tuning XCG based on 1-step and 2-step tuning procedures due to the same 72 sea states are illustrated in Figure 3.12. The applied power parameter ($p = 0.6$) in 1-step tuning must compromise between the tuning of sea state dependent and sea state independent parameters. Tuning of the sea state dependent parameter prefers a larger p_2, while a smaller p_1 is preferred for tuning the other parameters. Therefore, 2-step tuning should be preferred to avoid overconfident tuning of sea state independent parameters (by applying a smaller p_1). As illustrated in Figure 3.12, tuning of the XCG was even accelerated towards its true value approximately between sea state numbers 15 and 40. This is actually due to the slower reduced variance from the 2-step tuning, which offers a reasonably increased influence from the later sea states on the tuning results.

It is expected that the proposed procedure of tuning β_{44} and updating its GPR model can significantly improve the estimation accuracy of the onsite roll RAOs, especially for the sea states of most interest for the operation. However, it must be emphasized that such a procedure cannot replace model tests with a focus on the estimation of roll motions for extreme and accidental conditions, which are not expected to occur often in reality.

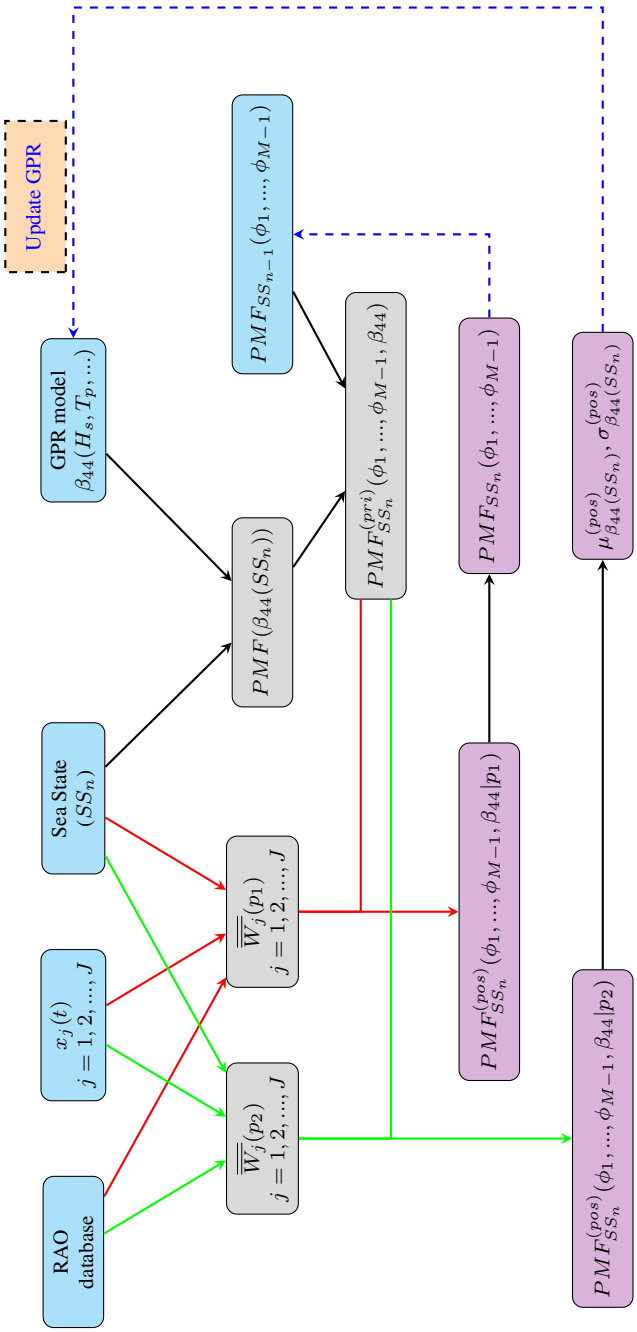

Figure 3.10: Process of the 2-step tuning of vessel parameters including sea state dependent β_{44} and updating the β_{44} GPR model, assuming $\phi_M = \beta_{44}$. Normally $p_1 < p_2$.

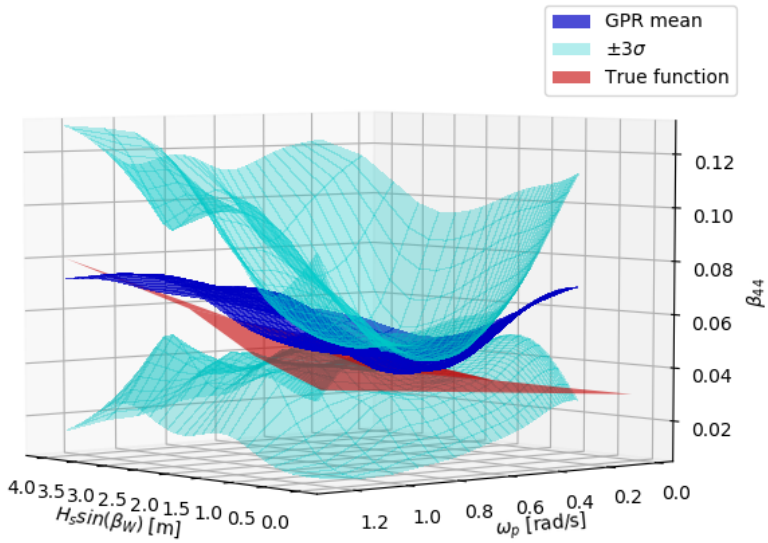

Figure 3.11: The updated β_{44} GPR model after tuning of β_{44} and XCG for 72 sea states, for Seed128 with a 2-step tuning procedure.

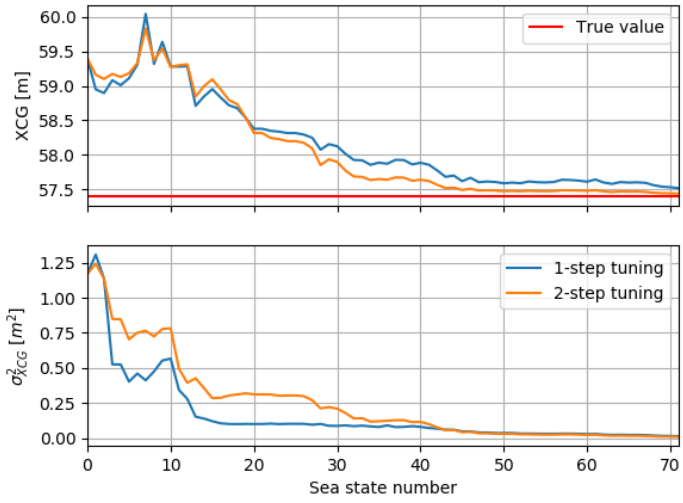

Figure 3.12: Comparison of the mean and the variance of the tuned XCG through the 72 simulated sea states obtained by application of the 1-step and the 2-step tuning procedures for Seed128.

3.5 Application: vessel condition monitoring and reliability-based onboard decision support

To date, the DBI-based model tuning algorithm has been proposed, developed, and demonstrated through numerical simulations. The tuning of those important but uncertain vessel parameters is expected to improve vessel motion prediction. The quantification of their uncertainties can even assist in quantifying the consequent vessel motion prediction uncertainties. This leads to potential applications of relevant operational decision support or decision making for maritime activities based on quantitative uncertainty assessment.

Paper A5 [103] proposed a decision support system based on quantitative risk assessment, taking into account the uncertainties of wave and vessel conditions by applying DBI-based model tuning as an adaptive vessel state observer. The DBI-based model tuning algorithm (Figure 3.1) is applied to monitor the vessel condition on board so that VCRPs can be actively updated according to available vessel (VMSs and VCRPs) and wave (forecast and historical) data. Furthermore, the updated probability distribution of VCRPs can be applied to the probabilistic prediction of critical structural response in combination with wave forecast information with uncertainties. The framework is illustrated in Figure 3.13.

Quantitative risk assessment for a preidentified potential event is always a challenge, and conservative prior knowledge about the relevant inputs (e.g., environments, vessel loading conditions, etc.) is usually considered, consequently leading to an overconservative risk assessment. Such conservatism (over vessel condition) can be identified and reduced by introducing the DBI-based tuning process. Formulation for calculating the probability of occurrence was proposed in Paper A5 and is summarized here.

The extreme value of the vertical velocity at the crane tip $\dot{\eta}_{max}$ may dominate lifting operations and therefore can be considered as a critical response. $\dot{\eta}_{max}$ means the maximum value of the response $\dot{\eta}$ during a stationary sea state which typically lasts between 30 minutes and 3 hours. For a safe operation, $\dot{\eta}_{max}$ should be less than $\dot{\eta}_0$ as a criterion. Therefore, the considered failure event can be expressed as $\dot{\eta}_{max} \geq \dot{\eta}_0$.

Considering the wave forecast $\boldsymbol{\theta}$ and updated VCRPs $\boldsymbol{\phi}$ in the form of a discrete joint probability distribution, i.e., $PMF(\boldsymbol{\theta}_s)$, for $s = 1, 2, \ldots, S$, and $PMF(\boldsymbol{\phi}_r)$ for $r = 1, 2, \ldots, R$, the response spectrum $S_{\dot{\eta},r,s}(\omega)$ for $\dot{\eta}$ at a specific combination of $\boldsymbol{\theta}_s$ and $\boldsymbol{\phi}_r$ can be calculated by:

$$S_{\dot{\eta},r,s}(\omega) = S_{\dot{\eta}}(\omega|\boldsymbol{\phi}_r, \boldsymbol{\theta}_s) = \sum_{\beta_\mathrm{W}} |H_{\dot{\eta},r}(\omega, \beta_\mathrm{W})|^2 S_{\zeta\zeta,s}(\omega, \beta_\mathrm{W}) \Delta\beta_\mathrm{W} \tag{3.10}$$

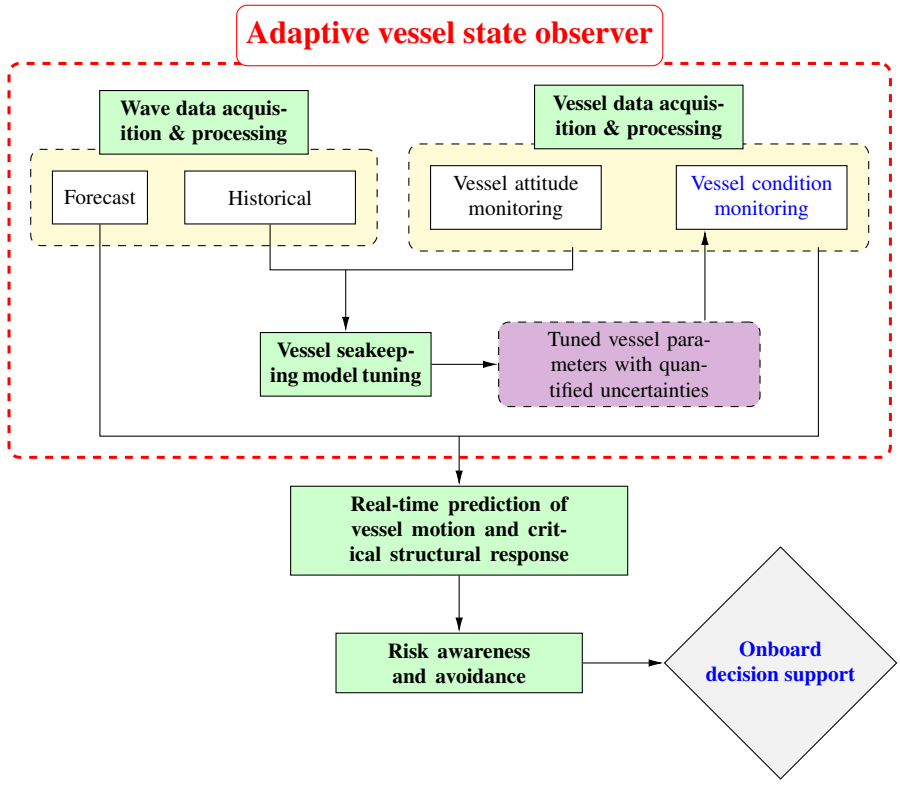

Figure 3.13: Overview of the proposed adaptive vessel state observer for vessel condition monitoring and decision support.

where $H_{\dot{\eta},r}(\omega, \beta_{\mathrm{W}})$ is the RAO of $\dot{\eta}$ based on $\boldsymbol{\phi}_r$, and $S_{\zeta\zeta,s}(\omega, \beta_{\mathrm{W}})$ is the wave spectrum based on $\boldsymbol{\theta}_s$.

$\dot{\eta}$, contributed from multiple rigid-body motion modes and possibly induced by broadband wave conditions with directional spreading, can be considered a broadband Gaussian process. Hence, the probability distribution of $\dot{\eta}_{max}$ for a specific response spectrum $S_{\dot{\eta},r,s}(\omega)$ with a duration of T (corresponding to one sea state) can be estimated by the Average Upcrossing Rate (AUR) method [118]:

$$PDF_{\dot{\eta}_{max},r,s}(v) = \frac{v}{m_{0,r,s}} \nu_X^+(0) T \exp\left(-\frac{v^2}{2m_{0,r,s}}\right) \exp\left(-\nu_X^+(0) \exp\left(-\frac{v^2}{2m_{0,r,s}}\right)\right) \tag{3.11a}$$

$$\nu_X^+(0) = \frac{1}{2\pi} \sqrt{\frac{m_{2,r,s}}{m_{0,r,s}}} \tag{3.11b}$$

where PDF means the probability density function. $m_{0,r,s}$ and $m_{2,r,s}$ are the

zeroth- and second-order spectral moments of $S_{\dot{\eta},r,s}(\omega)$. $\nu_X^+(0)$ is the zero-upcrossing period.

Furthermore, considering the probability distribution of $\boldsymbol{\theta}$ and $\boldsymbol{\phi}$, the probability of occurrence for the failure event $\dot{\eta}_{max} \geq \dot{\eta}_0$ can be calculated by:

$$PDF_{\dot{\eta}_{max}}(v) = \sum_{r=1}^{R}\sum_{s=1}^{S} PDF_{\dot{\eta}_{max},r,s}(v) \cdot PMF(\boldsymbol{\phi}_r) \cdot PMF(\boldsymbol{\theta}_s) \tag{3.12a}$$

$$P(\dot{\eta}_{max} \geq \dot{\eta}_0) = 1 - \int_{-\infty}^{\dot{\eta}_0} PDF_{\dot{\eta}_{max}}(v)dv \tag{3.12b}$$

Decision support may also provide timely and valuable suggestions to react to the identified potential risks. For example, the probability of failure can be significantly reduced by changing vessel heading β_V. Optimal heading β_V^* can be estimated leading to the minimum $P(\dot{\eta}_{max} \geq \dot{\eta}_0)$:

$$\begin{aligned}\beta_V^* &= \arg\min_{\beta_V} P(\dot{\eta}_{max} \geq \dot{\eta}_0|\beta_V) \\ &:= \{\beta_V|\forall y \in [0°, 360°) : P(\dot{\eta}_{max} \geq \dot{\eta}_0|y) > P(\dot{\eta}_{max} \geq \dot{\eta}_0|\beta_V)\}\end{aligned} \tag{3.13}$$

Chapter 4

Model Tuning by Unscented Kalman Filter

4.1 Motivation

The initially proposed DBI-based seakeeping model tuning algorithm was found to be less efficient when tuning many parameters. Due to the discretization of variables within their uncertainty ranges, the computational efforts increase exponentially to the number of considered uncertain vessel parameters (M). For an efficient algorithm, the computational efforts may preferably increase linearly to M. Naturally, instead of representing the joint probability distribution $P(\boldsymbol{\phi})$ by discrete points, it can be beneficial to express it by its mean and covariance. This further leads to an intuitive simplification of assuming the vessel state vector as being multivariate Gaussian distribution, which is widely applied to real engineering applications due to its unique advantages in terms of simple analytical solutions to linear systems.

The idea of simplifying $P(\boldsymbol{\phi})$ as being multivariate Gaussian distributed and updating its mean and covariance based on measurements intuitively leads to a proposal of applying Kalman filters, because the Kalman filter [102] is mathematically optimal for a linear system if all the variables are Gaussian processes. For a nonlinear system, the extended Kalman filter (EKF) is thus far the most popular model in practice, which uses the "first-order" linearization at the estimated state [119]. However, an EKF requires calculation of the Jacobian matrix, which may be difficult or computationally expensive. The error introduced by linearization could be accumulated with updating. Therefore, a convergent solution cannot be guaranteed, and poor performance has been observed, especially for highly nonlinear

systems. Instead of using a linear algebra formulation for nonlinear problems by linearization, it is preferable to directly use the more accurate nonlinear functions with Monte Carlo simulations to estimate the system state by generating many samples, transferring them to measurement space, and then presenting them statistically. This is the fundamental concept for the particle filter (PF) [120], which is also computationally expensive for large-dimensional systems.

In recent decades, the sigma-point Kalman filters (SPKFs) [119] have prevailed, at least in the research field. Instead of linearization at a single point, SPKFs linearize the model by implicitly applying weighted statistical linear regression based on information at several deterministic points [119]. SPKFs consider both the mean and uncertainty spreading of the state and therefore can at least guarantee a second-order approximation accuracy. There are mainly two types of SPKFs, i.e., the unscented Kalman filter (UKF) [121] and the central differential Kalman filter (CDKF) [119]. Both SPKFs perform equally well in practice with respect to the estimation accuracy.

A CDKF basically inherits the conventional Kalman filter formulation. However, instead of applying a truncated Taylor series expansion and calculating the Jacobian matrix at one point as for an EKF, a CDKF estimates the linearization based on Sterling's interpolation formula [122] by applying several points around the estimated mean state.

A UKF [82] is formulated based on the unscented transformation [123] directly through nonlinear functions. A UKF does not derive any linearized functions explicitly and therefore eases the usage of the linear algebra formulation, being convenient for systems involving very complex functions. Higher-order estimation accuracy can be achieved for a UKF by using a larger number of sigma points to include higher-order statistical characteristics such as skewness and kurtosis [124, 125].

4.2 Algorithm description

Based on the above discussions, UKF is believed to be a good solution as a compromise between implementation convenience, estimation accuracy, robustness, and computational efficiency. Therefore, a seakeeping model tuning algorithm based on a UKF was proposed in Paper A6 [93]. The uncertainties among vessel parameters, wave information, and vessel motions interact, meaning that increasing the accuracy of any one source can assist in improving knowledge on the others. The proposed UKF-based tuning algorithm, as illustrated in Figure 4.1, can simultaneously update important parameters with respect to wave and vessel conditions, containing four steps: weather update, sigma-point and weight calculation,

system propagation, and measurement update.

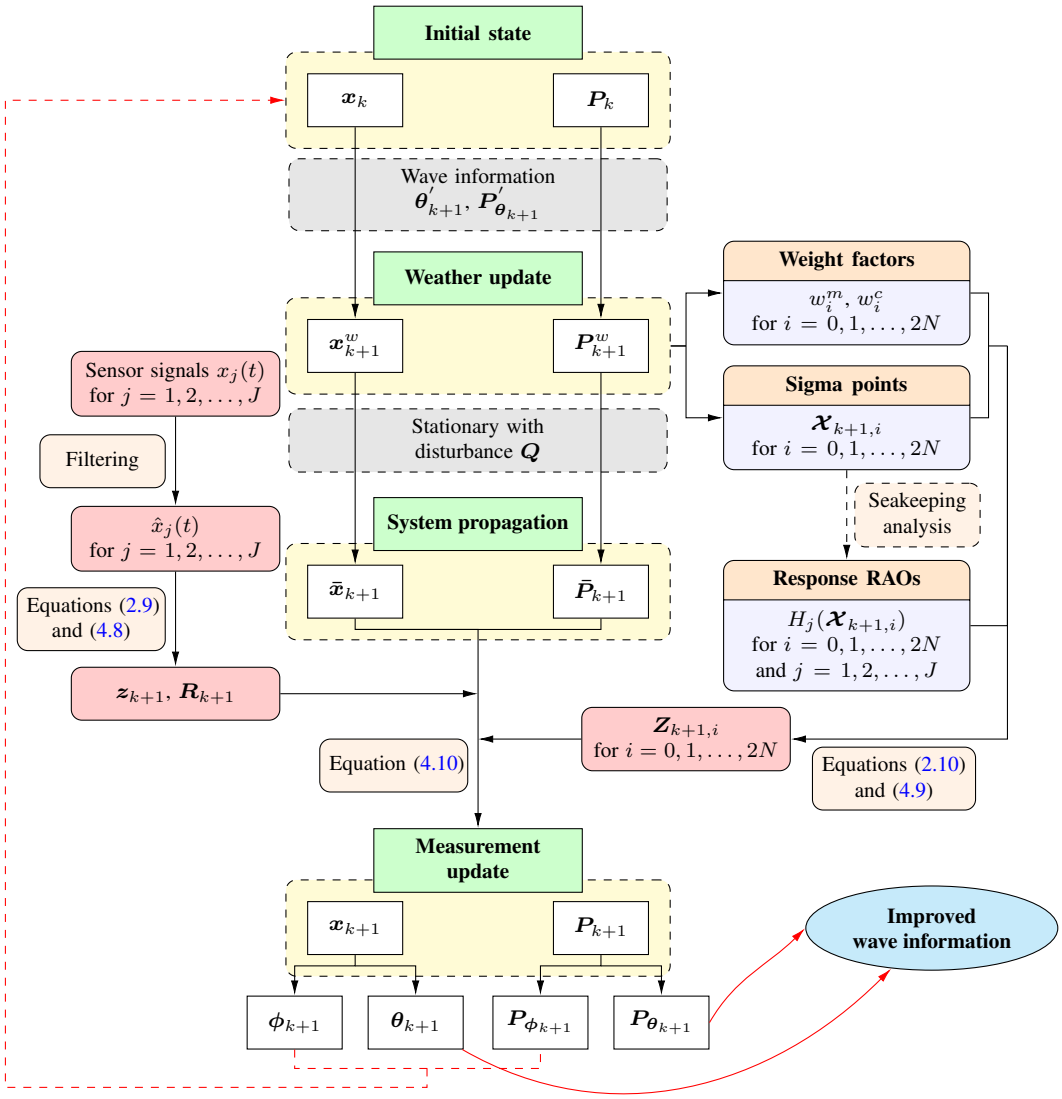

Figure 4.1: The process of tuning vessel parameters and sea state characteristics together with quantification of uncertainties.

4.2.1 Weather update

The tuning starts with initializing the system state and its covariance based on prior knowledge. A system state vector $\boldsymbol{x}$ consists of a vessel state vector $\boldsymbol{\phi}$ (including uncertain vessel parameters, i.e., VCRPs) and a sea state vector $\boldsymbol{\theta}$ (including un-

certain sea state characteristics). Stationary sea states are assumed, and they are assumed to be independent from each other. The system state after tuning k sea states is denoted by $\boldsymbol{x}_k$:

$$\boldsymbol{x}_k = \begin{bmatrix} \boldsymbol{\phi}_k \\ \boldsymbol{\theta}_k \end{bmatrix} \tag{4.1a}$$

$$\boldsymbol{P}_k = \begin{bmatrix} \boldsymbol{P}_{\boldsymbol{\phi}_k} & \boldsymbol{P}_{\boldsymbol{\phi}_k \boldsymbol{\theta}_k} \\ \boldsymbol{P}_{\boldsymbol{\theta}_k \boldsymbol{\phi}_k} & \boldsymbol{P}_{\boldsymbol{\theta}_k} \end{bmatrix} \tag{4.1b}$$

where $\boldsymbol{P}_k$, $\boldsymbol{P}_{\boldsymbol{\phi}_k}$, and $\boldsymbol{P}_{\boldsymbol{\theta}_k}$ are the covariance matrices of the system state, vessel state, and sea state, respectively. $\boldsymbol{P}_{\boldsymbol{\phi}_k \boldsymbol{\theta}_k}$ and $\boldsymbol{P}_{\boldsymbol{\theta}_k \boldsymbol{\phi}_k}$ are the cross covariance matrices between the vessel and sea state vectors.

When vessel and wave data of a new sea state (indexed by $k+1$) are acquired, the system state should first be updated according to the newly acquired wave information, i.e.,

$$\boldsymbol{x}^w_{k+1} = \begin{bmatrix} \boldsymbol{\phi}_k \\ \boldsymbol{\theta}'_{k+1} \end{bmatrix} \tag{4.2a}$$

$$\boldsymbol{P}^w_{k+1} = \begin{bmatrix} \boldsymbol{P}_{\boldsymbol{\phi}_k} & \boldsymbol{0} \\ \boldsymbol{0} & \boldsymbol{P}'_{\boldsymbol{\theta}_{k+1}} \end{bmatrix} \tag{4.2b}$$

where the superscript w represents the resulting state vector and its covariance matrix after a weather update. The sea state characteristics have been replaced by the acquired wave information $\boldsymbol{\theta}'_{k+1}$ and its covariance $\boldsymbol{P}'_{\boldsymbol{\theta}_{k+1}}$. In addition, the off-diagonal submatrices of the covariance matrix $\boldsymbol{P}^w_{k+1}$ are replaced by zeros.

4.2.2 Sigma-point and weight calculation

Then, the $2N+1$ sigma points $\boldsymbol{\mathcal{X}}_{k+1}$ are calculated based on the system state ($\boldsymbol{x}^w_{k+1}$ and $\boldsymbol{P}^w_{k+1}$) [102]:

$$\boldsymbol{\mathcal{X}}_{k+1,0} = \boldsymbol{x}^w_{k+1} \tag{4.3a}$$

$$\boldsymbol{\mathcal{X}}_{k+1,i} = \begin{cases} \boldsymbol{x}^w_{k+1} + \left[\sqrt{(N+\lambda)\boldsymbol{P}^w_{k+1}}\right]_i & \text{for } i = 1, 2, \ldots, N \\ \boldsymbol{x}^w_{k+1} - \left[\sqrt{(N+\lambda)\boldsymbol{P}^w_{k+1}}\right]_{i-N} & \text{for } i = N+1, \ldots, 2N \end{cases} \tag{4.3b}$$

$$\boldsymbol{\mathcal{X}}_{k+1} = [\boldsymbol{\mathcal{X}}_{k+1,0} \;\; \boldsymbol{\mathcal{X}}_{k+1,1} \;\; \cdots \;\; \boldsymbol{\mathcal{X}}_{k+1,2N}] \tag{4.3c}$$

where N is the system state dimension. Each column of $\boldsymbol{\mathcal{X}}_{k+1}$ is a sigma point. $\left[\sqrt{(N+\lambda)\boldsymbol{P}^w_{k+1}}\right]_i$ is the i^{th} column (or row) of the matrix square root of $(N+\lambda)\boldsymbol{P}^w_{k+1}$. There is no unique definition of the matrix square root operation since it is

extended from the square root of scalar numbers. A matrix $\boldsymbol{B}$ can be defined as the matrix square root of matrix $\boldsymbol{A}$ (positive semidefinite) if $\boldsymbol{B}\boldsymbol{B} = \boldsymbol{A}$ or $\boldsymbol{B}^\top\boldsymbol{B} = \boldsymbol{A}$ (factorization). There is often no unique solution of $\boldsymbol{B}$ following only one of these two definitions. $\boldsymbol{B}$ becomes unique when it fulfills both equations, and it is then called the principal square root of $\boldsymbol{A}$ [126]. In the relevant case studies within the present PhD project, the definition of principal square root was considered for the calculation in Equation (4.3b), based on the Schur method [127] from the SciPy package [95]. Note that even though the principal square root matrix is more intuitive, matrix factorization (e.g., Cholesky factorization) has been preferably applied as the matrix square root in the UKF algorithms due to its outstanding computational speed without compromising the UKF performance accuracy [127]. λ is calculated by [102]:

$$\lambda = \alpha^2(N + \kappa) - N \tag{4.4}$$

where α is called the scaling factor partially determining how far away the sigma points are from each other, and κ is normally set to be $3 - N$ or 0, as long as $N + \kappa \neq 0$.

According to Equation (4.3), $2N+1$ sigma points are calculated for a N-dimensional state. Each sigma point $\boldsymbol{\mathcal{X}}_{k+1,i}$, $i \in \{0, 1, \ldots, 2N\}$, is a deterministic system state vector that can be written as

$$\boldsymbol{\mathcal{X}}_{k+1,i} = \begin{bmatrix} \boldsymbol{\mathcal{X}}^{\boldsymbol{\phi}}_{k+1,i} \\ \boldsymbol{\mathcal{X}}^{\boldsymbol{\theta}}_{k+1,i} \end{bmatrix} \tag{4.5}$$

where $\boldsymbol{\mathcal{X}}^{\boldsymbol{\phi}}_{k+1,i}$ and $\boldsymbol{\mathcal{X}}^{\boldsymbol{\theta}}_{k+1,i}$ are the vessel state and sea state for $\boldsymbol{\mathcal{X}}_{k+1,i}$.

In addition, weight factors associated with those sigma points are calculated:

$$w_0^m = \frac{\lambda}{\lambda + N} \tag{4.6a}$$

$$w_0^c = \frac{\lambda}{\lambda + N} + 1 - \alpha^2 + \beta \tag{4.6b}$$

$$w_i^c = w_i^m = \frac{1}{2(\lambda + N)} \tag{4.6c}$$

where w^m and w^c are the weight factors for calculating the state mean and covariance matrix, respectively, and β, as a hyperparameter of UKF, equals 2 for Gaussian distributed variables.

4.2.3 System propagation

It is assumed to be a stationary system state during a sea state. Therefore, system propagation is simply formulated as:

$$\bar{\boldsymbol{x}}_{k+1} = \boldsymbol{x}^w_{k+1} + \boldsymbol{v} \tag{4.7a}$$

$$\bar{\boldsymbol{P}}_{k+1} = \boldsymbol{P}^{w}_{k+1} + \boldsymbol{Q} \tag{4.7b}$$

where $\bar{\boldsymbol{x}}_{k+1}$ and $\bar{\boldsymbol{P}}_{k+1}$ are the predicted state mean vector and covariance matrix after system propagation, respectively. Gaussian distributed $\boldsymbol{v} \sim \mathcal{N}(\boldsymbol{0}, \boldsymbol{Q})$ indicates the process disturbance, representing how well the stationary assumption holds for the considered state variables and the considered measurements within this updating loop $(k+1)$. $\boldsymbol{Q}$ is the process uncertainty covariance matrix.

4.2.4 Measurement update

The measurement update step plays a critical role in UKF-based tuning. First, design of the measurement space is very important for a successful tuning. Many quantities can be included to constitute the measurement space, such as STDs, variances, and zero-upcrossing periods of signals for (angular) displacements, velocities, and accelerations of 6-DOF vessel motions at a specific frequency or a range of frequencies. Those quantities considered in the designed measurement space can be estimated either from measurements or by calculations based on the predicted system state (i.e., sigma point). The measurement space where the considered quantities are derived directly from measurements is named the *observed measurement space*, while the measurement space where the considered quantities are estimated based on the predicted system state is named the *predicted measurement space*. Measurement signals should be filtered so that the first-order wave-induced vessel motions can be extracted as accurately as possible.

The observed measurement space, denoted by vector $\boldsymbol{z}$, can be formulated as:

$$\begin{aligned} \boldsymbol{z} =& [z_1 \quad z_2 \quad \dots \quad z_g \quad \dots \quad z_G]^\top \\ z_g \in& \{\dots, \sigma_{\eta_3}, \sigma_{\dot{\eta}_3}, \sigma_{\ddot{\eta}_3}, \sigma_{\eta_4}, \sigma_{\dot{\eta}_4}, \sigma_{\ddot{\eta}_4}, \dots, T_{z(\eta_3)}, T_{z(\eta_4)}, \dots\} \end{aligned} \tag{4.8}$$

where $T_{z(\eta_d)}$ is the zero-upcrossing period for vessel motion η_d of mode d, and $d \in \{1, 2, , \dots, 6\}$. Denote X to represent a specific vessel motion at a specific location, $X \in \{\eta_d, \dot{\eta}_d, \ddot{\eta}_d\}$ and $d = 1, 2, \dots, 6$. σ_X and $T_{z(X)}$ can be calculated, e.g., by Equation (2.10) in the frequency domain. The response spectrum can be obtained by estimating the periodogram [95] of the measurement signals. G is the total number of measurement quantities considered in the measurement space.

On the other hand, according to each sigma point $\boldsymbol{\mathcal{X}}_{k+1,i}$, the response spectrum $S_{XX,i}(\omega)$ can be calculated by:

Long-crested:

$$S_{XX,i}(\omega) = |H_X(\omega, \beta_W | \boldsymbol{\mathcal{X}}_{k+1,i})|^2 S_{\zeta\zeta,k+1}(\omega, \beta_W | \boldsymbol{\mathcal{X}}^{\boldsymbol{\theta}}_{k+1,i}) \tag{4.9a}$$

Short-crested:

$$S_{XX,i}(\omega) = \sum_{\beta_W} |H_X(\omega, \beta_W | \boldsymbol{\mathcal{X}}_{k+1,i})|^2 S_{\zeta\zeta,k+1}(\omega, \beta_W | \boldsymbol{\mathcal{X}}^{\boldsymbol{\theta}}_{k+1,i}) \Delta\beta_W \tag{4.9b}$$

where $H_X(\omega, \beta_W | \boldsymbol{\mathcal{X}}_{k+1,i})$ is the RAO between response X and wave elevation ζ according to the system state $\boldsymbol{\mathcal{X}}_{k+1,i}$ and $S_{\zeta\zeta,k+1}(\omega, \beta_W | \boldsymbol{\mathcal{X}}^{\boldsymbol{\theta}}_{k+1,i})$ is the wave spectrum according to the associated sea state $\boldsymbol{\mathcal{X}}^{\boldsymbol{\theta}}_{k+1,i}$.

Then, the quantities in the predicted measurement space can be calculated similarly by Equation (2.10), for each sigma point $\boldsymbol{\mathcal{X}}_{k+1,i}$. Subsequently, the predicted measurement vector corresponding to $\boldsymbol{\mathcal{X}}_{k+1,i}$, denoted by $\boldsymbol{\mathcal{Z}}_{k+1,i}$, can be assembled by those calculated quantities.

Finally, the measurement update step can be carried out by accounting for assessment at all the $2N + 1$ sigma points [102]:

$$\boldsymbol{\mathcal{Z}}_{k+1} = \sum_{i=0}^{2N} w_i^m \boldsymbol{\mathcal{Z}}_{k+1,i} \tag{4.10a}$$

$$\boldsymbol{y}_{k+1} = \boldsymbol{z}_{k+1} - \boldsymbol{\mathcal{Z}}_{k+1} \tag{4.10b}$$

$$\boldsymbol{P}_{\boldsymbol{z}_{k+1}} = \sum_{i=0}^{2N} w_i^c (\boldsymbol{\mathcal{Z}}_{k+1,i} - \boldsymbol{\mathcal{Z}}_{k+1})(\boldsymbol{\mathcal{Z}}_{k+1,i} - \boldsymbol{\mathcal{Z}}_{k+1})^\top + \boldsymbol{R}_{k+1} \tag{4.10c}$$

$$\boldsymbol{P}_{\boldsymbol{x}\boldsymbol{z}_{k+1}} = \sum_{i=0}^{2N} w_i^c (\boldsymbol{\mathcal{X}}_{k+1,i} - \bar{\boldsymbol{x}}_{k+1})(\boldsymbol{\mathcal{Z}}_{k+1,i} - \boldsymbol{\mathcal{Z}}_{k+1})^\top \tag{4.10d}$$

$$\boldsymbol{K} = \boldsymbol{P}_{\boldsymbol{x}\boldsymbol{z}_{k+1}} \boldsymbol{P}^{-1}_{\boldsymbol{z}_{k+1}} \tag{4.10e}$$

$$\boldsymbol{x}_{k+1} = \bar{\boldsymbol{x}}_{k+1} + \boldsymbol{K}\boldsymbol{y}_{k+1} \tag{4.10f}$$

$$\boldsymbol{P}_{k+1} = \bar{\boldsymbol{P}}_{k+1} - \boldsymbol{K}\boldsymbol{P}_{\boldsymbol{z}_{k+1}}\boldsymbol{K}^\top \tag{4.10g}$$

where $\boldsymbol{\mathcal{Z}}_{k+1} \in \mathbb{R}^G$ is the predicted measurement vector obtained by weighting the assessed $\boldsymbol{\mathcal{Z}}_{k+1,i}$ at all the $2N + 1$ sigma points. $\boldsymbol{y}_{k+1}$ is the residual vector between the observed and predicted measurement vector, and $\boldsymbol{P}_{\boldsymbol{z}_{k+1}} \in \mathbb{R}^{G\times G}$ approximately represents the covariance matrix of the system state in the measurement space, accounting for the uncertainties $\boldsymbol{R}_{k+1}$ from measurements and the applied measurement functions (i.e., Equations (2.9), (2.10), (4.8) and (4.9)). $\boldsymbol{P}_{\boldsymbol{x}\boldsymbol{z}_{k+1}} \in \mathbb{R}^{N\times G}$ represents the cross covariance of the system state in the state space and the measurement space. The updated state mean vector $\boldsymbol{x}_{k+1}$ and covariance matrix $\boldsymbol{P}_{k+1}$ are calculated based on the coefficient $\boldsymbol{K}$ known as the Kalman gain.

4.3 Demonstration by synthetic data

The proposed UKF-based algorithm was first demonstrated by numerical simulations based on Vessel A. Several case studies were documented in Paper A6 [93] to demonstrate that this algorithm can rationally tune both the vessel state and sea state simultaneously. Each case study considered 20 randomly generated sea states and the associated measurement signals of interesting vessel motion responses summarized in Table 2.5. Uncertainties of acquired sea state characteristics and measurement signals were considered, as shown in Table 4.1.

The tuning results of the base case in Paper A6 [93] are presented in the present section. The considered state space, its initialization, parameters related to synthetic signal generation, and hyperparameters related to the UKF are summarized in Table 4.1. The measurement space was selected, consisting of STDs of the 9 onboard vessel responses as shown in Table 2.5.

For illustrative purposes, new parameters are defined to quantify the performance for tuning sea state characteristics in terms of the reduction of absolute errors and variance:

$$\%\Delta\sigma^2_{H_s} = \frac{\sigma^2_{H_s} - \hat{\sigma}^2_{H_s}}{\sigma^2_{H_s}} \times 100\% \tag{4.11a}$$

$$\%\Delta\sigma^2_{T_p} = \frac{\sigma^2_{T_p} - \hat{\sigma}^2_{T_p}}{\sigma^2_{T_p}} \times 100\% \tag{4.11b}$$

$$\%\Delta\sigma^2_{\beta_W} = \frac{\sigma^2_{\beta_W} - \hat{\sigma}^2_{\beta_W}}{\sigma^2_{\beta_W}} \times 100\% \tag{4.11c}$$

$$\Delta\overline{H}_s = H^*_s - \overline{H}_s \tag{4.11d}$$

$$\Delta\overline{T}_p = T^*_p - \overline{T}_p \tag{4.11e}$$

$$\Delta\overline{\beta}_W = \beta^*_W - \overline{\beta}_W \tag{4.11f}$$

$$\Delta\hat{H}_s = H^*_s - \hat{H}_s \tag{4.11g}$$

$$\Delta\hat{T}_p = T^*_p - \hat{T}_p \tag{4.11h}$$

$$\Delta\hat{\beta}_W = \beta^*_W - \hat{\beta}_W \tag{4.11i}$$

where $\%\Delta\sigma^2_A$ represents the variance reduction in percentage, σ^2_A and $\hat{\sigma}^2_A$ are the variances of A before and after tuning, and $A \in \{H_s, T_p, \beta_W\}$. $\Delta\overline{A}$ is the difference between the true and acquired sea state characteristics, $\Delta\hat{A}$ is the difference between the true and updated A, and $\overline{A}$ and $\hat{A}$ represent the values of A after system propagation and after measurement update, respectively.

The tuning of vessel parameters β_{44} and XCG is illustrated in Figure 4.2. The

Table 4.1: Applied parameters for the base case simulation.

Parameter	Value
State $\boldsymbol{x}$	$\boldsymbol{x} = [\beta_{44}, XCG, H_s, T_p, \beta_W]^\top$
Initial $\boldsymbol{\phi}_0$	$\boldsymbol{\phi}_0 = [\beta_{44}, XCG]^\top = [7\%, 59.4m]^\top$
Initial $\boldsymbol{P}_{\boldsymbol{\phi}_0}$	$\boldsymbol{P}_{\boldsymbol{\phi}_0} = \text{diag}(0.035^2, 4.0^2)$
$\boldsymbol{R}$	$\boldsymbol{R} = 2\% \cdot \text{diag}(\hat{\sigma}_1^2, \ldots, \hat{\sigma}_J^2)$
$\boldsymbol{Q}$	$\boldsymbol{Q} = \text{diag}(0.005^2, 0.1, 0.05^2, 0.01, 0.25)$
α	0.01
β	2
κ	-2
H_s^* [1)]	Uniformly distributed in [1.0, 4.0] m
T_p^* [1)]	Uniformly distributed in [5.0, 20.0] s
β_W^* [1)]	Uniformly distributed in [0.0°, 360.0°]
σ_{H_s}	$10\% H_s^*$ m
σ_{T_p}	0.5 s
σ_{β_W}	5°
$\overline{H}_s$ [2)]	$H_s^* + \mathcal{N}(0, \sigma_{H_s}^2)$
$\overline{T}_p$ [2)]	$T_p^* + \mathcal{N}(0, \sigma_{T_p}^2)$
$\overline{\beta}_W$ [2)]	$\beta_W^* + \mathcal{N}(0, \sigma_{\beta_W}^2)$
Sea state duration	1800 s
SNR	50
f_{lp}	0.2 Hz

[1)] Superscript $*$ means the true value of the corresponding parameters, applied to generating synthetic signals.

[2)] The overlines over the parameters means that they are the simulated acquired values, which can be different from the true values.

tuned values approach their presumed true values, and the associated uncertainties are significantly reduced. Note that the simulated wave histories and vessel motion signals are different from the case studies presented in Chapter 3 due the different parameters applied for case simulations (e.g., the range of β_W, signal duration, and presumed true vessel loading condition) even though the same set of numerical

models of Vessel A is applied. Therefore, the tuning results illustrated in Figure 4.2 are not comparable to those presented in Chapter 3.

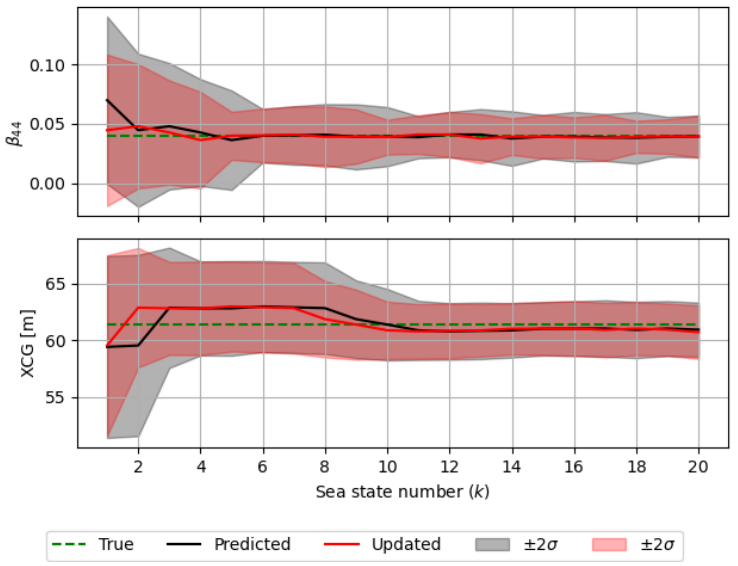

Figure 4.2: The results of tuning β_{44} and XCG for the base case.

Tunings of H_s, T_p, and β_W are illustrated in Figures 4.3–4.5. Clearly, the tuning algorithm proved to be capable of improving the knowledge about the corresponding sea states. It is worth mentioning that error reduction (i.e., $|\Delta\overline{A}| - |\Delta\hat{A}|$) and uncertainty reduction (i.e., $\%\Delta\sigma_A^2$) are different. For example, as shown in Figure 4.3 at $k = 13$, the tuned $\hat{H}_s$ has a larger error compared with the acquired $\overline{H}_s$, while the variance of H_s for this sea state reduces by approximately 40%. Due to the complex and nonmonotonous influence of T_p and β_W on the measurement space, tuning of T_p and β_W was less significant than that of H_s.

The uncertainties of variables in the system state are interactive. This means that improved knowledge on some variables can in return help to reduce uncertainties of the other variables in the system state, and vice versa. For example, when the uncertainties of the sea state vector $\boldsymbol{\theta}$ are increased compared with the presented case study, tuning will work harder to reduce the uncertainty of those sea state parameters [93]. This tuning algorithm has also proven to be feasible in the case of considering short-crested wave conditions in Paper A6 [93].

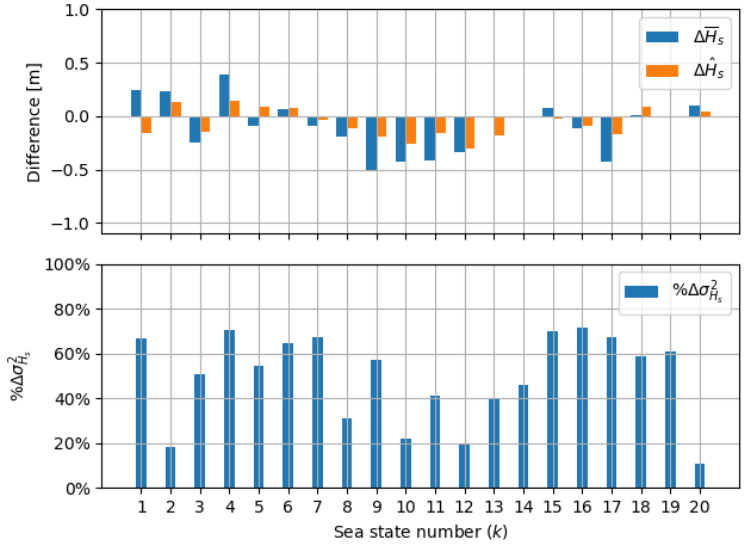

Figure 4.3: Illustration of the errors before and after tuning and the variance reduction for tuning of H_s for the base case.

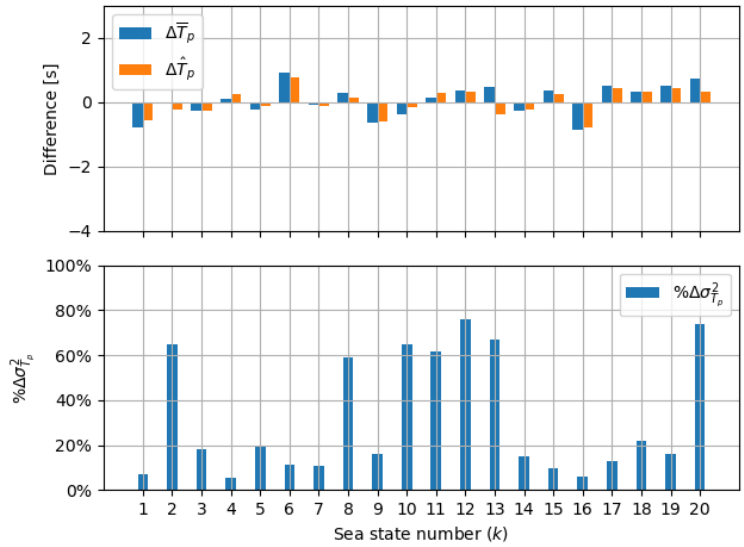

Figure 4.4: Illustration of the errors before and after tuning and the variance reduction for tuning T_p for the base case.

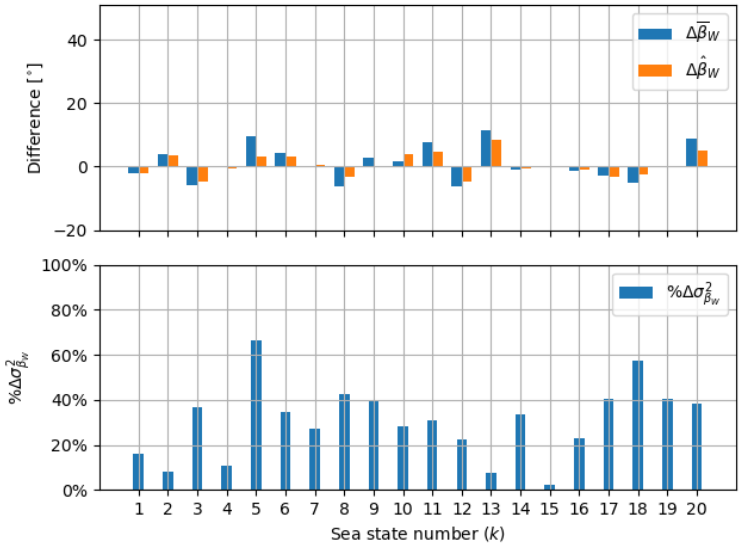

Figure 4.5: Illustration of the errors before and after tuning and the variance reduction for tuning of β_W for the base case.

4.4 Methodology validation by model-scale seakeeping tests

The UKF-based tuning algorithm was further validated by seakeeping model tests of Vessel B described in Section 2.2. Laboratory conditions provide perfect opportunity to control the environmental conditions (i.e., no influence from currents and wind and less uncertain wave spectra due to the calibration process) and relatively accurate vessel motion measurements.

The applied linear potential theory involves many simplifications, and consequently, the calculated RAOs may not be expected to perfectly represent the real vessel dynamics. In fact, seakeeping analysis through different codes can lead to significantly different RAOs [128, 129]. Generally, the estimated roll RAOs have the most significant uncertainties compared with the other 5 modes [128, 129].

The ShipX numerical model of Vessel B only considers the locations and dimensions of the three moonpools, in order to approximately obtain the correct vessel displacement volume and center of buoyancy. However, the applied ShipX model is not able to take into account the coupling and nonlinear effects between the moonpool resonance responses and the 6-DOF vessel rigid body motions, especially at the moonpool resonance periods [29, 130]. The seakeeping model tests were actually conducted to investigate the moonpool effects. Therefore, significant errors of the consequently calculated RAOs based on this simplified numerical

model of Vessel B are expected.

The seakeeping tests applied long-crested sea states, which allows direct calculation of the associated amplitudes of RAOs for that specific DOF, direction, and frequency range by $|H_X(\omega)| = \sqrt{S_{XX}(\omega)/S_{\zeta\zeta}(\omega)}$. The RAOs calculated based on wave and vessel motion measurements are named the *measured* RAOs, while the ShipX-simulated RAOs based on the numerical model with the specified true experimental loading condition ($\boldsymbol{x}^*$) are referred to as the *reference* RAOs. Significant errors due to simplifications of modeling and applied theory can be clearly observed by comparing the measured and reference RAOs, e.g., as illustrated in Figures 4.6 and 4.7. Such deviations are referred to as systematic errors.

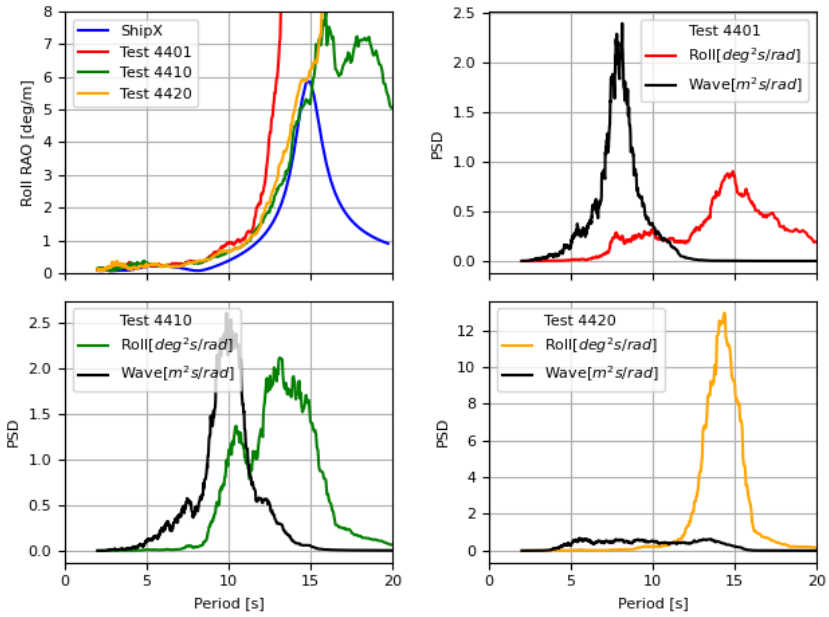

Figure 4.6: The measured roll RAOs and the reference roll RAO from the ShipX (VERES) simulation at beam sea (top left) and the power spectral densities (PSDs) of the measured waves and roll motions for Tests 4401, 4410, and 4420.

The systematic errors are inevitable in the seakeeping simulations, due to the imperfect representation of the real system dynamics. The systematic errors due to potential engineering errors and the ignorance of important effects (e.g., moonpool coupling effect) can usually be significant at the associated interesting frequencies; whereas, systematic errors due to reasonable simplifications (e.g., the infinitesimal response amplitude assumption in linear potential theory) are usually less significant.

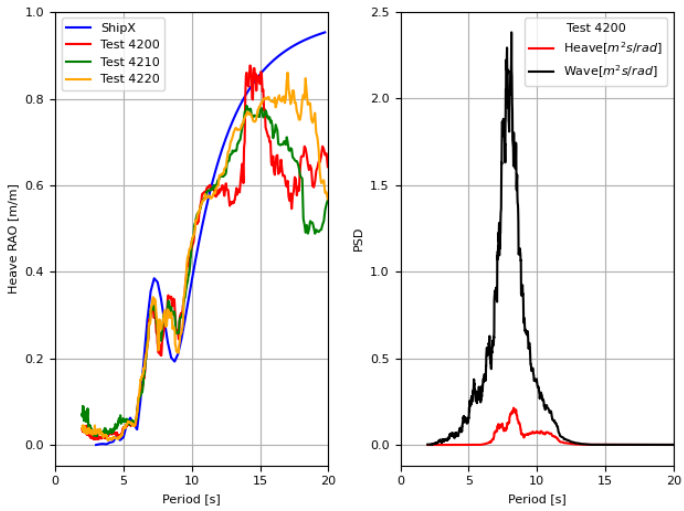

Figure 4.7: The measured heave RAO and the reference heave RAO from the ShipX (VERES) simulation for $\beta_W = 30°$ (left) and the power spectral densities (PSDs) of the measured waves and heave motions for Test 4200.

In practice, systematic errors cannot be determined deterministically and are usually case-dependent. Therefore, in order to identify and estimate the systematic errors for a proper design of the measurement space in the UKF model, sufficient theoretical background in hydrodynamics, engineering knowledge and experience on seakeeping modeling and selecting appropriate seakeeping analysis tools are highly required. Comprehensive benchmarking studies (e.g., [128, 129]) can help to identify these potential systematic errors.

The systematic errors of the seakeeping simulations can be reduced by, e.g., 1) increasing model fidelity; 2) removing some theoretical simplifications (e.g., by taking into account the moonpool coupling effects for this case study); 3) fusing seakeeping analysis results from multiple seakeeping programs; and 4) improving the modeling quality by e.g., thorough quality assurance.

It is important for successful tuning to carefully design the measurement space by taking into account such systematic errors. Paper A7 [87] demonstrated the critical influence of the design of the measurement space on the tuning results (Case 1, Case 2, and Case 4). It was concluded that a more informative measurement space (e.g., including measurement derivatives and higher-order moments of the associated response spectra) can improve tuning performance only if the software-simulated RAOs can sufficiently accurately present the real vessel dynamics.

As previously explained, the tuning of seakeeping parameters based on vessel and wave data is a multimodal and nonlinear problem. Therefore, the weighted statistical linear regression in UKF cannot perfectly capture the system nonlinearity either globally or locally. The tuning can be sensitive to the selection of sigma points, which can be influenced by the design of the state space. Paper A7 [87] also demonstrated the influence of the design of the state space on the tuning results (Case 3).

Through careful design of state and measurement spaces, deviated tuning results due to systematic errors can be largely overcome, such as the tuning results of Case 4, illustrated in Figure 4.8. Tables 4.2 and 4.3 summarizes the design of the state and measurement spaces, including considered variables in the state space and quantities in the measurement space, their initialization, and the design of the associated uncertainty covariance matrices $\boldsymbol{P}$, $\boldsymbol{Q}$, and $\boldsymbol{R}$. Due to quality control and calibration in a laboratory environment, the measurements of waves and vessel motions were quite accurate. Therefore, $\boldsymbol{\theta}$ is not included as part of the system state, as shown in Equation (4.1). The selection of state space was based on a parametric sensitivity study of the Vessel B seakeeping model. ShipX (VERES) can estimate the linearized additional roll damping based on semiempirical Ikeda's formulas [6, 131, 132, 112], denoted by β_{44}^{VER}. The state space hence consists of a variable $\beta_{44}^{'}$ representing the residual between the true and VERES estimated linearized additional roll damping. Those damping terms in $\boldsymbol{x}$ are in units of percentage.

Table 4.2: Parameters applied in Case 4 related to UKF modeling.

Parameter	**Value**
State space $\boldsymbol{x}$	$\boldsymbol{x} = [\beta_{33}, \beta_{44}^{'}, \beta_{55}, \text{ZCG}, r_{44}, r_{55}]^\top$
Initial $\boldsymbol{x}_0$	$\boldsymbol{x}_0 = [2, 2, 2, 10.79, 12, 41]^\top$
Initial $\boldsymbol{P}_0$	$\boldsymbol{P}_0 = \text{diag}(25, 64, 25, 0.04, 4, 25)$
$\boldsymbol{Q}$	$\boldsymbol{Q} = \text{diag}(0.25, 0.25, 0.25, 0.05^2, 0.09, 0.25)$
Measurement space	$\beta_W < 90°$: $[\sigma_{\eta_3}, \sigma_{\eta_5}, \sigma_{\dot{\eta}_3}, \sigma_{\dot{\eta}_5}, \sigma_{\ddot{\eta}_3}, \sigma_{\ddot{\eta}_5}, T_{z(\eta_3)}, T_{z(\eta_5)}]$ $\beta_W \geq 90°$: $[\sigma_{\eta_3}, \sigma_{\eta_4}, \sigma_{\dot{\eta}_3}, \sigma_{\ddot{\eta}_3}, T_{z(\eta_3)}]$
$\boldsymbol{R}$	Table 4.3

Like any other applications using the Kalman filter family, unbiased results require that the process model and measurement function reflect the real behavior of the system dynamics. However, the measurement functions applied in the case studies are simplified without accounting for the coupling and nonlinear effects

Table 4.3: Candidates of diagonal elements of $\boldsymbol{R}$ for Case 4.

Parameter	Description	Value
$\sigma_N^2(X_3)^*$	variance of σ_{X_3}	$\max(2\%\sigma_{X_3}^2, 10^{-6})$
$\sigma_N^2(X_4)^*$	variance of σ_{X_4} [2)]	$\max(9\%\sigma_{X_4}^2, 10^{-4})$
$\sigma_N^2(X_5)^*$	variance of σ_{X_5} [3)]	$\beta_W < 90°$: $\max(\underline{2\%}\sigma_{X_5}^2, 10^{-4})$; otherwise: $\max(5\%\sigma_{X_5}^2, 10^{-4})$
$\sigma_N^2(T_z)$	Noise variance of T_z for η_3, η_4, η_5	0.1 s^2 for η_3 and η_5; 0.25 s^2 for η_4

* $X_3 \in \{\eta_3, \dot{\eta}_3, \ddot{\eta}_3\}$; $X_4 \in \{\eta_4, \dot{\eta}_4, \ddot{\eta}_4\}$; $X_5 \in \{\eta_5, \dot{\eta}_5, \ddot{\eta}_5\}$

from moonpools. Consequently, the simulated RAOs applied in these measurement functions are significantly biased at some interesting frequencies, potentially leading to overall biased tuning of uncertain vessel parameters.

An example, named Case 1, is given in Paper A7 [87], where the zero up-crossing period of the pitch angular displacement and the STDs of the pitch angular displacement, velocity, and acceleration were included in the measurement space for all wave directions. As shown in Figure 4.9(f), the systematic errors for pitch estimation leads to a largely deviated tuning of r_{55}, e.g., at $k = 19$ in Case 1 ($r_{55} = 49.3$ m after $k = 19$, while $r_{55}^* = 44.8$ m). $k = 19$ corresponds to Test 4510 with $T_p = 10$ s and $\beta_W = 150°$.

However, the biased estimation of r_{55} in $\boldsymbol{x}_{19}$ actually reduces the residual $\boldsymbol{y}_{19}$, so that the updated prediction of quantities in the measurement space approaches the measured value for that specific sea state under tuning. This is demonstrated in Figure 4.10 that at $k = 19$ the updated pitch RAO at $\beta_W = 150°$ (i.e., the red curve) is significantly improved compared with the associated reference RAO (i.e., the blue curve), particularly at approximately $T_p = 10$ s. This is guaranteed because Kalman filters update the state estimate as a compromise between the predicted and observed measurement space at that time instant.

However, such biased vessel state estimation might significantly increase motion prediction errors for other frequencies and directions of interest. For example, as shown in Figure 4.11, the corresponding pitch RAO at $\beta_W = 0°$ based on $\boldsymbol{x}_{19}$ (i.e., the red curve) is significantly deviated from both the measured RAOs and the associated reference RAO. Based on the biasedly tuned vessel parameters at $k = 19$, significantly improved prediction accuracy for the pitch response can be

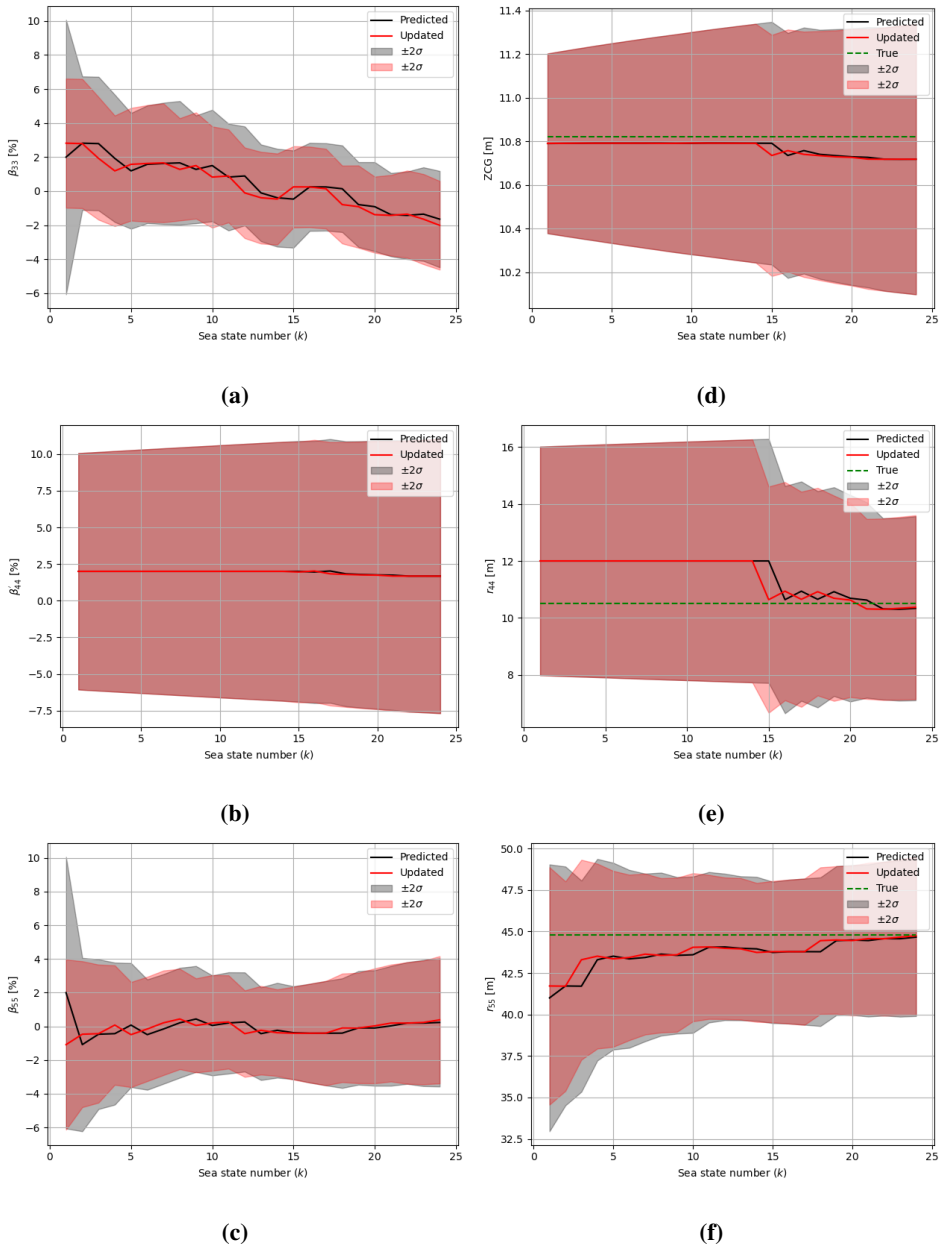

Figure 4.8: The state estimation for Case 4 after system propagation ("Predicted") and measurement update ("Updated") for each model test case described in Table 2.6. Subplots illustrate the tuning of (a) β_{33}; (b) $\beta_{44}^{'}$; (c) β_{55}; (d) ZCG; (e) r_{44}; (f) r_{55}.

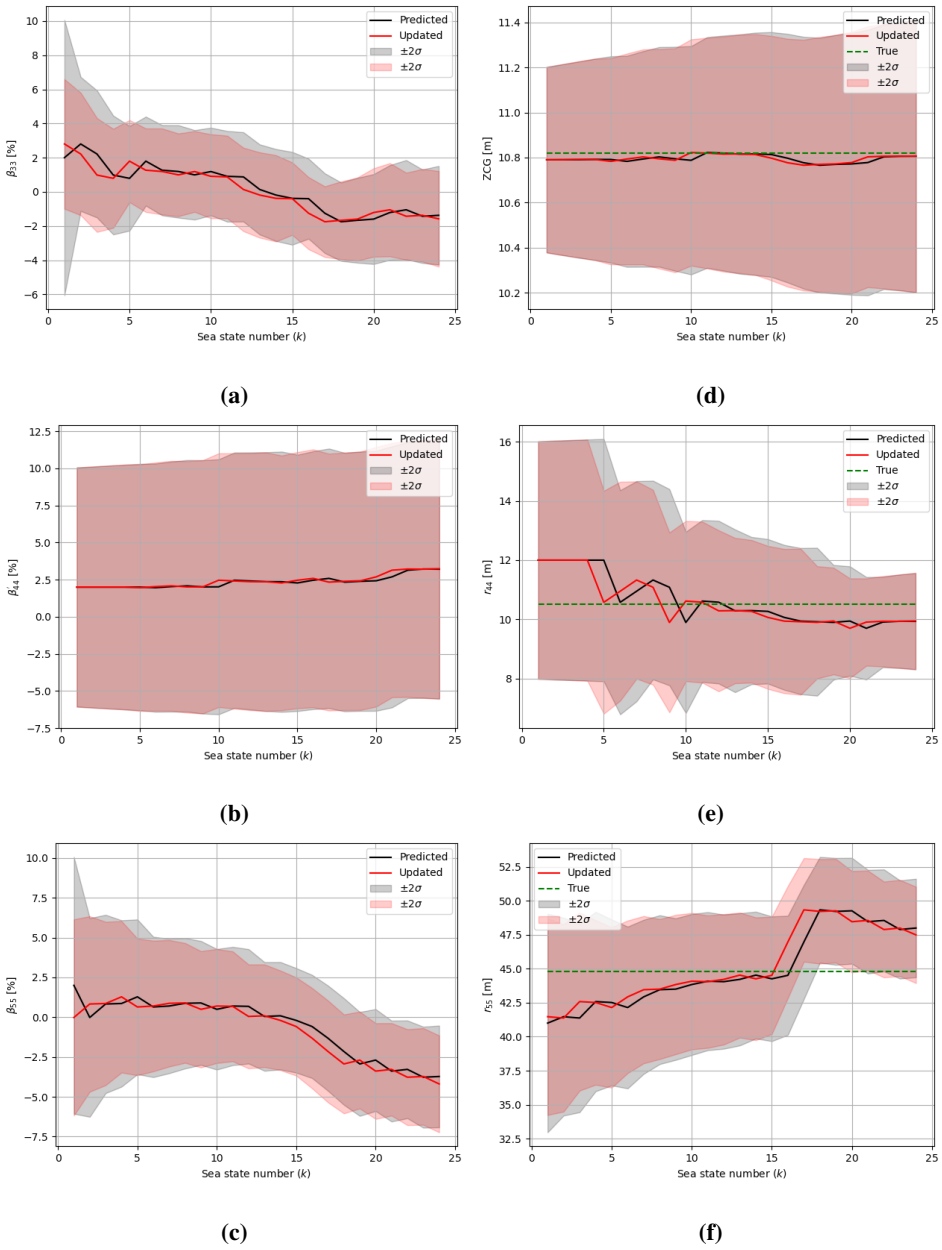

Figure 4.9: The state estimation for Case 1 after system propagation ("Predicted") and measurement update ("Updated") for each model test case described in Table 2.6. Subplots illustrate the tuning of (a) β_{33}; (b) $\beta_{44}^{'}$; (c) β_{55}; (d) ZCG; (e) r_{44}; (f) r_{55}.

expected for the sea states similar to the one at $k = 19$, but not for sea states at $\beta_W = 0°$.

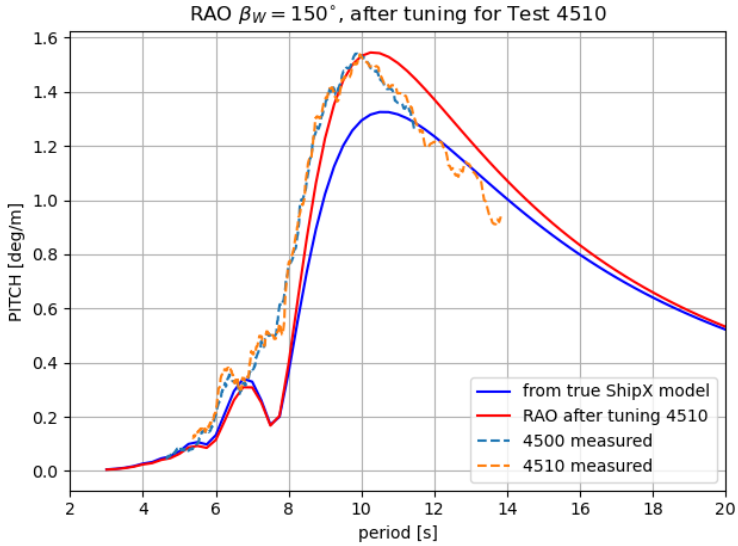

Figure 4.10: The pitch RAOs for $\beta_W = 150°$. Blue: the simulated reference RAO based on $\boldsymbol{x}^*$; red: the VERES-simulated RAO based on $\boldsymbol{x}_{19}$, i.e., after tuning for Test 4510 ($k = 19$); dashed: RAOs estimated directly from the measurements for $\beta_W = 150°$.

Considering environmental conditions with slow-varying sea states, when the objective of tuning is to improve vessel motion prediction accuracy for the next few sea states similar to the tuned sea states, systematic errors from seakeeping simulations and the consequent biased tuning of vessel parameters become less important. Thus, like demonstrated in Case 1, designing a more informative measurement space is recommended.

However, tuning vessel parameters based on a limited number of observations offers an unique opportunity of updating the complete RAO set for all directions and frequencies based on those tuned vessel parameters and potentially improving the prediction accuracy for the future unobserved sea states. Such a success of tuning vessel parameters and predicting vessel motions relies on a fundamental assumption that the applied seakeeping simulation and resulting RAOs can well represent the real system dynamics. This is usually acceptable for conventional ships at moderate seas which typical marine operations are mostly interested in. For an unbiased tuning of vessel parameters, a proper design of the measurement space becomes critical in the cases with significant systematic errors in the seakeeping simulations such as the presented study for Vessel B with open moonpools.

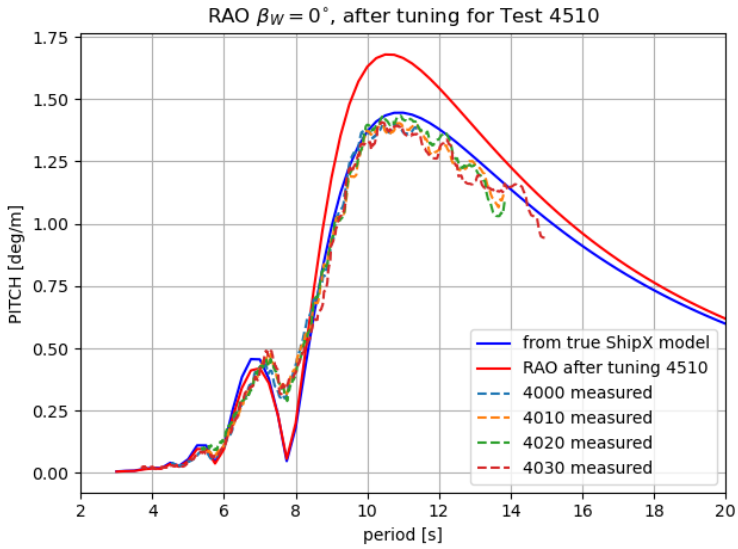

Figure 4.11: The pitch RAOs for $\beta_W = 0°$. Blue: the simulated reference RAO based on $\boldsymbol{x}^*$; red: the VERES-simulated RAO based on $\boldsymbol{x}_{19}$, i.e., after tuning for Test 4510 ($k = 19$); dashed: RAOs estimated directly from the measurements for $\beta_W = 0°$.

Designing the UKF model is expected to be project-dependent, such as depending on the seakeeping model tuning objective, the considered vessel and operational condition, the available seakeeping tools, the measuring system, the interesting vessel responses, etc.

The following practices of designing UKF model are recommended for an unbiased (or at least less biased) tuning of vessel parameters and securing proper response predictions being on the safe side in a probabilistic manner:

1) For the interesting responses with less systematic errors, larger variance values in $\boldsymbol{R}$ for the associated quantities in the measurement space can be designed to avoid overconfident tuning and response predictions.

2) While in the cases with significant systematic errors, less informative measurement space shall be designed for the relevant response modes. This is demonstrated by comparing the tuning results for Case 4 and Case 1. With the design of a less informative roll- and pitch-related measurement space, the tuning of r_{44} (Figure 4.8(e)) and r_{55} (Figure 4.8(f)) becomes less deviated but with larger variance values (so as to avoid overconfident tuning) in Case 4, compared with Case 1 (i.e., Figures 4.9(e) and 4.9(f)).

Chapter 5

Conclusions and Future Work

5.1 Conclusions

Research on the online identification and uncertainty estimation of vessel seakeeping model parameters based on onboard vessel and wave data has been conducted. Important VCRPs (contained in the vector ϕ) were identified through quantitative sensitivity assessment for the Vessel A seakeeping model. Their relative importance varies with wave and vessel conditions as well as the location and mode of the interesting response. It is necessary to include all uncertain vessel parameters throughout the tuning process to partially avoid tuning incorrect parameters.

Two tuning algorithms were proposed, developed and demonstrated, i.e., DBI-based and UKF-based tuning algorithms. For online tuning purposes, the DBI-based tuning algorithm requires predefining the uncertainty ranges of ϕ based on relevant prior knowledge and then establishing a corresponding RAO database at discrete points over the ϕ uncertainty domain. The tuning is performed by updating the discrete joint probability distribution of ϕ based on the Bayesian theorem. The likelihood at each discrete point is considered inversely proportional to the difference between the observed and predicted STDs of the interesting vessel response and hence estimated by inverse distance weighting formulation. Consequently, the nonlinear relationship between ϕ and the STD of the considered vessel response can be fully captured through this tuning process. This can be important in relation to a quantitative risk assessment.

However, it can be too computationally expensive to maintain such nonlinear information for real onboard applications when a large number of uncertain vessel parameters should be included. A UKF-based tuning algorithm is thus proposed,

assuming multivariate Gaussian distributed $\boldsymbol{\phi}$. Only the statistical information of the first two orders related to $P(\boldsymbol{\phi})$ is captured and updated through the tuning. The scaling factor α of the UKF model balances the influences of global and local system nonlinearity on the updating by determining the distances between the sigma points. For the purposes of online model tuning and real-time vessel motion prediction, the greatly improved computational efficiency of the UKF-based tuning algorithm is believed to have high potential for real applications. In addition, the online tuning system may have sufficient time to allow seakeeping simulations in the frequency domain during the tuning process. This means that the pre-established RAO database can be avoided, offering a more flexible way to handle the potentially varying uncertainty domain (e.g., due to variation of vessel conditions or uncertainties).

Uncertainties associated with the acquired measurements and wave information are considered in both algorithms. The framework of the UKF-based algorithm can further simultaneously reduce wave information uncertainties by including a sea state vector in the system state.

Success of the tuning process requires the following:

1. All the influential vessel parameters are included in $\boldsymbol{\phi}$ (i.e., state space). Both algorithms will tune $\boldsymbol{\phi}$ most efficiently to reduce the difference between interesting quantities from measurements and predictions (i.e., residual) within the entire uncertainty domain of $\boldsymbol{\phi}$. If an important uncertain vessel parameter is missed in $\boldsymbol{\phi}$, the algorithms will tune the others to reduce the residual. Consequently, the tuned $\boldsymbol{\phi}$ and RAOs probably still improve the response estimation at the present sea state; however, $\boldsymbol{\phi}$ will most likely deviate from the truth, leading to increased errors of RAOs for other wave conditions.

2. One should understand the systematic errors induced from seakeeping simulations. Different simplifications are made for different seakeeping analysis codes with varying levels of model fidelity, leading to a variety of model uncertainties (i.e., systematic errors). These systematic errors cannot be reduced by tuning $\boldsymbol{\phi}$. However, both tuning algorithms cannot distinguish the residuals caused by systematic errors versus random variations of $\boldsymbol{\phi}$.

3. Consequently, the interesting measurement quantities (i.e., measurement space) should be carefully selected to take care of the systematic errors. An increasingly informative measurement space including higher-order information in relation to the response spectrum (e.g., m_2, m_4, and T_z) can only improve the tuning performance for the motion modes with insignificant systematic

errors. A more informative measurement space generally increases the deviation of the tuned parameters related to the motion modes in the case of significant systematic errors (e.g., for the roll motion).

An adaptive lowpass filter was proposed, aiming at finding the sea state dependent optimal cutoff frequency f_{lp}^* to remove signal noise as accurately as possible. Instead of establishing a direct relation between the sea state and f_{lp}^*, two parameters θ and γ were introduced based on the special relationship between the lowpass filter cutoff frequency and the resulting σ and T_z of the filtered vessel motion signals to find f_{lp}^* without any sea state information being available. This algorithm does not require stationarity of the signals, but setting criteria on θ and γ may be vessel dependent. Overly relaxed θ and γ criteria are highly risky with respect to overfiltered signals. Statistical improvement in the tuning of ϕ was demonstrated by case studies applying this adaptive lowpass filter.

A GPR model using the RBF kernel was proposed to handle the sea state dependent parameters. The GPR model is involved in the tuning loop, updated by the available tuning results and providing improved prior knowledge of those sea state dependent parameters across the whole input uncertainty domain. Such a modification of the tuning process is necessary for real applications, which is expected to significantly improve the relevant motion prediction for the most interesting environmental conditions. However, such a model might not be applicable to motion prediction for extreme environmental conditions due to a lack of available samples.

5.2 Contributions

With reference to the research questions raised in Section 1.2, the main original contributions of the present PhD project based on the 7 included papers are summarized in this section.

Q1) *Which parameters are influential to the system dynamics and vessel motions, and therefore important to include in the tuning process?*

Through the sensitivity studies documented in Paper A1 [84], the important parameters were identified. The variation of their relative importance with sea state and loading conditions was also reported in Paper A1, which serves as a solid reference for the scope of the case studies in the following papers, supporting the explanation of some tuning results.

Q2) *How can those parameters be tuned?*

Paper A2 [90] initially answered this question by proposing a DBI-based seakeeping model tuning algorithm. Then, Paper A3 [91] proposed an algorithm,

aiming at finding the optimal sea state dependent lowpass filter cutoff frequency to optimally filter out high-frequency signal noise and improve the tuning results. Considering that some important uncertain vessel parameters are sea state dependent, Paper A4 [92] modified the original DBI-based algorithm by introducing a GPR model into the tuning process. This GPR model of sea state dependent parameters can be trained by new tuning results and in return improves the prior knowledge on those parameters for future sea states. Based on the algorithm proposed in Paper A2, Paper A5 [103] proposed how to account for the uncertainties of historical wave data. To solve the "curse of dimensionality" of this DBI-based algorithm [106], Paper A6 [93] proposed a new algorithm based on UKF, dramatically increasing the computational efficiency. As a compromise, the nonlinearity of model tuning is linearized by implicit weighted statistical linear regression, and the uncertain parameters are assumed to be multivariate Gaussian distributed. As a side bonus, this UKF-based tuning algorithm can also simultaneously improve the wave data accuracy.

Q3) *How can measurements be used?*

Papers A1 to A6 use the signal standard deviations of interesting responses for seakeeping model tuning. Paper A7 [87] further extended the possibility by using response zero-upcrossing periods (T_z) in the tuning procedure. In addition, Paper A7 has extensively demonstrated the importance of designing the measurement space with existing systematic errors for the sake of achieving unbiased tuning results.

Q4) *How should the uncertainties associated with environmental conditions, numerical vessel hydrodynamic model, and measurement data be represented, quantified, and considered through the tuning process, such that the uncertainties of the tuned parameters can be estimated?*

This question is answered by developing tuning algorithms that can quantitatively account for the aforementioned uncertainties. However, the DBI-based algorithm can only quantitatively account for uncertainties of wave data and deal with vessel motion measurement uncertainties by signal filtering. The DBI-based algorithm should be developed in the future to account for the uncertainties associated with the numerical vessel hydrodynamic model, i.e., the systematic errors. On the other hand, the UKF-based algorithm considers all three uncertainty sources by designing the state and measurement spaces and the associated covariance matrices $\boldsymbol{P}_0$, $\boldsymbol{Q}$, and $\boldsymbol{R}$. This has been thoroughly explained in Papers A6 [93] and A7 [87]. In addition, the possible change in vessel condition and the associated uncertainty of the system state can be

accounted for in $\boldsymbol{Q}$, possibly by introducing control inputs in the UKF-based tuning algorithm.

Q5) *How can such a tuning algorithm be applied to relevant applications?*

The fundamental objective is to improve the accuracy of vessel motion prediction in real time and to provide necessary onboard decision support to increase the safety and cost efficiency of any offshore activities involving floating structures. As a potential application, Paper A5 [103] describes a general framework for a quantitative risk-based decision support system involving online seakeeping model tuning to achieve such an objective. Operational safety and cost efficiency can consequently be increased by improving the knowledge about onboard vessel dynamics and the prediction accuracy of interesting responses and further by optimizing operations based on quantitative risk assessment.

5.3 Recommendations for future work

Admittedly, onboard tuning and uncertainty estimation of vessel seakeeping parameters is still at a very early conceptual development phase. Significant efforts on algorithm development and validation are expected in the future. Systematically selecting the important vessel parameters should be studied. The design of ϕ in the PhD project was based on simple parametric sensitivity studies. The resulting conclusions may not be generally applicable. Therefore, a reliable, robust, and efficient way of designing ϕ is needed in practice to optimize the computational efficiency by limiting the number of considered vessel parameters. More importantly, the design of the measurement space and handling the measurement uncertainties are extremely critical to the tuning results and therefore worth deeper investigation.

Most importantly, the algorithms should be validated based on full-scale on-site cases. Consequently, many previously simplified conditions must be taken into account:

1. Tuning algorithms should be further developed to account for the influences of vessel forward speed and water depth and the uncertainties of wave spreading, wave spectral type, etc. In addition, the effects of current and wind on the first-order vessel response should be considered.

2. Vessel motion measurement signals contain first-order and higher-order motions, noise, and even sensor faults. Fault detection, isolation, and diagnosis may be required for full-scale tests [133]. The accuracy associated with the

extraction of first-order wave-induced motions is essential for tuning performance. However, frequency overlap between first-order and higher-order motions has been observed. Future research should answer how to extract first-order vessel motions from signals containing all different components with overlapping frequencies.

3. Practically, the numerical seakeeping model assumes rigid body motions. However, the measured motion at the point of interest is not according to a perfect rigid body transformation relative to the reference point (e.g., COG). Therefore, a "flexibility" parameter might have to be introduced to take into account the uncertainties due to assuming the vessel dynamic system to be a perfect rigid body.

4. The proposed tuning algorithms assume stationary vessel and wave conditions within each tuning step. However, some critical marine operations are strongly nonstationary, e.g., heavy lift. Therefore, future research should solve how to apply the recently tuned vessel parameters to critical response prediction for nonstationary operations in real time. Further algorithm developments are preferred in terms of identifying such nonstationary conditions and possibly tuning parameters during the nonstationary phase.

Bibliography

[1] DNVGL-ST-N001. Marine operations and marine warranty. *Technical Report*, DNV GL 2016.

[2] BMT Fluid Mechanics Limited. Review of the role of response forecasting in decision-making for weather-sensitive offshore operations. *Technical Report*, HSE - Health & Safety Executive 2005. Research Report 347.

[3] Gudmestad OT. Waiting on suitable weather to perform marine operations. *Proceedings of the Fourth International Conference in Ocean Engineering (ICOE2018)*, Springer Singapore: Singapore, 2019; 3–12.

[4] Faltinsen OM. *Sea loads on ships and offshore structures*. Cambridge University Press Cambridge ; New York, 1990.

[5] Kring DC. Time domain ship motions by a three-dimensional rankine panel method. PhD Thesis, Massachusetts Institute of Technology, Department of Ocean Engineering 1994.

[6] Fathi DE, Hoff JR. Shipx vessel responses (VERES), theory manual. *Technical Report*, SINTEF Ocean AS 2017.

[7] Guachamin Acero W, Li L, Gao Z, Moan T. Methodology for assessment of the operational limits and operability of marine operations. *Ocean Engineering* 2016; **125**:308–327, doi:https://doi.org/10.1016/j.oceaneng.2016.08.015.

[8] Tan SG. Seakeeping considerations in ship design and operations. *MARIN, Wageningen, Presented at: Regional Maritime Conference, Indonesia, Report 635001-Paper*, 1995.

[9] Zhao X, Xu R, Kwan C. Ship-motion prediction: Algorithms and simulation results. *2004 IEEE International Conference on Acoustics, Speech, and Signal Processing*, vol. 5, IEEE, 2004; V–125.

[10] De Masi G, Gaggiotti F, Bruschi R, Venturi M. Ship motion prediction by radial basis neural networks. *2011 IEEE Workshop On Hybrid Intelligent Models And Applications*, 2011; 28–32, doi:10.1109/HIMA.2011.5953967.

[11] Zhang W, Liu Z. Real-time ship motion prediction based on time delay wavelet neural network. *Journal of Applied Mathematics* 2014; .

[12] Kawan B, Wang H, Li G, Chhantyal K. Data-driven modeling of ship motion prediction based on support vector regression. *Proceedings of the 58th Conference on Simulation and Modelling (SIMS 58)*, 2017.

[13] Li G, Kawan B, Wang H, Zhang H. Neural-network-based modelling and analysis for time series prediction of ship motion. *Ship Technology Research* 2017; **64**(1):30–39, doi:10.1080/09377255.2017.1309786.

[14] Nielsen UD, Brodtkorb AH, Jensen JJ. Response predictions using the observed autocorrelation function. *Marine Structures* 2018; **58**:31 – 52, doi:https://doi.org/10.1016/j.marstruc.2017.10.012.

[15] Takami T, Nielsen UD, Jensen JJ. Real-time deterministic prediction of wave-induced ship responses based on short-time measurements. *Ocean Engineering* 2021; **221**:108 503, doi:https://doi.org/10.1016/j.oceaneng.2020.108503. URL https://www.sciencedirect.com/science/article/pii/S0029801820314104.

[16] Makridakis S, Andersen A, Carbone R, Fildes R, Hibon M, Lewandowski R, Newton J, Parzen E, Winkler R. The accuracy of extrapolation (time series) methods: Results of a forecasting competition. *Journal of forecasting* 1982; **1**(2):111–153.

[17] Makridakis S, Chatfield C, Hibon M, Lawrence M, Mills T, Ord K, Simmons LF. The m2-competition: A real-time judgmentally based forecasting study. *International Journal of Forecasting* 1993; **9**(1):5 – 22, doi:https://doi.org/10.1016/0169-2070(93)90044-N.

[18] Makridakis S, Hibon M. The m3-competition: Results, conclusions and implications. *International journal of forecasting* 2000; **16**(4):451–476.

[19] Makridakis S, Spiliotis E, Assimakopoulos V. The m4 competition: Results, findings, conclusion and way forward. *International Journal of Forecasting* 2018; **34**(4):802–808.

[20] Assimakopoulos V, Nikolopoulos K. The theta model: a decomposition approach to forecasting. *International journal of forecasting* 2000; **16**(4):521–530.

[21] Hyndman RJ, Billah B. Unmasking the theta method. *International Journal of Forecasting* 2003; **19**(2):287 – 290, doi:https://doi.org/10.1016/S0169-2070(01)00143-1.

[22] Yue DK, Liu Y, Hendrickson K, Wu G, Xiao W, Henry L. Nonlinear wave environments for ship analysis. 27th Symposium on Naval Hydrodynamics, 2008.

[23] Nouguier F, Grilli ST, Guérin C. Nonlinear ocean wave reconstruction algorithms based on simulated spatiotemporal data acquired by a flash LIDAR camera. *IEEE Transactions on Geoscience and Remote Sensing* March 2014; **52**(3):1761–1771, doi:10.1109/TGRS.2013.2254494.

[24] Vestbøstad TM. A numerical study of wave-in-deck impact using a two-dimensional constrained interpolation profile method. PhD Thesis, Norwegian University of Science and Technology 2009.

[25] *Second Order Roll Motions for FPSO's Operating in Severe Environmental Conditions*, *OTC Offshore Technology Conference*, vol. All Days, doi:10.4043/18906-MS. URL https://doi.org/10.4043/18906-MS, oTC-18906-MS.

[26] Cao Y, Tahchiev G, Zhang F, Aarsnes JV, Glomnes EB. Effects of Hydrostatic Nonlinearity on Motions of Floating Structures. *Proceedings of ASME 2010 29th International Conference on Ocean, Offshore and Arctic Engineering*, *International Conference on Offshore Mechanics and Arctic Engineering*, vol. 4, 2010; 257–267, doi:10.1115/OMAE2010-20439.

[27] Faltinsen OM. Hydrodynamics of marine and offshore structures. *Journal of Hydrodynamics, Ser. B* 2015; **26**(6):835 – 847.

[28] Larsen CM, Lian W, Bachynski E, Kristiansen T, Myrhaug D. Lecture notes for course TMR4182 marine dynamics. *Technical Report*, Department of Marine Technology, NTNU, Trondheim 2019.

[29] Ravinthrakumar S, Kristiansen T, Molin B, Ommani B. Coupled vessel and moonpool responses in regular and irregular waves. *Applied Ocean Research* 2020; **96**.

[30] Hanssen FCW. Non-linear wave-body interaction in severe waves. PhD Thesis, Norwegian University of Science and Technology 2019.

[31] Kim SP. CFD as a seakeeping tool for ship design. *International Journal of Naval Architecture and Ocean Engineering* 2011; **3**(1):65 – 71, doi:https://doi.org/10.2478/IJNAOE-2013-0046.

[32] Irkal MA, Nallayarasu S, Bhattacharyya S. CFD approach to roll damping of ship with bilge keel with experimental validation. *Applied Ocean Research* 2016; **55**:1–17.

[33] ECMWF. *Part VII: ECMWF Wave Model*, chap. 7. IFS Documentation, ECMWF, 2016. URL https://www.ecmwf.int/node/16651.

[34] Hersbach H, Bell B, Berrisford P, Hirahara S, Horányi A, Muñoz-Sabater J, Nicolas J, Peubey C, Radu R, Schepers D, *et al.*. The ERA5 global reanalysis. *Quarterly Journal of the Royal Meteorological Society* 2020; **146**(730):1999–2049, doi:https://doi.org/10.1002/qj.3803. URL https://rmets.onlinelibrary.wiley.com/doi/abs/10.1002/qj.3803.

[35] Tolman HL, Balasubramaniyan B, Burroughs LD, Chalikov DV, Chao YY, Chen HS, Gerald VM. Development and implementation of wind-generated ocean surface wave modelsat ncep. *Weather and forecasting* 2002; **17**(2):311–333.

[36] Nielsen J, Pedersen N, Michelsen J, Nielsen U, Baatrup J, Jensen J, Petersen E. Seasense - real-time onboard decision support. *World Maritime Technology Conference*, 2006.

[37] Nielsen UD. Estimations of on-site directional wave spectra from measured ship responses. *Marine Structures* 2006; **19**(1):33 – 69, doi:https://doi.org/10.1016/j.marstruc.2006.06.001.

[38] Iseki T. Real-time estimation of directional wave spectra using non-stationary ship motion data. *Proceedings of ASME 2009 28th International Conference on Ocean, Offshore and Arctic Engineering*, International Conference on Offshore Mechanics and Arctic Engineering, 2009; 673–678, doi:10.1115/OMAE2009-79295.

[39] Nielsen UD. A concise account of techniques available for shipboard sea state estimation. *Ocean Engineering* 2017; **129**:352 – 362, doi:https://doi.org/10.1016/j.oceaneng.2016.11.035.

[40] Nielsen UD. Transformation of a wave energy spectrum from encounter to absolute domain when observing from an advancing ship. *Applied Ocean Research* 2017; **69**:160 – 172, doi:https://doi.org/10.1016/j.apor.2017.10.011.

[41] Brodtkorb AH, Nielsen UD, Sørensen AJ. Sea state estimation using vessel response in dynamic positioning. *Applied Ocean Research* 2018; **70**:76 – 86, doi:https://doi.org/10.1016/j.apor.2017.09.005.

[42] Ren Z, Han X, Verma AS, Dirdal JA, Skjetne R. Sea state estimation based on vessel motion responses: Improved smoothness and robustness using bézier surface and l1 optimization. *Marine Structures* 2021; **76**:102 904, doi:https://doi.org/10.1016/j.marstruc.2020.102904.

[43] Clauss GF, Kosleck S, Testa D. Critical situations of vessel operations in short crested seas - forecast and decision support system. *Journal of Offshore Mechanics and Arctic Engineering* 02 2012; **134**(3), doi:10.1115/1.4004515.

[44] Dannenberg J, Hessner K, Naaijen P, van den Boom H, Reichert K. The on board wave and motion estimator OWME. *Proceedings of the 20th international offshore and polar engineering conference*, ISOPE, 2010; 424–431.

[45] Naaijen P, Roozen DK, Huijsmans RHM. Reducing operational risks by on-board phase resolved prediction of wave induced ship motions. *Proceedings of ASME 2016 35th International Conference on Ocean, Offshore and Arctic Engineering*, International Conference on Offshore Mechanics and Arctic Engineering, 2016, doi:10.1115/OMAE2016-54591.

[46] Naaijen P, van Oosten K, Roozen K, van't Veer R. Validation of a deterministic wave and ship motion prediction system. *Proceedings of ASME 2018 37th International Conference on Ocean, Offshore and Arctic Engineering*, International Conference on Offshore Mechanics and Arctic Engineering, 2018, doi:10.1115/OMAE2018-78037.

[47] Huang W, Liu X, Gill EW. Ocean wind and wave measurements using x-band marine radar: A comprehensive review. *Remote Sensing* 2017; **9**(12), doi:10.3390/rs9121261. URL https://www.mdpi.com/2072-4292/9/12/1261.

[48] Hilmer T, Thornhill E. Deterministic wave predictions from the WaMoS II. *OCEANS 2014 - TAIPEI*, 2014; 1–8.

[49] Reichert K, Hessner K, Nieto Borge JC, Dittmer J. Wamos ii: A radar based wave and current monitoring system. *The Proceedings of the 9th (1999) International Offshore and Polar Engineering Conference*, International Society of Offshore and Polar Engineers: Brest, France, 1999.

[50] Stredulinsky DC, Thornhill EM. Ship motion and wave radar data fusion for shipboard wave measurement. *Journal of Ship Research* 2011; **55**:73 – 85.

[51] Naaijen P, Blondel-Couprie E. Reconstruction and Prediction of Short-Crested Seas Based on the Application of a 3D-FFT on Synthetic Waves: Part 1 — Reconstruction. *Proceedings of the ASME 2012 31st International Conference on Ocean, Offshore and Arctic Engineering*, vol. Volume 5: Ocean Engineering; CFD and VIV, 2012; 43–53, doi:10.1115/OMAE2012-83093.

[52] Blondel-Couprie E, Naaijen P. Reconstruction and Prediction of Short-Crested Seas Based on the Application of a 3D-FFT on Synthetic Waves: Part 2 — Prediction. *Proceedings of the ASME 2012 31st International Conference on Ocean, Offshore and Arctic Engineering*, vol. Volume 5: Ocean Engineering; CFD and VIV, 2012; 55–70, doi:10.1115/OMAE2012-83096.

[53] Connell BSH, Rudzinsky JP, Brundick CS, Milewski WM, Kusters JG, Farquharson G. Development of an environmental and ship motion forecasting system. *Proceedings of ASME 2015 34th International Conference on Ocean, Offshore and Arctic Engineering*, International Conference on Offshore Mechanics and Arctic Engineering, 2015, doi:10.1115/OMAE2015-42422.

[54] Kusters JG, Cockrell KL, Connell BSH, Rudzinsky JP, Vinciullo VJ. FutureWaves™: A real-time ship motion forecasting system employing advanced wave-sensing radar. *OCEANS 2016 MTS/IEEE Monterey*, 2016; 1–9, doi:10.1109/OCEANS.2016.7761478.

[55] Alford LK, Beck RF, Johnson JT, Lyzenga D, Nwogu O, Zundel A. A real-time system for forecasting extreme waves and vessel motions. *Proceedings of ASME 2015 34th International Conference on Ocean, Offshore and Arctic Engineering*, International Conference on Offshore Mechanics and Arctic Engineering, 2015, doi:10.1115/OMAE2015-42420.

[56] Chan HS, Armaoglu E, Thomson M, Garner A, Parisotto A, Sovilla S. Response forecasts for a suspended wellbay module and flare tower during

transit to shore. *The 29th International Ocean and Polar Engineering Conference*, Honolulu, Hawaii, USA, 2019.

[57] Tellkamp J, Bruns A, Gosch T, Günther H, Hansen PF, Nielsen UD, Papanikolaou A, Spanos D, Papatzanakis G, Kassner S, *et al.*. ADOPT summary of experiences and needs for further development. *Technical Report*, FORCE Technology and Uniresearch 2009.

[58] Journée J, Pinkster J. Introduction in ship hydromechanics. *Technical Report*, Delft University of Technology 2002.

[59] Tannuri EA, Sparano JV, Simos AN, Da Cruz JJ. Estimating directional wave spectrum based on stationary ship motion measurements. *Applied Ocean Research* 2003; **25**(5):243 – 261, doi:https://doi.org/10.1016/j.apor.2004.01.003.

[60] Alford LK, Beck RF, Johnson JT, Lyzenga D, Nwogu O, Zundel A. Design, implementation, and evaluation of a system for environmental and ship motion forecasting. 30th Symposium on Naval Hydrodynamics, Hobart, Australia, 2014.

[61] Nielsen UD, Mounet RE, Brodtkorb AH. Tuning of transfer functions for analysis of wave–ship interactions. *Marine Structures* 2021; **79**:103 029, doi:https://doi.org/10.1016/j.marstruc.2021.103029.

[62] Fossen T, Sagatun S, Sørensen A. Identification of dynamically positioned ships. *Control Engineering Practice* 1996; **4**(3):369 – 376, doi:https://doi.org/10.1016/0967-0661(96)00014-7.

[63] Fossen TI, Strand JP. Passive nonlinear observer design for ships using lyapunov methods: full-scale experiments with a supply vessel. *Automatica* 1999; **35**(1):3–16.

[64] Xu H, Soares CG. Hydrodynamic coefficient estimation for ship manoeuvring in shallow water using an optimal truncated LS-SVM. *Ocean Engineering* 2019; **191**:106 488.

[65] Yuan Y, Fu G, Zhang W. Extended and unscented Kalman filters for parameter estimation of a hydrodynamic model of vessel. *2016 35th Chinese Control Conference (CCC)*, 2016; 2051–2056.

[66] Ren Z, Han X, Yu X, Skjetne R, Leira BJ, Sævik S, Zhu M. Data-driven identification of 6dof dynamic model and wave load estimation for a ship in waves. *Mechanical Systems and Signal Processing* 2021; Revision under review.

[67] *Automatic Tuning of Vessel Models Offshore: A Feasibility Study Using High-Precision Data from Model Test*, Offshore Technology Conference, Houston, Texas, USA, 2020, doi:10.4043/30690-MS.

[68] Galvin J. The use of information technology at the met office. British Computer Society, Bristol Branch January Seminar 2014.

[69] Carrasco A, Sætra Ø. A limited-area wave ensemble prediction system for the nordic seas and the north sea. *Technical Report*, Norwegian Meteorological Institute, Oslo 2008.

[70] ECMWF. *Part V: Ensemble Prediction System*, chap. 5. IFS Documentation, ECMWF, 2016. URL https://www.ecmwf.int/node/16649.

[71] Natskår A, Moan T, Alvær P. Uncertainty in forecasted environmental conditions for reliability analyses of marine operations. *Ocean Engineering* 2015; **108**:636 – 647, doi:https://doi.org/10.1016/j.oceaneng.2015.08.034.

[72] Nessim M, Hong H, Jordaan I. Environmental load uncertainties for offshore structures. *Journal of Offshore Mechanics and Arctic Engineering* 11 1995; **117**(4):245–251, doi:10.1115/1.2827230.

[73] Li L, Haver S, Berlin N. Assessment of operational limits: Effects of uncertainties in sea state description. *Marine Structures* 2021; **77**:102 975, doi:https://doi.org/10.1016/j.marstruc.2021.102975. URL https://www.sciencedirect.com/science/article/pii/S095183392100037X.

[74] WMO. WMO guide to meteorological instruments and methods of observation. *Technical Report*, World Meteorological Organization (2014), Geneva 2014.

[75] Bitner-Gregersen EM, Øistein Hagen. Uncertainties in data for the offshore environment. *Structural Safety* 1990; **7**(1):11 – 34, doi:https://doi.org/10.1016/0167-4730(90)90010-M.

[76] Hagen Ø, Bitner-Gregersen EM, Vrouwenvelder A. JCSS probabilistic model code Part 2: Loads 2.15: Wave loads. *Technical Report*, Joint Committee on Structural Safety 2006.

[77] Orimolade AP, Furevik BR, Gudmestad OT. A comparison of wave height forecasts against wave measurements for a location in the Barents Sea and in the Norwegian Sea. *Proceedings of the Twenty-sixth (2016) International Ocean and Polar Engineering Conference*, International Society of Offshore and Polar Engineers, 2016.

[78] Hubbard DW. *How to Measure Anything*. John Wiley & Sons, Ltd, 2014.

[79] Bruserud K, Haver S. Uncertainties in current measurements in the northern North Sea. *Journal of Atmospheric and Oceanic Technology* 04 2017; **34**(4):855–876, doi:10.1175/JTECH-D-16-0192.1.

[80] Hafver A, Eldevik S, Pedersen FB. Probabilistic digital twins. https://ai-and-safety.dnvgl.com/probabilistic-twin/. DNV. Accessed: 2021-04-05.

[81] Natskår A. Reliability-based assessment of marine operations with emphasis on sea transport on barges. PhD Thesis, Norwegian University of Science and Technology 2020.

[82] Julier SJ. The scaled unscented transformation. *Proceedings of the 2002 American Control Conference (IEEE Cat. No. CH37301)*, vol. 6, IEEE, 2002; 4555–4559.

[83] DNV GL. Wasim user manual. *Technical Report*, DNV GL 2018.

[84] Han X, Sævik S, Leira BJ. A sensitivity study of vessel hydrodynamic model parameters. *Proceedings of the ASME 2020 39th International Conference on Ocean, Offshore and Arctic Engineering*, vol. 1, Virtual, Online, 2020.

[85] Saltelli A, Annoni P. How to avoid a perfunctory sensitivity analysis. *Environmental Modelling & Software* 2010; **25**(12):1508–1517, doi:https://doi.org/10.1016/j.envsoft.2010.04.012. URL https://www.sciencedirect.com/science/article/pii/S1364815210001180.

[86] Lewandowski EM. *The dynamics of marine craft: maneuvering and seakeeping*, vol. 22. World scientific, 2004.

[87] Han X, Leira BJ, Sævik S, Kaasen KE. Validation of vessel seakeeping model tuning algorithm based on measurements at model scale. *Marine Structures* 2021; **80**, doi:10.1016/j.marstruc.2021.103083.

[88] ITTC. Recommended procedures and guidelines: Global loads seakeeping procedure. *Technical Report*, International Towing Tank Conference 2011.

[89] Fathi DE. Shipx vessel responses (VERES), user's manual. *Technical Report*, SINTEF Ocean AS 2018.

[90] Han X, Leira BJ, Sævik S. Vessel hydrodynamic model tuning by discrete Bayesian updating using simulated onboard sensor data. *Ocean Engineering* 2021; **220**, doi:10.1016/j.oceaneng.2020.108407. URL https://www.sciencedirect.com/science/article/pii/S0029801820313147.

[91] Han X, Ren Z, Leira BJ, Sævik S. Adaptive identification of lowpass filter cutoff frequency for online vessel model tuning. *Ocean Engineering* 2021; **236**, doi:10.1016/j.oceaneng.2021.109483.

[92] Han X, Sævik S, Leira BJ. Tuning of vessel parameters including sea state dependent roll damping. *Ocean Engineering* 2021; **233**, doi:10.1016/j.oceaneng.2021.109084.

[93] Han X, Leira BJ, Sævik S, Ren Z. Onboard tuning of vessel seakeeping model parameters and sea state characteristics. *Marine Structures* 2021; **78**, doi:10.1016/j.marstruc.2021.102998.

[94] Jefferys E. Directional seas should be ergodic. *Applied Ocean Research* 1987; **9**(4):186 – 191, doi:https://doi.org/10.1016/0141-1187(87)90001-0. URL http://www.sciencedirect.com/science/article/pii/0141118787900010.

[95] Virtanen P, Gommers R, Oliphant TE, Haberland M, Reddy T, Cournapeau D, Burovski E, Peterson P, Weckesser W, Bright J, *et al.*. SciPy 1.0: Fundamental Algorithms for Scientific Computing in Python. *Nature Methods* 2020; **17**:261–272.

[96] Cooley JW, Tukey JW. An algorithm for the machine calculation of complex Fourier series. *Mathematics of computation* 1965; **19**(90):297–301.

[97] Grewal MS, Henderson VD, Miyasako RS. Application of kalman filtering to the calibration and alignment of inertial navigation systems. *IEEE Transactions on Automatic Control* Jan 1991; **36**(1):3–13, doi:10.1109/9.62283.

[98] Lee JK, Choi MJ. Effect of strapdown integration order and sampling rate on imu-based attitude estimation accuracy. *Sensors* 2018; **18**(9), doi:10.3390/s18092775. URL https://www.mdpi.com/1424-8220/18/9/2775.

[99] Blanke M. Fault-tolerant sensor fusion for marine navigation. *Proceedings of the 7th IFAC Conference on Manoeuvring and Control of Marine Craft*, IFAC Proceedings Volumes (IFAC-PapersOnline), Elsevier: United Kingdom, 2006; 1385–1390. URL http://mcmc2006.isr.ist.utl.

pt/, 7th IFAC Conference on Manoeuvring and Control of Marine Craft, MCMC'2006 ; Conference date: 20-09-2006 Through 22-09-2006.

[100] Blanke M. Diagnosis and fault-tolerant control for ship station keeping. *Proceedings of the 2005 IEEE International Symposium on, Mediterrean Conference on Control and Automation Intelligent Control, 2005.*, 2005; 1379–1384, doi:10.1109/.2005.1467217.

[101] Shukla SK, Talpin JP. *Synthesis of embedded software: frameworks and methodologies for correctness by construction*. Springer Science & Business Media, 2010.

[102] Labbe R. Kalman and Bayesian filters in Python. https://github.com/rlabbe/Kalman-and-Bayesian-Filters-in-Python 2018.

[103] Han X, Leira BJ, Sævik S, Radhakrishnan G, Skjong S, Kyllingstad LT. A framework for condition monitoring and risk-based decision support involving a vessel state observer. *Proceedings of the ASME 2021 40th International Conference on Ocean, Offshore and Arctic Engineering*, vol. 2, Virtual, Online, 2021.

[104] Shepard D. A two-dimensional interpolation function for irregularly-spaced data. *Proceedings of the 1968 23rd ACM National Conference*, ACM '68, Association for Computing Machinery: New York, NY, USA, 1968; 517–524, doi:10.1145/800186.810616.

[105] Scheick JT. *Linear algebra with applications*, vol. 81. McGraw-Hill New York, 1997.

[106] Gelman A, Carlin J, Stern H, Dunson D, Vehtari A, Rubin D. *Bayesian Data Analysis*. 3rd edn., Chapman and Hall/CRC, 2013, doi:10.1201/b16018.

[107] Godhaven JM. Adaptive tuning of heave filter in motion sensor. *IEEE Oceanic Engineering Society. OCEANS'98. Conference Proceedings (Cat. No.98CH36259)*, vol. 1, 1998; 174–178.

[108] Perez T, Blanke M. Ship roll damping control. *Annual Reviews in Control* 2012; **36**(1):129–147, doi:https://doi.org/10.1016/j.arcontrol.2012.03.010.

[109] Himeno Y. Prediction of ship roll damping - a state of the art. *Technical Report*, The University of Michigan, College of Engineering, Department of Naval Architecture and Marine Engineering, USA 1981.

[110] ITTC. Recommended procedures and guidelines: Numerical estimation of roll damping. *Technical Report*, International Towing Tank Conference 2011.

[111] Falzarano J, Somayajula A, Seah R. An overview of the prediction methods for roll damping of ships. *Ocean Systems Engineering* 2015; **5**(2):55–76.

[112] Ikeda Y, Komatsu K, Tanaka N. On roll damping force of ship-effects of hull surface pressure created by bilge keels. *Technical Report 00402*, Osaka Prefecture University 1979.

[113] Ikeda Y, Himeno Y, Tanaka N. A prediction method for ship roll damping. *Technical Report 00405*, Osaka Prefecture University 1978.

[114] Kaplan P. Lecture notes on nonlinear theory of ship roll motion in a random seaway 1966.

[115] Rasmussen CE, Williams CKI. *Gaussian Processes for Machine Learning (Adaptive Computation and Machine Learning)*. The MIT Press, 2005.

[116] Marriott FHC. Multivariate Statistics: A Vector Space Approach. *Journal of the Royal Statistical Society Series C* November 1984; **33**(3):319–319, doi:10.2307/2347710.

[117] Pedregosa F, Varoquaux G, Gramfort A, Michel V, Thirion B, Grisel O, Blondel M, Prettenhofer P, Weiss R, Dubourg V, *et al.*. Scikit-learn: Machine learning in Python. *Journal of Machine Learning Research* 2011; **12**:2825–2830.

[118] Naess A, Moan T. *Stochastic Dynamics of Marine Structures*. Cambridge University Press, 2012, doi:10.1017/CBO9781139021364.

[119] Van Der Merwe R, *et al.*. Sigma-point kalman filters for probabilistic inference in dynamic state-space models. PhD Thesis, OGI School of Science & Engineering at OHSU 2004.

[120] Del Moral P. Nonlinear filtering: Interacting particle resolution. *Comptes Rendus de l'Académie des Sciences-Series I-Mathematics* 1997; **325**(6):653–658.

[121] Julier SJ, Uhlmann JK. New extension of the kalman filter to nonlinear systems. *Signal processing, sensor fusion, and target recognition VI*, vol. 3068, International Society for Optics and Photonics, 1997; 182–193.

[122] Nørgaard M, Poulsen NK, Ravn O. New developments in state estimation for nonlinear systems. *Automatica* 2000; **36**(11):1627–1638.

[123] Julier SJ, Uhlmann JK. A general method for approximating nonlinear transformations of probability distributions. *Technical Report* 1996.

[124] Julier SJ. Skewed approach to filtering. *Signal and Data Processing of Small Targets 1998*, vol. 3373, Drummond OE (ed.), International Society for Optics and Photonics, SPIE, 1998; 271 – 282, doi:10.1117/12.324626.

[125] Julier SJ, Uhlmann JK. Consistent debiased method for converting between polar and cartesian coordinate systems. *Acquisition, Tracking, and Pointing XI*, vol. 3086, International Society for Optics and Photonics, 1997; 110–121.

[126] Horn RA, Johnson CR. *Matrix Analysis*. 2nd edn., Cambridge University Press, 2012, doi:10.1017/9781139020411.

[127] Deadman E, Higham NJ, Ralha R. Blocked schur algorithms for computing the matrix square root. *Applied Parallel and Scientific Computing*, Manninen P, Öster P (eds.), Springer Berlin Heidelberg: Berlin, Heidelberg, 2013; 171–182.

[128] Gourlay T, von Graefe A, Shigunov V, Lataire E. Comparison of AQWA, GL Rankine, MOSES, OCTOPUS, PDStrip and WAMIT With Model Test Results for Cargo Ship Wave-Induced Motions in Shallow Water. *Proceedings of the ASME 2015 34th International Conference on Ocean, Offshore and Arctic Engineering*, OMAE2015-41691, St. John's, Newfoundland, Canada, 2015.

[129] Dhavalikar SS. Comparative Study of Seakeeping Analysis Results From Various Methods. *Proceedings of the ASME 2011 30th International Conference on Ocean, Offshore and Arctic Engineering*, vol. Volume 1: Offshore Technology; Polar and Arctic Sciences and Technology, 2011; 217–223, doi:10.1115/OMAE2011-49223.

[130] Ravinthrakumar S, Kristiansen T, Ommani B. On the hydrodynamic interaction between ship and free-surface motions on vessels with moonpools. *Proceedings of the ASME 2019 38th International Conference on Ocean, Offshore and Arctic Engineering*, Glasgow, Scotland, UK, 2019.

[131] Ikeda Y. On roll damping force of ship - effect of friction of hull and normal force of bilge keels. *Technical Report 00401*, Osaka Prefecture University 1978.

[132] Ikeda Y, Himeno Y, Tanaka N. On eddy making component of roll damping force on naked hull. *Technical Report 00403*, Osaka Prefecture University 1978.

[133] Blanke M, Kinnaert M, Lunze J, Staroswiecki M. *Diagnosis and fault-tolerant control*. 3rd edn., Springer, 2015.

Appendices

Appendix A

Appended Papers

A.1 Paper A1

Paper A1:
X. Han, S. Sævik, and B. J. Leira, 2020. A sensitivity study of vessel hydrodynamic model parameters. In: *Proceedings of the ASME 2020 39th International Conference on Ocean, Offshore and Arctic Engineering*, volume 1, Virtual, Online.

Proceedings of the ASME 2020 39th International Conference on Ocean, Offshore and Arctic Engineering
OMAE2020
August 3-7, 2020, Virtual, Online

OMAE2020-19039

A SENSITIVITY STUDY OF VESSEL HYDRODYNAMIC MODEL PARAMETERS

Xu Han[1], Svein Sævik, Bernt Johan Leira
NTNU
Trondheim, Norway

ABSTRACT

In the recent decade, maritime and energy industries have realized the potential of using operational data in combination with a virtual replication of the real physical asset, termed the digital twin. The digital twin then serves as a platform for data management, asset monitoring, and inspection and maintenance management, featuring an improved basis for cost effective operations and future decision making in terms of e.g. life extension. The present paper deals with application of the digital twin concept in marine operations where it is essential to handle the inherent uncertainties of vessel performance by applying a model that can adapt to the real operating conditions. In this paper a case study is presented for identifying the most sensitive parameters in the vessel hydrodynamic model w.r.t. the vessel motion RAOs. The study also shows that the parametric sensitivity depends on the interesting vessel response parameter, wave direction and loading condition. A digital twin adaptive to various operational conditions may require parametric tuning of the numerical model. It is important to identify the correct parameter(s) for modification. A simplified and idealized case study is also carried out to test the requirements to a successful parameter identification for model tuning.

NOMENCLATURE

A_{P90}^{loc}	The P90 value of heave acceleration at the "loc" location, for a certain sea state
$A(\omega)$	Added mass coefficient
B	Vessel breadth
C_{ij}	Restoring stiffness to i[th] dof due to motion in j[th] dof
COG	Center of Gravity
D	Vessel draft
dof	Degree of freedom, 1 – Surge, 2 – sway, 3 – heave, 4 – roll, 5 – pitch, 6 – yaw
$F(\omega, u\|\beta_w)$	Excitation force from waves, on complex form, including Froude-Krylov and diffraction forces
GMT	Transverse metacentric height
GML	Longitudinal metacentric height
g	Gravity
H	water depth
H_S	Significant wave height
I_{xx}	moment of inertia w.r.t. vessel x-axis
I_{yy}	moment of inertia w.r.t. vessel y-axis
I_{zz}	moment of inertia w.r.t. vessel z-axis
k	Wave number
L_{PP}	Length between perpendiculars
loc	Location
M	Mass of vessel
MRU	Motion Reference Unit
OSV	Offshore Supply Vessel
RAO	Response Amplification Operator
SS	Sea state
T	Wave period
T_Z	Zero-upcrossing wave period
u	Vessel speed
Var	Variable, the parameter for sensitivity study
V_{P90}^{loc}	The P90 value of heave velocity at the "loc" location, for a certain sea state
w.r.t.	with respect to
XCG	longitudinal coordinate of vessel COG

[1] Contact author: xu.han@ntnu.no

YCG	transverse coordinate of vessel COG
ZCG	vertical coordinate of vessel COG
β_{ij}	The linear damping to the i[th] dof due to motion in j[th] dof, $\beta_{ij} = {\beta_{ij}}^{p} + {\beta_{ij}}^{a}$
${\beta_{ij}}^{p}$	Potential theory related damping
${\beta_{ij}}^{a}$	linearized damping in addition to the potential theory related damping term ${\beta_{ij}}^{a} = \xi \cdot \beta_{ij,cr}$
$\beta_{ij,cr}$	Critical damping, $\overline{\overline{\beta_{cr}}} = 2\sqrt{(\bar{\bar{A}}(\omega) + \bar{\bar{M}}) \cdot \bar{\bar{C}}}$
β_w	Wave direction w.r.t. vessel coordinate system
ω	Wave frequency
ω_e	Encounter frequency
λ	Wave length
ζ_a	Wave amplitude
ϕ_a	Wave slope amplitude $\phi_a = k \cdot \zeta_a$

INTRODUCTION

Industrial practice on vessel seakeeping analyses has been well standardized due to the developed theory of ocean waves and vessel hydrodynamics during the last century, see e.g., [1]. The theory and practice of modelling ocean waves and structural hydrodynamics is usually simplified and sometimes linearized. For example, the vessel response to ocean waves is very often simply represented in frequency domain by linear transfer functions (i.e. RAO) in 6 dof's. As a supplement, model tests in laboratory and virtual tests play an important role in the design phase when determining the hydrodynamic coefficients of vessels.

The numerical model developed in design phase can be extended to a digital twin of the real physical asset, supporting monitoring, maintenance, real-time decision making, remote control, automation etc. related to operations. Hundreds of sensors are installed in a typical offshore vessel. With developed technologies on sensors, data management, and remote communication, industries and researchers have started to explore different applications of the digital twin concept. Among them, onboard decision support systems (ODSS) have been a very promising application, aiming at real-time reliable prediction of critical responses.

Many ODSS for marine and offshore activities have been developed during the last decade, ref. [2], [3], [4], [5], [6], [7], [8], [9], mainly focusing on technologies providing more accurate wave prediction, in forms of either wave surface elevations or wave spectra. Linear transfer function between wave and vessel motion (i.e. RAO) has been applied in most ODSSs. The influences from the uncertainties of RAO have been studied, e.g., [10], [11], [12]. Challenges on insufficient accuracy of roll motion prediction by using RAO, is commonly observed, due to the highly nonlinear damping effect [13].

Sensor data with acceptable quality could be used to reduce the uncertainties and conservatism of the prediction through active modification of the numerical vessel hydrodynamic model. This has a huge commercial benefit regarding safety and reliability improvement, and potential cost reduction.

However, there are hundreds of parameters that can be varied in one hydrodynamic model, and normally very little prior knowledge is available on which parameters should be selected to modify. Considering measurement noises, information discretization, and uncertainties from model simplification, vessel hydrodynamic model tuning could be very challenging.

The work described in this paper, is based on a parametric sensitivity study of one OSV to identify which parameters that govern the vessel response to ocean waves in terms of RAOs, and to study the possibility of identifying the right parameters to tune based on acquired measurement data.

The paper is organized as follows. The basis of the vessel numerical hydrodynamic model is described in section "Case Study Basis". In section "Theory", the basic theories on linear dynamic systems in the frequency domain, wave dispersion and kinematics are briefly described. Then, the parametric sensitivity studies on water depth, vessel speed, inertia terms, metacentric heights and additional damping terms are reported in more detail in the section "Parametric Sensitivity Study", where the important parameters are identified. Afterwards, a simple case study is presented in section "Parameter Identification", aiming to identify the right tuning parameters. Then, some key findings and challenges are summarized in section "Conclusion and Discussion".

CASE STUDY BASIS

The case study was based on the hydrodynamic model for one OSV. The primary information of the vessel is summarized in Table 1. The coordinates refer to the reference coordinate system moving steadily at the vessel forward speed where the positive x-axis points from stern to bow (x=0 aft), the z-axis is pointing vertically upward from keel (z=0 at keel) and the y-axis is normal to the x-z plane where y=0 is at the longitudinal symmetric plane. Wave direction (heading) follows the same coordinate system, i.e. for waves at 0 heading propagates along the positive x-axis.

To investigate the sensitivity of hydrodynamic model parameters w.r.t. the vessel motion RAOs, both ballast and full loading conditions with infinite water depth were selected as base case. The base cases also included 0.5m GMT correction due to free surface effect and an addition roll damping (${\beta_{44}}^{a} = 5\% \cdot \beta_{44,cr}$). Only surge, sway, heave, roll and pitch amplitudes were considered, i.e. the influence on RAO phase angles were not included. The RAOs were calculated at the MRU location midship, approximately (60m,0m,11m).

The variables listed in Table 2 were included in the sensitivity studies. The ranges of water depth (H) and vessel speed (u) represented the normal operation conditions, while the ranges of the other variables reflected parametric uncertainties with prior knowledge of the operational conditions. The parameter variations were based on engineering judgement as the ranges can depend on many factors, such as the sensor accuracy, operational conditions, vessel type and vessel geometry.

Table 1: Vessel information, base cases

Parameters	Value	Unit
L_{PP}	~120	m
B	~27	m
D (Ballast)	~5.1	m
D (Full)	~6.8	m

Table 2: Studied variables

Variable	Range RAO visual inspection	Range numerical comparison
H*	20 – 2000 m	
u*	0 – 20 knots	
XCG	$\pm 4m$	$\pm 4m$
YCG	$\pm 1m$	$\pm 1m$
ZCG	$\pm 1m$	$\pm 1m$
M	$\pm 10\%$	$\pm 10\%$
I_{xx}	$\pm 10\%$	$\pm 10\%$
I_{yy}	$\pm 10\%$	$\pm 10\%$
I_{zz}	$\pm 10\%$	$\pm 10\%$
GMT	± 1.5m	± 0.5m
GML*	± 10 m	
${\beta_{11}}^{a}$ *	0 - 16% of $\beta_{11,cr}$	
${\beta_{22}}^{a}$ *	0 - 16% of $\beta_{22,cr}$	
${\beta_{33}}^{a}$	0 - 16% of $\beta_{33,cr}$	2 – 14%
${\beta_{44}}^{a}$	2 - 16% of $\beta_{44,cr}$	2 – 14%
${\beta_{55}}^{a}$ *	0 - 16% of $\beta_{55,cr}$	

*Parameters excluded for numerical comparison of sensitivity studies. Reasons are explained in sections "Metacentric height", "Additional damping" and "Numerical results".

THEORY

Frequency domain vessel motion RAOs can be calculated based on the equation of motion:

$$\left(\bar{\bar{A}}(\omega_e) + \bar{\bar{M}}\right)\ddot{\vec{x}} + \bar{\bar{\beta}}(\omega_e)\dot{\vec{x}} + C\vec{x} = \vec{F}(\omega, u|\beta_w) \quad \textbf{(1)}$$

$$RAO(\omega, u|\beta_w) = \frac{\vec{F}(\omega, u|\beta_w)}{-{\omega_e}^2\left(\bar{\bar{A}}(\omega_e) + \bar{\bar{M}}\right) + i\omega_e\bar{\bar{\beta}}(\omega_e) + \bar{\bar{C}}} = \bar{\bar{D}}(\omega_e) \cdot \vec{F}(\omega, u|\beta_w) \quad \textbf{(2)}$$

As a result, RAOs are complex-valued operators. The hydrodynamic coefficients and excitation forces were calculated by commercial software Wasim contained in the Sesam program package [14]. Wasim is a 3D time-domain hydrodynamic analysis software by Rankine panel method [15]. Luo [16] summarizes the common assumptions, boundary conditions and governing equations leading to the linear potential theory applied in Wasim. Each Wasim analysis was run for one wave period and operation condition where the "operation condition" herein is defined by vessel heading, loading condition, and vessel speed. The outputs of Wasim analyses from all wave periods are transferred to frequency domain. The database of hydrodynamic coefficients and excitation forces were therefore obtained for each operating condition and applied to generate the vessel motion RAO for each specific operation condition, based on formula (2).

For a valuable comparison, the quality of hydrodynamic coefficient calculation and RAO calculation should be assured. It is essential to make sure that the RAO peak is captured by having a sufficient number of hydrodynamic calculations around the peak period; that the time step applied for numerical simulation (time domain) is sufficiently small; and that the number of panels is sufficient, ref. [14].

Wave dispersion

The wave dispersion, referring to [1], can normally be expressed by:

$$\omega^2 = g \cdot k \cdot tanh(k \cdot H) \quad \textbf{(3)}$$

k is the wave number, $k = \frac{2\pi}{\lambda}$. So, the dispersion relation could also be written as:

$$\lambda = \frac{g}{2\pi}T^2 \tanh(2\pi\frac{H}{\lambda}) \quad \textbf{(4)}$$

It shows that the wave length, wave number and wave slope amplitude ($k\zeta_a$) are influenced by wave period and water depth.

Water particle motion

For linear potential wave theory, both the horizontal and vertical water particle velocity are dependent on water depth.

$$u = \omega a \cdot \frac{\cosh k(z+H)}{\sinh kd} \cdot \sin(\omega t - kx) \quad \textbf{(5)}$$

$$w = \omega a \cdot \frac{\sinh k(z+H)}{\sinh kd} \cdot \cos(\omega t - kx) \quad \textbf{(6)}$$

But at sea surface, the vertical velocity is independent of water depth:

$$u = \omega a \cdot \frac{\cosh k \cdot H}{\sinh k \cdot H} \cdot \sin(\omega t - kx) \quad \textbf{(7)}$$

$$w = \omega a \cdot \cos(\omega t - kx) \quad \textbf{(8)}$$

Therefore, as shown in Figure 1, the water particle trajectory is influenced by water depth and wave period. Larger wave period amplifies the water depth effect on the water particle horizontal motion.

Encounter frequency of advancing vessel

The vessel with forward speed experiences wave loads in encounter frequency instead of wave frequency. The encounter frequency is expressed:

$$\omega_e = |\omega - k \cdot u \cdot cos\beta_w| \quad \textbf{(9)}$$

For following wave conditions, i.e., $\beta_w = [0°, 90°)$, the term inside of absolute operator can be negative. This leads to a so-called 3-to-1 mapping problem between wave frequency and encounter frequency for following waves [17]. Therefore, for

simplification, this paper only considers head waves, $\beta_w = [90°, 180°]$.

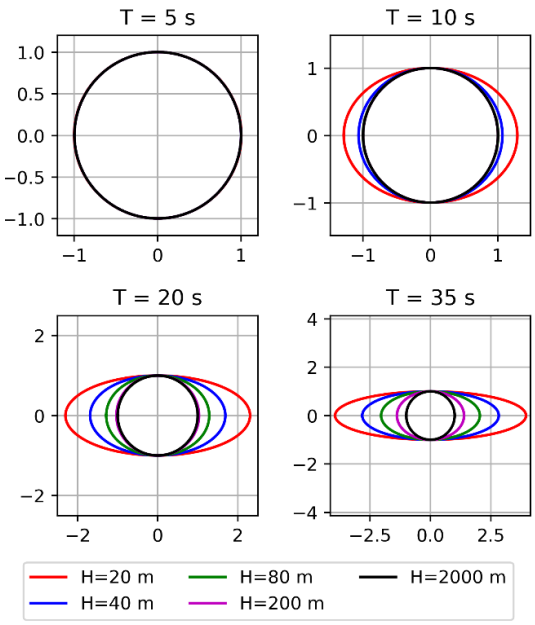

Figure 1: Trajectories of water particles, $\zeta_a = 1$

PARAMETRIC SENSITIVITY STUDY

Water depth

From equations (4) (7) and (9), the water depth influences the wave number k (Figure 2), and consequently the wave kinematics at sea surface and along water depth, wave length (and wave slope), and encounter frequency for advancing vessel. From Figure 3, the pitch RAO sensitivity to water depth shows a shift of the peak period for shallow water. This could be the effect of water depth on wave length (and wave steepness), which is also observed in [18]. Figure 4 shows that the excitation force on pitch is influenced by water depth on large wave periods due to its effect on wave steepness (shown in Figure 2). In addition to the water steepness influence on excitation force, the RAO peak amplitude also highly depends on the added mass and damping coefficients which are influenced by encounter frequency and wave kinematics on vessel wet body (e.g. Figure 5). Consequently, they are all influenced by water depth. In Figure 3, pitch RAOs at no forward speed was selected, intending to tell the shift of peak period is due to the water depth effects on λ (ϕ_a) and wave kinematics, instead of ω_e. For $u = 0kn$, $\omega_e = \omega$. Figure 6 shows that translational motion RAO amplitude does not converge at large periods when considering water depth effect on the horizontal water particle motion.

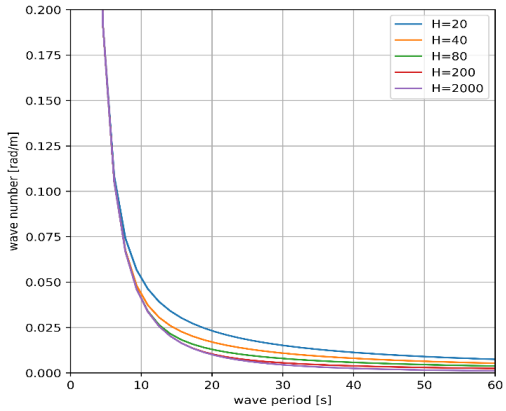

Figure 2: Wave number (k) influenced by wave period and water depth [m].

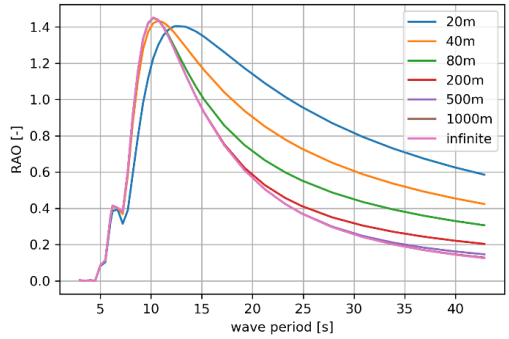

Figure 3: Pitch RAO for water depth sensitivity, ballast condition at 180° heading, with no forward speed.

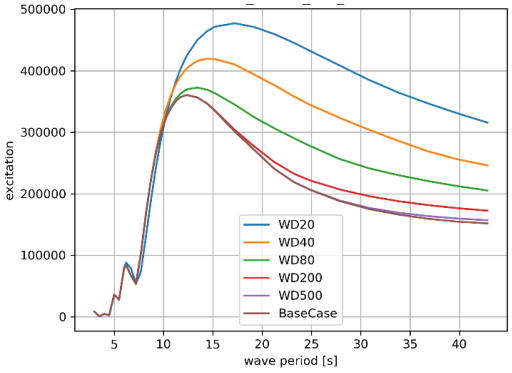

Figure 4: Pitch excitation moment for water depth sensitivity, ballast condition at 180° heading, with no forward speed. "WD" in legend means water depth [m].

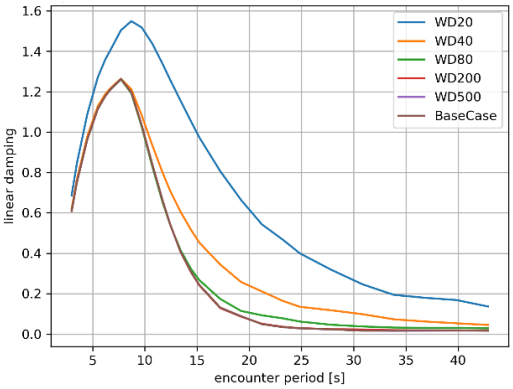

Figure 5: Damping on pitch for water depth sensitivity, ballast condition at 180° heading, with no forward speed. "WD" in legend means water depth [m].

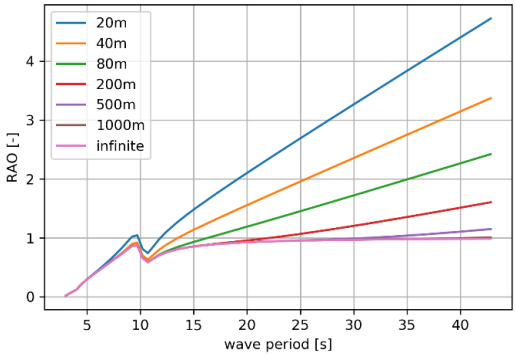

Figure 6: Sway RAO for water depth sensitivity, ballast condition at 90° heading, 10kn speed.

Vessel speed

The influence of vessel forward speed on vessel response is complex. For examples, Faltinsen [1] and MacTaggart [19] tried to show how the vessel speed can affect vessel motions. Simply speaking, vessel speed significantly affects the hydrodynamic coefficients, response period, total velocity potential and free surface conditions (i.e., kinematic and dynamic pressure) in the vessel moving reference system. Consequently, both diffraction and radiation are affected. The Froude-Krylov force is not dependent on speed but is oscillated with the encounter frequency.

Both $\overline{\overline{D}}(\omega_e)$ (free vibration) and $\vec{F}(\omega, u|\beta_w)$ (incident and wave diffraction loads) can possibly govern the peaks in RAO amplitudes (local and global peaks). For $\overline{\overline{D}}(\omega_e)$ term governed peaks (e.g. the peak at about 10s in Figure 7), the peak period usually locks to the encounter period. For $\vec{F}(\omega, u|\beta_w)$ term governed peaks (e.g. the peak at about 4s in Figure 7), the peak period usually links (but not strictly locks) to the wave period. Vessel speed influences the kinematic and dynamic pressure boundary conditions on surface, and consequently influences both the peak amplitude and peak period of the wave and vessel speed induced loads (i.e., $\vec{F}(\omega, u|\beta_w)$). When the peaks of $\overline{\overline{D}}(\omega_e)$ and $\vec{F}(\omega, u|\beta_w)$ are close, the peak could be located at any period in between.

In this case study, higher speed leads to smaller peak amplitude for roll RAO and its coupled sway RAO and larger peak amplitude for pitch RAO and its couple heave RAO, which were also observed in lecture notes [20].

Inertia terms

Inertia terms XCG, YCG, ZCG, M(D), I_{xx}, I_{yy} and I_{zz} were studied. In practice, those parameters vary from operation to operation and includes considerable uncertainty. Varying COG will change trim, heel, waterline and wet body surface. Varying moment of inertias will influence RAO for the corresponding rotational dof, and the coupled translational dof. Varying mass will change draft and consequently change the waterline and wet body surface. These will lead to any possible changes on RAOs, depending on hull geometry and mass distribution.

The case study shows that inertia terms can significantly influence the RAO amplitudes for a wide range of wave periods around the peak period. In addition, the RAO resonance period can also be influenced by inertia terms (e.g., moments of inertia). Roll and sway are sensitive to all of the studied relevant inertia terms, while pitch and heave are only sensitive to some of them. Studies show that the heave RAO at MRU is sensitive to XCG and M whereas pitch RAO at MRU is sensitive to XCG and I_{yy}.

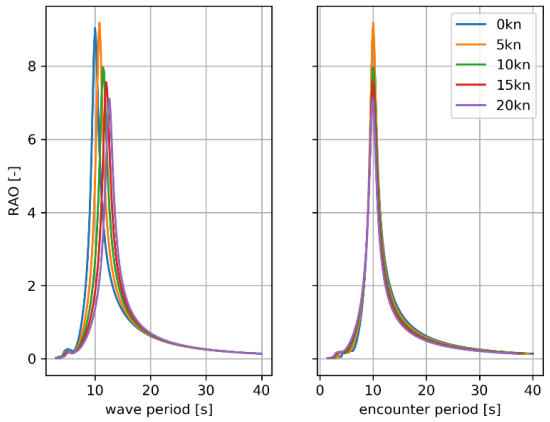

Figure 7: Roll RAO for vessel speed sensitivity, ballast condition at 120° heading.

Metacentric height

Metacentric heights GMT and GML directly determine the restoring moments for roll and pitch motions, as shown in equation (10). Variation of vessel inertia distribution will naturally lead to variation of metacentric heights, due to changes

of wet body shape, waterline etc. Here it was assumed that the uncertainty of GMs only comes from free surface effect.

More severe free surface correction leads to less restoring. Referring to equation (2), this consequently leads to larger natural period and larger RAO amplitudes for the corresponding dof. This effect is very important, especially for dofs where their resonances are dominated by natural responses, e.g., roll motion. An example is shown in Figure 8. In addition, a free surface correction leads to an amplification of RAO amplitude at large wave period.

$$C_{44} = \rho g V \cdot GMT \quad \textbf{(10)}$$

$$C_{55} = \rho g V \cdot GML$$

Roll motion can be significantly influenced by GMT, so as to its coupled sway motion. GML correction mainly influences the pitch RAO at large wave periods. Approximately, 10% GML difference leads to about 10% difference on the pitch RAO amplitude at large periods. Considering that GML is in the magnitude of few hundred meters, free surface correction of 10% is too much. Normally free surface correction of GML is not necessary due to large stiffness in pitch dof.

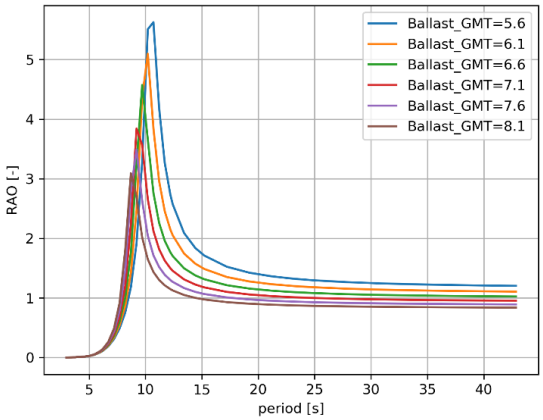

Figure 8: Roll RAO for GMT [m] sensitivity due to free surface correction, ballast condition at 90° heading, no forward speed. RAO amplitude unit in deg/deg.

Additional damping

It is well-known that there are many other types of damping in addition to potential theory related damping, for example, due to viscous effects, ref [13]. Damping plays an important role around the natural response periods. Please note that the response natural period could be different from its resonance period in the RAO. Therefore, the influence of additional damping is significant for the RAOs where the resonance is dominated by its natural response, such as roll and heave. However, it is difficult to judge how much the additional damping can be, simply due to its complexity and nonlinearity related to waves and vessel responses. Here a damping range of 0 – 16% of the critical damping for each dof at each frequency was applied, except for roll motion, where the additional damping range was assumed to be 2 – 16%.

The results show that around their resonance periods, the roll and heave RAO can be dramatically influenced by their additional damping. Also, the pitch RAO can be influenced by its additional damping, but not that significant as for roll and heave in beam sea conditions.

Numerical results

The influence of speed and water depth were considered small within their uncertainty ranges. Hence u and H were not included in the sensitivity ranking. However, speed and water depth are still important to consider when calculating RAO.

Base cases with 10kn forward speed were used. All sea states were described by long-crested Pierson Moskowitz wave spectra, with $H_S = 1m$. Tz of sea states varied from 4s to 25s with interval of 1s. and wave directions of 90˚, 120˚, 150˚, 180˚ w.r.t. the reference coordinate were considered. Each sea state was assumed 3-hour duration. The heave velocity time series were considered wide-banded and therefore, heave velocity amplitudes can be well described by the Rice distribution.

A criterion was introduced to quantify the parametric sensitivity. For each sea state, the 90-persentile value of heave velocity at the location of interest can be defined as V_{P90}^{loc}. The studied uncertainty ranges of interesting parameters are defined in Table 2. For each parameter, a number of values have been selected, and the corresponding sets of RAOs were calculated. Then for one particular parameter studied (defined as Var) and for each sea state (defined as SS), we could get several V_{P90}^{loc} values due to the variation of that parameter (values of Var defined as $\mathrm{Var(i)}, i = 1, 2, \ldots$) within the specified range. So, there will be a maximum and minimum value of V_{P90}^{loc}, defined as:

$$Vmax_{P90}^{loc}(Var, SS) = \max\{V_{P90}^{loc}(Var(i), SS)\},\ i = 1,2,\ldots \quad \textbf{(11)}$$

$$Vmin_{P90}^{loc}(Var, SS) = \min\{V_{P90}^{loc}(Var(i), SS)\},\ i = 1,2,\ldots \quad \textbf{(12)}$$

Parametric sensitivity studies of inertia terms show a weakly nonlinear effect on $V_{P90}^{loc}(Var, SS)$, while the influence from damping terms is significantly nonlinear. Here "nonlinear" means $\frac{\Delta V_{P90}^{loc}}{\Delta Var} \neq Constant$. The nonlinearity level depends on the vessel geometry, load condition, and environmental conditions such as wave direction and wave period in linear potential theory. Therefore, the difference between maximum and minimum of V_{P90}^{loc} may better indicate how sensitive the specific parameter (Var) is to RAOs and the interesting vessel response quantity within its uncertainty range, at specific location for a specific sea state, i.e., here defined as Equation (13). Alternatively, when the parameter value is close enough to the base case, $\theta_V^{loc}(Var, SS)$ defined in Equation (14) describes its parametric sensitivity near the base value, assuming that $\frac{\Delta V_{P90}^{loc}}{\Delta Var}$ is constant, for $\Delta Var \to 0$

$$Diff_V^{loc}(Var, SS) = Vmax_{P90}^{loc}(Var, SS) - Vmin_{P90}^{loc}(Var, SS) \quad \textbf{(13)}$$

$$\theta_V^{loc}(Var, SS) = \frac{dV_{P90}^{loc}(Var_0, SS)}{(dVar)/Var_0} \quad \textbf{(14)}$$

where, Var_0 is the value of Var in base case. This paper uses $Diff_V^{loc}(Var, SS)$ as the parametric sensitivity indicator.

Three locations were studied, i.e., at MRU location (loc = MRU), at crane tip starboard (loc = tip) of interest for a lift operation and at stern (loc = pip) of interest for pipelay operations. Both ballast and full loading conditions were studied. A "case" here is uniquely defined by Var, SS (H_S, T_Z, β_w), loc and loading condition. Figure 9, Figure 10 and Figure 11 show how the studied parameters affect RAOs for different sea states and locations. The oscillation noted in the figures are due to the variation of T_Z and β_w.

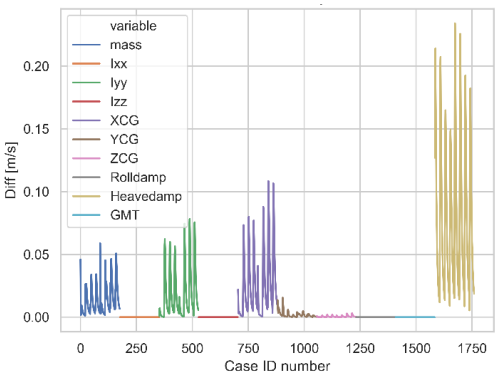

Figure 9: $Diff_V^{MRU}$ (at MRU) for all studied cases. Each Case ID number in x-axis represents a case.

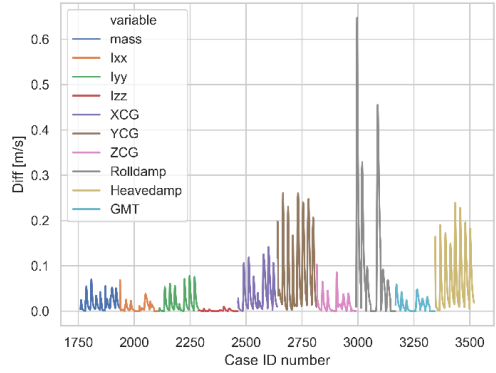

Figure 10: $Diff_V^{tip}$ (at crane tip) for all studied cases. Each Case ID number in x-axis represents a case.

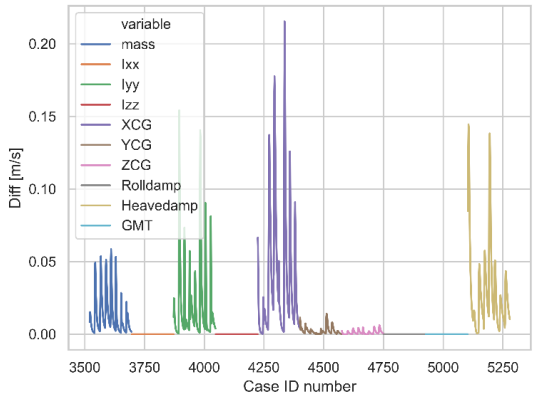

Figure 11: $Diff_V^{pip}$ (stern) for all studied cases. Each Case ID number in x-axis represents a case.

Table 3: Important parameters for RAO w.r.t. V_{P90}^{loc}

Location	Parameters
MRU	β_{33}, XCG, I_{yy}, M
Tip (crane tip)	β_{33}, β_{44}, XCG, YCG, ZCG, I_{yy}, GMT, M
Pip (stern)	XCG, I_{yy}, β_{33}, M

Table 3 summarizes the sensitive parameters for RAO w.r.t. V_{P90}^{loc} criteria for the three selected locations. The sensitivity ($Diff_V^{loc}$) for parameters listed in Table 3 are plotted on jittered polar form from Figure 12 to Figure 17 where the size of the scattered points represent the value of $Diff_V^{loc}$ for variation of Var, β_w and T_Z. Bold yellow lines separate the results for different headings. Table 4 details the heading dependent parametric sensitivity. Figures from Figure 12 to Figure 17 illustrate that the parametric sensitivity changes with T_Z and heading. One example could be for full load condition with beam sea (Figure 14). β_{33} and YCG rank first with small T_Z, while the importance of β_{44} increases with T_Z approaching resonance period. Furthermore, the sensitivity of β_{44} decreases when heading shifts towards head sea condition.

Table 4: Important parameters for RAO w.r.t. V_{P90}^{loc}, heading dependent

	MRU	tip (crane tip)	pip (stern)
90˚	β_{33}, XCG	β_{33}, β_{44},YCG,GMT	β_{33}
120˚	β_{33}, XCG	β_{33},β_{44},XCG,YCG, GMT	I_{yy}, XCG*
150˚	β_{33}, XCG	β_{33}, XCG, YCG	XCG, I_{yy}
180˚	β_{33}, XCG	β_{33}, XCG, YCG	XCG, I_{yy}

*XCG is only important for Full loading condition

The dominating parameters could change for different vessel loading conditions. For example, V_{P90}^{pip} is mostly influenced by only I_{yy} for ballast condition at 120˚ heading, while for full condition XCG also becomes very important.

However, this might not be the main consideration, because the uncertainty of the load condition normally will not be so large.

Please note that the conclusions in this chapter are sensitive to the selected criterion and uncertainty ranges of the considered parameters. The parametric uncertainty range may depend on vessel shape, loading condition, sensor quality, engineering experience, and etc. For example, the uncertainty studied here assumes 14% of the critical heave damping, which could be considered too much. So, in reality with reasonable uncertainty range of β_{33}, it may not show very significant influence on the interesting vessel response. Therefore, the conclusions here cannot be generalized.

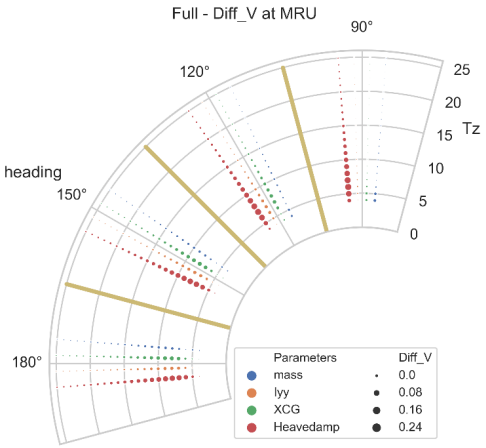

Figure 12: Jittered polar plots of $Diff_V^{MRU}$, full loading condition, for β_w= 90˚, 120˚, 150˚, 180˚, $T_Z \in [4, 25]s$

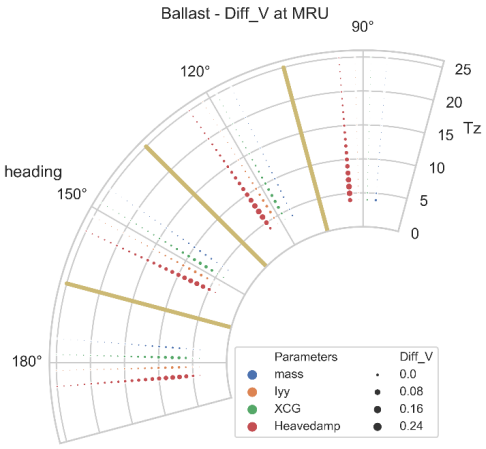

Figure 13: Jittered polar plots of $Diff_V^{MRU}$, ballast condition, for β_w= 90˚, 120˚, 150˚, 180˚, $T_Z \in [4, 25]s$

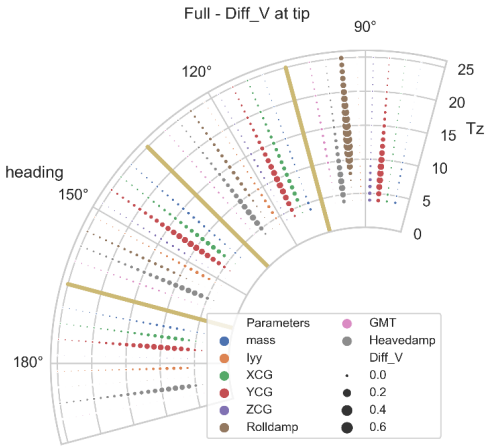

Figure 14: Jittered polar plots of $Diff_V^{tip}$, full loading condition, for β_w= 90˚, 120˚, 150˚, 180˚, $T_Z \in [4, 25]s$

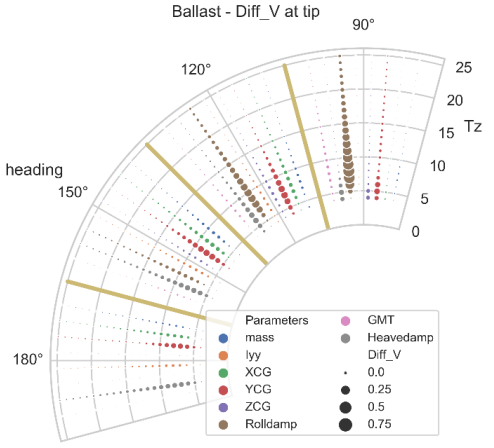

Figure 15: Jittered polar plots of $Diff_V^{tip}$, ballast condition, for β_w= 90˚, 120˚, 150˚, 180˚, $T_Z \in [4, 25]s$

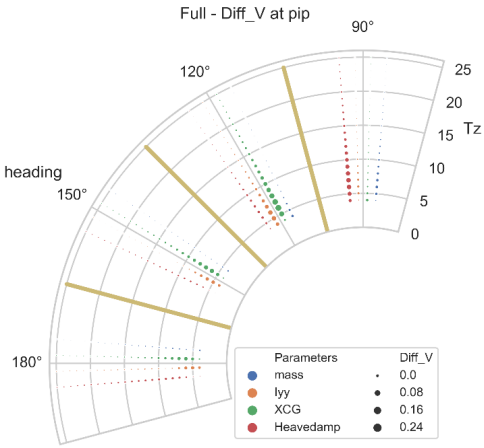

Figure 16: Jittered polar plots of $Diff_V^{pip}$, full loading condition, for β_w= 90˚, 120˚, 150˚, 180˚, $T_Z \in [4, 25]s$

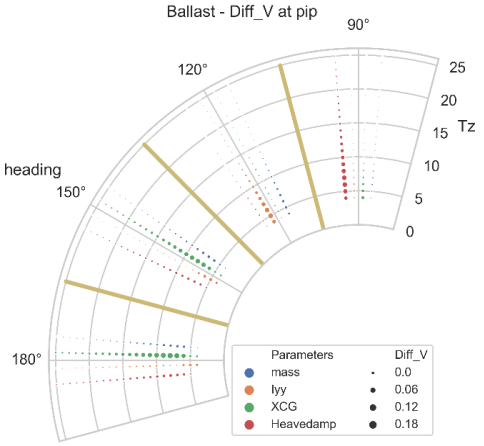

Figure 17: Jittered polar plots of $Diff_V^{pip}$, ballast condition, for β_w= 90˚, 120˚, 150˚, 180˚, $T_Z \in [4, 25]s$

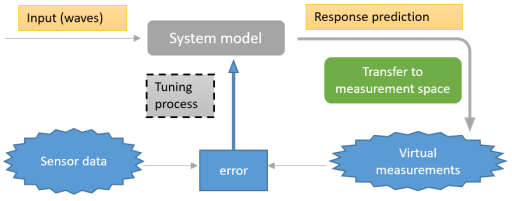

Figure 18: Example of a simple model tuning process

PARAMETER IDENTIFICATION

For digital twin application, it is essential that the numerical model can be actively adapted based on live measurements during the whole asset life time. Figure 18 shows a simple example process of system model modification. The potential applicable tuning process / methodology will not be discussed in this paper. The measurements could be, for example, the 90-percentile vertical velocity of the crane tip starboard for a duration of 3 hours where the criterion of complete tuning could be that the error of the V_{P90}^{tip} value from sensor data and prediction model is small enough, e.g., less than 10^{-4} m/s.

Assumptions and limitations

Assuming using V_{P90}^{tip} as measurement, could we succeed in tuning the hydrodynamic model to get the "right" RAO? In this paper, precise weather information and response measurements were assumed. In addition, it was also assumed that the potential linear theory perfectly describes the system except the additional damping terms. So, the only uncertainties are from the sensitive parameters of hydrodynamic model (system model in Figure 18). In this case study, it was also assumed that only one parameter was subject to modification.

The following sensor data were used, assuming no noises: 1) GPS data, so that the location, heading and speed of the vessel were known; 2) with known vessel location, weather information (e.g. sea state) could be obtained. Practically, 2D wave spectrum could be available and is considered reliable. In this study, the sea state was assumed to be perfectly described by a long-crest Pierson-Moskowitz spectrum; 3) Onboard MRU data, so the rigid body response (motion, velocity and acceleration, for all 6 dofs) at any location on vessel is known; 4) There are some sensors measuring ballast system and COG, etc. However, these measurements are subjected to uncertainties.

Case study

The sea state (SS1) and loading condition specified in Table 5 is studied, to test if we could find the right parameter for tuning in order to get the right RAO sets purely based on the criterion of the V_{P90}^{tip}:

Table 5: Study case information – SS1

Parameters	Value
H_S	2 m
T_Z	10 s
β_w	120 ˚
Loading condition	Ballast (approximately)

According to conclusion from Table 4 and to limit the scope, XCG, GMT and β_{44} were considered as candidate parameters for tuning in this case study. The 3-hour V_{P90}^{tip} at (60.0, 13.0, 12.0) w.r.t. the reference coordinate system, was set as criterion for model tuning. Tuning process was considered complete whenever the error of V_{P90}^{tip} was less than 10^{-2} m/s.

Applying the presumed base model (i.e. ballast condition, deep water, 10kn, with 5% additional roll damping and -0.5m GMT correction), $V_{P90}^{tip}(base\ model, SS1)$ is 1.31 m/s. Then the measurement $V_{P90}^{tip}(Var, SS1)$ of 1.29 m/s is received. The true parameter to tune from the base case of ballast condition is actually GMT from -0.5m to -0.25m. However, all the following 3 tuning results will meet the P90 criterion:

1. Case A: correction of XCG 1.0m towards stern
2. Case B: correction of β_{44} from 5% to 5.5%
3. Case C (True case): GMT free surface correction from -0.5m to -0.25m

Figure 19 shows the RAO of Heave velocity at the crane tip from Case A, B and C. Please note that the "true" model is actually quite close to the presumed base model. So, it may not expect large difference of heave velocity RAO among Case A, B and C. However, clear difference of crane tip heave velocity RAO is seen at response periods from 8s to 14s.

T_P of SS1 is about 14s for PM spectrum, ref [21]. At this peak period, there is insignificant RAO difference. However, if the tuned model from Case A or Case B is used, errors of future response predictions for sea states with T_P between 8s and 14s may be expected.

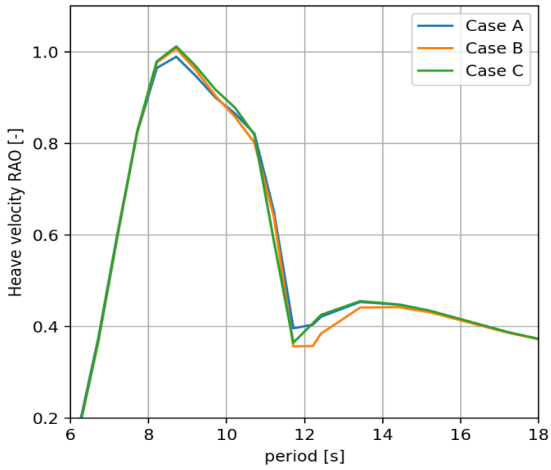

Figure 19: Heave Velocity RAO at crane tip, 120° wave heading.

From this case study, it can be concluded that it is not possible to identify the true parameter for tuning, only based on one criterion and one sea state measurement. Consequently, it would also be difficult to estimate how much the error could be due to using the tuned RAO from a wrong parameter.

Measurements from more sea states

Can the correct parameter be identified to tune by using more measurements from different sea states? In addition to measured V_{P90}^{tip} from SS1, measurement from another sea state, SS2 ($H_S = 3m$, $T_Z = 7$s, $\beta_w = 120^\circ$), is available. $V_{P90}^{tip}(base\ model, SS2) = 2.34\ m/s$. The measured V_{P90}^{tip} for SS2 is 2.32 m/s.

Table 6: Tuning results (from base case) – measurements from two sea states

Parameters	SS1	SS2
XCG	-1.0m	-0.4m
$\boldsymbol{\beta_{44}}$	+0.5%	+0.37%
GMT	**+0.25m**	**+0.25m**

Results in Table 6 show that only the tuning of GMT agrees perfectly between SS1 and SS2. Therefore, confidence is increased to exclude XCG from the three tuning candidates. However, one still cannot exclude β_{44} as a tuning candidate, because the additional roll damping is sea state dependent. This means that sea state dependent parameters cannot be identified by getting more measurement from other sea states. So, for model tuning, it is valuable to split the candidate parameters into categories of permanent, loading condition dependent and sea state dependent.

More criteria

As has been shown, different parameters influence the RAOs in different ways. Some parameters mainly influence RAO at a limited range of period (e.g., additional damping) and for some specific dofs (e.g., GMT). Some parameters only affect the amplitude of RAO (e.g. additional damping), while some parameters can affect both amplitude and peak period of RAO (e.g. GMT, XCG). It could be important to take these properties into account when identifying the right parameter to tune.

Vessel response at a specific location may contain vessel RAO information for multiple dofs. For example, heave motion at crane tip results from heave, roll and pitch motion RAO at midship. Different criteria, e.g., using measurements from other locations, V_{P90}^{locj}, may help to identify the right parameter to tune. In addition, the derivatives and integration of the velocity RAOs could also give more useful information. This means, applying motion and acceleration responses as additional criteria may help to identify the right parameters to tune.

SS1 is again used for case studies. Candidate parameters are still XCG, GMT and β_{44}. Case study "Locations" uses the P90 heave velocity for SS1 at two different locations, i.e., crane tip starboard (tip) and stern 10m starboard from vessel longitudinal axis (st10). Case study "Response" uses the P90 heave acceleration for SS1 at tip location, $A_{P90}^{tip}(SS1)$, in addition to $V_{P90}^{tip}(SS1)$.

Results in Table 7 and Table 8 show that multiple criteria for one sea state help exclude both loading condition dependent and sea state dependent parameters, promisingly leading to identify the right parameter for model tuning. Using different responses at the same location might be a better choice compared with same response type at different locations. Because response at

different locations is calculated based on rigid body motion assumption, which could be challenging for large vessels.

Table 7: Tuning results (from base case) – Case "Location"

Parameters	tip	st10
XCG	-1.0m	-1.37m
β_{44}	+0.5%	-0.25%
GMT	**+0.25m**	**+0.25m**

Table 8: Tuning results (from base case) – Case "Response"

Parameters	V_{P90}^{tip}	A_{P90}^{tip}
XCG	-1.0m	-0.68m
β_{44}	+0.5%	+0.3%
GMT	**+0.25m**	**+0.25m**

CONCLUSION AND DISCUSSION

It is important to consider the effects from water depth and vessel speed when building RAO functions. However, considering the uncertainty of the vessel speed and water depth measurements, and considering the simplifications of the applied theories for hydrodynamic analysis regarding vessel speed and shallow water effects, it might not be necessary to include those parameters for tuning purpose. When building RAO database, it is suggested to have sufficient resolution of water depths and vessel speeds to ensure the accuracy of RAO sets for the future use. Validation of potential theory could be challenging for very shallow water depth and uneven seabed conditions.

Ignoring the weak nonlinearity of parametric sensitivity to RAOs discussed in "Numerical results" section, the uncertainty of most interesting parameters could be well described by a Gaussian model, with the prior value representing the most probable (mean) value. However, for modelling uncertainty of additional damping, this might be questionable, because 1) biased engineering judgement usually is applied; 2) and the uncertainty is usually not symmetric w.r.t. the prior damping value used.

This paper describes how the selected vessel hydrodynamic model parameters affect response RAOs. Parametric sensitivity to RAOs depends on T_Z, β_w, location, load condition and corresponding parametric uncertainty range, etc. The study shows that β_{33}, β_{44}, COG, I_{yy}, GMT and M are important parameters with respect to the vessel response sensitivity, and therefore could be selected for model tuning.

Model tuning requires to identify the correct parameter(s) first. The case study for parameter identification shows that measurements from different sea states cannot help identifying sea state dependent parameters. It is valuable to apply multiple criteria and multiple types of measurements (e.g., different locations and responses) to identify the correct parameter. The case study on parameter identification assumed precise knowledge on weather information and vessel response measurements, and only one parameter was subject to model tuning. However, real world is noisy and uncertain. The number of tuning parameters is normally also unknown. In addition, there is an uncertainty due to model simplification of vessel response system in potential theory. These uncertainties can lead to potentially overfitting or underfitting problems. Future work is required on how to identify multiple parameters for tuning process. In reality, no candidate parameters can be excluded due to uncertainties and noises from input and measurements. However, this can hopefully be circumvented by probabilistic modelling of candidate parameters.

ACKNOWLEDGEMENTS

This work was made possible through the Centre for Research based Innovation MOVE, financially supported by the Norwegian Research Council, NFR project no. 237929 and the consortium partners, http://www.ntnu.edu/move. Special thanks are given to Olav Rognebakke, Jens Bloch Helmers, Håvard Nordtveit Austefjord and Hui Sun in Section of Hydrodynamics & Stability in DNV GL for providing models, and various helpful technical discussions and supports. Thanks are also given to DNV GL Riser Technology Section for providing office and facilities when the first author studied at Høvik.

REFERENCES

[1] O. Faltinsen, "Sea Loads on Ships and Offshore Structures," Cambridge University Press, 1993.

[2] L. K. Alford, R. F. Beck, J. T. Johnson, D. Lyzenga, O. Nwogu og A. Zundel, «A Real-time System for Forecasting Extreme Waves and Vessel Motions,» i *OMAE*, 2015.

[3] B. Connell, J. Rudzinsky og C. Brundick, «Development of an environmental and ship motion forecasting system,» i *OMAE*, St. John's, 2015.

[4] J. Kusters, K. Cockrell, B. Connell, J. Rudzinsky og V. Vinciullo, «FutureWavesTM: a Real-time Ship Motion Forecasting SYstem employing Advanced Wave-Sensing Radar,» i *IEEE*, 2016.

[5] G. F. Clauss, S. Kosleck og D. Testa, «Critical Situations of Vessel Operations in Short Crested Seas - Forecast and Decision Support System,» *Journal of OMAE,* vol. 134, 2012.

[6] J. Dannenberg, K. Hessner, P. Naaijen, H. Boom og K. Reichert, «The On Board Wave and Motion Estimator OWME,» i *ISOPE*, Beijing, 2011.

[7] G. Clauss, S. Kosleck, D. Testa og K. Hessner, «Forecast of critical situations in short-crested seas,» i *OMAE*, Estoril, 2008.

[8] P. Naaijen, D. Roozen og R. Huijsmans, «Reducing operational risks by on-board phase resolved prediction of wave induced ship motions,» i *OMAE*, Busan, 2016.

[9] J. Nielsen, N. Pedersen, J. Michelsen, U. Nielsen, J. Baatrup, J. Jensen og E. Petersen, «SeaSense - Realtime Onboard Decision Support,» WMTC, 2006.

[10] E. A. Tannuri, J. V. Sparano, A. N. Simos and J. J. D. Cruz, "Estimating directional wave spectrum based on stationary ship motion measurements," *Applied Ocean Research,* vol. 25, pp. 243-261, 2003.

[11] U. D. Nielsen, A. H. Brodtkorb and A. J. Sørensen, "A brute-force spectral approach for wave estimation using measured vessel motions," *Marine Structures,* pp. 101-121, 2018.

[12] W. Qiu, J. Junior, D. Lee, H. Lie, V. Magarovskii, T. Mikami, J. Rousset, S. Sphaier, L. Tao and X. Wang, "Uncertainties related to predictions of loads and responses for ocean and offshore structures," *Ocean Engineering,* vol. 86, pp. 58-67, 2014.

[13] ITTC, "ITTC Quality System Manual Recommended Procedures and Guidelines - Numerical Estimation of Roll Damping," 2011.

[14] «Wasim User Manual,» DNV GL, 2018.

[15] D. Kring, «Time Domain Ship Motions by a Three-Dimensional Rankine Panel Method,» 1988.

[16] Y. Luo, «Numerical Investigation of Wave-Body Interactions in Shallow Water,» NTNU, 2013.

[17] U. D. Nielsen, «Transformation of a wave energy spectrum from encounter toabsolute domain when observing from an advancing ship,» *Applied Ocean Research,* vol. 69, pp. 160-172, 2017.

[18] G. Clauss, F. Stempinski, M. Dudek and M. Klein, "Water depth influence on wave-structure-interaction," *Ocean Engineering,* vol. 36, pp. 1396-1403, 2009.

[19] K. McTaggart, «Ship Radiation and Diffraction Forces at Moderate Forward Speed,» 2015.

[20] J. Journee og J. Pinkster, Introduction in Ship Hydromechanics, Lecture MT519, 2002.

[21] "DNVGL-RP-C205 Environmental conditions and environmental loads," DNV GL, 2017.

A.2 Paper A2

Paper A2:
X. Han, B. J. Leira, and S. Sævik, 2021. Vessel hydrodynamic model tuning by discrete Bayesian updating using simulated onboard sensor data. *Ocean Engineering* 220.

Ocean Engineering 220 (2021) 108407

Contents lists available at ScienceDirect

Ocean Engineering

journal homepage: www.elsevier.com/locate/oceaneng

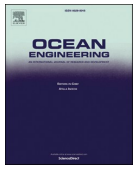

Vessel hydrodynamic model tuning by Discrete Bayesian updating using simulated onboard sensor data

Xu Han [a,b,*], Bernt Johan Leira [a,b], Svein Sævik [a,b]

[a] Department of Marine Technology, Norwegian University of Science and Technology (NTNU), 7491, Trondheim, Norway
[b] Centre for Research-based Innovation on Marine Operations (SFI MOVE), Norway

ARTICLE INFO

Keywords:
Tuning of seakeeping model
Wave-induced vessel responses
Sensor signal processing
Discrete Bayesian updating
Inverse distance weighting
Sensitivity studies
Validation analysis

ABSTRACT

Vessel and wave hydrodynamics are fundamental for vessel motion prediction. Improving hydrodynamic model accuracy without compromising computational efficiency has always been of high interest for safe and cost-effective marine operations. With continuous development of sensor technology and computational capacity, an improved digital twin concept for vessel motion prediction can be realized based on an onboard online adaptive hydrodynamic model. This article proposes and demonstrates a practical approach for tuning of important vessel hydrodynamic model parameters based on simulated onboard sensor data of vessel motion response. The algorithm relies fundamentally on spectral analysis, probabilistic modelling and the discrete Bayesian updating formula. All case studies show promising and reasonable tuning results. Sensitivities of the approach with respect to its key parameters were also studied. Sensor noise has been considered. The algorithm is found to be computationally efficient, robust and stable when tuning the values of hydrodynamic parameters and updating their uncertainties, within reasonable sensor noise levels.

1. Introduction

The energy sector is experiencing rapid change with a fast growth in offshore wind and solar farms, an increased number of subsea installations to provide tie-backs to existing oil and gas facilities as well as a continuous drive towards exploration of natural resources in deeper and colder ocean areas. These trends lead to more challenging marine operations, facing heavier offshore lifts, more complex operation systems, and severe operational environments. Hence, the economic incentives for obtaining broader operational weather windows by reducing the inherent uncertainties of marine operations increase. As of today, engineering practice considers uncertainties conservatively and marine operations are designed and simulated according to rules (e.g., DNVGL-ST-N001 (2016)) before they are executed. Uncertainty reduction in vessel seakeeping analysis has been focused on by both industry and research institutions for decades. Knowledge on modelling of wave and vessel hydrodynamics has been rather well developed, with respect to engineering practice (Faltinsen, 1990; DNVGL-RP-C205, 2017). In principle one can design the marine operation by application of the most computational demanding and accurate hydrodynamic models, e.g., by including nonlinear wave kinematics (Yue et al., 2008; Nouguier et al., 2014) and vessel hydrodynamics (Cao et al., 2010; Larsen et al., 2019; Himeno, 1981; Faltinsen, 2015), and even by applying computational fluid dynamics (CFD) (Kim, 2011).

However, the on-site uncertainties related to wave and vessel condition may reduce the value of engineering efforts during the design phase. Instead of applying very high fidelity models in the operation design phase to increase the accuracy (e.g., by using nonlinear or CFD programs), a lot of efforts have been made on increasing the knowledge of the on-site wave forecast and real-time vessel operational condition. With the development in sensor technology and computational process capacity during the last two decades, many research-oriented onboard decision support systems (ODSS) for marine and offshore activities have been developed aiming at improving vessel motion predictions. Examples are: 1) SeaSense system (Nielsen et al., 2006); 2) CASH system (Clauss et al., 2012); 3) OWME project (Onboard Wave and Motion Estimator) applying non-coherent WaMoS II radar (Dannenberg et al., 2010; Naaijen et al., 2016, 2018); 4) ESMF project (Environment and Ship Motion Forecasting) applying coherent wave radar systems (Connell et al., 2015; Kusters et al., 2016; Alford et al., 2015). On-site full-scale tests have been performed for validation of the different proposed methods (Naaijen et al., 2016, 2018; Connell et al., 2015; Alford et al.,

* Corresponding author. Department of Marine Technology, Norwegian University of Science and Technology (NTNU), 7491, Trondheim, Norway.
E-mail address: xu.han@ntnu.no (X. Han).

https://doi.org/10.1016/j.oceaneng.2020.108407
Received 30 April 2020; Received in revised form 21 September 2020; Accepted 22 November 2020
Available online 9 December 2020

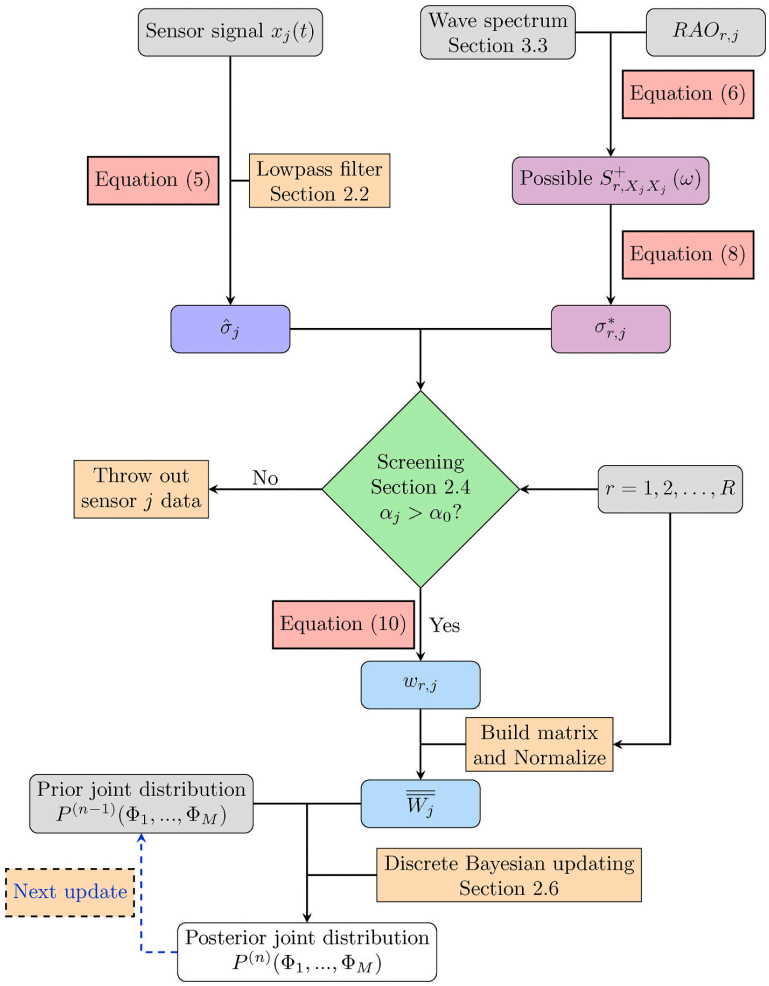

Fig. 1. Process of tuning vessel hydrodynamic model parameters, based on vessel response sensor signal.

2015). Challenges on roll motion prediction based on the vessel being modelled as a linear transfer function, known as response amplitude operator (RAO), have been reported in all the relevant tests.

A successful wave-induced vessel motion prediction requires two sources, i.e., a sufficiently accurate wave forecast and a numerical vessel model which describes the relationship between wave and vessel motion for the current operational condition. Most developed ODSS's focus on improving wave prediction, either by wave radar systems, or by the "ship as a wave buoy" analogy. Those approaches are all influenced by the vessel motion. The wave radar approaches could possibly predict the encounter waves a few minutes ahead based on a linear wave propagation model, and hence a vessel response envelope can be well estimated. However, the predicted time series of the encounter waves at the vessel position will not be accurate enough. On the other hand, nonlinear wave propagation models could better forecast the encounter waves at the vessel position, but the computational time is a challenge for real-time application (Alford et al., 2015; Grilli et al., 2011). The "ship as a wave buoy" analogy, estimating waves in the form of wave spectrum, requires good prior knowledge on vessel conditions (Nielsen, 2006; Brodtkorb et al., 2018a; Nielsen et al., 2019; Ren et al., 2021). Nielsen (2007) and Tannuri et al. (2003) demonstrated the influence of vessel condition uncertainty on the sea state estimation. Most sea state estimation approaches presume stationary environmental and vessel conditions. Iseki (2009) and (Brodtkorb et al., 2018b) investigated the influence of using non-stationary ship motion data on sea state estimation. In addition, with developed information technology, numerical weather prediction (NWP) can be improved with increased spatial and temporal resolution. Instead of only reporting the wave forecast in terms of significant wave height (H_s), peak period (T_p), and direction (β_W), a full 2D wave spectral description now can be provided by several weather forecasters (e.g., Galvin (2014)). This may also help reducing uncertainties of vessel motion prediction.

Simplifications in vessel seakeeping models have to be made in order to design the ODSS's for real-time purposes. Most ODSS's use linear transfer functions (i.e., RAOs) between wave and vessel response. Application of vessel motion RAOs has proven to be reliable, computationally cheap and practically accurate for moderate seas. Some advanced programs use retardation functions based on the hydrodynamic coefficient database to predict real-time motion in the time domain, e.g., Milewski et al. (2015). The interest of using machine learning for vessel motion analysis has increased in recent years, e.g., Cheng et al. (2019); De Masi et al. (2011); Nielsen et al. (2018). Pure

data driven and so-called physical based data-driven machine learning methods are hot research topics within several disciplines related to digitalization. The Artificial intelligence (AI) models trained by available data, are however very sensitive to the provided historical data. For nonlinear systems, the AI models may therefore fail if the training data set is insufficient with respect to describing the nonlinearity. For vessels with frequently changing loading conditions, it may be challenging to obtain sufficient training data and to generalize. AI approaches have also faced difficulties of being accepted by energy and maritime industries due to lack of physics reasoning and documented reliability.

Traditionally, hydrodynamic coefficients are calibrated to scale experiments (van Daalen et al., 2014), for predefined vessel loading conditions where the uncertainties from vessel inertia distribution and viscous roll damping could be significant. The situation onboard may be different from the designed or simulated conditions, e.g. due to the vessel having a different load condition than that originally assumed. Consequently, the presumed RAOs may not be appropriate to apply for onboard vessel motion prediction. However, improving the accuracy of RAOs based on vessel motion and wave information (e.g., H_s, T_p, β_W, and directional spreading) is practically very challenging. Normally vessel motion (e.g., heave motion η_{33}) can be estimated (Faltinsen, 1990) by

$$\eta_{33}(\omega) = \sum_{\beta_W} \zeta(\omega, \beta_W) \cdot H_{33}(\omega, \beta_W) \tag{1}$$

where $\eta_{33}(\omega)$ is the heave motion at frequency ω, $\zeta(\omega, \beta_W)$ is the wave elevation at frequency ω along the direction β_W, and $H_{33}(\omega, \beta_W)$ is the corresponding heave motion RAO. Calculating the RAO $H_{33}(\omega, \beta_W)$ represents the inverted problem of vessel motion estimation. There is typically no unique solution for such inversion problems, because $H_{33}(\omega, \beta_W)$ is direction dependent, while $\eta_{33}(\omega)$ carries no such information. Alford et al. (2014) tried to solve the inversion problem using singular value decomposition (SVD) technique to solve the ill-conditioned equation $H_{yx}(\omega) = \frac{S_{yx}(\omega)}{S_{xx}(\omega)}$. As a consequence, the directional dependency characteristics of the true transfer function will be sacrificed, making it questionable whether the calculated transfer function can be applied to a new sea state.

Instead, this paper tries to improve the RAO accuracy by modifying the important parameters in vessel seakeeping model based on wave information and vessel motion measurements. Based upon an updated hydrodynamic model, the RAO can be recalculated and possibly applied to other sea states, potentially increasing the accuracy of seakeeping prediction and the safety of marine operations. However, there are some challenges: 1) It is a multi-dimensional problem. There could be hundreds of parameters subject to uncertainty. 2) It is a multi-modal problem. Many combinations of parameters can possibly fit perfectly with the measurement data, e.g. in terms of response power spectrum, but those combinations may be far away from each other. 3) It is a nonlinear problem with respect to the relationship between hydrodynamic parameters and the resulting vessel motion RAO. In this paper, a probabilistic approach of vessel hydrodynamic parameter tuning based on onboard motion measurements is proposed, where the adaptive model will both update the parameter values and their confidence, quantitatively. This is an important step towards reliability-based marine operations and reducing inherent conservatism. The adaptive model can be continuously applied throughout the whole lifetime of the vessel, assisting in monitoring, inspection, management, life extension, etc., in accordance with the digital twin concept.

The paper is organized as follows. Section 2 details the proposed model tuning algorithm. Then the algorithm is demonstrated by case studies of a selected vessel model. The inputs and basis of the case studies are described in Section 3. Results of two studied cases are described in Section 4. Results of sensitivity analyses for key parameters in the proposed method are reported in Section 5. The proposed tuning methodology is validated by extensively simulated tuning analyses in Section 6. Conclusions and future work are then summarized in Section 7.

2. Model tuning procedure

Assume that there are M uncertain vessel parameters $(\Phi_1, \Phi_2, \ldots, \Phi_M)$ and there are J sensors measuring interesting vessel motions (e.g., displacement, velocity, and acceleration of heave and roll at different locations onboard). Based on the prior knowledge on the uncertain vessel parameters and available vessel sensors $j = 1, 2, \ldots, J$, a RAO database covering all possible vessel conditions for all sensors should be available for the tuning process. The procedure for tuning of vessel parameters $(\Phi_1, \Phi_2, \ldots, \Phi_M)$ based on measurements from onboard sensors at a specific sea state can be divided into the following steps as illustrated in Fig. 1:

1. Initialize the discrete joint probability distribution $P^{(0)}(\Phi_1, \Phi_2, \ldots, \Phi_M)$ based on prior knowledge on the vessel condition.
2. Process the sensor measurements (e.g., signal $x_j(t)$ from sensor j), including signal filtering and calculation of the filtered signal standard deviation $\widehat{\sigma}_j$.
3. Calculate the standard deviations of the possible responses $\sigma^*_{r,j}$, based on the candidate RAOs from the RAO database. $r \in \{1, 2, \ldots, R\}$ represents the r^{th} combination of variables in the RAO database, i.e., $(\Phi_{i1}, \Phi_{i2}, \ldots, \Phi_{im}, \ldots, \Phi_{iM})$, where Φ_{im} the im^{th} discrete value for the vessel parameter Φ_m and $m \in \{1, 2, \ldots, M\}$. R is the total number of possible combinations of uncertain vessel parameters.
4. Screen out less significant sensors.
5. Calculate the weight matrix $\overline{\overline{W_j}}$ for the considered whole range of uncertain vessel parameters, if sensor j passes the above screening phase.
6. Normalize $\overline{\overline{W_j}}$, and interpolate the weight matrix $\overline{\overline{W_j}}$ from the size $I1 \times I2 \times \cdots \times IM$ (variable resolution in the RAO database) to the size $K1 \times K2 \times \cdots \times KM$ (variable resolution in the discrete probability distribution model).
7. Update the joint probability distribution $P^{(1)}(\Phi_1, \Phi_2, \ldots, \Phi_M)$.
8. Repeat the previous steps, and continuously update the variable distribution, $P^{(2)}(\Phi_1, \ldots, \Phi_M)$, …, $P^{(n)}(\Phi_1, \ldots, \Phi_M)$, ….

All steps are explained in the following subsections. The detailed parameter explanations can be found in Nomenclature.

2.1. Initialization of joint probability distribution

The probabilistic model of the M uncertain vessel parameters can be initialized as independent Gaussian distributions with presumed mean μ_m and variance σ_m^2 for each variable, based on prior knowledge on the vessel.

$$\Phi_m \sim Gaussian\left(\mu_m, \sigma_m^2\right) \tag{2}$$

The variance of each variable depends on vessel geometry, loading condition, engineering judgement and etc. It is further assumed that the possible values of the variable Φ_m are within the range of $\mu_m \pm 3\sigma_m$. In the joint probability distribution model, each variable was discretized into Km number of values. A multivariate probabilistic model with M uncertain variables can be expressed by a discrete joint probability distribution $P(\Phi_1, \Phi_2, \ldots, \Phi_M)$. The probability density function of one possible combination of $(\Phi_1, \Phi_2, \ldots, \Phi_M)$ is expressed by $PDF(\Phi_{k1}, \Phi_{k2}, \ldots, \Phi_{kM})$, which is established by

$$PDF(\Phi_{k1}, \Phi_{k2}, \ldots, \Phi_{kM}) = \prod_{m=1}^{M} PDF(\Phi_{km}) \tag{3}$$

The probability for this combination can then be calculated by

$$P(\Phi_{k1}, \Phi_{k2}, \ldots, \Phi_{kM}) = PDF(\Phi_{k1}, \Phi_{k2}, \ldots, \Phi_{kM}) \cdot \prod_{m=1}^{M} \Delta\Phi_m \tag{4}$$

where $\Delta\Phi_m$ means the interval of values for the variable Φ_m. Unrealistic values such as negative values for damping were removed in the initialization step for probabilistic modelling. In addition, normalization of the probability distribution was done through every tuning step. This was to ensure that the cumulative probability sums to 1.0.

2.2. Signal processing

Sensitivity analysis with respect to signal lowpass filtering demonstrated that it is essential to filter out noise before the probability updating process. The fast Fourier transform (FFT) lowpass filtering approach was applied with 1.0 Hz as the cutoff frequency (f_{lp}) for the base case in the case studies. The filtered signal for sensor j is denoted as $\widehat{x}_j(t)$. After filtering, the signal standard deviation can be calculated by means of the unbiased sample standard deviation:

$$\widehat{\sigma}_j = \sqrt{\frac{\sum_{t=1}^{N_t}\left(\widehat{x}_j(t) - \overline{x}_j\right)^2}{(N_t - 1)}} \tag{5a}$$

$$\overline{x}_j = \frac{\sum_{t=1}^{N_t}\widehat{x}_j(t)}{N_t} \tag{5b}$$

where $\widehat{x}_j(t)$ is the filtered vessel response time series from sensor j for the time step t and N_t is the number of time steps. The original noisy sensor signal $x_j(t)$ (in time domain) or $X_j(\omega)$ (in frequency domain) can be measurement of the vessel displacement, velocity, or acceleration for any degree of freedom (DOF).

2.3. Calculation of possible response spectra based on candidate RAOs

For a certain sensor numbered as j, within the known ranges of the uncertain vessel hydrodynamic parameters, the corresponding possible response spectra can be calculated by

$$S^+_{r,X_jX_j}(\omega) = \left|H_{r,X_j\zeta}(\omega,\beta_W)\right|^2 \cdot S^+_{\zeta\zeta}(\omega,\beta_W) \tag{6}$$

where S^+ means single sided power spectrum, $H_{r,X_j\zeta}(\omega,\beta_W)$ represents the linear transfer function (i.e., RAO) between the interesting vessel response $X_j(\omega)$ at the sensor j and wave elevation $\zeta(\omega,\beta_W)$, for the r^{th} combination of variables in the RAO database, $r \in \{1,2,\ldots,R\}$ and

$$R = \prod_{m=1}^{M} Im \tag{7}$$

where Im is the number of discrete values for variable Φ_m in the RAO database. Then the possible response standard deviation for the r^{th} combination can be calculated by

$$\sigma^*_{r,j} = \sqrt{\sum_{n=1}^{N_\omega} S^+_{r,X_jX_j}(\omega_n)\cdot\Delta\omega} \tag{8}$$

where N_ω is the total number of discretized frequencies for the response spectrum.

2.4. Screening of sensors

If the variation of the considered parameters influences the sensor j measurements very little, all calculated $\sigma^*_{r,j}$ values will be very close. Then this sensor should be considered as valueless, based on the following arguments:

1. The other uncertainties from e.g., simplification of vessel hydrodynamics, measurement noise, discretization of signals and power spectra, and wave hindcast, will be much more significant than the present parameter variations. Under such condition, updating parameters becomes unreasonable.
2. For the weight calculation to be described in Section 2.5, if $\left|\sigma^*_{r,j} - \widehat{\sigma}_j\right| \to 0$, the weight $w_{r,j}$ could be very large. A small amount of noise or other uncertainties may result in a significantly biased weight matrix.

Therefore, it is important to identify and ignore valueless sensors for each sea state before updating the joint probability distribution of the uncertain vessel parameters. Consequently, a new parameter α_j is introduced, named SSR (sensor screening ratio) which is defined by

$$\alpha_j = \frac{\sigma_{\sigma^*_{r,j}}}{\widehat{\sigma}_j} \tag{9a}$$

$$\sigma_{\sigma^*_{r,j}} = \sqrt{\frac{\sum_{r=1}^{R}\left(\sigma^*_{r,j} - \overline{\sigma^*_j}\right)^2}{R-1}} \tag{9b}$$

$$\overline{\sigma^*_j} = \frac{\sum_{r=1}^{R}\sigma^*_{r,j}}{R} \tag{9c}$$

where $\sigma_{\sigma^*_{r,j}}$ is the standard deviation of $\sigma^*_{r,j}$, $r = 1,2,\ldots,R$. The base case studies used a screening criterion of $\alpha_j = 0.05$. For a certain sensor j, if $\alpha_j < 0.05$, then the sensor j will be excluded when updating the parameters. Selection of the α_j value may depend on the quantity and location of the sensor, the sea state, and the selected vessel parameters to be modified.

2.5. Weight calculation

The distance between $\sigma^*_{r,j}$ and $\widehat{\sigma}_j$ represents how much the r^{th} combination of the parameters can be believed in based on the received measurements at sensor j. The weight factor can be calculated by inverse distance weighting introduced by Shepard (1968). Normalization is applied to the weight matrix before updating the joint probability distribution of parameters.

$$w_{r,j} = \left\| \frac{1}{\left|\sigma^*_{r,j} - \widehat{\sigma}_j\right|^p} \right\| \tag{10}$$

where $p \in (0,\infty)$ is called the power parameter and $\|\cdot\|$ is a normalization operator.

2.6. Discrete Bayesian updating

Classical discrete Bayes' theorem may be simply expressed as

$$P(U|V) = \frac{P(U)\cdot P(V|U)}{P(V)} \tag{11}$$

where U and V are events. $P(U|V)$ is the likelihood of event U occurring given that V is true while $P(V|U)$ is the likelihood of event V occurring given that U is true. For the tuning of vessel hydrodynamic parameters, U can be considered as those uncertain parameters, while V corresponds to the received sensor signals. However, the Bayesian inference may not seem so simple as shown in Equation (11), due to the practical difficulties of estimating $P(V|U)$ and $P(V)$. Inspired by Labbe (2018), the Bayesian updating applied for model tuning could also be understood as:

$$posterior = \frac{prior\cdot likelihood}{normalization} \tag{12}$$

where *likelihood* means the possibility of getting such measurement (e.g., sensor j) result for the particular combination (e.g., r) of uncertain vessel

Table 1
Vessel information, base case.

Parameters	Description	Value	Unit
L_{PP}	Length between perpendiculars	~120	m
B	Breadth	~27	m
D (Ballast)	Draft	~5.1	m

parameters, which can be reasonably represented by the weight factor $w_{r,j}$. This is the key to updating our belief to the prior knowledge after receiving the sensor data. With Equation (10), $w_{r,j}$ is calculated based on the discrete vessel parameter values used in the RAO database. For one sensor j, the size of the calculated weight matrix $\overline{\overline{W_j}}$ for M variables by Equation (10) is $I1 \times I2 \times \cdots \times IM$. However, the joint probability distribution of variables uses much more discrete values than was used to build RAO database. In order to update the joint distribution of variables, the weight matrix needs to be interpolated to the size of $K1 \times K2 \times \cdots \times KM$. Multi-dimensional linear interpolation was performed by means of the Python xarray package (Hoyer and Hamman, 2017).

Discrete Bayesian updating could easily apply to nonlinear systems such as the described hydrodynamic parameter tuning challenge. Due to the nonlinearity, the updated probability distribution will have no closed-form mathematical description after the first update, and the updated probability distribution will no longer be Gaussian. The n^{th} updating for the r^{th} combination of uncertain vessel parameters based on the valuable sensor j data can then be formulated as:

$$PDF^{(n)}(\Phi_{k1}, \ldots, \Phi_{kM}) = PDF^{(n-1)}(\Phi_{k1}, \ldots, \Phi_{kM}) \cdot w_{r,j} \tag{13}$$

3. Case study basis

3.1. Numerical vessel model

The case study was based on an offshore supply vessel (OSV) hydrodynamic seakeeping model. The primary vessel dimensions are summarized in Table 1. The coordinates refer to the reference coordinate system moving steadily at the vessel forward speed, as illustrated in Fig. 2. The positive x-axis points from stern to bow ($x = 0$ aft), the z-axis is pointing vertically upward from keel ($z = 0$ at keel) and the y-axis is normal to the $x - z$ plane where $y = 0$ is at the longitudinal symmetric plane. The wave direction β_W follows the same coordinate system, i.e. waves at 0° heading propagates along the positive x-axis. Table 2 summarizes the location and ID of the virtual sensors considered in the paper. The sensor locations are illustrated in Fig. 2. Practically, the vessel heave response could dominate the operation limit, and hence it is usually of interest to monitor the heave response. Earlier parametric sensitivity study (Han et al., 2020) suggests that measuring different quantities of vessel response (i.e., displacement, velocity, and acceleration) at different locations onboard can help identifying the right uncertain parameter to tune. Therefore, the RAO database contains the heave response (displacement, velocity and acceleration), at three different locations, see Fig. 2. Rigid body motion transformation was assumed in the study.

3.2. RAO database

A RAO database was established based on the ballast condition as the base case. Wasim (DNV GL, 2018) was used for hydrodynamic analysis to create the RAO database. Being a computer program in the DNV GL Sesam family, Wasim is a 3D time-domain hydrodynamic analysis software based on the Rankine panel method (Kring, 1994). Wasim analyses were run through all wave periods for each combination of the studied parameters in the time domain. The outputs were transferred to the frequency domain so as to build the frequency dependent database of hydrodynamic coefficients and thereafter calculate the vessel RAOs by

Table 2
Description of sensor measurements.

Sensor ID	Location	Coordinate (x,y,z) [m]	Signal/measurements
Disp_A	A	(60.0, 0.0, 10.0)	$\eta_{33}(t)$ at location A
Disp_B	B	(60.0, 13.0, 10.0)	$\eta_{33}(t)$ at location B
Disp_C	C	(0.0, 10.0, 14.0)	$\eta_{33}(t)$ at location C
Vel_A	A	(60.0, 0.0, 10.0)	$\dot{\eta}_{33}(t)$ at location A
Vel_B	B	(60.0, 13.0, 10.0)	$\dot{\eta}_{33}(t)$ at location B
Vel_C	C	(0.0, 10.0, 14.0)	$\dot{\eta}_{33}(t)$ at location C
Acc_A	A	(60.0, 0.0, 10.0)	$\ddot{\eta}_{33}(t)$ at location A
Acc_B	B	(60.0, 13.0, 10.0)	$\ddot{\eta}_{33}(t)$ at location B
Acc_C	C	(0.0, 10.0, 14.0)	$\ddot{\eta}_{33}(t)$ at location C

$\eta_{33}(t)$: time series of heave displacement; $\dot{\eta}_{33}(t)$: time series of heave velocity; $\ddot{\eta}_{33}(t)$: time series of heave acceleration.

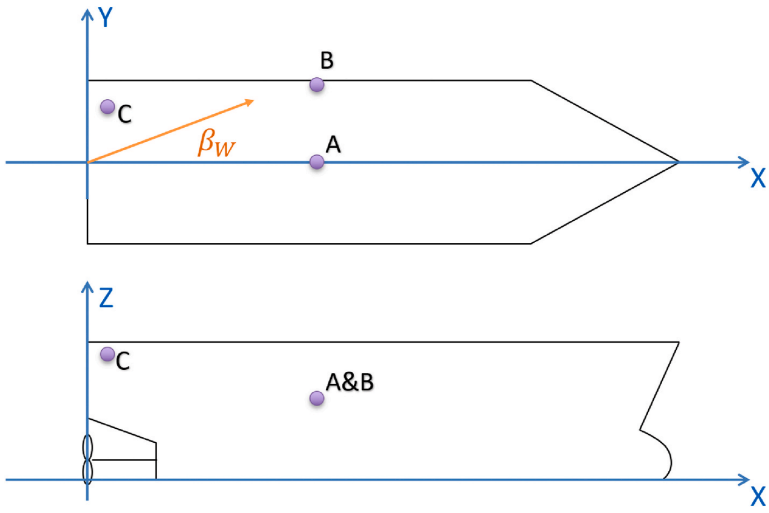

Fig. 2. Illustration of vessel coordinate system and locations of considered interesting points.

Table 3
Parametric range for the considered variables.

Parameters	Variation range	Number of values
Mass	[-6%, +6%]	7
XCG	[-4 m, +4 m]	5
r_{55}	[-9%, +9%]	7
GMT[a]	[0, 1 m]	6
β_{44}	[2%, 14%]	7

[a] Here "GMT" represents the free surface correction to the transverse metacentric height. $GMT = 0.5$m here means that the transverse metacentric height is corrected with -0.5m due to free surface effects. It is not the value of the transverse metacentric height.

$$RAO(\omega, u|\beta_W) = \frac{\overrightarrow{F}(\omega, u|\beta_W)}{-\omega_e^2\left(\overline{\overline{A}}(\omega_e) + \overline{\overline{M_0}}\right) + i\omega_e\overline{\overline{\beta}}(\omega_e) + \overline{\overline{C}}} \tag{14}$$

where ω is the wave frequency, u is the vessel advancing speed, and β_W is the wave heading as illustrated in Fig. 2. $\overrightarrow{F}(\omega, u|\beta_W)$ is the complex-valued wave-induced excitation force, and ω_e is the encounter frequency. $\overline{\overline{A}}$, $\overline{\overline{M_0}}$, $\overline{\overline{\beta}}$ and $\overline{\overline{C}}$ are the added mass matrix, inertia matrix, damping matrix and restoring stiffness matrix of the vessel, respectively.

Only heave RAOs corresponding to the sensors described in Table 2 were included in the RAO database. As summarized in Table 3, variation of 5 parameters were considered for the RAO database, with the described number of discrete values for each parameter. Selection of parameters was based on sensitivity studies of hydrodynamic parameters that influence the vessel motions of interest. Some key findings on the parametric sensitivity study (Han et al., 2020) are: 1) GMT and additional roll damping (β_{44}) both have a strong influence on the roll motion response; 2) Parameters related to the inertia distribution such as XCG, YCG, ZCG, mass and r_{55} have a strong influence on the vessel heave motion at different locations onboard, among which XCG and r_{55} are the most important parameters; 3) YCG only has significant influence on the vessel roll motion and its coupled motions. The ranges represent prior knowledge and the corresponding uncertainties for the parameters. Zero vessel speed was considered in order to avoid dealing with the 3-to-1 mapping problem between wave frequency and encounter frequency for following waves (Nielsen, 2017). In total, 13 wave headings between 0° and 180° with 15° interval were included. Therefore, each sensor in Table 2 has hundreds of thousands heave RAOs prepared.

3.3. Wave spectrum

Ocean waves are usually short-crested in reality. In addition, a sea state may contain both wind sea and swells coming from totally different main directions with significantly distinct peak periods. Precise knowledge on the wave condition was assumed for the studied cases, i.e. uncertainties from wave hindcast/forecast were not considered. For simplicity, the long-crested Pierson-Moskowitz (PM) spectrum $S_{PM}(\omega)$ was used (DNVGL-RP-C205, 2017).

$$S_{PM}(\omega) = 5 \Big/ 16 \cdot H_s^2 \omega_p^2 \omega^{-5} exp\left(-5 \Big/ 4\left(\frac{\omega}{\omega_p}\right)^{-4}\right) \tag{15}$$

where H_s is the significant wave height, and ω_p is the sea state peak frequency.

3.4. Sensor signal simulation

Virtual sensor signals were numerically simulated for the case studies. For each of the 9 virtual sensors described in Table 2, the signals were generated, according to the procedure illustrated in Fig. 3. Firstly, with known wave spectrum $S^+_{\zeta\zeta}(\omega, \beta_W)$ and the true RAO values for

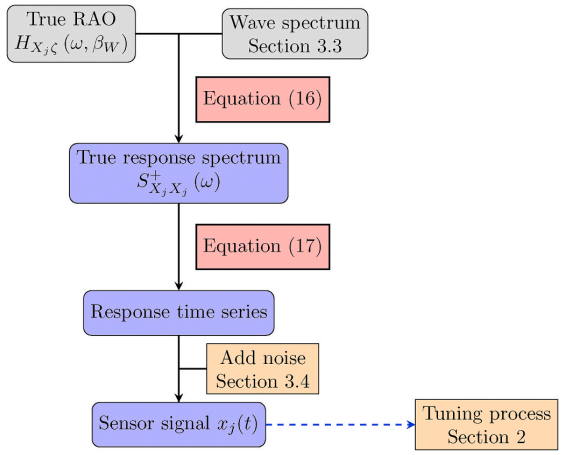

Fig. 3. Process of generating virtual sensor signal $x_j(t)$ for sensor j.

sensor j, the response spectrum can be calculated by

$$S^+_{X_jX_j}(\omega) = \left|H_{X_j\zeta}(\omega, \beta_W)\right|^2 \cdot S^+_{\zeta\zeta}(\omega, \beta_W) \tag{16}$$

where $H_{X_j\zeta}(\omega, \beta_W)$ represents the true RAO for vessel response $X_j(\omega)$. Then the signal of 3-hour response time series with time step of 0.1s was generated by

$$x_j(t) = \sum_{n=1}^{N\omega} N_\omega C_n(\omega_n)\cos(\omega_n t + \phi_n) \tag{17a}$$

$$C_n(\omega_n) = \sqrt{2S^+_{X_jX_j}(\omega_n)\cdot\Delta\omega} \tag{17b}$$

where $\phi_n \in [0, 2\pi)$ is a random phase angle which is continuous and uniformly distributed, $\Delta\omega$ is the width of the radial frequency interval of ω_n, and N_ω is the total number of the discrete frequencies for the response spectrum. Deterministic amplitudes were applied according to Equation (17b). This means that theoretically all possible realizations will return exactly the same response power spectrum when $\Delta\omega \to 0$.

Sensor signal noises were included. Gaussian distributed white noise was assumed with mean value $\mu_N = 0$ and a specified covariance σ_N^2. The noise was added to each time step of the time series independently, according to the specified signal-to-noise Ratio (SNR), defined by

$$SNR = \frac{\sigma_X^2}{\sigma_N^2} \tag{18}$$

where, σ_X^2 is the variance of the true response time series.

However, note that in reality, the sensor noise may be biased and non-Gaussian distributed (Labbe, 2018). Practically, the velocity can be calculated by integration of acceleration time series, while the displacement can be calculated by another integration over the velocity time series. The noise associated with displacement, velocity and acceleration signals are therefore correlated. However, this correlation is currently not considered. The noises of acceleration, velocity and displacement time series were added independently.

4. Case study results

Case studies were conducted to test the proposed methodology. For illustration purposes, each case only includes two parameters to tune. The sea states in Table 4 were applied. The key parameters used in the tuning process are summarized in Table 5.

Table 4
Sea states for the case studies.

Sea state ID	H_s [m]	T_z [s]	β_W [°]	Seed number
SS1	2.0	6.0	90	11
SS2	4.0	10.0	30	27
SS3	3.0	7.0	45	52
SS4	1.5	4.0	60	19
SS5	2.5	8.5	105	43

Table 5
Key parameters of tuning approach in the base case studies.

Parameters	Value	Unit
SNR (Equation (18))	100	–
α_j (Equation (9a))	0.05	–
p (Equation (10))	0.3	–

Table 6
Prior information and true values of GMT and β_{44}.

Parameter	Mean	σ^2	$\pm 3\sigma$	True value
GMT [m]	0.5	0.015	[0.13, 0.87]	0.40
β_{44} [-]	0.07	4.00E-04	[0.01, 0.13]	0.04

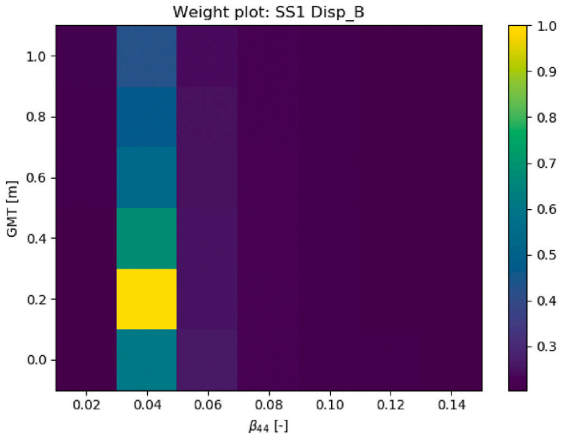

Fig. 4. Example of weight matrix, based on Disp_B sensor measurement for SS1.

4.1. GMT and β_{44}

The first case study considered GMT and β_{44} as the uncertain vessel hydrodynamic parameters. The other three parameters (i.e., XCG, mass and r_{55}) were set as deterministic. The prior knowledge and the true values of GMT and β_{44} are summarized in Table 6.

The calculated weight matrix illustrated in Fig. 4, indicates that the considered parameters GMT and β_{44} are sensitive to the Disp_B sensor for the SS1 sea state. It is obvious that GMT and β_{44} influence the roll motion very much, and SS1 is a beam sea condition with the peak period approximately near the heave RAO peak amplitude period for the location B. On the other hand, Fig. 5 illustrates a confusing weight matrix. The weight factor is spreading over a large variable range, because the sea state SS4 is with $T_z = 4.0$ s ($T_p = 5.6$ s). There was barely no significant vessel response around that small response period due to the lowpass filtering nature of the vessel. This means that GMT and β_{44} do not have significant influence on the RAOs and vessel motion for the

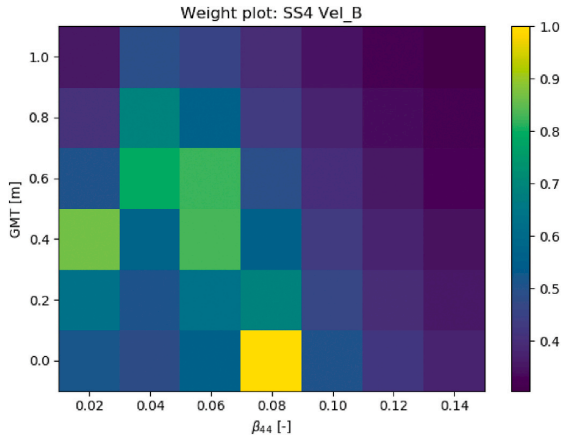

Fig. 5. Example of weight matrix, based on Vel_B sensor measurement for SS4.

Table 7
Intermediate tuning results - *GMT* [m] and β_{44}.

Sea state	μ_{GMT}	σ^2_{GMT}	$\mu_{\beta_{44}}$	$\sigma^2_{\beta_{44}}$	Number of valuable sensors
Initial	0.5	0.0145[a]	0.07	3.86E-04[a]	N/A
SS1	0.34	0.0145	0.042	4.61E-05	6
SS2	0.31	0.0112	0.041	1.97E-05	2
SS3	0.33	0.0125	0.041	1.08E-05	3
SS4	0.38	0.0180	0.041	1.17E-05	2
SS5	0.35	0.0128	0.041	5.85E-06	6

[a] It is different from the initial variance summarized in Table 6, due to a normalization procedure during initialization described in Section 2.1.

given sea state SS4. The variance of GMT and β_{44} were increased after tuning based on SS4, as shown in Table 7, meaning that the tuning system got confused by the sensor data for SS4. Both parameters do not influence the heave motion at the COG and therefore, the measurements at the location A near the COG were screened out for all tuning steps.

Fig. 6 illustrates the tuning results based on response measurements from each sea state. SS1 and SS5 played important roles with respect to the successful tuning, while SS4 attempted to degrade the tuning results. It is noted that sensor data from SS1 over-tuned the probability distribution of GMT, due to signal noises. This problem is discussed in detail in Section 5.4 and Section 5.5.

4.2. XCG and mass

The same sea states defined in Table 4 were applied for tuning the XCG and the mass, however, with a different vessel condition. The prior knowledge and the true values of XCG and mass are summarized in Table 8.

The results in Fig. 7 and Table 10 show that SS3 and SS4 significantly contributed to the tuning of XCG in the correct direction. Both sea states are oblique waves with small wave periods, where the hydrodynamic parametric sensitivity studies (Han et al., 2020) showed that the vessel heave motion are sensitive to XCG. As illustrated in Fig. 7, the joint probability distribution was not updated from SS5, meaning that all sensor measurements from SS5 were screened out. In other words, XCG and mass have negligible effects to the considered vessel response at SS5. The weight matrix examples shown in Fig. 8 indicate the system "confusion". All the 4 sensor measurements successfully gave high weight to the correct XCG value, but failed with respect to tuning vessel mass. The measurements from sensor Acc_B gave approximately the same weight factor through the whole range of mass values.

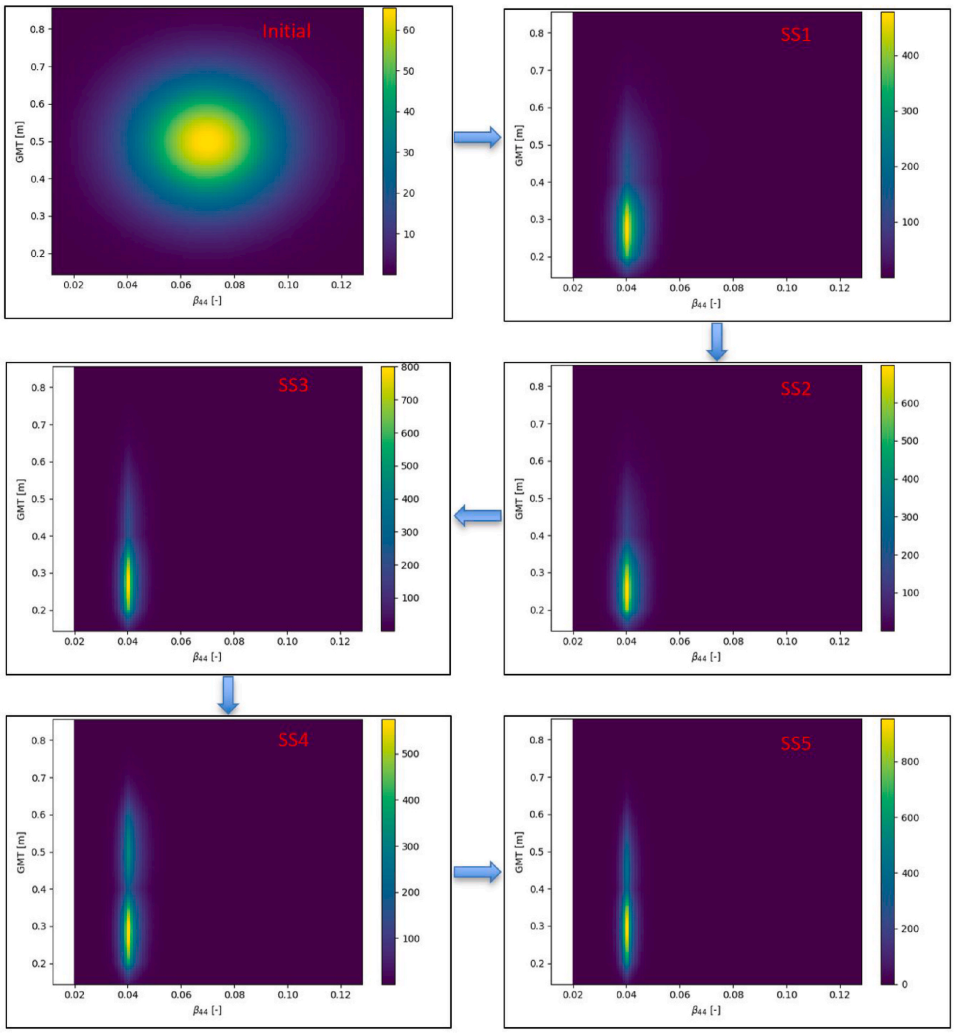

Fig. 6. Intermediate tuning results of the joint probability distribution of GMT and β_{44} from measurements for each sea state.

Table 8
Prior information and true values of XCG and Mass.

Parameter	Mean	σ^2	$\pm 3\sigma$	True value
XCG [m]	59.4	1.21	[56.23, 62.56]	57.4
Mass [t]	12,166.5	59,000	[11,467, 12,865]	11,680

Measurements from Disp_C and Vel_B sensors gave almost the opposite weighting distribution along mass values. The parametric sensitivity study (Han et al., 2020) showed that vessel mass influences the heave velocity mostly at small response periods for head and following sea conditions. At the given uncertainty ranges, the mass variation is less important with respect to the vessel response compared with XCG. Therefore, it is not very surprising that the measurements from the selected sea states failed to tune the vessel mass, due to 1) its less sensitivity for the considered sea states; 2) the nonlinear nature of the vessel response to the hydrodynamic parameters; 3) the measurement noise and uncertainties by e.g., seed variation. Therefore, measurements from one more sea state (SS6 in Table 9) were provided. SS6 was expected to be relatively sensitive with respect to the mass coefficient. Fig. 9 shows a dramatic shift of the peak of the joint distribution to a lower mass value.

5. Parametric sensitivity study

The case study of tuning GMT and β_{44} presented in Section 4.1 was chosen as the base case for the sensitivity study of some key parameters in the tuning algorithm.

5.1. Power parameter p

$p = 0.1, 0.5$ and 1.0 were chosen as the sensitivity study cases. The tuning results are summarized in Table 11. As shown in Fig. 10, large p leads to very large weight factor, which could be risky especially when $\left|\sigma^*_{r,j} - \hat{\sigma}_j\right| \to 0$. Therefore large p may lead to quick and abrupt change of

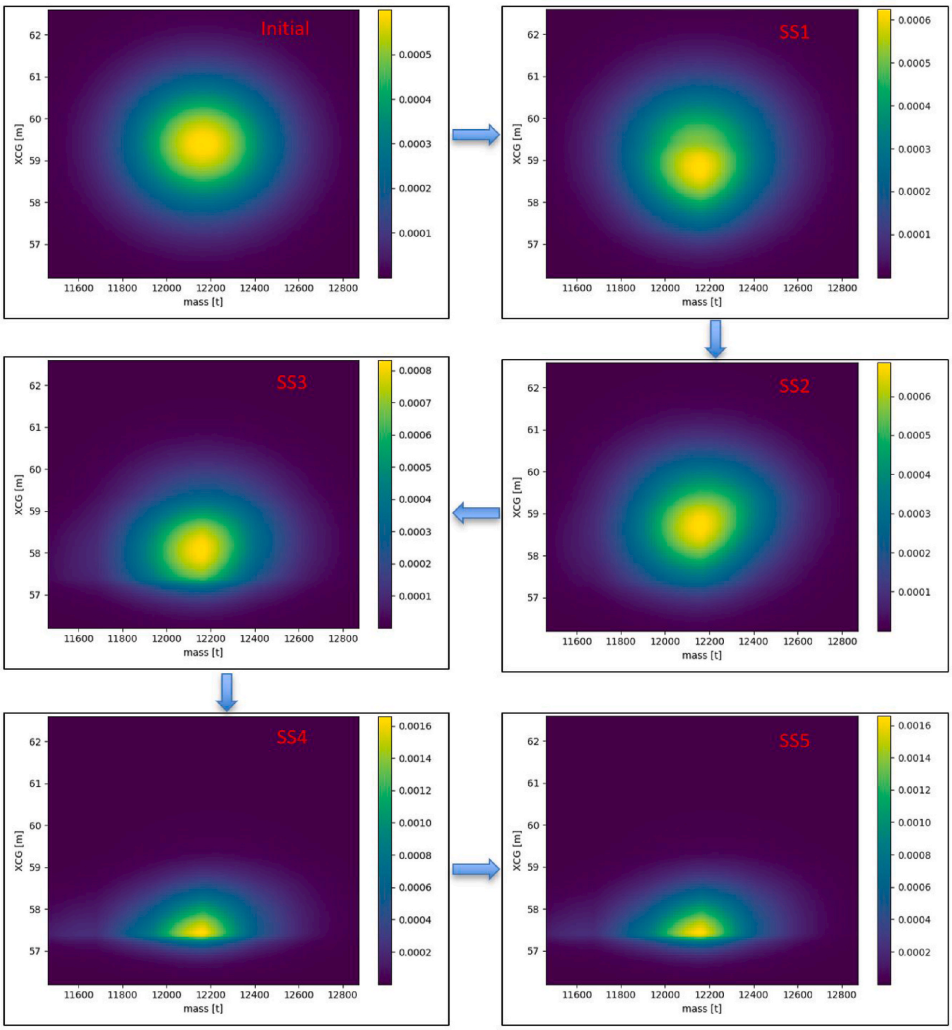

Fig. 7. Intermediate tuning results of the joint probability distribution of XCG and mass from measurements for each sea state.

Table 9
Additional sea state for model tuning of mass coefficient.

Sea state ID	H_s [m]	T_z [s]	β_W [°]	Seed number
SS6	1.5	5.5	15	8

the joint probability distribution of parameters, as illustrated in Fig. 11. Larger p value leads to less "memory" of the tuning results from the previous sea states. This may not be practically reasonable, especially for a stationary vessel situation, due to the existing uncertainties. The vessel loading condition could be considered as stationary for a relatively long time, e.g., in terms of days. If the focus is only to tune the sea state dependent parameters, e.g., β_{44}, larger p value might be preferable. But cautions are required to use large p for tuning multiple parameters at the same time.

Table 10
Intermediate tuning results - XCG [m] and mass [t].

Sea state	μ_{XCG}	σ^2_{XCG}	μ_{mass}	σ^2_{mass}	Number of **valuable sensors**
Initial	59.4	1.17[a]	12,166	56,969[a]	N/A
SS1	59.1	1.2	12,153	54,231	1
SS2	58.9	1.01	12,154	56,177	2
SS3	58.4	0.77	12,150	57,587	3
SS4	57.8	0.33	12,145	58,806	6
SS5	57.8	0.33	12,145	58,806	0
SS6	57.6	0.18	11,910	11,4640	7

[a] It is different from the initial variance summarized in Table 8, due to the normalization procedure described in Section 2.1.

5.2. SNR

It is interesting to test the performance of the proposed tuning approach with respect to the signal noise level. The sensitivity analysis

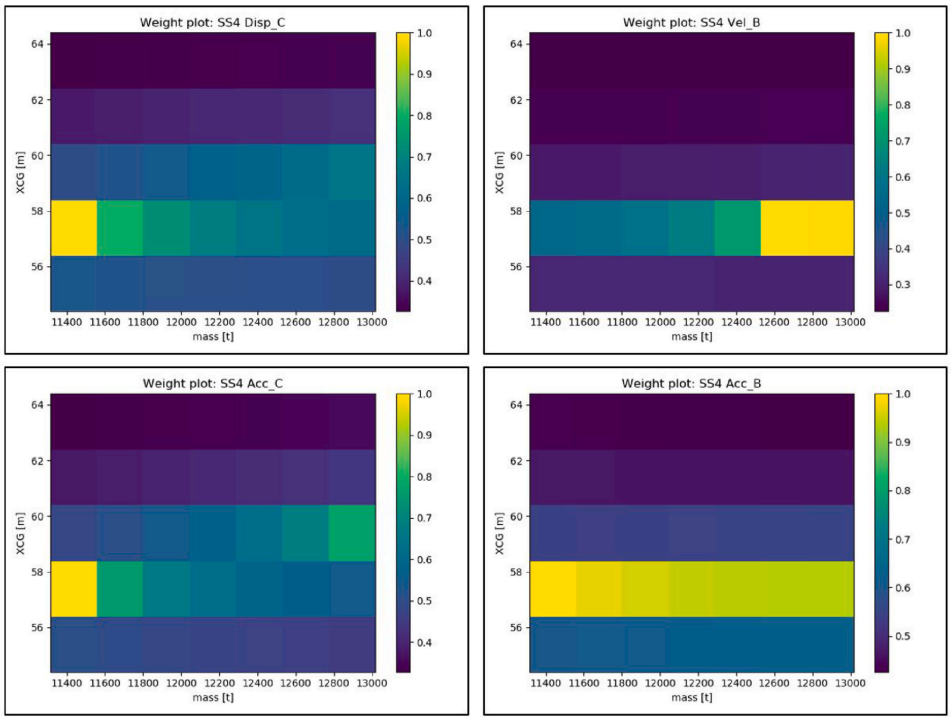

Fig. 8. Examples of weight matrix for tuning of XCG and mass from measurements for SS4.

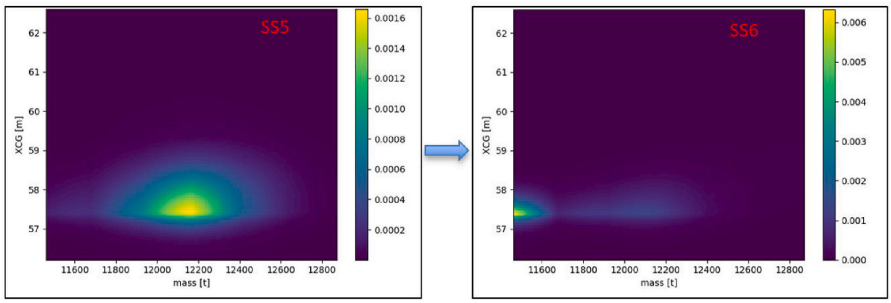

Fig. 9. Tuning results of probability distribution of XCG and mass due to measurements from SS6.

Table 11
Sensitivity with respect to power parameter.

p	μ_{GMT}	σ^2_{GMT}	GMT P90 interval[a]	$\mu_{\beta_{44}}$	$\sigma^2_{\beta_{44}}$
0.1	0.46	0.0150	[0.26, 0.66]	0.044	8.95E-05
0.3	0.35	0.0128	[0.17, 0.54]	0.041	5.85E-06
0.5	0.28	0.0057	[0.16, 0.41]	0.040	3.48E-06
1	0.26	0.0020	[0.19, 0.33]	0.040	2.70E-06

[a] 5− and 95− percentile values.

on SNR therefore also serves a purpose of validating the methodology. The lowpass filter method does not require to know the noise level explicitly. Results in Table 12 show that the methodology is quite stable with respect to dealing with signal noises. The tuning results in terms of mean and variance of the parameters are close for all SNR values varying from 10 to 10,000.

5.3. Seed variation

The seeds for generating vessel response sensor signals had been selected for all previous studies, ensuring exactly the same signals for tuning result comparison. The importance of seed variation with respect to the tuned results was investigated. Seeds were randomly generated for the same 5 sea states. In total, 10 sets of randomly generated seeds were used for the 5 sea states, corresponding to 10 tuning results, named as from Case1 to Case10. As shown in Fig. 12, the tuning results of β_{44} were very stable, in terms of its expected value and variance. This is due to very sensitive and monotonic influences from β_{44} to vessel response (i.e., RAO). The additional roll damping only influences the RAO amplitude, but not the RAO peak period. Fig. 12 shows that seed variation could significantly influence the tuning results for the parameters which

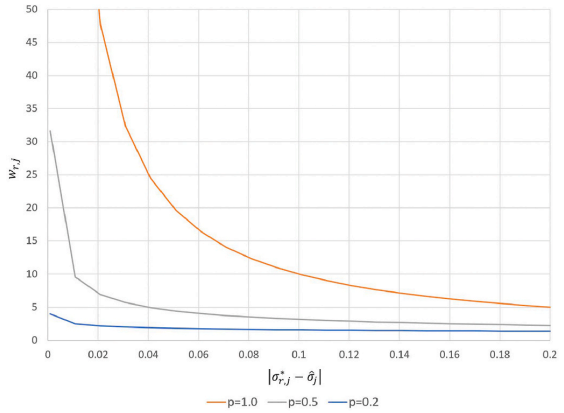

Fig. 10. Influence of power parameter on weight factor along $\left|\sigma^*_{r,j} - \hat{\sigma}_j\right|$.

are not very sensitive to the vessel response at those sea states (e.g., GMT) as variation in tuned GMT was observed. This is because 1) vessel response RAO is less sensitive to GMT; 2) the correlation between GMT and vessel RAO is complex. GMT shifts the RAO amplitude peak period, and changes the amplitude magnitude, as GMT determines the restoring stiffness for roll response. It is also noted that the variance of GMT did not reduce significantly through tuning based on measurements from the selected sea states.

5.4. Lowpass filtering cutoff frequency

Considering noise, the signal variance is equal to:

$$\sigma^2_{signal} = \sigma^2_X + \sigma^2_N \tag{19}$$

where σ^2_X and σ^2_N are the variance of the true response time series and the signal noise, respectively. Theoretically without processing signal noise, the variance of the signal will always be larger than the true response variance, potentially leading to biased tuning results. Therefore, the noise should be removed as much as possible. The noise power cannot be known exactly by nature. Section 5.2 demonstrated the robustness of applying a lowpass filter to deal with noise. A sensitivity study with respect to the cutoff frequency was carried out. The results are summarized in Table 13 for tuning GMT and β_{44}, and Table 14 for tuning XCG and mass.

Both Tables 13 and 14 show that $f_{lp} = 0.2$ Hz almost always gave the best tuned results in terms of being closer to the true values and with less variance. Exceptions were observed for the variance of the tuned vessel mass in Table 14. The mass variance σ^2_{mass} after tuning was larger than the initiated variance for all seed variations, indicating the system "confusion" mentioned in Section 4.2 due to the less sensitivity of mass on the vessel response for the considered sea states. Deep investigation of intermediate results indicated that the noise variance filtered out was actually always less than the true noise variance for the base case (i.e., $f_{lp} = 1.0$ Hz). Consequently, the variances of the filtered signal time series were all biased to a higher value than the true response. This led to biased tuning results.

Table 12
Sensitivity with respect to SNR.

SNR	μ_{GMT}	σ^2_{GMT}	GMT P90 interval[a]	$\mu_{\beta_{44}}$	$\sigma^2_{\beta_{44}}$
10	0.41	0.0182	[0.18, 0.63]	0.041	9.33E-06
100	0.35	0.0128	[0.17, 0.54]	0.041	5.85E-06
1000	0.39	0.0110	[0.22, 0.56]	0.041	5.91E-06
10,000	0.39	0.0108	[0.22, 0.56]	0.041	5.89E-06

[a] 5– and 95– percentile values.

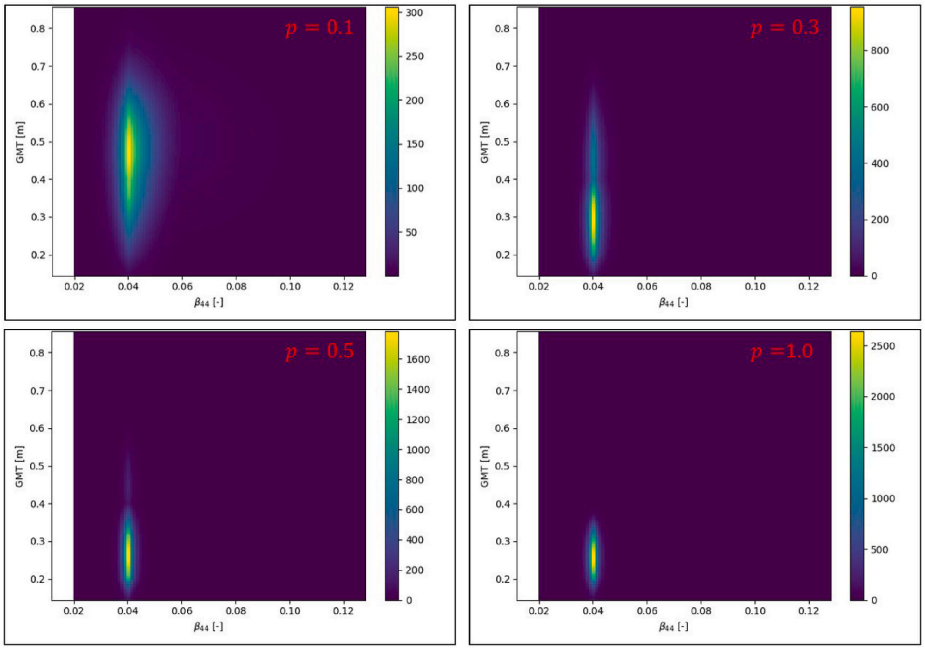

Fig. 11. Parameter tuning results from sea states in Table 4 for different power parameters.

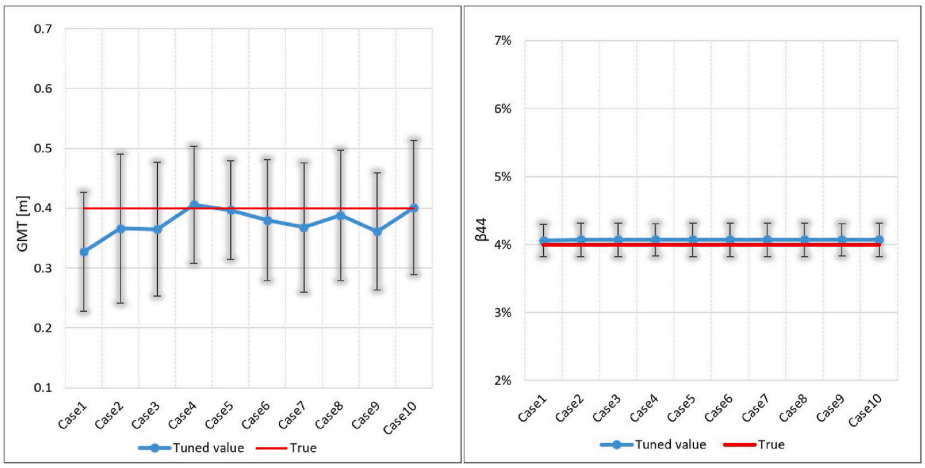

Fig. 12. Variation of tuned GMT and β_{44} due to seed variation, error bars indicate $\pm 1\sigma$.

Table 13
Sensitivity with respect to f_{lp} - tuning GMT [m] and β_{44} [-].

f_{lp} [Hz]	μ_{GMT}	σ^2_{GMT}	$\mu_{\beta_{44}}$	$\sigma^2_{\beta_{44}}$
0.2	0.411	0.004	0.0406	4.73E-06
0.33	0.386	0.0113	0.0407	5.92E-06
0.5	0.384	0.0118	0.0407	5.97E-06
1.0 (Base case)	0.353	0.0128	0.0407	5.85E-06
1.5	0.368	0.0150	0.0407	6.00E-06
2.0	0.318	0.0117	0.0406	5.86E-06

5.5. Sensor screening ratio - α

The selection of α depends on the uncertainty ranges of the considered parameters, and the uncertainties from input such as waves and response measurements. For a given uncertainty range of parameters, larger α leads to model tuning with less valuable sensor data, which may slow down the convergence speed. Smaller α helps to tune the model with more sensor data, but on the other hand, may lead to wrong results because the noise cannot be always perfectly treated.

Table 15 shows how the tuned results vary with α. It is clear that when α is reduced, more sensors which are less influenced by the considered uncertain vessel hydrodynamic parameters are included. Due to noise, the filtered signal variance deviates from the true response variance. If the noise was not appropriately filtered, those less important sensors generally would accelerate the tuning to a deviated value. Therefore, it is important to ensure a good selection of f_{lp} value, or acquire some additional knowledge on the noise and uncertainties. Based on Section 5.4, $f_{lp} = 0.2$ Hz suits better for the case study. Therefore, a sensitivity of α with respect to the lowpass filter cutoff frequency of 0.2 Hz was also studied, as shown in Table 16. With better handling of noise, more sensors were used with smaller α, generally leading to better model tuning results. Therefore, a trade-off between α and f_{lp} should be considered for practical purposes, due to the existence of uncertainties and limitations of noise filtering.

Table 14
Sensitivity with respect to f_{lp} - tuning XCG [m] and mass [t].

f_{lp} [Hz]	μ_{XCG}	σ^2_{XCG}	μ_{mass}	σ^2_{mass}
0.20	57.70	0.248	12099	62368
0.33	57.81	0.314	12131	62498
0.5	57.82	0.322	12137	60358
1.0 (Base case)	57.84	0.334	12145	58806
1.5	57.86	0.346	12149	58758
2.0	57.87	0.356	12155	57998

Table 15
Sensitivity with respect to SSR α with $f_{lp} = 1.0$ Hz - tuning GMT [m] and β_{44} [-].

α	μ_{GMT}	σ^2_{GMT}	$\mu_{\beta_{44}}$	$\sigma^2_{\beta_{44}}$	N_{out} [a]
0.01	0.294	0.0091	0.0408	4.98E-06	19
0.02	0.317	0.0106	0.0407	5.06E-06	22
0.05 (base case)	0.353	0.0128	0.0407	5.85E-06	26
0.1	0.339	0.0103	0.0408	7.53E-06	31
0.2	0.358	0.0108	0.0413	1.65E-05	36

[a] Number of sensors screened out. For each study, there were 45 sensor data (5 sea states × 9 sensors).

Table 16
Sensitivity with respect to SSR α with $f_{lp} = 0.2$ Hz - tuning GMT [m] and β_{44} [-].

α	μ_{GMT}	σ^2_{GMT}	$\mu_{\beta_{44}}$	$\sigma^2_{\beta_{44}}$	N_{out} [a]
0.01	0.401	0.0026	0.0405	3.76E-06	19
0.02	0.4	0.0032	0.0406	4.08E-06	21
0.05 (base case)	0.411	0.004	0.0406	4.73E-06	25
0.1	0.426	0.0046	0.0407	6.77E-06	31
0.2	0.418	0.0042	0.0411	1.33E-05	36

[a] Number of sensors screened out. For each study, there were 45 sensor data (5 sea states × 9 sensors).

6. Validation and robustness

So far, only two 2-dimensional model tuning cases have been studied, for 5 sea states. In order to validate the proposed tuning approach, more extensive hydrodynamic model tuning analyses were carried out. For one selected true vessel condition, sensor signals were simulated for 6 sea states. The duration for each sea state was 1 hour. Parameters defining the sea states (i.e., H_s, T_z, β_W and seed) were randomly selected within the range described in Table 17. GMT, r_{55}, XCG and β_{44} were selected for model tuning. The reason to exclude mass coefficient was because the results from Section 4.2 indicate that the vessel mass does not have a significant influence within its considered uncertainty range. The validation analyses included 120 tuning results. All 4 parameters were tuned simultaneously.

Tuning 4 parameters at the same time became slower compared with the previous cases of tuning 2 parameters. Therefore, the power

Table 17
Applied parameters related to the model tuning process for method validation.

Parameter	Value
H_s	Uniformly distributed in [1.0, 3.0] m
T_z	Uniformly distributed in [4.0, 15.0] s
β_W	Randomly selected among 13 discrete values $\beta_W \in \{0°, 15°, \ldots, 180°\}$
Seed	Randomly generated
Duration	3600 s
SNR	50
f_{lp}	0.2 Hz
α	0.05
p	0.4

parameter p was increased to 0.4. The joint probability distribution of the parameters was initiated as shown in Table 18. The key parameters needed for sensor signal generation and the tuning methodology are summarized in Table 17.

Due to limited computational processing capacity of the available laptop (CPU Intel(R) TM i7-8650U @ 1.90 GHz, 32 GB memory), a limited number of discretized values had to be applied for each parameter. To tune 4 parameters, the acceptable total number of discrete combinations was below 1.3E+07. This might be due to the large memory demands from Python Numpy operations during 4-dimensional interpolation of the calculated weight matrices described in Section 2.6. The computational capacity can be increased by optimizing the codes, changing the data structure, or simply increase the computer memory capacity. Table 18 describes the applied number of discrete parameter values for the joint probability distribution. The resolution for the uncertain parameters is considered sufficient with respect to the studied parameter ranges. For tuning a 4-dimensional model, with the considered uncertain range and resolution, the computational time for each sea state was about 90 s. For the 2-dimensional tuning model with 100×100 resolution for the probability distribution, the computational time for each sea state was about 10 s.

From Figs. 13 and 14, it is clear that the proposed tuning procedure succeeds to tune β_{44} and XCG in most cases. However, a large variation of tuning results for GMT and r_{55} were also experienced. This is consistent with the findings from the earlier hydrodynamic parametric sensitivity studies (Han et al., 2020), showing that the vessel RAO is much less sensitive to GMT and r_{55} compared to β_{44} and XCG. For illustration purposes, each figure only contains information on 2 parameters.

Similar to all other experiment or test calibration methodologies (e.g., machine learning algorithms, hydrodynamic coefficients fitted based

Table 18
Prior information and true values of the considered vessel parameters.

Parameter	Mean	σ^2	$\pm 3\sigma$	True value	N_{prob} [a]	N_{RAO} [b]
GMT [m]	0.5	0.015	[0.13, 0.87]	0.4	40	6
β_{44}	0.07	4.0E-04	[1%, 13%]	0.04	50	7
r_{55} [·m]	32.5	1.0	[29.5, 35.5]	30.55	30	7
XCG [m]	59.4	1.21	[56.1,62.7]	61.4	30	5

[a] Number of discrete variable values for the joint probability model.
[b] Number of discrete parameter values used in the RAO database.

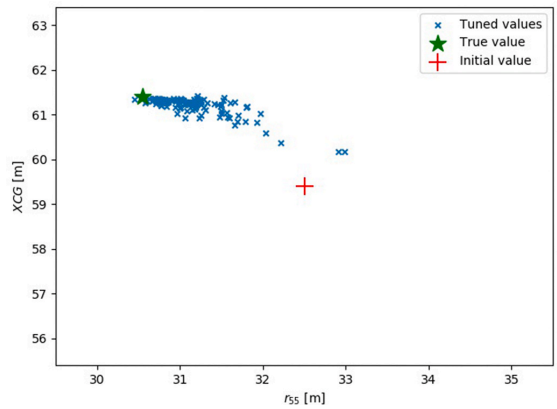

Fig. 14. Tuning results for validation analyses, expected values of r_{55} and XCG.

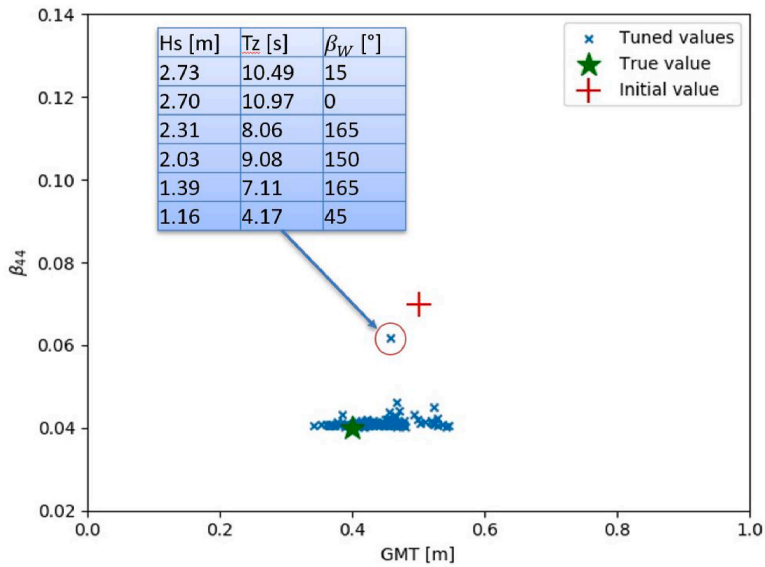

Fig. 13. Tuning results for validation analyses, expected values of GMT and β_{44}.

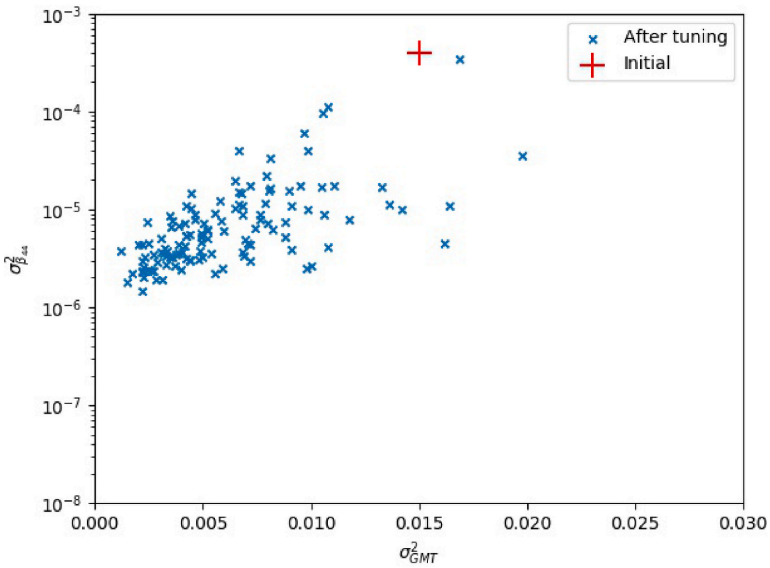

Fig. 15. Tuning results for validation analyses, variance of GMT and β_{44}.

on laboratory tests), relevant and valuable cases (sea states) are required in order to tune the parameters. But different from the complex AI algorithms like neural networks, the physics-based model tuning is better at extrapolation from the available data and does not require a huge amount of data samples. This is particularly important for nonlinear problems. Extrapolation here means good vessel response predictions for outlier sea states. The process for tuning hydrodynamic parameters still requires that the available RAO database covers the entire range of hydrodynamic parameter uncertainties. The validation analyses were limited to only 6 sea states for each tuning. Therefore, failure of model tuning is, by nature, possible. For example, one out of the 120 tuning simulations failed to report good enough additional roll damping, highlighted in Fig. 13. A deep investigation showed that all the generated sensor signals were basically from head and following sea states where β_{44} played a negligible role, and none of the sea states were near the roll resonance period.

Figs. 15 and 16 illustrate how the variance changes after tuning. Analyses show that the variable variance significantly reduces after tuning especially for the important parameters (i.e., β_{44} and XCG), as expected. Note that the y-axis of Fig. 15 is log-scaled.

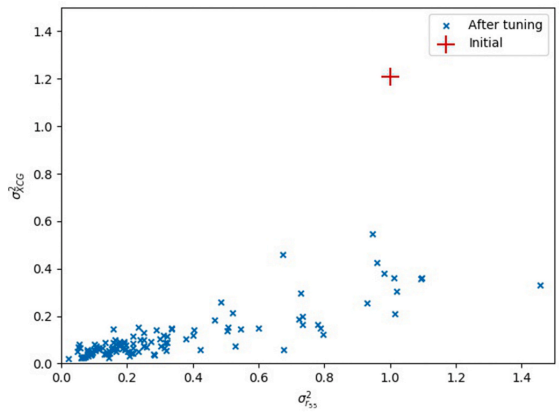

Fig. 16. Tuning results for validation analyses, variance of r_{55} and XCG.

Table 19
Summary of validation analyses results.

Parameter	Mean			Variance	
	Initial	Tuned	True	Initial	Tuned
GMT [m]	0.5	0.43	0.4	0.015	6.11E-03
β_{44} [-]	0.07	0.041	0.04	4.00E-04	1.26E-05
r_{55} [· m]	32.5	31.13	30.55	1.0	0.437
XCG [m]	59.4	61.2	61.4	1.21	0.141

The expected mean and variance of the parameters are summarized in Table 19. The tuning methodology succeeds to modify the parameters such that they approach the true values with significantly increased confidence. Therefore, the validation analyses demonstrated the robustness and stability of the proposed tuning methodology.

7. Conclusions and future work

A procedure with great potential for practical implementation with respect to tuning of vessel hydrodynamic seakeeping model parameters based on onboard vessel motion measurements has been proposed. Similar to model calibration based on laboratory tests, hydrodynamic coefficients can be modified based on available data by the tuning approach. Therefore, the improved vessel motion prediction is supported by physics and common engineering practice. But different from model calibration by laboratory tests, more uncertainties are in reality observed onboard. Therefore, it is more natural to present the important hydrodynamic parameters and RAOs in a probabilistic way. The proposed tuning approach combines engineering practice with the random nature, quantitatively improving the knowledge on the vessel conditions and response. Hence, the reliability of the vessel motion RAO and motion prediction can be documented quantitatively as well. Therefore, some of the safety factors in engineering practice related to marine operation design (e.g., DNVGL-ST-N001, 2016) may be reduced, and reliability-based marine operations may be possible. Consequently, the approach could potentially help to reduce the operational cost and

increase safety. The tuning process is fast and suitable for onboard application which could improve the quality of digital twins and assist within the context of onboard decision support.

Analyses demonstrate that the tuning approach is robust, and stable to deal with noise. Better tuning results were observed for the parameters which have stronger influence on the measured vessel response. The tuning algorithm also showed reasonable behaviour when updating the hydrodynamic parameters for cases where the sea states or the measurements were not very relevant for those uncertain parameters. Key parameters of the tuning methodology were also studied by sensitivity analyses. Relatively large values of the power parameter p led to higher belief in sensor data, and hence less memory to the prior knowledge. It was found important to select the cutoff frequency f_{lp} of the lowpass filter in a proper way for an unbiased tuning result. Practically, a trade-off between α and f_{lp} should be considered to optimally use the available measurement data. Inspired by Godhaven (1998), the lowpass filter cutoff frequency f_{lp} could be preferably modelled as sea state dependent, automatically selected based on measurements and environment information. The tuning methodology was also validated by using virtual sensor signals from randomly selected sea states by tuning 4 parameters simultaneously.

Even though a considerable amount of analyses were carried out for validation, more work is still required for methodology verification. Only one vessel condition was studied in Section 6. More vessel conditions and broader ranges of hydrodynamic parameters should be studied. More importantly, scaled experimental data and on-site full scale data should be used to verify the tuning methodology. The presented case studies of tuning vessel parameters (Fig. 1) and virtual sensor signal simulation (Fig. 3) apply the RAOs from the same RAO database which are generated based on seakeeping analyses by Wasim software. However, the real on-site vessel motion measurements will fully reflect the reality while the established RAO database to be used for vessel model tuning will be potentially subject to bias introduced by the simplifications made in the applied seakeeping software and the vessel numerical model. This software introduced bias should also be investigated in the future research work.

Practically, if the RAO database can be extended to various vessel advancing speeds with sufficient speed resolution, much more on-site measurements can be used to tune the important vessel parameters. Consequently, the cutoff frequency will therefore depend on vessel speed.

So far, the additional roll damping β_{44} was considered only operational condition dependent, which assumes a constant value throughout all sea states for the current vessel loading condition. Some parameters are sea state dependent (e.g., roll damping), some other parameters are operational condition dependent (such as inertia distribution), while others could be permanent (e.g., vessel geometry). Each parameter should be categorized accordingly and different model tuning strategy might be considered for each category.

So far, only uncertainties from sensor noise were considered. In reality, the uncertainties from wave information are significant, such as directional spreading, wave spectral shape, and uncertainties from wave forecast and hindcast modelling. Other environmental loads have not been considered, such as wind and current, leaving the procedure with a considerable gap towards on-site practice. Practically, these challenges can be solved by modifying the signal filter and by also including a highpass filter.

In addition, rigid body motion was assumed when calculating heave RAO functions at different locations. In reality for large slender vessels, more advanced models might therefore be required due to the increasing importance of hydroelastic effects.

CRediT authorship contribution statement

Xu Han: Conceptualization, Methodology, Software, Formal analysis, Data curation, Writing - original draft & Editing. **Bernt Johan Leira:** Writing - review & editing, Supervision, Project administration, Funding acquisition. **Svein Sævik:** Writing - review & editing, Supervision, Project administration.

Declaration of competing interest

The authors declare that they have no known competing financial interests or personal relationships that could have appeared to influence the work reported in this paper.

Acknowledgement

This work was made possible through the Center for Research based Innovation MOVE, financially supported by the the Research Council of Norway, NFR project No. 237929 and the consortium partners, http://www.ntnu.edu/move. Special thanks are given to Section of Hydrodynamics & Stability in DNV GL for providing hydrodynamic models and software support.

Nomenclature

$(\Phi_{i1},\ldots,\Phi_{iM})$ The combination of variable values from the $i1^{th}$ value of Φ_1,$i2^{th}$ value of Φ_2, …, and the iM^{th} value of Φ_M. $im \in [1,Im]$, Im is the number of discrete values for Φ_m in the RAO database, $m \in [1,M]$

$(\Phi_{k1},\ldots,\Phi_{kM})$ The combination of variable values from the $k1^{th}$ value of Φ_1, $k2^{th}$ value of Φ_2, …, and the kM^{th} value of Φ_M. $km \in [1,Km]$, Km is the number of discrete values for Φ_m in the joint distribution model, $m \in [1,M]$

α_j Sensor screening ratio (SSR) for sensor j

β_{44} Ratio between the additional roll damping and the critical roll damping. The additional damping can be expressed as $\beta_{44}\cdot\beta_{cr,44} = \beta_{44}\cdot 2\sqrt{(\overline{\overline{A}}(\omega_e)+\overline{\overline{M_0}})\cdot\overline{\overline{C}}}$

β_W Wave direction with respect to. vessel coordinate system

$\eta_{33},\dot{\eta_{33}},\ddot{\eta_{33}}$ Heave displacement, velocity, acceleration

$\widehat{\sigma}_j$ Standard deviation of the filtered signal from sensor j

$\widehat{x}_j(t)$ Filtered signal from sensor j

μ Variable mean value

ω Wave frequency

ω_e Encounter frequency

ω_p Spectral peak frequency, $\omega_P = 2\pi/T_p$

$\overline{\overline{\beta}}$ Vessel damping matrix

$\overline{\overline{A}}$ Vessel added mass matrix

$\overline{\overline{C}}$	Vessel restoring stiffness matrix
$\overline{\overline{M_0}}$	Vessel inertia matrix
$\overline{\overline{W_j}}$	Weight matrix based on measurement from sensor j
Φ	Random variable
σ_N^2	Variance of noise
σ_X^2	Variance of response
$\sigma_{r,j}^*$	The predicted standard deviation by using $RAO_{r,j}$
$\sigma_{\sigma_{r,j}^*}$	The standard deviation of $\sigma_{r,j}^*$ over $r \in \{1, 2, \ldots, R\}$
ϕ	Phase angle
ζ	Wave elevation
B	Vessel breadth
$C(\omega)$	The amplitude of the sinusoidal response at frequency of ω
D	Vessel draft
f_{lp}	Lowpass filter cutoff frequency in Hz
$H_{33}(\omega, \beta_W)$	Heave motion RAO
$H_{r,X_j\zeta}(\omega, \beta_W)$	Linear transfer function between wave and vessel response at sensor j based on r^{th} combination of uncertain vessel parameters
H_s	Significant wave height
r_{55}	Radius of gyration for pitchn
Im	The total number of discrete values for Φ_m in the RAO database
im	The im^{th} value of the variable in the RAO database for Φ_m
J	The number of sensors
j	Sensor ID, the j^{th} sensor, representing different quantities (displacement, velocity, acceleration) and locations
Km	The number of discrete values for Φ_m in the joint probability distribution
km	The km^{th} value of the discretized variable in the probability distribution model for Φ_m
L_{pp}	Length between perpendiculars
M	The number of considered variables for tuning
N_ω	The number of discretized frequencies
N_t	The number of discretized time steps
p	Power parameter
$P^{(n)}(\Phi_1, \ldots, \Phi_M)$	The updated discrete joint probability distribution after the n^{th} updating step
R	The total number of possible combinations of uncertain vessel parameters in the RAO database
$RAO_{r,j}$	The RAO based on the variable combination r, corresponding to the response sensor j (location and quantity)
$S_{\zeta\zeta}^{+}(\omega, \beta_W)$	Single-sided power spectral density of waves
$S_{r,X_jX_j}^{+}(\omega)$	Calculated single-sided power spectral density of vessel response at sensor j based on RAO candidate $RAO_{r,j}$
$S_{X_jX_j}^{+}(\omega)$	Single-sided power spectral density of vessel response at sensor j
T_p	Spectral peak period, $T_p = 1.4049T_z$ for PM spectrum (DNVGL-RP-C205, 2017)
T_z	Zero-upcrossing wave period
u	Vessel speed
$w_{r,j}$	Weight factor for the r^{th} variable combination based on measurement from sensor j
$x_j(t)$	Signal from sensor j
$\overrightarrow{F}(\omega, u\|\beta_W)$	Excitation force from waves including Froude-Krylov and diffraction forces
AI	Artificial intelligence
CFD	Computational fluid dynamics
COG	Center of gravity
DOF	Degree of freedom
FFT	Fast Fourier transform
GMT	Free surface correction to the transverse metacentric height
ODSS	Onboard decision support system
OSV	Offshore supply vessel
PDF	Probability density function
PM	Pierson-Moskowitz spectrum
RAO	Response amplitude operator
SNR	Signal-to-noise ratio
SS	Sea state
SSR	Sensor screening ratio
XCG	Longitudinal coordinate of vessel COG
YCG	Transverse coordinate of vessel COG
ZCG	Vertical coordinate of vessel COG

References

Alford, L.K., Beck, R.F., Johnson, J.T., Lyzenga, D., Nwogu, O., Zundel, A., 2014. Design, Implementation, and Evaluation of a System for Environmental and Ship Motion Forecasting. Proceedings of the 30th Symposium on Naval Hydrodynamics. Hobart, Australia.

Alford, L.K., Beck, R.F., Johnson, J.T., Lyzenga, D., Nwogu, O., Zundel, A., 2015. A real-time system for forecasting extreme waves and vessel motions. Proceedings of the ASME 2015 34th International Conference on Ocean, Offshore and Arctic Engineering, 11. Newfoundland, Canada.

Brodtkorb, A.H., Nielsen, U.D., Sørensen, A.J., 2018b. Online wave estimation using vessel motion measurements. IFAC-PapersOnLine 51 (29), 244–249. https://doi.org/10.1016/j.ifacol.2018.09.510. ISSN 2405–8963, 11th IFAC Conference on Control Applications in Marine Systems, Robotics, and Vehicles CAMS 2018.

Brodtkorb, A.H., Nielsen, U.D., Sørensen, A.J., 2018a. Sea state estimation using vessel response in dynamic positioning. Appl. Ocean Res. 70, 76–86. https://doi.org/10.1016/j.apor.2017.09.005. ISSN 0141–1187.

Cao, Y., Tahchiev, G., Zhang, F., Aarsnes, J.V., Glomnes, E.B., 2010. Effects of Hydrostatic Nonlinearity on Motions of Floating Structures. Proceedings of the ASME 2010 29th International Conference on Ocean, Offshore and Arctic Engineering, 4. Shanghai, China.

Cheng, X., Li, G., Skulstad, R., Major, P., Chen, S., Hildre, H.P., Zhang, H., 2019. Data-driven uncertainty and sensitivity analysis for ship motion modeling in offshore operations. Ocean. Eng. 179, 261–272. https://doi.org/10.1016/j.oceaneng.2019.03.014. ISSN 0029–8018.

Clauss, G.F., Kosleck, S., Testa, D., 2012. Critical Situations of Vessel Operations in Short Crested Seas - Forecast and Decision Support System. Journal of Offshore Mechanics and Arctic Engineering 134.

Connell, B.S.H., Rudzinsky, J.P., Brundick, C.S., Milewski, W.M., Kusters, J.G., Farquharson, G., 2015. Development of an Environmental and Ship Motion Forecasting System. Proceedings of the ASME 2015 34th International Conference on Ocean, Offshore and Arctic Engineering. Newfoundland, Canada.

Dannenberg, J., Hessner, K., Naaijen, P., van den Boom, H., Reichert, K., 2010. The on board wave and motion estimator OWME. In: Proceedings of the 20th International Offshore and Polar Engineering Conference. ISOPE, pp. 424–431. ISBN 978-1-880653-77-7.

De Masi, G., Gaggiotti, F., Bruschi, R., Venturi, M., 2011. Ship motion prediction by radial basis neural networks. In: IEEE Workshop on Hybrid Intelligent Models and Applications. IEEE, Paris, France, pp. 28–32. ISSN 2167-8219.

DNV GL, 2018. Wasim User Manual. Tech. Rep. DNV GL.

DNVGL-RP-C205, 2017. Environmental Conditions and Environmental Loads. Tech. Rep. DNV GL.

DNVGL-ST-N001, 2016. Marine Operations and Marine Warranty. Tech. Rep. DNV GL.

Faltinsen, O.M., 1990. Sea Loads on Ships and Offshore Structures. Cambridge University Press Cambridge, New York. ISBN 0521372852 0521458706.

Faltinsen, O.M., 2015. Hydrodynamics of marine and offshore structures. Journal of Hydrodynamics, Ser. B 26 (6), 835–847.

Galvin, J., 2014. The Use of Information Technology at the Met Office. British Computer Society, Bristol Branch January Seminar.

Godhaven, J.-M., 1998. Adaptive tuning of heave filter in motion sensor. In: IEEE Oceanic Engineering Society. OCEANS'98. Conference Proceedings (Cat. No.98CH36259), vol. 1. IEEE, pp. 174–178.

Grilli, S.T., Guérin, C.-A., Goldstein, B.I., 2011. Ocean Wave Reconstruction Algorithms Based on Spatio-Temporal Data Acquired by a Flash LIDAR Camera. International Society of Offshore and Polar Engineers, Hawaii, USA.

Han, X., Sævik, S., Leira, B.J., 2020. A sensitivity study of vessel hydrodynamic model parameters. Proceedings of the ASME 2020 39th International Conference on Ocean, Offshore and Arctic Engineering. Virtual, Online, OMAE2020-19039.

Himeno, Y., 1981. Prediction of Ship Roll Damping - A State of the Art. Tech. Rep. The University of Michigan, College of Engineering, Department of Naval Architecture and Marine Engineering, USA.

Hoyer, S., Hamman, J., 2017. xarray: N-D labeled Arrays and Datasets in Python. Journal of Open Research Software 5 (1), 10. http://doi.org/10.5334/jors.148.

Iseki, T., 2009. Real-time estimation of directional wave spectra using non-stationary ship motion data. In: Proceedings of the ASME 2009 28th International Conference on Ocean, Offshore and Arctic Engineering, pp. 673–678. https://doi.org/10.1115/OMAE2009-79295.

Kim, S.P., 2011. CFD as a seakeeping tool for ship design. International Journal of Naval Architecture and Ocean Engineering 3 (1), 65–71. https://doi.org/10.2478/IJNAOE-2013-0046. ISSN 2092–6782.

Kring, D.C., 1994. Time Domain Ship Motions by a Three-Dimensional Rankine Panel Method. Ph.D. thesis. Massachusetts Institute of Technology, Department of Ocean Engineering.

Kusters, J.G., Cockrell, K.L., Connell, B.S.H., Rudzinsky, J.P., Vinciullo, V.J., 2016. FutureWavesTM: a real-time ship motion forecasting system employing advanced wave-sensing radar. In: OCEANS 2016 MTS/IEEE Monterey. IEEE, pp. 1–9.

Labbe, R., 2018. Kalman and Bayesian Filters in Python.

Larsen, C.M., Lian, W., Bachynski, E., Kristiansen, T., Myrhaug, D., 2019. Lecture Notes for Course TMR4182 Marine Dynamics. Tech. Rep. Department of Marine Technology, NTNU, Trondheim.

Milewski, W.M., Connell, B.S.H., Vinciullo, V.J., Kirschner, I.N., 2015. Reduced Order Model for Motion Forecasts of One or More Vessels. Proceedings of the ASME 2015 34th International Conference on Ocean, Offshore and Arctic Engineering, 11. Newfoundland, Canada.

Naaijen, P., Roozen, D.K., Huijsmans, R.H.M., 2016. Reducing Operational Risks by On-Board Phase Resolved Prediction of Wave Induced Ship Motions. Proceedings of the ASME 2016 35th International Conference on Ocean, Offshore and Arctic Engineering, 7. Busan, South Korea.

Naaijen, P., van Oosten, K., Roozen, K., van't Veer, R., 2018. Validation of a Deterministic Wave and Ship Motion Prediction System. Proceedings of the ASME 2018 37th International Conference on Ocean, Offshore and Arctic Engineering, 7B. Madrid, Spain.

Nielsen, U.D., 2006. Estimations of on-site directional wave spectra from measured ship responses. Mar. Struct. 19 (1), 33–69. https://doi.org/10.1016/j.marstruc.2006.06.001. ISSN 0951–8339.

Nielsen, U.D., 2007. Response-based estimation of sea state parameters - influence of filtering. Ocean. Eng. 34 (13), 1797–1810. https://doi.org/10.1016/j.oceaneng.2007.03.002. ISSN 0029–8018.

Nielsen, U.D., 2017. Transformation of a wave energy spectrum from encounter to absolute domain when observing from an advancing ship. Appl. Ocean Res. 69, 160–172. https://doi.org/10.1016/j.apor.2017.10.011. ISSN 0141–1187.

Nielsen, J.K., Pedersen, N.H., Michelsen, J., Nielsen, U.D., Baatrup, J., Jensen, J.J., Petersen, E.S., 2006. SeaSense - real-time onboard decision support. In: World Maritime Technology Conference. London, UK.

Nielsen, U.D., Brodtkorb, A.H., Jensen, J.J., 2018. Response predictions using the observed autocorrelation function. Mar. Struct. 58, 31–52. https://doi.org/10.1016/j.marstruc.2017.10.012. ISSN 0951–8339.

Nielsen, U.D., Brodtkorb, A.H., Sørensen, A.J., 2019. Sea state estimation using multiple ships simultaneously as sailing wave buoys. Appl. Ocean Res. 83, 65–76. https://doi.org/10.1016/j.apor.2018.12.004. ISSN 0141–1187.

Nouguier, F., Grilli, S.T., Guérin, C., 2014. Nonlinear ocean wave reconstruction algorithms based on simulated spatiotemporal data acquired by a flash LIDAR camera. IEEE Trans. Geosci. Rem. Sens. 52 (3), 1761–1771. https://doi.org/10.1109/TGRS.2013.2254494. ISSN 1558–0644.

Ren, Z., Han, X., Verma, A.S., Dirdal, J.A., Skjetne, R., 2021. Sea state estimation based on vessel motion responses: improved smoothness and robustness using Bézier surface and L1 optimization. Mar. Struct. In press.

Shepard, D., 1968. A two-dimensional interpolation function for irregularly-spaced data. In: Proceedings of the 1968 23rd ACM National Conference, ACM '68. Association for Computing Machinery, New York, NY, USA, pp. 517–524. ISBN 9781450374866.

Tannuri, E.A., Sparano, J.V., Simos, A.N., Da Cruz, J.J., 2003. Estimating directional wave spectrum based on stationary ship motion measurements. Appl. Ocean Res. 25 (5), 243–261. https://doi.org/10.1016/j.apor.2004.01.003. ISSN 0141–1187.

van Daalen, E., Fehribach, J., van Leeuwen, T., Reinhardt, C., Schenkels, N., Sheombarsing, R., 2014. Model calibration for ship simulations. In: Proceedings of the 98th Study Group Mathematics with Industry. TU Delft, pp. 68–91.

Yue, D.K., Liu, Y., Hendrickson, K., Wu, G., Xiao, W., Henry, L., 2008. Nonlinear Wave Environments for Ship Analysis. Proceedings of the 27th Symposium on Naval Hydrodynamics. Seoul, South Korea.

A.3 Paper A3

Paper A3:
X. Han, Z. Ren, B. J. Leira, and S. Sævik, 2021. Adaptive identification of lowpass filter cutoff frequency for online vessel model tuning. *Ocean Engineering* 236.

Ocean Engineering 236 (2021) 109483

Contents lists available at ScienceDirect

Ocean Engineering

journal homepage: www.elsevier.com/locate/oceaneng

Adaptive identification of lowpass filter cutoff frequency for online vessel model tuning

Xu Han *, Zhengru Ren, Bernt Johan Leira, Svein Sævik

Department of Marine Technology, Norwegian University of Science and Technology (NTNU), 7491 Trondheim, Norway
Centre for Research-based Innovation on Marine Operations (SFI MOVE), Norway

ARTICLE INFO

Keywords:
Adaptive lowpass filtering
Optimal cutoff frequency
Wave-induced vessel responses
On-site measurements
Online vessel model tuning
Discrete Bayesian updating

ABSTRACT

Tuning of vessel models in real-time based on vessel measurements and weather information is of great interest in order to increase the safety and efficiency of marine operations. Vessel motion signals usually contain high-frequency noise. For an unbiased model tuning algorithm, it is essential to filter the noisy signals in order to identify the power of the wave-induced first-order vessel response. Lowpass filters with high accuracy should therefore be applied. However, it is a challenge to design such a filter since the optimal cutoff frequency can vary with sea states, vessel dimensions, vessel conditions, etc. This paper proposes a novel algorithm to adaptively search for the optimal cutoff frequency for a lowpass filter with high accuracy. The algorithm is fundamentally based on the facts that the vessel naturally acts as a lowpass filter and the energy from the high-frequency components, e.g., signal noise, is significantly smaller than that from the wave-induced vessel response. The algorithm is validated by 500 numerically simulated vessel motion signals with quite high noise levels and also by analysis of several on-site full-scale vessel motion signals. The improvements to the tuning results for the vessel parameters are demonstrated.

1. Introduction

Marine operations are usually designed onshore before they are executed. Operational limits are determined based on presumed operational scenarios, loading conditions, etc. Practically, it is common to calculate the wave-induced loads and motions based on linear transfer functions, named response amplitude operators (RAOs) (DNVGL-ST-N001, 2016). However, the applied RAOs at the design stage may not represent the true vessel conditions during operation in an adequate manner, because (1) conservative engineering assumptions are usually made to cover the variation of vessel loading conditions during marine operations, e.g., pipe laying; and (2) the onboard vessel loading condition (inertia distribution) may deviate from the presumed one.

These limitations could lead to over-conservative and inefficient marine operations, or even risky operations with increased possibility of accidents. Therefore, a dynamically adaptive tuning of vessel numerical models could continuously help to improve the knowledge on the real-time vessel condition, and hence increase the efficiency and safety of the marine operations. Han et al. (2021a) proposed an algorithm based on Bayesian inference to improve the knowledge about these real-time vessel conditions and to reduce the model uncertainty quantitatively by using (1) onboard data from sensor systems, e.g., motion reference unit (MRU) and global navigation satellite system (GNSS); (2) wave information such as H_s (significant wave height), T_p (spectral peak period), β_W (wave direction), directional spreading, and spectral shape. As explained in Han et al. (2021a), tuning of a vessel hydrodynamic model is a multi-modal, multi-dimensional, and nonlinear problem.

The vessel motion measurements are extremely important for many onboard systems, e.g., dynamic positioning (DP) systems and active heave compensators (AHCs). A typical MRU system uses measurements from an inertial measurement unit (IMU) which consists of accelerometers measuring translational accelerations and gyroscopes measuring rotational velocities. It is well recognized that all measurements are inexact but usually they can statistically represent the true value (Hubbard, 2014). The accuracy and precision of the measurements depend on the involved methods, processes, and instruments. IMU measurements may contain errors due to misalignment, mis-scaling, constant and slow-varying biases, gravity-related terms, and nonlinearities from the gyro torque and accelerometers (Grewal et al., 1991). Sensor fusion and signal filtering techniques should therefore be applied to achieve high-fidelity motion monitoring, reduce sensor noise, and avoid measurement drift (Fossen, 2011).

Filters can be categorized into model-free and model-based approaches, depending on whether a representative model is applied. Kalman filters and the associated extended methods have been the most

* Corresponding author at: Department of Marine Technology, Norwegian University of Science and Technology (NTNU), 7491 Trondheim, Norway.
E-mail address: xu.han@ntnu.no (X. Han).

https://doi.org/10.1016/j.oceaneng.2021.109483
Received 7 July 2020; Received in revised form 23 March 2021; Accepted 11 July 2021
Available online 21 July 2021

Nomenclature

α_j	Sensor screening ratio (SSR) for sensor j
$\bar{x}_j$	The mean of the measured filtered time series for sensor j
β_{44}	Ratio between the additional roll damping and the critical roll damping
β_W	Wave direction w.r.t. vessel coordinate system
$\eta_{33}, \dot{\eta_{33}}, \ddot{\eta_{33}}$	Heave displacement, velocity, acceleration
γ_p	Peak enhancement factor
$\hat{\sigma}_j\left(f_{lp}\right)$	The standard deviation of signal from sensor j after filtered at cutoff frequency f_{lp}
$\hat{\sigma}_X$	The filtered vessel motion signal STD
$\hat{T}_z$	The zero-upcrossing period of the filtered vessel motion signal
$\hat{x}_j(t)$	The filtered time series for sensor j at time step t
ω	Wave frequency
ω_p	Wave spectral peak frequency
$\overline{\overline{W_j}}$	The weight matrix (likelihood function) based on the received measurements from sensor j
$\boldsymbol{\Phi}_m$	The uncertain vessel parameter to be tuned, $m \in \{1, 2, ..., M\}$
σ_X^*	The true vessel motion signal STD
σ_N^2	Variance of noise
σ_X^2	Variance of response
$\sigma_{\sigma_{r,j}}$	The STD of $\sigma_{r,j}$ over $r \in \{1, 2, ..., N_{RAO}\}$
$\sigma_{r,j}$	The predicted STD by using $RAO_{r,j}$
f_{lp}^*	The optimal cutoff frequency [Hz] for a lowpass filter
f_{lp}	Lowpass filter cutoff frequency [Hz]
$H\left(\omega, \beta_W\right)$	Linear transfer function between wave and vessel (heave) response, i.e. RAO
H_s	Significant wave height
Im	The number of the discrete values used for RAO database for the vessel parameter $\boldsymbol{\Phi}_m$
im	The imth value of the variable $\boldsymbol{\Phi}_m$ in the RAO database
j	Sensor ID, the jth sensor, representing different quantities (displacement, velocity, acceleration) and locations
Km	The number of the discrete values use for the probability distribution model for the vessel parameter $\boldsymbol{\Phi}_m$
km	The kmth value of the discretized variable $\boldsymbol{\Phi}_m$ in the probability distribution model
M	The number of considered variables for tuning
N_ω	The number of discretized frequencies
N_t	The number of discretized time steps
N_{Prob}	The total number of the discrete points for the joint probability distribution model, $N_{Prob} = \prod_{m=1}^{M}(Km)$
N_{RAO}	The total number of possible vessel parameter combinations to build the RAO database, $N_{RAO} = \prod_{m=1}^{M}(Im)$
p	Power parameter
$P^{(n)}\left(\boldsymbol{\Phi}_1, ..., \boldsymbol{\Phi}_M\right)$	The updated discrete joint probability distribution after the nth updating step
r_{55}	Pitch radius of gyration
$RAO_{r,j}$	The RAO based on the variable combination r, for the sensor j (location and quantity)
$S_{\zeta\zeta}^+\left(\omega, \beta_W\right)$	Single-sided power spectral density of long-crested waves
$S_{XX}^+(\omega)$	Single-sided power spectral density of vessel response X
T_p	Spectral peak period
T_z	Zero-upcrossing period
$w_{r,j}$	Weight factor for the rth variable combination based on measurement from sensor j
$x_j(t)$	The original signal for sensor j at time step t
FFT	Fast Fourier transform
GMT	Correction to the transverse metacentric height due to free surface effects
IMU	Inertial measurement unit
MRU	Motion reference unit
OSV	Offshore supply vessel
PDF	Probability density function
PM	Pierson–Moskowitz spectrum
RAO	Response amplitude operator
SNR	Signal-to-noise ratio
STD	Standard deviation
WN	White noise
XCG	Longitudinal coordinate of vessel center of gravity

popular model-based approaches, due to their convenient formulation for state estimation and feasibility in relation to time-varying systems in the time domain (Simon, 2006). Most MRU applications use model-based advanced Kalman filters for the convenient applications of sensor fusion. Ren et al. (2019) proposed motion estimation algorithms by fusing the IMU and GNSS measurements. Grewal et al. (1991) introduced a dual extended Kalman filter for estimating the measurement errors from gyroscopes and accelerometers separately. The separated filtering of gyro and accelerometer measurements reduces the number of coefficients to be tuned. Besides, significant amounts of motion estimation algorithms have been developed based on various Kalman filters, such as unscented Kalman filter (Zhang et al., 2005), adaptive Kalman filter (Li and Wang, 2013), and exogenous Kalman filter (Stovner et al., 2018). An alternative type of model-based filtering technique is based on the Lyapunov stability concept (Fossen and Strand, 1999; Grip et al., 2015). The residual error converges to zero or a bounded region according to online approximation and adaptive updating.

Taking advantage of their simple form, model-free filter techniques are easier to apply. Usually, one is interested to extract the signals within a certain frequency range by applying a bandpass, notch, low-pass, or highpass filter. Many different signal filters have been developed and applied in different fields, e.g., Butterworth filters (Butterworth, 1930) and Kolmogorov filters (Challa and Bar-Shalom, 2000). However, the cutoff frequency should be designed and tuned, either explicitly or implicitly in the filter models. As the first statistically designed filter, the Wiener filter (Wiener, 1964) can optimally extract the true signal from noise within the frequency domain by designing the

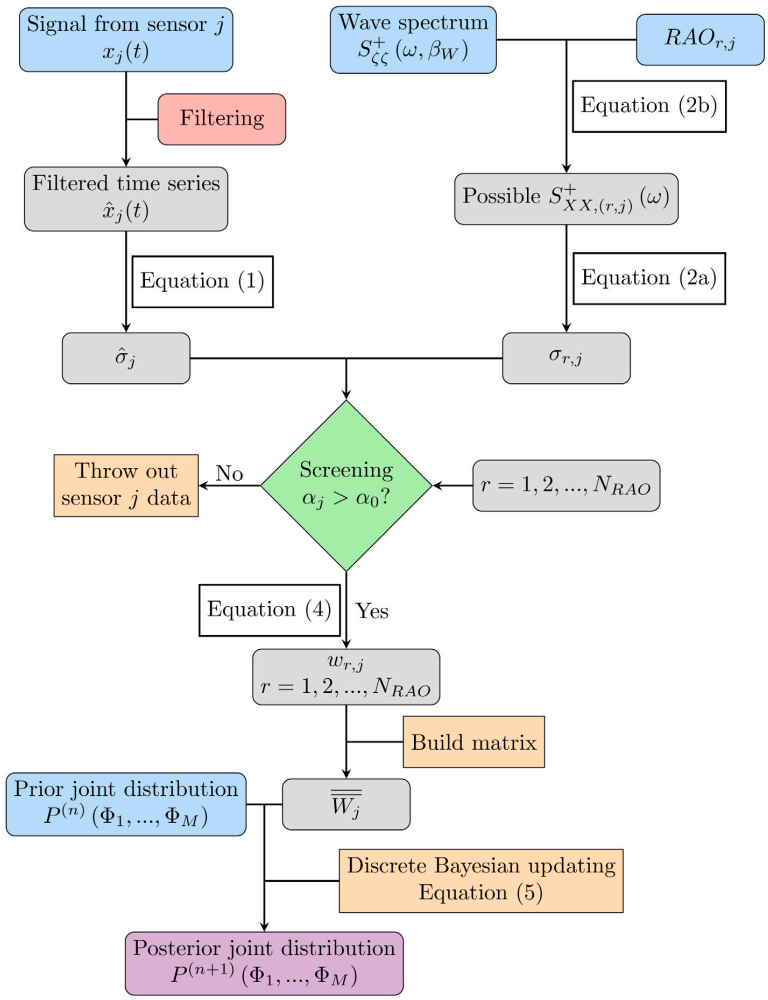

Fig. 1. Process of tuning vessel hydrodynamic model parameters, based on the vessel motion measurements and wave spectrum. Precise knowledge about wave spectrum is assumed.

filter as a linear time-invariant system, requiring knowledge about the noise-free signal spectrum and the noise spectrum. For processing with heave motion measurements, Godhaven (1998) proposed an adaptive highpass filter where the optimal cutoff frequency was obtained by minimizing the measurement errors, which depends on the measured wave condition, the selected filter model and filter order, the considered error sources, etc.

Parametric sensitivity studies of the vessel model tuning algorithm proposed by Han et al. (2021a) showed that the quality of the tuned results highly relies on a reliable filtering of signal noise to identify the vessel motion energy in the wave frequency region. Assuming that the noise energy is mainly within the high-frequency region, a lowpass filter should therefore be applied to remove the high-frequency components (e.g., noises) from the vessel motion signals. Its optimal cutoff frequency depends on many parameters such as sea state, vessel advancing speed, vessel heading, etc. This paper focuses on developing an adaptive algorithm to find the optimal cutoff frequency for the lowpass filter.

The paper is organized as follows. Section 2 briefly describes the procedures of the proposed model tuning algorithm. Section 3 describes the basic inputs of the performed analyses and the scope of work to find an algorithm or a function which could calculate the optimal cutoff frequency. Being the core of this paper, Section 4 aims to identify the important parameters correlated to the optimal cutoff frequency and explore the properties associated with the signals and the cutoff frequencies. Consequently, a novel algorithm is then proposed in Section 4, which can adaptively tune the optimal cutoff frequencies. Then the proposed algorithm is verified by means of 500 randomly generated time series in addition to several on-site vessel motion measurements, described in Section 5. The influence of the proposed adaptive lowpass filter on the vessel model tuning results is then evaluated. Conclusions and future work are presented in Section 6.

2. Basic vessel model tuning procedure

The considered vessel seakeeping model tuning procedure proposed by Han et al. (2021a) is briefly repeated in this section and illustrated in Fig. 1. The joint probability distribution of the uncertain vessel parameters ($\boldsymbol{\Phi}_1, \ldots, \boldsymbol{\Phi}_m, \ldots, \boldsymbol{\Phi}_M$, $m \in \{1, 2, \ldots, M\}$), after tuning

n times based on the proposed tuning procedure can be expressed as $P^{(n)}(\Phi_1, \Phi_2, \ldots, \Phi_M)$. The update is based on the provided wave information, vessel motion measurements (e.g., at a sensor numbered as j), and a prepared RAO database which covers all the considered sensors and the whole uncertainty ranges of the considered vessel parameters:

1. Filter the vessel motion measurements from sensor j, $x_j(t)$. In reality, the raw motion signal includes noise in the high-frequency range, a low-frequency signal bias, and environment-induced low-frequency motions. It is important to filter out such disturbances and to identify the first-order wave-induced motions.
2. Calculate the standard deviation (STD) of the filtered signal, $\hat{\sigma}_j$, by

$$\hat{\sigma}_j = \sqrt{\frac{\sum_{t=1}^{N_t} \left(\hat{x}_j(t) - \bar{x}_j\right)^2}{N_t - 1}} \tag{1a}$$

$$\bar{x}_j = \frac{\sum_{t=1}^{N_t} \hat{x}_j(t)}{N_t} \tag{1b}$$

where $\hat{x}_j(t)$ means the estimated time series of the filtered signal for sensor j at the time step t, N_t is the total number of discrete time steps of the signal, and $\bar{x}_j$ is the mean value of the filtered signal.
3. Calculate the standard deviations of the possible vessel response $\sigma_{r,j}$, based on the corresponding wave spectrum and the candidate RAO from the RAO database

$$\sigma_{r,j} = \sqrt{\sum_{n=1}^{N_\omega} S^+_{XX,(r,j)}(\omega_n) \cdot \Delta\omega} \tag{2a}$$

$$S^+_{XX,(r,j)}(\omega) = \left|H_{r,j}(\omega, \beta_W)\right|^2 \cdot S^+_{\zeta\zeta}(\omega, \beta_W) \tag{2b}$$

where N_ω is the total number of discretized frequencies for the response spectrum, $S^+_{XX,(r,j)}(\omega)$ is the spectrum for response X, $S^+_{\zeta\zeta}(\omega, \beta_W)$ is the long-crested wave spectrum without considering directional spreading. S^+ means single-sided power spectrum, $H_{r,j}(\omega, \beta_W)$ represents the RAO candidate calculated based on vessel parameter combination r for sensor j. Each possible combination of the considered vessel parameters, i.e., $(\Phi_{i1}, \Phi_{i2}, \ldots, \Phi_{iM})$, is subscripted with number $r \in \{1, 2, \ldots, N_{RAO}\}$, where $N_{RAO} = \prod_{m=1}^{M} Im$ is the total number of vessel parameter combinations and Im is the number of the discretized values of the considered uncertain vessel parameter Φ_m. The possible response STD with the rth combination of parameters for the sensor j is denoted by $\sigma_{r,j}$.
4. Screen out insensitive sensor measurements with respect to the considered vessel model parameters for the current sea state. A new parameter α_j, named sensor screening ratio (SSR), is introduced

$$\alpha_j = \frac{\sigma_{\sigma_{r,j}}}{\hat{\sigma}_j} \tag{3a}$$

$$\sigma_{\sigma_{r,j}} = \sqrt{\frac{\sum_{r=1}^{N_{RAO}} \left(\sigma_{r,j} - \bar{\sigma}_{R,j}\right)^2}{N_{RAO} - 1}} \tag{3b}$$

$$\bar{\sigma}_{R,j} = \frac{\sum_{r=1}^{N_{RAO}} \sigma_{r,j}}{N_{RAO}} \tag{3c}$$

where $\sigma_{\sigma_{r,j}}$ is the STD of $\sigma_{r,j}$ for $r \in \{1, 2, \ldots, N_{RAO}\}$. The previous study used a screening criterion of $\alpha_0 = 0.05$. For a certain sensor j, if $\alpha_j < 0.05$, then the sensor j will be excluded when updating the parameters. SSR basically represents how important the considered vessel parameters are under the current sea state at sensor j.
5. Calculate the weight factor for each $\sigma_{r,j}$ by

$$w_{r,j} = \frac{1}{\left|\sigma_{r,j} - \hat{\sigma}_j\right|^p} \tag{4}$$

where $p \in \mathbb{R}^+$ is called the power parameter. The choice of p value depends on the number of dimensions (M) for the model tuning, the sensitivity and uncertainty range of the considered vessel parameters, and the engineering judgment.
6. Establish the weight matrix $\overline{\overline{W_j}}$, i.e., the likelihood function, for all possible combinations of vessel parameters in the RAO database. The weight matrix has the size of $I1 \times I2 \times \cdots \times IM$.
7. Linearly interpolate the weight matrix $\overline{\overline{W_j}}$ from the size of $I1 \times I2 \times \cdots \times IM$ (variable resolution in the RAO database) to the size of $K1 \times K2 \times \cdots \times KM$ (variable resolution in the discrete joint probability distribution model).
8. Update the joint probability distribution $P^{(n+1)}(\Phi_1, \Phi_2, \ldots, \Phi_M)$ by multiplying the prior discrete joint probability density with the weight matrix $\overline{\overline{W_j}}$ element-wise

$$PDF^{(n+1)}(\Phi_1, \ldots, \Phi_M) = \mathcal{NO}\left(PDF^{(n)}(\Phi_1, \ldots, \Phi_M) \odot \overline{\overline{W_j}}\right) \tag{5}$$

where PDF means the probability density function, $\odot$ operator means the element-wise multiplication of two matrices, i.e., a Hadamard product (Scheick, 1997). $\mathcal{NO}(\cdot)$ is a normalization operator, so that the sum of the probabilities in the joint probability distribution remains 1.0 after every tuning.

The main idea is to transfer the objective of recursively calculating direction-dependent vessel motion RAOs based on vessel motion measurements and wave information to the statistical inference on the vessel model parameters which are direction-independent. The benefits are (1) the tuned results also indicate the confidence; (2) the tuned results can be used to predict the future vessel responses for different sea states and wave directions.

3. Problem statement

Early case studies (Han et al., 2021a) indicated the key role of signal filtering for unbiased vessel model tuning results. Both over-filtering and under-filtering of signal noise could lead to biased tuning results. The high-frequency components of the motion signal which are mainly due to the signal noise and the local vibrations can be removed by a lowpass filter. For the lowpass filter, it is essential to find the optimal cutoff frequency which depends on the sea state, vessel dimension, and vessel condition. However, the wave spectrum can be represented in terms of a number of parameters, such as H_s, T_p, β_W, wave spreading and spectral shape which in reality may not be accurately described by any of the well-known wave spectral types, e.g., Pierson–Moskowitz (PM), JONSWAP, and Thorsethaugen. Therefore, it is difficult to find a general function relating the optimal cutoff frequency to the sea state, vessel dimensions, and vessel condition. In addition, due to the random nature of signal noises, mathematically accurate expression for the function of the optimal cutoff frequency f^*_{lp} becomes a challenge.

This paper focuses on finding the optimal lowpass filter cutoff frequency (f^*_{lp}) in order to estimate the energy of the true wave-induced first-order vessel motion as accurately as possible. The signals are assumed to have no low-frequency components, and therefore only a lowpass filter was required for the signal. With the ambition of finding relations between sea states and f^*_{lp}, the analysis scope described in Section 3.2 is performed. All the analyses were based on one selected vessel with several sensor systems as described in Section 3.1.

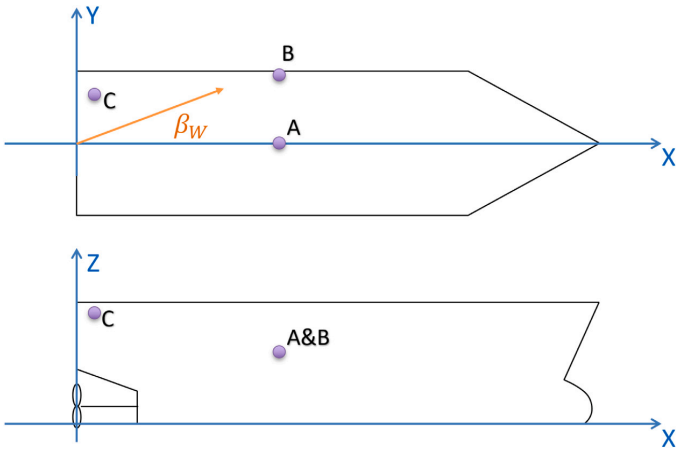

Fig. 2. Illustration of vessel coordinate system and locations of considered measurement points.

Table 1
Vessel information, base case.

Parameters	Description	Value	Unit
L_{PP}	Length between perpendiculars	~120	m
B	Breadth	~27	m
D (Ballast)	Draft	~5.1	m

Table 2
Range of vessel model parameters in RAO database.

Parameters	Variation range	Number of values
Mass	[−6%, +6%]	7
XCG	[−4 m, +4 m]	5
r_{55}	[−9%, +9%]	7
GMT[a]	[0, 1 m]	6
β_{44}	[2%, 14%]	7

[a]Here "GMT" represents the free surface correction to the transverse metacentric height. $GMT = 0.5$ m here means that the transverse metacentric height is corrected with −0.5 m due to free surface effects. It is not the value of the transverse metacentric height.

Table 3
Description of sensor measurements.

Sensor ID	Location	Coordinate (x,y,z) [m]	Signal/measurements
Disp_A	A	(60.0, 0.0, 10.0)	$\eta_{33}(t)$ at location A
Disp_B	B	(60.0, 13.0, 10.0)	$\eta_{33}(t)$ at location B
Disp_C	C	(0.0, 10.0, 14.0)	$\eta_{33}(t)$ at location C
Vel_A	A	(60.0, 0.0, 10.0)	$\dot{\eta}_{33}(t)$ at location A
Vel_B	B	(60.0, 13.0, 10.0)	$\dot{\eta}_{33}(t)$ at location B
Vel_C	C	(0.0, 10.0, 14.0)	$\dot{\eta}_{33}(t)$ at location C
Acc_A	A	(60.0, 0.0, 10.0)	$\ddot{\eta}_{33}(t)$ at location A
Acc_B	B	(60.0, 13.0, 10.0)	$\ddot{\eta}_{33}(t)$ at location B
Acc_C	C	(0.0, 10.0, 14.0)	$\ddot{\eta}_{33}(t)$ at location C

$\eta_{33}(t)$: time series of heave displacement;
$\dot{\eta}_{33}(t)$: time series of heave velocity;
$\ddot{\eta}_{33}(t)$: time series of heave acceleration.

3.1. Vessel model

The numerical studies are based on an offshore supply vessel (OSV) close to its ballast condition (Han et al., 2021a). The primary vessel dimensions are summarized in Table 1. The vessel reference coordinate system moves steadily at the vessel forward speed, as illustrated in Fig. 2. The positive X-axis along the longitudinal symmetric axis points from the stern to the bow ($X = 0$ aft), the Z-axis is pointing vertically upwards from the keel ($Z = 0$), and the Y-axis is normal to the X–Z plane where $Y = 0$ is at the vessel longitudinal symmetry plane. The wave direction β_W follows the same coordinate system, i.e. waves at 180° heading propagate along the negative X-axis.

The RAO database was established (1) to generate signals for different locations and responses of the vessel; and (2) to evaluate the effects of the adaptive lowpass filter on the model tuning performance. Based on the early sensitivity studies of the hydrodynamic model parameters in relation to the vessel motions of interest (Han et al., 2020), variation of five vessel parameters was considered for the RAO database. The considered uncertainty ranges are summarized in Table 2. The discrete values for each parameter are evenly distributed within its uncertainty range. Seakeeping analyses were performed by Wasim (DNV, 2018) (from the DNV Sesam family), applying the Rankine panel method (Kring, 1994). Running analyses through all wave periods in the time domain, the outputs can then be transferred to the frequency domain in order to build the RAOs. A RAO database was then established by considering all possible combinations of the discrete values for the five vessel parameters. Heave responses are often of interest for marine operations (e.g., heavy lift). Therefore, heave RAOs (i.e. displacement, velocity and acceleration) at three different locations (see Fig. 2) were included in the RAO database, for each combination of vessel parameters. As described in Table 3, 9 different measured quantities (sensors) associated with heave response were considered in the model tuning simulations. Only zero advancing speed was considered for simplicity in order to avoid dealing with the 3-to-1 mapping problem between the absolute wave frequency and encounter frequency for following waves (Lewandowski, 2004). In total, 13 Wave headings between 0° and 180° with a 15° interval were considered in the RAO database for the 9 sensor measurements.

3.2. Finding the optimal cutoff frequency

It is assumed that the high-frequency signal errors can be represented by white noise

$$WN \sim \mathcal{N}\left(0, \sigma_N^2\right) \tag{6}$$

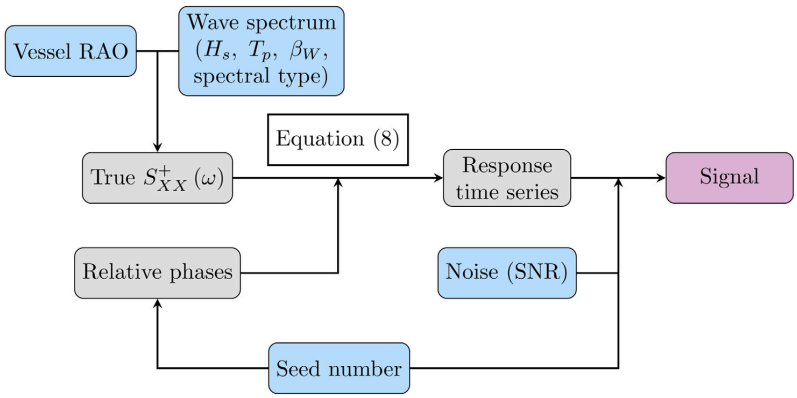

Fig. 3. Flow chart for the purpose of simulating noisy vessel response measurements.. (For interpretation of the references to colour in this figure legend, the reader is referred to the web version of this article.)

where the variance of the noise σ_N^2 is determined by the signal-to-noise ratio (SNR)

$$SNR = \frac{\sigma_X^2}{\sigma_N^2} \tag{7}$$

where σ_X^2 is the variance of the true signal.

The response signal can be simulated according to the process in Fig. 3. Blocks in blue are the required inputs which together can uniquely determine the output signal. The seed number was used to generate both the relative phase φ_n for each frequency component ω_n and the noise for each time step. A massive amount of vessel heave motion signals were generated by varying all the input parameters in Fig. 3, in order to investigate the relations between inputs and f^*_{lp}.

The considered variation of inputs are summarized in Table 4. Each simulation lasts for 1 h. The time series were generated based on the corresponding response spectrum by application of the following relationships:

$$x(t) = \sum_{n=1}^{N_\omega} C_n(\omega_n)\cos(\omega_n t + \varphi_n) \tag{8a}$$

$$C_n(\omega_n) = \sqrt{2S^+_{XX}(\omega_n)\cdot \Delta\omega} \tag{8b}$$

$$S^+_{XX}(\omega) = |H_X(\omega,\beta_W)|^2 \cdot S^+_{\zeta\zeta}(\omega,\beta_W) \tag{8c}$$

where $\varphi_n \in [0, 2\pi)$ is a random phase angle which is continuous and uniformly distributed, $\Delta\omega$ is the width of the radial frequency interval of ω_n, and N_ω is the total number of the discrete frequencies for the response spectrum. $S^+_{XX}(\omega_n)$ is the single-sided response spectrum for the response X, calculated by Eq. (8c). $|H_X(\omega,\beta_W)|$ is the RAO of the response X for a specific vessel condition. The vessel condition in the present paper is defined by the 5 vessel parameters in Table 2. One vessel condition was randomly selected among the RAO database for the studies of finding the optimal cutoff frequency. $S^+_{\zeta\zeta}(\omega,\beta_W)$ is the wave spectrum. The influence of wave spectral type on the optimal cutoff frequency was studied where three wave spectral types (DNVGL-RP-C205, 2017) were considered, i.e., PM, JONSWAP, and Torsethaugen.

The PM wave spectrum $S_{PM}(\omega)$, originally proposed for fully-developed sea, can be calculated based on H_s and T_p:

$$S_{PM}(\omega) = \frac{5}{16}H_s^2\omega_p^4\omega^{-5}\exp(-\frac{5}{4}(\frac{\omega}{\omega_p})^{-4}) \tag{9}$$

where $\omega_p = 2\pi/T_p$ is the wave spectral peak frequency.

The JONSWAP spectrum $S_{JON}(\omega)$, representing a fetch limited developing sea state, can be calculated by

$$S_{JON}(\omega) = (1-0.287\ln(\gamma_p))S_{PM}(\omega,\omega_p,H_s)\gamma_p^{\exp(-0.5(\frac{\omega-\omega_p}{\sigma_w\omega_p})^2)} \tag{10a}$$

$$\gamma_p = \begin{cases} 5 & \text{for } T_p/\sqrt{H_s} \le 3.6 \\ \exp(5.75 - 1.15\frac{T_p}{\sqrt{H_s}}) & \text{for } 3.6 < T_p/\sqrt{H_s} < 5 \\ 1 & \text{for } T_p/\sqrt{H_s} \ge 5 \end{cases} \tag{10b}$$

$$\sigma_w = \begin{cases} 0.07 & \text{for } \omega \le \omega_p \\ 0.09 & \text{for } \omega > \omega_p \end{cases} \tag{10c}$$

where γ_p is the peak enhancement factor calculated based on H_s and T_p, and σ_w is the spectral width parameter.

The double-peaked Torsethaugen spectrum can be calculated based on the simplified form described in Appendix A.2 in DNVGL-RP-C205 (2017). It is the sum of two JONSWAP spectra described in Eq. (10). The simplified formulation of the Torsethaugen spectrum $S_{Tor}(\omega)$ is different for the case of sea states dominated by wind seas versus those dominated by swells. These are distinguished based on the value of the parameter $T_f = 6.6H_s^{1/3}$:

$$S_{Tor}(\omega) = S_{JON,w}(\omega|H_{s,w},T_{p,w},\gamma_{p,w}) + S_{JON,sw}(\omega|H_{s,sw},T_{p,sw},\gamma_{p,sw}) \tag{11a}$$

For wind dominated sea ($T_p \le T_f$):

$$H_{s,w} = r_{pw}H_s \tag{11b}$$

$$T_{p,w} = T_p \tag{11c}$$

$$\gamma_{p,w} = 35[\frac{2\pi}{g}\frac{H_{s,w}}{T_p^2}]^{0.857} \tag{11d}$$

$$H_{s,sw} = \sqrt{1-r_{pw}^2}H_s \tag{11e}$$

$$T_{p,sw} = T_f + 2.0 \tag{11f}$$

$$\gamma_{p,sw} = 1 \tag{11g}$$

$$r_{pw} = 0.7 + 0.3\exp(-(2\frac{T_f - T_p}{T_f - 2\sqrt{H_s}})^2) \tag{11h}$$

For swell dominated sea ($T_p > T_f$):

$$H_{s,w} = \sqrt{1-r_{ps}^2}H_s \tag{11i}$$

$$T_{p,w} = 6.6H_{s,w}^{1/3} \tag{11j}$$

$$\gamma_{p,w} = 1 \tag{11k}$$

$$H_{s,sw} = r_{ps}H_s \tag{11l}$$

$$T_{p,sw} = T_p \tag{11m}$$

$$\gamma_{p,sw} = 35[\frac{2\pi}{g}\frac{H_s}{T_f^2}]^{0.857}(1+6\frac{T_p - T_f}{25 - T_f}) \tag{11n}$$

Table 4
Parameter variation for generating heave response signals.

Parameter	Values	Unit	Number of values
H_s	{1, 4}	m	2
T_p	{5, 6, … , 25}	s	21
β_W	{0, 30, 60, 90}	°	4
Wave spectrum	{PM, JONSWAP, Torsethaugen}	–	3
Seed variation	Random [1, 300]	–	10
SNR	{10, 30, 100}	–	3
Sensor	Described in Table 3	–	9

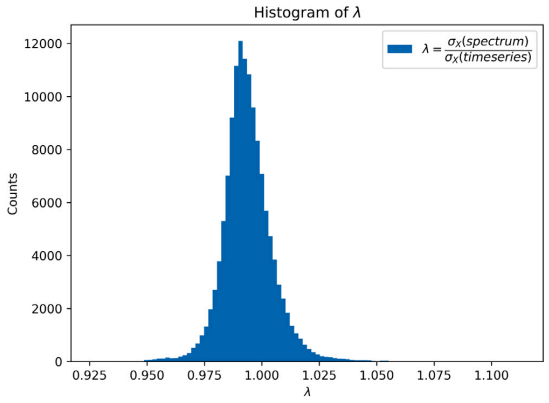

Fig. 4. Distribution of λ, i.e., the ratio between standard deviations calculated based on the spectrum by Eq. (2a) and the time series by Eq. (1a) without noises.

$$r_{ps} = 0.6 + 0.4\exp\left(-\left(\frac{T_p - T_f}{0.3(25 - T_f)}\right)^2\right) \tag{11o}$$

where $H_{s,w}$, $T_{p,w}$, and $\gamma_{p,w}$ stand for the associated H_s, T_p, and γ_p of the wind sea component $S_{JON,w}(\omega|H_{s,w}, T_{p,w}, \gamma_{p,w})$, while $H_{s,sw}$, $T_{p,sw}$, $\gamma_{p,sw}$ correspond to the swell component $S_{JON,sw}(\omega|H_{s,sw}, T_{p,sw}, \gamma_{p,sw})$.

A FFT (Cooley and Tukey, 1965) lowpass filter using the Python SciPy package (Virtanen et al., 2020) was applied to filter each signal, by application of many different cutoff frequencies $f_{lp} \in [0.05, 2.0]$ Hz. The optimal cutoff frequency f_{lp}^*, therefore, can be determined by comparing the STD of the filtered signal $\hat{\sigma}_X(f_{lp})$ with the STD of the true response time series σ_X^*. The study tested 25 cutoff frequencies for each signal, i.e., $f_{lp} \in \{0.050, 0.053, 0.056, 0.059, 0.063, 0.067, 0.071, 0.077, 0.083, 0.091, 0.10, 0.111, 0.125, 0.143, 0.167, 0.20, 0.25, 0.30, 0.33, 0.40, 0.50, 0.60, 0.75, 1.0, 1.5, 2.0\}$ Hz.

4. Data exploration

This section aims to identify the most relevant input parameters for the optimal cutoff frequency f_{lp}^* and to propose a way to find f_{lp}^*. Due to the limited number of discretized frequencies and discretized time steps for a given simulation length based on Eq. (8), the generated response time series will not contain exactly the same power as the response power spectrum. Fig. 4 indicates that there may be up to about a ±2.5% error/
uncertainty for the studied 1-h response realizations with a limited number of discrete frequencies and time steps. This approximately corresponds to a SNR of 20. The uncertainty can be reduced by increasing the number of discretized frequencies, reducing the time series sampling interval, and increasing the duration of the realization. The studies did not attempt to reduce this error.

Fig. 5 shows the overall distribution of the optimal cutoff frequency f_{lp}^* together with the 5-, 25-, 50-, 75-, and 95-percentile values. The optimal cutoff frequencies are well concentrated between 0.15 Hz and 0.3 Hz. However, further data exploration has to be performed in order to find any possible relation between f_{lp}^* and the input parameters quantitatively.

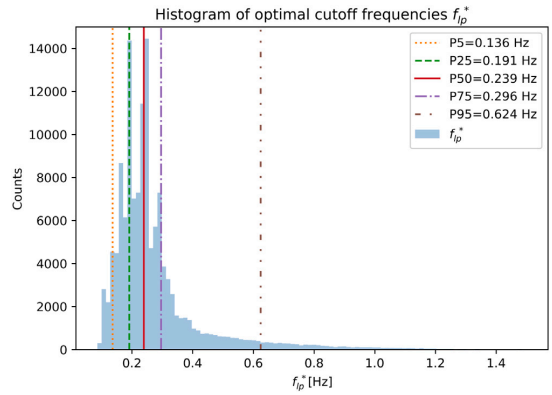

Fig. 5. Histogram of the optimal lowpass filter cutoff frequencies.

Initial data exploration shows that the optimal cutoff frequency f_{lp}^* can be influenced by the characteristic spectral period (e.g., T_p), incoming wave direction β_W, wave spectral shape, the sensor location, and noise level SNR. In addition, the significant influence from seed variation is also observed. The optimal cutoff frequency value from signals with higher SNR (less noise) seems to be more affected by seed variation.

Note that there were very few cases (0.005%) that failed to find an optimal cutoff frequency within the tested range ([0.05,2.0] Hz), mostly due to the effects from seed variation, and the limitations in accuracy which are associated with numerical calculations based on discrete frequencies and time steps. It only happened for SNR = 100.

Plots show that the function $f_{lp}^*(T_p)$ could be well fitted by a linear function (e.g., $f_{lp}^* = aT_p + b$) or a bi-linear function (e.g., $f_{lp}^* = aT_p + b$ for all $T_p \le T_0$; $f_{lp}^* = cT_p + d$ for all $T_p > T_0$). However, the fitted parameters (e.g., a, b, T_0, etc.) depend on many input parameters, such as β_W, wave spectral shape, sensor location, vessel condition, etc. Therefore, it is difficult to find a clear function for the optimal cutoff frequency directly with respect to the wave and sensor inputs, i.e., $f_{lp}^*(T_p, \beta_W$, spectral type, sensor, etc.).

4.1. Standard deviation and zero-upcrossing period of filtered signals

Therefore, it is of interest to further investigate details on how the standard deviation (STD) and zero-upcrossing period of the filtered signal ($\hat{\sigma}_X(f_{lp})$ and $\hat{T}_z(f_{lp})$) changes with changing cutoff frequency. For example, Figs. 6 and 7 show that:

1. The optimal cutoff frequency f_{lp}^* always stays at or near the turning point of the $\hat{\sigma}_X$-f_{lp} curve.
2. The optimal cutoff frequency f_{lp}^* is always on the "plateau" of the $\hat{T}_z$-f_{lp} curves, but not necessarily at the turning point.
3. When a larger f_{lp} applies, less noise is filtered out. But $\hat{\sigma}_X(f_{lp})$ increases very slowly with increasing f_{lp} for $f_{lp} > f_{lp}^*$. This means that even though applying larger f_{lp} may lead to biased tuning results, it is still much safer to use a slightly larger f_{lp} than a slightly smaller f_{lp} relative to f_{lp}^*.

The reason for the existence of the "plateau" in the $\hat{T}_z$-f_{lp} curve is the clear distinction between the main frequency regions for the true vessel response versus the signal noise. In addition, the less the noise level is (i.e., larger SNR), the flatter and longer the "plateau" will be.

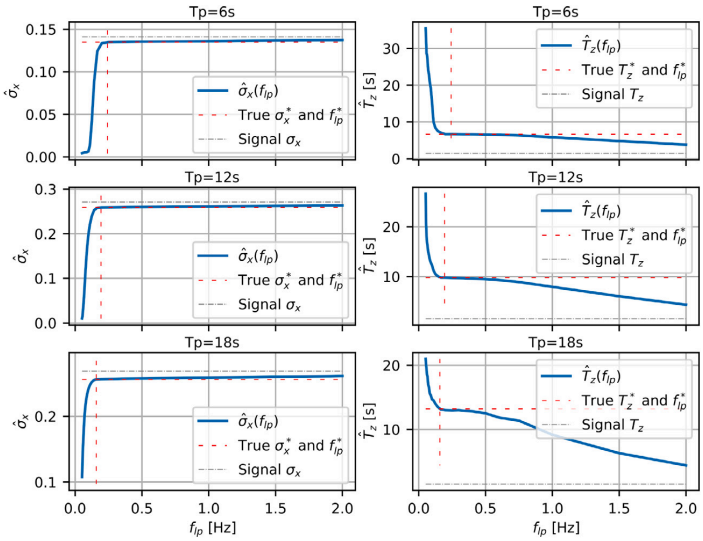

Fig. 6. $\hat{\sigma}_X$-f_{lp} and $\hat{T}_z$-f_{lp} curves for Disp_A sensor, SNR = 10, $\beta_W = 90°$, $T_p = 6$ s, 12 s, and 18 s.

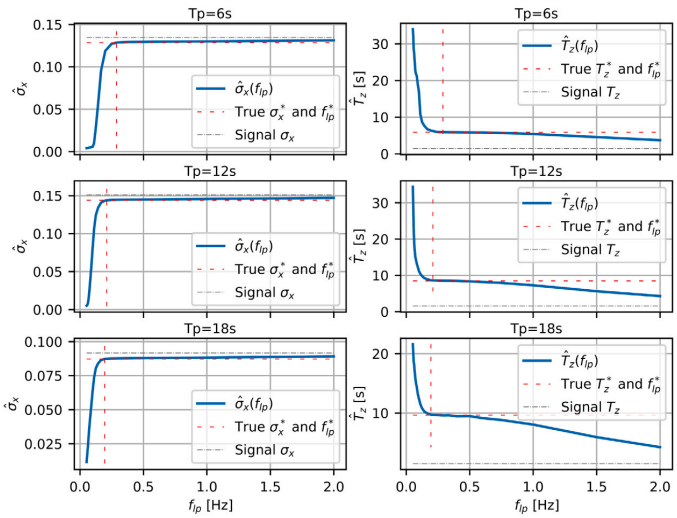

Fig. 7. $\hat{\sigma}_X$-f_{lp} and $\hat{T}_z$-f_{lp} curves for Acc_C sensor, SNR = 10, $\beta_W = 0°$, $T_p = 6$ s, 12 s, and 18 s.

This is because less noise will have less influence on the overall signal zero-upcrossing period.

Therefore, it can be helpful to determine the optimal cutoff frequency based on the characteristics of the $\hat{\sigma}_X$-f_{lp} and $\hat{T}_z$-f_{lp} curves. Two parameters are introduced, representing the absolute values of the normalized slopes of the $\hat{T}_z$ - f_{lp} and $\hat{\sigma}_X$ - f_{lp} curves. The hat operator $\hat{}$ means the filtered results.

The efficiency of increasing or reducing the cutoff frequency on the change of the filtered signal energy, is referred to as $\theta\left(f_{lp}\right)$, defined by

$$\theta\left(f_{lp,i}\right) = \frac{\hat{\sigma}_X\left(f_{lp,i}\right) - \hat{\sigma}_X\left(f_{lp,i-1}\right)}{\hat{\sigma}_X\left(f_{lp,i}\right) \cdot \left(f_{lp,i} - f_{lp,i-1}\right)} \tag{12}$$

where $\hat{\sigma}_X\left(f_{lp,i}\right)$ means the filtered signal STD by application of the cutoff frequency $f_{lp,i}$

The effect of increasing or reducing the cutoff frequency on the change of the zero-upcrossing period of the filtered signal, is referred to as $\lambda\left(f_{lp}\right)$

$$\gamma\left(f_{lp,i}\right) = \frac{\hat{T}_z\left(f_{lp,i-1}\right) - \hat{T}_z\left(f_{lp,i}\right)}{\hat{T}_z\left(f_{lp,i}\right) \cdot \left(f_{lp,i} - f_{lp,i-1}\right)} \tag{13}$$

where $\hat{T}_z\left(f_{lp,i}\right)$ means the zero-upcrossing period of the filtered signal based on the cutoff frequency of $f_{lp,i}$. Please note that γ is positive when the slope of the $\hat{T}_z$-f_{lp} curve is negative. When $\left(f_{lp,i} - f_{lp,i-1}\right) \to 0$, $\theta\left(f_{lp,i}\right)$ represents the normalized slope of the $\hat{\sigma}_X$-f_{lp} curve at $f_{lp,i}$, while $\gamma\left(f_{lp,i}\right)$ represents the opposite value of the normalized slope of the $\hat{T}_z$-f_{lp} curve at $f_{lp,i}$. The true response STD is in the following defined as σ_X^*.

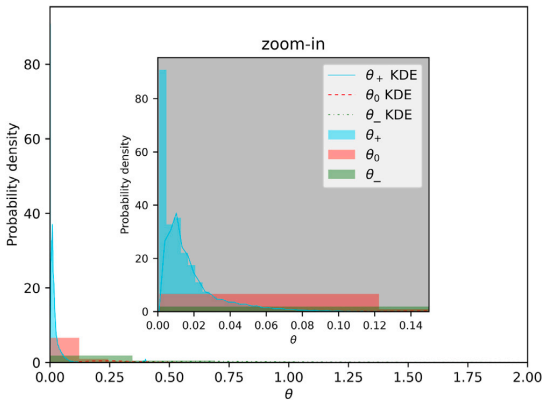

Fig. 8. Normalized histogram of θ_-, θ_0, and θ_+ based on all studied signals. The fitted lines are the estimated Gaussian kernel densities (Waskom et al., 2020) based on the corresponding normalized histograms. KDE: kernel density estimation.

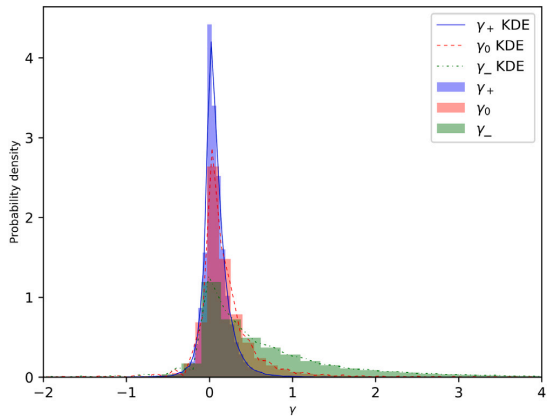

Fig. 9. Normalized histogram of γ_-, γ_0, and γ_+ based on all studied signals. The fitted lines are the estimated Gaussian kernel densities based on the corresponding normalized histograms. KDE: kernel density estimation.

The program tested a limited number of discrete f_{lp} values gradually as described in Section 3.2. Therefore, the optimal frequency is actually found by interpolation between the neighboring frequencies, f_{lp,i^*} and f_{lp,i^*+1}, where $\hat{\sigma}_X\left(f_{lp,i^*}\right) \le \sigma_X^* \le \hat{\sigma}_X\left(f_{lp,i^*+1}\right)$ for $f_{lp,i^*} \le f_{lp}^* \le f_{lp,i^*+1}$. Due to the mentioned findings of the two curves, the distributions of the θ and γ values around the optimal cutoff frequency f_{lp}^* are of great interest to further investigate, and these are therefore defined as follows:

$$\theta_- = \frac{\hat{\sigma}_X\left(f_{lp,i^*}\right) - \hat{\sigma}_X\left(f_{lp,i^*-1}\right)}{\hat{\sigma}_X\left(f_{lp,i^*}\right) \cdot \left(f_{lp,i^*} - f_{lp,i^*-1}\right)} \tag{14a}$$

$$\theta_0 = \frac{\hat{\sigma}_X\left(f_{lp,i^*+1}\right) - \hat{\sigma}_X\left(f_{lp,i^*}\right)}{\hat{\sigma}_X\left(f_{lp,i^*+1}\right) \cdot \left(f_{lp,i^*+1} - f_{lp,i^*}\right)} \tag{14b}$$

$$\theta_+ = \frac{\hat{\sigma}_X\left(f_{lp,i^*+2}\right) - \hat{\sigma}_X\left(f_{lp,i^*+1}\right)}{\hat{\sigma}_X\left(f_{lp,i^*+2}\right) \cdot \left(f_{lp,i^*+2} - f_{lp,i^*+1}\right)} \tag{14c}$$

$$\gamma_- = \frac{\hat{T}_z\left(f_{lp,i^*-1}\right) - \hat{T}_z\left(f_{lp,i^*}\right)}{\hat{T}_z\left(f_{lp,i^*}\right) \cdot \left(f_{lp,i^*} - f_{lp,i^*-1}\right)} \tag{15a}$$

$$\gamma_0 = \frac{\hat{T}_z\left(f_{lp,i^*}\right) - \hat{T}_z\left(f_{lp,i^*+1}\right)}{\hat{T}_z\left(f_{lp,i^*+1}\right) \cdot \left(f_{lp,i^*+1} - f_{lp,i^*}\right)} \tag{15b}$$

$$\gamma_+ = \frac{\hat{T}_z\left(f_{lp,i^*+1}\right) - \hat{T}_z\left(f_{lp,i^*+2}\right)}{\hat{T}_z\left(f_{lp,i^*+2}\right) \cdot \left(f_{lp,i^*+2} - f_{lp,i^*+1}\right)} \tag{15c}$$

Note that the values of θ and γ can be influenced by the resolution of the tested f_{lp} values. The histograms of the parameters θ_-, θ_0, θ_+, γ_-, γ_0, and γ_+ are shown in Figs. 8 and 9. Because of the large difference between the bin ranges for the parameters (e.g., θ_-, θ_0, and θ_+), the plotted histograms were normalized for the purpose of easier comparison between them. The histogram of each variable considered 100 bins, and the histogram was normalized so that the height (denoted as h) of the histogram plot represents the probability density of the parameter (denoted as v). The bins are evenly distributed, so that $\Delta v = \frac{v_{max} - v_{min}}{100}$. The plotted normalized histogram plots fulfill

$$\sum_{i=1}^{100} h_i \cdot \Delta v = 1.0. \tag{16}$$

It is clear that θ_+ is highly concentrated in a much smaller θ value range, as compared with the distributions of θ_- and θ_0. However, γ_-, γ_0 and γ_+ are all distributed around zero, with γ_+ having the smallest variance. These observations positively support the findings from Figs. 6 and 7. The statistical percentile values of all these 6 parameters are summarized in Table 5.

Table 5
Distribution of θ and γ values near the optimal cutoff frequency.

Parameter	P5	P25	P50	P75	P95
f_{lp}^*	0.136	0.191	0.239	0.296	0.624
θ_-	0.0011	0.0258	0.189	0.569	2.263
θ_0	0.001	0.0082	0.0371	0.0989	0.341
θ_+	0.001	0.0033	0.009	0.0181	0.0502
γ_-	−0.111	0.062	0.359	0.961	2.591
γ_0	−0.137	0.000559	0.109	0.285	0.841
γ_+	−0.136	−0.00056	0.053	0.139	0.36

It is also interesting to find that the uncertainty of $\theta\left(f_{lp}^*\right)$ is highly correlated with the SNR. Larger noise leads to larger variation of $\theta\left(f_{lp}^*\right)$ for different signals (seed variation) from the same response spectrum. However, this does not conflict with the previous findings that higher noise leads to less variation of f_{lp}^* for different signals due to seed variation for the same response spectrum. The distributions of θ_-, θ_0, θ_+ become even more distinguishable for a certain SNR value (e.g., Figs. 10 and 11).

As shown in Table 5 and Fig. 9, the γ values are small and stable near f_{lp}^*, which means that the optimal cutoff is on the "plateau" of the $\hat{T}_z$-f_{lp} curve. As γ_-, γ_0, γ_+ are similarly distributed, the criterion for γ must be relaxed, acting as a supplementary rule for the θ criterion.

4.2. Proposed strategy to find optimal cutoff frequency

Due to the large slope of the $\hat{\sigma}_X$ - f_{lp} curve for $f_{lp} < f_{lp}^*$, it is better to filter slightly less noise than risking to filter out too much energy. Assuming no low-frequency motion, the proposed strategy to find the optimal lowpass filter cutoff frequency f_{lp}^* in order to retain only the signals within the wave frequency region is summarized as follows.

1. Starting from a small cutoff frequency $f_{lp,1}$ of, e.g., 0.02 Hz, filter the noisy signal $x(t)$, and calculate the STD and zero-upcrossing period of the filtered signal, i.e., $\hat{\sigma}_X(f_{lp,1})$ and $\hat{T}_z(f_{lp,1})$.
2. Repeat step 1 by gradually increasing the cutoff frequency $f_{lp,i}, i = 2, 3, \ldots$. Calculate $\hat{\sigma}(f_{lp,i})$, $\hat{T}_z(f_{lp,i})$, $\theta(f_{lp,i})$, and $\gamma(f_{lp,i})$ for $i = 2, 3, \ldots$.

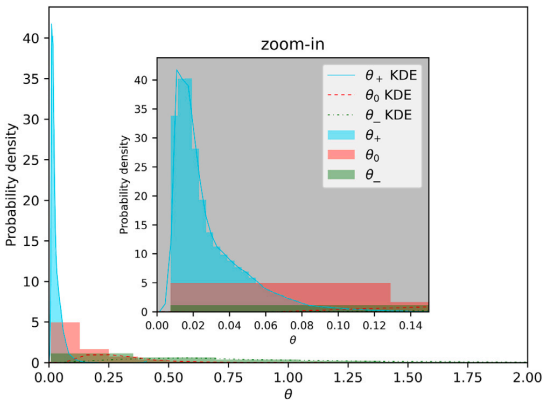

Fig. 10. Normalized histogram of θ_-, θ_0, and θ_+ based on the studied signals for a SNR of 10. The fitted lines are the estimated Gaussian kernel densities based on the corresponding normalized histograms. KDE: kernel density estimation.

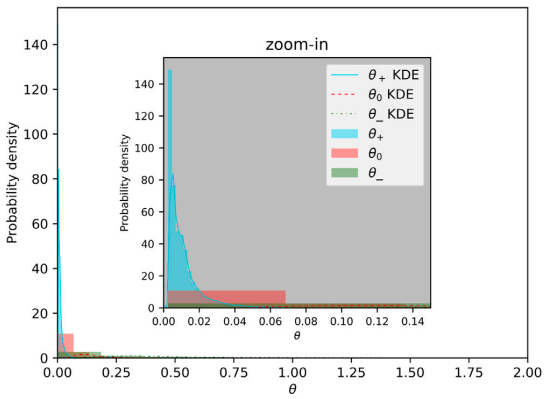

Fig. 11. Normalized histogram of θ_-, θ_0, and θ_+ based on the studied signals for a SNR of 30. The fitted lines are the estimated Gaussian kernel densities based on the corresponding normalized histograms. KDE: kernel density estimation.

3. Then the first cutoff frequency f_{lp,i^*} where both the values of $\theta_{f_{lp,i^*}}$ and $\gamma_{f_{lp,i^*}}$ meet the preset criteria, will be considered as the optimal cutoff frequency, denoted as $\tilde{f}^*_{lp}$.

It is not necessary to explicitly define the "turning" point of the $\hat{\sigma}_X$-f_{lp} curve. When the resolution of the tested f_{lp} is sufficiently fine, θ_0 and θ_+ will be very close, and practically it does not matter which of these values is selected. Based on the statistical distribution of θ and γ summarized in Table 5, the following criteria are considered as the base case.

$$\theta(f^*_{lp}) \leq 0.05 \tag{17a}$$

$$\gamma(f^*_{lp}) \leq 0.9 \tag{17b}$$

The $\theta(f^*_{lp}) \leq 0.05$ was chosen based on statistical information about θ_0 and θ_+ so that θ_+ meets the criterion for 95% of the cases, and more than half of θ_0 meets the criterion. The histograms of θ_-, θ_0, θ_+ indicate that the selected criterion is statistically appropriate.

As the θ and γ criteria are based on statistics of a case study, it cannot guarantee that the present procedure will find the optimal cutoff frequency for all signals. Therefore, one supplementary requirement was introduced to ensure returning an "optimal" cutoff frequency value for signal filtering, i.e., f^*_{lp} must be within [0.1, 0.9] Hz, i.e.,

$$f^*_{lp} = \begin{cases} 0.1 \text{ Hz}, & \text{if } \tilde{f}^*_{lp} < 0.1 \text{ Hz} \\ 0.9 \text{ Hz}, & \text{if } \tilde{f}^*_{lp} > 0.9 \text{ Hz} \\ \tilde{f}^*_{lp}, & \text{otherwise} \end{cases} \tag{18}$$

where $\tilde{f}^*_{lp}$ means the identified optimal cutoff frequency based on the main proposed strategy with the criteria in Eq. (17). The algorithm are also summarized in pseudo code format.

Algorithm 1: Recursive searching of optimal cutoff frequency.

Initialize: i=0, $\theta = 1.0$, $\gamma = 10.0$;
Input: Predefined f_{lp} values in ascending order and the signal $x(t)$;
while $\theta > 0.05$ *or* $\gamma > 0.9$ **do**
  $i = i + 1$;
  Obtain $\hat{x}(t)$ by filtering $x(t)$ at cutoff frequency of $f_{lp,i}$;
  Calculate $\hat{\sigma}_X(f_{lp,i})$ and $\hat{T}_z(f_{lp,i})$;
  if $i > 1$ **then**
    Calculate $\theta(f_{lp,i})$ by Equation (12) and $\gamma(f_{lp,i})$ by Equation (13);
    $\theta = \theta(f_{lp,i})$;
    $\gamma = \gamma(f_{lp,i})$;
  end
end
$\tilde{f}^*_{lp} = f_{lp,i}$;
if $\tilde{f}^*_{lp} < 0.1\ Hz$ **then**
  $f^*_{lp} = 0.1 Hz$;
else if $\tilde{f}^*_{lp} > 0.9\ Hz$ **then**
  $f^*_{lp} = 0.9$ Hz;
else
  $f^*_{lp} = \tilde{f}^*_{lp}$;
end
return f^*_{lp};

5. Test of strategy

5.1. Simulated signals

The proposed strategy was tested for 500 randomly generated vessel motion signals, based on randomly selecting the values of the input parameters summarized in Table 6.

In total, 83 values of $f_{lp} \in [0.06, 5.13]$ Hz were considered for the lowpass filter, as shown in Fig. 12. The resolution was gradually increased with decreasing f_{lp}, especially for $f_{lp} \in [0.1, 0.3]$ Hz.

Different values of θ and γ criteria were also tested, as summarized in Table 7. The parameter κ was defined in order to evaluate the results of the adaptive filtering based on different criteria,

$$\kappa = \frac{\hat{\sigma}_X\left(\tilde{f}^*_{lp}\right)}{\sigma^*_X} \tag{19}$$

where $\hat{\sigma}_X\left(\tilde{f}^*_{lp}\right)$ is the filtered signal STD at the found optimal cutoff frequency $\tilde{f}^*_{lp}$.

Fig. 13 shows the distributions of κ from the 500 test cases (Table 6) for the 4 different sets of criteria (Table 7). Among the results, $\theta = 0.05$ with $\gamma = 0.9$ generally leads to the best filtering results with respect to the response STD, for which the filtered signal STDs are concentrated mostly around the true values. The distribution of κ for Crit2 shows slightly more spreading when using a smaller γ criterion, indicating that γ serves to provide a supplementary criterion for the adaptive filtering process. Results from Crit3 with a much higher θ value are the worst with respect to the filtered signal STD. The distribution is dramatically skewed to the left, indicating that many signals were over-filtered. This is due to a too "relaxed" θ criterion. Crit4 is most strict,

Table 6
Applied parameters related to the strategy test for the adaptive lowpass filter.

Parameter	Values	Unit
H_s	Uniformly distributed in [1.0, 4.0]	m
T_p	Uniformly distributed in [5.0, 22.0]	s
β_W	Randomly selected among 13 discrete directions within [0,180]	°
Seed	Uniformly distributed in [1, 300]	–
Duration	3600	s
SNR[a]	Randomly selected among 15 discrete values within $[int(5 \times 1.2^i), i \in [0, 15]]$	–
Vessel condition	Randomly selected among 10 vessel conditions within the RAO database	–
Sensor	Randomly selected among the 9 sensors described in Table 3	–

[a]The discrete SNR values are determined with approximately 20% difference between neighboring values, for SNR∈ [5, 64].

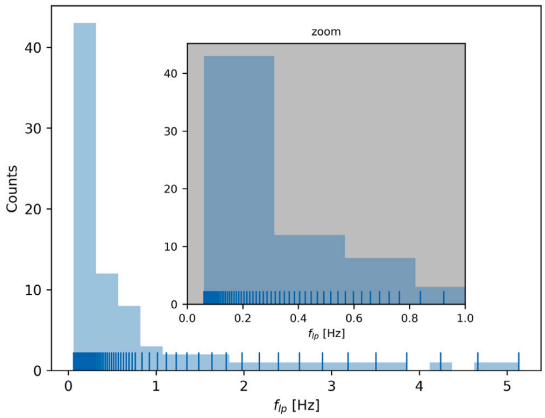

Fig. 12. Histogram of tested f_{lp} values. The blue sticks along the f_{lp} axis represent the data points.

Table 7
Tested θ and γ criteria.

Case ID	θ	γ
Crit1	0.05	0.9
Crit2	0.05	0.36
Crit3	0.3	0.9
Crit4	0.02	0.2

which, however, did not lead to better filtering results than the base case (Crit1). It can be seen in Fig. 13 that there is a notable skewing to the right, indicating that the signals may be under-filtered.

5.2. On-site MRU measurements

It is interesting to test the proposed strategy by application of on-site measurements. However, it is impossible to know the vessel's true on-site response due to the inevitable measurement uncertainties (Hubbard, 2014). Therefore, it was only possible to test whether or not the $\hat{\sigma}_X$ - f_{lp} and $\hat{T}_z$ - f_{lp} curves show similar characteristics as described in Section 4.1, and to discuss the limitations. It is worth mentioning that the vessel motion signals obtained from MRU are already filtered through, e.g., application of an extended Kalman filter, to avoid drift.

5.2.1. Gunnerus seakeeping and DP tests

The MRU measurements of the NTNU research vessel Gunnerus during seakeeping and DP tests in 2013 (Steen et al., 2016) were

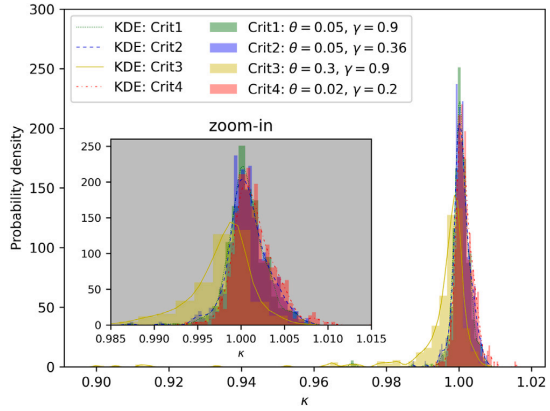

Fig. 13. Normalized histograms of κ values for the strategy test with different criteria. The fitted lines are the estimated Gaussian kernel densities based on the corresponding normalized histograms (Waskom et al., 2020).

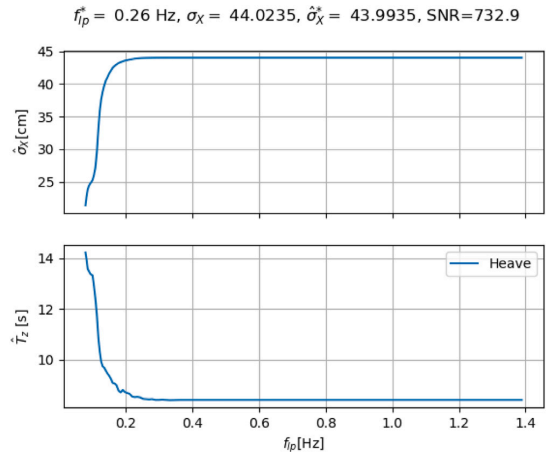

Fig. 14. $\hat{\sigma}_X$ - f_{lp} and $\hat{T}_z$ - f_{lp} curves of heave motion for CaseA1.

considered. Two test cases were reported, one 2-hour DP test (CaseA1) under a sea state with 2 significant peak periods (8.5 s and 13.3 s), and one half-hour seakeeping test (CaseA2) with 10.4kn speed under a swell-dominated sea state.

The quickly reduced slopes of the $\hat{\sigma}_X$-f_{lp} curves were observed for both cases for all MRU measurements with respect to heave, pitch, and roll, e.g., Fig. 14. Because the received MRU signals were already filtered, the noise level was low, as expected. In addition, Gunnerus is a research vessel with a relatively small dimension (about 30 m long), and accordingly its resonance response periods are relatively small. Therefore, the $\hat{T}_z$-f_{lp} curves, as expected, becomes very flat when the cutoff frequency is sufficiently large.

It is interesting to observe the reduced slopes for the $\hat{\sigma}_X$-f_{lp} and $\hat{T}_z$-f_{lp} curves within the wave frequency region for heave and pitch measurements (e.g., Fig. 15). This is because CaseA2 was a swell-dominated sea condition (T_p = 13.5 s) with a small wind sea. The vessel was mostly excited within a relatively low frequency region, while the vessel response resonance was in a relatively high frequency region due to Gunnerus' small dimensions. Therefore, there was a clear gap with respect to the frequencies of the excited vessel motion by the swell and the wind sea.

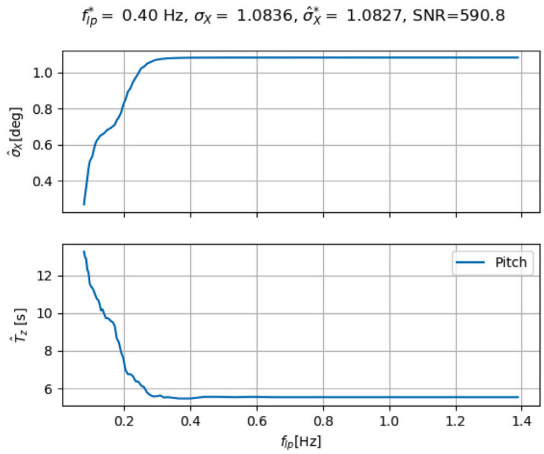

Fig. 15. $\hat{\sigma}_X$ - f_{lp} and $\hat{T}_z$ - f_{lp} curves of pitch motion for CaseA2.

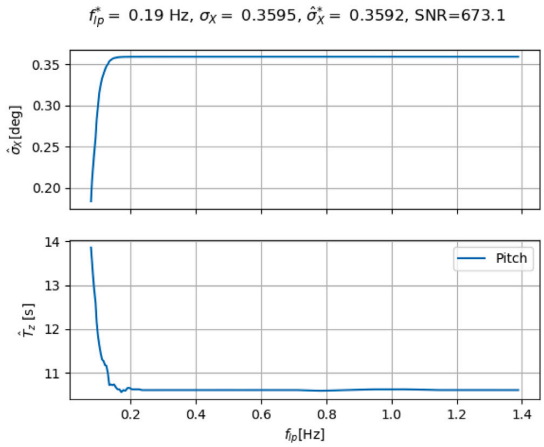

Fig. 16. $\hat{\sigma}_X$ - f_{lp} and $\hat{T}_z$ - f_{lp} curves of pitch motion for CaseB1.

5.2.2. Normand vision

The MRU measurements (CaseB1) from Normand Vision during a lifting operation in 2017 were also tested. The operation lasted for a total of 2 hours. The $\hat{\sigma}_X$ - f_{lp} and $\hat{T}_z$ - f_{lp} curves for the 2-hour pitch and roll responses are shown in Figs. 16 and 17. The $\hat{T}_z$ - f_{lp} curve for pitch is not smooth near the turning point. For roll motion, the $\hat{T}_z$ - f_{lp} curve shows an oscillatory behavior, with the $\hat{T}_z$ value converging around 44 s which is larger than the wave periods.

A closer look at the time series of pitch and roll motions indicates that the unstable behavior of the $\hat{T}_z$ - f_{lp} curves were due to the additional low-frequency motion caused by the lift-off and landing operations, see Fig. 18. Consequently as shown in Fig. 19, the vessel trim was also changed due to the change of vessel CoG during the operation.

Then a highpass filter with cutoff frequency of 0.04 Hz was applied to filter out the low-frequency motions before applying the adaptive lowpass filter. The updated $\hat{\sigma}_X$ - f_{lp} and $\hat{T}_z$ - f_{lp} curves of roll motion are shown in Fig. 20. Compared with Fig. 17, the $\hat{T}_z$ - f_{lp} curve in Fig. 20 becomes smoother and converges to a reasonable value.

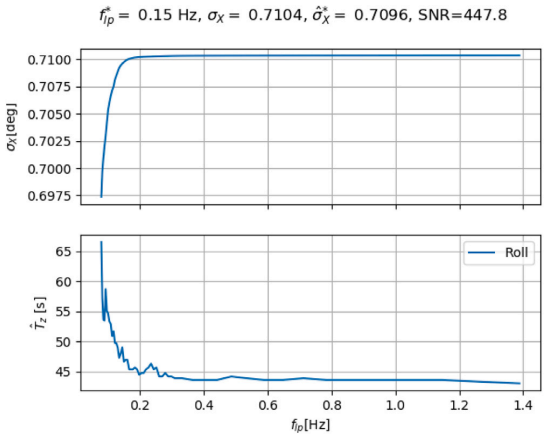

Fig. 17. $\hat{\sigma}_X$ - f_{lp} and $\hat{T}_z$ - f_{lp} curves of roll motion for CaseB1.

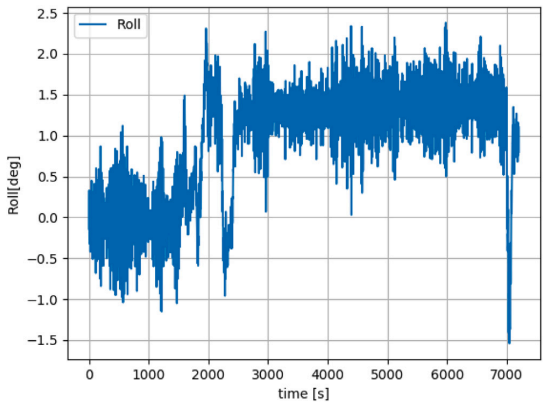

Fig. 18. Time series of roll motion for CaseB1.

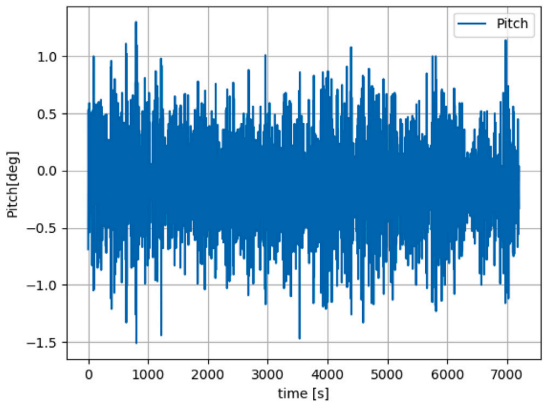

Fig. 19. Time series of pitch motion for CaseB1.

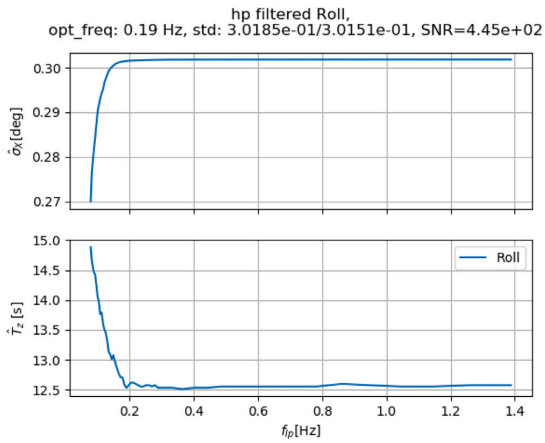

Fig. 20. $\hat{\sigma}_X$ - f_{lp} and $\hat{T}_z$ - f_{lp} curves of the highpass filtered roll motion for CaseB1.

Table 8
Applied parameters related to the model tuning process for method validation.

Parameter	Value	Unit
H_s	Uniformly distributed in [1.0, 4.0]	m
T_p	Uniformly distributed in [5.0, 20.0]	s
β_W	Randomly selected among 13 discrete directions within [0,180]	°
Seeds	Randomly generated within [1,300][a]	-
Duration	3600	s
SNR	Randomly selected among [5, 10, 20, 40, 80]	–
α	0.05	–
p	0.4	–

[a]Two seeds were generated for each sea state. One was applied for the generation of true response time series, the other was applied in order to add noise to the signal.

5.3. Influence on the model tuning results

So far, the proposed adaptive lowpass filter has been shown to be stable with respect to variation of sea states, vessel conditions and noise levels. This section focuses on investigating how much benefit the model tuning can get from the adaptive lowpass filter with the proposed procedure of finding the optimal cutoff frequency. In total, 200 model tuning cases were run with both the adaptive lowpass filter and a lowpass filter with a fixed cutoff frequency of 1.0 Hz. Each model tuning case used vessel response measurements and wave information from 6 randomly generated sea states. The main wave information, the parameters applied to generating measurements, and the parameters used for model tuning are summarized in Table 8. The true vessel condition and the initial probability distributions of the considered vessel model parameters are summarized in Table 9, which is different from the considered vessel condition for algorithm development described in Section 3.2 and Section 4. It is worth mentioning that the important uncertain vessel parameter β_{44}, representing the ratio between the additional (mainly caused by viscous effect) and critical roll damping, actually varies with sea states (Han et al., 2021b). However, a constant true value of β_{44} was considered for simplicity. The considered vessel parameters were tuned simultaneously.

Compared with the model tuning results with a fixed cutoff frequency of 1.0 Hz, the results show that the adaptive filter approach statistically improved the accuracy with respect to the expected values (see Fig. 21) and reduced the variance of the considered parameters

Table 9
Prior information and true values of the considered vessel parameters.

Parameter	Mean	σ^2	$\pm 3\sigma$	True value	Ik[a]	Im[b]
GMT [m]	0.5	0.015	[0.13, 0.87]	0.4	40	6
β_{44}	0.07	4.0E−04	[1%, 13%]	0.04	50	7
r_{55} [m]	32.5	1.0	[29.5, 35.5]	30.55	30	7
XCG [m]	59.4	1.21	[56.1, 62.7]	61.4	30	5

[a]Number of discrete variable values for the joint probability model.
[b]Number of discrete parameter values used in the RAO database.

(see Fig. 22). However, the improvements of the less sensitive parameters (GMT and r_{55}) were not very significant, particularly in terms of the tuned expected values.

6. Conclusions and future work

An algorithm to find the sea state and vessel dependent optimal cutoff frequency for a lowpass filter has been proposed, to improve extracting vessel motions in the wave frequency region from the noisy vessel motion measurement signals. It is difficult to find and express the explicit relation between the optimal cutoff frequency and the characteristics of the sea state, vessel dimensions, and vessel condition. In addition, the environmental uncertainties are difficult to measure, quantify, and control. The proposed algorithm significantly eases these challenges by introducing two parameters θ and γ, based on the statistical characteristics of the $\hat{\sigma}_X$ - f_{lp} and $\hat{T}_z$ - f_{lp} curves around the optimal cutoff frequencies, and these characteristics are not explicitly linked to any sea state or vessel property.

Applying the algorithm to the vessel model tuning process, statistically improves the tuning results, however, to a limited degree for some parameters due to (1) the numerical errors from STD calculations of vessel motions based on discrete time series and spectral densities; and (2) the fact that the considered parameters (e.g., GMT and r_{55}) may not be very sensitive to the involved sea states. The improvements in relation to tuning of β_{44} and XCG are rather significant because they are more sensitive to the considered vessel motions at the involved sea states.

It has been found important to choose a reasonable set of criteria for θ and γ. A relaxed θ criterion can lead to significant signal over-filtering, while too strict criteria may cause the signal under-filtered. Too strict criteria may also make the algorithm fail to find the optimal cutoff frequency based on the proposed normal procedure. Even though the capability of extending the algorithm and the preset θ and γ criteria for other vessel conditions and dimensions has not been fully demonstrated, all the validation tests described in Section 5 used either different vessel conditions (i.e., Sections 5.1 and 5.3) or different vessels (i.e., Section 5.2), rather than the one used for deriving the algorithm (Section 4). This tends to support the hypothesis that the proposed adaptive lowpass filter would work for different vessels and vessel conditions. Section 5 showed that the algorithm is stable and the on-site full-scale measurements also fulfill the characteristics of the $\hat{\sigma}_X$ - f_{lp} and $\hat{T}_z$ - f_{lp} curves as described in Section 4.1. The algorithm works because:

1. The vessel itself is by nature a lowpass filter of the wave energy. Therefore, the high-frequency response normally has much less energy.
2. The noise mainly carries energy in the high-frequency domain distinguishably outside of the frequency region for the main vessel response. Sensor misalignment and bias are slowly varying, i.e., with low frequencies.
3. Signal noise has considerably less energy compared with the true vessel response energy. The SNR values applied for all presented case studies were higher than 5.

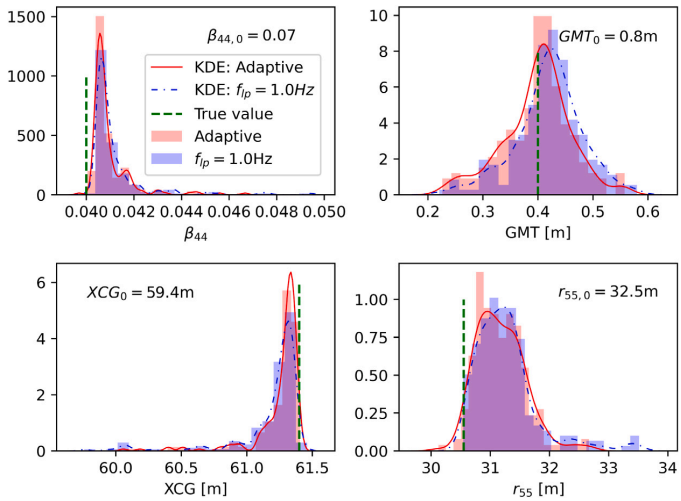

Fig. 21. Normalized histograms (vertical axes) of the expected values for the tuned vessel parameters, comparing the adaptive filter approach with use of a fixed cutoff frequency $f_{lp} = 1.0$ Hz. The red and blue lines are the corresponding estimated Gaussian kernel densities. KDE: kernel density estimation. The parameters with subscript of 0 in the legends refer to the initial values.

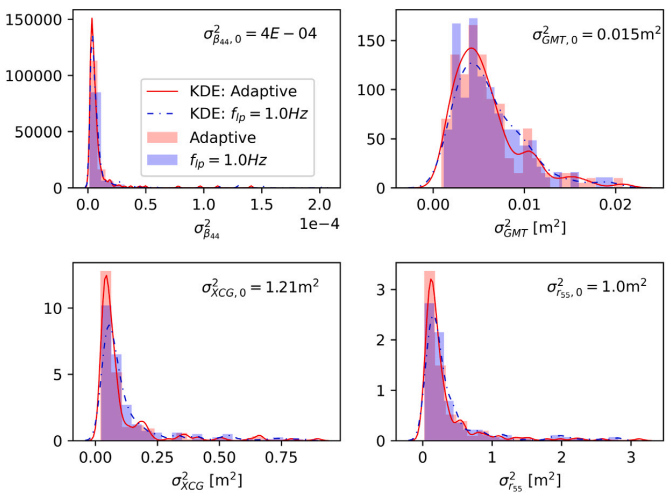

Fig. 22. Normalized histograms (vertical axes) of the variances for the tuned vessel parameters, comparing the adaptive filter approach with use of a fixed cutoff frequency $f_{lp} = 1.0$ Hz. The red and blue lines are the corresponding estimated Gaussian kernel densities. KDE: kernel density estimation. The parameters with subscript of 0 in the legends refer to the initial values.

The proposed adaptive filter algorithm is believed to be a flexible solution, because:

1. It does not require to know the weather or vessel conditions.
2. It is not directly linked to any specific filter. The algorithm uses properties of the standard deviation and zero-upcrossing period of the filtered signal which are available for most signal filters. Even though the present study made use of the FFT filter, the method can be applied based on any other normal filters of any order, as long as the cutoff frequency of that filter model can be explicitly expressed.
3. It does not strictly require a stationary condition. It has been demonstrated in Section 5.2.2 that the $\hat{\sigma}$-f_{lp} and $\hat{T}_z$-f_{lp} curves for the non-stationary signals are similar to the curves for stationary signals (e.g., as illustrated in Figs. 6 and 7) as discussed in Section 4.1. However, special attention should be paid to those non-stationary conditions which may introduce low-frequency components with high energy.
4. It is expected to be stable at least for vessels with similar dimensions and displacement.

More comprehensive analyses should be performed to verify that the proposed adaptive lowpass filter and its preset θ and γ criteria work for other and significantly different vessels and vessel conditions. The proposed adaptive lowpass filter requires that the power of the response spectrum should be sufficient in magnitude for frequencies less than the optimal cutoff frequency. For a sea state consisting of one wind sea component with a small $T_{p,w}$ and one swell component with a large $T_{p,sw}$ and with two different directions, there might be no wave energy in some periods between $T_{p,w}$ and $T_{p,sw}$. The proposed

method might fail if the search for f_{lp}^* stops immediately after fulfilling the criteria with respect to θ and λ. However, this could be solved by continuously checking the θ and γ values with increasing f_{lp}, ensuring all the considered f_{lp} values larger than f_{lp}^* meet the preset θ and γ criteria as well. Alternatively, the algorithm can be modified so that searching f_{lp}^* starts from the smaller wave spectral peak period (e.g., corresponding to f_{lp} of $1/T_{p,w}$ Hz).

The cases of model tuning considered four uncertain vessel parameters. The interpolation and multiplication operators within the 4-dimensional space requires a significant amount of computer memory. In reality, additional uncertain parameters should be included in the algorithm of model tuning, e.g., vessel heading, vessel speed and wave spectrum related parameters such as H_s, T_p, β_W, directional spreading, etc. As a consequence, the methodology could face the common challenge referred to as the curse of dimensionality in connection with discrete Bayesian inference (Gelman et al., 2013). Modification of the model tuning algorithm should be considered in the future in order to improve the computational efficiency, e.g., by only taking into account the mean vector and covariance matrix of the uncertain vessel parameters (Han et al., 2021c).

CRediT authorship contribution statement

Xu Han: Conceptualization, Methodology, Software, Formal analysis, Data curation, Writing - original draft & editing. **Zhengru Ren:** Writing - review & editing. **Bernt Johan Leira:** Writing - review & editing, Supervision, Project administration, Funding acquisition. **Svein Sævik:** Writing - review & editing, Supervision, Project administration.

Declaration of competing interest

The authors declare that they have no known competing financial interests or personal relationships that could have appeared to influence the work reported in this paper.

Acknowledgments

This work was made possible through the Centre for Research-based Innovation MOVE, financially supported by the Research Council of Norway, NFR project no. 237929 and the consortium partners, http://www.ntnu.edu/move. Thanks are given to Section of Hydrodynamics & Stability in DNV for providing hydrodynamic models.

The data presented in Section 5.2.1 was collected during sea trials in 2013 in connection with the SIM-VAL KPN project (grant number 225141/O70). The data collection was financed by Rolls-Royce Marine and the Research Council of Norway through grant number 226412/O70. Thanks to Rolls-Royce Marine for permission to publish the results. Thanks is also given to Astrid H. Brodtkorb for assistance with the datasets.

Thanks are given to Ocean Installer for providing the on-site measurement data for a lift operation in 2017 presented in Section 5.2.2 as well as giving permission to use it.

References

Butterworth, S., 1930. Experimental wireless and the wireless engineer. Wireless Eng. 7, 536.

Challa, S., Bar-Shalom, Y., 2000. Nonlinear filter design using fokker-Planck-Kolmogorov probability density evolutions. IEEE Trans. Aerosp. Electron. Syst. 36 (1), 309–315.

Cooley, J.W., Tukey, J.W., 1965. An algorithm for the machine calculation of complex fourier series. Math. Comp. 19 (90), 297–301.

DNV, 2018. Wasim User Manual. Technical Report, DNV.

DNVGL-RP-C205, 2017. Environmental conditions and environmental loads. Technical Report, DNV.

DNVGL-ST-N001, 2016. Marine operations and marine warranty. Technical Report, DNV.

Fossen, T.I., 2011. Handbook of Marine Craft Hydrodynamics and Motion Control. John Wiley & Sons.

Fossen, T.I., Strand, J.P., 1999. Passive nonlinear observer design for ships using Lyapunov methods: full-scale experiments with a supply vessel. Automatica 35 (1), 3–16.

Gelman, A., Carlin, J., Stern, H., Dunson, D., Vehtari, A., Rubin, D., 2013. Bayesian Data Analysis. CRC press.

Godhaven, J.-M., 1998. Adaptive tuning of heave filter in motion sensor. In: IEEE Oceanic Engineering Society. OCEANS'98. Conference Proceedings (Cat. No.98CH36259), Vol. 1. pp. 174–178.

Grewal, M.S., Henderson, V.D., Miyasako, R.S., 1991. Application of Kalman filtering to the calibration and alignment of inertial navigation systems. IEEE Trans. Automat. Control 36 (1), 3–13. http://dx.doi.org/10.1109/9.62283.

Grip, H.F., Fossen, T.I., Johansen, T.A., Saberi, A., 2015. Globally exponentially stable attitude and gyro bias estimation with application to GNSS/INS integration. Automatica 51, 158–166.

Han, X., Leira, B.J., Sævik, S., 2021a. Vessel hydrodynamic model tuning by discrete Bayesian updating using simulated onboard sensor data. Ocean Eng. 220, http://dx.doi.org/10.1016/j.oceaneng.2020.108407.

Han, X., Leira, B.J., Sævik, S., Ren, Z., 2021c. Onboard tuning of vessel seakeeping model parameters and sea state characteristics. Mar. Struct. 78, http://dx.doi.org/10.1016/j.marstruc.2021.102998.

Han, X., Sævik, S., Leira, B.J., 2020. A sensitivity study of vessel hydrodynamic model parameters. In: Proceedings of the ASME 2020 39th International Conference on Ocean, Offshore and Arctic Engineering, Vol. 1. Virtual, Online.

Han, X., Sævik, S., Leira, B.J., 2021b. Tuning of vessel parameters including sea state dependent roll damping. Ocean Eng. 233, http://dx.doi.org/10.1016/j.oceaneng.2021.109084.

Hubbard, D.W., 2014. How to Measure Anything. John Wiley & Sons, Ltd.

Kring, D.C., 1994. Time Domain Ship Motions by a Three-Dimensional Rankine Panel Method (Ph.D. thesis). Massachusetts Institute of Technology, Doctor of Philosophy in Hydrodynamics, May 1994, Department of Ocean Engineering.

Lewandowski, E.M., 2004. The Dynamics of Marine Craft: Maneuvering and Seakeeping, Vol. 22. World scientific.

Li, W., Wang, J., 2013. Effective adaptive Kalman filter for MEMS-IMU/magnetometers integrated attitude and heading reference systems. J. Navig. 66 (1), 99–113.

Ren, Z., Skjetne, R., Jiang, Z., Gao, Z., Verma, A.S., 2019. Integrated GNSS/IMU hub motion estimator for offshore wind turbine blade installation. Mech. Syst. Signal Process. 123, 222–243.

Scheick, J.T., 1997. Linear Algebra with Applications, Vol. 81. McGraw-Hill New York.

Simon, D., 2006. Optimal State Estimation. John Wiley & Sons, Ltd.

Steen, S., Selvik, Ø., Hassani, V., 2016. Experience with rim-driven azimuthing thrusters on the research ship Gunnerus, In: Proc. of High-Performance Marine Vessels.

Stovner, B.N., Johansen, T.A., Fossen, T.I., Schjølberg, I., 2018. Attitude estimation by multiplicative exogenous Kalman filter. Automatica 95, 347–355.

Virtanen, P., Gommers, R., Oliphant, T.E., Haberland, M., Reddy, T., Cournapeau, D., Burovski, E., Peterson, P., Weckesser, W., Bright, J., van der Walt, S.J., Brett, M., Wilson, J., Jarrod Millman, K., Mayorov, N., Nelson, A.R.J., Jones, E., Kern, R., Larson, E., Carey, C., Polat, İ., Feng, Y., Moore, E.W., Vand erPlas, J., Laxalde, D., Perktold, J., Cimrman, R., Henriksen, I., Quintero, E.A., Harris, C.R., Archibald, A.M., Ribeiro, A.H., Pedregosa, F., van Mulbregt, P., Contributors, S..., 2020. Scipy 1.0: Fundamental algorithms for scientific computing in python. Nature Methods 17, 261–272.

Waskom, M., Botvinnik, O., Ostblom, J., Gelbart, M., Lukauskas, S., Hobson, P., Gemperline, D.C., Augspurger, T., Halchenko, Y., Cole, J.B., Warmenhoven, J., de Ruiter, J., Pye, C., Hoyer, S., Vanderplas, J., Villalba, S., Kunter, G., Quintero, E., Bachant, P., Martin, M., Meyer, K., Swain, C., Miles, A., Brunner, T., O'Kane, D., Yarkoni, T., Williams, M.L., Evans, C., Fitzgerald, C., Brian, 2020. Mwaskom/seaborn: v0.10.1 (april 2020). http://dx.doi.org/10.5281/zenodo.3767070.

Wiener, N., 1964. Extrapolation, Interpolation, and Smoothing of Stationary Time Series. The MIT Press.

Zhang, P., Gu, J., Milios, E.E., Huynh, P., 2005. Navigation with IMU/GPS/digital compass with unscented Kalman filter. In: IEEE International Conference Mechatronics and Automation, 2005, Vol. 3. IEEE, pp. 1497–1502.

A.4 Paper A4

Paper A4:
X. Han, S. Sævik, and B. J. Leira, 2021. Tuning of vessel parameters including sea state dependent roll damping. *Ocean Engineering* 233.

Ocean Engineering 233 (2021) 109084

Contents lists available at ScienceDirect

Ocean Engineering

journal homepage: www.elsevier.com/locate/oceaneng

Tuning of vessel parameters including sea state dependent roll damping

Xu Han *, Svein Sævik, Bernt Johan Leira

Department of Marine Technology, Norwegian University of Science and Technology (NTNU), 7491 Trondheim, Norway
Centre for Research-based Innovation on Marine Operations (SFI MOVE), Norway

ARTICLE INFO

Keywords:
Online model tuning
Discrete Bayesian updating
Roll damping
Gaussian process regression
Stochastic Kriging
Wave-induced vessel motion

ABSTRACT

Online tuning of vessel models based on onboard measurement data can reduce the uncertainties of vessel motion prediction, and therefore potentially increase the safety and cost efficiency for marine operations. Among the uncertain vessel parameters, the roll damping coefficient is very important and highly nonlinear. In reality, roll damping depends on the sea state and vessel condition. This paper proposes two different procedures for tuning the sea state dependent roll damping coefficient together with other uncertain vessel parameters, i.e., 1-step tuning and 2-step tuning procedures. In addition, a roll damping prediction model based on Gaussian process regression is also proposed to predict the roll damping for future sea states based on historical data. The tuning procedure together with the proposed prediction model form an iterative closed loop of continuously improving the knowledge about the roll damping online, also estimating the model uncertainty based on prior knowledge, sampling uncertainties, and the applied kernel. Case studies are presented to demonstrate the procedures.

1. Introduction

Reliable vessel motion prediction plays a key role for the safety and optimization of maritime and offshore activities. Among the vessel motions induced by different environmental sources, the wave-frequent ones can be most critical to predict because they are most difficult to control. In engineering practice, it is acceptable to simplify the relation between wave elevation and the rigid body vessel motions by linearization of the transfer functions in the frequency domain, especially for typical marine operations executed at moderate seas (DNVGL-ST-N001, 2016). The vessel motion linear transfer functions for the 6 degrees of freedom (DOFs) in complex form are usually also referred to as Response Amplitude Operators (RAOs). The roll motion is widely recognized as the most critical and challenging response quantity to predict, because the critical roll motion near resonance is extremely influenced by the estimated damping which is significantly underpredicted by the linear potential theory.

Roll damping is highly nonlinear and has therefore attracted huge research interest for more than a century (Falzarano et al., 2015). System modelling usually requires simplifications which result in model uncertainties and errors. Linearization of roll damping is common practice for seakeeping analysis in order to estimate the linear transfer function between wave elevation and vessel roll motion, i.e., the roll RAO. For irregular waves, the roll damping is linearized by minimizing the error between the linearized and the real system with the assumption that both input to and output from the system are Gaussian processes (Kaplan, 1966). This is called stochastic linearization.

The Watanabe–Inoue–Takahashi formula may be applied to estimate the total roll damping for varying u (vessel forward speed), ϕ_A (roll amplitude), ω (wave frequency), and ship forms (Himeno, 1981). However, the estimation seems only acceptable for normally loaded ships near their natural frequencies (Himeno, 1981). A third-order polynomial formula may well model the nonlinearity between the non-dimensional equivalent linear roll damping ($\hat{B}_{44}$) and the non-dimensional frequency ($\hat{\omega}$) for each combination of u, ϕ_A, vessel loading, and ship form based on Tasai–Takaki's Table reported in English by Himeno (1981). However, the $\hat{B}_{44}$ as a function of e.g., ship form and speed is not clear.

About half a century ago, Ikeda, Himeno, Tanaka, and their teams from Osaka Prefecture University heavily contributed to understanding and modelling the nonlinear roll damping in a systematic manner. Their work of separating the roll damping into several components and ignoring their interactions recommended by ITTC (2011), basically forms the present engineering practice of ship roll damping estimation in the absence of experimental data. Known as Ikeda's method, the equivalent linear roll damping B_{44} can be separated as follows Himeno (1981)

$$B_{44} = B_W + B_F + B_E + B_L + B_{BK} \tag{1}$$

* Corresponding author at: Department of Marine Technology, Norwegian University of Science and Technology (NTNU), 7491 Trondheim, Norway.
E-mail address: xu.han@ntnu.no (X. Han).

https://doi.org/10.1016/j.oceaneng.2021.109084
Received 29 September 2020; Received in revised form 14 April 2021; Accepted 24 April 2021
Available online 1 June 2021

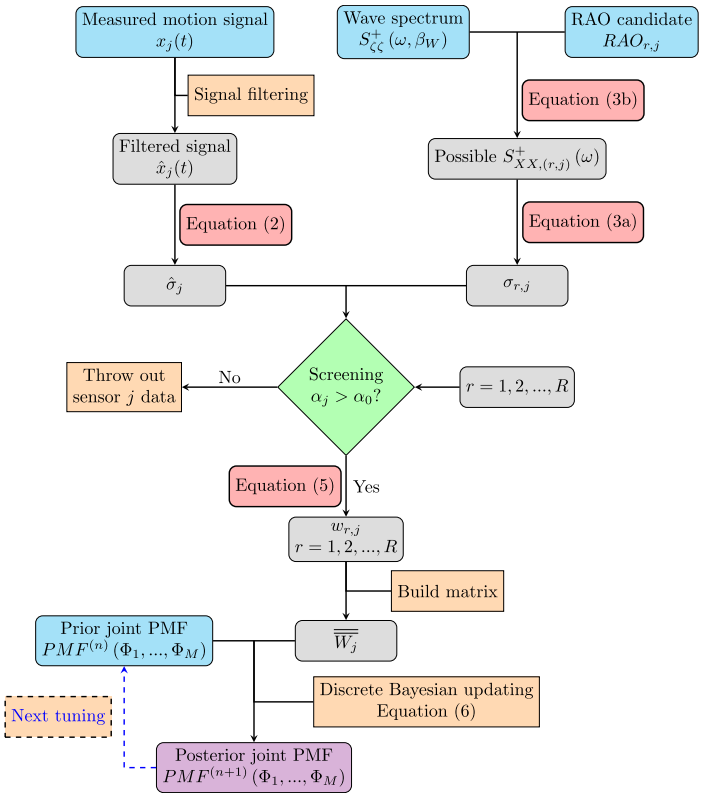

Fig. 1. Process of tuning vessel model parameters, based on the vessel motion signal $x_j(t)$ and the wave spectrum. Precise knowledge about the wave spectrum is assumed.

where B_W is the wave damping, B_F is the friction damping caused by hull skin-friction, B_E is the damping due to eddy making, B_L is the linear lift damping, B_{BK} is the damping due to the bilge keels. Among them, B_W and B_L are linearly proportional to roll angular velocity, while the other components are nonlinear. B_F is relatively less important and may be neglected for full scale ships (Himeno, 1981). Ikeda et al. (1978a,b,c, 1979) proposed formulas for estimating most of the important roll damping components by a semi-empirical approach. Even though Ikeda's formulas are recommended by ITTC (2011), cautions should be taken, because (1) Ikeda's formulas are limited to certain ship forms; and (2) Ikeda's formulas were derived for pure roll motion based on still water condition (Larsen et al., 2019). For example, the use of panel methods to predict the wave damping (B_W) with forward speed is theoretically accurate and recommended (Falzarano et al., 2015) over the semi-empirical Ikeda's formulas (Ikeda et al., 1978b). Söder et al. (2017) found that the Ikeda's formulas significantly overestimated the hull lift damping component while underestimating the bilge keel damping by benchmarking with model test data.

Consequently, model tests or empirical data are always preferred for new vessel design in order to model the roll damping with sufficient accuracy. Free decay model tests are normally performed to obtain the roll damping, however, only at the important damped roll resonance frequency. Forced rolling model tests can be performed to obtain the roll damping at other frequencies. However, this is frequently not performed. In addition, much more model tests are required if the roll amplitude dependent damping coefficients are wanted. By fitting to the empirical data, the total roll damping can be modelled as functions of vessel speed u, vessel draught D, roll amplitude ϕ_A (or wave amplitude A), wave frequency ω, etc.

However, the scale effects of model tests may significantly affect the accuracy of the roll damping estimation (Söder and Rosén, 2015). At present, prediction of roll damping based on numerical simulation by computational fluid dynamics (CFD) codes has also received considerable attention, e.g., Irkal et al. (2016). However, a reliable CFD analysis requires high competence in modelling and understanding the limitations of the codes and the applied algorithms. Usually, results from CFD analyses require validation from model tests. Both model tests and high-fidelity analyses are expensive and time-consuming. Therefore, it is of great interest to improve the knowledge of the roll damping for the specific vessel throughout its whole life cycle by using the weather information and the vessel motion measurements onboard. In practice, the additional damping can be considered as a function of parameters related to the sea state and vessel condition, i.e., $B_{44} = f(\boldsymbol{x})$ where $\boldsymbol{x} = [u, D, H_s, T_p, \beta_W, \dots]$, H_s is the significant wave height, T_p is the spectral wave peak period, β_W is the wave direction. With such a roll damping function, the RAO and roll motions can be estimated at a specific wave and vessel condition by assuming stationarity. Consequently the improved roll damping model built upon on-site measurements can potentially increase the cost efficiency and safety for marine operations.

It is very challenging to update the roll damping by on-site measurements and weather information, because (1) measurements and weather information are subject to significant uncertainties (Bitner-Gregersen and Hagen, 1990; Qiu et al., 2014); and (2) there are also many other vessel parameters subject to uncertainties, e.g., inertia items (Han et al., 2020). Therefore, all the uncertain parameters should

be identified first and tuned simultaneously in a probabilistic way. An earlier case study by Han et al. (2020) indicates that multiple sensors at different locations providing signals of displacements, velocities, and accelerations can help identifying the uncertain vessel parameters. Han et al. (2021a) proposed an algorithm for tuning of vessel model parameters by Bayesian inference. Tuning of the uncertain vessel parameters in a probabilistic approach can improve the knowledge about the real-time vessel condition and reduce the model uncertainties quantitatively, based on onboard vessel motion measurements and wave information such as H_s, T_p, β_W, directional spreading, and spectral shape.

Vessel parameters can be sea state dependent, vessel condition dependent, or permanent (Han et al., 2020). The sea state dependent parameters (e.g., roll damping) usually also depend on vessel conditions (e.g., loading conditions and vessel forward speed). Han et al. (2021a) considered a constant roll damping coefficient through different sea states for tuning, and pointed out that the algorithm should be further developed to tune vessel roll damping as being sea state dependent. The present paper describes the algorithm for tuning of sea state dependent roll damping coefficient together with other vessel parameters. In addition, it is even more important for this paper to establish an algorithm which prescribes how to model the roll damping as sea state dependent and predict it for the unobserved future sea states. This is considered particularly challenging because:

1. The tuned roll damping value is only valid for the current sea state, which does not directly help predicting the vessel roll damping for other sea states. Therefore, the algorithm should be able to predict the roll damping for the unobserved sea states with improved accuracy based on prior knowledge and historical tuning results for different sea states and vessel conditions.
2. As discussed previously, it is difficult to define a function in advance that is sufficiently accurate for modelling of roll damping.
3. The number of available full-scale measurements can be very limited and insufficient. Under-fitting or over-fitting can be expected.
4. The available measurements may also be concentrated around certain sea states. It is questionable to predict roll damping for other sea states by extrapolation based on any fitted curve.

The paper is organized as follows. The basic vessel model tuning algorithm is described in Section 2 (Han et al., 2021a). For flexible modelling of roll damping, Gaussian process regression is introduced in Section 3. In Section 4, two procedures are proposed to modify the basic model tuning algorithm in order to tune and represent roll damping as being sea state dependent. Numerical case studies are carried out to demonstrate the performance of the proposed tuning procedures and the corresponding roll damping prediction model. The basis of the case studies are described in Section 5, and the results are shown in Section 6. Finally, Section 7 concludes and discusses the findings, limitations, and future work related to the present research.

2. Basic vessel model tuning procedure

The applied algorithm for tuning of vessel seakeeping parameters based on wave information and vessel motion measurements proposed by Han et al. (2021a) is briefly repeated here for completeness purposes. The algorithm is also illustrated in Fig. 1.

Firstly, the uncertain vessel parameters (i.e., $\boldsymbol{\Phi}_1, \boldsymbol{\Phi}_2, \ldots, \boldsymbol{\Phi}_m, \ldots, \boldsymbol{\Phi}_M$, $m \in \{1, 2, \ldots, M\}$) are identified based on their sensitivities with respect to the measured vessel motions of primary interest. This can be achieved by performing uncertainty and sensitivity analyses, e.g., Han et al. (2020). The uncertainty ranges of those parameters can be determined based on the relevant prior information such as available design and analysis documentation, accuracy of onboard monitoring data, and engineering judgement. Each uncertain parameter $\boldsymbol{\Phi}_m$ is then discretized evenly into Im values within its uncertainty range. For a successful tuning, it is important to have a sufficiently large uncertainty range for each $\boldsymbol{\Phi}_m$ while the spacing between the discretized values should be sufficiently small to capture any critical nonlinear behaviour. Considering reasonable uncertainty ranges based on practical prior information, 5 to 8 discrete values for each vessel parameter can be sufficient for the tuning. Combining the uncertain parameters at their discrete values, a total number of $R = I1 \times I2 \times \cdots \times IM$ discrete assessment points are defined, for calculating the possible RAOs. In addition, multiple quantities of vessel motions (e.g., displacement, velocity, and acceleration for different DOFs at different locations) are normally required for the tuning process. Each of the considered measured vessel motion quantities is indexed by $j \in \{1, 2, \ldots, J\}$. Consequently, a RAO database containing $R \times J$ RAOs can be established by performing seakeeping analysis for those measured quantities at those discrete combinations of the uncertain parameters.

The joint probability distribution of the identified uncertain vessel parameters is denoted as $P^{(n)}\left(\boldsymbol{\Phi}_1, \boldsymbol{\Phi}_2, \ldots, \boldsymbol{\Phi}_M\right)$. The superscript n stands for the number of completed iterative updates based on the proposed tuning procedure. The joint probability distribution is tuned for each stationary wave and vessel condition. Typically, for a vessel in steady condition with respect to heading, advancing speed, and inertia distribution, the stationarity is determined by the duration of a stationary sea state which could vary from 20 min to 3 hr, depending on geometrical location. With the information on waves (e.g., a wave spectrum), vessel motion measurements (e.g., signal $x_j(t)$ for the measured quantity j), and a RAO database covering the uncertainty ranges of the uncertain vessel parameters, the tuning can be performed as follows:

1. Filter the vessel motion measurements $x_j(t)$ to obtain the vessel motion time series in the wave frequency domain. The high-frequency components (e.g., signal noise) and the low-frequency components (e.g., signal bias, second-order motions) are important to be filtered out. The filtered signal is denoted as $\hat{x}_j(t)$
2. Calculate the standard deviation of the filtered signal, $\hat{\sigma}_j$, by

$$\hat{\sigma}_j = \sqrt{\frac{\sum_{t=1}^{N_t}\left(\hat{x}_j(t) - \bar{x}_j\right)^2}{\left(N_t - 1\right)}} \tag{2a}$$

$$\bar{x}_j = \frac{\sum_{t=1}^{N_t}\hat{x}_j(t)}{N_t} \tag{2b}$$

where N_t is the total number of time steps of the signal, and $\bar{x}_j$ is the mean value of the filtered signal. The duration of the signal $x_j(t)$, $T = N_t \Delta t$ (where Δt is the time interval), should be selected such that the sea state and vessel condition remains stationary within the duration of T, while the sampling variability should be sufficiently small. A typical value of T can be 20 min to 1 hr.
3. Calculate the standard deviations of the possible vessel response $\sigma_{r,j}$, based on the wave spectrum and the candidate RAO from the RAO database for the measured quantity j (i.e., $RAO_{r,j}$)

$$\sigma_{r,j} = \sqrt{\sum_{n=1}^{N_\omega} S^+_{XX,(r,j)}\left(\omega_n\right) \cdot \Delta\omega} \tag{3a}$$

$$S^+_{XX,(r,j)}(\omega) = \left|H_{r,j}\left(\omega, \beta_W\right)\right|^2 \cdot S^+_{\zeta\zeta}\left(\omega, \beta_W\right) \tag{3b}$$

where N_ω is the total number of the discretized frequencies for the response spectrum, $S^+_{\zeta\zeta}\left(\omega, \beta_W\right)$ is the long-crested wave spectrum, and S^+ stands for a single-sided power spectrum. $S^+_{XX,(r,j)}(\omega)$ is the possible response spectrum for the response X corresponding to the measured quantity j based on the vessel parameter combination r, $H_{r,j}\left(\omega, \beta_W\right)$ is the corresponding linear transfer function (i.e., $RAO_{r,j}$) between wave elevation and vessel response. Each possible combination of the considered vessel parameters, i.e., $\left(\phi_{i1}, \phi_{i2}, \ldots, \phi_{iM}\right)$, is subscripted with

number $r \in \{1, 2, \ldots, R\}$, where ϕ_{im} for $m \in \{1, 2, \ldots, M\}$ is the imth discrete value of the considered uncertain vessel parameter $\boldsymbol{\Phi}_m$ in the RAO database. $R = \prod_{m=1}^{M}(Im)$, is the total number of vessel parameter combinations and Im is the number of the discretized values of $\boldsymbol{\Phi}_m$ in the RAO database. For all possible vessel parameter combinations, $\sigma_{r,j}$ should be calculated.

4. Less sensitive measured quantities for the considered uncertain vessel parameters at the current sea state $S^{+}_{\zeta\zeta}(\omega, \beta_W)$ should be screened out. The sensor screening ratio (SSR) α_j is introduced to quantify the importance of the measured quantity j

$$\alpha_j = \frac{\sigma_{\sigma_{r,j}}}{\hat{\sigma}_j} \tag{4a}$$

$$\sigma_{\sigma_{r,j}} = \sqrt{\frac{\sum_{r=1}^{R}\left(\sigma_{r,j} - \bar{\sigma}_{R,j}\right)^2}{R-1}} \tag{4b}$$

$$\bar{\sigma}_{R,j} = \frac{\sum_{r=1}^{R}\sigma_{r,j}}{R} \tag{4c}$$

where $\sigma_{\sigma_{r,j}}$ is the standard deviation of $\sigma_{r,j}$ over $r = 1, 2, \ldots, R$. The case study uses a screening criterion of $\alpha_0 = 0.05$. If $\alpha_j < \alpha_0$, the signal of the quantity j will be excluded during the process of tuning the parameters. SSR basically represents the importance of the obtained measurements for tuning of the considered vessel parameters for the present sea state. The selection of the criterion value α_0 depends on the uncertainties of the measurements and the system errors introduced by application of linear potential theory to represent the true vessel dynamics within the wave frequency band. The influence of the introduced screening criterion on the final tuning results is discussed by detailed sensitivity studies in Han et al. (2021a).

5. Calculate the weight factor for each parameter combination r by inverse distance weighting (Shepard, 1968)

$$w_{r,j} = \frac{1}{\left|\sigma_{r,j} - \hat{\sigma}_j\right|^p} \tag{5}$$

where $p \in \mathbb{R}^+$ is called the power parameter. The choice of the p value depends on the number of considered uncertain parameters, their sensitivity and uncertainty ranges, and engineering judgements. The influence of the p value on the tuning results was studied by Han et al. (2021a).

6. Build the likelihood function for updating the joint probability distribution of the considered uncertain parameters $(\boldsymbol{\Phi}_1, \boldsymbol{\Phi}_2, \ldots, \boldsymbol{\Phi}_M)$. First, establish the weight matrix $\overline{\overline{W_j}}$ for all $r \in \{1, 2, \ldots, R\}$ in the RAO database. The weight matrix would have M dimensions with the size of $I1 \times I2 \times \cdots \times IM$. Then linearly interpolate the weight matrix $\overline{\overline{W_j}}$ from the size of $I1 \times I2 \times \cdots \times IM$ (variable resolution in the RAO database) to the size of $K1 \times K2 \times \cdots \times KM$ (variable resolution in the discrete joint probability distribution).

7. Update the joint probability distribution $P^{(n+1)}(\boldsymbol{\Phi}_1, \boldsymbol{\Phi}_2, \ldots, \boldsymbol{\Phi}_M)$. Since the likelihood function (i.e., weight matrix $\overline{\overline{W_j}}$) is presented at limited number of parameter combinations, $r \in \{1, 2, \ldots, N_{Prob}\}$, where $N_{Prob} = \prod_{m=1}^{M}(Km)$ and Km is the number of the discretized values of $\boldsymbol{\Phi}_m$ in the discrete joint probability distribution, updating the joint probability distribution based on discrete Bayesian inference (Labbe, 2018) must therefore be calculated at those discretized points, i.e.,

$$PMF^{(n+1)}(\boldsymbol{\Phi}_1, \ldots, \boldsymbol{\Phi}_M) = \mathcal{NO}\left(PMF^{(n)}(\boldsymbol{\Phi}_1, \ldots, \boldsymbol{\Phi}_M) \odot \overline{\overline{W_j}}\right) \tag{6}$$

where PMF means the joint probability mass function, $\odot$ operator means the element-wise multiplication of the two matrices of the same dimension, i.e., a Hadamard product (Scheick, 1997).

To ensure that the sum of the joint probability mass function remains 1.0, normalization $\mathcal{NO}(\cdot)$ is required. Physically, the uncertain vessel parameters are continuous variables. Therefore, the joint probability density function (PDF) is more appropriate to represent their uncertainties. Numerically, the relation between joint PMF and joint PDF can be approximated by:

$$PMF(\phi_{k1}, \phi_{k2}, \ldots, \phi_{kM}) = PDF(\phi_{k1}, \phi_{k2}, \ldots, \phi_{kM}) \prod_{m=1}^{M} \Delta\boldsymbol{\Phi}_m \tag{7}$$

where ϕ_{km} for $m \in \{1, 2, \ldots, M\}$ is the kmth discrete value for the variable $\boldsymbol{\Phi}_m$, $\Delta\boldsymbol{\Phi}_m$ is the interval between the discrete values of variable $\boldsymbol{\Phi}_m$.

The algorithm applies statistical inference of the direction-independent vessel parameters based on onboard measurements and wave information. Consequently, the tuned vessel model can be applied to predict the vessel motion for other sea states and wave directions, with quantified parameter uncertainties.

3. GaussIan process regression

Gaussian process regression (GPR) is found to be a very promising solution for roll damping modelling and prediction, because (1) it does not require to decide the format of the roll damping function; (2) the tuned values of roll damping for the previous sea states and vessel conditions can reasonably influence the prediction of roll damping for future sea states and vessel conditions, through the covariance function; (3) it also indicates the estimation uncertainty based on the prior knowledge, the available samples, and the selected kernel function.

GPR is fundamentally based on the conditional distribution of multivariate Gaussian vectors (Rasmussen and Williams, 2006). For a $N+M$ dimensional multivariate Gaussian vector $\boldsymbol{y}$

$$\boldsymbol{y} = \begin{bmatrix}\boldsymbol{y}_1 \\ \boldsymbol{y}_2\end{bmatrix} \text{ (with sizes } \begin{bmatrix}N \times 1 \\ M \times 1\end{bmatrix}) \tag{8}$$

where $\mathbf{y}_1$ and $\mathbf{y}_2$ are also multivariate Gaussian vectors and the mean vector $\boldsymbol{\mu}$ and the covariance matrix $\boldsymbol{\Sigma}$ can be written as

$$\boldsymbol{\mu} = \begin{bmatrix}\boldsymbol{\mu}_1 \\ \boldsymbol{\mu}_2\end{bmatrix} \text{ (with sizes } \begin{bmatrix}N \times 1 \\ M \times 1\end{bmatrix}) \tag{9a}$$

$$\boldsymbol{\Sigma} = \begin{bmatrix}\boldsymbol{\Sigma}_{11} & \boldsymbol{\Sigma}_{12} \\ \boldsymbol{\Sigma}_{21} & \boldsymbol{\Sigma}_{22}\end{bmatrix} \text{ (with sizes } \begin{bmatrix}N \times N & N \times M \\ M \times N & M \times M\end{bmatrix}) \tag{9b}$$

then the conditional distribution of $\boldsymbol{y}_2$ on $\boldsymbol{y}_1 = \tilde{\boldsymbol{y}}_1$ is also a multivariate Gaussian distribution, i.e.,

$$(\boldsymbol{y}_2 | \boldsymbol{y}_1 = \tilde{\boldsymbol{y}}_1) \sim \mathcal{N}(\bar{\boldsymbol{\mu}}_2, \bar{\boldsymbol{\Sigma}}_{22}) \tag{10a}$$

$$\bar{\boldsymbol{\mu}}_2 = \boldsymbol{\mu}_2 + \boldsymbol{\Sigma}_{21}\boldsymbol{\Sigma}_{11}^{-1}(\tilde{\boldsymbol{y}}_1 - \boldsymbol{\mu}_1) \tag{10b}$$

$$\bar{\boldsymbol{\Sigma}}_{22} = \boldsymbol{\Sigma}_{22} - \boldsymbol{\Sigma}_{21}\boldsymbol{\Sigma}_{11}^{-1}\boldsymbol{\Sigma}_{12} \tag{10c}$$

This means that the distribution of $\boldsymbol{y}_2$ can be updated based on the known samples $\boldsymbol{y}_1 = \tilde{\boldsymbol{y}}_1$ and the covariance matrix for $\boldsymbol{y}_2$ and $\boldsymbol{y}_1$. It is worth noting that updating of the variance matrix $\boldsymbol{\Sigma}_{22}$, i.e., Eq. (10c), does not rely on the observed values of $\boldsymbol{y}_1$, i.e., $\tilde{\boldsymbol{y}}_1$.

For a continuous function $y = f(x)$, each y value (i.e. $y_i = f(x_i)$, $i \in \mathbb{Z}^+$) can be considered as a Gaussian distributed random variable, i.e., $y_i \sim \mathcal{N}(\mu_i, \sigma_i)$, and all variables are correlated. By having samples at some known points $\boldsymbol{x}_1$ (i.e., $\boldsymbol{y}_1 = f(\boldsymbol{x}_1) = \tilde{\boldsymbol{y}}_1$), the corresponding predictions at other points (e.g., $\boldsymbol{y}_2 = f(\boldsymbol{x}_2)$) can be estimated based on Eqs. (9) and (10) if the covariance matrix of the variables for $\boldsymbol{y}_1$ and $\boldsymbol{y}_2$ (i.e., $\boldsymbol{\Sigma}$) can be established.

The covariance matrix is called the kernel or the similarity function, which establishes the correlation among data points. It is physically reasonable to consider the kernel (covariance coefficient) $K(x_i, x_j) = cov(i, j)$ between $y_i = f(x_i)$ and $y_j = f(x_j)$ to be a function of the distance along the input axis (i.e. $K(x_i, x_j) = g(|x_i - x_j|)$). Among

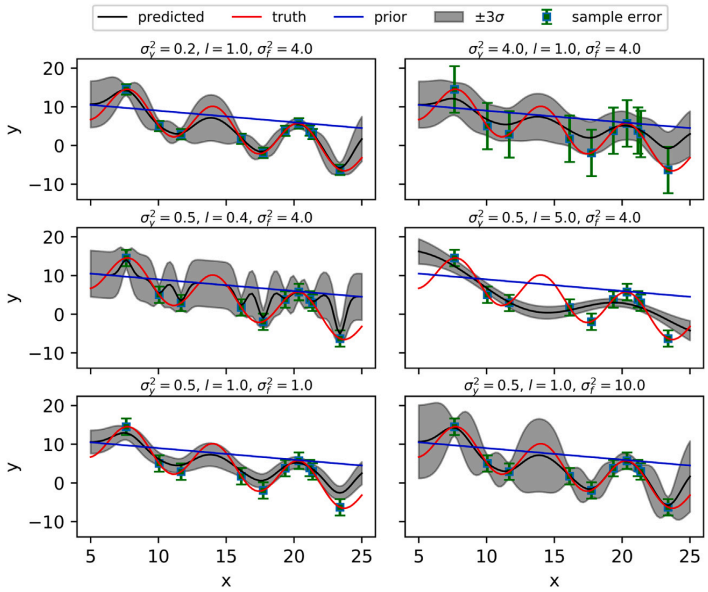

Fig. 2. The influence of GPR hyperparameters on the prediction curve.

many kernel designs, the radial-basis function (RBF) is the most popular kernel, i.e.,

$$K(x_i, x_j) = \sigma_f^2 \exp(-\frac{1}{2l^2}(x_i - x_j)^2) \tag{11}$$

where two hyperparameters are introduced. σ_f^2 is called signal variance which represents the prior knowledge about the variance of the random process. l is called length-scale.

In reality, samples are also subject to uncertainties. In the input space $\boldsymbol{Y}$, the observed samples $\tilde{\boldsymbol{Y}}$ can be written as

$$\tilde{\boldsymbol{Y}} = f(\boldsymbol{X}) + \boldsymbol{\epsilon} \tag{12}$$

where the $\boldsymbol{\epsilon}$ vector represents the uncertainties for the samples. For each sample $\tilde{y}_i$, the uncertainty ϵ_i is also considered to be a Gaussian variable:

$$\epsilon_i \sim \mathcal{N}(0, \sigma_{y_i}^2) \tag{13}$$

where $\sigma_{y_i}^2$ represents the uncertainty level for the observed sample y_i. Consequently, for predicting $\boldsymbol{y}_* = f(\boldsymbol{x}_*)$, Eq. (10) can be modified to account for sampling noise:

$$(\boldsymbol{y}_* | \boldsymbol{Y} = \tilde{\boldsymbol{Y}}) \sim \mathcal{N}(\bar{\boldsymbol{\mu}}_*, \bar{\boldsymbol{K}}_{**}) \tag{14a}$$

$$\bar{\boldsymbol{\mu}}_* = \boldsymbol{\mu}_* + \boldsymbol{K}_{*Y} \boldsymbol{K}_{\tilde{Y}}^{-1} (\tilde{\boldsymbol{Y}} - \boldsymbol{\mu}_Y) \tag{14b}$$

$$\bar{\boldsymbol{K}}_{**} = \boldsymbol{K}_{**} - \boldsymbol{K}_{*Y} \boldsymbol{K}_{\tilde{Y}}^{-1} \boldsymbol{K}_{Y*} \tag{14c}$$

where $\boldsymbol{Y}$ is the input space, $\tilde{\boldsymbol{Y}}$ is the observed samples for the input space, $\boldsymbol{y}_*$ is the space to be predicted (prediction space). $\bar{\boldsymbol{\mu}}_*$ and $\bar{\boldsymbol{K}}_{**}$ are the conditional mean and the updated kernel (i.e., the similarity function) for the prediction space. $\boldsymbol{\mu}_*$ and $\boldsymbol{\mu}_Y$ represent the prior means. $\boldsymbol{K}_{*Y}$ and $\boldsymbol{K}_{Y*}$ are the kernels representing the correlations between the input space and the prediction space, calculated based on Eq. (11). $\boldsymbol{K}_{\tilde{Y}}$ can be calculated by

$$\boldsymbol{K}_{\tilde{Y}} = \boldsymbol{K}_Y + \boldsymbol{\Sigma}_Y \tag{15a}$$

$$\boldsymbol{K}_Y = \begin{bmatrix} K(x_1,x_1) & \dots & K(x_1,x_j) & \dots & K(x_1,x_N) \\ & \ddots & & & \vdots \\ & & K(x_i,x_j) & \dots & K(x_i,x_N) \\ & & & \ddots & \vdots \\ & & & & K(x_N,x_N) \end{bmatrix} \tag{15b}$$

$$\boldsymbol{\Sigma}_Y = \begin{bmatrix} \sigma_{y1}^2 & & & & \\ & \ddots & & & \\ & & \sigma_{yi}^2 & & \\ & & & \ddots & \\ & & & & \sigma_{yN}^2 \end{bmatrix} \tag{15c}$$

where $\boldsymbol{K}_Y$ is the kernel for the input space with each element calculated based on Eq. (11). $\boldsymbol{\Sigma}_Y$ is a $N \times N$ diagonal matrix. Note that $\boldsymbol{K}_{\tilde{Y}}$ is no longer the covariance matrix for the input space, because it includes the uncertainties of the observations. Eqs. (14) and (15) including the sampling uncertainties is called stochastic Kriging.

GPR is a "non-parametric" method, meaning that the regression does not require knowing the form or the order of the function. GPR is sometimes also considered as an "infinite-parametric" method, because it ideally requires infinite samples in order to perfectly model the function.

Fig. 2, as an example, illustrates how the GPR hyperparameters influence the prediction. Larger σ_y^2 helps to smoothen the fitted curve/surface. For the sample with uncertainties, σ_y^2 represents its sample uncertainty/error. The length-scale l indicates how strong the correlation is between the points in that dimension. In addition to σ_y^2, the length-scale may also help the regression avoiding over-fitting and under-fitting. σ_f^2 represents the variance of the prior knowledge about the model. It can be interpreted as the variance of a point that is far away from all the available sample points (i.e., negligible correlation).

The stochastic Kriging algorithm (Rasmussen and Williams, 2006) as implemented in the Python package scikit-learn (sklearn hereafter) (Pedregosa et al., 2011) has been used. The GPR in sklearn has been demonstrated as "near the best" GPR programme with respect to its analysis performance and computational speed (Erickson et al., 2018). The GPR model in sklearn assumes zero prior mean. It is practically acceptable since the GPR model converges according to the available samples and independent of the provided prior mean if the amount of training data is sufficiently large. However, to ensure accuracy for research purpose, non-zero prior mean is considered in the study. Based on the fact that the prior mean vector does not influence the covariance matrix for the multivariate Gaussian distribution, i.e.,

$$\begin{bmatrix} \boldsymbol{Y} \\ \boldsymbol{y}_* \end{bmatrix} \sim \mathcal{N}\left(\begin{bmatrix} \boldsymbol{\mu}_Y \\ \boldsymbol{\mu}_* \end{bmatrix}, \begin{bmatrix} \boldsymbol{K}_{\tilde{Y}} & \boldsymbol{K}_{Y*} \\ \boldsymbol{K}_{*Y} & \boldsymbol{K}_{**} \end{bmatrix} \right) \text{ is equivalent to,}$$

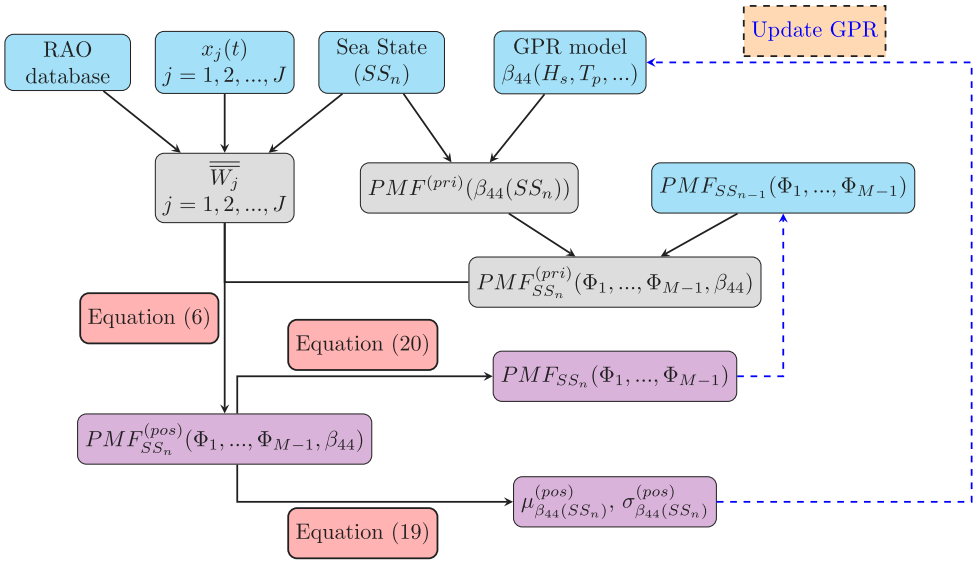

Fig. 3. Process of the 1-step tuning of vessel parameters including sea state dependent β_{44} and updating the β_{44} GPR model, assuming $\Phi_M = \beta_{44}$.

$$\begin{bmatrix} \boldsymbol{Y} - \boldsymbol{\mu_Y} \\ \boldsymbol{y}_* - \boldsymbol{\mu}_* \end{bmatrix} \sim \mathcal{N}\left(\begin{bmatrix} \boldsymbol{0} \\ \boldsymbol{0} \end{bmatrix}, \begin{bmatrix} \boldsymbol{K}_{\tilde{Y}} & \boldsymbol{K}_{Y*} \\ \boldsymbol{K}_{*Y} & \boldsymbol{K}_{**} \end{bmatrix} \right) \tag{16}$$

The prior mean will accordingly be subtracted from the values at the data points before the GPR model fitting, whereas it will be added to the predicted value for the prediction based on the fitted GPR model.

Tuning the hyperparameters may be based on personal experience and engineering judgement. However, these hyperparameters can also be automatically optimized, by assuming that the input data points ($\tilde{\boldsymbol{Y}}$) are given at their maximum likelihood. The log marginal likelihood for a zero mean prior can be written as (Rasmussen and Williams, 2006)

$$\log p(\tilde{\boldsymbol{Y}}|\boldsymbol{X}) = \log \mathcal{N}(\tilde{\boldsymbol{Y}}|\boldsymbol{0}, \boldsymbol{K}_{\tilde{Y}}) = -\frac{1}{2}\tilde{\boldsymbol{Y}}^T \boldsymbol{K}_{\tilde{Y}}^{-1}\tilde{\boldsymbol{Y}} - -\frac{1}{2}\log|\boldsymbol{K}_{\tilde{Y}}| - \frac{N}{2}\log(2\pi) \tag{17}$$

where N is the number of samples. In order to better control the GPR model for the present research, the hyperparameters of the kernel are manually determined without applying the sampling dependent optimization in Eq. (17).

4. Proposed procedure for tuning of vessel parameters including sea state dependent roll damping

4.1. One-step tuning procedure

In order to interactively tune sea state dependent roll damping and improve the roll damping prediction model (i.e., the GPR model), the model tuning algorithm described in Section 2 is modified, as illustrated in Fig. 3. Assume that the joint probability distribution of the uncertain vessel parameters have been tuned for $n-1$ sea states (and so as to the GPR model of β_{44}). The procedure of tuning vessel parameters and updating the GPR model based on the measurements (i.e., $x_j(t)$, $j = 1, 2, \ldots, J$) and the corresponding wave information for the next sea state SS_n is described below. $SS_n \in \mathbb{Z}^+$, is the index of the sea state (i.e., sea state number).

1. Given the wave information for the sea state SS_n and the updated GPR model from previous sea states, the additional roll damping coefficient β_{44} can be predicted, in terms of its mean and variance values. Then the probability mass function of $\beta_{44}(SS_n)$ can be established at the discrete values, assuming it is Gaussian distributed.
2. Together with the available knowledge about other uncertain vessel parameters after the previous sea state SS_{n-1}, i.e., $PMF_{SS_{n-1}}(\boldsymbol{\Phi}_1, \ldots, \boldsymbol{\Phi}_{M-1})$, the joint probability distribution including β_{44} can be calculated by multiplying the probability mass functions of $\beta_{44}(SS_n)$ and the other parameters at their discrete values, i.e.,

$$PMF^{(pri)}_{SS_n}(\phi_{k1}, \ldots, \phi_{k(M-1)}, \phi_{kM}) = PMF_{SS_{n-1}}(\phi_{k1}, \phi_{k2}, \ldots, \phi_{k(M-1)}) \cdot PMF(\phi_{kM}(SS_n)) \tag{18}$$

where ϕ_{km} for $m \in \{1, 2, \ldots, M-1\}$ is the $k$$m$th discrete value of the parameter $\boldsymbol{\Phi}_m$. $\phi_{kM}(SS_n)$ is the $k$$M$th discrete value of β_{44} predicted by the GPR model for the sea state SS_n, $\boldsymbol{\Phi}_M = \beta_{44}(SS_n)$.
3. With the pre-established RAO database and the received vessel motion measurements for all the J quantities for the sea state SS_n, the weight matrices can be calculated for each sensor measurement based on the previously described tuning procedure in Section 2.
4. Then the joint probability mass function of vessel parameters can be updated based on Eq. (6), as the posterior of the vessel parameters for the wave information SS_n.
5. The posterior mean $\mu_{\beta_{44}(SS_n)}$ and standard deviation $\sigma_{\beta_{44}(SS_n)}$ can be calculated by

$$PMF^{(pos)}_{SS_n}(\phi_{kM}) = \sum_{k1=1}^{K1} \cdots \sum_{k(M-1)=1}^{K(M-1)} PMF^{(pos)}_{SS_n}(\phi_{k1}, \ldots, \phi_{kM}) \tag{19a}$$

$$\mu^{(pos)}_{\beta_{44}(SS_n)} = \sum_{kM=1}^{KM} \phi_{kM} PMF^{(pos)}_{SS_n}(\phi_{kM}) \tag{19b}$$

$$\sigma^{(pos)}_{\beta_{44}(SS_n)} = \sqrt{\sum_{kM=1}^{KM} (\phi_{kM} - \mu^{(pos)}_{\beta_{44}(SS_n)})^2 PMF(\phi_{kM})} \tag{19c}$$

and the posterior of the other parameters can be calculated for each combination by

$$PMF^{(pos)}_{SS_n}(\phi_{k1}, \ldots, \phi_{k(M-1)}) = \sum_{kM=1}^{KM} PMF^{(pos)}_{SS_n}(\phi_{k1}, \ldots, \phi_{kM}) \tag{20}$$

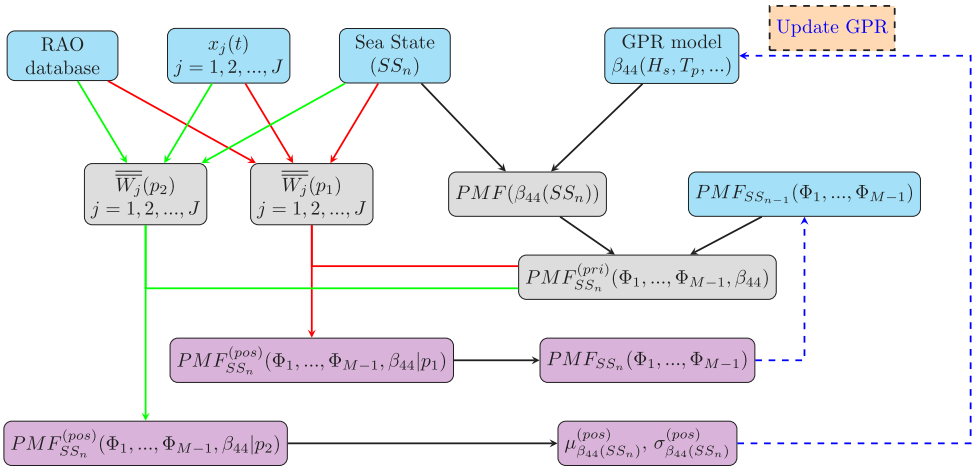

Fig. 4. Process of the 2-step tuning of vessel parameters including sea state dependent β_{44} and updating the β_{44} GPR model, assuming $\Phi_M = \beta_{44}$. Normally $p_1 < p_2$.

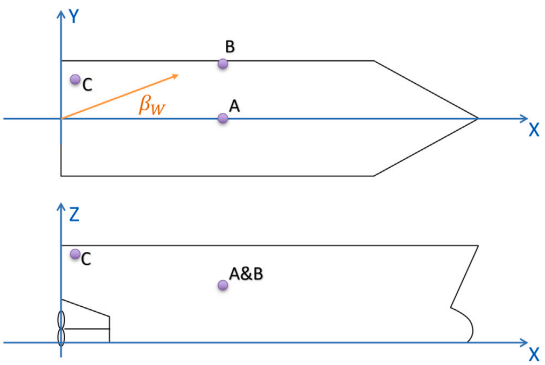

Fig. 5. The reference coordinate system and the locations of the sensors measuring vessel motions such as displacements, velocities, and accelerations.

The GPR model of β_{44} can be updated with the new available information $\mu^{(pos)}_{\beta_{44}(SS_n)}$ and $\sigma^{(pos)}_{\beta_{44}(SS_n)}$.

6. Then for the next sea state, the joint $PMF^{(pos)}_{SS_n}(\Phi_1, \ldots, \Phi_{M-1})$ will become the prior information.

4.2. Two-step tuning procedure

For tuning of sea state dependent parameters, a larger power parameter p is usually desired, due to the very limited number of available measurements for that particular sea state. However, tuning of other parameters may not require (and may not benefit from) application of such a large p value. The larger the p value is, the faster the variance of the parameters can be reduced, potentially leading to an overconfidence issue. The tuning results could be biased (Han et al., 2021a). Once the variance becomes relatively small, the expected value of the tuned parameter becomes very difficult to change.

Considering that all the vessel parameters must be tuned simultaneously, the one-step tuning procedure could be modified by splitting the Bayesian updating into two steps, as illustrated in Fig. 4. The basic idea is to apply two different power parameters, p_1 and p_2 where $p_1 < p_2$, to calculate the $PMF^{(pos)}_{SS_n}(\Phi_1, \ldots, \Phi_{M-1})$ and $PMF^{(pos)}_{SS_n}(\beta_{44})$ separately.

5. Case study basis

Case studies were performed in order to investigate the proposed algorithm in detail. For illustrative purpose, tuning of only 2 vessel parameters simultaneously was considered. The roll damping was assumed to be a function of only three independent wave-related parameters (i.e., H_s, T_p, and β_W), and can be written as a function of two input characteristics (i.e., $H_s \sin\beta_W$ and T_p).

5.1. Vessel information and RAO database

All case studies were based on numerical models for an offshore supply vessel (OSV) close to its ballast condition. Zero forward speed has been considered. The reference coordinate system for the seakeeping analysis is illustrated in Fig. 5. The X–Z plane is at the vessel longitudinal symmetry plane, and the origin is at the stern of the keel elevation. The positive X-axis points towards the bow, the positive Y-axis points towards the port, and the positive Z-axis points vertically upwards. The wave heading β_W, as illustrated in Fig. 5, follows the same coordinate system, in a positive going-to convention.

As described in Section 2, the RAO database should be established to represent the RAOs for all the considered motions, sensor locations, and covering the whole uncertainty ranges for the considered uncertain vessel parameters. The measurements of vessel heave displacements, velocities, and accelerations at three locations (see Fig. 5) have been considered, as summarized in Table 1, assuming that the measurements are independent. It is also assumed that there is much available supplementary information regarding the vessel design properties (e.g., operation design report and arrangement drawing) and onboard sensors (e.g., ballast monitoring) to approximately identify the vessel condition in real time. Therefore, the online vessel model tuning is focused on reducing the uncertainties of the estimated vessel condition resulting from new information becoming available based on measurements. The considered uncertain vessel parameters were selected based on the previous parametric sensitivity study (Han et al., 2020). Their uncertainty ranges are summarized in Table 2. Each of the considered vessel parameters was discretized within the specified uncertainty range. The number of discrete values is also shown in Table 2. In total, 9 wave headings between 30° and 150° with a 15° interval were considered in the RAO database, for all the 9 sensor measurements described in Table 1. All the RAOs were calculated by means of the DNV GL commercial software Wasim (DNV GL, 2018) which is based on application of the Rankine panel method (Kring, 1994).

Table 1
Description of sensor measurements.

Sensor ID	Location	Coordinate (x,y,z) [m]	Signal/measurements
Disp_A	A	(60.0, 0.0, 10.0)	$\eta_3(t)$ at location A
Disp_B	B	(60.0, 13.0, 10.0)	$\eta_3(t)$ at location B
Disp_C	C	(0.0, 10.0, 14.0)	$\eta_3(t)$ at location C
Vel_A	A	(60.0, 0.0, 10.0)	$\dot{\eta}_3(t)$ at location A
Vel_B	B	(60.0, 13.0, 10.0)	$\dot{\eta}_3(t)$ at location B
Vel_C	C	(0.0, 10.0, 14.0)	$\dot{\eta}_3(t)$ at location C
Acc_A	A	(60.0, 0.0, 10.0)	$\ddot{\eta}_3(t)$ at location A
Acc_B	B	(60.0, 13.0, 10.0)	$\ddot{\eta}_3(t)$ at location B
Acc_C	C	(0.0, 10.0, 14.0)	$\ddot{\eta}_3(t)$ at location C

$\eta_3(t)$: time series of heave displacement;
$\dot{\eta}_3(t)$: time series of heave velocity;
$\ddot{\eta}_3(t)$: time series of heave acceleration.

Table 2
Range of vessel model parameters in the RAO database.

Parameters	Variation range	Number of values
Mass	[−6%, +6%]	7
XCG	[−4 m, +4 m]	5
I_{yy}	[−9%, +9%]	7
GMT[a]	[0, 1 m]	6
β_{44}	[2%, 14%]	7

[a]Here "GMT" represents the free surface correction to the transverse metacentric height. $GMT = 0.5$ m here means that the transverse metacentric height is corrected with −0.5 m due to free surface effects. It is not the value of the transverse metacentric height.

Table 3
Data points for building the linear function of β_{44}.

T_p [s]	ω_p [rad/s]	$H_s \sin\beta_W$ [m]	β_{44} [–]
5	1.2566	0.0	0.04
25	0.2513	0.0	0.03
5	1.2566	1.0	0.05
25	0.2513	1.0	0.03
5	1.2566	2.0	0.065
25	0.2513	2.0	0.03
5	1.2566	4.0	0.08
25	0.2513	4.0	0.03

5.2. Assumed function of additional roll damping

As discussed in Section 1, the linearized roll damping B_{44} can be a function of many parameters, e.g.,

$$B_{44} \sim g(H_s, T_p, \beta_W, COG, mass, u, \phi_A ...) \tag{21}$$

where COG is the vessel centre of gravity, $mass$ is the vessel mass. In real applications, the GPR model of the roll damping B_{44} can be initiated based on the Ikeda's formulas mentioned in Section 1. Then the acquired wave and vessel motion measurements can assist in tuning B_{44} and updating the GPR model according to the proposed procedures in Section 4. For the purpose of demonstration, it was assumed that the roll damping according to the potential theory has been accurately calculated by seakeeping analysis software, and the linearized additional roll damping coefficient β_{44} can be accurately described as:

$$\beta_{44} \sim f(H_s \sin\beta_W, \omega_p) \tag{22a}$$

$$\beta_{44} = \frac{B_{44} - B_W}{B_{44,crit}} \tag{22b}$$

where $f()$ is a linear function, $\omega_p = \frac{2\pi}{T_p}$, $B_{44,crit}$ is the critical roll damping calculated based on vessel hydrodynamic coefficient matrices of added mass, inertia, and stiffness. The true linear function $f()$, illustrated in Fig. 6, was defined by the data points as summarized in Table 3. Linear interpolation between the data points was applied. Extrapolation was not allowed.

Table 4
Prior information and true values of GMT and XCG.

Case ID	Parameter	Mean	σ^2	True value
Case_GMT	GMT [m]	0.5	0.015	0.6
Case_XCG	XCG [m]	59.4	1.21	57.4

The prior knowledge about β_{44} was considered as a constant Gaussian process, with prior mean of 0.07 and variance of 0.02^2 i.e.,

$$\beta_{44,0} \sim \mathcal{N}(0.07, 0.02^2) \tag{23}$$

The prior mean and prior variance of β_{44} is also illustrated in Fig. 6.

5.3. Scope of case studies

Two separate cases were studied in detail. Case_GMT investigated the algorithm performance for tuning of GMT and β_{44} and updating the prediction model for β_{44} simultaneously, whereas, Case_XCG investigated the algorithm performance for tuning of XCG and β_{44} and updating the prediction model for β_{44} simultaneously. The prior and true β_{44} are described in Section 5.2. For demonstration purposes, the assumed true values and prior knowledge about the GMT and XCG in the case studies are defined in Table 4. Demonstration on tuning and prediction of β_{44} is the key objective of the case studies. Therefore, no head seas or following seas have been considered.

It is worth mentioning that the proposed GPR model can also be used for designing experimental test scopes actively, i.e., an adaptive sequential experimental design, e.g., Neumann-Brosig et al. (2020). Based on available experimental data, the GPR model can indicate where the largest uncertainty is to be found. Consequently the next test can be designed at that point to optimize the test scope. However, for the vessel in operations, the occurrence of sea states is decided by nature. Consequently, the sampling scheme cannot be established in the same way as for adaptive sequential experimental design. For the case studies, the sea states were randomly simulated as shown in Table 5. Similar to the case studies demonstrated by Han et al. (2021a,b), H_s, T_p, and β_W were also assumed to be evenly distributed random variables within the specified ranges, only for demonstration purposes. Note that the variables which represent the long-term wave conditions are usually not uniformly distributed in the real world. All the sea states were assumed to be adequately represented by the Pierson–Moskowitz (PM) spectrum. Directional spreading of the sea states was not considered.

Many initial simulations were performed in order to understand how the proposed algorithms will work. The initial findings were:

1. More samples are required in order to train the GPR model for the case of higher dimension. The considered GPR model actually have 3 random input parameters, i.e., ω_p, H_s, and β_W. The random generation of the uniformly and independently distributed H_s and β_W variables actually leads to a non-uniformly distributed $H_s \sin\beta_W$. Consequently, a much smaller likelihood of occurrence should be expected along the edges of the considered surface of the β_{44} GPR model.
2. For the β_{44} GPR model, the prior variance described in Eq. (23) should be applied as the hyperparameter signal variance (σ_f^2).
3. Each of the two input characteristics of the GPR model (i.e., $H_s \sin\beta_W$ and ω_p) requires an independent length-scale l. For an uncomplicated and smooth true surface such as a polynomial function, it seems reasonable to set l to be 10%–20% of the total range of each axis parameter.
4. For sea state SS_n, the variance of $\beta_{44}(SS_n)$ after tuning represents the uncertainty of that data point. Therefore, $\sigma_y(SS_n) = \sigma^{(pos)}_{\beta_{44}(SS_n)}$.
5. Tuning of the sea state dependent β_{44} requires a relatively large power parameter p.

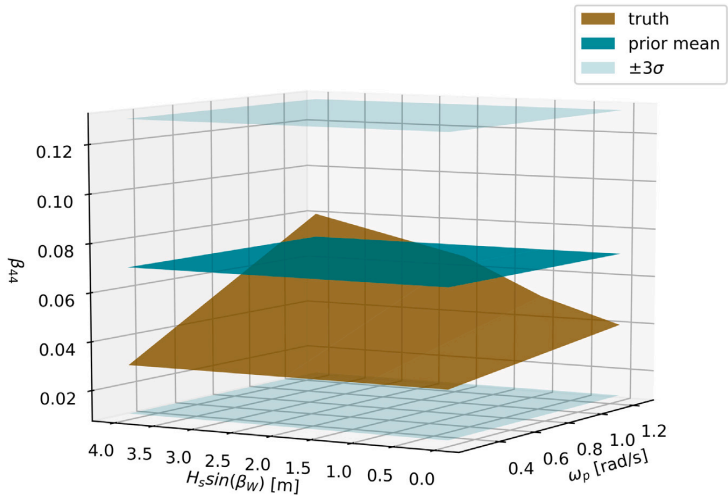

Fig. 6. The true function surface of $\beta_{44}(H_s \sin\beta_W, \omega_p)$ and the associated prior knowledge.

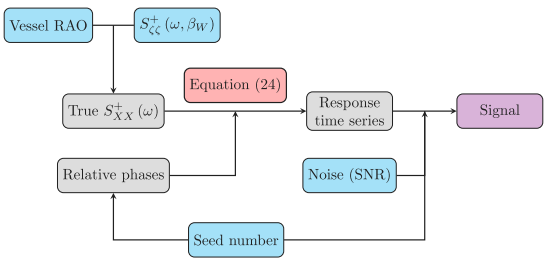

Fig. 7. Flow chart for the purpose of simulating noisy vessel response measurements.

The vessel motion signals were numerically simulated. Noise was also added to the signals. The considered input parameters for noisy signal simulation and case studies are summarized in Table 5. The vessel motion measurements for each sea state were simulated for 1 h. Each case study included 72 sea states. The procedure of simulating the noisy vessel motion measurements is illustrated in Fig. 7. The true response spectrum for response X, i.e., $S^+_{XX}(\omega)$ can be calculated based on the wave spectrum of the randomly simulated sea state and the corresponding vessel response RAO. A realization of that response can be generated by:

$$x(t) = \sum_{n=1}^{N_\omega} C_n(\omega_n)\cos(\omega_n t + \varphi_n) \tag{24a}$$

$$C_n(\omega_n) = \sqrt{2S^+_{XX}(\omega_n)\cdot \Delta\omega} \tag{24b}$$

where $\varphi_n \in [0, 2\pi)$ is a random phase angle which is continuous and uniformly distributed, $\Delta\omega$ is the interval of the discrete radial frequencies ω_n, and N_ω is the total number of discrete frequencies for the response spectrum. Then the signal noise can be added to each time step of the time series, assuming that (1) the signal noise is white noise, i.e., $WN \sim \mathcal{N}(0, \sigma_N^2)$; (2) and the variance of noise σ_N^2 is proportional to the true signal variance σ_X^2, defined as SNR (signal-to-noise ratio).

$$SNR = \frac{\sigma_X^2}{\sigma_N^2} \tag{25}$$

Table 5
Applied parameters related to the signal simulation, model tuning, and GPR model fitting.

Parameter	Value
H_s	Uniformly distributed in [1.0, 4.0] m
T_p	Uniformly distributed in [5.0, 25.0] s
β_W	Randomly selected among 9 discrete directions within $[30°, 150°]$
Seeds	Randomly generated within [1, 300]
Duration	3600 s
SNR	30
α	0.05
f_{lp}	0.2 Hz
p	0.6*
$l(H_s \sin\beta_W)$	0.7 m
$l(\omega_p)$	0.2 rad/s
σ_f^2	0.02^2

*$p = 0.6$ was applied to the case studies for the 1-step tuning procedure. $p_1 = 0.3$ and $p_2 = 0.7$ were applied to the case studies for the 2-step tuning procedure.

6. Results

6.1. One-step tuning

A number of cases have been analysed, also including stochastic variability obtained by means of seed variation. A summary of the aggregated results are reported for the purpose of demonstration and documentation of the algorithm performance.

6.1.1. Case_GMT

Representative results corresponding to two different realizations are included, with initial seed number 128 (denoted as "Seed128") and seed number 45 (denoted as "Seed45"). Note that different initial seed number will determine different sea states with respect to different H_s, T_p, β_W, and seeds for generating virtual noisy signals. Figs. 8 and 9 illustrate the updated GPR model for β_{44} after tuning the vessel parameters for 72 sea states. Information on the randomly generated sea states and the intermediate results with respect to tuning of β_{44} are summarized in Tables A.6 and A.7 in Appendix for Seed128 and Seed45 respectively. The expected values of the tuned β_{44} for those 72 sea states are also illustrated as samples in Figs. 8 and 9. Figs. 10 and 11 illustrate the tuned results of GMT throughout the 72 sea states for Seed128 and Seed45, respectively. As expected, both β_{44} GPR models

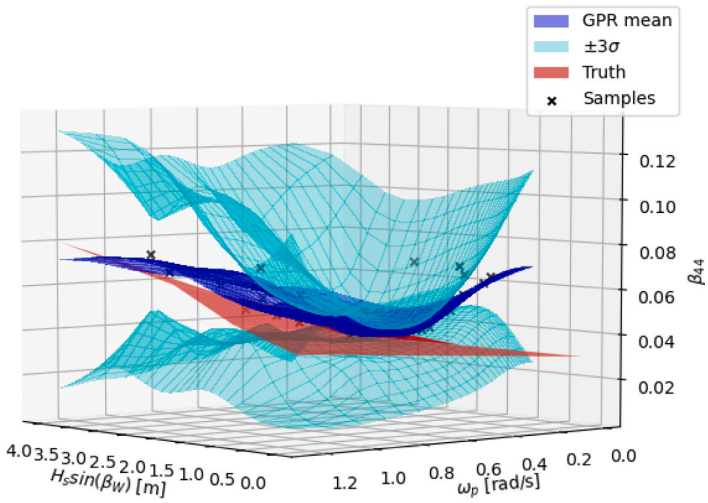

Fig. 8. The updated β_{44} GPR model after tuning of β_{44} and GMT for 72 sea states, for Seed128.

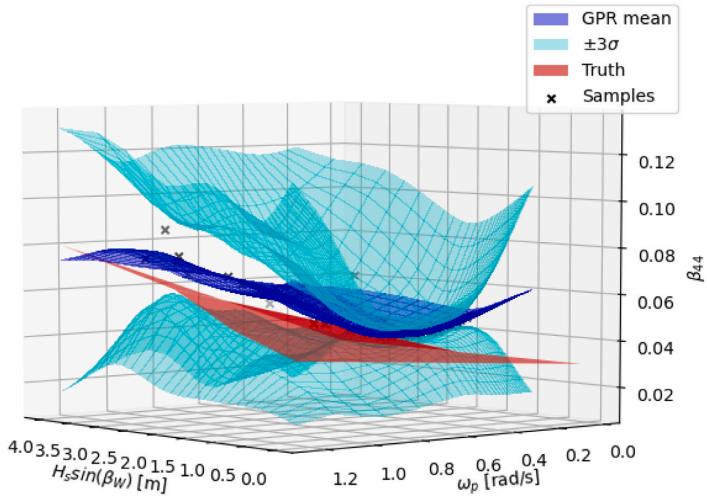

Fig. 9. The updated β_{44} GPR model after tuning of β_{44} and GMT for 72 sea states, for Seed45.

are found to converge towards the presumably true function. The posterior knowledge on β_{44}, in terms of the mean and variance, improves significantly based on the simulated vessel motion measurements for 3 days. However, the results of the tuned GMT become very different for the two presented cases. For Seed128 case (Fig. 10), the GMT mean fluctuates around the true value. When the tuning algorithm finds that the previously tuned GMT deviates significantly from the current observation, the variance dramatically increases, reflecting the confusion of the system. The increasing variance helps the system to adjust the tuning direction. Note that more simulations with different initial seeds were performed. For most simulated cases, the tuned GMT fluctuates about 0.5 m and 0.6 m throughout the 72 sea states, similarly to the behaviour illustrated in Fig. 10. On the contrary, Fig. 11 shows that the tuned GMT for case Seed45 significantly deviates from the true value. The variance was reduced significantly, while the mean value of the GMT was quickly tuned to a wrong value. This leads to an over-confident situation, where the tuning system was not able to bounce back to the true value. As shown in Fig. 11, the variance increased significantly between sea state number 45 and 50, and sea state number 66 and 68. The system tried very hard to bounce back towards the true value. However, it did not manage to change the tuned mean value of the GMT significantly.

This type of over-confidence is dangerous. Hence, a too rapid decrease of the variance for parameters that are not sea state dependent should be avoided. The bias associated with the tuned value of the GMT also indicates that the GMT may not be very sensitive to vessel motions for most wave conditions.

It is worth mentioning that the sequence of the occurring sea states and the corresponding measurements can influence the tuning of the sea state independent parameters (i.e., GMT in this case) as well as the updated GPR model for the sea state dependent β_{44}. However, such influence is usually very limited for convergent tuning results with sufficient amount of data and carefully selected power parameter

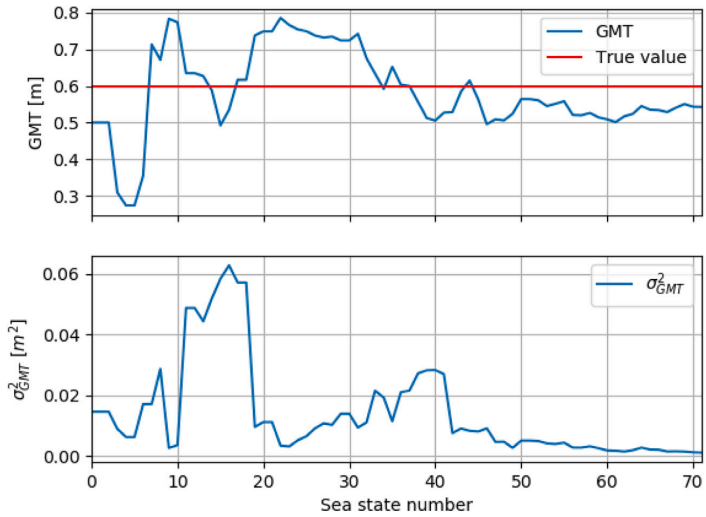

Fig. 10. The mean and the variance of the tuned GMT through the simulated 72 sea states, for Seed128.

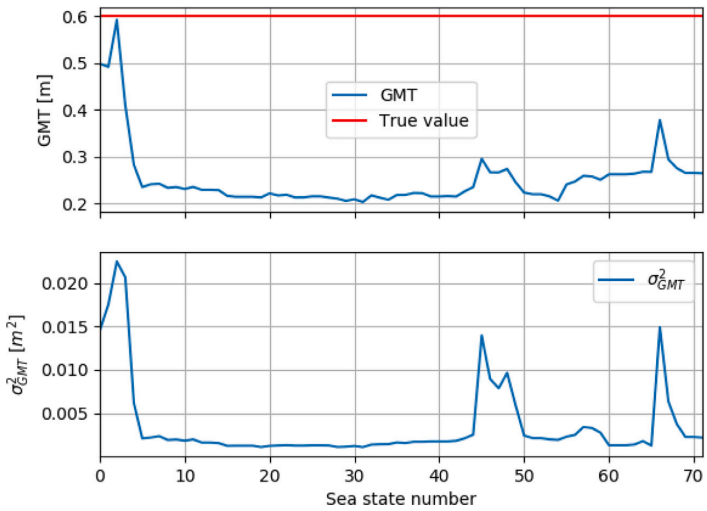

Fig. 11. The mean and the variance of the tuned GMT through the simulated 72 sea states, for Seed45.

p so that over-confident tuning can be avoided. Divergent tuning results, however, can be more influenced by the order of the sea state occurrence. In reality, the tuning is carried out in the sequence of occurrence by nature, which means that changing the tuning sequence is not relevant in practice.

6.1.2. Case_XCG

Based on earlier studies (Han et al., 2020, 2021a,c), the value of XCG is found to have a stronger influence on the vessel motions than the value of GMT. Therefore, as expected, tuning of XCG was much more stable than tuning of GMT. Fig. 12 shows the significantly improved GPR model of β_{44}, compared with the prior knowledge (Fig. 6). The intermediate tuning results of β_{44} are summarized in Table A.8 in Appendix. Fig. 13 shows that the tuned XCG gradually approaches the true value.

6.2. Two-step tuning

Based on the findings in Section 6.1.1, the over-confidence (low variance) implies that the 1-step parameter tuning procedure has difficulties in counteracting the convergence to the wrong value. Therefore, it is of great interest to apply the proposed 2-step tuning procedure, as described in Section 4.2, so that the sea state independent vessel parameters can be tuned relatively slowly.

Compared with results based on the 1-step tuning procedure, the trained GPR models of β_{44} approach the true surface in a better way, due to the applied higher power parameter for tuning of β_{44}. Tables A.9 and A.10 in Appendix summarize the intermediate tuning results of β_{44} for Case_GMT (Seed45) and Case_XCG (Seed128), respectively, based on 2-step tuning procedure.

With respect to tuning of GMT, as shown in Fig. 14, the 2-step tuning algorithm by application of a smaller power parameter leads

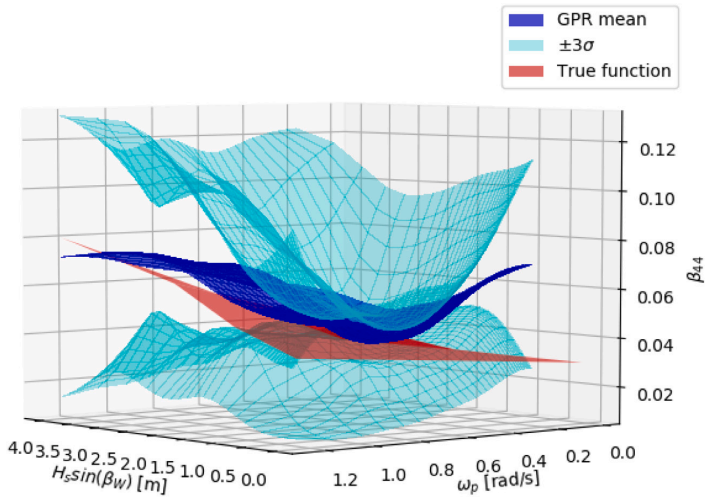

Fig. 12. The updated β_{44} GPR model after tuning of β_{44} and XCG for 72 sea states, for Seed128.

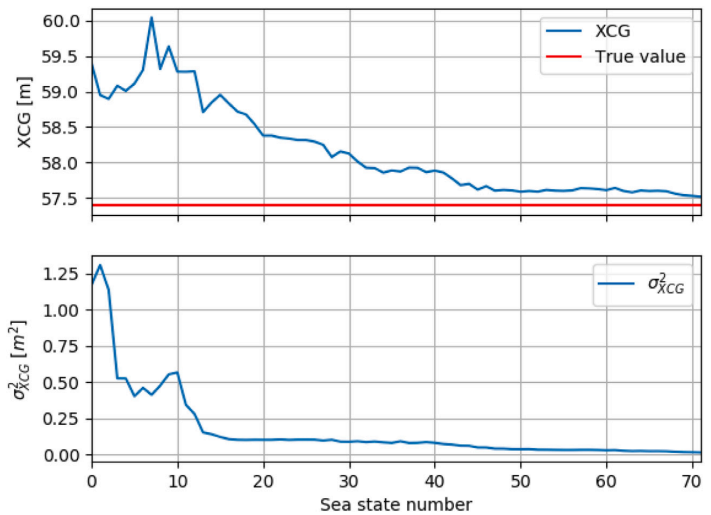

Fig. 13. The mean and the variance of the tuned XCG through the simulated 72 sea states, for Seed128.

to smaller fluctuations of the tuned mean values based on the measurements from different sea states. The over-confidence issue with respect to the GMT variance could therefore mainly be avoided. A large variance is preferred instead of a biased estimate resulting from over-confidence due to a fictitiously small variance.

As shown in Fig. 15, with a smaller power parameter p, tuning of the XCG was even accelerated towards the true value approximately between sea state number 15 and 40. The variance decreased more slowly, but the expected value converged faster towards the true value.

7. Conclusions and future work

The paper has proposed an algorithm for tuning and prediction of sea state dependent roll damping by an iterative closed loop between the tuning procedure and the GPR based prediction model. The tuned β_{44} for the current sea state updates the GPR model which in return improves the β_{44} prediction for future sea states. A simple and representative roll damping function was presumed for the numerical studies for demonstration purposes. The numerical case studies have shown that the tuning procedure succeeds to improve the roll damping coefficient estimation. The true variation of β_{44} is expected to be identified based on the real on-site vessel motion measurements and the environment, although subjected to some uncertainties.

With the 1-step tuning algorithm, the sea state independent parameters such as GMT and XCG may suffer from the over-confidence issue due to the applied large power parameter. Therefore, a 2-step tuning algorithm was proposed by applying two sets of different likelihood functions to update the prior knowledge, in order to tune roll damping and other parameters with different confidence level. Case studies showed that the 2-step tuning algorithm may even accelerate the tuning towards the true value. In addition, for the biased tuning (e.g., tuning of GMT for initial seed number of 45) the 2-step tuning can at least slow down the divergence.

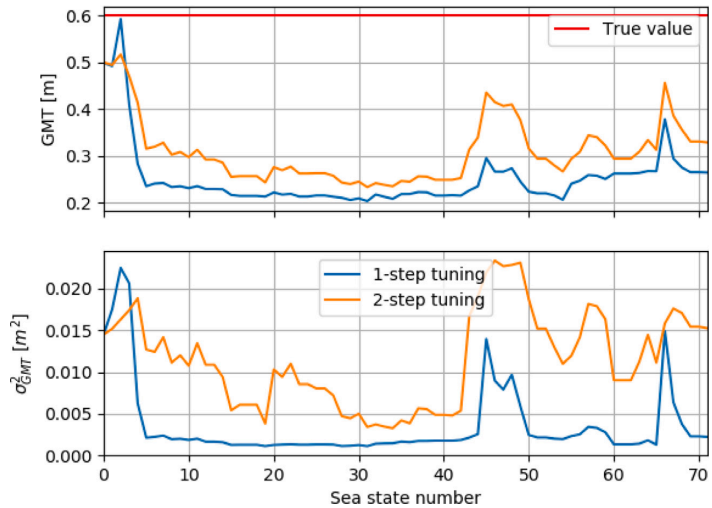

Fig. 14. Comparison of the mean and the variance of the tuned GMT through the simulated 72 sea states obtained respectively by application of the 1-step and the 2-step tuning procedures, for Seed45.

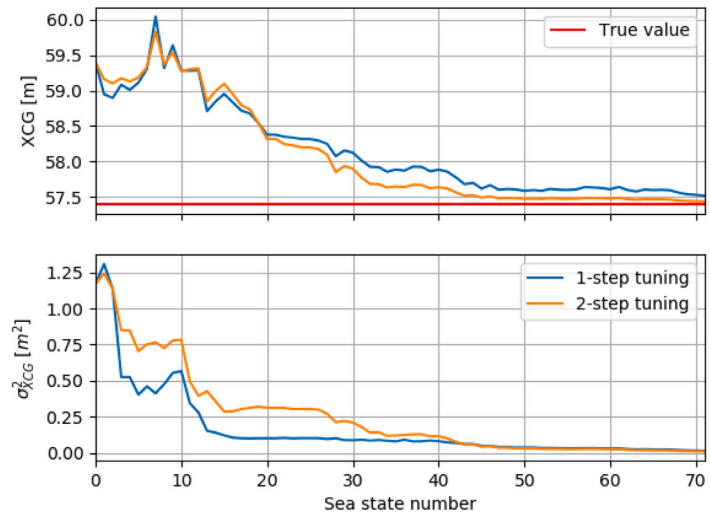

Fig. 15. Comparison of the mean and the variance of the tuned XCG through the simulated 72 sea states obtained respectively by application of the 1-step and the 2-step tuning procedures, for Seed128.

Even though the proposed tuning framework is expected to improve the estimation of sea state dependent vessel parameters, several important limitations should be emphasized for real applications:

1. The amount of on-site measurements can be limited especially for operations with frequently changing vessel conditions. There might be only a few available sea states for a certain vessel condition with respect to inertia distribution and vessel speed. Therefore, it might be reasonable to apply larger length-scale l in the RBF kernel of the GPR model in order to make the available updates influence the GPR model as much as possible. However, "under-fitting" may occur, as illustrated in Fig. 2.
2. The proposed algorithm for online tuning of sea state and vessel condition dependent roll damping based on on-site measurements cannot fully substitute lab experiments. The vessels are designed to survive at extreme and accidental scenarios, which probably do not happen on-site for a considerably long period. Therefore, tuning based on on-site measurements is probably insufficient to find a complete and sufficiently accurate function for representation of roll damping, covering the most extreme weather conditions and accidental scenarios. Lab tests can be designed and optimized, but not for on-site conditions. Using on-site measurements to improve the knowledge of roll damping for moderate seas is reasonable. However, predicting the extremes should still rely on model tests and CFD analysis.

3. The on-site sea states usually vary slowly, meaning that the sea state occurring afterwards is normally close to the current sea state. This slowly-varying characteristics negatively influence the global performance of the GPR model updating. However, this could also be an advantage in terms of better accuracy in relation to the local input domain of highest interest. More useful data can be available in a concentrated sub-space of the input parameters (e.g. H_s and T_p), and the environmental condition for the operation in the near future is probably located close to or within this concentrated input space. Consequently, more confidence could be obtained within such input space of great interest for the near future operation.

In addition, future work is essentially required before real applications on board can be achieved:

1. As stated in Items 2 and 3 of the algorithm limitations, the probability of occurrence for wave conditions is not uniformly distributed in the real world. Hence, insufficient observations with respect to GPR modelling are expected at those wave conditions with low probability of occurrence. The RBF kernel may be modified so that the length-scale l can be location dependent in the input space of the GPR model. A larger value of l may be applied for the input sub-space with low probability of occurrence so that those less frequently observed samples can have increased influence on a wider range of the input domain.
2. The proposed tuning framework as described in Section 4 introduces a GPR model which relies on the selection of the kernel and its hyperparameters. The hyperparameters of the GPR model can be optimized as described in Section 3. However, it was found that the optimal solution depends on the initial searching values, bounds, the amount of training data, and the applied algorithm (Erickson et al., 2018). Therefore, future research should investigate the effects of applying other kernels (e.g., Matérn kernel, Rational quadratic kernel, and Dot-Product kernel) and the effects of applying the automatic tuning of the kernel's hyperparameters on the results of tuning and predicting vessel parameters.
3. The GPR prediction model must be continuously quality checked. Usually a stopping criterion should be introduced in the future to avoid analysis divergence. For the β_{44} GPR model, the stopping criterion could be related to the prediction error. For example, if the tuned roll damping based on the new measurements is outside of the 99-percentile interval of the available GPR model at that sea state, then it might indicate that (1) the GPR model is over-confident; (2) the tuned results are biased; or (3) the vessel condition is changed, etc.
4. Roll damping depends not only on the sea states, but also on the vessel conditions such as vessel forward speed and loading conditions. Future research should demonstrate the tuning algorithm with a more complete roll damping GPR model which is sea state and vessel condition dependent. The proposed procedure could be modified by just including parameters with respect to vessel conditions as input parameters to the GPR model.
5. In reality, the acquired wave information e.g., on H_s and T_p, is always subject to uncertainties, which was not considered in the present paper. It is important as part of future work to systematically consider the effects of the weather uncertainties on the model tuning algorithm and the roll damping GPR model.
6. In the tuning procedure, the values of the power parameter p and the SSR criterion parameter α_0 can significantly influence the tuning results, and the selection of both values is at the moment based on trial and error. How to determine their values based on available quantitative information about system dimension, measurement uncertainty, etc., can be important to investigate as part of future work.

Nomenclature

Abbreviations

CFD	Computational Fluid Dynamics
COG	Centre of gravity
GMT	Correction to the transverse metacentric height due to free surface effects
GPR	Gaussian process regression
ITTC	International Towing Tank Conference
OSV	Offshore supply vessel
PDF	Probability density function
PM	Pierson–Moskowitz spectrum
PMF	Probability mass function
RAO	Response amplitude operator
RBF	Radial-basis function
SNR	Signal-to-noise ratio
SSR	Sensor screening ratio
WN	White noise
XCG	Longitudinal coordinate of vessel centre of gravity

Vectors and matrices

$\bar{\boldsymbol{\mu}}_*$	The conditional mean for the prediction space with the given observations
$\bar{\boldsymbol{K}}_{**}$	The updated kernel for the prediction space with the given observations
$\boldsymbol{\epsilon}$	The noise of the observations $\tilde{\boldsymbol{Y}}$
$\boldsymbol{\mu}_*$	The prior mean for the prediction space
$\boldsymbol{\mu}_Y$	The prior mean for the input space
$\boldsymbol{K}_{**}$	The prior covariance for the prediction space
$\boldsymbol{K}_{\tilde{Y}}$	The kernel for the input space with noise
$\boldsymbol{K}_{Y*}$	The kernel between input and prediction spaces
$\boldsymbol{K}_Y$	The kernel for the input space
$\boldsymbol{y}_*$	The prediction space for the function $y = f(x)$ at $\boldsymbol{x} = \boldsymbol{x}_*$
$\overline{\overline{W}}_j$	The weight matrix (likelihood function) based on the received measurements $x_j(t)$
$\tilde{\boldsymbol{Y}}$	The observations related to the input space $\boldsymbol{Y}$

Other Symbols

α_j	Sensor screening ratio (SSR) for the measured quantity j
β_{44}	Ratio between the additional roll damping and the critical roll damping
β_W	Wave direction w.r.t. vessel coordinate system
$\eta_3, \dot{\eta}_3, \ddot{\eta}_3$	Heave displacement, velocity, acceleration
ω	Wave frequency
ω_p	Wave spectral peak frequency
ϕ_A	Roll amplitude
$\boldsymbol{\Phi}_m$	The uncertain vessel parameter to be tuned, $m \in \{1, 2, ..., M\}$
ϕ_{im}	The imth discrete value of the vessel parameter $\boldsymbol{\Phi}_m$ in the RAO database
ϕ_{km}	The kmth discrete value of the vessel parameter $\boldsymbol{\Phi}_m$ in the discrete joint probability distribution
$\sigma^2_{y_i}$	The variance of the observation y_i
σ^2_N	Variance of noise
$\sigma^2_{\tilde{Y}}$	Variance of response
σ^2_f	Signal variance
$\sigma_{\sigma_{r,j}}$	The standard deviation of $\sigma_{r,j}$ over $r \in \{1, 2, ldots, R\}$
$\sigma_{r,j}$	The predicted standard deviation by using $RAO_{r,j}$
$\hat{\sigma}_j$	The standard deviation of the filtered signal $\hat{x}_j(t)$
B_{44}	Roll damping
B_{BK}	The damping component of B_{44} due to bilge keels
B_E	The damping component of B_{44} due to eddy making
B_F	Friction damping component of B_{44}
B_L	Linear lift damping component of B_{44}
B_W	Wave damping component of B_{44}
f_{lp}	lowpass filter cutoff frequency [Hz]

$H_{r,j}(\omega, \beta_W)$	Linear transfer function between wave and vessel (heave) response for the measured quantity j based on the combination r for the uncertain vessel parameters, i.e. $RAO_{r,j}$
H_s	Significant wave height
Im	The number of discrete values used for RAO database for the vessel parameter Φ_m
im	The imth value of the variable Φ_m in the RAO database
J	The total number of the measured quantities
j	The index of the measured quantities, representing different motions and their derivatives (i.e., displacement, velocity, acceleration) at various locations
Km	The number of discrete values used for the probability distribution model for the vessel parameter Φ_m
km	The kmth value of the discretized variable Φ_m in the probability distribution model
l	Length-scale
M	The number of considered variables for tuning
N_ω	The number of discretized frequencies
N_t	The number of discretized time steps
N_{Prob}	The total number of the discrete points for the joint probability distribution, $N_{Prob} = \prod_{m=1}^{M}(Km)$
p	Power parameter
R	The total number of possible vessel parameter combinations to build the RAO database, $R = \prod_{m=1}^{M}(Im)$
$RAO_{r,j}$	The RAO based on the variable combination r, for the measured quantity j, i.e., $H_{r,j}(\omega, \beta_W)$
$S^+_{\zeta\zeta}(\omega, \beta_W)$	Single-sided power spectral density of long-crested waves
$S^+_{XX}(\omega)$	Single-sided power spectral density of vessel response X
SS_n	The index of the occurring sea state, i.e., the sea state number
T_p	Spectral peak period
u	Vessel forward speed
$w_{r,j}$	Weight factor for the rth variable combination based on measurement of quantity j
$x_j(t)$	The original signal for the measured quantity j at time step t
$\bar{x}_j$	The mean of the filtered time series $\hat{x}_j(t)$
$\hat{x}_j(t)$	The filtered time series of $x_j(t)$

CRediT authorship contribution statement

Xu Han: Conceptualization, Methodology, Software, Formal analysis, Data curation, Writing - original draft, Writing - review & editing. **Svein Sævik:** Writing - review & editing, Supervision, Project administration. **Bernt Johan Leira:** Writing - review & editing, Supervision, Project administration, Funding acquisition.

Declaration of competing interest

The authors declare that they have no known competing financial interests or personal relationships that could have appeared to influence the work reported in this paper.

Acknowledgements

This work was made possible through the Centre for Research based Innovation MOVE, financially supported by the Research Council of Norway, NFR project no. 237929 and the consortium partners, http://www.ntnu.edu/move. Special thanks are given to Section of Hydrodynamics & Stability in DNV for providing the numerical seakeeping models.

Appendix. The simulated sea states and tuning of β_{44}

The parameters summarized in the tables are described as follows:

- SS_n: sea state number (index)
- H_s [m]: significant wave height
- β_W [°]: wave direction
- T_p [s]: wave spectral peak period
- β^*_{44}: the true value of β_{44} according to Table 3
- $\tilde{\beta}_{44}$: the GPR model predicted β_{44} before tuning for sea state SS_n
- $\tilde{\sigma}^2_{\beta_{44}}$: the GPR model predicted variance of β_{44} before tuning for sea state SS_n
- $\hat{\beta}_{44}$: the tuned β_{44} for sea state SS_n
- $\hat{\sigma}^2_{\beta_{44}}$: the variance of β_{44} after tuning for sea state SS_n

Table A.6
The simulated sea states and the tuning inputs and outputs of β_{44} — Case_GMT for Seed128 with 1-step tuning.

SS_n	H_s	β_W	T_p	β^*_{44}	$\tilde{\beta}_{44}$	$\tilde{\sigma}^2_{\beta_{44}}$	$\hat{\beta}_{44}$	$\hat{\sigma}^2_{\beta_{44}}$
1	3.60	150	22.59	0.0366	0.0700	4.0E−04	0.0700	3.9E−04
2	1.79	30	19.40	0.0346	0.0700	4.0E−04	0.0700	3.9E−04
3	1.39	45	22.73	0.0341	0.0700	4.0E−04	0.0658	3.9E−04
4	1.12	75	15.63	0.0365	0.0690	1.9E−04	0.0428	2.0E−05
5	1.72	90	20.17	0.0372	0.0597	1.5E−04	0.0442	3.9E−05
6	2.94	150	20.40	0.0362	0.0467	3.6E−05	0.0467	3.5E−05
7	3.37	90	15.17	0.0443	0.0694	4.0E−04	0.0435	4.4E−05
8	2.80	90	15.59	0.0426	0.0494	1.9E−04	0.0411	1.5E−05
9	2.00	45	17.27	0.0372	0.0430	2.1E−05	0.0424	1.7E−05
10	1.36	105	11.12	0.0408	0.0462	1.9E−04	0.0412	1.7E−05
11	1.93	135	16.25	0.0375	0.0411	1.0E−05	0.0410	8.5E−06
12	1.33	120	15.00	0.0371	0.0420	9.8E−06	0.0416	7.7E−06
13	2.81	150	18.00	0.0369	0.0437	5.1E−06	0.0437	4.9E−06
14	1.75	75	6.48	0.0533	0.0685	3.9E−04	0.0713	2.3E−04
15	1.90	120	7.72	0.0490	0.0641	1.9E−04	0.0585	1.3E−04
16	2.55	120	8.27	0.0518	0.0605	2.4E−04	0.0587	1.1E−04
17	3.15	60	8.94	0.0523	0.0579	2.0E−04	0.0540	8.9E−05
18	3.79	60	13.38	0.0461	0.0442	5.2E−05	0.0451	3.5E−05
19	1.31	30	24.86	0.0331	0.0654	1.6E−04	0.0654	1.5E−04
20	3.12	60	11.44	0.0471	0.0450	7.6E−05	0.0420	2.0E−05
21	3.96	60	8.82	0.0555	0.0599	2.2E−04	0.0584	5.5E−05
22	2.68	150	22.73	0.0351	0.0518	2.4E−05	0.0518	2.3E−05
23	2.78	135	14.87	0.0411	0.0399	6.5E−05	0.0409	2.9E−05
24	3.23	90	22.04	0.0393	0.0499	1.1E−04	0.0420	2.2E−05
25	3.46	90	24.63	0.0386	0.0464	5.2E−05	0.0432	2.6E−05
26	1.38	105	22.24	0.0352	0.0511	9.5E−06	0.0504	9.0E−06
27	3.72	135	22.40	0.0382	0.0472	6.8E−05	0.0457	5.4E−05
28	2.72	30	17.03	0.0371	0.0423	2.0E−06	0.0423	2.0E−06
29	3.19	45	10.69	0.0469	0.0447	4.8E−05	0.0441	3.2E−05
30	1.90	135	20.10	0.0359	0.0475	2.1E−06	0.0474	2.1E−06
31	1.20	30	21.08	0.0335	0.0630	7.1E−05	0.0630	6.8E−05
32	1.49	30	9.75	0.0388	0.0547	1.8E−04	0.0440	5.3E−05
33	1.40	60	8.80	0.0430	0.0502	6.2E−05	0.0431	1.9E−05
34	2.97	105	24.73	0.0377	0.0454	3.1E−05	0.0437	2.2E−05
35	2.27	135	12.44	0.0413	0.0391	1.6E−05	0.0395	1.0E−05
36	3.95	90	13.38	0.0479	0.0568	1.7E−04	0.0444	4.1E−05
37	2.21	105	23.40	0.0371	0.0496	4.3E−05	0.0458	2.8E−05
38	1.76	45	21.29	0.0352	0.0504	2.8E−06	0.0503	2.7E−06
39	1.65	105	21.79	0.0362	0.0477	5.8E−06	0.0471	5.4E−06
40	3.53	120	5.73	0.0673	0.0706	3.8E−04	0.0751	1.1E−04
41	3.07	45	23.35	0.0372	0.0469	1.5E−05	0.0465	1.4E−05
42	1.61	120	6.32	0.0504	0.0667	1.6E−04	0.0615	6.1E−05
43	3.12	75	17.62	0.0415	0.0416	9.6E−06	0.0408	4.8E−06
44	3.52	30	12.51	0.0422	0.0401	8.5E−06	0.0401	6.1E−06
45	3.24	90	12.25	0.0475	0.0452	2.1E−05	0.0437	1.4E−05
46	3.25	60	5.83	0.0651	0.0744	1.1E−04	0.0675	7.6E−05
47	1.67	75	17.27	0.0380	0.0416	2.8E−06	0.0412	2.2E−06
48	1.72	60	11.88	0.0412	0.0395	4.8E−06	0.0398	3.0E−06
49	3.63	60	24.95	0.0380	0.0434	1.1E−05	0.0430	9.4E−06
50	3.61	105	17.85	0.0423	0.0421	1.6E−05	0.0411	7.7E−06
51	2.83	75	13.71	0.0443	0.0409	8.8E−06	0.0407	5.2E−06
52	1.62	150	16.24	0.0353	0.0508	1.9E−05	0.0508	1.8E−05
53	1.62	30	10.67	0.0383	0.0434	3.0E−05	0.0422	1.9E−05
54	2.31	60	18.50	0.0389	0.0426	5.6E−06	0.0421	4.7E−06
55	2.70	135	21.01	0.0375	0.0450	2.7E−06	0.0449	2.5E−06

(*continued on next page*)

Table A.6 (*continued*).

SS_n	H_s	β_W	T_p	β^*_{44}	$\bar{\beta}_{44}$	$\bar{\sigma}^2_{\beta_{44}}$	$\hat{\beta}_{44}$	$\hat{\sigma}^2_{\beta_{44}}$
56	3.27	60	22.06	0.0387	0.0431	5.4E−06	0.0427	4.9E−06
57	2.55	75	24.19	0.0373	0.0458	6.7E−06	0.0447	6.0E−06
58	3.06	45	20.93	0.0381	0.0441	2.0E−06	0.0440	2.0E−06
59	1.77	120	8.54	0.0461	0.0500	2.6E−05	0.0484	2.3E−05
60	3.80	135	18.02	0.0405	0.0412	3.3E−06	0.0411	2.9E−06
61	3.46	120	18.07	0.0411	0.0410	2.0E−06	0.0409	1.7E−06
62	1.60	60	17.73	0.0369	0.0432	5.8E−07	0.0432	5.6E−07
63	1.52	30	8.08	0.0408	0.0479	8.6E−05	0.0426	2.8E−05
64	3.77	150	11.76	0.0438	0.0417	5.8E−06	0.0417	5.2E−06
65	3.36	90	21.67	0.0397	0.0420	4.0E−06	0.0416	3.2E−06
66	2.60	60	18.56	0.0394	0.0420	2.0E−06	0.0418	1.9E−06
67	1.21	120	23.76	0.0340	0.0571	6.9E−06	0.0567	6.7E−06
68	2.90	30	5.96	0.0524	0.0659	7.4E−05	0.0642	5.2E−05
69	1.57	30	7.58	0.0416	0.0458	3.6E−05	0.0429	1.8E−05
70	2.35	135	12.39	0.0417	0.0398	1.4E−06	0.0398	1.2E−06
71	3.45	45	24.22	0.0373	0.0453	2.6E−06	0.0452	2.5E−06
72	1.54	135	11.92	0.0387	0.0402	5.6E−06	0.0402	4.3E−06

Table A.7
The simulated sea states and the tuning inputs and outputs of β_{44} — Case_GMT for Seed45 with 1-step tuning.

SS_n	H_s	β_W	T_p	β^*_{44}	$\bar{\beta}_{44}$	$\bar{\sigma}^2_{\beta_{44}}$	$\hat{\beta}_{44}$	$\hat{\sigma}^2_{\beta_{44}}$
1	3.97	45	22.60	0.0384	0.0700	4.0E−04	0.0637	3.8E−04
2	2.65	135	8.23	0.0499	0.0699	4.0E−04	0.0607	2.3E−04
3	1.84	105	11.10	0.0439	0.0660	3.0E−04	0.0444	5.1E−05
4	1.23	120	17.10	0.0358	0.0613	3.5E−04	0.0435	6.6E−05
5	2.33	75	23.81	0.0372	0.0606	2.7E−04	0.0424	3.0E−05
6	2.42	90	19.66	0.0391	0.0467	5.9E−05	0.0416	1.4E−05
7	1.15	30	5.79	0.0435	0.0699	4.0E−04	0.0679	4.2E−04
8	1.49	135	8.20	0.0425	0.0636	3.1E−04	0.0565	1.8E−04
9	1.35	90	6.28	0.0500	0.0668	2.9E−04	0.0651	9.9E−05
10	2.88	30	13.89	0.0392	0.0411	7.6E−05	0.0419	4.8E−05
11	3.57	45	21.80	0.0383	0.0458	2.1E−05	0.0448	1.8E−05
12	2.95	60	16.15	0.0416	0.0450	5.1E−05	0.0432	2.8E−05
13	3.97	135	24.76	0.0376	0.0531	6.5E−05	0.0481	4.2E−05
14	2.41	150	20.26	0.0353	0.0461	7.8E−05	0.0461	7.5E−05
15	2.85	60	23.82	0.0375	0.0447	9.8E−06	0.0439	8.5E−06
16	1.85	105	19.53	0.0377	0.0407	5.5E−05	0.0404	1.5E−05
17	3.93	150	10.05	0.0468	0.0507	6.4E−05	0.0535	4.6E−05
18	3.02	30	23.15	0.0355	0.0450	3.6E−05	0.0450	3.4E−05
19	2.32	150	18.69	0.0357	0.0456	2.8E−05	0.0456	2.7E−05
20	1.87	75	7.10	0.0524	0.0648	1.4E−04	0.0612	3.5E−05
21	2.53	105	17.08	0.0407	0.0421	1.1E−05	0.0413	6.2E−06
22	1.34	135	19.75	0.0346	0.0494	3.6E−05	0.0479	3.1E−05
23	1.68	105	9.74	0.0448	0.0517	4.4E−05	0.0484	3.2E−05
24	2.44	90	24.78	0.0371	0.0444	6.0E−06	0.0437	5.3E−06
25	1.73	30	21.82	0.0340	0.0509	3.4E−05	0.0509	3.2E−05
26	2.16	150	13.66	0.0375	0.0453	5.0E−05	0.0441	3.8E−05
27	3.46	30	19.46	0.0375	0.0408	9.5E−06	0.0408	9.2E−06
28	1.22	135	18.37	0.0348	0.0489	1.6E−05	0.0479	1.4E−05
29	3.77	150	15.47	0.0403	0.0392	1.5E−05	0.0394	1.2E−05
30	1.67	45	10.96	0.0401	0.0466	4.3E−05	0.0434	2.2E−05
31	3.12	30	16.42	0.0382	0.0405	7.4E−06	0.0405	6.5E−06
32	1.33	120	16.48	0.0364	0.0437	6.4E−06	0.0430	5.5E−06
33	2.80	105	5.89	0.0641	0.0686	3.6E−04	0.0764	1.2E−04
34	2.22	150	14.07	0.0374	0.0427	7.2E−06	0.0425	6.6E−06
35	3.51	45	24.80	0.0372	0.0445	2.8E−06	0.0444	2.7E−06
36	1.75	135	9.53	0.0421	0.0484	2.7E−05	0.0467	2.2E−05
37	2.37	150	14.46	0.0376	0.0420	2.8E−06	0.0419	2.6E−06
38	2.67	60	6.58	0.0582	0.0698	1.0E−04	0.0680	1.3E−04
39	1.76	45	24.35	0.0345	0.0484	1.9E−05	0.0478	1.7E−05
40	1.33	45	13.15	0.0371	0.0446	1.3E−05	0.0435	1.0E−05
41	3.18	75	5.61	0.0683	0.0749	1.8E−04	0.0749	1.7E−04
42	1.93	120	6.50	0.0530	0.0640	4.4E−05	0.0622	2.7E−05
43	3.48	75	6.49	0.0646	0.0735	2.5E−04	0.0862	1.3E−04
44	2.35	60	12.47	0.0437	0.0441	1.8E−05	0.0432	1.2E−05
45	1.28	150	8.69	0.0393	0.0565	1.4E−04	0.0511	9.6E−05
46	3.66	75	7.58	0.0604	0.0793	2.2E−04	0.0658	4.8E−05
47	3.23	60	9.73	0.0506	0.0599	1.9E−04	0.0590	6.5E−05
48	1.37	150	13.14	0.0362	0.0475	2.9E−05	0.0463	2.4E−05
49	3.57	120	6.41	0.0635	0.0781	6.4E−05	0.0729	5.4E−05
50	1.20	150	11.91	0.0365	0.0480	2.6E−05	0.0461	2.1E−05

Table A.7 (*continued*).

SS_n	H_s	β_W	T_p	β^*_{44}	$\bar{\beta}_{44}$	$\bar{\sigma}^2_{\beta_{44}}$	$\hat{\beta}_{44}$	$\hat{\sigma}^2_{\beta_{44}}$
51	1.55	60	7.95	0.0456	0.0551	3.7E−05	0.0490	2.0E−05
52	1.52	45	12.61	0.0381	0.0427	2.9E−06	0.0424	2.6E−06
53	3.77	30	19.75	0.0379	0.0401	4.3E−06	0.0401	4.1E−06
54	3.00	45	22.49	0.0374	0.0411	5.9E−06	0.0410	5.2E−06
55	1.77	120	23.59	0.0355	0.0450	7.4E−06	0.0445	6.9E−06
56	1.75	45	7.27	0.0461	0.0545	2.8E−05	0.0499	2.2E−05
57	3.95	75	15.69	0.0448	0.0660	3.4E−04	0.0497	1.1E−04
58	3.04	135	13.27	0.0431	0.0425	7.1E−06	0.0421	5.8E−06
59	2.21	60	24.30	0.0364	0.0424	4.3E−06	0.0422	4.0E−06
60	1.19	45	17.09	0.0351	0.0470	5.5E−06	0.0465	5.2E−06
61	2.33	75	21.20	0.0381	0.0408	1.7E−06	0.0407	1.4E−06
62	1.62	150	20.07	0.0342	0.0498	6.3E−06	0.0498	6.1E−06
63	1.97	150	18.11	0.0352	0.0461	1.9E−06	0.0461	1.9E−06
64	2.95	60	12.56	0.0451	0.0476	1.9E−05	0.0474	1.6E−05
65	3.17	135	11.35	0.0458	0.0485	9.0E−06	0.0484	8.6E−06
66	2.40	90	7.19	0.0562	0.0684	6.8E−05	0.0640	2.4E−05
67	1.56	105	11.18	0.0421	0.0442	7.4E−06	0.0427	5.3E−06
68	1.89	105	16.77	0.0392	0.0392	2.0E−06	0.0394	1.5E−06
69	1.42	150	12.77	0.0365	0.0456	5.3E−06	0.0452	5.0E−06
70	1.28	135	20.01	0.0345	0.0485	1.6E−06	0.0484	1.5E−06
71	2.48	30	22.41	0.0349	0.0468	3.1E−06	0.0468	3.0E−06
72	3.97	45	23.64	0.0380	0.0487	1.3E−05	0.0482	1.3E−05

Table A.8
The simulated sea states and the tuning inputs and outputs of β_{44} — Case_XCG for Seed128 with 1-step tuning.

SS_n	H_s	β_W	T_p	β^*_{44}	$\bar{\beta}_{44}$	$\bar{\sigma}^2_{\beta_{44}}$	$\hat{\beta}_{44}$	$\hat{\sigma}^2_{\beta_{44}}$
1	3.60	150	22.59	0.0366	0.0700	4.0E−04	0.0700	3.9E−04
2	1.79	30	19.40	0.0346	0.0700	4.0E−04	0.0665	3.4E−04
3	1.39	45	22.73	0.0341	0.0683	1.8E−04	0.0649	2.0E−04
4	1.12	75	15.63	0.0365	0.0673	1.7E−04	0.0437	2.8E−05
5	1.72	90	20.17	0.0372	0.0607	1.5E−04	0.0470	7.5E−05
6	2.94	150	20.40	0.0362	0.0505	4.6E−05	0.0480	3.6E−05
7	3.37	90	15.17	0.0443	0.0697	4.0E−04	0.0416	1.8E−05
8	2.80	90	15.59	0.0426	0.0483	1.8E−04	0.0408	1.4E−05
9	2.00	45	17.27	0.0372	0.0452	2.5E−05	0.0437	1.7E−05
10	1.36	105	11.12	0.0408	0.0470	1.9E−04	0.0413	1.9E−05
11	1.93	135	16.25	0.0375	0.0426	1.1E−05	0.0426	9.6E−06
12	1.33	120	15.00	0.0371	0.0431	1.2E−05	0.0422	8.6E−06
13	2.81	150	18.00	0.0369	0.0454	5.5E−06	0.0451	5.3E−06
14	1.75	75	6.48	0.0533	0.0685	3.9E−04	0.0764	3.8E−04
15	1.90	120	7.72	0.0490	0.0655	2.1E−04	0.0611	4.9E−05
16	2.55	120	8.27	0.0518	0.0613	2.2E−04	0.0605	4.3E−05
17	3.15	60	8.94	0.0523	0.0583	1.6E−04	0.0583	9.7E−05
18	3.79	60	13.38	0.0461	0.0425	3.8E−05	0.0451	2.8E−05
19	1.31	30	24.86	0.0331	0.0663	1.4E−04	0.0649	1.4E−04
20	3.12	60	11.44	0.0471	0.0475	7.2E−05	0.0466	4.3E−05
21	3.96	60	8.82	0.0555	0.0627	2.2E−04	0.0616	6.1E−05
22	2.68	150	22.73	0.0351	0.0533	2.3E−05	0.0533	2.2E−05
23	2.78	135	14.87	0.0411	0.0428	6.9E−05	0.0462	5.1E−05
24	3.23	90	22.04	0.0393	0.0452	1.0E−04	0.0411	1.9E−05
25	3.46	90	24.63	0.0386	0.0454	4.8E−05	0.0427	2.3E−05
26	1.38	105	22.24	0.0352	0.0524	9.4E−06	0.0516	8.8E−06
27	3.72	135	22.40	0.0382	0.0473	6.8E−05	0.0461	5.5E−05
28	2.72	30	17.03	0.0371	0.0438	2.2E−06	0.0437	2.1E−06
29	3.19	45	10.69	0.0469	0.0499	5.4E−05	0.0515	3.8E−05
30	1.90	135	20.10	0.0359	0.0488	2.1E−06	0.0486	2.1E−06
31	1.20	30	21.08	0.0335	0.0635	6.8E−05	0.0634	6.9E−05
32	1.49	30	9.75	0.0388	0.0538	1.8E−04	0.0422	3.3E−05
33	1.40	60	8.80	0.0430	0.0492	5.0E−05	0.0425	1.4E−05
34	2.97	105	24.73	0.0377	0.0449	3.1E−05	0.0433	2.1E−05
35	2.27	135	12.44	0.0413	0.0420	1.8E−05	0.0414	1.2E−05
36	3.95	90	13.38	0.0479	0.0560	1.6E−04	0.0443	3.9E−05
37	2.21	105	23.40	0.0371	0.0517	4.9E−05	0.0470	3.4E−05
38	1.76	45	21.29	0.0352	0.0515	2.7E−06	0.0512	2.6E−06
39	1.65	105	21.79	0.0362	0.0494	6.5E−06	0.0487	6.1E−06
40	3.53	120	5.73	0.0673	0.0704	3.8E−04	0.0773	1.4E−04
41	3.07	45	23.35	0.0372	0.0484	1.7E−05	0.0478	1.6E−05
42	1.61	120	6.32	0.0504	0.0693	1.8E−04	0.0636	7.2E−05
43	3.12	75	17.62	0.0415	0.0404	8.2E−06	0.0402	4.3E−06

(*continued on next page*)

Table A.8 (*continued*).

SS_n	H_s	β_W	T_p	β^*_{44}	$\bar{\beta}_{44}$	$\bar{\sigma}^2_{\beta_{44}}$	$\hat{\beta}_{44}$	$\hat{\sigma}^2_{\beta_{44}}$
44	3.52	30	12.51	0.0422	0.0436	1.0E−05	0.0426	7.6E−06
45	3.24	90	12.25	0.0475	0.0464	1.9E−05	0.0446	1.4E−05
46	3.25	60	5.83	0.0651	0.0755	1.3E−04	0.0697	8.2E−05
47	1.67	75	17.27	0.0380	0.0436	3.3E−06	0.0430	2.9E−06
48	1.72	60	11.88	0.0412	0.0407	5.4E−06	0.0405	3.3E−06
49	3.63	60	24.95	0.0380	0.0427	1.0E−05	0.0424	8.5E−06
50	3.61	105	17.85	0.0423	0.0410	1.3E−05	0.0406	6.5E−06
51	2.83	75	13.71	0.0443	0.0432	1.0E−05	0.0421	6.6E−06
52	1.62	150	16.24	0.0353	0.0514	2.0E−05	0.0510	1.9E−05
53	1.62	30	10.67	0.0383	0.0417	2.2E−05	0.0416	1.3E−05
54	2.31	60	18.50	0.0389	0.0448	6.6E−06	0.0438	5.7E−06
55	2.70	135	21.01	0.0375	0.0467	3.0E−06	0.0466	2.9E−06
56	3.27	60	22.06	0.0387	0.0425	5.3E−06	0.0422	4.5E−06
57	2.55	75	24.19	0.0373	0.0462	6.9E−06	0.0451	6.3E−06
58	3.06	45	20.93	0.0381	0.0454	2.3E−06	0.0453	2.2E−06
59	1.77	120	8.54	0.0461	0.0510	1.7E−05	0.0498	1.6E−05
60	3.80	135	18.02	0.0405	0.0411	3.3E−06	0.0410	2.9E−06
61	3.46	120	18.07	0.0411	0.0402	1.9E−06	0.0402	1.6E−06
62	1.60	60	17.73	0.0369	0.0446	6.4E−07	0.0445	6.1E−07
63	1.52	30	8.08	0.0408	0.0469	7.8E−05	0.0414	1.8E−05
64	3.77	150	11.76	0.0438	0.0453	6.6E−06	0.0447	6.1E−06
65	3.36	90	21.67	0.0397	0.0414	3.5E−06	0.0411	2.8E−06
66	2.60	60	18.56	0.0394	0.0433	2.2E−06	0.0429	2.1E−06
67	1.21	120	23.76	0.0340	0.0576	6.7E−06	0.0572	6.6E−06
68	2.90	30	5.96	0.0524	0.0679	8.3E−05	0.0661	6.8E−05
69	1.57	30	7.58	0.0416	0.0447	2.8E−05	0.0421	1.3E−05
70	2.35	135	12.39	0.0417	0.0417	1.6E−06	0.0415	1.4E−06
71	3.45	45	24.22	0.0373	0.0458	2.7E−06	0.0457	2.6E−06
72	1.54	135	11.92	0.0387	0.0399	5.4E−06	0.0399	4.1E−06

Table A.9
The simulated sea states and the tuning inputs and outputs of β_{44} — Case_GMT for Seed45 with 2-step tuning.

SS_n	H_s	β_W	T_p	β^*_{44}	$\bar{\beta}_{44}$	$\bar{\sigma}^2_{\beta_{44}}$	$\hat{\beta}_{44}$	$\hat{\sigma}^2_{\beta_{44}}$
1	3.97	45	22.60	0.0384	0.0700	4.0E−04	0.0624	3.8E−04
2	2.65	135	8.23	0.0499	0.0699	4.0E−04	0.0593	2.1E−04
3	1.84	105	11.10	0.0439	0.0653	3.0E−04	0.0435	3.5E−05
4	1.23	120	17.10	0.0358	0.0607	3.5E−04	0.0423	3.9E−05
5	2.33	75	23.81	0.0372	0.0597	2.7E−04	0.0420	2.6E−05
6	2.42	90	19.66	0.0391	0.0460	5.6E−05	0.0415	1.3E−05
7	1.15	30	5.79	0.0435	0.0699	4.0E−04	0.0726	4.3E−04
8	1.49	135	8.20	0.0425	0.0633	3.1E−04	0.0509	1.6E−04
9	1.35	90	6.28	0.0500	0.0661	2.8E−04	0.0644	8.3E−05
10	2.88	30	13.89	0.0392	0.0392	6.4E−05	0.0405	3.8E−05
11	3.57	45	21.80	0.0383	0.0454	2.1E−05	0.0445	1.7E−05
12	2.95	60	16.15	0.0416	0.0448	4.9E−05	0.0427	2.5E−05
13	3.97	135	24.76	0.0376	0.0527	6.4E−05	0.0477	4.0E−05
14	2.41	150	20.26	0.0353	0.0445	6.3E−05	0.0445	6.1E−05
15	2.85	60	23.82	0.0375	0.0444	9.2E−06	0.0436	7.9E−06
16	1.85	105	19.53	0.0377	0.0401	5.2E−05	0.0402	1.4E−05
17	3.93	150	10.05	0.0468	0.0496	5.3E−05	0.0521	4.2E−05
18	3.02	30	23.15	0.0355	0.0443	3.3E−05	0.0443	3.2E−05
19	2.32	150	18.69	0.0357	0.0439	2.0E−05	0.0439	1.9E−05
20	1.87	75	7.10	0.0524	0.0633	1.3E−04	0.0606	3.1E−05
21	2.53	105	17.08	0.0407	0.0417	1.0E−05	0.0409	5.1E−06
22	1.34	135	19.75	0.0346	0.0474	3.0E−05	0.0463	2.6E−05
23	1.68	105	9.74	0.0448	0.0492	3.9E−05	0.0462	2.5E−05
24	2.44	90	24.78	0.0371	0.0442	5.6E−06	0.0434	4.9E−06
25	1.73	30	21.82	0.0340	0.0492	3.0E−05	0.0492	2.9E−05
26	2.16	150	13.66	0.0375	0.0429	4.4E−05	0.0423	3.2E−05
27	3.46	30	19.46	0.0375	0.0404	8.7E−06	0.0404	8.4E−06
28	1.22	135	18.37	0.0348	0.0470	1.4E−05	0.0462	1.2E−05
29	3.77	150	15.47	0.0403	0.0388	1.4E−05	0.0390	1.1E−05
30	1.67	45	10.96	0.0401	0.0438	3.8E−05	0.0419	1.9E−05
31	3.12	30	16.42	0.0382	0.0397	6.5E−06	0.0398	5.7E−06
32	1.33	120	16.48	0.0364	0.0422	5.3E−06	0.0418	4.4E−06
33	2.80	105	5.89	0.0641	0.0690	3.6E−04	0.0774	7.9E−05
34	2.22	150	14.07	0.0374	0.0413	6.2E−06	0.0412	5.6E−06
35	3.51	45	24.80	0.0372	0.0442	2.6E−06	0.0441	2.5E−06
36	1.75	135	9.53	0.0421	0.0457	2.3E−05	0.0441	1.7E−05
37	2.37	150	14.46	0.0376	0.0407	2.3E−06	0.0407	2.2E−06
38	2.67	60	6.58	0.0582	0.0709	9.1E−05	0.0704	1.2E−04

Table A.9 (*continued*).

SS_n	H_s	β_W	T_p	β^*_{44}	$\bar{\beta}_{44}$	$\bar{\sigma}^2_{\beta_{44}}$	$\hat{\beta}_{44}$	$\hat{\sigma}^2_{\beta_{44}}$
39	1.76	45	24.35	0.0345	0.0471	1.7E−05	0.0465	1.6E−05
40	1.33	45	13.15	0.0371	0.0432	1.2E−05	0.0424	8.8E−06
41	3.18	75	5.61	0.0683	0.0758	1.5E−04	0.0758	1.5E−04
42	1.93	120	6.50	0.0530	0.0637	4.0E−05	0.0620	2.3E−05
43	3.48	75	6.49	0.0646	0.0743	2.5E−04	0.0866	1.2E−04
44	2.35	60	12.47	0.0437	0.0434	1.6E−05	0.0417	7.8E−06
45	1.28	150	8.69	0.0393	0.0541	1.3E−04	0.0457	5.8E−05
46	3.66	75	7.58	0.0604	0.0797	2.1E−04	0.0620	1.8E−05
47	3.23	60	9.73	0.0506	0.0571	1.8E−04	0.0569	6.7E−05
48	1.37	150	13.14	0.0362	0.0459	2.6E−05	0.0449	2.2E−05
49	3.57	120	6.41	0.0635	0.0783	5.9E−05	0.0715	4.4E−05
50	1.20	150	11.91	0.0365	0.0460	2.3E−05	0.0446	1.8E−05
51	1.55	60	7.95	0.0456	0.0518	3.4E−05	0.0473	1.8E−05
52	1.52	45	12.61	0.0381	0.0413	2.5E−06	0.0411	2.2E−06
53	3.77	30	19.75	0.0379	0.0399	3.9E−06	0.0399	3.8E−06
54	3.00	45	22.49	0.0374	0.0411	5.5E−06	0.0410	4.9E−06
55	1.77	120	23.59	0.0355	0.0443	6.9E−06	0.0439	6.3E−06
56	1.75	45	7.27	0.0461	0.0524	2.6E−05	0.0476	1.7E−05
57	3.95	75	15.69	0.0448	0.0654	3.4E−04	0.0462	7.1E−05
58	3.04	135	13.27	0.0431	0.0413	5.5E−06	0.0411	4.3E−06
59	2.21	60	24.30	0.0364	0.0423	4.1E−06	0.0421	3.8E−06
60	1.19	45	17.09	0.0351	0.0454	4.8E−06	0.0450	4.6E−06
61	2.33	75	21.20	0.0381	0.0407	1.6E−06	0.0406	1.3E−06
62	1.62	150	20.07	0.0342	0.0481	5.7E−06	0.0481	5.5E−06
63	1.97	150	18.11	0.0352	0.0445	1.6E−06	0.0445	1.6E−06
64	2.95	60	12.56	0.0451	0.0462	1.8E−05	0.0457	1.5E−05
65	3.17	135	11.35	0.0458	0.0469	7.9E−06	0.0463	7.6E−06
66	2.40	90	7.19	0.0562	0.0685	6.4E−05	0.0640	2.1E−05
67	1.56	105	11.18	0.0421	0.0427	6.3E−06	0.0416	4.0E−06
68	1.89	105	16.77	0.0392	0.0389	1.8E−06	0.0391	1.4E−06
69	1.42	150	12.77	0.0365	0.0443	4.7E−06	0.0439	4.4E−06
70	1.28	135	20.01	0.0345	0.0469	1.4E−06	0.0468	1.4E−06
71	2.48	30	22.41	0.0349	0.0455	2.8E−06	0.0455	2.7E−06
72	3.97	45	23.64	0.0380	0.0480	1.3E−05	0.0475	1.2E−05

Table A.10
The simulated sea states and the tuning inputs and outputs of β_{44} — Case_XCG for Seed128 with 2-step tuning.

SS_n	H_s	β_W	T_p	β^*_{44}	$\bar{\beta}_{44}$	$\bar{\sigma}^2_{\beta_{44}}$	$\hat{\beta}_{44}$	$\hat{\sigma}^2_{\beta_{44}}$
1	3.60	150	22.59	0.0366	0.0700	4.0E−04	0.0700	3.9E−04
2	1.79	30	19.40	0.0346	0.0700	4.0E−04	0.0665	3.3E−04
3	1.39	45	22.73	0.0341	0.0682	1.8E−04	0.0638	1.9E−04
4	1.12	75	15.63	0.0365	0.0670	1.7E−04	0.0431	2.1E−05
5	1.72	90	20.17	0.0372	0.0601	1.5E−04	0.0456	5.6E−05
6	2.94	150	20.40	0.0362	0.0486	4.0E−05	0.0465	3.1E−05
7	3.37	90	15.17	0.0443	0.0696	4.0E−04	0.0414	1.6E−05
8	2.80	90	15.59	0.0426	0.0477	1.8E−04	0.0407	1.2E−05
9	2.00	45	17.27	0.0372	0.0436	2.2E−05	0.0425	1.4E−05
10	1.36	105	11.12	0.0408	0.0463	1.8E−04	0.0411	1.7E−05
11	1.93	135	16.25	0.0375	0.0413	9.4E−06	0.0414	7.7E−06
12	1.33	120	15.00	0.0371	0.0422	1.0E−05	0.0416	7.0E−06
13	2.81	150	18.00	0.0369	0.0441	4.7E−06	0.0438	4.4E−06
14	1.75	75	6.48	0.0533	0.0685	3.9E−04	0.0748	2.9E−04
15	1.90	120	7.72	0.0490	0.0652	2.0E−04	0.0611	4.1E−05
16	2.55	120	8.27	0.0518	0.0612	2.2E−04	0.0605	3.6E−05
17	3.15	60	8.94	0.0523	0.0583	1.6E−04	0.0579	9.1E−05
18	3.79	60	13.38	0.0461	0.0421	3.6E−05	0.0448	2.5E−05
19	1.31	30	24.86	0.0331	0.0660	1.4E−04	0.0643	1.4E−04
20	3.12	60	11.44	0.0471	0.0474	7.0E−05	0.0455	3.8E−05
21	3.96	60	8.82	0.0555	0.0625	2.2E−04	0.0611	4.7E−05
22	2.68	150	22.73	0.0351	0.0519	2.2E−05	0.0519	2.1E−05
23	2.78	135	14.87	0.0411	0.0415	6.6E−05	0.0451	4.7E−05
24	3.23	90	22.04	0.0393	0.0452	1.0E−04	0.0410	1.8E−05
25	3.46	90	24.63	0.0386	0.0452	4.7E−05	0.0424	2.1E−05
26	1.38	105	22.24	0.0352	0.0510	8.8E−06	0.0502	8.2E−06
27	3.72	135	22.40	0.0382	0.0472	6.6E−05	0.0458	5.1E−05
28	2.72	30	17.03	0.0371	0.0426	1.9E−06	0.0425	1.8E−06
29	3.19	45	10.69	0.0469	0.0492	5.1E−05	0.0505	3.4E−05
30	1.90	135	20.10	0.0359	0.0474	2.0E−06	0.0473	1.9E−06
31	1.20	30	21.08	0.0335	0.0631	6.6E−05	0.0632	6.7E−05
32	1.49	30	9.75	0.0388	0.0539	1.8E−04	0.0423	3.0E−05

(*continued on next page*)

Table A.10 (*continued*).

SS_n	H_s	β_W	T_p	β^*_{44}	$\bar{\beta}_{44}$	$\bar{\sigma}^2_{\beta_{44}}$	$\hat{\beta}_{44}$	$\hat{\sigma}^2_{\beta_{44}}$
33	1.40	60	8.80	0.0430	0.0491	4.6E−05	0.0423	1.2E−05
34	2.97	105	24.73	0.0377	0.0448	2.9E−05	0.0431	1.9E−05
35	2.27	135	12.44	0.0413	0.0413	1.6E−05	0.0409	1.0E−05
36	3.95	90	13.38	0.0479	0.0556	1.6E−04	0.0437	3.2E−05
37	2.21	105	23.40	0.0371	0.0508	4.6E−05	0.0460	2.8E−05
38	1.76	45	21.29	0.0352	0.0502	2.6E−06	0.0499	2.4E−06
39	1.65	105	21.79	0.0362	0.0479	5.8E−06	0.0472	5.5E−06
40	3.53	120	5.73	0.0673	0.0705	3.8E−04	0.0770	1.1E−04
41	3.07	45	23.35	0.0372	0.0474	1.5E−05	0.0468	1.4E−05
42	1.61	120	6.32	0.0504	0.0691	1.7E−04	0.0625	5.8E−05
43	3.12	75	17.62	0.0415	0.0403	7.7E−06	0.0402	4.0E−06
44	3.52	30	12.51	0.0422	0.0428	9.2E−06	0.0420	6.6E−06
45	3.24	90	12.25	0.0475	0.0460	1.8E−05	0.0442	1.3E−05
46	3.25	60	5.83	0.0651	0.0755	1.2E−04	0.0691	6.8E−05
47	1.67	75	17.27	0.0380	0.0423	2.9E−06	0.0418	2.4E−06
48	1.72	60	11.88	0.0412	0.0403	4.8E−06	0.0402	2.9E−06
49	3.63	60	24.95	0.0380	0.0426	9.4E−06	0.0422	7.8E−06
50	3.61	105	17.85	0.0423	0.0408	1.2E−05	0.0404	6.0E−06
51	2.83	75	13.71	0.0443	0.0427	9.4E−06	0.0417	5.8E−06
52	1.62	150	16.24	0.0353	0.0510	1.9E−05	0.0506	1.8E−05
53	1.62	30	10.67	0.0383	0.0418	2.0E−05	0.0417	1.2E−05
54	2.31	60	18.50	0.0389	0.0436	6.1E−06	0.0428	4.9E−06
55	2.70	135	21.01	0.0375	0.0455	2.7E−06	0.0453	2.6E−06
56	3.27	60	22.06	0.0387	0.0424	4.9E−06	0.0420	4.2E−06
57	2.55	75	24.19	0.0373	0.0456	6.4E−06	0.0446	5.7E−06
58	3.06	45	20.93	0.0381	0.0445	2.1E−06	0.0444	2.0E−06
59	1.77	120	8.54	0.0461	0.0510	1.6E−05	0.0496	1.4E−05
60	3.80	135	18.02	0.0405	0.0409	3.1E−06	0.0408	2.7E−06
61	3.46	120	18.07	0.0411	0.0402	1.7E−06	0.0402	1.5E−06
62	1.60	60	17.73	0.0369	0.0433	5.5E−07	0.0433	5.3E−07
63	1.52	30	8.08	0.0408	0.0462	7.5E−05	0.0411	1.7E−05
64	3.77	150	11.76	0.0438	0.0447	6.0E−06	0.0440	5.4E−06
65	3.36	90	21.67	0.0397	0.0412	3.3E−06	0.0410	2.5E−06
66	2.60	60	18.56	0.0394	0.0426	2.1E−06	0.0422	1.9E−06
67	1.21	120	23.76	0.0340	0.0565	6.5E−06	0.0561	6.2E−06
68	2.90	30	5.96	0.0524	0.0670	7.3E−05	0.0650	5.5E−05
69	1.57	30	7.58	0.0416	0.0441	2.6E−05	0.0419	1.2E−05
70	2.35	135	12.39	0.0417	0.0412	1.4E−06	0.0410	1.2E−06
71	3.45	45	24.22	0.0373	0.0452	2.5E−06	0.0451	2.4E−06
72	1.54	135	11.92	0.0387	0.0397	4.9E−06	0.0398	3.8E−06

References

Bitner-Gregersen, E.M., Hagen, Ø., 1990. Uncertainties in data for the offshore environment. Struct. Saf. 7 (1), 11–34. http://dx.doi.org/10.1016/0167-4730(90)90010-M.

DNV GL, 2018. Wasim user manual. Technical Report.

DNVGL-ST-N001, 2016. Marine operations and marine warranty.

Erickson, C.B., Ankenman, B.E., Sanchez, S.M., 2018. Comparison of Gaussian process modeling software. European Journal of Operational Research (ISSN: 0377-2217) 266 (1), 179–192. http://dx.doi.org/10.1016/j.ejor.2017.10.002.

Falzarano, J., Somayajula, A., Seah, R., 2015. An overview of the prediction methods for roll damping of ships. Ocean Syst. Eng. 5 (2), 55–76.

Han, X., Leira, B.J., Sævik, S., 2021a. Vessel hydrodynamic model tuning by discrete Bayesian updating using simulated onboard sensor data. Ocean Eng. 220, http://dx.doi.org/10.1016/j.oceaneng.2020.108407, URL: https://www.sciencedirect.com/science/article/pii/S0029801820313147.

Han, X., Leira, B.J., Sævik, S., Ren, Z., 2021b. Onboard tuning of vessel seakeeping model parameters and sea state characteristics. Mar. Struct. 78, http://dx.doi.org/10.1016/j.marstruc.2021.102998.

Han, X., Ren, Z., Leira, B.J., Sævik, S., 2021c. Adaptive identification of lowpass filter cutoff frequency for online vessel model tuning. Ocean Eng. Revision under review.

Han, X., Sævik, S., Leira, B.J., 2020. A sensitivity study of vessel hydrodynamic model parameters. In: Proceedings of the ASME 2020 39th International Conference on Ocean, Offshore and Arctic Engineering, Vol. 1. Virtual, Online.

Himeno, Y., 1981. Prediction of ship roll damping - state of the art. Technical Report, The University of Michigan, College of Engineering, Department of Naval Architecture and Marine Engineering, USA.

Ikeda, Y., Himeno, Y., Tanaka, N., 1978a. On eddy making component of roll damping force on naked hull. Technical Report 00403, Osaka Prefecture University.

Ikeda, Y., Himeno, Y., Tanaka, N., 1978b. Components of roll damping of ship at forward speed. Technical Report 00404, Osaka Prefecture University.

Ikeda, Y., Himeno, Y., Tanaka, N., 1978c. A prediction method for ship roll damping. Technical Report 00405, Osaka Prefecture University.

Ikeda, Y., Komatsu, K., Tanaka, N., 1979. On roll damping force of ship-effects of hull surface pressure created by bilge keels. Technical Report 00402, Osaka Prefecture University.

Irkal, M.A.R., Nallayarasu, S., Bhattacharyya, S.K., 2016. CFD approach to roll damping of ship with bilge keel with experimental validation. Appl. Ocean Res. 55, 1–17.

ITTC, 2011. Recommended procedures and guidelines: Numerical estimation of roll damping. Technical Report, International Towing Tank Conference.

Kaplan, P., 1966. Lecture notes on nonlinear theory of ship roll motion in a random seaway.

Kring, D.C., 1994. Time domain ship motions by a three-dimensional Rankine panel method (Ph.D. thesis). Massachusetts Institute of Technology.

Labbe, R., 2018. Kalman and Bayesian filters in Python. https://github.com/rlabbe/Kalman-and-Bayesian-Filters-in-Python,

Larsen, C.M., Lian, W., Bachynski, E.E., Kristiansen, T., Myrhaug, D., 2019. Lecture notes in TMR4182 marine dynamics.

Neumann-Brosig, M., Marco, A., Schwarzmann, D., Trimpe, S., 2020. Data-efficient autotuning with Bayesian optimization: An industrial control study. IEEE Trans. Control Syst. Technol. 28 (3), 730–740.

Pedregosa, F., Varoquaux, G., Gramfort, A., Michel, V., Thirion, B., Grisel, O., Blondel, M., Prettenhofer, P., Weiss, R., Dubourg, V., Vanderplas, J., Passos, A., Cournapeau, D., Brucher, M., Perrot, M., Duchesnay, E., 2011. Scikit-learn: Machine learning in python. J. Mach. Learn. Res. 12, 2825–2830.

Qiu, W., Junior, J.S., Lee, D., Lie, H., Magarovskii, V., Mikami, T., Rousset, J.-M., Sphaier, S., Tao, L., Wang, X., 2014. Uncertainties related to predictions of loads and responses for ocean and offshore structures. Ocean Eng. 86, 58–67.

Rasmussen, C.E., Williams, C.K.I., 2006. Gaussian processes for machine learning. The MIT Press, ISBN: 026218253X, URL: https://www.GaussianProcess.org/gpml.

Scheick, J.T., 1997. Linear algebra with applications, Vol. 81. McGraw-Hill New York.

Shepard, D., 1968. A two-dimensional interpolation function for irregularly-spaced data. In: Proceedings of the 1968 23rd ACM National Conference. In: ACM '68, Association for Computing Machinery, New York, NY, USA, pp. 517–524. http://dx.doi.org/10.1145/800186.810616.

Söder, C.-J., Rosén, A., 2015. A framework for holistic roll damping prediction. In: International Ship Stability Workshop.

Söder, C.-J., Rosén, A., Huss, M., 2017. Ikeda revisited. J. Mar. Sci. Technol..

A.5 Paper A5

Paper A5:
X. Han, B. J. Leira, S. Sævik, G. Radhakrishnan, S. Skjong, and L. T. Kyllingstad, 2021. A framework for condition monitoring and risk-based decision support involving a vessel state observer. In: *Proceedings of the ASME 2021 40th International Conference on Ocean, Offshore and Arctic Engineering*, volume 2, Virtual, Online.

Proceedings of the ASME 2021 40th International Conference on Ocean, Offshore and Arctic Engineering
OMAE2021
June 21-30, 2021, Virtual, Online

OMAE2021-61850

A FRAMEWORK FOR CONDITION MONITORING AND RISK-BASED DECISION SUPPORT INVOLVING A VESSEL STATE OBSERVER

Xu Han*, Bernt J. Leira, Svein Sævik, Gowtham Radhakrishnan
Department of Marine Technology, SFI MOVE
Norwegian University of Science and Technology
Trondheim, Norway

Stian Skjong, Lars T. Kyllingstad
SINTEF Ocean AS
Trondheim, Norway

ABSTRACT

Digital twins have attracted significant attention across different domains for decades. In the maritime and the energy industries, digital twins have been mainly used for system condition monitoring, project visualization, crew training, real-time decision making/support, and predictive maintenance based on onsite measurement data from onboard sensors. Such a digital twin normally presumes the vessel's operational condition by assistance from sensors and engineering judgement. However, a vessel's operational condition and loading state may shift quite often due to the frequently changing operational scenarios, tasks, and environmental conditions. In addition, the true vessel state (e.g., inertia distribution) may deviate from the intended one according to planning due to possible engineering errors. Even though there are sensors helping to monitor vessel condition such as draft monitoring systems and ballast systems, several important vessel parameters are difficult to measure directly, e.g., moment of inertia, center of gravity, and nonlinear hydrodynamic damping. This paper proposes a framework for monitoring vessel condition and providing decision support based on quantitative risk assessment, through a vessel state observer which is able to self-tune the important but uncertain vessel parameters by utilizing the available prior knowledge, vessel measurements, and information about the associated sea states. The tuned vessel parameters improve the information about the real-time vessel condition and consequently assist to improve the prediction accuracy of vessel seakeeping performance in the near future for the emerging wave conditions. Furthermore, the tuned results and the response prediction can then be applied to a decision support system, quantitatively evaluating potential risk and providing suggestions. The framework consists of 5 modules, i.e., wave data acquisition and processing, vessel data acquisition and processing, vessel seakeeping model tuning, real-time vessel motion and critical structural response prediction, and risk awareness and avoidance. Details of each module are described in the paper. The proposed framework can also assist in the development of autonomous ships.

Nomenclature

β_{33}	Additional heave damping coefficient
β_{44}	Additional roll damping coefficient
β_{Wp}	The prevailing wave direction for short-crested waves
β_{W}	Wave direction w.r.t. vessel coordinate system
$\boldsymbol{\phi}$	The random variable vector representing uncertain VCRPs
$\boldsymbol{\phi}_r$	The r^{th} point of the discrete distribution of $\boldsymbol{\phi}$, $r \in [1,R]$
$\boldsymbol{\theta}$	The random variable vector representing uncertain wave data
$\boldsymbol{\theta}_s$	The s^{th} point of the discrete distribution of $\boldsymbol{\theta}$, $s \in [1,S]$
$\hat{\sigma}_j$	The standard deviation of the filtered signal $\hat{x}_j(t)$
$\hat{x}_j(t)$	The filtered time series for sensor signal $x_j(t)$
ω	Wave frequency
$\overline{\overline{W}}_{j,s}$	Likelihood function of $\boldsymbol{\theta}_s$ being the truth with respect

*Address all correspondence to this author (email: xu.han@ntnu.no).

	to the measuring quantity j, across all the considered $\boldsymbol{\phi}_r$ for $r = 1,2,\ldots,R$
$\overline{\overline{W}}_j$	Likelihood function for the measuring quantity j, across all the considered $\boldsymbol{\phi}_r$ for $r = 1,2,\ldots,R$ and $\boldsymbol{\theta}_s$ for $s = 1,2,\ldots,S$
ϕ_m	The m^{th} VCRP variable in the vector $\boldsymbol{\phi}$
$\sigma_{r,j,s}$	The standard deviation of $S_{r,j,s}(\omega)$
θ_n	The n^{th} variable in the vector $\boldsymbol{\theta}$
H_s	Significant wave height
$H_{r,j}$	The RAO based on VCRPs $\boldsymbol{\phi}_r$, corresponding to the measuring quantity index j
J	The total number of measuring vessel motion quantities for one sea state
j	Index of measuring vessel motion quantity
k	The sea state number
M	The number of considered variables for tuning
N	The number of considered variables in $\boldsymbol{\theta}$
n_s	Spreading parameter for short-crested waves
N_t	Number of time steps for the sensor signals
N_ω	Number of discrete frequencies for each 1D spectrum
p	Power parameter
R	The total number of discrete points over the joint distribution of uncertain VCRPs
S	The total number of discrete points over the joint distribution of uncertain wave data
$S_{\zeta\zeta,s}$	Wave spectrum based on wave information $\boldsymbol{\theta}_s$
$S_{r,j,s}$	The possible response spectrum based on VCRPs $\boldsymbol{\phi}_r$ and wave information $\boldsymbol{\theta}_s$, corresponding to the measuring quantity index j
T_p	Wave spectral peak period
$w_{r,j,s}$	Likelihood of the considered $\boldsymbol{\phi}_r$ and $\boldsymbol{\theta}_s$ being the truth with respect to the measuring quantity j
$x_j(t)$	The original signal for the j^{th} sensor measurement for a certain sea state
COG	Center of gravity
DOF	Degree of freedom
GMT	Free surface correction to the transverse metacentric height
GPS	Global positioning system
MRU	Motion reference unit
ODSS	Onboard decision support system
PDF	Probability density function
PMF	Probability mass function
RAO	Response amplitude operator
RESP	Module of real-time vessel motion and critical structural response prediction
RISK	Module of risk awareness and avoidance
SSR	Sensor screening ratio, i.e., α
TUN	Module of vessel seakeeping model tuning
VAP	Vessel data acquisition and processing
VARP	Vessel attitude related parameter
VCRP	Vessel condition related parameter
WAP	Wave data acquisition and processing
XCG	Longitudinal coordinate of vessel COG
ZCG	Vertical coordinate of vessel COG

1 INTRODUCTION

With the increasing interest for exploring sustainable energy, aquaculture, and many other sources towards harsher, deeper, and colder ocean environments, safety and cost-efficiency of marine operations can play a crucial role for some emerging industries, such as offshore wind energy. Heavier, larger, and more complex structures and systems are designed and installed offshore. Marine operations such as transportation, installation, and underwater inspection and maintenance usually involve cooperation and interaction among many systems, subject to complicated environmental loads. In addition, the offshore environments such as winds, waves, and currents are well known to be associated with high uncertainties and random nature. Considering the complexities and uncertainties, it is therefore critical to design marine operation onshore before the execution so that operational limits with respect to environmental conditions are clearly given to operators. In addition, conservative assumptions are usually involved in order to reduce the dimension of the reported operational limit diagrams, and to improve the readability. Therefore, a reliable, safe, but also cost-efficient marine operation should put efforts on 1) reducing and even quantifying the uncertainties of the influential structural and environmental parameters and 2) reducing the aforementioned conservatism by increasing the reporting dimension of the operational limit diagrams and adaptively visualizing the limit without compromising the readability.

Floating structures are heavily involved in various marine operations. The floater dynamics when exposed to environmental loads may dominate the operational limit, where wave-induced floater motions in wave frequency region are the most difficult to control. Therefore, only waves and the wave-induced motions within the wave frequency domain for vessels are considered in the present research. Knowledge about the waves is one of the three most important parts for a reliable vessel motion prediction. The other two are the knowledge about the vessel condition and the theoretical modelling about vessel hydrodynamics in response to the waves. In practice, a floater may be considered as a rigid body and its dynamics may be well represented by linearized transfer functions [1] for moderate seas, primarily based on the linear potential theory. The linear transfer functions typically describe the relation between wave elevation and rigid body motions in 6 degrees of freedom (DOFs), which are also known as the response amplitude operators (RAOs), and are widely applied in the design of marine operations [1].

Uncertainty reduction of information about waves, vessel conditions, and the vessel dynamics are therefore of great aca-

demic and engineering interest for safe and cost-efficient marine operations, as well as for developing reliable and robust autonomous ships. So far, most researches have been focused on reducing the uncertainties of wave predictions [2–4], and hydrodynamic system modelling [5]. Through the authors' many years of industrial and engineering working experience, almost every project involves discussions arguing that the applied RAOs are conservative due to some assumptions. And sometimes such arguments about conservatism can be skeptical. On the other hand, the introduced conservatism will reduce the operational limit based on the current engineering practices. There are so many possibilities making the applied vessel RAOs wrongly determined and used, e.g., due to mutual misunderstanding, misinterpretation of engineering results from different disciplines, engineering errors, some unplanned arrangements, and the fact that the operation may just be different from the planned simply due to some emergent or urgent issues. Reducing the uncertainties of onsite vessel conditions has been a challenge even though the significance has been well recognized [6]. Tuning or updating vessel condition related parameters (VCRPs) based on onboard vessel data and wave data is challenging because this is a multimodal, multi-dimensional, and nonlinear problem [7].

Han et al. [7] recently proposed a tuning algorithm which can tune the expectation and the variance of VCRPs based on available onboard data. This paper further develops the conceptual tuning algorithm, including the wave data uncertainties. Then such a tuning system, functioning as a vessel state observer, can monitor the vessel conditions especially for the important vessel parameters that are difficult to measure directly, such as moment of inertia, center of gravity, and nonlinear hydrodynamic damping. In addition, an embedded risk-based onboard decision support system (ODSS) can be implemented, providing warnings of potential risks and suggesting actions for risk avoidance, by performing real-time simulations based on the monitored vessel conditions and forecasted sea states. Such ODSS can be further applied to operation optimisation by giving suggestions on operational actions to adjust some critical parameters (e.g., vessel speed u, vessel heading β_V, and the vessel's loading condition). Suggestions may be achieved by quickly exploring the influences on the critical structural responses from possible system parameters, identifying the sensitive parameters, and then searching for the optimal solution in balance with risk reduction and additional cost. All the involved calculations from tuning of uncertain parameters, vessel motion prediction, to quantitative risk assessment and operation optimization, must be carried out in real time. By "real time" we here mean that the assessment must be completed and the consequent decision support information must be provided within a short enough time frame so that the users can take the suggested relevant actions. Thus, an adaptive vessel state observer can help to improve the safety and cost efficiency of marine operations through a risk-based ODSS.

The paper is organized as follows. Section 2 provides an overview of the proposed framework involving a vessel state observer. Following the overview, Sections 3 to 7 explain each of the five modules of the framework, respectively. Finally, Section 8 summarizes the current work and suggests some important future work.

2 FRAMEWORK OVERVIEW

The framework overview is illustrated in Figure 1, which indicates the relations between modules and shows how the model tuning can assist on vessel condition monitoring and decision support through the vessel state observer. The framework mainly consists of 5 interactive modules. The main inputs and outputs of the 5 modules are summarized in Table 1.

Two data streaming modules are required, namely wave information acquisition and processing (WAP), and vessel data acquisition and processing (VAP). These two modules mainly acquire and process the necessary input data for the next three modules. The state observer is aimed at making full use of available environmental data and onboard vessel data. Therefore, the quality and amount of available data can be critical. However, data are subject to measurement errors, while the true values are also normally unknown. When combining data from different sources, data synchronization and fusion are typically challenging [8]. In reality, data streaming has to consider signal filtering, fault detection, sensor fusion, synchronization, and preferably assess the data quality along the data streaming pipeline. DNV GL [9] proposed a framework on data quality assessment in order to ensure sufficient data quality. In practice, different data sources are subject to different uncertainties. Therefore, uncertainty quantification is of huge interest and can assist the data streaming process including data acquisition and processing. Based on the valuable data from WAP and VAP modules, VCRPs can then be tuned in the next module of vessel seakeeping model tuning. The tuning results will in return benefit the vessel condition monitoring in VAP. Furthermore, prediction of vessel motions and critical structural responses can be performed based on wave forecast data in WAP and vessel data in VAP. Lastly, quantitative risk assessment can be conducted in the module of risk awareness and avoidance, aiming at quantifying the probability of occurrence for the pre-identified events and providing suggestions through ODSS by searching for optimal solutions. The critical response limit is considered as being the input to the module RESP which predicts the vessel motion and critical response, while the permissible probability of occurrence for the event is considered as being the required input to the module RISK which quantifies the associated exceedance probability of the critical response and takes care of the risk awareness and avoidance. Details are provided in the following sections.

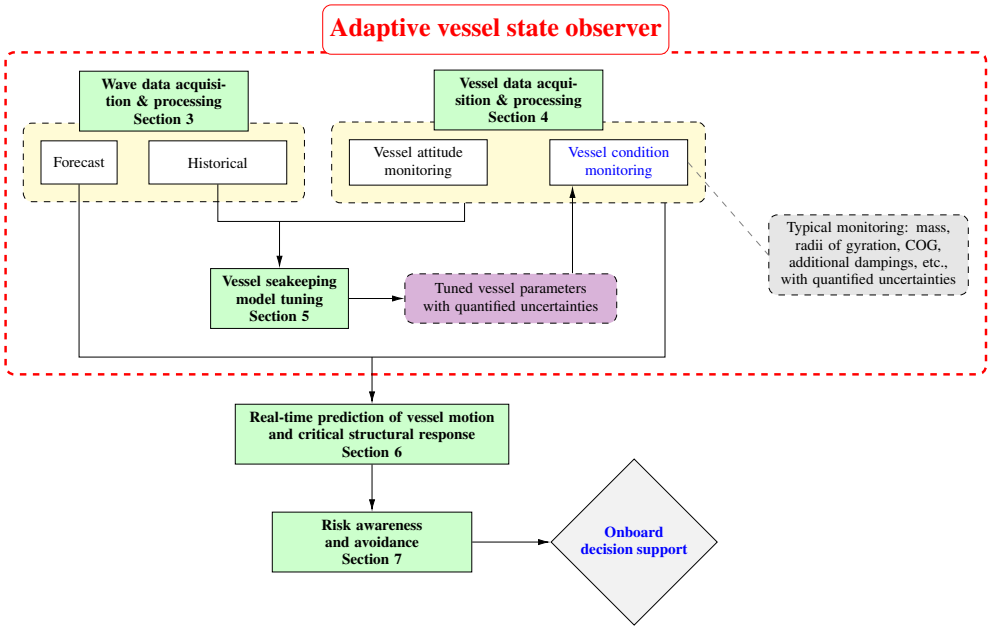

FIGURE 1. OVERVIEW OF THE PROPOSED ADAPTIVE VESSEL STATE OBSERVER FOR VESSEL CONDITION MONITORING AND DECISION SUPPORT.

3 WAVE DATA ACQUISITION AND PROCESSING

This section describes the WAP module. Wave data can be categorized into historical and forecast data, as shown in Figures 1 and 2. The historical wave data are normally subject to less uncertainty than forecast, and therefore are preferred to apply to seakeeping model parameter tuning process. Whereas, real-time vessel motion and critical structural response predictions have to consider the forecasts corresponding to the predicting timeline.

As illustrated in Figure 2, historical wave data can be obtained from instrumental measurements, wave model analysis (i.e., hindcast), or their combination. Wave data measured by instruments such as waverider buoys, shipborne wave recorders, satellite altimeters, and wave radars may be considered to have less uncertainties than from visual observations or wave model analyses. Onboard wave measuring instruments are preferred for vessel condition monitoring and decision support, in order to avoid potential remote communicating challenges. Researches on ODSSs in the last two decades mostly focused on developing and applying onboard wave measuring systems to ensure timely and sufficiently accurate wave forecast for real-time vessel and structural response predictions. For examples, waves can be measured on board by 1) coherent Doppler marine radar systems [10, 11]; 2) non-coherent nautical radar systems, e.g.,

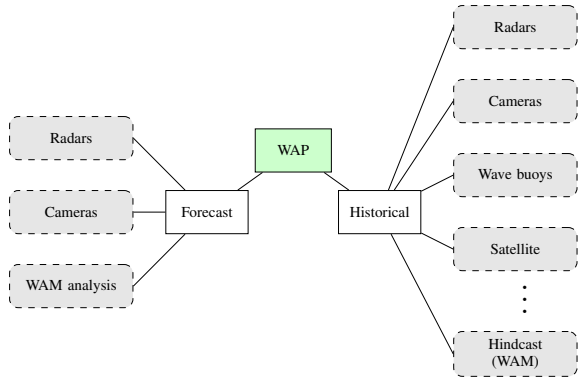

FIGURE 2. WAVE DATA SOURCES.

WaMoS II system [3, 12]; 3) special cameras based on light detection and ranging (LIDAR) technology [13,14]; 4) using vessel responses and applying "ship as a wave buoy" analogy [4, 15]; and 5) deploying wave buoys near the operating location and connecting to the floater directly. The WAP module should also be able to acquire historical wave data from other instruments or

TABLE 1. INPUTS AND OUTPUTS OF THE FRAMEWORK MODULES.

Module	Input	Output
WAP [a)]	1) Measured historical waves (time records); 2) Historical waves by wave model analysis ($S_{\zeta\zeta}(\omega,\beta_W)$ or $\boldsymbol{\theta}$); 3) Measured forecasted waves (time records); 4) Wave forecast by wave model analysis ($S_{\zeta\zeta}(\omega,\beta_W)$ or $\boldsymbol{\theta}$); 5) The measuring or analysis uncertainties.	Cleaned and quality-controlled: 1) $\boldsymbol{\theta}$ and $P(\boldsymbol{\theta})$ for historical waves; 2) $\boldsymbol{\theta}$ and $P(\boldsymbol{\theta})$ for forecasted waves; 3) $S_{\zeta\zeta}(\omega,\beta_W)$ for forecasted waves.
VAP [b)]	1) Time records of measurements from onboard systems (GPS, INS, etc.); 2) Information on VCRPs (technical reports, previously tuned VCRPs).	Cleaned and quality-controlled: 1) VARPs $\boldsymbol{\gamma}$; 2) VCRPs $\boldsymbol{\phi}$ and $P(\boldsymbol{\phi})$.
TUN [c)]	1) $\boldsymbol{\theta}$ and $P(\boldsymbol{\theta})$ for historical waves from WAP; 2) VARPs $\boldsymbol{\gamma}$ from VAP; 3) VCRPs $\boldsymbol{\phi}$ and $P(\boldsymbol{\phi})$ from VAP as prior; 4) RAO database for $x_j(t)$, $j=1,2,...,J$ and $\boldsymbol{\phi}_r$, $r=1,2,...,R$.	1) Tuned VCRPs $\boldsymbol{\phi}$ and $P(\boldsymbol{\phi})$ back to VAP module; 2) Report the tuned $PMF(\boldsymbol{\phi})$, or $\mathbf{E}(\boldsymbol{\phi})$ and $\mathbf{CoV}(\boldsymbol{\phi})$.
RESP [d)]	1) Wave forecast $S_{\zeta\zeta}(\omega,\beta_W)$ (or $\boldsymbol{\theta}$, $P(\boldsymbol{\theta})$) from WAP; 2) The critical vessel / structural response and its limiting criteria; 3) VARPs $\boldsymbol{\gamma}$ and VCRPs $\boldsymbol{\phi}$ and $P(\boldsymbol{\phi})$ from VAP; 4) RAOs between wave elevations and the critical response based on $\boldsymbol{\gamma}$ and $\boldsymbol{\phi}$.	1) Predicted response spectrum; 2) Predicted extreme response.
RISK [e)]	1) Wave forecast $S_{\zeta\zeta}(\omega,\beta_W)$ (or $\boldsymbol{\theta}$, $P(\boldsymbol{\theta})$) from WAP; 2) Identified failure event and its criteria; 3) VARPs $\boldsymbol{\gamma}$ and VCRPs $\boldsymbol{\phi}$ and $P(\boldsymbol{\phi})$ from VAP; 4) RAOs between wave elevations and the critical response based on $\boldsymbol{\gamma}$ and $\boldsymbol{\phi}$.	1) Probability of event occurrence; 2) Warning if necessary; 3) Optimal suggestion on risk avoidance.

[a)] WAP: module of wave data acquisition and processing
[b)] VAP: module of vessel data acquisition and processing
[c)] TUN: module of vessel seakeeping model tuning
[d)] RESP: module of real-time vessel motion and critical structural response prediction
[e)] RISK: module of risk awareness and avoidance

hindcast when remote communication allows so.

The uncertainties of measured wave data depend on the type and the installation of instruments, the sensor quality, the sampling, temporal and spatial variability, etc. [16, 17]. The uncertainties from some types of instruments are more stable across mild to harsh seas, while some other types may outperform with much less measuring errors for a specific range of wave powers [18]. The World Meteorological Organization (WMO) published general requirements with respect to the instrumental performance [19], as shown in Table 2.

Nowadays, the third-generation wave models (e.g., WAM [20] and WaveWatch III [21]) are widely applied for wave forecast and hindcast. WAM estimate wind generated waves and their propagation based on information about winds, geographics, etc. Wave reanalyses [22] have been continuously carried out to improve the historical wave data quality by using the continuously developed methodologies, increased computational capacity and resolutions. The uncertainties of the hindcast wave data may be represented by the ensemble spreading [23]. However, such ensemble spreading may underestimate the analysis uncertainties because it only considers the random errors but not the systematic ones. Wave data accuracy can be further improved

TABLE 2. TYPICAL WAVE MEASUREMENT UNCERTAINTIES (2σ) [19]

Variable	H_s	T_p	β_W
WMO required	0.5m for $H_s \leq 5$m; 10% for $H_s > 5$m	0.5 s	10°
Typical moored buoy	0.2m or 10%	1.0 s	10°

H_s: significant wave height
T_p: wave spectral peak period
β_W: wave direction

by combining multiple measuring sources and analyzed wave results.

Wave forecast data are usually from the wave model analysis (e.g., WAM) considering nonlinear interactions between wave components. The uncertainties of the forecast data depend on the location, season, resolution, the forecasting time, etc. It is therefore important to take such uncertainties into account in marine operations, e.g., by reducing the operational window based on the suggested alpha factor [1]. Typically, prediction of T_p is subject to much higher uncertainty than prediction of H_s [24]. Marine radars and LIDAR systems measure the wave field before waves approaching to vessel. Therefore, they can also be used as wave forecast information in a very short time ahead (e.g., up to few minutes) for real-time vessel and structural response prediction [25].

A sea state may be represented by its characteristics. For example, wave characteristics $\boldsymbol{\theta}$ may include H_s, T_p, β_W, and spreading parameter n_s for each independent wave source such as wind sea and swells in one sea state. For example, a sea state with a short-crested wind sea and a short-crested swell, $\boldsymbol{\theta}$ may be written as:

$$\begin{aligned}\boldsymbol{\theta} &= [H_{s,1} \quad T_{p,1} \quad \beta_{W,1} \quad n_{s,1} \quad H_{s,2} \quad T_{p,2} \quad \beta_{W,2} \quad n_{s,2}]^\top \\ &= [\theta_1 \quad \theta_2 \quad \dots \quad \theta_n \quad \dots \quad \theta_N]^\top\end{aligned} \tag{1}$$

where θ_n represents one wave characteristic, $n \in \{1,2,\dots,N\}$, and N is the number of wave characteristics in $\boldsymbol{\theta}$. Those parameters are also subject to uncertainties, described by discrete joint probability distribution $P(\boldsymbol{\theta})$.

The output of WAP module should contain 1) the wave characteristics $\boldsymbol{\theta}$ and their uncertainties $P(\boldsymbol{\theta})$ for historical sea states, which will be used for the module of vessel seakeeping model tuning; and 2) the forecasted wave characteristics $\boldsymbol{\theta}$ and their uncertainties $P(\boldsymbol{\theta})$, which will be used for the modules of real-time critical response prediction (RESP) and risk awareness and avoidance (RISK). WAP can also provides the wave forecast in form of wave spectrum $S_{\zeta\zeta}(\omega,\beta_W)$ for RESP module.

4 VESSEL DATA ACQUISITION AND PROCESSING

A VAP module with high quality, monitoring the vessel attitudes and conditions with uncertainty quantification is also vital for the vessel state observer and the whole framework. The vessel attitude related parameters (VARPs) include vessel speed, heading, draft, trim, heel, and the rigid body motions, while the vessel condition related parameters (VCRPs) include damping terms and inertia distribution related terms such as mass, radii of gyration (i.e., r_{44}, r_{55}, r_{66}), center of gravity (COG), and transverse metacentric height (GMT). The VARPs mostly can be measured directly on board or easily deduced from measurements, e.g., by Speed and Distance Log Device, Global Positioning System (GPS), Motion Reference Unit (MRU), etc. However, the VCRPs may not be easily measured or deduced from measurements. Even though marine operations should be designed cautiously before execution, vessel conditions should be presumed in the design phase. However, the real vessel condition in operation may deviate significantly from the designed one due to simplifications, conservatism, and even mistakes made in the design and execution phases. Therefore, it is important to be able to monitor and update the VCRPs and quantify their uncertainties for the risk-based onboard decision support [6]. The proposed framework focuses on the vessel 6-DOF rigid body motions and resulting critical response of onboard structures in wave frequency region.

The VARPs are normally given in the form of time records, containing noises and errors. Signal processing including fault detection, synchronization, band-pass filtering should be applied to ensure reliable vessel motion data only in the wave frequency ranges. The vessel condition monitoring system is aimed to improve the accuracy of the relevant vessel parameters and quantify the associated uncertainties, to ensure the quality of the real-time vessel motion and critical structural response prediction (Section 6) and the quantitative risk assessment (Section 7). Therefore, the module of vessel seakeeping model tuning is the core of such a monitoring system.

5 VESSEL SEAKEEPING MODEL TUNING

Benefiting from WAP and VAP modules, quality-controlled wave and vessel data are available for tuning of VCRPs. The proposed model tuning algorithm is based on the assumption that the vessel motions can be well estimated by the linearized transfer functions between wave elevations and vessel motions, at least for the moderate seas. First of all, it is essential for a successful tuning to take all the important but uncertain VCRPs into account [7,26]. Han et al. [26] and Radhakrishnan et al. [27] quantitatively investigated the sensitivities of VCRPs on the ves-

sel seakeeping responses in operation, while Gutsch et al. [28] investigated such effects with respect to ship design.

VCRPs are formed as a random vector (denoted by $\boldsymbol{\phi}$), e.g.,

$$\begin{aligned}\boldsymbol{\phi} &= [\text{mass} \quad r_{44} \quad r_{55} \quad \text{XCG} \quad \text{ZCG} \quad \beta_{33} \quad \beta_{44} \quad \text{GMT}\ldots]^\top \\ &= [\phi_1 \quad \phi_2 \quad \ldots \quad \phi_m \quad \ldots \quad \phi_M]^\top\end{aligned} \tag{2}$$

where XCG and ZCG represent the COG coordinate along longitudinal and vertical directions. β_{33} and β_{44} are the linearized "additional" dampings for heave and roll DOFs, in addition to the damping terms calculated based on the linear potential theory. Normally, stochastic linearization is applied to linearize such nonlinear terms [29]. ϕ_m is a random variable, representing a VCRP, $m \in \{1,2,\ldots,M\}$, where M is the total number of uncertain VCRPs considered in the tuning process. In the framework, the vessel condition monitoring system can provide and obtain the probabilistic information about the uncertain VCRPs in discrete forms. In addition to VCRPs, any VARPs that can significantly influence the vessel motion RAOs within their considered uncertainty ranges should be included in the vector $\boldsymbol{\phi}$, e.g., vessel draft and trim. Due to the well developed sensor and filtering technologies, normally VARPs subject to much less uncertainties than VCRPs. In the proposed framework, all the processed data and signals for VARPs are considered deterministically.

The vessel condition monitoring system requires manually initializing the uncertain VCRPs by giving the expected value and variance for each ϕ_m. The initiated values and variances can be based on the available engineering knowledge from design of the operation, and the variance may be based on engineering confidence and expert opinion. The variance may preferably be initiated larger than the actual value, to ensure the sufficient uncertainty ranges and the corresponding RAO database, according to [7]. Then the joint probability distribution can be established, e.g., by assuming a multivariate Gaussian distribution and independence between VCRPs. Any other joint probability distribution model can replace the multivariate Gaussian one if this is found to be relevant e.g., based on engineering judgement. For a convergent tuning, the resulting joint probability distribution is normally less affected by the applied initial joint distribution.

Figure 3 illustrates the process of tuning VCRPs based on wave and vessel data which are also subject to uncertainties. The algorithm, based on the previous work by Han et al. [7], is further developed here to account for the uncertainties of the wave data.

The proposed tuning algorithm discretizes the random variables, and consequently, discrete joint probability distribution $P(\boldsymbol{\phi})$ is actually achieved through the process. At each discrete point $\boldsymbol{\phi}_r$, the corresponding probability mass function is denoted by $PMF(\boldsymbol{\phi}_r)$ for $r \in \{1,2,\ldots,R\}$, where R is the total number of considered discrete combinations of random VCRPs. Correspondingly, a RAO database $H_{r,j}(\omega,\beta_\text{W})$ ($r = 1,2,\ldots,R,\ j = 1,2,\ldots,J$) at each $\boldsymbol{\phi}_r$ for each quantity measured by the inertial navigation system (INS) is established. ω is the response frequency in rad/s. The INS-measured quantity can be e.g., displacement, velocity and acceleration of heave, roll, and pitch.

Wave characteristics $\boldsymbol{\theta}$ should be acquired from WAP module, according to the vessel heading and location information from the VAP module. The probability distribution of $\boldsymbol{\theta}$ are discretized into S points $\boldsymbol{\theta}_s$, for $s = 1,2,\ldots,S$. The probability mass function of $\boldsymbol{\theta}_s$ is denoted by $PMF(\boldsymbol{\theta}_s)$. Accordingly, for a wave vector $\boldsymbol{\theta}_s = [H_{\text{s},1} \quad T_{\text{p},1} \quad \beta_{\text{W},1} \quad n_{\text{s},1} \quad \ldots H_{\text{s},i} \quad T_{\text{p},i} \quad \beta_{\text{W},i} \quad n_{\text{s},i} \quad \ldots]^\top$, the wave spectrum can be estimated based on presumed spectral type (e.g., Pierson-Moskowitz spectrum) and spreading function $D(\beta_\text{W})$ [30], considering a multi-peak spectrum:

$$S_{\zeta\zeta,s}(\omega,\beta_\text{W}) \approx \sum_i S_{\zeta\zeta,i}(\omega) D_i(\beta_\text{W}) \tag{3a}$$

$$D_i(\beta_\text{W}) = \frac{\Gamma(1+n_{\text{s},i}/2)}{\sqrt{\pi}\Gamma(1/2+n_{\text{s},i}/2)} \cos^{n_{\text{s},i}}(\beta_\text{W} - \beta_{\text{Wp},i}) \tag{3b}$$

$$S_{\zeta\zeta,i}(\omega) = \frac{5}{16} H_{\text{s},i}^2 \omega_{p,i}^4 \omega^{-5} \exp(-\frac{5}{4}(\frac{\omega}{\omega_{p,i}})^{-4}) \tag{3c}$$

where Γ is the Gamma function, $\beta_{\text{Wp},i}$ is the prevailing wave direction for each independent wave source and $|\beta_\text{W} - \beta_{\text{Wp},i}| \le \frac{\pi}{2}$. $n_{\text{s},i}$ is the spreading parameter, $2 \le n_{\text{s},i} \le 4$ for wind seas, and $n_{\text{s},i} > 7$ for swells [30]. $\omega_{p,i} = 2\pi/T_{\text{p},i}$ is the sea state peak frequency. The subscript i represents one of the independent wave sources in the multi-peak spectrum.

Then the corresponding possible response spectrum $S_{r,j,s}(\omega)$ and the response standard deviation $\sigma_{r,j,s}$ can be calculated with respect to vessel condition $\boldsymbol{\phi}_r$ for the motion measuring quantity j:

$$S_{r,j,s}(\omega) = \sum_{\beta_\text{W}} |H_{r,j}(\omega,\beta_\text{W})|^2 S_{\zeta\zeta,s}(\omega,\beta_\text{W}) \Delta\beta_\text{W} \tag{4a}$$

$$\sigma_{r,j,s} = \sqrt{\sum_{n=1}^{N_\omega} S_{r,j,s}(\omega_n) \cdot \Delta\omega_n} \tag{4b}$$

where $\Delta\beta_\text{W}$ is the wave direction interval, $\Delta\omega_n$ is the frequency interval which may be different for different discrete frequency ω_n, and whereN_ω is the number of discrete frequencies.

The vessel motion signals $x_j(t)$ are processed (e.g., for fault detection and band-pass filtering) in the VAP module, before being used in the seakeeping model tuning module. The processed signal for quantity j is denoted by $\hat{x}_j(t)$. Its standard deviation

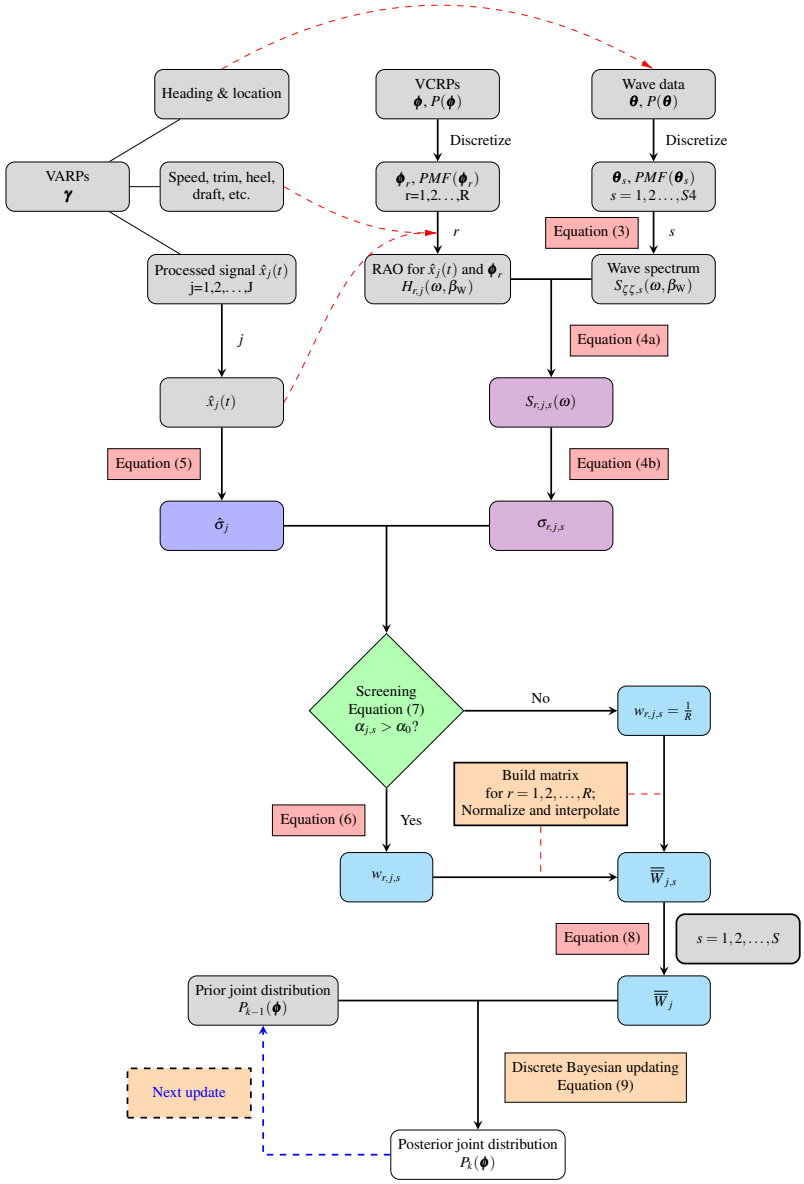

FIGURE 3. TUNING OF VCRPS FOR SEAKEEPING, BASED ON WAVE AND VESSEL DATA.

$\hat{\sigma}_j$ can thus be calculated by:

$$\hat{\sigma}_j = \sqrt{\frac{\sum_{t=1}^{N_t} \left(\hat{x}_j(t) - \bar{x}_j\right)^2}{(N_t - 1)}} \tag{5a}$$

$$\bar{x}_j = \frac{\sum_{t=1}^{N_t} \hat{x}_j(t)}{N_t} \tag{5b}$$

where N_t is the total number of time steps of the signal, and $\bar{x}_j$ is the mean value of the filtered signal.

Then the closeness between $\hat{\sigma}_j$ and $\sigma_{j,r,s}$ represents the likelihood of the considered $\boldsymbol{\theta}_s$ and $\boldsymbol{\phi}_r$ being the vectors holding the actual state values with respect to the vessel motion quantity j. Such likelihood is formulated based on inverse distance weighting [31]:

$$w_{r,j,s} = \frac{1}{\left|\sigma_{r,j,s} - \hat{\sigma}_j\right|^p} \tag{6}$$

where $p \in \mathbb{R}^+$ is called the power parameter. The value of p can be selected based on e.g., 1) the confidence of the vessel motion measurements, 2) how well the RAOs can actually represent the true relation to the wave elevations, 3) number of considered uncertain VCRP, and 4) their sensitivity and uncertainty ranges. However, application of Equation (6) may cause unrealistic likelihood estimation especially when $\sigma_{r,j,s} - \hat{\sigma}_j$ approaches zero for all $r \in [1, R]$. Therefore, a screening process is required before likelihood calculation. The less sensitive measuring quantity j for the considered VCRPs $\boldsymbol{\phi}$ at the possible sea state $\boldsymbol{\theta}_s$ should be screened out. Sensor screening ratio (SSR) $\alpha_{j,s}$ is therefore introduced as a criterion of the screening process, representing the importance of $x_j(t)$:

$$\alpha_{j,s} = \frac{\sigma^*_{R,j,s}}{\hat{\sigma}_j} \tag{7a}$$

$$\sigma^*_{R,j,s} = \sqrt{\frac{\sum_{r=1}^{R} (\sigma_{r,j,s} - \overline{\sigma}_{R,j,s})^2}{R - 1}} \tag{7b}$$

$$\overline{\sigma}_{R,j,s} = \frac{\sum_{r=1}^{R} \sigma_{r,j,s}}{R} \tag{7c}$$

where $\sigma^*_{R,j,s}$ is the standard deviation of $\sigma_{r,j,s}$, over $r = 1, 2, ..., R$. The screening criterion can for example be set to $\alpha_0 = 0.05$ [7]. If $\alpha_{j,s} < \alpha_0$, the likelihood $w_{r,j,s} = \frac{1}{R}$ applies for all $r = 1, 2, ..., R$, for the sea state $\boldsymbol{\theta}_s$, indicating the equal likelihood over the whole $\boldsymbol{\phi}$ uncertainty space.

For valid measurements, the likelihood $w_{r,j,s}$ is firstly calculated for all $r = 1, 2, \ldots, R$. Then a likelihood function $\overline{\overline{W}}_{j,s}$ can be established. Normally the resolution of the discrete VCRPs $\boldsymbol{\phi}$ into R points is numerically insufficient for a smooth representation of the joint distribution $P(\boldsymbol{\phi})$. Therefore, interpolation is required when building $\overline{\overline{W}}_{j,s}$ for the Bayesian updating. Consequently, the number of discrete points for modelling the discrete joint probability distribution increases from R to V. Each discrete point in the probability distribution model is denoted by $\boldsymbol{\phi}_v$. Normalization of $\overline{\overline{W}}_{j,s}$ is required such that the sum of the likelihood function remains 1.0, ensuring a fair likelihood calculation (i.e., Equation (8)) over the uncertain wave space. The probabilistic distribution of wave characteristics $\boldsymbol{\theta}$ should be taken into account before the Bayesian updating, i.e.,

$$\overline{\overline{W}}_j = \sum_{s=1}^{S} \overline{\overline{W}}_{j,s} PMF(\boldsymbol{\theta}_s) \tag{8}$$

where $\overline{\overline{W}}_j$ is the likelihood function to be applied for the Bayesian updating.

Finally, the joint probability distribution of VCRPs can be updated by Bayesian updating at each discrete point $\boldsymbol{\phi}_v$:

$$PMF_{k+1}(\boldsymbol{\phi}_v) = \mathcal{NO}(PMF_k(\boldsymbol{\phi}_v) \odot \overline{\overline{W}}_j) \tag{9}$$

where the $\odot$ operator means the element-wise multiplication of the two matrices of the same dimension, i.e., a Hadamard product [32]. To ensure that the sum of the joint probability mass function remains 1.0, normalization $\mathcal{NO}(\cdot)$ is required. $k \in \mathbb{Z}^+$ represents the tuning step index, which increases when j or sea state changes.

The tuned VCRPs may be reported in terms of the discrete joint probability distribution (i.e., $PMF(\boldsymbol{\phi})$), or the expectation and the covariance matrix (i.e., $\mathbf{E}(\boldsymbol{\phi})$ and $\mathbf{CoV}(\boldsymbol{\phi})$). Correlations between VCRPs can be captured automatically through the tuning process. Due to the nonlinearity between $\boldsymbol{\phi}$ and vessel responses, the tuned distribution will no longer be multivariate Gaussian.

6 REAL-TIME VESSEL MOTION AND CRITICAL STRUCTURAL RESPONSE PREDICTION

With such a vessel seakeeping model tuning module, VCRPs can be actively monitored with considerably improved confidence, see examples in [7]. In addition, the change of vessel conditions could also be detected automatically. As a result, accuracy of vessel motion predictions can be improved and the prediction uncertainties inherited from the uncertainties in WAP and VAP modules can be assessed.

For the real-time vessel motion prediction, very high fidelity prediction models e.g., by applying computational fluid dynamics (CFD) [33] become unrealistic. Aligning with the engineer-

ing practices [1], it is usually sufficient to predict the wave-induced vessel motions and the critical structural responses based on linear transfer functions deduced from the available VARPs and VCRPs. Wave forecast should be used for the prediction. For example, the vertical velocity $\dot{\eta}(x_p, y_p, z_p)$ on the crane tip at port side midship with coordinates (x_p, y_p, z_p) could be interesting and critical to monitor for lifting operations. Considering 2D wave spectrum, such response can be quickly calculated in the frequency domain by:

$$S_{\dot{\eta}\dot{\eta}}(\omega|x_p, y_p, z_p) = \sum_{\beta_W} S_{\zeta\zeta}(\omega, \beta_W)|H_{\dot{\eta}}(\omega, \beta_W|(x_p, y_p, z_p), E(\boldsymbol{\phi}), E(\boldsymbol{\gamma}))|^2 \Delta\beta_W \tag{10}$$

where $E(\boldsymbol{\phi})$ and $E(\boldsymbol{\gamma})$ are the expected values of VCRP and VARP vectors. $H_{\dot{\eta}}(\omega, \beta_W|(x_p, y_p, z_p), E(\boldsymbol{\phi}), E(\boldsymbol{\gamma}))$ represents the corresponding RAO for the critical vessel motion $\dot{\eta}(x_p, y_p, z_p)$ based on $E(\boldsymbol{\phi})$ and $E(\boldsymbol{\gamma})$. Based on normal wave forecasts at Met offices and Equation (10), critical response $\dot{\eta}(x_p, y_p, z_p)$ can be predicted sufficiently long time ahead, e.g., in terms of hours or days. Thus, the prediction uncertainty depends on the quality, time ahead of the wave forecast, and how well the linearized transfer function $H_{\dot{\eta}}(\omega, \beta_W|(x_p, y_p, z_p), E(\boldsymbol{\phi}), E(\boldsymbol{\gamma}))$ can represent the reality. In case of forecasting waves by onboard radar systems, the encountered waves can be forecasted only in a very short time ahead, e.g., in magnitude of seconds or minutes. Less forecast uncertainty and richer wave information including relative phases of wave components can be obtained from such a forecast method. However, due to the nonlinear nature of wave propagation [34], it is challenging to estimate the arriving waves at the vessel sufficiently ahead of time, based on the observed wave field several hundred to thousand meters away from the vessel. Thus, the consequent response predictions in terms of time records based on linear wave propagation are normally less reliable. Instead, extreme values of responses are of larger interest and higher reliability.

The nonlinearity of vessel roll motion is well-known due to the dominated nonlinear damping terms [35]. Therefore, it is often challenging to get acceptable quality of roll motion prediction when linear roll RAO is applied and the additional linearized damping term cannot be sufficiently tuned based on the full-scale measurements [10–12, 25]. Better correlation between the extreme responses from the prediction and the measurement of roll motion has been normally observed. It is believed that roll motion prediction can be significantly improved in term of the extreme value by applying the re-calculated RAOs based on the tuned VCRPs described in Section 5.

7 RISK AWARENESS AND AVOIDANCE

The purposes of vessel condition monitoring, seakeeping model tuning, and real-time critical response prediction are to reduce uncertainties in the entire operation system, reduce conservatism, improve the accuracy of risk assessment, and potentially reduce the costs and operational risks. Quantification of the risk requires to quantify the probability of occurrence $P(\mathscr{X})$ and the consequence $C(\mathscr{X})$ of pre-identified potential events $\mathscr{X}$. Only quantification of $P(\mathscr{X})$ is discussed. Benefiting from the quantified VCRPs uncertainties and the discretization of variables and probability distributions, the probability of occurrence for event $\mathscr{X}$ can be calculated. For example, lifting operations may be restricted by the vertical velocity at crane tip (e.g., $\dot{\eta}_{max}(x_p, y_p, z_p) < \dot{\eta}_0$ m/s) as a limiting criteria for heave compensation systems. For easier expression, the quantity $\dot{\eta}(x_p, y_p, z_p)$ herein is written as $\dot{\eta}$, and its maximum value is denoted by $\dot{\eta}_{max}$. $\dot{\eta}$ is a wide-banded Gaussian process, i.e., $\dot{\eta} \sim \mathscr{N}(0, \sigma_{\dot{\eta}}^2)$. The corresponding probability of failure is expressed as $P(\dot{\eta}_{max} \geq \dot{\eta}_0)$.

The example considers the uncertain VCRPs $\boldsymbol{\phi}$ by its discrete points $\boldsymbol{\phi}_r$ and the corresponding probability mass function $PMF(\boldsymbol{\phi}_r)$ for $r = 1, 2, \ldots, R$. The uncertain wave data $\boldsymbol{\theta}$ is similarly represented by the discrete points $\boldsymbol{\theta}_s$ and probability mass function $PMF(\boldsymbol{\theta}_s)$, for $s = 1, 2, \ldots, S$. At a specific combination of $\boldsymbol{\phi}_r$ and $\boldsymbol{\theta}_s$, the corresponding response spectrum $S_{\dot{\eta},r,s}(\omega)$ can be calculated as:

$$S_{\dot{\eta},r,s}(\omega) = S_{\dot{\eta}}(\omega|\boldsymbol{\phi}_r, \boldsymbol{\theta}_s) = \sum_{\beta_W} |H_{\dot{\eta},r}(\omega, \beta_W)|^2 S_{\zeta\zeta,s}(\omega, \beta_W) \Delta\beta_W \tag{11}$$

where $H_{\dot{\eta},r}(\omega, \beta_W)$ is the linear transfer function calculated based on $\boldsymbol{\phi}_r$, $S_{\zeta\zeta,s}(\omega, \beta_W)$ is the wave spectrum based on $\boldsymbol{\theta}_s$. The zeroth, second and fourth order spectral moments can then be calculated by:

$$m_{0,r,s} = \sum_{\omega} S_{\dot{\eta},r,s}(\omega) \Delta\omega \tag{12a}$$

$$m_{2,r,s} = \sum_{\omega} \omega^2 S_{\dot{\eta},r,s}(\omega) \Delta\omega \tag{12b}$$

$$m_{4,r,s} = \sum_{\omega} \omega^4 S_{\dot{\eta},r,s}(\omega) \Delta\omega \tag{12c}$$

Then the probability distribution of the response peaks (maxima), i.e., $\dot{\eta}_{max}$, can be considered as a Rice distribution,

i.e.,

$$PDF_{\dot{\eta}_{max},r,s}(v) = \frac{\varepsilon_{r,s}}{\sqrt{2\pi m_{2,r,s}}}\exp(-\frac{v^2}{2\varepsilon_{r,s}^2 m_{2,r,s}}) + \sqrt{1-\varepsilon_{r,s}^2}\frac{v}{m_{2,r,s}}\exp(-\frac{v^2}{2m_{2,r,s}})\Phi(G_{r,s}) \tag{13a}$$

$$\varepsilon_{r,s} = \sqrt{1-\frac{m_{2,r,s}^2}{m_{0,r,s}m_{4,r,s}}} \tag{13b}$$

$$\Phi(G_{r,s}) = \int_{-\infty}^{G_{r,s}} \frac{1}{\sqrt{2\pi}}\exp(-\frac{G_{r,s}^2}{2})dG_{r,s} \tag{13c}$$

$$G_{r,s} = \frac{v\sqrt{1-\varepsilon_{r,s}^2}}{\varepsilon_{r,s}\sqrt{m_{2,r,s}}} \tag{13d}$$

where *PDF* means the probability density function. Finally, the probability distributions of $\boldsymbol{\phi}$ and $\boldsymbol{\theta}$ are taken into account, and the corresponding probability distribution of $\dot{\eta}_{max}$ is:

$$PDF_{\dot{\eta}_{max}}(v) = \sum_{r=1}^{R}\sum_{s=1}^{S} PDF_{\dot{\eta}_{max},r,s}(v)\cdot PMF(\boldsymbol{\phi}_r)\cdot PMF(\boldsymbol{\theta}_s) \tag{14}$$

and consequently the probability of occurrence for the event $\dot{\eta}_{max} \geq \dot{\eta}_0$ can be calculated by:

$$P(\dot{\eta}_{max} \geq \dot{\eta}_0) = 1 - \int_{-\infty}^{\dot{\eta}_0} PDF_{\dot{\eta}_{max}}(v)dv \tag{15}$$

If $P(\dot{\eta}_{max} \geq \dot{\eta}_0)$ exceeds the allowable value, risk assessment module will send a warning message to the operators through ODSS, indicating the predicted potential risk. Consequently, the possible measures will be automatically screened in the risk assessment module. Typically, VARPs such as vessel speed, heading, and draft can be screened first since they can be controlled and adjusted quickly on board. For example, risk avoidance module can evaluate $P(\dot{\eta}_{max} \geq \dot{\eta}_0|\beta_V)$ for $\beta_V \in [0^\circ, 360^\circ)$, where β_V is the vessel heading. Then the optimal heading β_V^* can be determined as the one leading to the minimum probability of occurrence:

$$\begin{aligned}\beta_V^* &= \arg\min_{\beta_V} P(\dot{\eta}_{max} \geq \dot{\eta}_0|\beta_V) \\ &:= \{\beta_V | \forall y \in [0^\circ, 360^\circ) : P(\dot{\eta}_{max} \geq \dot{\eta}_0|y) > P(\dot{\eta}_{max} \geq \dot{\eta}_0|\beta_V)\}\end{aligned} \tag{16}$$

Such optimal value can then be suggested through ODSS.

8 CONCLUSION AND FUTURE WORK

Knowledge about vessel conditions is important for the vessel motions in the wave frequency region. However, some VCRPs are difficult to measure directly and therefore real-time onboard monitoring of such parameters can be challenging. This paper describes a vessel state observer, which can actively monitor and tune those VCRPs and quantify the uncertainties, fundamentally based on the previously proposed seakeeping model tuning algorithm [7]. This algorithm applies the method of discrete Bayesian inference and represents the likelihood function based on inverse distance weighting. The tuning algorithm is now further developed in this paper to include uncertainties from wave data. Furthermore, the tuned VCRPs with quantified uncertainties are considered as inputs to a proposed risk awareness and avoidance module where the probability of occurrence for critical events can be quantified. Followed by the risk assessment, suggestions can be given to the operator through the ODSS system.

The vessel condition monitoring system and the onboard decision support system can therefore benefit significantly from the model tuning module and the whole vessel state observer. However, this is at very early conceptual development stage. Future work should be aimed to implement such a framework onboard vessels for verification purposes. Towards such an ambition, several issues must be addressed with respect to the tuning algorithm. Firstly, limitations of applying such an algorithm should be identified through comprehensive model-scaled and full-scaled tests. Due to the stochastic linearization of the nonlinear terms for the dynamic equations of vessel motions, some VCRPs are linearized and therefore become sea state dependent. For example, the linearized additional roll damping is highly sea state dependent. For a sea state dependent parameter, the tuned value is only valid for a particular sea state, and therefore becomes questionable to apply to future sea states. The illustrated tuning algorithm has not considered tuning of sea state dependent parameters together with the others. This has to be addressed before considering real applications, for example, as proposed by Han et al. [36].

Discrete Bayesian inference can be challenging for real applications due to the "curse of dimensionality" [37] when the number of uncertain parameters increases. Han et al. [38] therefore proposed a more efficient tuning algorithm by only considering the first two orders of the joint probability distribution properties. However, as a compromise, nonlinearity can not be fully represented in the tuning results. In addition, issues on tuning together with sea state dependent parameters has not been addressed in that algorithm.

Lastly, a risk-based ODSS requires real-time risk assessment. However, the proposed algorithm in Section 7 might not be that computationally efficient due to the discretizations. Algorithm modifications should be expected as a result of future research work.

ACKNOWLEDGMENT

This work was made possible through the Centre for Research based Innovation MOVE, financially supported by the Research Council of Norway, NFR project no. 237929 and the consortium partners, http://www.ntnu.edu/move. The authors also thank Karl Erik Kaasen at SINTEF Ocean for valuable commenting and discussions.

REFERENCES

[1] DNVGL-ST-N001, 2016. Marine operations and marine warranty. Tech. rep., DNV GL.

[2] Dannenberg, J., Hessner, K., Naaijen, P., van den Boom, H., and Reichert, K., 2010. "The on board wave and motion estimator OWME". In Proceedings of the 20th international offshore and polar engineering conference, ISOPE, pp. 424–431.

[3] Hilmer, T., and Thornhill, E., 2014. "Deterministic wave predictions from the WaMoS II". In OCEANS 2014 - TAIPEI, pp. 1–8.

[4] Ren, Z., Han, X., Verma, A. S., Dirdal, J. A., and Skjetne, R., 2021. "Sea state estimation based on vessel motion responses: Improved smoothness and robustness using Bézier surface and L1 optimization". *Marine Structures,* ***76***, p. 102904.

[5] Faltinsen, O. M., 2015. "Hydrodynamics of marine and offshore structures". *Journal of Hydrodynamics, Ser. B,* ***26***(6), pp. 835 – 847.

[6] Tellkamp, J., Bruns, A., Gosch, T., Günther, H., Hansen, P. F., Nielsen, U. D., Papanikolaou, A., Spanos, D., Papatzanakis, G., Kassner, S., Wittkuhn, D., Tränkmann, I., Ehrke, K.-C., Krüger, S., Vorhoelter, H., Kluwe, F., and Jaap Struijk, J. K. N., 2009. ADOPT summary of experiences and needs for further development. Tech. rep., FORCE Technology and Uniresearch.

[7] Han, X., Leira, B. J., and Sævik, S., 2021. "Vessel hydrodynamic model tuning by discrete Bayesian updating using simulated onboard sensor data". *Ocean Engineering,* ***220***.

[8] Skjong, S., Kyllingstad, L., Reite, K.-J., Haugen, J., Ladstein, J., and Aarsæther, K., 2019. "Generic On-Board Decision Support System Framework for Marine Operations". In Proceedings of the ASME 2019 38th International Conference on Ocean, Offshore and Arctic Engineering, Vol. 7A.

[9] DNVGL-RP-0497, 2017. Data quality assessment framework. Tech. rep., DNV GL.

[10] Alford, L. K., Beck, R. F., Johnson, J. T., Lyzenga, D., Nwogu, O., and Zundel, A., 2015. "A real-time system for forecasting extreme waves and vessel motions". International Conference on Offshore Mechanics and Arctic Engineering.

[11] Connell, B. S. H., Rudzinsky, J. P., Brundick, C. S., Milewski, W. M., Kusters, J. G., and Farquharson, G., 2015. "Development of an environmental and ship motion forecasting system". International Conference on Offshore Mechanics and Arctic Engineering.

[12] Naaijen, P., Roozen, D. K., and Huijsmans, R. H. M., 2016. "Reducing operational risks by on-board phase resolved prediction of wave induced ship motions". International Conference on Offshore Mechanics and Arctic Engineering.

[13] Grilli, S. T., Guérin, C.-A., and Goldstein, B. I., 2011. "Ocean wave reconstruction algorithms based on spatiotemporal data acquired by a flash LIDAR camera". the International Offshore and Polar Engineering Conference.

[14] Nouguier, F., Grilli, S. T., and Guérin, C., 2014. "Nonlinear ocean wave reconstruction algorithms based on simulated spatiotemporal data acquired by a flash LIDAR camera". *IEEE Transactions on Geoscience and Remote Sensing,* ***52***(3), March, pp. 1761–1771.

[15] Nielsen, U. D., 2017. "A concise account of techniques available for shipboard sea state estimation". *Ocean Engineering,* ***129***, pp. 352 – 362.

[16] Bitner-Gregersen, E. M., and øistein Hagen, 1990. "Uncertainties in data for the offshore environment". *Structural Safety,* ***7***(1), pp. 11 – 34.

[17] Hagen, Ø., Bitner-Gregersen, E. M., and Vrouwenvelder, A., 2006. JCSS probabilistic model code Part 2: Loads 2.15: Wave loads. Tech. rep.

[18] Orimolade, A. P., Furevik, B. R., and Gudmestad, O. T., 2016. "A comparison of wave height forecasts against wave measurements for a location in the Barents Sea and in the Norwegian Sea". In Proceedings of the Twenty-sixth (2016) International Ocean and Polar Engineering Conference, International Society of Offshore and Polar Engineers.

[19] World Meteorological Organization (2014), 2014. "WMO guide to meteorological instruments and methods of observation".

[20] ECMWF, 2016. *Part VII: ECMWF Wave Model*. No. 7 in IFS Documentation. ECMWF.

[21] Tolman, H. L., Balasubramaniyan, B., Burroughs, L. D., Chalikov, D. V., Chao, Y. Y., Chen, H. S., and Gerald, V. M., 2002. "Development and implementation of wind-generated ocean surface wave modelsat ncep". *Weather and forecasting,* ***17***(2), pp. 311–333.

[22] Hersbach, H., Bell, B., Berrisford, P., Hirahara, S., Horányi, A., Muñoz-Sabater, J., Nicolas, J., Peubey, C., Radu, R., Schepers, D., Simmons, A., Soci, C., Abdalla, S., Abellan, X., Balsamo, G., Bechtold, P., Biavati, G., Bidlot, J., Bonavita, M., De Chiara, G., Dahlgren, P., Dee, D., Diamantakis, M., Dragani, R., Flemming, J., Forbes, R., Fuentes, M., Geer, A., Haimberger, L., Healy, S., Hogan,

R. J., Hólm, E., Janisková, M., Keeley, S., Laloyaux, P., Lopez, P., Lupu, C., Radnoti, G., de Rosnay, P., Rozum, I., Vamborg, F., Villaume, S., and Thépaut, J.-N., 2020. "The ERA5 global reanalysis". *Quarterly Journal of the Royal Meteorological Society,* ***146***(730), pp. 1999–2049.

[23] ECMWF, 2016. *Part V: Ensemble Prediction System*. No. 5 in IFS Documentation. ECMWF.

[24] Natskår, A., Moan, T., and Alvær, P., 2015. "Uncertainty in forecasted environmental conditions for reliability analyses of marine operations". *Ocean Engineering,* ***108***, pp. 636 – 647.

[25] Naaijen, P., van Oosten, K., Roozen, K., and van't Veer, R., 2018. "Validation of a deterministic wave and ship motion prediction system". International Conference on Offshore Mechanics and Arctic Engineering.

[26] Han, X., Sævik, S., and Leira, B. J., 2020. "A sensitivity study of vessel hydrodynamic model parameters". In Proceedings of the ASME 2020 39th International Conference on Ocean, Offshore and Arctic Engineering, Vol. 1, Virtual, Online.

[27] Radhakrishnan, G., Han, X., Sævik, S., Gao, Z., and Leira, B. J., 2021. "System uncertainty effects on wave frequency response of floating vessels based on polynomial chaos expansion". In Proceedings of the ASME 2021 40th International Conference on Ocean, Offshore and Arctic Engineering, Virtual, Online.

[28] Gutsch, M., Sprenger, F., and Steen, S., 2017. "Design parameters for increased operability of offshore crane vessels". In Proceedings of the ASME 2017 36th International Conference on Ocean, Offshore and Arctic Engineering, Trondheim, Norway.

[29] Kaplan, P., 1966. Lecture notes on nonlinear theory of ship roll motion in a random seaway.

[30] DNVGL-RP-C205, 2017. Environmental conditions and environmental loads. Tech. rep., DNV GL.

[31] Shepard, D., 1968. "A two-dimensional interpolation function for irregularly-spaced data". In Proceedings of the 1968 23rd ACM National Conference, ACM '68, Association for Computing Machinery, p. 517–524.

[32] Scheick, J. T., 1997. *Linear algebra with applications*, Vol. 81. McGraw-Hill New York.

[33] Kim, S. P., 2011. "CFD as a seakeeping tool for ship design". *International Journal of Naval Architecture and Ocean Engineering,* ***3***(1), pp. 65 – 71.

[34] Yue, D. K., Liu, Y., Hendrickson, K., Wu, G., Xiao, W., and Henry, L., 2008. "Nonlinear wave environments for ship analysis". 27th Symposium on Naval Hydrodynamics.

[35] ITTC, 2011. Recommended procedures and guidelines: Numerical estimation of roll damping. Tech. rep., International Towing Tank Conference.

[36] Han, X., Sævik, S., and Leira, B. J., 2021. "Tuning of vessel parameters including sea state dependent roll damping". *Ocean Engineering*. Revision under review.

[37] Gelman, A., Carlin, J., Stern, H., Dunson, D., Vehtari, A., and Rubin, D., 2013. *Bayesian Data Analysis*, 3 ed.

[38] Han, X., Leira, B. J., Sævik, S., and Ren, Z., 2021. "Onboard tuning of vessel seakeeping model parameters and sea state characteristics". *Marine Structures,* ***78***.

A.6 Paper A6

Paper A6:
X. Han, B. J. Leira, S. Sævik, and Z. Ren, 2021. Onboard tuning of vessel seakeeping model parameters and sea state characteristics. *Marine Structures* 78.

Marine Structures 78 (2021) 102998

Contents lists available at ScienceDirect

Marine Structures

journal homepage: www.elsevier.com/locate/marstruc

Onboard tuning of vessel seakeeping model parameters and sea state characteristics

Xu Han *, Bernt Johan Leira, Svein Sævik, Zhengru Ren

Department of Marine Technology, Norwegian University of Science and Technology (NTNU), 7491 Trondheim, Norway
Centre for Research-based Innovation on Marine Operations (SFI MOVE), Norway

ARTICLE INFO

Keywords:
Wave-induced vessel responses
Vessel seakeeping model parameters
Sea state characteristics
Unscented transformation
Unscented Kalman filter
Uncertainty reduction

ABSTRACT

It is essential for a safe and cost-efficient marine operation to improve the knowledge about the real-time onboard vessel conditions. This paper proposes a novel algorithm for simultaneous tuning of important vessel seakeeping model parameters and sea state characteristics based on onboard vessel motion measurements and available wave data. The proposed algorithm is fundamentally based on the unscented transformation and inspired by the scaled unscented Kalman filter, which is very computationally efficient for large dimensional and nonlinear problems. The algorithm is demonstrated by case studies based on numerical simulations, considering realistic sensor noises and wave data uncertainties. Both long-crested and short-crested wave conditions are considered in the case studies. The system state of the proposed tuning framework consists of a vessel state vector and a sea state vector. The tuning results reasonably approach the true values of the considered uncertain vessel parameters and sea state characteristics, with reduced uncertainties. The quantification of the system state uncertainties helps to close a critical gap towards achieving reliability-based marine operations.

1. Introduction

For marine operations, operational limit diagrams are normally provided in operating reports or operation manual booklets. Normally, there are many variables that influence these diagrams, such as vessel heading, loading condition, vessel speed, water depth, wave condition, and operation phase, so that dimension reduction must be considered as a compromise with readability. As a result, conservatism is typically increased. By means of IT tools and increased onboard communicating and computing capacity, real-time and interactively updated operational limit diagrams can be available without sacrificing useful information and knowledge.

It is also well recognized that the vessel operational conditions (defined by vessel inertia distribution, damping, forward speed, and the encountered weather and water depth conditions) are always subject to uncertainties [1], and those uncertain parameters can significantly influence the resulting vessel motion estimation [1–3]. A successful onboard decision support system (ODSS) for operation optimization and risk avoidance normally requires accurate real-time vessel motion prediction. For decades, there has been a strong research interest in relation to wave-induced vessel motion prediction in real time. Without wave prediction, one is still able to predict vessel motions by extrapolation of the recorded motion time series based on various approaches. Li et al. [4] qualitatively compared different typical predictive models within the machine learning domain. In general, the applicable predictive models for nonlinear time series involving machine learning could (1) be too computationally expensive to use online (e.g., support vector machine [5], fuzzy logic, and decision tree methods); (2) require highly customized modeling (e.g., wavelet neural network [6]); (3)

* Corresponding author at: Department of Marine Technology, Norwegian University of Science and Technology (NTNU), 7491 Trondheim, Norway.
E-mail address: xu.han@ntnu.no (X. Han).

https://doi.org/10.1016/j.marstruc.2021.102998
Received 23 October 2020; Received in revised form 16 January 2021; Accepted 8 March 2021

Nomenclature

$\%\Delta\sigma_A^2$	The variance reduction for parameter A due to tuning. A can be H_s, T_p, β_W, etc.
α	Scaling factor for the UKF model
$\bar{x}_j$	The mean value of the filtered sensor signal $\hat{x}_j(t)$
β	Hyperparameter in the UKF model in order to partially account for higher order statistical properties
β_{44}	Ratio between the additional roll damping and the critical roll damping
β_{Wp}	The prevailing wave direction for short-crested waves
β_W	Wave direction w.r.t. vessel coordinate system
$\bar{\boldsymbol{P}}_k$	The state covariance matrix for $\bar{\boldsymbol{x}}_k$
$\bar{\boldsymbol{x}}_k$	The predicted system state for the kth update
$\boldsymbol{\mathcal{X}}_{k,i}^{\boldsymbol{\phi}}$	The vessel state for the sigma point $\boldsymbol{\mathcal{X}}_{k,i}$
$\boldsymbol{\mathcal{X}}_{k,i}^{\boldsymbol{\theta}}$	The sea state for the sigma point $\boldsymbol{\mathcal{X}}_{k,i}$
$\boldsymbol{\mathcal{X}}_{k,i}$	The ith sigma point for the system state $\boldsymbol{x}_k$, i.e., the ith column of $\boldsymbol{\mathcal{X}}_k$
$\boldsymbol{\mathcal{X}}_k$	The sigma points for the system state $\boldsymbol{x}_k$
$\bar{\boldsymbol{\mathcal{Z}}}_k$	The predicted measurement vector estimated based on all sigma points
$\boldsymbol{\phi}_k$	The vessel state after the kth update
$\boldsymbol{\theta}'_k$	The acquired sea state information for the kth update
$\boldsymbol{\theta}_k$	The sea state after the kth update
$\boldsymbol{K}$	Kalman gain
$\boldsymbol{P}_k^w$	The covariance matrix for $\boldsymbol{x}_k^w$
$\boldsymbol{P}'_{\theta_k}$	The prior uncertainty of $\boldsymbol{\theta}'_k$
$\boldsymbol{P}_k$	The system state covariance matrix for $\boldsymbol{x}_k$
$\boldsymbol{P}_{\boldsymbol{\phi}_k}$	The covariance matrix for $\boldsymbol{\phi}_k$
$\boldsymbol{P}_{\theta_k}$	The covariance matrix for $\boldsymbol{\theta}_k$
$\boldsymbol{P}_{\boldsymbol{x}\boldsymbol{z}_k}$	The cross covariance matrix for the system state in state space and measurement space at kth measurement update step
$\boldsymbol{P}_{\boldsymbol{z}_k}$	The covariance matrix for the system state in measurement space at kth measurement update step
$\boldsymbol{Q}$	Process uncertainty covariance matrix
$\boldsymbol{R}$	Measurement uncertainty covariance matrix
$\boldsymbol{v}$	Process disturbance
$\boldsymbol{x}_k^w$	The system state after weather update step for the kth sea state
$\boldsymbol{x}_k$	The system state after the kth update
$\boldsymbol{y}_k$	The residual at kth measurement update step
$\boldsymbol{Z}_{k,i}$	The predicted measurement vector at $\boldsymbol{\mathcal{X}}_{k,i}$, built based on all sensor signals $x_j(t)$, for $j = 1, 2, \ldots, J$
$\boldsymbol{z}_k$	The acquired measurements at the kth update step (i.e., the standard deviations of sensor signals)
$\Delta\hat{A}$	The error between the true and the tuned values for parameter A. A can be H_s, T_p, β_W, etc.
$\eta_3, \dot{\eta}_3, \ddot{\eta}_3$	Heave displacement, velocity, acceleration
$\hat{\sigma}_A$	The standard deviation of the tuned parameter A. A can be H_s, T_p, β_W, etc.
$\hat{\sigma}_j$	The standard deviation of the filtered signal $\hat{x}_j(t)$
$\hat{A}$	The tuned value of parameter A. A can be H_s, T_p, β_W, etc.
$\hat{x}_j(t)$	The filtered time series for sensor signal $x_j(t)$
κ	Hyperparameter in the UKF model
ω	Wave frequency
$\overline{\sigma}_A$	The standard deviation of the acquired parameter A. A can be H_s, T_p, β_W, etc.
$\overline{A}$	The acquired value of parameter A. A can be H_s, T_p, β_W, etc.
ψ	Phase angle between the wave elevation and the vessel response in the RAO
σ_N^2	Variance of signal noise
σ_A	The standard deviation of the random variable A. A can be H_s, T_p, β_W, β_{44}, XCG, etc.
$\sigma_{j,i}$	The predicted measurement (response standard deviation) corresponding to the sensor measurement $x_j(t)$ based on the sigma point $\boldsymbol{\mathcal{X}}_{k,i}$
τ	Initial seed for case simulations

and lack of physical reasoning. Despite the complexity and computational cost, purely machine learning based predictive models such as neural network in general do not outperform compared with other classical prediction methods such as autoregressive models and minor component analysis [7]. Nielsen et al. [8] proposed a ship motion prediction algorithm based on the autocorrelation

ε_A	The error between the true and the acquired values for parameter A. A can be H_s, T_p, β_W, etc. $\varepsilon_A = \Delta\overline{A}$
φ	Random phase angle for wave components
A^*	The true value of parameter A. A can be H_s, T_p, β_W, etc.
f_{lp}	Lowpass filter cutoff frequency [Hz]
$H_j(\omega, \beta_W \mid \boldsymbol{\mathcal{X}}_{k,i})$	The RAO corresponding to the system state $\boldsymbol{\mathcal{X}}_{k,i}$ and the sensor signal $x_j(t)$
H_s	Significant wave height
J	The total number of sensor measurements for one sea state
j	Sensor ID, the jth sensor measurement, representing different quantities (displacement, velocity, acceleration) and locations
k	The sea state number
N	The dimension of the system state
n_s	Spreading parameter for short-crested waves
N_t	Number of time steps for the sensor signals
N_{β_W}	Number of discrete directions for each spectrum
N_ω	Number of discrete frequencies for each 1D spectrum
$S^*_{X_j X_j}(\omega)$	The true vessel motion spectrum for sensor j
$S_{\zeta\zeta}(\omega, \beta_W \mid \boldsymbol{\mathcal{X}}^{\boldsymbol{\theta}}_{k,i})$	The single-sided wave spectrum corresponding to the sea state $\boldsymbol{\mathcal{X}}^{\boldsymbol{\theta}}_{k,i}$
$S_{\zeta\zeta}\left(\omega, \beta_W\right)$	Single-sided wave spectrum
$S_{j,i}(\omega)$	The estimated vessel motion spectrum based on the sigma point $\boldsymbol{\mathcal{X}}^{\boldsymbol{\theta}}_{k,i}$ corresponding to the signal $x_j(x)$
T_p	Wave spectral peak period
w_i^c	The weight factor for state mean calculation at the ith sigma point, $i = 0, 1, 2, \ldots, 2N$
w_i^m	The weight factor for state covariance calculation at the ith sigma point, $i = 0, 1, 2, \ldots, 2N$
$x_j(t)$	The original signal for the jth sensor measurement for a certain sea state
DP	Dynamic positioning
ODSS	Onboard decision support system
OSV	Offshore supply vessel
PM	Pierson–Moskowitz spectrum
RAO	Response amplitude operator
SNR	Signal-to-noise ratio
UKF	Unscented Kalman filter
WMO	World Meteorological Organization
XCG	Longitudinal coordinate of vessel center of gravity

function of the measured motion time series. Due to the highly random nature of the encountered waves, it is challenging to ensure the time series extrapolation quality. The algorithms mentioned above reported reliable predictions of wave-induced vessel motions from a few seconds up to less than a minute ahead.

Alternatively, the wave-induced vessel motion can be predicted by seakeeping analysis based on wave forecast and predefined vessel conditions, without taking advantage of historical motion records. Seakeeping analysis has been commonly applied for design of floaters and floater-involved marine operations [9]. Usually transfer functions between vessel motions and wave elevations from seakeeping analysis can be linearized [10] and applied for real-time motion prediction. The corresponding prediction capacity is limited by the accuracy of the wave forecast and the applied linear transfer functions, i.e., response amplitude operators (RAOs). In recent decades, research about ODSS has been mainly focused on improving vessel motion prediction by improving the wave prediction for the near future by: (1) processing of coherent wave radar signals [11,12]; (2) using non-coherent wave radar signals combined with ship motion measurements [13–15]; (3) applying "ship as a wave buoy" analogy [16,17] assuming stationary sea states and predicting the future sea state by extrapolation; (4) or improving the accuracy of the wave analysis model [18–20].

Although seldom addressed, it is equally important to quantify and reduce the uncertainties associated with vessel seakeeping model parameters for a risk-based ODSS [1]. Practically, the uncertainties of vessel parameters for marine operations can be reduced by (1) careful design and organization of marine operation activities; (2) directly using available vessel condition monitoring systems such as the ballasting system and draft measurement. However, important vessel parameters related to inertia distribution and damping are challenging to measure directly and still expected to be subject to significant uncertainties. Identification of these important vessel hydrodynamic parameters has been mainly studied for maneuvering [21–23] and dynamic positioning (DP) [24] scenarios, where the responses at wave frequencies are considered as a disturbance or simply ignored. The estimated hydrodynamic coefficients such as added mass and damping may be questionable to apply for future wave conditions. Compared with tuning DP and maneuvering models, seakeeping model tuning is even more challenging because it must explicitly consider the highly variable wave loads.

Han et al. [25] proposed a promising online algorithm to improve the knowledge about the important vessel parameters and quantify the uncertainties, based on onboard vessel motion measurements and wave information (in terms of wave spectrum). The algorithm is based on discrete Bayesian inference and the tuned parameters can improve the accuracy of the RAOs to be applied for future sea states. Roll motion is subject to high nonlinearity due to the significant influence from nonlinear roll damping sources such as eddy making and bilge keel induced damping [26]. Such damping terms are defined as "additional" damping, differing from the damping derived from the linear potential theory. However in practice, such additional roll damping is usually linearized at each sea state by e.g., stochastic linearization [27] so that the roll motion transfer function can represent a linear behavior. As a consequence, the additional roll damping becomes sea state dependent. Han et al. [28] proposed two procedures for tuning and predicting such sea state dependent parameters together with other vessel parameters.

However, the algorithm of vessel seakeeping model tuning is still at an early developing stage with many identified challenges towards industrial applications. The acquired wave information can never be exact. Precise knowledge about the wave spectrum was assumed in the previous research [25,28]. The feasibility of the previously proposed tuning algorithms with Bayesian inference technique have been demonstrated, by considering up to 4 uncertain vessel parameters. In reality, more uncertain parameters should be included in the tuning model, e.g., vessel heading and speed, wave spectrum related parameters such as H_s (significant wave height), T_p (wave spectral peak period), β_W (wave direction), directional spreading, and many other hydrodynamic parameters. As a consequence, the previously developed methodology faces a common challenge with respect to the curse of dimensionality [29]. This makes the discrete Bayesian inference based model tuning approach time-consuming, computationally expensive, and hence unrealistic for practical applications within such an extended system framework.

To solve the curse of dimensionality, this paper proposes a novel and much more efficient algorithm to tune the vessel seakeeping model parameters by applying a second-order statistical inference algorithm based on the mean and variance of the variables. The newly proposed algorithm also considers the uncertainties from waves and can even reduce these uncertainties through the proposed tuning procedure. The paper is organized as follows. The uncertainties from wave information are discussed in Section 2. Then the new tuning algorithm is described in Section 3. The proposed algorithm is demonstrated numerically by case studies. The basis of the considered seakeeping model, generation of synthetic sensor signals, and the base case inputs are described in Section 4. The results of the base case and associated sensitivity studies are presented in Section 5. Finally, Section 6 summarizes the main findings from the present study and gives suggestions for future work.

2. Wave data and the associated uncertainties

Wave field data can be collected through forecast, hindcast, visual observation, or instrumental measurements, among which the measurements by instruments such as wave buoys, shipborne wave recorders, satellite altimeters, and onboard radars may be subject to minimum error. Practically, any type of wave data can be valuable for tuning of the seakeeping model parameters.

Nowadays wave forecast and hindcast mostly use the third-generation wave models, e.g., WAM, accounting for the nonlinear interaction between wave components [30]. The uncertainty of wave forecast may be well quantified by the spread of the wave ensemble prediction [31,32]. The wave forecast could be biased, especially in sheltered or coastal areas. Natskår et al. [33] compared the wave data between forecast and hindcast. Biased H_s was observed in the forecast data.

The comparison study by Orimolade et al. [34] indicates that (1) the wave forecast uncertainty also depends on the location to be forecasted; (2) and the instrumental error of the MIROS microwave radar onboard the Heidrun platform may be generally higher than the wave buoy measurements used for Barents Sea. Comparisons between summer and winter seas [34] may suggest that the wave information obtained by wave radar measurements performed in a more stable way across mild and harsh seas, even with relatively large measuring errors. The measurement errors by wave buoys are much smaller at moderate seas but can be significantly increased at harsh environmental conditions. Hagen et al. [35] also argued that breaking waves or slamming acting on a wave buoy may lead to overestimation of wave heights, while underestimation may occur for severe seas due to the buoy being drawn through the wave crest, or for large surface current.

To assure a globally aligned measurement quality, the World Meteorological Organization (WMO) has published recommendations and requirements for instrument performance [36]. The specified measurement uncertainties corresponds to a 95% probability level, i.e., two standard deviations (2σ) for a Gaussian distribution. The measurements should, where possible, record the sea state characteristics (e.g., H_s, T_p, and β_W) for wind sea and swell, separately.

Please note that the specified uncertainties of the WaMoSII system and the WAM results are only based on the available indicative accuracy information [1,37]. It is assumed that the accuracy approximately corresponds to a 95% confidence level. The term "accuracy" is less preferred compared with "uncertainty" [36] because "accuracy" can be determined only when the true value is perfectly known. Natskår et al. [33] reported even higher uncertainties on the forecast T_p, in comparison with hindcast wave data.

The freely accessible ERA5 datasets [38] and toolbox provide comprehensive opportunities of reanalyzing wave data both in terms of the expectation and the uncertainty assessment, based on the Integrated Forecasting System (IFS) Cy41r2 which combines WAM forecast and available observations. However, it is worth noting that ERA5 mostly considers random errors in terms of ensemble spread [32] but not systematic errors. The uncertainties of the ERA5 datasets are highly dependent on the amount and quality of available observations, resolution, location, and season. The wave analysis results and their uncertainty assessment may be biased, due to the potential systematic errors, e.g., in the cases of tropical and extra-tropical cyclones. By benefiting from the development of the wave model [30], data assimilation [39], and observation handling [40], the uncertainties of the ocean wave analysis in terms of both bias and variance have been significantly reduced [20].

Table 1
Operational measurement uncertainties (2σ) [36].

Variable	H_s	T_p	β_W
WMO required[a]	0.5 m for $H_s \leq 5$ m; 10% for $H_s > 5$ m	0.5 s	10°
WMO achievable[b]	0.5 m for $H_s \leq 5$ m; 10% for $H_s > 5$ m	0.5 s	20°
Typical moored buoy	0.2 m or 10%	1.0 s	10°
WaMoSII radar [1,37]	0.5 m or 10%	0.5 s	2°
Wave model (WAM) [1]	0.5 m or 15%	10%	15°

[a] "WMO required" corresponds to the recommended requirements about the measurement uncertainty for general operational use [36].
[b] "WMO achievable" corresponds to the realistic measurement uncertainty that the sensor can be achieved in normal operational practice [36].

Table 2
Applied uncertainties of the measured sea state characteristics.

Variable	Standard deviation	Unit
H_s	10%	m
T_p	0.5	s
β_W	5	°

The wave information used in the state estimation model should include uncertainties from instrumental sensors, sampling variability (e.g., due to discrete measured data with limited duration for a relatively large recording interval), temporal and spatial variability (i.e., using the imperfectly synchronized measurement data from another location), and inaccurate description of waves caused by e.g., the selection of wave models and probability distribution models. However, in reality the mentioned uncertainties are very challenging to quantify and estimate independently. The reported uncertainties from sampling variability and temporal and spatial variability by Bitner-Gregersen and Hagen [41] are well within the WMO required measurement accuracy. Therefore, it is rational to consider that the specified measurement uncertainties in Table 1 have included the sampling, temporal, and spatial variability to some degree. Due to the sampling variation, the Joint Committee on Structural Safety suggests longer wave recording length (even with less accuracy) for each recording interval rather than too short wave records within each interval (even with high accuracy) [35].

Based on the discussion above, the considered uncertainties of sea state characteristics are summarized in Table 2, assuming that the sea state information is from measurements or hindcast. A sensitivity case considering larger uncertainties was also carried out, see Section 5.4.

The long-term distribution of T_p is normally modeled as conditional upon H_s with a log-normal distribution [42]. However, the short-term distribution of T_p with a prior knowledge with respect to H_s and T_p from measurements, hindcast, or forecast can be reasonably approximated as being Gaussian distributed, i.e., $P(T_p|\overline{H}_s, \overline{T}_p) \sim \mathcal{N}(\overline{T}_p, \overline{\sigma}^2_{T_p})$, where $\overline{H}_s$ and $\overline{T}_p$ represent the prior, and $\overline{\sigma}^2_{T_p}$ represents the uncertainties (variance) of the prior $\overline{T}_p$.

3. Formulation of algorithm

Real applications of vessel seakeeping model tuning must consider many uncertain sea state characteristics as described in Section 2, as well as a large number of uncertain vessel parameters. Consequently, the curse of dimensionality from the previously proposed discrete Bayesian inference approach [25] must be overcome for practical applications. The most common practice is to approximate the joint probability distribution of the random variables by taking account of their properties related to the first two orders, i.e., the mean vector and the covariance matrix, and assuming the variables are multivariate Gaussian distributed. The Kalman filter and its extended forms are the most popular algorithms updating the assumed Gaussian distributed state based on measurements. Tuning of vessel seakeeping parameters is a multi-dimensional, multi-modal and nonlinear problem [25]. As shown later, it is difficult to express the measurement function from the system state (including vessel parameters and sea state characteristics) to the measurement (i.e., the standard deviation of vessel motion) in an algebraic format. Comparing the performance among the popular nonlinear Kalman filters [43–47], the unscented Kalman filter (UKF) [46] is found to be relatively feasible for the seakeeping model tuning problem, with respect to estimation accuracy, implementation convenience, numerical robustness, and computational expense. UKF is formulated based on the unscented transformation [48] directly through nonlinear functions.

The proposed tuning algorithm is then based on the UKF model, consisting of four steps: weather update, sigma-point and weight calculation, system propagation, and measurement update. Different from the typical UKF models which update the state of the dynamic system for each time instant, the proposed UKF model updates the system state for each sea state, assuming that the system state is approximately stationary during each sea state. The tuning procedure is illustrated in Fig. 1. Details are described in the following sections.

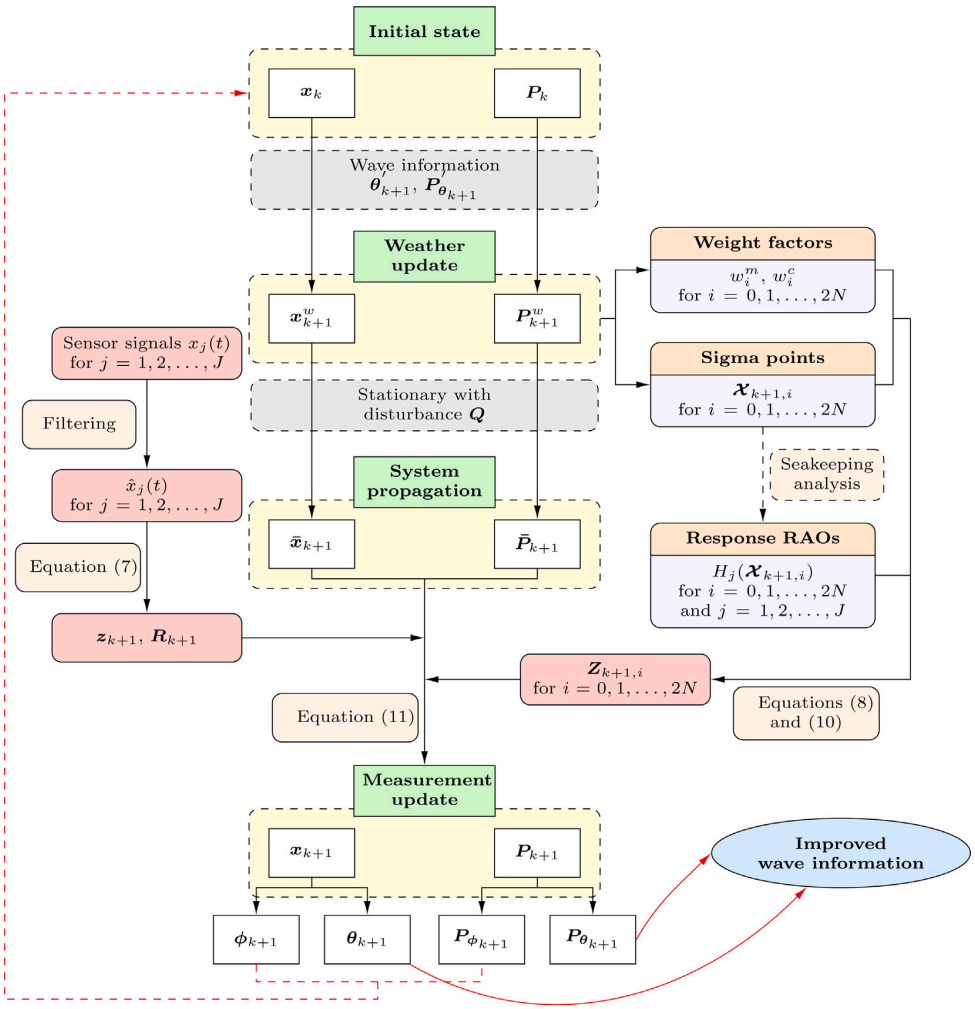

Fig. 1. The process of tuning vessel parameters and sea state characteristics together with quantification of uncertainties.

3.1. Weather update

The system state $\boldsymbol{x}_k$ at the sea state indexed by k consists of a vessel state $\boldsymbol{\phi}_k$ including uncertain vessel parameters and a sea state $\boldsymbol{\theta}_k$ including uncertain sea state characteristics such as H_s, T_p, and β_W. The subscript k indicates the corresponding parameter that has been tuned for k sea states. Wave conditions can be considered stationary within a sea state. Normally a stationary sea state can last from 20 min up to 3 h, depending on the location. $\boldsymbol{\phi}_k$ and $\boldsymbol{\theta}_k$ are approximately constant within that sea state. For the next sea state with the acquired wave information $\boldsymbol{\theta}'_{k+1}$ and its uncertainty $\boldsymbol{P}'_{\boldsymbol{\theta}_{k+1}}$, the system state should be updated accordingly. This step is referred to as weather update:

$$\boldsymbol{x}^w_{k+1} = \begin{bmatrix} \boldsymbol{\phi}_k \\ \boldsymbol{\theta}'_{k+1} \end{bmatrix} \tag{1a}$$

$$\boldsymbol{P}^w_{k+1} = \begin{bmatrix} \boldsymbol{P}_{\boldsymbol{\phi}_k} & \boldsymbol{0} \\ \boldsymbol{0} & \boldsymbol{P}'_{\boldsymbol{\theta}_{k+1}} \end{bmatrix} \tag{1b}$$

where the superscript w means the corresponding variable after the weather update step. Compared with the state after the kth update i.e., $\boldsymbol{x}_k$ and $\boldsymbol{P}_k$, the sub-variables $\boldsymbol{\theta}_k$ and $\boldsymbol{P}_{\boldsymbol{\theta}_k}$ have been replaced by $\boldsymbol{\theta}'_{k+1}$ and $\boldsymbol{P}'_{\boldsymbol{\theta}_{k+1}}$ respectively. In addition, the off-diagonal sub-matrices $\boldsymbol{P}_{\boldsymbol{\phi}_k\boldsymbol{\theta}_k}$ and $\boldsymbol{P}_{\boldsymbol{\theta}_k\boldsymbol{\phi}_k}$ are replaced by zeros.

3.2. Calculation of sigma points and weight factors

The sigma points $\boldsymbol{\mathcal{X}}_{k+1}$ in the state space are calculated by [43]

$$\boldsymbol{\mathcal{X}}_{k+1,0} = \boldsymbol{x}^{w}_{k+1} \tag{2a}$$

$$\boldsymbol{\mathcal{X}}_{k+1,i} = \begin{cases} \boldsymbol{x}^{w}_{k+1} + \left[\sqrt{(N+\lambda)\boldsymbol{P}^{w}_{k+1}}\right]_{i} & \text{for } i = 1, 2, \dots, N \\ \boldsymbol{x}^{w}_{k+1} - \left[\sqrt{(N+\lambda)\boldsymbol{P}^{w}_{k+1}}\right]_{i-N} & \text{for } i = N+1, \dots, 2N \end{cases} \tag{2b}$$

$$\boldsymbol{\mathcal{X}}_{k+1} = [\boldsymbol{\mathcal{X}}_{k+1,0} \quad \boldsymbol{\mathcal{X}}_{k+1,1} \quad \cdots \quad \boldsymbol{\mathcal{X}}_{k+1,2N}] \tag{2c}$$

where $\left[\sqrt{(N+\lambda)\boldsymbol{P}^{w}_{k+1}}\right]_{i}$ means the ith column (or row) of the matrix square root of $(N+\lambda)\boldsymbol{P}^{w}_{k+1}$. N is the dimension of the system state vector. $\boldsymbol{\mathcal{X}}_{k+1}$ has a size of $N \times (2N+1)$. Each sigma point $\boldsymbol{\mathcal{X}}_{k+1,i}$ ($i \in \{0, 1, \dots, 2N\}$) is a deterministically selected state vector, and it can be written as

$$\boldsymbol{\mathcal{X}}_{k+1,i} = \begin{bmatrix} \boldsymbol{\mathcal{X}}^{\boldsymbol{\phi}}_{k+1,i} \\ \boldsymbol{\mathcal{X}}^{\boldsymbol{\theta}}_{k+1,i} \end{bmatrix} \tag{3}$$

where $\boldsymbol{\mathcal{X}}^{\boldsymbol{\phi}}_{k+1,i}$ and $\boldsymbol{\mathcal{X}}^{\boldsymbol{\theta}}_{k+1,i}$ are the corresponding vessel state and sea state at the sigma point $\boldsymbol{\mathcal{X}}_{k+1,i}$. Coefficient λ in Eq. (2) is calculated by [43]:

$$\lambda = \alpha^2(N+\kappa) - N \tag{4}$$

where α is the so-called scaling factor, and the parameter κ can have any value as long as $N+\kappa \neq 0$, and is normally set to be $3-N$ or 0.

The weight factors corresponding to the calculated sigma points are independent of updating step k and can be calculated by [43]:

$$w^{m}_{0} = \frac{\lambda}{\lambda+N} \tag{5a}$$

$$w^{c}_{0} = \frac{\lambda}{\lambda+N} + 1 - \alpha^2 + \beta \tag{5b}$$

$$w^{c}_{i} = w^{m}_{i} = \frac{1}{2(\lambda+N)} \tag{5c}$$

where $i = 1, 2, \dots, 2N$. w^{m} are the weight factors for the state mean calculation while w^{c} are the weight factors for the state covariance matrix calculation. β is introduced in the scaled UKF by Julier [46] to partially include the higher order statistical information, and $\beta = 2$ for Gaussian distributed variables. To ensure a positive semi-definite covariance matrix, all the weight factors w^{c}_{i} for $i = 0, 1, \dots, 2N$ should be non-negative [46]. Consequently, it requires (1) $\kappa > -N$; (2) and approximately $\alpha > \sqrt{\frac{N}{4(N+\kappa)}}$ assuming a relatively small α value. The criterion (2) is practically difficult to achieve because the UKF normally performs better with a very small α value such as 0.01 [46]. Julier et al. [49] proposed a modified formulation for covariance calculation in order to guarantee a positive semi-definite covariance matrix.

3.3. System propagation

The vessel state and the sea state are assumed approximately stationary during an update. Therefore, the system propagation can be formulated as

$$\bar{\boldsymbol{x}}_{k+1} = \boldsymbol{x}^{w}_{k+1} + \boldsymbol{v} \tag{6a}$$

$$\bar{\boldsymbol{P}}_{k+1} = \boldsymbol{P}^{w}_{k+1} + \boldsymbol{Q} \tag{6b}$$

where $\bar{\boldsymbol{x}}_{k+1}$ is the predicted state, $\bar{\boldsymbol{P}}_{k+1}$ is the predicted state covariance. $\boldsymbol{v}$ is a $N \times 1$ vector representing the process disturbance, and is assumed to be multivariate Gaussian processes, i.e., $\boldsymbol{v} \sim \mathcal{N}(\boldsymbol{0}, \boldsymbol{Q})$ where $\boldsymbol{Q}$ is the process uncertainty covariance matrix.

3.4. Measurement update

Firstly, the acquired vessel motion signals $x_j(t)$ shall be filtered to remove the low-frequency components, bias, and high-frequency noises, in order to keep only the response energy within the wave frequency domain. $j = 1, 2, \dots, J$, where $J = 9$ in the case studies, is the number of available sensor measurements for one sea state. The filtered signal is denoted by $\hat{x}_j(t)$ for each measured quantity, e.g., displacement, velocity, or acceleration of the heave or roll motions. The standard deviations of the filtered vessel motion signals at different locations and quantities (i.e., displacement, velocity, and acceleration) are considered to constitute the measurement space, denoted by $\boldsymbol{z}_{k+1} \in \mathbb{R}^{J}$. $\boldsymbol{z}_{k+1}$ is calculated by:

$$\boldsymbol{z}_{k+1} = \begin{bmatrix} \hat{\sigma}_1 \\ \hat{\sigma}_2 \\ \vdots \\ \hat{\sigma}_J \end{bmatrix} \tag{7a}$$

$$\hat{\sigma}_j = \sqrt{\frac{\sum_{t=1}^{N_t} \left(\hat{x}_j(t) - \bar{x}_j\right)^2}{\left(N_t - 1\right)}} \tag{7b}$$

$$\bar{x}_j = \frac{\sum_{t=1}^{N_t} \hat{x}_j(t)}{N_t} \tag{7c}$$

where N_t is the total number of time steps for the sensor measurement $x_j(t)$, and $\bar{x}_j$ is the mean value of the filtered signal $\hat{x}_j(t)$.

Transferring the states (i.e., sigma points) from the state space to the measurement space involves highly nonlinear functions, and the functions depend on the states as well. The transferred states in the measurement space is called "the predicted measurements". For a specific sensor signal $x_j(t)$ ($j \in \{1, 2, \ldots, J\}$), the corresponding predicted measurement (i.e., the standard deviation) can be calculated at each selected sigma point by Eq. (8) assuming long-crested waves.

$$S_{j,i}(\omega) = |H_j(\omega, \beta_W | \boldsymbol{\mathcal{X}}_{k+1,i})|^2 S_{\zeta\zeta}(\omega, \beta_W | \boldsymbol{\mathcal{X}}^{\boldsymbol{\theta}}_{k+1,i}) \tag{8a}$$

$$\sigma_{j,i} = \sqrt{\sum_{n=1}^{N_\omega} S_{j,i}\left(\omega_n\right) \cdot \Delta\omega_n} \tag{8b}$$

where $H_j(\omega, \beta_W | \boldsymbol{\mathcal{X}}_{k+1,i})$ is the linear transfer function (i.e., RAO) between wave elevation and the vessel motion of interest corresponding to $x_j(t)$, which depends on the state sigma point $\boldsymbol{\mathcal{X}}_{k+1,i}$ and the location and quantity j. $S_{\zeta\zeta}(\omega, \beta_W | \boldsymbol{\mathcal{X}}^{\boldsymbol{\theta}}_{k+1,i})$ is the single-sided wave spectrum, $S_{j,i}$ is the corresponding response spectrum, its standard deviation $\sigma_{j,i}$ is the predicted measurement for the measured quantity j at sigma point $\boldsymbol{\mathcal{X}}_{k+1,i}$, N_ω is the number of discrete frequencies of the response spectrum, and $\Delta\omega_n$ is the frequency interval for ω_n. $\Delta\omega_n$ may be different for different discrete frequencies ω_n. For cases considering long-crested waves, 241 discrete frequencies were applied.

When a 2D wave or a short-crested wave is considered, Eq. (8) will consequently become:

$$S_{j,i}(\omega) = \sum_{\beta_W} |H_j(\omega, \beta_W | \boldsymbol{\mathcal{X}}_{k+1,i})|^2 S_{\zeta\zeta}(\omega, \beta_W | \boldsymbol{\mathcal{X}}^{\boldsymbol{\theta}}_{k+1,i}) \Delta\beta_W \tag{9a}$$

$$\sigma_{j,i} = \sqrt{\sum_{n=1}^{N_\omega} S_{j,i}\left(\omega_n\right) \cdot \Delta\omega_n} \tag{9b}$$

where $\Delta\beta_W$ is the wave direction interval and $\Delta\beta_W = 2°$ was applied. Evenly distributed frequencies ($N_\omega = 400$) at each discrete direction between periods of 3 s and 40 s were applied in the sensitivity study for short-crested waves when calculating the predicted measurements $\sigma_{j,i}$.

The predicted measurement $\boldsymbol{Z}_{k+1,i}$ based on the sigma point $\boldsymbol{\mathcal{X}}_{k+1,i}$ for $j = 1, 2, \ldots, J$ can be written as

$$\boldsymbol{Z}_{k+1,i} = \begin{bmatrix} \sigma_{1,i} \\ \sigma_{2,i} \\ \vdots \\ \sigma_{J,i} \end{bmatrix} \tag{10}$$

Accordingly, the measurement update step can be formulated as

$$\boldsymbol{\mathcal{Z}}_{k+1} = \sum_{i=0}^{2N} w_i^m \boldsymbol{Z}_{k+1,i} \tag{11a}$$

$$\boldsymbol{y}_{k+1} = \boldsymbol{z}_{k+1} - \boldsymbol{\mathcal{Z}}_{k+1} \tag{11b}$$

$$\boldsymbol{P}_{\boldsymbol{z}_{k+1}} = \sum_{i=0}^{2N} w_i^c (\boldsymbol{Z}_{k+1,i} - \boldsymbol{\mathcal{Z}}_{k+1})(\boldsymbol{Z}_{k+1,i} - \boldsymbol{\mathcal{Z}}_{k+1})^\top + \boldsymbol{R}_{k+1} \tag{11c}$$

$$\boldsymbol{P}_{\boldsymbol{x}\boldsymbol{z}_{k+1}} = \sum_{i=0}^{2N} w_i^c (\boldsymbol{\mathcal{X}}_{k+1,i} - \bar{\boldsymbol{x}}_{k+1})(\boldsymbol{Z}_{k+1,i} - \boldsymbol{\mathcal{Z}}_{k+1})^\top \tag{11d}$$

$$\boldsymbol{K} = \boldsymbol{P}_{\boldsymbol{x}\boldsymbol{z}_{k+1}} \boldsymbol{P}^{-1}_{\boldsymbol{z}_{k+1}} \tag{11e}$$

$$\boldsymbol{x}_{k+1} = \bar{\boldsymbol{x}}_{k+1} + \boldsymbol{K}\boldsymbol{y}_{k+1} \tag{11f}$$

$$\boldsymbol{P}_{k+1} = \bar{\boldsymbol{P}}_{k+1} - \boldsymbol{K}\boldsymbol{P}_{\boldsymbol{z}_{k+1}}\boldsymbol{K}^\top \tag{11g}$$

where $\boldsymbol{\mathcal{Z}}_{k+1} \in \mathbb{R}^J$ is the predicted measurement vector based on the sigma points $\boldsymbol{\mathcal{X}}_{k+1}$, $\boldsymbol{y}_{k+1}$ is the residual between the predicted measurement $\boldsymbol{\mathcal{Z}}_{k+1}$ and the acquired measurement $\boldsymbol{z}_{k+1}$. $\boldsymbol{R}_{k+1}$ represents the measurement noise and the uncertainties of the measurement functions as shown in Eq. (8). $\boldsymbol{R}_{k+1}$ can be sensor and sea state dependent. $\boldsymbol{P}_{\boldsymbol{z}_{k+1}} \in \mathbb{R}^{J \times J}$ is the covariance matrix of the sigma points in measurement space, $\boldsymbol{P}_{\boldsymbol{x}\boldsymbol{z}_{k+1}} \in \mathbb{R}^{N \times J}$ is the cross covariance of the state and the measurement. $\boldsymbol{K}$ is known as the Kalman gain which is used for updating the state and its covariance matrix. The updated state and its covariance for step $k+1$ are denoted by $\boldsymbol{x}_{k+1}$ and $\boldsymbol{P}_{k+1}$ respectively.

Accordingly, a complete loop is described for recursively tuning of the uncertain vessel parameters and the sea state characteristics, and reducing their uncertainties.

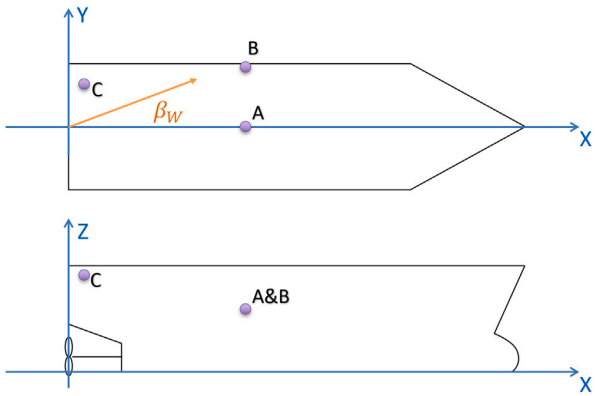

Fig. 2. The reference coordinate system and the locations of the virtual sensors measuring vessel motions.

Table 3
Description of sensor measurements.

Sensor ID	Location	Signal/measurements
Displacement_A	A	$\eta_3(t)$ at location A
Displacement_B	B	$\eta_3(t)$ at location B
Displacement_C	C	$\eta_3(t)$ at location C
Velocity_A	A	$\dot{\eta}_3(t)$ at location A
Velocity_B	B	$\dot{\eta}_3(t)$ at location B
Velocity_C	C	$\dot{\eta}_3(t)$ at location C
Acceleration_A	A	$\ddot{\eta}_3(t)$ at location A
Acceleration_B	B	$\ddot{\eta}_3(t)$ at location B
Acceleration_C	C	$\ddot{\eta}_3(t)$ at location C

$\eta_3(t)$: time series of heave displacement;
$\dot{\eta}_3(t)$: time series of heave velocity;
$\ddot{\eta}_3(t)$: time series of heave acceleration.

4. Basis of case studies

The algorithm is demonstrated by case studies based on a typical offshore supply vessel (OSV) where the wave information and vessel motion measurements are numerically simulated with addition of white noise. It is assumed that the wave-induced vessel motion in the wave frequency range can be well estimated by the linear transfer functions (i.e., RAOs) and the wave spectrum in the frequency domain, for moderate seas. The RAOs were generated by application of DNV GL advanced seakeeping analysis software Wasim [50].

4.1. Scope of the base case

Earlier research [2] suggests that multiple vessel motion sensors at different locations providing signals of displacements, velocities, and accelerations can help to identify the correct uncertain vessel parameters and tune towards their true values. Therefore, the case studies considered virtual sensors at three different locations onboard (i.e., locations A, B, and C) as illustrated in Fig. 2 and summarized in Table 3, measuring the corresponding heave displacements, velocities, and accelerations. The vessel coordinate system is also illustrated in Fig. 2. The origin is at the stern of the keel elevation. The positive X-axis points towards the bow, the positive Y-axis points towards the port, and the positive Z-axis points vertically upwards. The wave direction β_W, also shown in Fig. 2, follows the same coordinate system, in a positive going-to convention, where for example, $\beta_W = 180°$ corresponds to a head sea condition.

Zero vessel forward speed was considered for simplicity to avoid the 3-to -1 mapping problem for following seas [51]. However, the proposed algorithm and framework is so flexible that vessel forward speed can definitely be included in the vessel state $\boldsymbol{\phi}$. Earlier studies [2,25] show that the interesting vessel motions listed in Table 3 are sensitive to the linearized additional roll damping coefficient β_{44} and the longitudinal center of gravity XCG. In reality, application of a multi-peak wave spectrum consisting of both wind sea and swell components might be needed. However, single peak long-crested Pierson–Moskowitz (PM) wave spectra [42] as shown in Eq. (12) are assumed for simplification.

$$S_{\zeta\zeta}(\omega) = \frac{5}{16} H_s^2 \omega_p^4 \omega^{-5} \exp\left(-\frac{5}{4}\left(\frac{\omega}{\omega_p}\right)^{-4}\right) \tag{12}$$

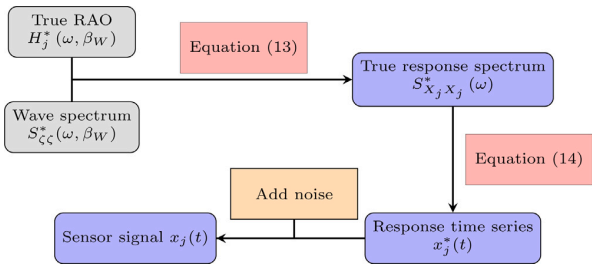

Fig. 3. Process of generating virtual sensor signal $x_j(t)$ for sensor j.

where ω_p is the sea state peak frequency. The error due to the uncertain wave spectral shape may be included in the measurement noise covariance matrix $\boldsymbol{R}$.

For demonstration purposes, the uncertain vessel parameters $\boldsymbol{\phi} = [\beta_{44}, XCG]^\top$ as the vessel state, and the uncertain sea state characteristics $\boldsymbol{\theta} = [H_s, T_p, \beta_W]^\top$ as the sea state, were considered for the base case study. The selected true vessel state is $\boldsymbol{\phi}^* = [\beta^*_{44}, XCG^*]^\top = [4\%, 61.4\ \text{m}]^\top$. Consequently, the true RAO for each virtual sensor can be determined, denoted by $H_j^*(\omega, \beta_W)$. Virtual sensor signals are numerically simulated, as illustrated in Fig. 3. Based on the true vessel motion RAO $H_j^*(\omega, \beta_W)$ corresponding to the sensor measurement $x_j(t)$ and the true wave spectrum $S^*_{\zeta\zeta}(\omega, \beta_W)$, the corresponding true vessel motion spectrum $S^*_{X_j X_j}(\omega)$ can be calculated by Eq. (13) assuming long-crested wave conditions as the base case.

$$S^*_{X_j X_j}(\omega) = |H_j^*(\omega, \beta_W)|^2 S^*_{\zeta\zeta}(\omega, \beta_W) \tag{13}$$

Then a vessel motion realization (i.e., $x_j^*(t)$) can be generated by:

$$x_j^*(t) = \sum_{n=1}^{N_\omega} C_n(\omega_n) \cos(\omega_n t + \varphi_n + \psi_{j,n}) \tag{14a}$$

$$C_n(\omega_n) = \sqrt{2 S^*_{X_j X_j}(\omega_n) \cdot \Delta\omega_n} \tag{14b}$$

where ω_n is the discrete frequency, $\Delta\omega_n$ is the interval of ω_n, and N_ω is the total number of discrete frequencies for $S^*_{X_j X_j}(\omega_n)$. $\varphi_n \in [0, 2\pi)$ is a continuous and uniformly distributed random phase angle for the wave component at ω_n, $\psi_{j,n} \in [-\pi, \pi)$ is the phase angle between the wave elevation and the vessel response at ω_n corresponding to the signal $x_j(t)$. For example, the complex-valued linear transfer function $H_j(\omega, \beta_W)$ equals to $|H_j(\omega_n, \beta_W)| \exp(1i \times \psi_{j,n})$. $S^*_{X_j X_j}(\omega_n)$ for periods between 3 s and 40 s was considered. In order to sufficiently capture the spectral information at the periods of main interest and reduce the numerical integration error, the period intervals (i.e., ΔT_n) for the discrete periods from 5 s to 25 s were set to 0.125 s. For periods from 3 s to 5 s and from 25 s to 26 s, ΔT_n was set to 0.25 s; and for periods from 26 s to 40 s, ΔT_n is 0.5 s. Consequently, the frequency intervals $\Delta\omega_n$ applied in Eq. (14) were unevenly distributed, thus avoiding time record repetition.

Finally, the virtual signal $x_j(t)$ was generated by adding noise to each time step of $x_j^*(t)$. Independent Gaussian distributed white noise was assumed with specified signal-to-noise ratio (SNR):

$$SNR = \frac{\sigma^2_{X_j}}{\sigma^2_N} \tag{15}$$

where $\sigma^2_{X_j}$ is the variance of the true response spectrum and σ^2_N is the noise variance.

Each case study considered 20 randomly generated sea states. Each sea state was assumed to last for 30 min. No transition between sea states was considered, thus assuming that each sea state is independent from the others. The values of the key parameters for the base case study are summarized in Table 4 with respect to case simulations and in Table 5 with respect to UKF modeling. The initial state is also summarized in Table 5.

Please note that ε_{H_s}, ε_{T_p}, and ε_{β_W} are the errors from the acquired wave information which are random and Gaussian distributed, i.e.,

$$\varepsilon_{H_s} = \sigma_{H_s} \cdot \text{rand}[\mathcal{N}(0,1)] \sim \mathcal{N}(0, \sigma^2_{H_s}) \tag{16a}$$

$$\varepsilon_{T_p} = \sigma_{T_p} \cdot \text{rand}[\mathcal{N}(0,1)] \sim \mathcal{N}(0, \sigma^2_{T_p}) \tag{16b}$$

$$\varepsilon_{\beta_W} = \sigma_{\beta_W} \cdot \text{rand}[\mathcal{N}(0,1)] \sim \mathcal{N}(0, \sigma^2_{\beta_W}) \tag{16c}$$

where σ_{H_s}, σ_{T_p}, and σ_{β_W} are the standard deviations of the acquired wave information (i.e., H_s, T_p, and β_W) as indicated in Table 2, representing their uncertainties. rand$[\mathcal{N}(0,1)]$ means a randomly selected value from an unit normal distribution i.e., $\mathcal{N}(0,1)$. A lowpass filter based on fast Fourier transform (FFT) was applied for each sensor signal to remove the signal noises as much as

Table 4
Applied parameters in the base case simulation.

Parameter	Value
H_s^*[a]	Uniformly distributed in [1.0, 4.0] m
T_p^*[a]	Uniformly distributed in [5.0, 20.0] s
β_W^*[a]	Uniformly distributed in [0.0°, 360.0°]
σ_{H_s}	$10\%H_s^*$ m
σ_{T_p}	0.5 s
σ_{β_W}	5°
$\overline{H}_s$[b]	$H_s^* + \varepsilon_{H_s}$
$\overline{T}_p$[b]	$T_p^* + \varepsilon_{T_p}$
$\overline{\beta}_W$[b]	$\beta_W^* + \varepsilon_{\beta_W}$
Initial seed τ	44
Sea state duration	1800 s
Number of sea states	20
SNR	50
f_{lp}	0.2 Hz

[a]Superscript $*$ means the true value of the corresponding parameters. The acquired wave information ($\overline{H}_s$, $\overline{T}_p$, $\overline{\beta}_W$) is subject to errors (i.e., ε_{H_s}, ε_{T_p}, and ε_{β_W}).

[b]The overlines over the parameters means that they are the simulated acquired values which can be different from the true values.

Table 5
Applied parameters in the base case related to UKF modeling.

Parameter	Value
State $\boldsymbol{x}$	$\boldsymbol{x} = [\beta_{44}, XCG, H_s, T_p, \beta_W]^\top$
Initial $\boldsymbol{\phi}_0$	$\boldsymbol{\phi}_0 = [\beta_{44}, XCG]^\top = [7\%, 59.4\text{ m}]^\top$
Initial $\boldsymbol{P}_{\boldsymbol{\phi}_0}$	$\boldsymbol{P}_{\boldsymbol{\phi}_0} = \text{diag}(0.035^2, 4.0^2)$
$\boldsymbol{R}$	$\boldsymbol{R} = 2\% \cdot \text{diag}(\hat{\sigma}_1^2, \ldots, \hat{\sigma}_J^2)$
$\boldsymbol{Q}$	$\boldsymbol{Q} = \text{diag}(0.005^2, 0.1, 0.05^2, 0.01, 0.25)$
α	0.01
β	2
κ	−2

possible. A SNR of 50 was considered. Sensitivity studies with respect to the SNR (varied from 30 to 200) showed very stable tuning performance due to the application of a lowpass filter to remove the high-frequency noises as accurately as possible. Ideally, the cutoff frequency f_{lp} should be sea state and vessel dependent. For simplicity, a constant cutoff frequency $f_{lp} = 0.2$ Hz was applied. Please note that the initial seed τ uniquely determines the true sea states, the normalized random values of rand$[\mathcal{N}(0,1)]$ (and consequently the acquired wave information with the same parameter uncertainties), and the random phase angles φ_n for the time series from the deterministic discrete frequencies. Consequently, τ uniquely determines the simulated sea states and the virtual sensor signals in the coded program for the long-crested wave conditions. The randomly generated values of rand$[\mathcal{N}(0,1)]$ for ε_{H_s}, ε_{T_p}, and ε_{β_W} are independent.

The measurement uncertainty covariance matrix $\boldsymbol{R}$ is a diagonal matrix. For each sensor j, the measurement variance was set to be 2% of the variance of the filtered sensor signal $\hat{\sigma}_j^2$. Small values were used for the process uncertainty covariance matrix $\boldsymbol{Q}$, which represents how well the propagation model can describe the process. For the numerical simulation, a stationary condition was fulfilled so that the proposed propagation model can very well represent the simulated conditions. However, slow-varying characteristics may be commonly seen in reality for the vessel and wave conditions. Therefore, the values of the $\boldsymbol{Q}$ matrix should be increased to reflect this effect. Initial sensitivity studies of key parameters in the UKF model indicate that a smaller α generally leads to better performance. UKF with smaller α selects the sigma points closer to each other so that the local effects are more displayed, while UKF with larger α tends to focus more on the global system behavior. Therefore, a smaller value of α is preferred for highly nonlinear problems. On the other hand, a small α easily leads to a negative weight factor w_0^c for large dimensional problems, and thus cannot guarantee a positive semi-definite state covariance matrix $\boldsymbol{P}$. Such a challenge was not noted during the performance of the simulations and therefore, no modification to the proposed algorithm was made.

Initial studies also indicated that it is beneficial to use a slightly larger initial covariance matrix for the vessel state, $\boldsymbol{P}_{\boldsymbol{\phi}_0}$. A larger initial $\boldsymbol{P}_{\boldsymbol{\phi}_0}$ will accelerate the vessel state convergent towards their true values, and $\boldsymbol{P}_{\boldsymbol{\phi}}$ will approach its convergent value which is independent from its initial value.

Table 6
Range of vessel model parameters in the RAO database.

Parameters	Variation range	Number of values
β_{44}	[2%, 14%]	7
XCG	[55.4 m, 63.4 m]	5

Table 7
Applied parameters in the base case related to UKF modeling.

Parameter	Value
n_s^*	Uniformly distributed in [2.0, 5.0]
$\overline{n}_s$	3.5
σ_{n_s}	1.0
State $\boldsymbol{x}$	$\boldsymbol{x} = [\beta_{44}, XCG, H_s, T_p, \beta_W, n_s]^\top$
$\boldsymbol{Q}$	$\boldsymbol{Q} = \mathrm{diag}(0.005^2, 0.1, 0.05^2, 0.01, 0.25, 0.09)$
κ	−3

4.2. Measurement functions

The measurement function as shown in Eqs. (8) and (10) varies with the calculated sigma points. Therefore, seakeeping analysis is preferably performed for each determined sigma point as illustrated in Fig. 1. However, for simplicity, a RAO database with limited amount of combinations of uncertain vessel parameters inherited from earlier research work [25] was used. The available discrete values of β_{44} and XCG in the RAO database are summarized in Table 6. The measurement estimation (i.e., the standard deviations of the interesting vessel motions $\sigma_j(\beta_{44}, XCG)$) can be approximated by linear interpolation of neighboring values $\sigma_j(\beta'_{44}, XCG')$, $\sigma_j(\beta''_{44}, XCG')$, $\sigma_j(\beta'_{44}, XCG'')$, $\sigma_j(\beta''_{44}, XCG'')$ calculated based on the available RAOs in the RAO database, where β'_{44}, XCG', β''_{44}, XCG'' are the available values in the RAO database and $\beta'_{44} < \beta_{44} < \beta''_{44}$, $XCG' < XCG < XCG''$.

The uncertainties caused by applying linear RAOs as the system model may consist of model bias and model scatter. The model bias is the average model error compared with the actual system, whereas the random component with respect to the model bias refers to the model scatter [52]. The model bias may be introduced by simplifications and assumptions made in the seakeeping software and the numerical model. However, zero model bias was assumed for the measurement function. The model scatter is accounted for by means of the measurement uncertainty covariance matrix $\boldsymbol{R}$.

4.3. Short-crested waves

Long-crested waves barely exist in the real world. Therefore, it is worth demonstrating, as a sensitivity case study, how the short-crested waves can be considered in the proposed tuning framework. The short-crested wave condition may be approximated by multiplying the uni-directional PM wave spectrum with a directional spreading function $D(\beta_W)$ [42]:

$$S_{\zeta\zeta}(\omega, \beta_W) \approx S_{\zeta\zeta}(\omega) D(\beta_W) \tag{17a}$$

$$D(\beta_W) = \frac{\Gamma(1 + n_s/2)}{\sqrt{\pi}\Gamma(1/2 + n_s/2)} \cos^{n_s}(\beta_W - \beta_{Wp}) \tag{17b}$$

where Γ is the Gamma function, β_{Wp} is the prevailing wave direction and $|\beta_W - \beta_{Wp}| \leq \frac{\pi}{2}$. n_s is the spreading parameter, $2 \leq n_s \leq 4$ for wind sea, and $n_s > 7$ for swells [42]. Consequently, the spreading parameter n_s should therefore be included in the sea state vector $\boldsymbol{\theta}$. For the sensitivity study on short-crested waves, the applied key parameters that are different from the base case are summarized in Table 7. In reality, the acquired wave information may not contain the spreading information, e.g., in terms of n_s value. Therefore, the sensitivity study assumed that the estimation of n_s was not acquired from wave measurements, hindcast, or forecast. For each new sea state, n_s is set to be 3.5, with a variance of 1.0.

When short-crested waves are considered, Eqs. (13) and (14) are substituted by:

$$x_j^*(t) = \sum_{u=1}^{N_{\beta_W}} \sum_{v=1}^{N_\omega} C_{u,v} \cos(\omega_{u,v} t + \varphi_{u,v} + \psi_{j,u,v}) \tag{18a}$$

$$C_{u,v} = \sqrt{2 S^*_{X_j X_j}(\omega_{u,v}, \beta_{W_u}) \Delta\omega_{u,v} \Delta\beta_W} \tag{18b}$$

$$S^*_{X_j X_j}(\omega_{u,v}, \beta_{W_u}) = |H_j^*(\omega_{u,v}, \beta_{W_u})|^2 S_{\zeta\zeta}(\omega_{u,v}, \beta_{W_u}) \tag{18c}$$

where N_ω is the number of discrete frequencies $\omega_{u,v}$ for each wave direction β_{W_u}. The subscript of $\omega_{u,v}$ indicates that the values of discrete frequencies also depend on the wave direction. For each β_{W_u} in the sensitivity study of short-crested wave conditions, 800 discrete frequencies were randomly generated, assuming that frequencies are uniformly distributed between 0.157 rad/s and 2.094 rad/s (i.e., periods between 3 s and 40 s), in order to avoid non-ergodic wave realizations [53]. Compared with long-crested wave conditions, much more discrete frequencies were generated for each direction in order to assure a sufficiently small frequency

interval at the frequency range of main interest. Consequently, $\Delta\omega_{u,v}$ differs for each $\omega_{u,v}$. Constant $\Delta\beta_W$ of 2° was considered. $\varphi_{u,v} \in [0, 2\pi)$ is the random phase angle for wave component at $(\omega_{u,v}, \beta_{W_u})$, $\psi_{j,u,v} \in [-\pi, \pi)$ is the phase angle for the linear transfer function $H_j^*(\omega_{u,v}, \beta_{W_u})$. The power spectral density of the short-crested waves $S_{\zeta\zeta}(\omega_{u,v}, \beta_{W_u})$ can be calculated according to Eq. (17).

5. Results

New parameters $\%\Delta\sigma^2_{H_s}$, $\%\Delta\sigma^2_{T_p}$, and $\%\Delta\sigma^2_{\beta_W}$ are defined in order to present the relative reduction of the variance in percentage for the corresponding sea state characteristics.

$$\%\Delta\sigma^2_{H_s} = \frac{\sigma^2_{H_s} - \hat{\sigma}^2_{H_s}}{\sigma^2_{H_s}} \times 100\% \tag{19a}$$

$$\%\Delta\sigma^2_{T_p} = \frac{\sigma^2_{T_p} - \hat{\sigma}^2_{T_p}}{\sigma^2_{T_p}} \times 100\% \tag{19b}$$

$$\%\Delta\sigma^2_{\beta_W} = \frac{\sigma^2_{\beta_W} - \hat{\sigma}^2_{\beta_W}}{\sigma^2_{\beta_W}} \times 100\% \tag{19c}$$

where $\sigma^2_{H_s}$, $\sigma^2_{T_p}$, and $\sigma^2_{\beta_W}$ represents the variance of the acquired sea state characteristics, while $\hat{\sigma}^2_{H_s}$, $\hat{\sigma}^2_{T_p}$, and $\hat{\sigma}^2_{\beta_W}$ indicate their tuned values after measurement update.

$\Delta\overline{H}_s$, $\Delta\overline{T}_p$, and $\Delta\overline{\beta}_W$ are also defined to represent the difference between the true and the acquired wave information, while $\Delta\hat{H}_s$, $\Delta\hat{T}_p$, and $\Delta\hat{\beta}_W$ are defined to represent the difference between the true and the tuned values of the wave parameters after measurement update stage, i.e.,

$$\Delta\overline{H}_s = \varepsilon_{H_s} = H_s^* - \overline{H}_s \tag{20a}$$

$$\Delta\overline{T}_p = \varepsilon_{T_p} = T_p^* - \overline{T}_p \tag{20b}$$

$$\Delta\overline{\beta}_W = \varepsilon_{\beta_W} = \beta_W^* - \overline{\beta}_W \tag{20c}$$

and

$$\Delta\hat{H}_s = H_s^* - \hat{H}_s \tag{21a}$$

$$\Delta\hat{T}_p = T_p^* - \hat{T}_p \tag{21b}$$

$$\Delta\hat{\beta}_W = \beta_W^* - \hat{\beta}_W \tag{21c}$$

5.1. Base case

The randomly generated sea states according to Table 4 for the base case are summarized in Table 8 and the tuning results are summarized in Table 9. k indicates the sea state number. A superscript $*$ indicates the true value of the parameter, while an overline over the parameter means the corresponding acquired (prior) information. A hat $\hat{}$ over the parameter indicates its value after the measurement update step for the corresponding sea state k.

Fig. 4 shows the standard deviations of the filtered sensor signals (blue points) and the corresponding estimated standard deviations of the vessel responses (i.e., the "predicted measurements") by transferring the system states from the state space to the measurement space based on the unscented transformation described in Section 3.4. The difference between the acquired and the predicted measurement is the residual $\boldsymbol{y}$ defined in Eq. (11b). Fig. 5 illustrates how the uncertain vessel parameters β_{44} and XCG vary through the simulation. The dotted green lines are the true values. The black lines are the predicted values of the uncertain parameters after the system propagation described in Section 3.3, while the filled gray areas indicate the corresponding 95% confidence interval for the parameters, i.e., $\pm 2\sigma$ where σ is the variable standard deviation. The red lines are the updated values after the measurement update step described in Section 3.4, and the filled red areas indicate the corresponding 95% confidence interval. Fig. 5 shows a successful tuning of β_{44} and XCG and reduction of their uncertainties.

While the proposed algorithm managed to tune the uncertain vessel parameters, knowledge about the sea state characteristics were also improved simultaneously, as shown in Figs. 6 to 8. Generally, the tuning algorithm helped to reduce the overall errors and variance from the acquired wave information. For example, the largest error of the acquired H_s (i.e., $\Delta\overline{H}_s$) happened at $k = 9$. The tuning algorithm managed to reduce such errors from 0.5 m to 0.2 m. Furthermore, the information variance on H_s was reduced by 58%. Even though increased errors after tuning were observed for some sea states (e.g., $k = 6,\ 13,\ 18$), it only happened when the error from the acquired information was already relatively small. In addition, such increased errors did not prevent the system from significantly reducing the uncertainty (variance). In comparison, error reduction with respect to T_p and β_W may not be that dramatic, because the influence of T_p and β_W on the vessel motions is not as monotonous and simple as that of H_s. Please note that error reduction is different from uncertainty reduction. There is a significant possibility that for a certain parameter (e.g., H_s) the error increases while its variance reduces.

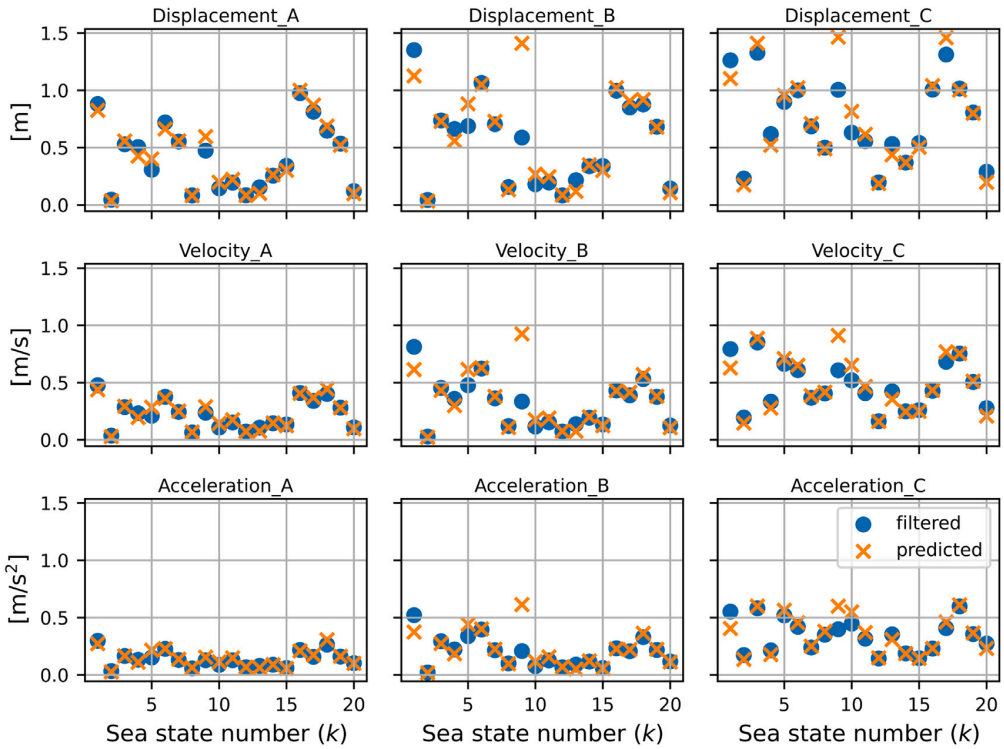

Fig. 4. The acquired (after signal filtering) and predicted measurements for the base case from the 9 virtual sensors described in Table 3 for the 20 sea states, base case $\tau = 44$.

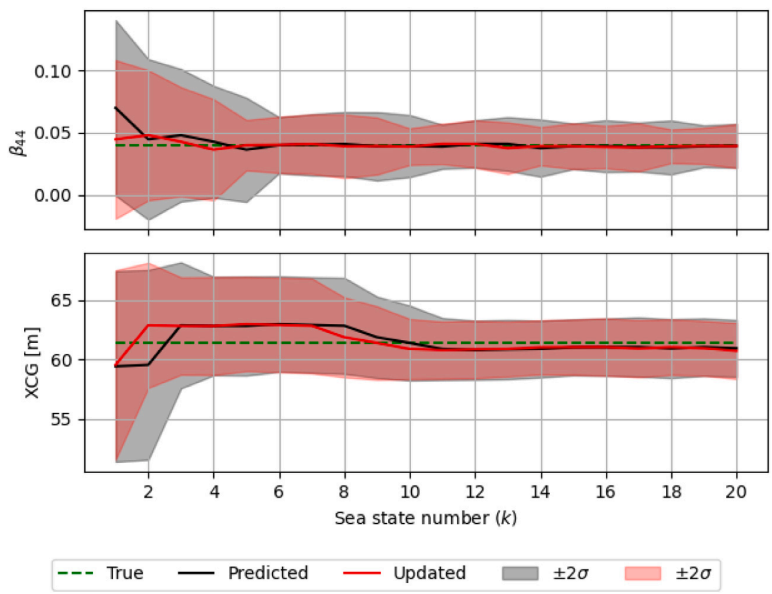

Fig. 5. The results of tuning β_{44} and XCG for the base case $\tau = 44$. (For interpretation of the references to color in this figure legend, the reader is referred to the web version of this article.)

Table 8
The true and the acquired sea state characteristics for the base case.

k	H_s^*	T_p^*	β_W^*	$\overline{H}_s$	$\overline{T}_p$	$\overline{\beta}_W$
1	3.5	14.6	256.0	3.3	15.3	257.9
2	1.3	7.1	26.1	1.1	7.1	22.1
3	3.2	11.9	317.7	3.5	12.2	323.5
4	2.1	18.1	261.4	1.7	18.0	261.5
5	2.1	8.9	300.0	2.2	9.1	290.5
6	2.8	15.0	255.7	2.8	14.1	251.4
7	2.2	17.9	251.1	2.3	18.0	250.8
8	2.2	7.2	334.8	2.4	6.9	341.0
9	2.5	13.4	317.4	3.0	14.1	314.7
10	3.1	7.4	34.2	3.6	7.8	32.5
11	3.9	7.6	164.3	4.3	7.5	156.6
12	2.4	6.6	177.4	2.7	6.2	183.5
13	2.3	8.0	39.2	2.3	7.6	27.9
14	1.3	11.8	55.3	1.4	12.1	56.4
15	1.7	16.9	354.3	1.6	16.6	354.1
16	3.9	19.9	97.8	4.0	20.7	99.2
17	3.8	17.1	323.0	4.3	16.5	326.0
18	3.6	10.7	59.1	3.6	10.3	64.3
19	2.9	12.7	47.6	2.9	12.2	47.7
20	1.6	5.9	114.2	1.5	5.2	105.5

Table 9
Tuning results for base case.

k	$\hat{H}_s$	$\hat{T}_p$	$\hat{\beta}_W$	$\%\Delta\sigma^2_{\hat{H}_s}$	$\%\Delta\sigma^2_{\hat{T}_p}$	$\%\Delta\sigma^2_{\hat{\beta}_W}$	$\hat{\beta}_{44}$	$\widehat{\mathrm{XCG}}$	$\hat{\sigma}^2_{\hat{\beta}_{44}}$	$\hat{\sigma}^2_{\widehat{XCG}}$
1	3.7	15.1	258.0	67%	7%	16%	0.045	59.53	1.02E−03	15.87
2	1.2	7.3	22.6	18%	65%	8%	0.048	62.86	6.88E−04	6.94
3	3.4	12.1	322.4	51%	18%	37%	0.043	62.80	4.84E−04	4.21
4	2.0	17.9	261.8	69%	5%	10%	0.036	62.80	4.15E−04	4.25
5	2.0	9.0	297.1	54%	20%	67%	0.040	62.97	1.03E−04	3.94
6	2.7	14.2	252.4	57%	8%	35%	0.040	62.89	1.28E−04	3.95
7	2.2	18.1	250.5	67%	10%	27%	0.041	62.82	1.42E−04	3.98
8	2.3	7.1	338.2	31%	59%	43%	0.039	61.85	1.64E−04	2.83
9	2.7	14.0	317.8	58%	18%	55%	0.039	61.37	1.31E−04	2.38
10	3.4	7.5	29.8	34%	64%	33%	0.039	60.86	5.41E−05	1.60
11	4.1	7.3	159.4	41%	62%	31%	0.041	60.77	6.61E−05	1.45
12	2.7	6.2	182.2	20%	76%	22%	0.041	60.82	9.11E−05	1.46
13	2.5	8.4	30.7	40%	68%	8%	0.038	60.86	1.08E−04	1.33
14	1.3	12.0	55.6	47%	15%	34%	0.039	61.01	5.94E−05	1.30
15	1.6	16.6	354.1	72%	10%	2%	0.039	61.02	8.44E−05	1.35
16	4.0	20.6	98.8	72%	6%	23%	0.039	61.03	7.28E−05	1.45
17	3.9	16.6	326.6	69%	14%	42%	0.038	60.90	9.29E−05	1.44
18	3.6	10.3	61.5	59%	22%	58%	0.039	61.02	4.59E−05	1.37
19	2.9	12.3	47.7	61%	16%	40%	0.039	60.92	5.29E−05	1.33
20	1.6	5.5	109.1	11%	74%	39%	0.039	60.70	7.78E−05	1.39

The base case took approximately 120 s to run on the available laptop (CPU Intel(R) TM i7-8650U @ 1.90 GHz, 32 GB memory), from generating signals for the first sea state to updating the state vector for the last sea state, meaning that tuning of 5 parameters for each sea state approximately needs 6 s (including virtual sensor signal generation time). As an indicative comparison, Han et al. [25] reported that tuning of 4 parameters for one sea state approximately needs 90 s, running on the same laptop. Extraordinary improvement of computational efficiency is therefore demonstrated.

5.2. Seed variation

Simulations with different initial seed (τ) values other than 44 were performed. Generally, very stable tuning of β_{44} has been observed across all initial seeds. However, a convergent tuning result for XCG may not be observed after 20 sea states for some initial seed values, e.g., as shown in Fig. 9 with a value of $\tau = 16$. Earlier vessel parametric sensitivity studies [2] documented that the sensitivity of XCG on the vessel response varies with wave headings and wave periods, and the influence of XCG to the vessel response is generally less than the additional roll damping coefficient β_{44}. Therefore, a less accurately tuned XCG can be rational.

In general, tuning performance is very stable. Divergent tuning results have not been observed. However, less stable tuning may occur when insignificant vessel response is expected, e.g., at sea states with very small wave spectral peak periods. Consequently, the tuning can be very sensitive to the quality of signal filtering.

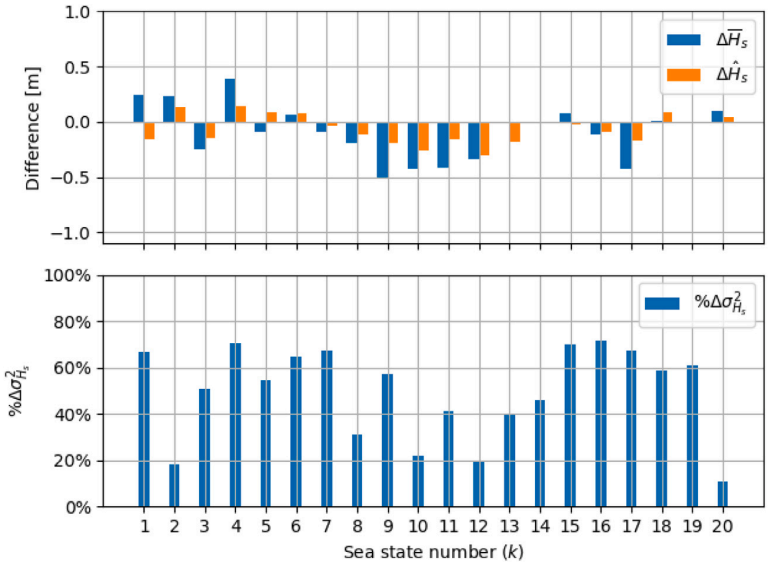

Fig. 6. Illustration of the errors before and after the tuning, and the variance reduction after tuning of H_s, for the base case $\tau = 44$.

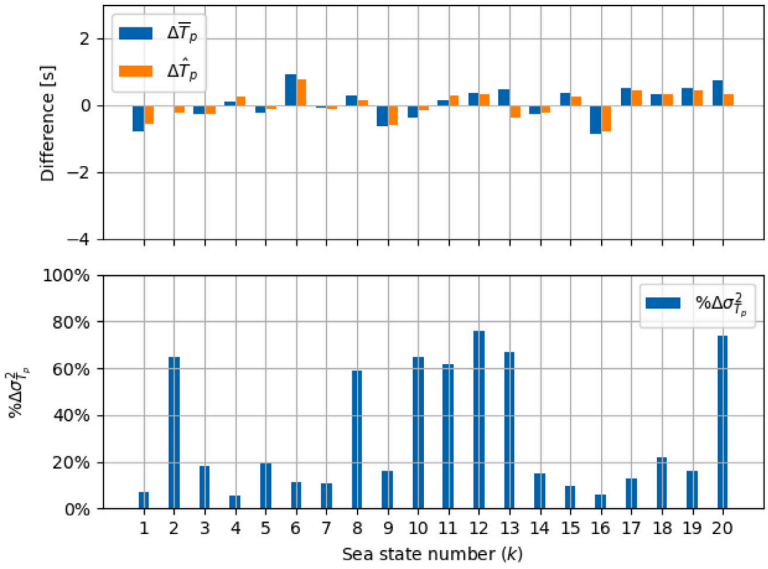

Fig. 7. Illustration of the errors before and after the tuning, and the variance reduction after tuning of T_p, for the base case $\tau = 44$.

5.3. Short-crested waves

As described in Section 4.3, a sensitivity case study was performed, considering short-crested wave conditions. The applied parameters that are different from Tables 4 and 5 are summarized in Table 7.

As shown in Fig. 10, tuning of uncertain vessel parameters was slightly influenced due to the introduced additional uncertainty from the wave spreading parameter n_s. The tuning of H_s and T_p (Figs. 11 and 12) are much less influenced by the introduced wave spreading and the uncertain n_s. Including uncertainty of wave spreading n_s can significantly influence the tuning of wave direction β_W, in terms of both the tuned expected value and the variance reduction. Comparing between Figs. 13 and 8, significantly reduced

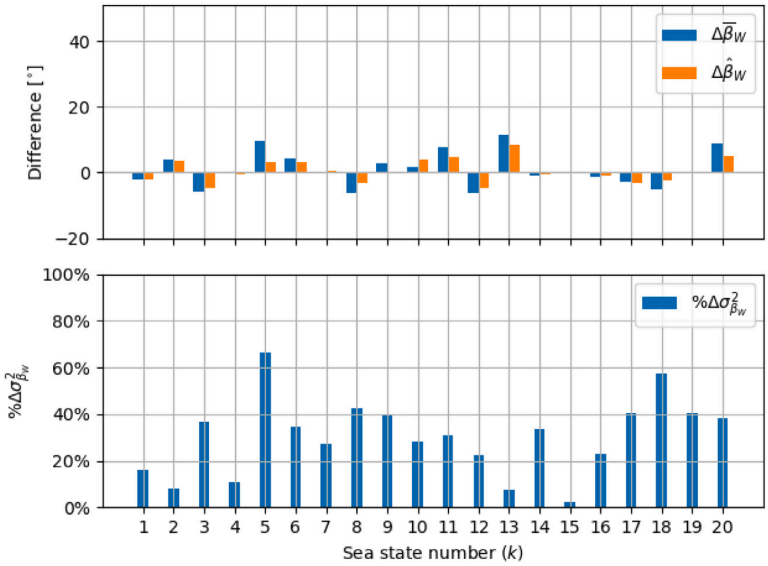

Fig. 8. Illustration of the errors before and after the tuning, and the variance reduction after tuning of β_W, for the base case $\tau = 44$.

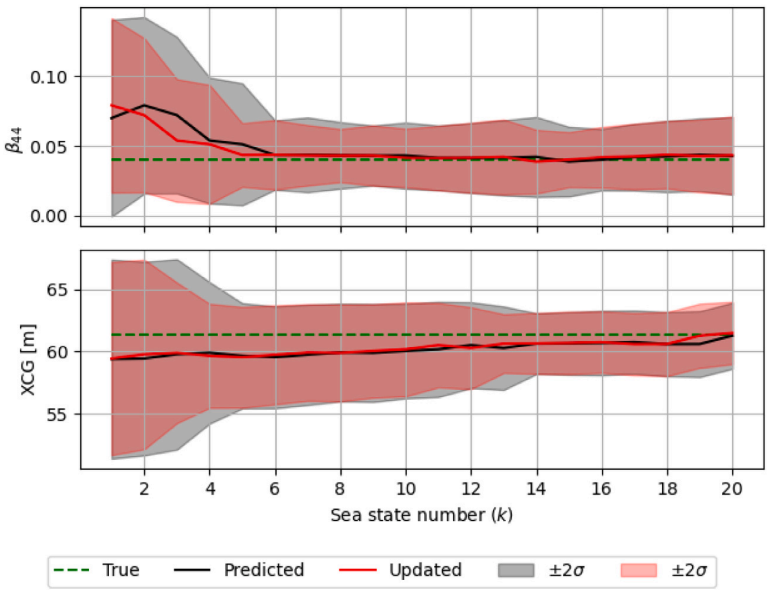

Fig. 9. The results of tuning β_{44} and XCG for the case with $\tau = 16$.

$\%\Delta\sigma^2_{\hat{\beta}_W}$ are generally observed, indicating less confidence improvement of the prevailing wave direction when considering short-crested waves with the uncertain spreading parameter. In addition, information on n_s itself was not significantly improved as shown in Fig. 14. Negative $\%\Delta\sigma^2_{n_s}$ indicates the increased uncertainty on spreading parameter after tuning.

5.4. Sensitivity of wave information uncertainty

Uncertainties of the vessel state and the sea state are interacting in the proposed algorithm. An increasingly confident vessel seakeeping model can help improving the wave information, while more accurate wave information will help reducing the

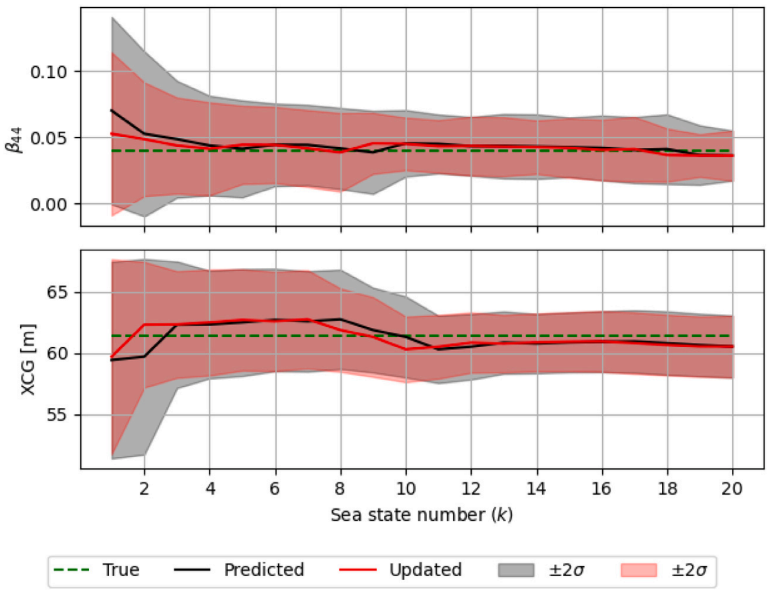

Fig. 10. The results of tuning β_{44} and XCG for the sensitivity study with respect to short-crested waves with $\tau = 44$.

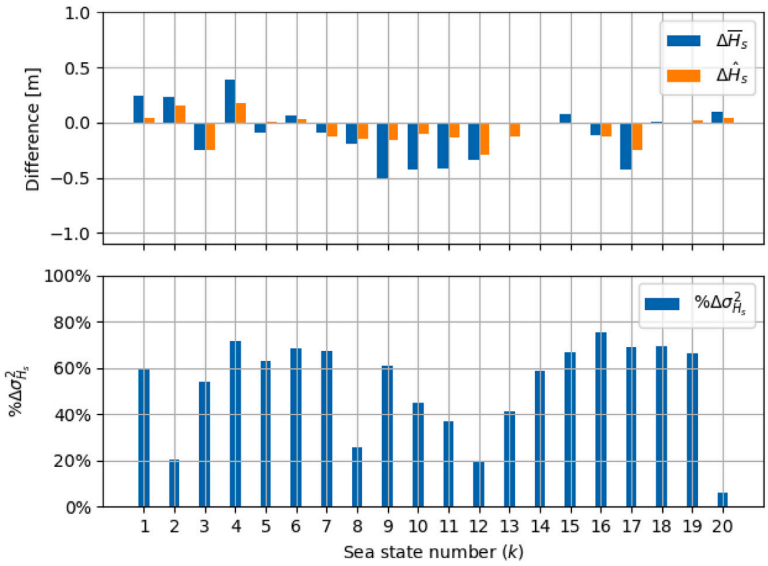

Fig. 11. Illustration of the errors before and after the tuning, and the variance reduction after tuning of H_s, for the sensitivity study with respect to short-crested waves with $\tau = 44$.

uncertainties of the vessel state. The base case assumed that the wave information can be acquired from measurements or hindcast, with a reasonably low uncertainty. However, such wave information may be delayed for several hours or up to some days. Therefore, it is interesting to test the algorithmic performance if the acquired wave information is subject to larger uncertainties when such wave measurements or hindcast data are not available. The alternative wave information source may come from forecast, visual observation, etc. Compared with the uncertainties of the WAM model in Table 1, much larger uncertainty of wave information was therefore considered in the sensitivity study, as shown in Table 10.

The same initial seed as for the base case was applied. Therefore, the same true sea states as shown in Table 8 were applied. The acquired sea states were consequently different from the base case, but the errors from the true sea states were proportional to

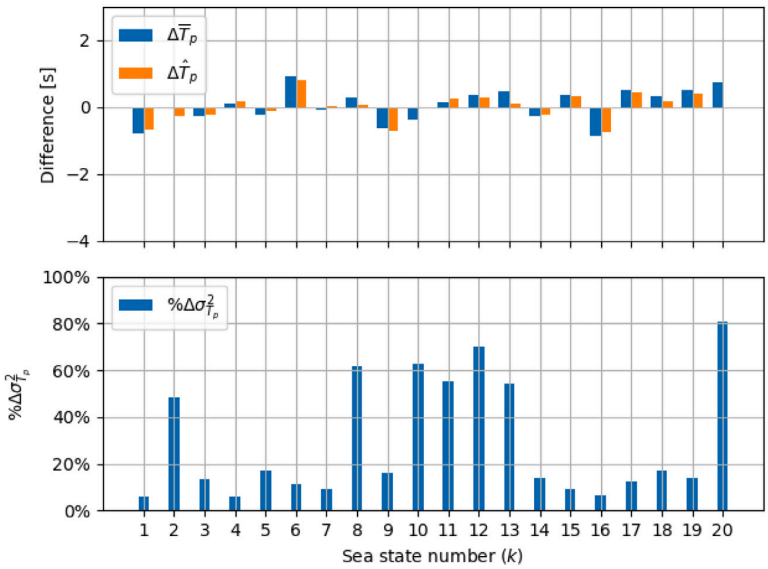

Fig. 12. Illustration of the errors before and after the tuning, and the variance reduction after tuning of T_p, for the sensitivity study with respect to short-crested waves with $\tau = 44$.

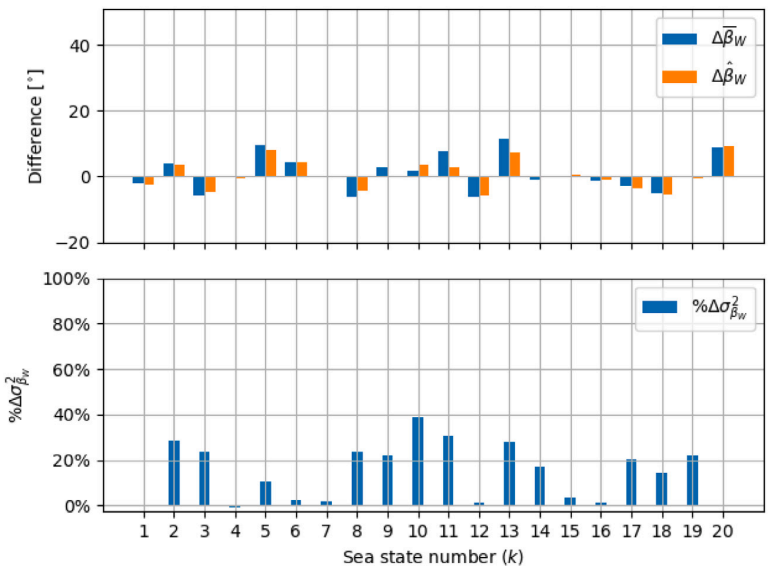

Fig. 13. Illustration of the errors before and after the tuning, and the variance reduction after tuning of β_W, for the sensitivity study with respect to short-crested waves with $\tau = 44$.

Table 10
Applied uncertainties of sea state characteristics in the sensitivity study with respect to wave information uncertainty.

Parameter	Standard deviation
σ_{H_s}	$20\%H_s^*$ m
σ_{T_p}	$10\%T_p^*$ s
σ_{β_W}	15°

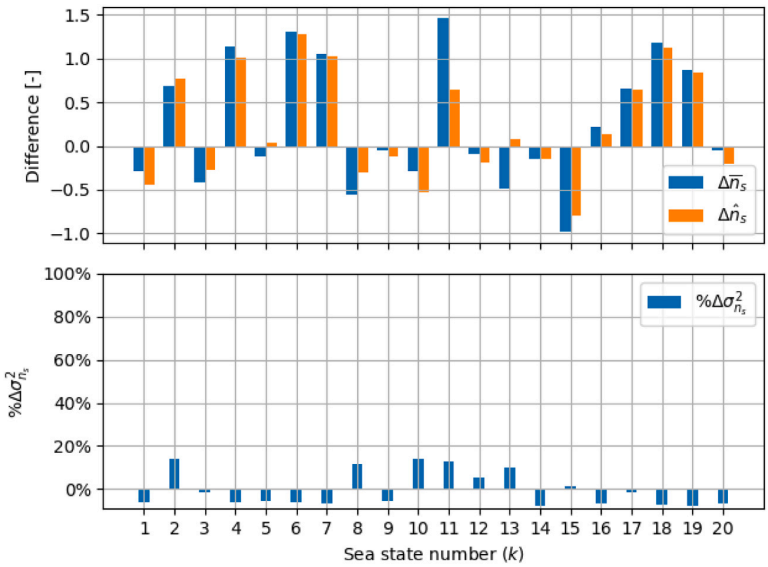

Fig. 14. Illustration of the errors before and after the tuning, and the variance reduction after tuning of n_s, for the sensitivity study with respect to short-crested waves with $\tau = 44$.

the corresponding errors in the base case. For example, the ratio of ϵ_{H_s} values between the base case and this sensitivity study was equal to the ratio of σ_{H_s} values between the base case and this sensitivity study.

Figs. 15 to 18 illustrate the tuning results of the vessel parameters and sea state characteristics based on larger wave information uncertainty. Fig. 15 shows a successful tuning of β_{44}. Whereas, convergent but slightly deviated tuning of XCG was observed when considering larger wave uncertainties. Compared with Fig. 5, the convergent XCG variance is larger when wave information is subject to larger variance, as shown in Fig. 15. Compared with the base case (e.g., at $k = 2$), the tuning of vessel state becomes smoother because of a relatively small Kalman gain in this sensitivity case. This means that the tuning algorithm rationally identifies larger uncertainty in the predicted measurements due to the specified larger wave information uncertainty. Consequently, the system reasonably focused more on improving the accuracy of the acquired wave information, as shown in Figs. 16 to 18. Significantly improved H_s, T_p, and β_W were observed compared with the base case. Much larger $\%\Delta\sigma^2_{H_s}$, $\%\Delta\sigma^2_{T_p}$, and $\%\Delta\sigma^2_{\beta_W}$ are shown in Figs. 16 to 18 compared with Figs. 6 to 8 in the base case.

6. Conclusions and future work

A computationally cheap and efficient algorithm for tuning of uncertain vessel seakeeping model parameters and important characteristics of wave information has been proposed. The algorithm is founded on the so-called unscented transformation and the corresponding scaled unscented Kalman filter, which can efficiently handle large dimensional problems and take the system nonlinearity into account. Its performance has been demonstrated by numerically simulated case studies based on an OSV. The benefit of including sea state characteristics in the system state vector is that the uncertainties of wave information can also be reduced through the process. The proposed method continuously improves the simultaneous knowledge about the vessel state and the sea state information based on the onboard vessel motion measurements and the acquired wave data. Reasonable tuning results can still be achieved even with higher wave information uncertainties as described in Section 5.4. In reality, wave information can be improved before the tuning procedure by fusion of wave data from multiple resources, such as from wave forecast, hindcast, onboard wave radar, visual observation, and nearby wave buoy measurements [33].

The algorithm contains several important parameters to tune, such as α, $\boldsymbol{Q}$, $\boldsymbol{R}$, and the initial $\boldsymbol{P}$ matrices. Experience suggests to apply a small α value (e.g., 0.1 or 0.01) for a better algorithmic performance. Normally, vessel heading and forward speed can vary slowly or be subjected to disturbance within a sea state. The process uncertainty $\boldsymbol{Q}$ should reflect how well the assumption about stationarity holds true in reality. Moreover, the vessel heading, forward speed, and inertia distribution can be frequently shifted depending on the operation scenarios (e.g., transportation, docking, and lifting). For such scenarios, control parameters should be introduced in the system propagation model. The measurement uncertainty $\boldsymbol{R}$ should in reality account for the possibly biased, non-Gaussian signal errors. It is also very important to filter the signal at the measurement update step in order to keep the vessel motion signals only in the wave frequency domain. It can be beneficial to initiate the vessel state covariance as being considerably larger than expected. Too small initial vessel state covariance indicates overconfidence in relation to the uncertain vessel parameters, leading to a too small Kalman gain $\boldsymbol{K}$ and thus slowing down the tuning towards convergence.

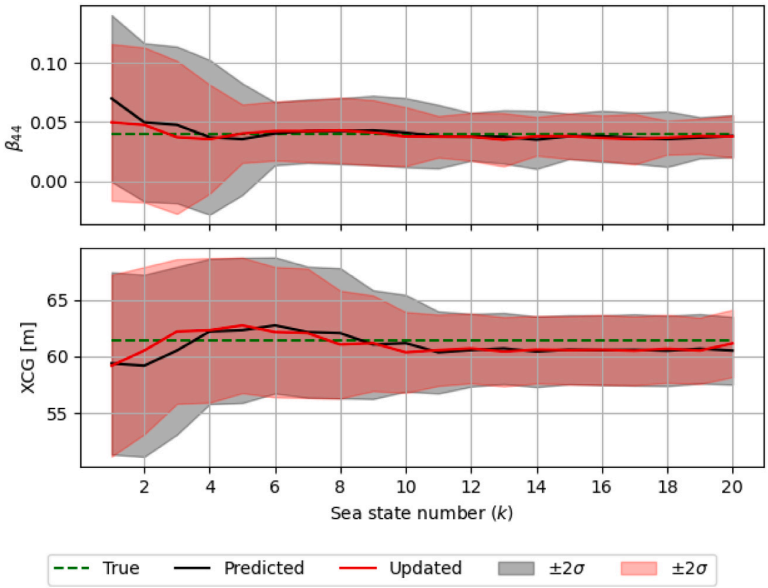

Fig. 15. The results of tuning β_{44} and XCG for the sensitivity study by using increasingly uncertain wave information with $\tau = 44$.

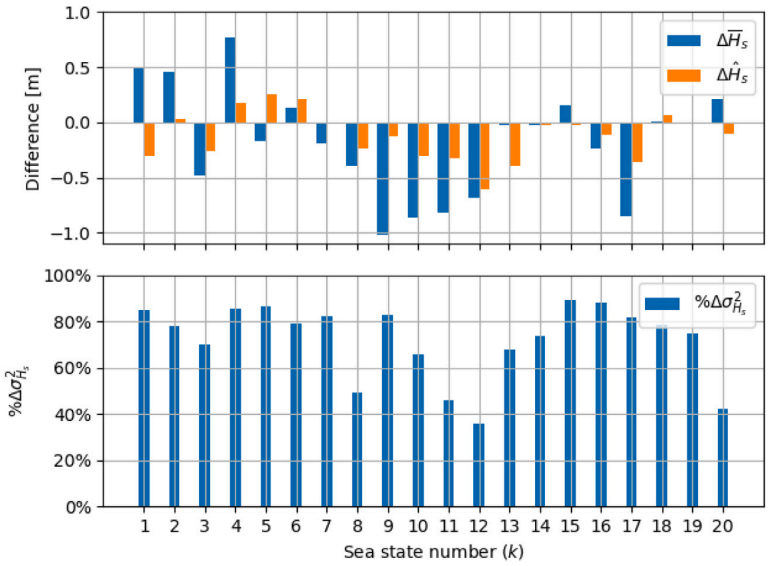

Fig. 16. Illustration of the errors before and after the tuning, and the variance reduction after tuning of H_s, for the sensitivity study by using increasingly uncertain wave information with $\tau = 44$.

The proposed algorithm is so flexible that the system state can basically include any uncertain parameters in relation to modeling of the linear potential theory based vessel seakeeping and description of sea state. A case study considering short-crested wave conditions with uncertain spreading parameter was also performed. As expected, the introduced uncertain spreading parameter n_s mainly affects the tuning of the wave direction related parameters such as β_W. n_s has very limited influence on tuning of the other sea state characteristics and vessel parameters simply because the wave direction related parameters influence the vessel motion measurements (i.e., the measurement space) differently from the other parameters.

In reality, a 2D wave spectrum with specified uncertainties in relation to each frequency component for each direction could be considered. The wave information uncertainties may be unbiased in the long term, whereas, these errors could be biased in the short

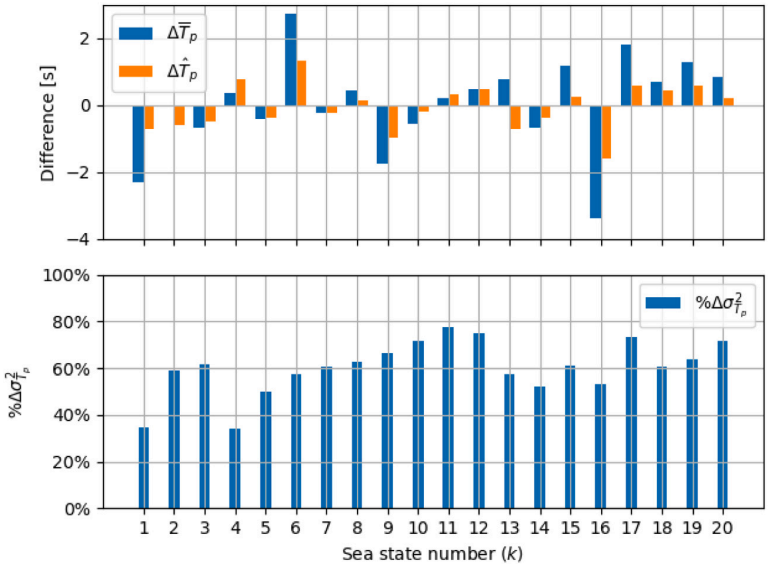

Fig. 17. Illustration of the errors before and after the tuning, and the variance reduction after tuning of T_p, for the sensitivity study by using increasingly uncertain wave information with $\tau = 44$.

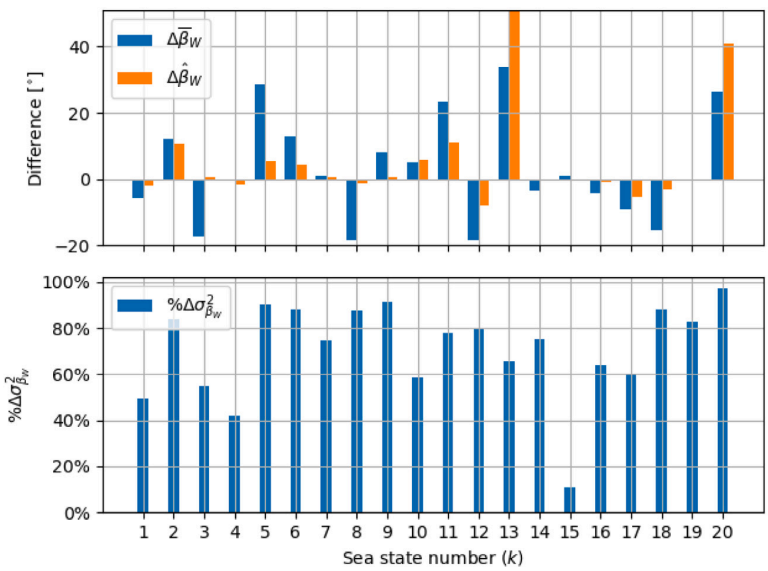

Fig. 18. Illustration of the errors before and after the tuning, and the variance reduction after tuning of β_W, for the sensitivity study by using increasingly uncertain wave information with $\tau = 44$.

term. This may therefore lead to divergent tuning results. The tuning model should, to a certain degree, tolerate those uncertainties, which might be challenging.

In reality, several other uncertain parameters should be considered including the vessel forward speed. Consequently, handling the response spectrum based on the encountered frequencies may become a challenge due to the well-known 3-to-1 mapping issue for following seas. The surface current, acting on the vessel as an additional "vessel speed", could also influence many important hydrodynamic coefficients such as damping and added mass. The measurements of surface current suffer from large uncertainties partly due to the influence from surface waves, the types and set-ups of instruments, and variation of the instrument quality for measuring current speed [35,54].

The vessel parameters related to inertia distribution and even geometry are time-variant in the long term. The real system should be able to detect the possible change of e.g., the vessel loading condition, and adaptively adjust the state accordingly. For example, this could be triggered when any of the updated vessel parameters is outside of its $\pm 3\sigma$ range.

So far, a constant value of the additional roll damping coefficient β_{44} for all sea states has been considered in the proposed UKF based tuning algorithm and the case studies. However, in reality β_{44} is sea state dependent. Han et al. [28] proposed an algorithm for tuning and prediction of sea state dependent roll damping, by application of discrete Bayesian inference with a surrogate model of roll damping. However, the procedure for the tuning of sea state dependent parameters is not straight forward for the proposed UKF based tuning algorithm. Tuning and predicting sea state dependent vessel parameters together with other uncertain parameters for the proposed UKF model considering uncertain wave information should be addressed in the future. Furthermore, the proposed algorithm should be validated by scaled tests and on-site measurement data.

It is also worth mentioning that the proposed UKF based tuning is an online algorithm. Since the vessel condition (in terms of vessel geometry, inertia distribution, etc.) typically does not change for a considerable period of time (e.g., few hours or days), the tuned vessel parameters and the corresponding vessel motion RAOs can therefore be applied to improve the prediction accuracy of vessel motions for real-time applications. However, vessel loading conditions can vary continuously and significantly during many critical marine operations, such as heavy lift and pipe laying. Consequently, the tuned vessel parameters based on available data before such operations may not be suitable to apply directly. Future research should consider how to tune and predict the vessel parameters, and consequently improve the prediction accuracy of critical responses during such non-stationary operations.

Declaration of competing interest

The authors declare that they have no known competing financial interests or personal relationships that could have appeared to influence the work reported in this paper.

Acknowledgments

This work was made possible through the Centre for Research based Innovation MOVE, financially supported by the Research Council of Norway, NFR project no. 237929 and the consortium partners, http://www.ntnu.edu/move. Special thanks are given to Section of Hydrodynamics & Stability in DNV GL for providing the seakeeping models.

References

[1] Tellkamp J, Bruns A, Gosch T, Günther H, Hansen PF, Nielsen UD, Papanikolaou A, Spanos D, Papatzanakis G, Kassner S, Wittkuhn D, Tränkmann I, Ehrke K-C, Krüger S, Vorhoelter H, Kluwe F, Jaap Struijk JKN. ADOPT summary of experiences and needs for further development. Technical report, FORCE Technology and Uniresearch; 2009.

[2] Han X, Sævik S, Leira BJ. A sensitivity study of vessel hydrodynamic model parameters. In: Proceedings of the ASME 2020 39th international conference on ocean, offshore and arctic engineering, Vol. 1. Virtual, Online; 2020, http://dx.doi.org/10.1115/OMAE2020-19039.

[3] Journée J, Pinkster J. Introduction in ship hydromechanics. Technical report, Delft University of Technology; 2002.

[4] Li G, Kawan B, Wang H, Zhang H. Neural-network-based modelling and analysis for time series prediction of ship motion. Ship Technol Res 2017;64(1):30–9. http://dx.doi.org/10.1080/09377255.2017.1309786.

[5] Kawan B, Wang H, Li G, Chhantyal K. Data-driven modeling of ship motion prediction based on support vector regression. In *Proceedings of the 58th conference on simulation and modelling (SIMS 58)*, 2017.

[6] Zhang W, Liu Z. Real-time ship motion prediction based on time delay wavelet neural network. J Appl Math 2014.

[7] Zhao X, Xu R, Kwan C. Ship-motion prediction: Algorithms and simulation results. In: 2004 IEEE international conference on acoustics, speech, and signal processing, Vol. 5. IEEE; 2004, p. V–125.

[8] Nielsen UD, Brodtkorb AH, Jensen JJ. Response predictions using the observed autocorrelation function. Mar Struct 2018;58:31–52. http://dx.doi.org/10.1016/j.marstruc.2017.10.012.

[9] DNVGL-ST-N001. Marine operations and marine warranty. Technical report, DNV GL; 2016.

[10] Faltinsen OM. Sea loads on ships and offshore structures. New York: Cambridge University Press Cambridge; 1990.

[11] Alford LK, Beck RF, Johnson JT, Lyzenga D, Nwogu O, Zundel A. A real-time system for forecasting extreme waves and vessel motions. International conference on offshore mechanics and arctic engineering, Volume 11: Prof. Robert F. Beck Honoring Symposium on Marine Hydrodynamics, 2015, http://dx.doi.org/10.1115/OMAE2015-42420.

[12] Connell BSH, Rudzinsky JP, Brundick CS, Milewski WM, Kusters JG, Farquharson G. Development of an environmental and ship motion forecasting system. In: International conference on offshore mechanics and arctic engineering, Volume 11: Prof. Robert F. Beck Honoring Symposium on Marine Hydrodynamics, 2015, http://dx.doi.org/10.1115/OMAE2015-42422.

[13] Stredulinsky DC, Thornhill EM. Ship motion and wave radar data fusion for shipboard wave measurement. J Ship Res 2011;55:73–85.

[14] Naaijen P, Roozen DK, Huijsmans RHM. Reducing operational risks by on-board phase resolved prediction of wave induced ship motions. International conference on offshore mechanics and arctic engineering, Volume 7: Ocean Engineering, 2016, http://dx.doi.org/10.1115/OMAE2016-54591.

[15] Hilmer T, Thornhill E. Deterministic wave predictions from the WaMoS II. In: OCEANS 2014 - taipei. 2014, p. 1–8. http://dx.doi.org/10.1109/OCEANS-TAIPEI.2014.6964526.

[16] Nielsen UD. A concise account of techniques available for shipboard sea state estimation. Ocean Eng 2017;129:352–62. http://dx.doi.org/10.1016/j.oceaneng.2016.11.035.

[17] Ren Z, Han X, Verma AS, Dirdal JA, Skjetne R. Sea state estimation based on vessel motion responses: Improved smoothness and robustness using Bézier surface and L1 optimization. Mar Struct 2021;76:102904. http://dx.doi.org/10.1016/j.marstruc.2020.102904.

[18] Galvin J. The use of information technology at the Met Office. British Computer Society, Bristol Branch January Seminar; 2014.

[19] Gusdal Y, Carrasco A, Furevik BR, Sætra Ø. Validation of the operational wave model WAM at met.no - report 2010. Technical report, Oslo: Norwegian Meteorological Institute; 2011.

[20] Hersbach H, Bell B, Berrisford P, Hirahara S, Horányi A, Muñoz Sabater J, Nicolas J, Peubey C, Radu R, Schepers D, Simmons A, Soci C, Abdalla S, Abellan X, Balsamo G, Bechtold P, Biavati G, Bidlot J, Bonavita M, De Chiara G, Dahlgren P, Dee D, Diamantakis M, Dragani R, Flemming J, Forbes R, Fuentes M, Geer A, Haimberger L, Healy S, Hogan RJ, Hólm E, Janisková M, Keeley S, Laloyaux P, Lopez P, Lupu C, Radnoti G, de Rosnay P, Rozum I, Vamborg F, Villaume S, Thépaut J-N. The ERA5 global reanalysis. Q J R Meteorol Soc 2020;146(730):1999–2049. http://dx.doi.org/10.1002/qj.3803, URL: https://rmets.onlinelibrary.wiley.com/doi/abs/10.1002/qj.3803 arXiv:https://rmets.onlinelibrary.wiley.com/doi/pdf/10.1002/qj.3803.

[21] Xu H, Hassani V, Guedes Soares C. Uncertainty analysis of the hydrodynamic coefficients estimation of a nonlinear manoeuvring model based on planar motion mechanism tests. Ocean Eng 2019;173:450–9. http://dx.doi.org/10.1016/j.oceaneng.2018.12.075.

[22] Xu H, Guedes Soares C. Hydrodynamic coefficient estimation for ship manoeuvring in shallow water using an optimal truncated LS-SVM. Ocean Eng 2019;191:106488.

[23] Yuan Y, Fu G, Zhang W. Extended and unscented Kalman filters for parameter estimation of a hydrodynamic model of vessel. In: 2016 35th chinese control conference (CCC). 2016, p. 2051–6.

[24] Fossen T, Sagatun S, SØrensen A. Identification of dynamically positioned ships. Control Eng Pract 1996;4(3):369–76. http://dx.doi.org/10.1016/0967-0661(96)00014-7.

[25] Han X, Leira BJ, Sævik S. Vessel hydrodynamic model tuning by discrete Bayesian updating using simulated onboard sensor data. Ocean Eng 2021;220. http://dx.doi.org/10.1016/j.oceaneng.2020.108407.

[26] ITTC. Recommended procedures and guidelines: Numerical estimation of roll damping. Technical report, International Towing Tank Conference; 2011.

[27] Kaplan P. Lecture notes on nonlinear theory of ship roll motion in a random seaway. 1966.

[28] Han X, Sævik S, Leira BJ. Tuning of vessel parameters including sea state dependent roll damping. Ocean Eng 2021. Revision under review.

[29] Gelman A, Carlin J, Stern H, Dunson D, Vehtari A, Rubin D. Bayesian data analysis. 3rd ed.. 2013.

[30] ECMWF. Part VII: ECMWF wave model. IFS documentation, vol. 7, ECMWF; 2016, URL: https://www.ecmwf.int/node/16651.

[31] Carrasco A, Saetra Ø. A limited-area wave ensemble prediction system for the Nordic Seas and the North Sea. Technical report, Oslo: Norwegian Meteorological Institute; 2008.

[32] ECMWF. Part V: Ensemble prediction system. IFS documentation, vol. 5, ECMWF; 2016, URL: https://www.ecmwf.int/node/16649.

[33] Natskår A, Moan T, Alvær P. Uncertainty in forecasted environmental conditions for reliability analyses of marine operations. Ocean Eng 2015;108:636–47.

[34] Orimolade AP, Furevik BR, Gudmestad OT. A comparison of wave height forecasts against wave measurements for a location in the barents sea and in the norwegian sea. In: Proceedings of the twenty-sixth (2016) international ocean and polar engineering conference. International Society of Offshore and Polar Engineers; 2016.

[35] Hagen Ø, Bitner-Gregersen EM, Vrouwenvelder A. JCSS probabilistic model code part 2: loads 2.15: wave loads. Technical report, Joint Committee on Structural Safety; 2006.

[36] World Meteorological Organization (2014). WMO guide to meteorological instruments and methods of observation. 2014.

[37] Reichert K, Hessner K, Nieto Borge JC, Dittmer J. WaMoS II: A radar based wave and current monitoring system. In: The Proceedings of the 9th (1999) International Offshore and Polar Engineering Conference. Brest, France: International Society of Offshore and Polar Engineers; 1999.

[38] Hersbach H, Bell B, Berrisford P, Biavati G, Horányi A, Muñoz Sabater J, Nicolas J, Peubey C, Radu R, Rozum I, Schepers D, Simmons A, Soci C, Dee D, Thépaut J-N. ERA5 hourly data on single levels from 1979 to present. 2021, http://dx.doi.org/10.24381/cds.adbb2d47, Copernicus Climate Change Service (C3S) Climate Data Store (CDS). Accessed on < 02-01-2021 >.

[39] ECMWF. Part II: Data assimilation. IFS documentation, vol. 2, ECMWF; 2016, URL: https://www.ecmwf.int/node/16666.

[40] ECMWF. Part I: Observations. IFS documentation, vol. 1, ECMWF; 2016, URL: https://www.ecmwf.int/node/16646.

[41] Bitner-Gregersen EM, Hagen Ø. Uncertainties in data for the offshore environment. Struct Saf 1990;7(1):11–34. http://dx.doi.org/10.1016/0167-4730(90)90010-M.

[42] DNVGL-RP-C205. Environmental conditions and environmental loads. Technical report, DNV GL; 2017.

[43] Labbe R. Kalman and bayesian filters in python. 2018, https://github.com/rlabbe/Kalman-and-Bayesian-Filters-in-Python.

[44] Van Der Merwe R, et al. Sigma-point Kalman filters for probabilistic inference in dynamic state-space models (Ph.D. thesis), OGI School of Science & Engineering at OHSU; 2004.

[45] Julier SJ, Uhlmann JK. New extension of the Kalman filter to nonlinear systems. In: Signal processing, sensor fusion, and target recognition VI. vol. 3068, International Society for Optics and Photonics; 1997, p. 182–93.

[46] Julier SJ. The scaled unscented transformation. In: Proceedings of the 2002 american control conference (IEEE Cat. No. CH37301), Vol. 6. IEEE; 2002, p. 4555–9.

[47] Nørgaard M, Poulsen NK, Ravn O. New developments in state estimation for nonlinear systems. Automatica 2000;36(11):1627–38. http://dx.doi.org/10.1016/S0005-1098(00)00089-3.

[48] Julier SJ, Uhlmann JK. A general method for approximating nonlinear transformations of probability distributions. Citeseer; 1996.

[49] Julier S, Uhlmann J, Durrant-Whyte HF. A new method for the nonlinear transformation of means and covariances in filters and estimators. IEEE Trans Automat Control 2000;45(3):477–82.

[50] DNV GL. Wasim user manual. Technical report, DNV GL; 2018.

[51] Lewandowski EM. The dynamics of marine craft: maneuvering and seakeeping, Vol. 22. World scientific; 2004.

[52] Nessim MA, Hong HP, Jordaan IJ. Environmental load uncertainties for offshore structures. Journal of Offshore Mechanics and Arctic Engineering 1995;117(4):245–51. http://dx.doi.org/10.1115/1.2827230.

[53] Jefferys E. Directional seas should be ergodic. Appl Ocean Res 1987;9(4):186–91. http://dx.doi.org/10.1016/0141-1187(87)90001-0, URL: http://www.sciencedirect.com/science/article/pii/0141118787900010.

[54] Bruserud K, Haver S. Uncertainties in current measurements in the northern north sea. J Atmos Ocean Technol 2017;34(4):855–76. http://dx.doi.org/10.1175/JTECH-D-16-0192.1.

A.7 Paper A7

Paper A7:
X. Han, B. J. Leira, S. Sævik, and K. E. Kaasen, 2021. Validation of vessel seakeeping model tuning algorithm based on measurements at model scale. *Marine Structures* 80.

Marine Structures 80 (2021) 103083

Contents lists available at ScienceDirect

Marine Structures

journal homepage: www.elsevier.com/locate/marstruc

Validation of vessel seakeeping model tuning algorithm based on measurements at model scale

Xu Han [a,b,*], Bernt Johan Leira [a,b], Svein Sævik [a,b], Karl Erik Kaasen [b,c]

[a] Department of Marine Technology, Norwegian University of Science and Technology (NTNU), 7491 Trondheim, Norway
[b] Centre for Research-based Innovation on Marine Operations (SFI MOVE), Norway
[c] Department of Ships and Ocean Structures, SINTEF Ocean AS, Trondheim, Norway

ARTICLE INFO

Keywords:
Vessel seakeeping
Model tuning
Model-scale tests
Unscented transformation
Systematic errors

ABSTRACT

Wave-induced vessel motion prediction plays a critical role in ensuring safe marine operations. The operational limiting criteria can usually be calculated by applying presumed linearized vessel motion transfer functions based on the specified vessel loading condition, which may deviate from the real vessel condition when the operation is executed. Reducing the uncertainties of the onboard vessel loading condition can therefore improve the accuracy of vessel motion prediction and hence improve the safety and cost-efficiency for marine operations. However, parameters related to the onboard vessel loading condition can be difficult to measure directly, such as the center of gravity and moments of inertia. In addition, the hydrodynamic viscous damping terms are always subject to significant uncertainties and sometimes become critical for accurate vessel motion predictions. A very promising algorithm for the tuning of these important uncertain vessel parameters based on the unscented Kalman filter (UKF) that uses onboard vessel motion measurements and synchronous wave information was proposed and demonstrated previously by application to synthetic data. The present paper validates the UKF-based vessel seakeeping model tuning algorithm by considering measurements from model-scale seakeeping tests. Validation analyses demonstrate rational tuning results. The observed random errors and bias in relation to the measurement functions due to the applied simplification and linearization in the seakeeping simulations can lead to biased tuning. The importance of designing the state space and the measurement space is demonstrated by case studies. Due to the nonlinear relationship between the uncertain vessel parameters and the vessel motions, the tuning is shown to be sensitive to the mean state vector and selection of the surrounding sigma points.

1. Introduction

Improving the accuracy of vessel motion prediction is important for safe and cost-efficient marine operations. Compared with second-order difference-frequency motions, the wave-induced vessel responses in the wave frequency region are more difficult to control due to their high-frequency dynamics, which may therefore practically dominate the operational limiting criteria for typical marine operations such as transportation and lifting. Hence, the wave-induced vessel response at wave frequencies, i.e, the seakeeping performance, is focused on in the present paper. The uncertainty of this vessel motion prediction can be reduced by (1) reducing the uncertainties of the wave forecast; (2) improving the knowledge and control of the vessel conditions on board, such

* Corresponding author at: Department of Marine Technology, Norwegian University of Science and Technology (NTNU), 7491 Trondheim, Norway.
E-mail address: xu.han@ntnu.no (X. Han).

https://doi.org/10.1016/j.marstruc.2021.103083
Received 28 March 2021; Received in revised form 25 May 2021; Accepted 27 June 2021

Nomenclature

α	Scaling factor for the UKF model
β	Hyperparameter in the UKF model in order to partially account for higher order statistical properties
β'_{44}	The difference of the VERES estimated linearized additional roll damping coefficient from its true value
β_{dd}	The linearized additional damping coefficient at mode d
β_W	Wave direction w.r.t. vessel coordinate system
$\bar{\boldsymbol{P}}_k$	The state covariance matrix for $\bar{\boldsymbol{x}}_k$
$\bar{\boldsymbol{x}}_k$	The predicted system state for the kth update
$\boldsymbol{\mathcal{X}}_{k,i}$	The ith sigma point for the system state $\boldsymbol{x}_k$, i.e., the ith column of $\boldsymbol{\mathcal{X}}_k$
$\boldsymbol{\mathcal{X}}_k$	The sigma points for the system state $\boldsymbol{x}_k$
$\bar{\boldsymbol{\mathcal{Z}}}_k$	The predicted measurement vector estimated based on all sigma points $\boldsymbol{\mathcal{X}}_k$ for the kth update
$\boldsymbol{K}$	Kalman gain
$\boldsymbol{P}_k$	The system state covariance matrix for $\boldsymbol{x}_k$
$\boldsymbol{P}_{\boldsymbol{x}\boldsymbol{z}_k}$	The cross covariance matrix for the system state in state space and measurement space at kth measurement update step
$\boldsymbol{P}_{\boldsymbol{z}_k}$	The covariance matrix for the system state in measurement space at kth measurement update step
$\boldsymbol{Q}$	Process uncertainty covariance matrix
$\boldsymbol{R}$	Measurement uncertainty covariance matrix
$\boldsymbol{x}_k$	The system state after the kth update
$\boldsymbol{y}_k$	The residual at kth measurement update step
$\boldsymbol{Z}_{k,i}$	The predicted measurement vector at $\boldsymbol{\mathcal{X}}_{k,i}$
$\boldsymbol{Z}_{k,i}$	The predicted measurement vector based on the sigma point $\boldsymbol{\mathcal{X}}_{k,i}$
$\boldsymbol{z}_k$	The measurement vector containing the measured response characteristics at the kth update step
$\eta_d, \dot{\eta}_d, \ddot{\eta}_d$	Displacement, velocity, acceleration of response for mode d
κ	Hyperparameter in the UKF model
ω	Wave or response frequency
σ	The standard deviation of random variable
$\zeta(t)$	Wave elevation time series
$B_{a,dd}$	The linearized additional damping
$B_{cr,dd}$	The critical damping at mode d
d	The index of vessel rigid body modes. $d = 1$: surge, $d = 2$: sway, $d = 3$: heave, $d = 4$: roll, $d = 5$: pitch, $d = 6$: yaw
H_s	Significant wave height
$\boldsymbol{J}$	The total number of the considered measured response characteristics in the measurement space for one sea state
j	Index of the considered measured response characteristics
k	The index of each model test case
L_{PP}	Length between perpendiculars
N	The dimension of the system state
r_{44}	Radius of gyration for roll
r_{55}	Radius of gyration for pitch
$S_{\zeta\zeta}(\omega, \beta_W)$	Single-sided wave spectrum
$S_{XX}(\omega, \beta_W)$	Response spectrum for X
T_z	Zero-up-crossing period
T_p	Wave spectral peak period
w_i^c	The weight factor for state mean calculation at the ith sigma point, $i = 0, 1, 2, \ldots, 2N$
w_i^m	The weight factor for state covariance calculation at the ith sigma point, $i = 0, 1, 2, \ldots, 2N$
X	Vessel response
$x(t)$	Vessel response in form of time records, $x(t) \in \{\eta_d(t)\dot{\eta}_d, \ddot{\eta}_d\}$, $d \in \{3, 4, 5\}$ considered in the present paper
z_j	The considered jth quantity in the measurement space
BL	Baseline of vessel hull
CL	Centerline of vessel hull

COG	Center of gravity
DOF	Degree of freedom
FFT	Fast Fourier transform
OCV	Offshore Construction Vessel
ODSS	Onboard decision support system
PSD	Power spectral density
RAO	Response amplitude operator
UKF	Unscented Kalman filter
ZCG	Vertical coordinate of vessel COG

Many real-time onboard decision support systems (ODSSs) have been developed to assist marine operations based on vessel motion prediction. Computational efficiency is critical for a real-time vessel motion prediction, and therefore, the analytical model for vessel response prediction in an ODSS must be simplified. Normally, for marine operations, the wave-induced vessel response in the wave frequency region can be estimated based on linear transfer functions in relation to the wave elevation [1]. These linear transfer functions are also called response amplitude operators (RAOs), which can be calculated by seakeeping analysis software based on 3D panel methods or 2D strip theory [2–4].

Research on ODSSs [5–9] in recent decades has mainly focused on reducing the wave forecast uncertainty by, e.g., (1) developing high-fidelity wave forecast models [10] for forecasts of a few hours up to some days in advance; (2) calibrating the local alpha factor [1] with wave-measuring instruments deployed near the floater [11]; (3) measuring the wave field in front of the vessel and predicting the encountered waves through noncoherent or coherent radar systems or special cameras [8,12–14]; and (4) estimating the wave spectrum by applying the "ship as a wave buoy" analogy [15,16] and predicting the sea state by extrapolation. Similar to the design of marine operations, such an ODSS predicts wave-induced vessel responses based on the presumed deterministic vessel condition in terms of, e.g., the load distribution and linearized viscous damping, which may deviate from the real condition at the operation execution phase. These uncertainties of the vessel condition can significantly contribute to the errors of the predicted vessel motions and the consequent decision making [5,8,9]. Therefore, it is important to identify the on-site vessel conditions based on the information available on board and from the operation design phase. Some important vessel parameters such as the draft, trim, and heel can be measured directly, while other parameters such as the moment of inertia, center of gravity (COG), and linearized viscous damping may not be so easy to measure. Identification of these immeasurable vessel hydrodynamic parameters is therefore of great interest. For example, Xu and Soares [17] and Fossen et al. [18] proposed algorithms for the parameter identification of maneuvering and dynamic positioning scenarios; however, the responses in the wave frequency region were considered disturbances. Kaasen et al. [19] developed an automatic procedure for the tuning of a commercial simulation model based on output error minimization and tested it based on data from model tests, considering precise wave and vessel motion measurements, and accurate fundamental seakeeping theory.

Han et al. [20] proposed an algorithm for the identification of the immeasurable vessel seakeeping parameters based on onboard vessel motion measurements and wave information, considering data uncertainties. The uncertainties of the tuning results were quantified. The algorithm is based on discrete Bayesian inference with a predefined RAO database representing the parametric uncertainty ranges. Even though the parametric uncertainties can be quantified and the nonlinear relation between vessel parameters and responses can be captured, the algorithm faces a common challenge for large-dimensional problems due to discretization, i.e., the curse of dimensionality [21]. Therefore, Han et al. [22] developed a new and computationally efficient algorithm for the tuning and uncertainty quantification of the important vessel parameters based on the unscented transformation [23] and the unscented Kalman filter (UKF) [24] by assuming multivariate Gaussian distributed vessel variables. However, the algorithm has been demonstrated only in connection with case studies based on synthetic data. Method validations based on model-scale and full-scale measurements are therefore required.

This paper tests the performance of the UKF-based model tuning algorithm by applying measurements from model-scale seakeeping tests. The model tests are first described in Section 2. Then, the applied tuning algorithm is briefly summarized in Section 3. Afterwards, the scope of the validation analysis is described in Section 4. The results are shown and explained in Section 5. Finally, Section 6 summarizes the findings, discusses the limitations, and suggests future research work to modify the seakeeping model tuning algorithm.

2. Seakeeping model tests

Seakeeping model tests with zero forward speed for a state-of-the-art offshore construction vessel (OCV) were selected for the validation analyses of the UKF-based tuning algorithm. The vessel is approximately 150 m long and 27 m wide, and the tested loading condition approximately corresponds to a displacement of 20 000 m^3, a draft of 6.8 m, and a transverse metacentric height of 2.7 m. With one main work moonpool and two ROV moonpools, the OCV is also equipped with bilge keels (approximately 54 m long with a breadth of 1.0 m) and roll reduction tanks to reduce the roll motions.

Only one loading condition was considered in the model tests, with all three moonpools open. The model, at a scale of approximately 1:23, as illustrated in Fig. 1, was manufactured with 3 moonpools, 2 bow thruster tunnels, 3 stern thruster tunnels, 3

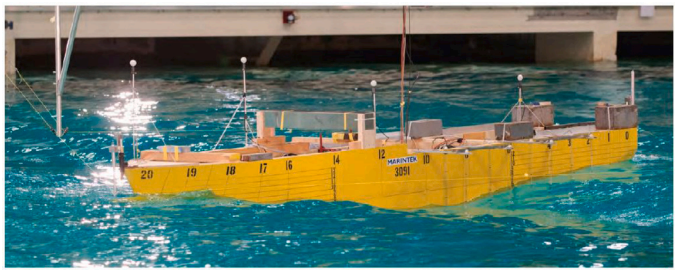

Fig. 1. Illustration of the seakeeping test.

Table 1
Seakeeping model tests performed for irregular waves.

k	Test No.	Spectral type	H_s [m]	T_p [s]	β_W [°]	Roll reduction tank
1	4000	JONSWAP	3	8	0	Frozen
2	4010	JONSWAP	3	10	0	Frozen
3	4020	JONSWAP	5	10	0	Frozen
4	4030	RECT	3	5–16	0	Frozen
5	4100	JONSWAP	3	8	15	Frozen
6	4110	JONSWAP	3	10	15	Frozen
7	4120	JONSWAP	5	10	15	Frozen
8	4130	RECT	3	5–16	15	Frozen
9	4200	JONSWAP	3	8	30	Frozen
10	4210	JONSWAP	3	10	30	Frozen
11	4220	RECT	3	5–16	30	Frozen
12	4300	JONSWAP	3	8	45	Frozen
13	4310	JONSWAP	3	10	45	Frozen
14	4320	RECT	3	5–16	45	Frozen
15	4401	JONSWAP	3	8	90	Frozen
16	4410	JONSWAP	3	10	90	Frozen
17	4420	RECT	3	5–16	90	Frozen
18	4500	JONSWAP	3	8	150	Frozen
19	4510	JONSWAP	3	10	150	Frozen
20	4600	JONSWAP	3	8	165	Frozen
21	4610	JONSWAP	3	10	165	Frozen
22	4700	JONSWAP	3	8	180	Frozen
23	4710	JONSWAP	3	10	180	Frozen
24	4720	RECT	3	5–16	180	Frozen

roll reduction tanks, and bilge keels. Only cases with the roll reduction tanks deactivated (namely, "frozen") were considered in the validation analyses. The model was weighed and balanced to obtain the specified loading condition as accurately as possible, w.r.t. the COG, radii of gyration for the roll and pitch, and volume displacement. The model tests were performed with only long-crested waves and without disturbance from current or wind. The main focus of the tests was to investigate the local effect of moonpool resonance. Therefore, most tests were carried out for sea states with peak periods (T_p) around the moonpool resonance periods, i.e., between 8 s and 10 s. Narrowband JONSWAP wave spectra with a peak enhancement factor of 3.3 were applied for the tests. For each wave direction β_W, an additional test case was conducted with a broadband and approximately rectangular wave spectrum (denoted by "RECT") for wave periods from 5 s to 16 s with a significant wave height (H_s) of 3 m. The considered test cases are summarized in Table 1.

A reference coordinate system was defined for the convenience of reporting. All the quantities reported hereafter correspond to this coordinate system. The origin of the coordinate system is at the baseline (BL) of the midship ($L_{pp}/2$) along the longitudinal symmetric axis, i.e., the centerline (CL). The positive x-axis points towards the bow, positive y-axis points towards port, and positive z-axis points upwards vertically. The definition of β_W in the present paper follows the coming-from convention, i.e., 0° for head sea, 180° for following sea, and 90° for beam seas coming from the port side.

A soft mooring system consisting of 4 horizontal springs was used to keep the model on station. This mooring system leads to low-frequency motions in surge, sway and yaw at periods of approximately 100 s. In the model tests, vessel motions and wave elevations were recorded in the form of time series. The measurement instruments, locations (at full scale) and quantities are summarized in Table 2.

Measurements from accelerometers were used for quality control of the OQUS camera outputs. The wave elevation measurements from the wave probes were calibrated prior to the model tests, e.g., as illustrated in Fig. 2. The OQUS camera measured motion signals of heave [m], roll [deg], and pitch [deg], and the calibrated wave elevation [m] measurements were used in the validation analyses. The nominal accuracy of the OQUS camera measurements was 0.8 mm for translational motions and 0.1° for angular

Table 2
Summary of measurements.

Instrument	Location [m]	Quantities
OQUS camera[a]	(0, 0, 0)	(Angular) Displacements of 6 DOFs[b]
Accelerometers	(−58.6, −10.4, 7.5)	Translational accelerations
Probes	8 port side, 2 starboard side, 1 in each of the moonpools	Relative water elevations

[a]OQUS electronic-optical positioning system.
[b]DOF: degree of freedom.

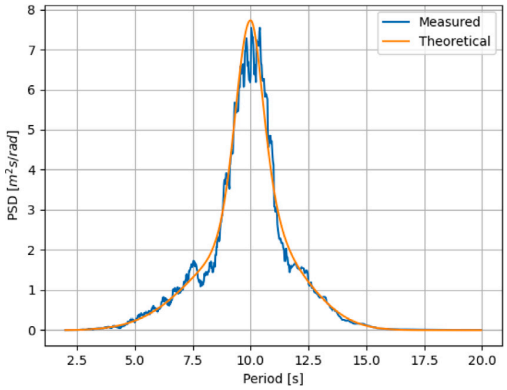

Fig. 2. Comparison of wave spectra between the theoretical and the measured for Test 4020. PSD: power spectral density. (For interpretation of the references to color in this figure legend, the reader is referred to the web version of this article.)

motions, while the accuracy of the wave measurements was 1 mm. All the measurements were transferred to full scale according to the Froude scaling laws [25]. At full scale, the duration of each seakeeping test was approximately 4500 s and the associated sampling frequency was approximately 41.6 Hz. The numerical seakeeping models were also made at full scale.

3. Formulation of the tuning algorithm

Han et al. [22] proposed a tuning algorithm based on the unscented transformation [23] and the corresponding scaled unscented Kalman filter (UKF) [24], which is computationally efficient for large-dimensional problems and guarantees second-order approximation accuracy for nonlinear systems. The UKF, belonging to the family of sigma-point Kalman filters [26], linearizes a model by implicitly applying weighted statistical linear regression based on the information at several deterministic points (i.e., the so-called sigma points). It uses nonlinear functions explicitly at the sigma points and therefore does not require the linear algebra formulation. This has been shown as an advantage for the problem of seakeeping model tuning heavily involving complex and state-dependent measurement functions [22].

The original tuning procedure contains a weather update step so that the wave characteristics for a sea state (e.g., H_s, T_p, and β_W) are included in the system state and tuned together with the uncertain vessel parameters [22]. As shown in Fig. 2, the wave measurements are subjected to insignificant uncertainties under laboratory conditions. Therefore, wave characteristics are not included in the system state, and the weather update step becomes irrelevant. Instead, the measured wave time series $\zeta(t)$ is considered as an input affecting the measurement function, which is used as part of the measurement update step. The complete tuning procedure for one sea state indexed by $k+1$ is illustrated in Fig. 3. The tuning process mainly consists of 3 steps, i.e., calculation of the sigma points and their weight factors, system propagation, and measurement update.

The state vector includes uncertain vessel parameters such as those related to the inertia distribution and the linearized viscous damping terms. The initial state vector and the state covariance matrix are denoted by $\boldsymbol{x}_0$ and $\boldsymbol{P}_0$, respectively. The state vector and covariance matrix after updating by k sea states are denoted by $\boldsymbol{x}_k$ and $\boldsymbol{P}_k$, respectively. Each sea state is assumed stationary and independent from other sea states.

When measurements of vessel responses and wave elevations are acquired for sea state $k+1$, the sigma points should be calculated based on the updated N-dimensional state $\boldsymbol{x}_k$ and $\boldsymbol{P}_k$:

$$\boldsymbol{\mathcal{X}}_{k+1,0} = \boldsymbol{x}_k \tag{1a}$$

$$\boldsymbol{\mathcal{X}}_{k+1,i} = \begin{cases} \boldsymbol{x}_k + \left[\sqrt{(N+\lambda)\boldsymbol{P}_k}\right]_i & \text{for } i = 1, 2, \ldots, N \\ \boldsymbol{x}_k - \left[\sqrt{(N+\lambda)\boldsymbol{P}_k}\right]_{i-N} & \text{for } i = N+1, \ldots, 2N \end{cases} \tag{1b}$$

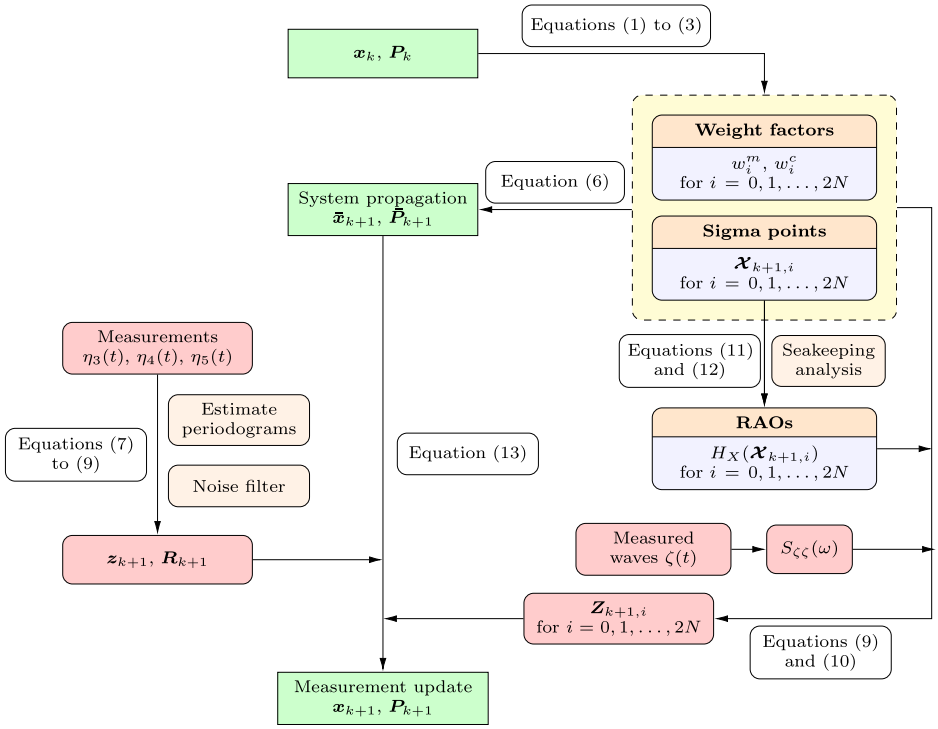

Fig. 3. The process of tuning vessel seakeeping model parameters, together with the quantification of uncertainties.

$$\boldsymbol{\mathcal{X}}_{k+1} = [\boldsymbol{\mathcal{X}}_{k+1,0} \quad \boldsymbol{\mathcal{X}}_{k+1,1} \quad \cdots \quad \boldsymbol{\mathcal{X}}_{k+1,2N}] \tag{1c}$$

where $\left[\sqrt{(N+\lambda)\boldsymbol{P}_k}\right]_i$ is the ith column (or row) of the matrix square root of $(N+\lambda)\boldsymbol{P}_k$. Each sigma point $\boldsymbol{\mathcal{X}}_{k+1,i}$ for $i \in \{0, 1, \ldots, 2N\}$ is deterministically selected according to Eq. (1a) or Eq. (1b). The matrix $\boldsymbol{\mathcal{X}}_{k+1}$ has a size of $N \times (2N+1)$, where each column represents a sigma point. The hyperparameter λ in Eq. (1) is calculated by:

$$\lambda = \alpha^2(N + \kappa) - N \tag{2}$$

where α is the scaling factor, the hyperparameter κ is normally set to either $3 - N$ or 0, and $\kappa \neq -N$. The corresponding weight factors for the sigma points to be used for estimation of the mean and the covariance can be calculated by:

$$w_0^m = \frac{\lambda}{\lambda + N} \tag{3a}$$

$$w_0^c = \frac{\lambda}{\lambda + N} + 1 - \alpha^2 + \beta \tag{3b}$$

$$w_i^c = w_i^m = \frac{1}{2(\lambda + N)} \tag{3c}$$

where w^m denotes the weight factors for the mean calculation, w^c denotes the weight factors for the covariance matrix calculation, and $i = 1, 2, \ldots, 2N$. The hyperparameter β equals to 2 for Gaussian distributed variables [24]. The weight factors depend only on the dimension and the values of the UKF-related hyperparameters.

With the deterministically selected sigma points and their corresponding weight factors, the system state can be predicted for sea state number $k+1$ through the system propagation step by:

$$\bar{\boldsymbol{x}}_{k+1} = \sum_{i=0}^{2N} w_i^m f(\boldsymbol{\mathcal{X}}_{k+1,i}) \tag{4a}$$

$$\bar{\boldsymbol{P}}_{k+1} = \sum_{i=0}^{2N} w_i^c (f(\boldsymbol{\mathcal{X}}_{k+1,i}) - \bar{\boldsymbol{x}}_{k+1})(f(\boldsymbol{\mathcal{X}}_{k+1,i}) - \bar{\boldsymbol{x}}_{k+1})^\top + \boldsymbol{Q} \tag{4b}$$

where $\bar{\boldsymbol{x}}_{k+1}$ and $\bar{\boldsymbol{P}}_{k+1}$ are the predicted state vector and covariance matrix. $f()$ is the process model, i.e., the state propagation function. $\boldsymbol{Q}$ is the process uncertainty covariance matrix representing the process disturbance and the process model uncertainties.

Eq. (4) is generally valid for any nonlinear process models. However, the system propagation step can be very much simplified when the propagation function is linear, such as the presently considered tuning of the vessel seakeeping model parameters. Stationary sea states and vessel conditions are assumed, leading to a simple linear function:

$$f(\boldsymbol{\mathcal{X}}_{k+1,i}) = \boldsymbol{I}_N \boldsymbol{\mathcal{X}}_{k+1,i} = \boldsymbol{\mathcal{X}}_{k+1,i} \tag{5}$$

where $\boldsymbol{I}_N$ is an N-dimensional identity matrix. Consequently, Eq. (4) can be replaced by Eq. (6) for the present study:

$$\bar{\boldsymbol{x}}_{k+1} = \boldsymbol{x}_k \tag{6a}$$

$$\bar{\boldsymbol{P}}_{k+1} = \boldsymbol{P}_k + \boldsymbol{Q} \tag{6b}$$

Following the system propagation, the system state can now be updated through the measurement update step by application of the acquired wave and vessel motion measurements for sea state $k+1$. As illustrated in Fig. 3, heave $\eta_3(t)$, roll $\eta_4(t)$, and pitch $\eta_5(t)$ measured by the OQUS camera and wave elevations $\zeta(t)$ measured by the probes are used in the validation analyses. Second-order surge, sway, and yaw motions are significant. Therefore, the corresponding measurements are excluded. Considering that the measurements are associated with high accuracy due to the application of advanced instruments, calibration, and quality control under laboratory conditions as mentioned in Section 2, signal noise is considered negligible. A previous vessel seakeeping parametric sensitivity study [27] suggests including the derivative information regarding the vessel motions (e.g., the velocity and acceleration) to improve the tuning accuracy for the uncertain parameters. Therefore, in the validation analyses, the measurement space in the UKF-based tuning model is considered to include the standard deviations of the (angular) displacement, velocity, acceleration, and corresponding zero-up-crossing periods (T_z) for heave, roll, and pitch in the wave frequency range. The measurement space and the measurement vector $\boldsymbol{z}$ can be formulated as:

$$\begin{aligned} \boldsymbol{z} &= [z_1 \quad z_2 \quad \dots \quad z_j \quad \dots \quad z_J]^\top \\ z_j &\in \{\sigma_{\eta_3}, \sigma_{\dot{\eta}_3}, \sigma_{\ddot{\eta}_3}, \sigma_{\eta_4}, \sigma_{\dot{\eta}_4}, \sigma_{\ddot{\eta}_4}, \dots, T_{z(\eta_3)}, T_{z(\eta_4)}, \dots\} \end{aligned} \tag{7}$$

where σ is the standard deviation and η_d, $\dot{\eta}_d$, $\ddot{\eta}_d$ represent the (angular) displacement, velocity, and acceleration for the considered responses in 6 DOFs. d is usually referred to as the index of the vessel rigid body modes. $d = 1, 2, 3, 4, 5, 6$ correspond to surge, sway, heave, roll, pitch, and yaw, respectively. The vessel motions of mode d are also referred to as the motions in the dth DOF. $j = 1, 2, \dots, J$, where J is the number of considered measured response characteristics in the measurement space for one sea state. Selecting the quantities for the measurement vector can be critical to the tuning results, especially when the measurement function is subject to significant uncertainty, e.g., due to simplification of the seakeeping model.

In the following, a scalar quantity X denotes a vessel response, with $X \in \{\eta_d, \dot{\eta}_d, \ddot{\eta}_d\}$ and $d = \{1, 2, \dots, 6\}$. $X(\omega)$ represents the response in the frequency domain, while $x(t)$ represents the corresponding time domain signal. The numerical differentiation of discrete signals $x(t)$ is well known to generate very high noises. These noises are usually at high frequencies and can be distinguished outside the frequency interval of the real motions. Therefore, the measured $\eta_3(t)$, $\eta_4(t)$, $\eta_5(t)$, and $\zeta(t)$ are first transferred to the frequency domain by estimating their periodograms [28]. The corresponding power spectral densities (PSDs), i.e., $S_{\eta_3\eta_3}(\omega)$, $S_{\eta_4\eta_4}(\omega)$, $S_{\eta_5\eta_5}(\omega)$, and $S_{\zeta\zeta}(\omega)$, are subsequently calculated. Then, the corresponding spectra of the velocities and accelerations can be calculated by:

$$S_{\dot{X}\dot{X}}(\omega) = \omega^2 S_{XX}(\omega) \tag{8a}$$

$$S_{\ddot{X}\ddot{X}}(\omega) = \omega^4 S_{XX}(\omega) \tag{8b}$$

where $\dot{X}(\omega)$ in the frequency domain represents the first derivative of X, i.e., $\dot{x}(t) = \frac{d\,x(t)}{d\,t}$ in the time domain, while $\ddot{X}(\omega)$ represents its second derivative, i.e., $\ddot{x}(t) = \frac{d^2\,x(t)}{d\,t^2}$. The PSDs outside the wave frequencies should be removed before the measurement update step. This is considered equivalent to a fast Fourier transform (FFT) bandpass filter. Then, the quantities in the measurement space $\boldsymbol{z}$ can be calculated:

$$\sigma_X = \sqrt{m_0} \tag{9a}$$

$$T_{z(X)} = 2\pi\sqrt{\frac{m_0}{m_2}} \tag{9b}$$

$$m_0 = \sum_{\omega} S_{XX}(\omega)\Delta\omega \tag{9c}$$

$$m_2 = \sum_{\omega} \omega^2 S_{XX}(\omega)\Delta\omega \tag{9d}$$

Once the quantities of the measurement space have been selected, the system state including the uncertain vessel parameters should be transferred from the state space to the measurement space by applying the measurement functions. It is obvious that these measurement functions are highly nonlinear and dependent on the state as well. The system state in the measurement space is called "the predicted measurements", denoted by $\boldsymbol{\mathcal{Z}}$. First, the response spectrum should be calculated for each sigma point $\boldsymbol{\mathcal{X}}_{k+1,i}$:

$$S_{XX,i}(\omega) = |H_X(\omega, \beta_W | \boldsymbol{\mathcal{X}}_{k+1,i})|^2 S_{\zeta\zeta,k+1}(\omega, \beta_W) \tag{10}$$

where $S_{\zeta\zeta,k+1}(\omega, \beta_W)$ is the wave spectrum for sea state $k+1$, which is calculated based on the periodogram of the calibrated probe measurements. The linear transfer function $H_X(\omega, \beta_W | \boldsymbol{\mathcal{X}}_{k+1,i})$ for the response X varies with the sigma point $\boldsymbol{\mathcal{X}}_{k+1,i}$. Subsequently, the

elements of the predicted measurements can be calculated based on Eq. (9). At each sigma point $\boldsymbol{\mathcal{X}}_{k+1,i}$, the predicted measurement vector can be assembled according to Eq. (7) based on the selected measurement space, denoted by $\boldsymbol{Z}_{k+1,i}$.

As illustrated in Fig. 3, seakeeping analysis is carried out at each sigma point $\boldsymbol{\mathcal{X}}_{k+1,i}$ to obtain $|H_X(\omega, \beta_W|\boldsymbol{\mathcal{X}}_{k+1,i})|$. The simulated linear transfer functions of heave $H_{\eta_3^*}(\omega)$ are reported at a dedicated location on the vessel, depending on the software and the numerical modeling. The superscript $*$ for η_3^* indicates that the software-reported heave RAO may be at a location different from the measured location. Therefore, the software-calculated complex-valued heave RAOs must be transferred to the measured location, i.e., the origin of the reference coordinate system in the present case studies, by:

$$H_{\eta_3}(\omega) = H_{\eta_3^*}(\omega) - y_0 H_{\eta_4}(\omega) + x_0 H_{\eta_5}(\omega) \tag{11}$$

where $H_{\eta_3}(\omega)$ is the complex-valued heave motion RAO at the OQUS-measured location, i.e., (0, 0, 0) in the reference coordinate system. (x_0, y_0, z_0) are the coordinates of the software-reported RAOs in the same reference coordinate system. The roll and pitch RAOs remain the same at different locations on a rigid body. Afterwards, the RAO amplitudes of the velocity and acceleration can be calculated based on the (angular) displacement:

$$|H_{\dot{X}}(\omega)| = \omega |H_X(\omega)| \tag{12a}$$

$$|H_{\ddot{X}}(\omega)| = \omega^2 |H_X(\omega)| \tag{12b}$$

Eqs. (7) and (9) to (12) should be treated as a complete set of the measurement functions to calculate the predicted measurement vector $\boldsymbol{Z}_{k+1,i}$ at each sigma point, while Eqs. (7) to (9) provide the procedure to calculate the measurement vector $\boldsymbol{z}_{k+1}$. The measurement functions are very difficult to express in a compact mathematical formulation because (1) many different response characteristics can be included in the measurement space (e.g., σ and T_z); (2) it involves seakeeping simulations, rigid body motion transformations, derivative calculations, etc.; and (3) the applied RAOs again depend on the state and subsequent selection of the sigma points. Finally, the measurement update step can be performed based on:

$$\boldsymbol{\mathcal{Z}}_{k+1} = \sum_{i=0}^{2N} w_i^m \boldsymbol{Z}_{k+1,i} \tag{13a}$$

$$\boldsymbol{y}_{k+1} = \boldsymbol{z}_{k+1} - \boldsymbol{\mathcal{Z}}_{k+1} \tag{13b}$$

$$\boldsymbol{P}_{\boldsymbol{z}_{k+1}} = \sum_{i=0}^{2N} w_i^c (\boldsymbol{Z}_{k+1,i} - \boldsymbol{\mathcal{Z}}_{k+1})(\boldsymbol{Z}_{k+1,i} - \boldsymbol{\mathcal{Z}}_{k+1})^\top + \boldsymbol{R}_{k+1} \tag{13c}$$

$$\boldsymbol{P}_{\boldsymbol{x}\boldsymbol{z}_{k+1}} = \sum_{i=0}^{2N} w_i^c (\boldsymbol{\mathcal{X}}_{k+1,i} - \bar{\boldsymbol{x}}_{k+1})(\boldsymbol{Z}_{k+1,i} - \boldsymbol{\mathcal{Z}}_{k+1})^\top \tag{13d}$$

$$\boldsymbol{K} = \boldsymbol{P}_{\boldsymbol{x}\boldsymbol{z}_{k+1}} \boldsymbol{P}_{\boldsymbol{z}_{k+1}}^{-1} \tag{13e}$$

$$\boldsymbol{x}_{k+1} = \bar{\boldsymbol{x}}_{k+1} + \boldsymbol{K}\boldsymbol{y}_{k+1} \tag{13f}$$

$$\boldsymbol{P}_{k+1} = \bar{\boldsymbol{P}}_{k+1} - \boldsymbol{K}\boldsymbol{P}_{\boldsymbol{z}_{k+1}}\boldsymbol{K}^\top \tag{13g}$$

where the residual $\boldsymbol{y}_{k+1}$ is the difference between the predicted measurement $\boldsymbol{\mathcal{Z}}_{k+1}$ and the realized measurement vector $\boldsymbol{z}_{k+1}$ in the measurement space and $\boldsymbol{R}_{k+1}$ represents the uncertainties from the measurements and the measurement functions. $\boldsymbol{P}_{\boldsymbol{z}_{k+1}} \in \mathbb{R}^{J\times J}$ is the covariance matrix of the sigma points in the measurement space, and $\boldsymbol{P}_{\boldsymbol{x}\boldsymbol{z}_{k+1}} \in \mathbb{R}^{N\times J}$ is the cross covariance of the state and the measurement. $\boldsymbol{x}_{k+1}$ and $\boldsymbol{P}_{k+1}$ are the updated state mean and covariance matrix based on the calculated Kalman gain $\boldsymbol{K}$ for the sea state indexed by $k+1$.

4. Scope of the validation analysis

The vessel seakeeping model tuning algorithm described in Section 3 was validated based on the seakeeping (zero speed) model tests described in Section 2.

4.1. Numerical seakeeping model and response measurements

In the validation analyses, the RAOs at the sigma points were calculated by means of the ShipX (VERES) software developed by SINTEF Ocean [3] and based on 2D strip theory. The adequate meshing of the ShipX model is illustrated in Fig. 4.

A simplified representation of the moonpools was applied in ShipX. The locations and dimensions of the three moonpools were specified as inputs to ShipX in order to approximately obtain the correct vessel displacement volume and longitudinal center of buoyancy [29]. Due to the relatively small volume ratio between the moonpools and vessel, the coupling effects between the moonpool and vessel responses were considered small [30]. Ravinthrakumar et al. [31] also shows negligible coupling effects between vessel motions and moonpool response for a volume ratio less than 4.5%. However, the coupling effects are not only dependent on the volume ratio but also highly dependent on the location of the moonpool(s) and the wave heading [32]. Such coupling effects mostly influence the vessel motions (e.g., heave and pitch) around the moonpool resonance periods with respect to the piston and sloshing modes. It is believed that the coupling between moonpool and roll can be much more complicated

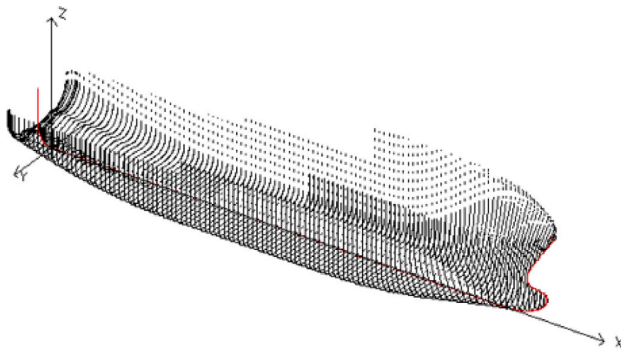

Fig. 4. Screenshot of the ShipX strip model.

owing to (1) the significant nonlinear sloshing effects from the water in the moonpool on the roll motion; (2) the significant viscous damping contributed by the sharp edges of the moonpools; and (3) the nonlinear swirling effects. Moreover, for vessels with multiple moonpools, even though the moonpool arrangement is normally symmetric with respect to the centerline, the moonpool response can be different between symmetric moonpools for oblique and beam seas due to the shielding effects and the encountered wave phase differences. All of these facts make the roll motion estimation complicated. Therefore, this simplified ShipX model is expected to have relatively high uncertainties associated with the roll RAO estimation.

VERES in ShipX is based on linear potential theory with the assumption of inviscid and incompressible fluid and irrotational flow condition [33]. However, damping terms in addition to that based on linear potential theory may play critical roles in the vessel motion estimation, particularly for the roll around its resonance [34]. This "additional" damping is in fact nonlinear due to viscous effects, dependent on the amplitudes and frequencies of the considered vessel motion velocities and waves. The stochastic linearization technique [35] is usually applied to express the relationship between vessel motion and wave elevation in the frequency domain. Consequently, this linearized "additional" damping becomes sea-state dependent. Han et al. [36] proposed to a method to handle such important sea-state dependent parameters in the tuning process based on discrete Bayesian inference so that the prediction accuracy for those parameters can be improved and quantified by the tuning results at the observed sea states. The linearized additional damping coefficient β_{dd} for mode d is defined as the ratio between the linearized additional damping and the critical damping for mode d as a percentage (i.e., 100 times the ratio):

$$\beta_{dd} = \frac{B_{a,dd}}{B_{cr,dd}} \times 100\ [\%] \tag{14a}$$

$$B_{cr,dd} = 2\sqrt{(M_{dd} + A_{dd}(\infty))C_{dd}} \tag{14b}$$

where M_{dd}, A_{dd}, and C_{dd} are the vessel inertia, added mass, and restoring stiffness for the motion mode d, respectively. The vessel added mass is frequency dependent. For simplicity, a constant added mass A_{dd} for each motion mode d has been considered in Eq. (14b), taken as the added mass at the infinite frequency $\omega \to \infty$. $B_{a,dd}$ is the linearized additional damping, and $B_{cr,dd}$ is the critical damping for the dth DOF. In the case studies, constant values of $B_{cr,dd}$ for $d = 3, 4, 5$ were applied independent of tuning results. In fact, it is mostly important to find the best $B_{a,dd}$ to represent the vessel dynamics for the present vessel and wave conditions. β_{dd} was introduced mainly to ensure that all the parameters considered in the system state space are of similar magnitudes for the purpose of numerical stability, as explained in Section 4.2. Tuning of β_{dd} with reference to a constant $B_{cr,dd}$ helps revealing the change of $B_{a,dd}$ through tuning simulations.

The geometry and location of the bilge keels are specified in the ShipX model. VERES estimates the linearized viscous roll damping from the hull and bilge keels based on Ikeda's formulas [37–40]. Hence, β_{44} is automatically included in the simulation based on the semiempirical solutions. However, this estimation of β_{44} is still subject to considerable uncertainties. Instead, for the validation analysis in the application of the VERES simulations, the parameter β'_{44} is considered in the state vector, representing the error of the additional roll damping coefficient between the VERES estimated and the true value:

$$\beta'_{44} = \beta_{44} - \beta_{44}^{VER} \tag{15}$$

where β_{44} is the previously defined additional roll damping and β_{44}^{VER} is the additional roll damping estimated by ShipX (VERES). β'_{44} may therefore be expected to vary around zero.

For verification of the model, the resonance periods of the output roll ($\beta_W = 90°$) and pitch ($\beta_W = 0°$) RAOs were first benchmarked based on the roll and pitch decay tests. RAOs are always reported at the COG in VERES, i.e., (−3.81 m, 0, 10.82 m) with respect to the reference coordinate system defined in Section 2. The heave RAOs should therefore be transferred to the reference coordinate system origin according to Eq. (11). The set of VERES-simulated RAOs based on the tested loading condition and benchmarked based on the decay tests are hereby referred to as the "reference" RAOs.

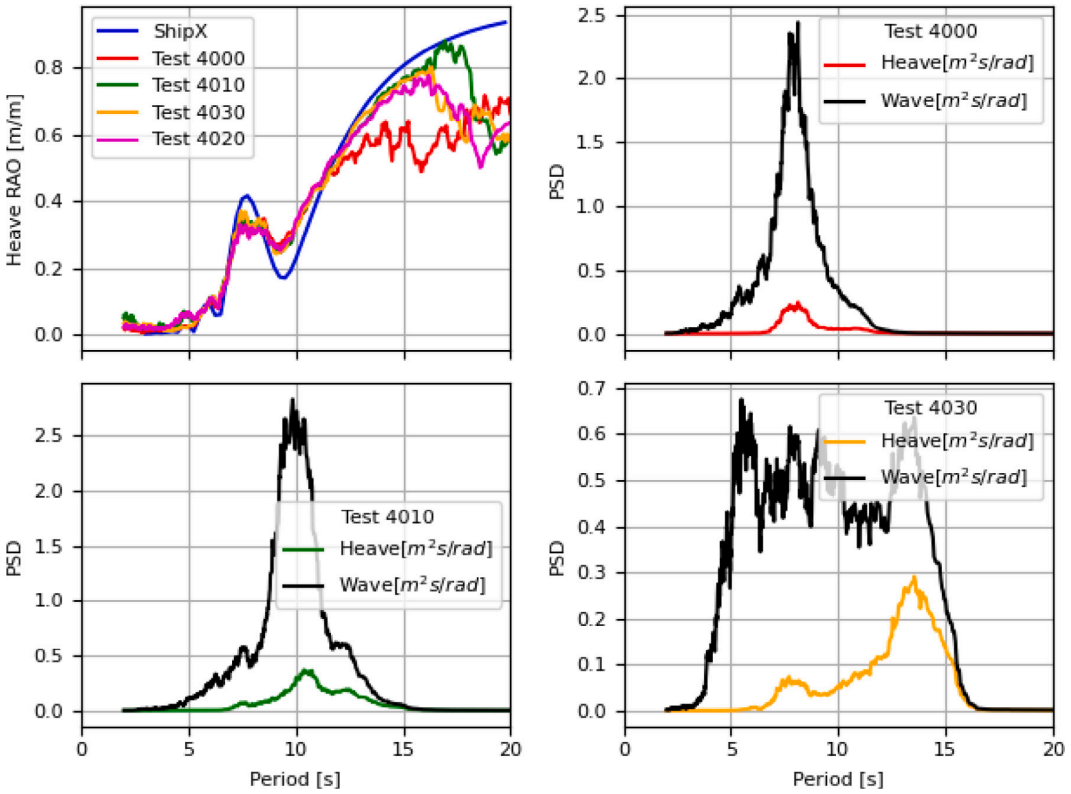

Fig. 5. The measured heave RAOs and the reference heave RAO from the ShipX (VERES) simulation at head sea (top left), and the power spectral densities (PSDs) of the measured waves and heave motions for Tests 4000, 4010, and 4030. (For interpretation of the references to color in this figure legend, the reader is referred to the web version of this article.)

The applied unidirectional wave conditions in the laboratory provide the perfect opportunity to compare the measured RAOs with the corresponding simulated RAOs from the seakeeping software. The measured RAO amplitudes can therefore be calculated by:

$$|H_X(\omega)| = \sqrt{\frac{S_{XX}(\omega)}{S_{\zeta\zeta}(\omega)}} \tag{16}$$

where $S_{XX}(\omega)$ and $S_{\zeta\zeta}(\omega)$ are power spectral densities of the response X and wave elevation ζ from the measurements. Several critical issues are hence identified: (1) numerical error magnification due to very small wave energies away from the peak frequencies; (2) second-order effect on the roll motion; (3) moonpool coupling effects on the vessel motions; and (4) generally larger estimation errors on the roll motion. Detailed explanations are given in the following.

The reference RAOs for heave and pitch are shown under the head sea condition in Figs. 5 and 6, while the reference roll RAO is shown for beam sea in Fig. 7, with comparison of the RAOs calculated for the relevant test cases. Due to the limited dimensions of the ocean basin laboratory and the applied model scale, wave components with wave periods larger than 15 s at full scale become unreliable. Therefore, the vessel response and wave components with periods larger than 15 s were disregarded in the tuning process. When the wave PSD is sufficiently small, numerical issues may occur if applying Eq. (16). For example, as illustrated in Fig. 6, the measured pitch RAO amplitudes at small periods (i.e., 2 to 5 s) from Test 4020 are overestimated due to the very small wave energies and measurement errors. Large RAO estimation errors can also be observed at large periods (e.g., $>$ 15 s) due to the same numerical issue. However, it is worth mentioning that the proposed tuning algorithm may not be highly influenced by these numerical errors because the measurement space focuses on the overall characteristics of the response spectra (e.g., parameters related to m_0 and m_2) instead of directly calculating the RAOs based on Eq. (16). Hence, the small energies or measurement errors usually do not significantly influence those characteristics.

However, special attention should be paid to the measured roll motions, as shown in Fig. 7. Very large roll motions are observed around the resonance, i.e., at approximately 15 s, where very little wave energies exist. These significant roll motions outside the main wave frequency range are believed to be due to the second-order difference-frequency responses from the interactions of wave

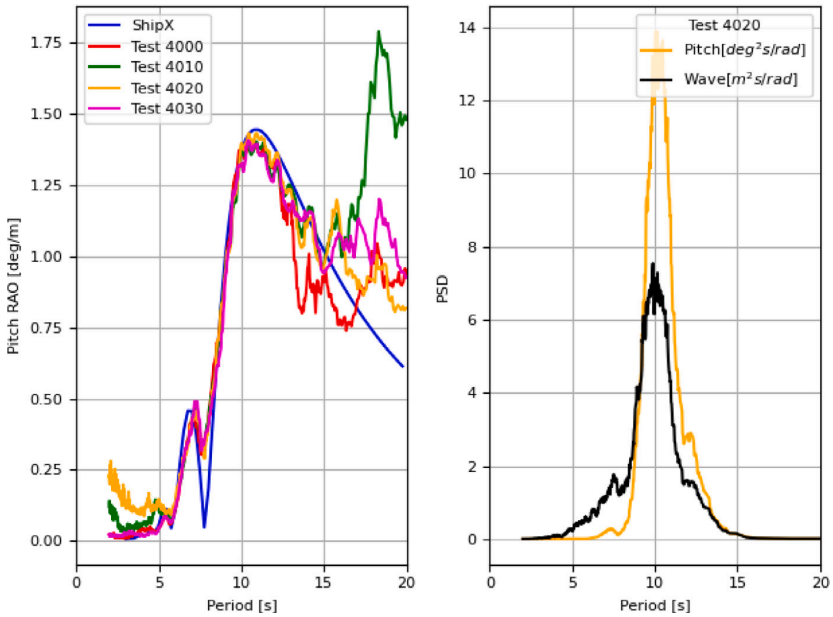

Fig. 6. The measured pitch RAOs and the reference pitch RAO from the ShipX (VERES) simulation at head sea (left), and the power spectral densities (PSDs) of the measured waves and pitch motions for Test 4020. (For interpretation of the references to color in this figure legend, the reader is referred to the web version of this article.)

loads at different frequencies. This type of phenomenon has been observed, explained, and reported by researchers, e.g., by Rezende et al. [41]. For example, wave components at 6 s and 10 s will lead to a difference-frequency response at a period of 15 s. Motions due to the second-order effects must be excluded from the seakeeping model tuning because only the first-order wave-induced vessel motions are considered in the algorithm. From Fig. 7, the good matching of the VERES-simulated and the measured roll RAOs within the wave frequency ranges indicates that these second-order roll motions are mostly outside the wave frequency range for each individual sea state. Therefore, these second-order motions can be largely excluded by applying a high-pass FFT filter for periods with very small wave energies. For each sea state, the wave and response components at frequencies with wave PSDs less than 5% of the maximum wave PSD value were removed.

In addition, coupling effects between the moonpool piston mode and vessel motions were observed in the case of oblique seas. As illustrated in Fig. 8, the measured heave RAOs based on those test cases with a wave heading of 30° show a second peak at approximately 8 to 9 s, which is significantly different from the VERES-simulated RAO without considering the coupling effects. Similarly, Fig. 9 shows local RAO amplitude peaks at the moonpool piston resonance period for the roll motion at oblique seas (e.g., at 30° and 150°). However, this coupling has significantly less influence for a wave heading of 150° than for 30°, which may be due to the shielding effect from the vessel body on the wave kinematics at the moonpools. The moonpools are located in the vessel forepart. These deviations contribute to the uncertainties of the measurement functions and consequently the predicted measurements. Therefore, the measurement noise matrix $\boldsymbol{R}$ should consider these errors due to simplifications of the seakeeping simulation.

4.2. State space

In practice, the vessel attitude-related parameters, e.g., draft, trim, heel, heading, and forward speed, can be measured by various onboard monitoring systems and hence may be less uncertain. In addition, the vessel geometry can normally be treated deterministically, subject to minor uncertainty due to thorough design and manufacturing work at shipyards. Therefore, within their practical uncertainty ranges, the variation of parameters related to vessel attitude and geometry may have very limited influence on the wave-induced vessel motions. However, due to the frequently shifted vessel loading conditions, potential engineering errors, and considered simplifications and assumptions in the theory, the parameters related to the inertia distribution and hydrodynamic damping may be subject to significant uncertainties.

Similar to [27], the sensitivity of the important uncertain vessel parameters was studied based on the ShipX model, which was deployed during the model testing project. The sensitivity results are qualitatively summarized in Table 3. The RAOs for heave, roll and pitch at the COG are compared within the considered uncertainty range for each uncertain parameter. The influential vessel parameters, i.e., β_{33}, β_{44}, β_{55}, ZCG, r_{44}, and r_{55}, were therefore considered in the system state vector for the model tuning.

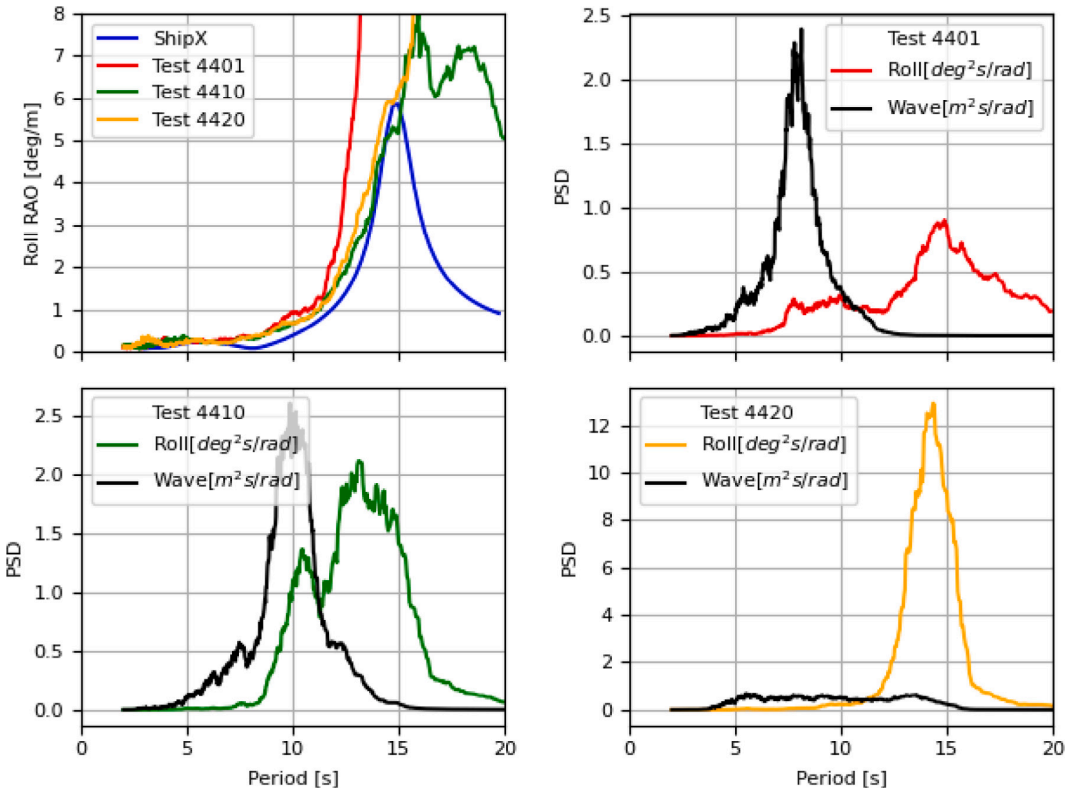

Fig. 7. The measured roll RAOs and the reference roll RAO from the ShipX (VERES) simulation at beam sea (top left), and the power spectral densities (PSDs) of the measured waves and roll motions for Tests 4401, 4410, and 4420. (For interpretation of the references to color in this figure legend, the reader is referred to the web version of this article.)

Table 3
Sensitivity of uncertain vessel parameters.

Parameter	Range	Heave	Roll	Pitch
β_{33}	[0, 10%]	Significant	No	No
β'_{44}	[−7, 7%]	No	Significant	No
β_{55}	[0, 10%]	Minor	No	Significant
ZCG	[6.8, 13.8] m	No	Significant	Minor
r_{44}	[9.5, 11.5] m	No	Significant	No
r_{55}	[41, 49] m	Minor	No	Significant

The linearized additional damping coefficients were assumed constant. The dependency on the sea state characteristics (i.e., H_s, T_p, β_W, etc.) should be considered in practical applications. However, the number of available model tests was limited. Roll motion is most sensitive to the additional damping, particularly around the resonance period. However, the wave peak periods for most tests were 8 s or 10 s, which are outside the resonance; therefore, the additional roll damping plays a very limited role with respect to the measured roll motions. Thus, constant additional damping was believed sufficient for the validation analyses based on these model test cases.

According to Eq. (1), the covariance matrix $\boldsymbol{P}_k$ should be positive semidefinite. Non-negative weight factors w^c guarantee this positive semidefinite property for $\boldsymbol{P}_k$ [24]. However, in practice, it is challenging to have a positive weight factor w_0^c for the state mean $\boldsymbol{\mathcal{X}}_{k+1,0}$ because a very small α is preferred in the algorithm. Non-positive semidefinite $\boldsymbol{P}$ was observed in the initial studies due to the system nonlinearity and the numerical issue caused by too large difference in the order of magnitudes for the diagonal elements of $\boldsymbol{P}$. In addition, when divergent or irrational tuning results occur, unexpected and extremely nonlinear behavior may lead to a non-positive semidefinite covariance matrix. Therefore, the additional damping coefficients (as a percentage) instead of the additional damping and the radii of gyration instead of the moments of inertia are considered in the system state space.

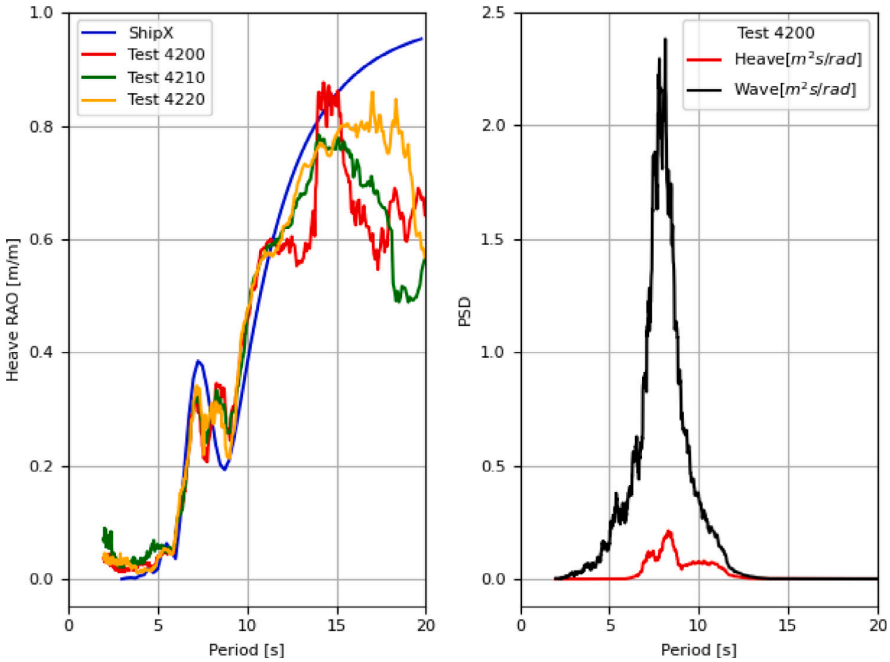

Fig. 8. The measured heave RAO and the reference heave RAO from the ShipX (VERES) simulation for $\beta_W = 30°$ (left), and the power spectral densities (PSDs) of the measured waves and heave motions for Test 4200. (For interpretation of the references to color in this figure legend, the reader is referred to the web version of this article.)

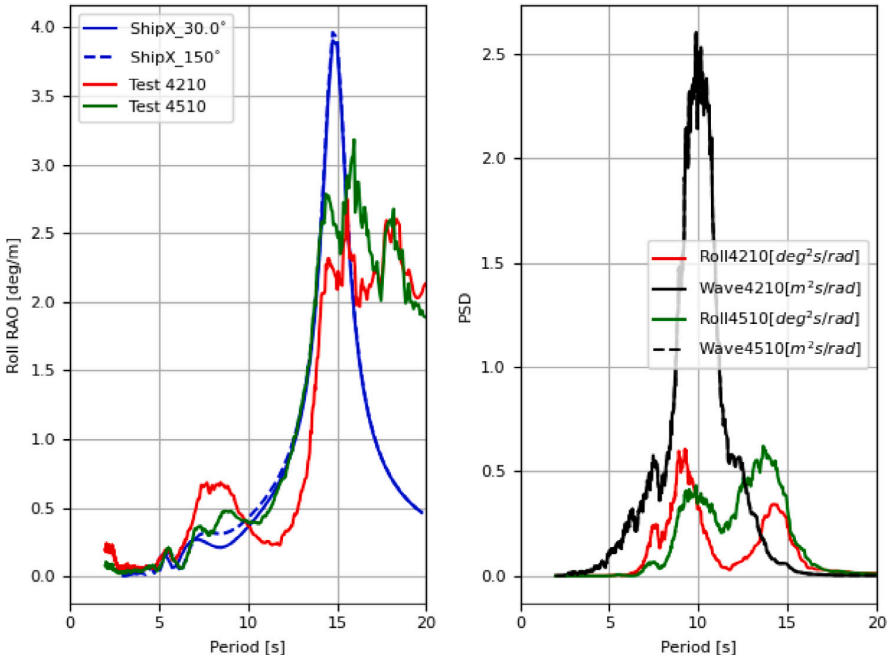

Fig. 9. The measured roll RAOs for Tests 4210 and 4510 and the reference roll RAOs from the ShipX (VERES) simulation for $\beta_W = 30°$and150° (left), and the power spectral densities (PSDs) of the measured waves and roll motions for Tests 4210 and 4510. The wave spectra of Tests 4210 and 4510 are nearly identical. (For interpretation of the references to color in this figure legend, the reader is referred to the web version of this article.)

Table 4
Candidates of diagonal elements of measurement uncertainty variance matrix $\boldsymbol{R}$.

Parameter	Description	Value
$\sigma_N^2(X_3),\ X_3 \in \{\eta_3, \dot{\eta}_3, \ddot{\eta}_3\}$	Noise variance of σ_{X_3} [a]	$\max(2\%\sigma_{X_3}^2, 10^{-6})$
$\sigma_N^2(X_4),\ X_4 \in \{\eta_4, \dot{\eta}_4, \ddot{\eta}_4\}$	Noise variance of σ_{X_4} [b]	$\max(9\%\sigma_{X_4}^2, 10^{-4})$
$\sigma_N^2(X_5),\ X_5 \in \{\eta_5, \dot{\eta}_5, \ddot{\eta}_5\}$	Noise variance of σ_{X_5} [c]	$\max(5\%\sigma_{X_5}^2, 10^{-4})$
$\sigma_N^2(T_z)$	Noise variance of T_z for η_3, η_4, η_5	0.1 s^2 for η_3 and η_5; 0.25 s^2 for η_4

[a] σ_{X_3}: the standard deviation of the heave displacement, velocity, and acceleration measurements.
[b] σ_{X_4}: the standard deviation of the roll rotation, velocity, and acceleration measurements.
[c] σ_{X_5}: the standard deviation of the pitch rotation, velocity, and acceleration measurements.

4.3. Measurement space

One of the keys to success for the tuning process is the selection of the measurement space and the determination of the corresponding errors from measurements (i.e., random errors) and measurement functions (i.e., systematic errors). Initial studies indicate that including derivative information of the measured positions and orientations (i.e., heave, roll and pitch) helps to improve the convergence of the tuning results. However, this applies only if the simulated RAOs based on the true vessel parameters can represent the real responses well. When the reference RAOs are significantly deviated from the true system dynamics, a more informative measurement space (e.g., including the velocity, acceleration, and zero-up-crossing period) for that specific DOF will generally lead to more biased tuning results.

For the model tests, the error sources of the simulated RAOs and the consequent predicted measurements are explained in Section 4.1 and are mainly due to ignoring or linearizing the nonlinear effects and the limitations of linear potential theory and strip theory. Consequently, the measurement uncertainty matrix $\boldsymbol{R}$ has to include these errors and uncertainties. Compared with the measured RAOs, significant errors of the simulated reference RAOs based on the true vessel parameters were observed for the pitch with wave headings between 90° and 180° and all the roll responses. Even more errors were seen for the roll response with wave headings from 0° (not inclusive) to 90° (not inclusive). The measurement space related to the roll motion should therefore be associated with a larger variance in $\boldsymbol{R}$.

For the algorithm to work, note that one fundamental assumption should be fulfilled, i.e., the wave-induced vessel motions can be well represented by the linear transfer functions (RAOs) simulated by the seakeeping analysis. This normally holds for conventional vessels on moderate seas, especially for heave and pitch. The RAOs generated by different software can be different [4,42]. However, benchmarking of the results generated by software in comparison with the results from experiments and onsite measurements has not been extensively performed and published. Comparison studies [4,42] indicate that

(1) The estimated heave and pitch motion RAOs from most seakeeping solvers match each other well, and they are in agreement with experiments.
(2) Strip theory generally overestimates the local trough (i.e., the RAO amplitude at trough is too small) regarding the cancellation effects for pitch and heave at high frequencies.
(3) Much more deviations and uncertainties of the estimated roll motion RAO are often observed when comparing with various seakeeping solvers, and generally none of the programs or theories outperforms the others when benchmarking with experiments.
(4) A deviated estimation of the roll resonance period between programs is often observed.
(5) Largely deviated estimation of the roll RAO amplitudes is observed across all wave periods, partly due to the applied different approaches for viscous damping estimation.
(6) Seakeeping programs based on strip theories perform equally as well (or equally as poorly) as panel-model-based programs.

The vessel position and orientation measured by the OQUS cameras are subject to measurement errors, which should also be considered in $\boldsymbol{R}$, but these are less significant within the main wave frequencies. For the derivative information, the power and the associated noise of the position and orientation measurements are weighted by ω^2 and ω^4 at each frequency according to Eq. (8). The considered range of ω is usually $[0.5, 1.26]$ rad/s. Therefore, the standard deviations of the derived velocity and acceleration are approximately at the same level as that of the (angular) displacement after bandpass filtering of the signals described in Section 3. Consequently, the random errors of those calculated response standard deviations with different derivative orders are also expected to be approximately of the same magnitude for each motion mode.

The diagonal elements in $\boldsymbol{R}$ are summarized in Table 4 with consideration of the aforementioned systematic and measurement errors. The off-diagonal elements of $\boldsymbol{R}$ are all zero. The designed $\boldsymbol{R}$ matrix in Table 4, without optimization, was applied to investigate the UKF-based tuning algorithm performance, which is considered sufficient for demonstration purposes.

For vessel motion measurements with significant energies, the associated measurement uncertainties were assumed to be proportional to the measured response energies. A lower bound value for each $\sigma_N^2(X_d)$ was set mainly to avoid over-confident and biased tuning. For certain combinations of β_W and T_p, some vessel motions can be less significant, e.g., roll motions around head sea outside of roll resonance period. Consequently, the corresponding random and numerical errors will become more predominant in percentage of the associated motion signal energy, compared with the percentage at other wave conditions. Hence, the measurement

Table 5
Parameters applied in Case 1 related to UKF modeling.

Parameter	Value
State space $\boldsymbol{x}$	$\boldsymbol{x} = [\beta_{33}, \beta'_{44}, \beta_{55}, \mathrm{ZCG}, r_{44}, r_{55}]^{\mathrm{T}}$
Initial $\boldsymbol{x}_0$	$\boldsymbol{x}_0 = [2, 2, 2, 10.79, 12, 41]^{\mathrm{T}}$
Initial $\boldsymbol{P}_0$	$\boldsymbol{P}_0 = \mathrm{diag}(25, 64, 25, 0.04, 4, 25)$
$\boldsymbol{Q}$	$\boldsymbol{Q} = \mathrm{diag}(0.25, 0.25, 0.25, 0.05^2, 0.09, 0.25)$
Measurement space $\boldsymbol{z}$	$\boldsymbol{z} = [\sigma_{\eta_3}, \sigma_{\eta_4}, \sigma_{\eta_5}, \sigma_{\dot{\eta}_3}, \sigma_{\dot{\eta}_5}, \sigma_{\ddot{\eta}_3}, \sigma_{\ddot{\eta}_5}, T_{z(\eta_3)}, T_{z(\eta_5)}]$
$\boldsymbol{R}$	Per Table 4
α	0.01
β	2
κ	−3

uncertainties of certain motions may be underestimated at the less critical sea states if the same ratio of the signal energy is applied across different motion energy levels. Therefore, a minimum value for each $\sigma_N^2(X_d)$ was introduced. Considering $\omega \in [0.5, 1.26]$ rad/s and Eqs. (8) and (9), the same lower bound of measurement uncertainties was applied for displacement, velocity, and acceleration of each motion mode, assuming that the response measurement uncertainties at those less critical wave conditions are mostly contributed from random and numerical errors. Design of $\boldsymbol{R}$ can be optimized, but is considered out of the present research scope.

4.4. Validation analysis cases

Based on initial studies of the model tests, numerical simulations, and the important concerns regarding the selection of the state space and measurement space described in Sections 4.1 to 4.3, the scope of the validation analyses is summarized in this section. Four validation analysis cases are included (referred to as Case 1 to Case 4) to demonstrate the performance and limitations of the algorithm. Tables 5 to 8 summarize the UKF modeling for the 4 cases. All the model tests in Table 1 are considered. The differences among the 4 cases are emphasized through the use of underlines.

The applied values of the initial state vector $\boldsymbol{x}_0$, its initial covariance matrix $\boldsymbol{P}_0$, and the process covariance matrix $\boldsymbol{Q}$ are tentative. Selection of the initial state vector $\boldsymbol{x}_0$ and its initial covariance matrix $\boldsymbol{P}_0$ should reflect the relevant prior knowledge in real applications, based on available technical documentation and engineering judgement. In practice, a slightly larger $\boldsymbol{P}_0$ could increase the initial rate of the state tuning towards the true values [22]. After tuning, the convergent state vector should ideally approach the true state while its convergent covariance matrix should basically reflect the uncertainties of the system propagation model, measurement functions, measurement uncertainties, etc. Therefore, the mean vector of the convergent state and the corresponding covariance are ideally independent of their initial choices. However, due to the nonlinear and multimodal characteristics, the tuning is still expected to be dependent on the initialization, especially before asymptotic convergence of the tuning results. The system propagation model, i.e., Eq. (6), assumes a constant system state for all sea states. The process uncertainty $\boldsymbol{Q}$ should reflect the possible variations of the true state across the different tested sea states. In the case studies, the true values of ZCG, r_{44}, and r_{55} remain unchanged while the linearized additional damping terms (i.e., β_{33}, β'_{44}, and β_{55}) are not strictly constant across sea states as explained in Section 4.2. Hence, compared with the process uncertainties of those linearized additional damping terms, relatively small process uncertainties were applied to the terms that are related to the inertia distribution (i.e., ZCG, r_{44}, and r_{55}). In principle, $\boldsymbol{Q}$ should account for possible state variation across different sea states and operational scenarios [22].

The hyperparameters α, β, κ are the same for all cases and are therefore shown only in Table 5. For the seakeeping model parameter tuning, a very small α helps to stabilize the tuning and to capture the important local nonlinear effects. The values of β and κ have less influence on the tuning results. The same parameters are included as the state space in all 4 cases, as described in Section 4.2.

Due to the significant errors of the measurement characteristics between the predicted and the measured described in Section 4.1, it is important to determine the measurement space with extra caution. The standard deviations of η_3, η_5, the first two orders of their derivatives, and their zero-up-crossing periods (T_z) are included in the measurement space for Case 1, considering the fact that the seakeeping analyses normally predict the heave and pitch motions well. However, only roll angular displacement η_4 is included in the measurement space for Case 1 due to (1) the generally less accurate seakeeping simulations; (2) the significant errors due to the ignorance of the moonpool coupling and the second-order motion effects (e.g., Figs. 7 and 9); and (3) the fact that the mean wave loads are outside the roll resonance period.

In Case 2 (Table 6), the measurement space and the measurement noise matrix $\boldsymbol{R}$ are further modified. It was observed that the simulated pitch RAOs were significantly underestimated compared with the measured ones for wave headings between 90° and 180° (e.g., Fig. 10). This result may be caused by the moonpool effects. Therefore, the derivatives and T_z for pitch motion are not included for $\beta_W \geq 90°$ in Case 2. In addition, less measurement noise variance is considered for pitch-related measurements with $\beta_W < 90°$ due to the relatively accurate simulation.

Both Case 1 and Case 2 considered ZCG to be associated with a relatively high confidence, i.e., a standard deviation of 0.2 m, corresponding to ±0.4 m for a 95% confidence interval. Much higher uncertainty of ZCG is considered in Case 3, as shown in Table 7. This case is provided to show the tuning challenges of nonlinear and multimodal systems caused by the interactions of some vessel parameters for the same DOF as well as interactions with multiple DOFs affected by the same vessel parameter.

Compared with Case 2, the measurement space in Case 4 (Table 8) is further modified. Roll motion is not included in the measurement space for $\beta_W < 90°$, while pitch motion is not considered for $\beta_W \geq 90°$.

Table 6
Parameters applied in Case 2 related to UKF modeling. Differences from Case 1 are underlined.

Parameter	Value
State space $\boldsymbol{x}$	$\boldsymbol{x} = [\beta_{33}, \beta'_{44}, \beta_{55}, \mathrm{ZCG}, r_{44}, r_{55}]^\top$
Initial $\boldsymbol{x}_0$	$\boldsymbol{x}_0 = [2, 2, 2, 10.79, 12, 41]^\top$
Initial $\boldsymbol{P}_0$	$\boldsymbol{P}_0 = \mathrm{diag}(25, 64, 25, 0.04, 4, 25)$
$\boldsymbol{Q}$	$\boldsymbol{Q} = \mathrm{diag}(0.25, 0.25, 0.25, 0.05^2, 0.09, 0.25)$
Measurement space $\boldsymbol{z}$	$\beta_W < 90°$: $\boldsymbol{z} = [\sigma_{\eta_3}, \sigma_{\eta_4}, \sigma_{\eta_5}, \sigma_{\dot{\eta}_3}, \sigma_{\dot{\eta}_5}, \sigma_{\ddot{\eta}_3}, \sigma_{\ddot{\eta}_5}, T_{z(\eta_3)}, T_{z(\eta_5)}]$ $\beta_W \geq 90°$: $\boldsymbol{z} = [\sigma_{\eta_3}, \sigma_{\eta_4}, \sigma_{\eta_5}, \sigma_{\dot{\eta}_3}, \sigma_{\ddot{\eta}_3}, T_{z(\eta_3)}]$
$\boldsymbol{R}$	σ_{x_5} for $\beta_W < 90°$: $\max(\underline{2\%}\sigma^2_{x_5}, 10^{-4})$; otherwise: Per Table 4

Table 7
Parameters applied in Case 3 related to UKF modeling. Differences from Case 2 are underlined.

Parameter	Value
State space $\boldsymbol{x}$	$\boldsymbol{x} = [\beta_{33}, \beta'_{44}, \beta_{55}, \mathrm{ZCG}, r_{44}, r_{55}]^\top$
Initial $\boldsymbol{x}_0$	$\boldsymbol{x}_0 = [2, 2, 2, \underline{11.5}, 12, 41]^\top$
Initial $\boldsymbol{P}_0$	$\boldsymbol{P}_0 = \mathrm{diag}(25, 64, 25, \underline{1.0}, 4, 25)$
$\boldsymbol{Q}$	$\boldsymbol{Q} = \mathrm{diag}(0.25, 0.25, 0.25, 0.05^2, 0.09, 0.25)$
Measurement space $\boldsymbol{z}$	Per Case 2 (Table 6)
$\boldsymbol{R}$	Per Case 2 (Table 6)

Table 8
Parameters applied in Case 4 related to UKF modeling. Differences from Case 2 are underlined.

Parameter	Value
State space $\boldsymbol{x}$	$\boldsymbol{x} = [\beta_{33}, \beta'_{44}, \beta_{55}, \mathrm{ZCG}, r_{44}, r_{55}]^\top$
Initial $\boldsymbol{x}_0$	$\boldsymbol{x}_0 = [2, 2, 2, 10.79, 12, 41]^\top$
Initial $\boldsymbol{P}_0$	$\boldsymbol{P}_0 = \mathrm{diag}(25, 64, 25, 0.04, 4, 25)$
$\boldsymbol{Q}$	$\boldsymbol{Q} = \mathrm{diag}(0.25, 0.25, 0.25, 0.05^2, 0.09, 0.25)$
Measurement space $\boldsymbol{z}$	$\beta_W < 90°$: $\boldsymbol{z} = [\sigma_{\eta_3}, \sigma_{\eta_5}, \sigma_{\dot{\eta}_3}, \sigma_{\dot{\eta}_5}, \sigma_{\ddot{\eta}_5}, T_{z(\eta_3)}, T_{z(\eta_5)}]$ $\beta_W \geq 90°$: $\boldsymbol{z} = [\sigma_{\eta_3}, \sigma_{\eta_4}, \sigma_{\dot{\eta}_3}, \sigma_{\ddot{\eta}_3}, T_{z(\eta_3)}]$
$\boldsymbol{R}$	Per Case 2 (Table 6)

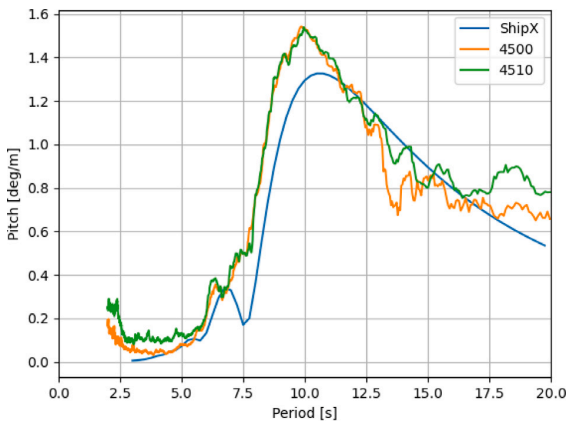

Fig. 10. The reference pitch RAO from the ShipX (VERES) simulation and the measured pitch RAOs based on Tests 4500 and 4510 for a wave heading of 150°. (For interpretation of the references to color in this figure legend, the reader is referred to the web version of this article.)

5. Results

The tuning results from the 4 cases described in Section 4.4 are summarized, discussed, and compared in this section. The objectives of the tuning are not only to improve the vessel motion estimation at the present tuning sea state but much more importantly to improve the knowledge regarding the uncertain vessel parameters to achieve more accurate RAOs for better vessel motion prediction in relation to future unobserved sea states, especially for the most critical wave conditions. For convenience of discussion, the true values of the uncertain vessel parameters are denoted by $\boldsymbol{x}^* = [\beta^*_{33}, \beta'^*_{44}, \beta^*_{55}, \mathrm{ZCG}^*, r^*_{44}, r^*_{55}]^\top = [0, 0, 0, 10.82, 10.5, 44.8]^\top$.

It is worth mentioning that the proposed tuning algorithm is computationally very efficient for large-dimensional nonlinear systems. For the case studies with a 6-dimensional state vector and the seakeeping simulation by ShipX (VERES), the validation analysis took less than 2 h to tune through all 24 test cases in Table 1 when running 7 VERES analyses in parallel, i.e., less than 5 min per model test case. The time spent was dominated by the seakeeping simulations. Having completed the seakeeping simulations, the tuning for each model test case took approximately 3 s.

5.1. Case 1

The tuning of the uncertain vessel parameters for Case 1 is shown in Fig. 11. The "Predicted" lines in black indicate the prediction of those parameters after the system propagation step corresponding to Eq. (6), and the filled gray areas illustrate their 95% confidence intervals (i.e., $\pm 2\sigma$ for Gaussian variables). The "Updated" lines in red indicate the updated estimation of those uncertain vessel parameters after the measurement update step corresponding to Eqs. (7)–(13), and the filled red areas illustrate their 95% confidence intervals. The dashed lines in green indicate the corresponding true values specified in the model tests. For the additional damping terms, true values are not available.

As illustrated in Fig. 11a, β_{33} varies around zero, as expected. The negative β_{33} for the following sea conditions ($k > 17$) suggests a possible underestimation of the heave responses from the VERES simulation at the relevant wave conditions. The heave resonance is at approximately 6 to 9 s, where significant wave loads are present in the model tests. Referring to Table 3, only β_{33} in the system state can significantly influence the heave RAO amplitude around the periods of interest. A greatly reduced uncertainty of β_{33} is also shown in Fig. 11a.

The peak of the pitch RAO also occurs at approximately 7 to 10 s. Therefore, β_{55} is expected to have a significant influence on the pitch response for the tested wave conditions. For $\beta_W < 90°$, β_{55} was quickly tuned to 0%, while r_{55} (Fig. 11f) gradually approached its true value. This suggests that the VERES-simulated pitch RAOs based on the true value of r_{55} without additional damping match the measurements very well, as shown in Fig. 6. However, for $\beta_W < 90°$, a dramatic decrease in β_{55} and increase in r_{55} are observed, both leading to an increase in the pitch motions for the tested wave conditions. This outcome also reveals the deviation in the pitch estimation by the ShipX (VERES) simulations based on the true r_{55} and zero β_{55} for $\beta_W \geq 90°$, e.g., as shown in Fig. 10. Even though the tuned r_{55} in Case 1 largely deviated from the true value when $k > 15$, in fact, the corresponding pitch estimations for those testing wave conditions were significantly improved. For example, Fig. 12 compares the pitch motion spectra estimated based on the true vessel parameters $\boldsymbol{x}^*$ (blue), the tuned vessel parameters $\boldsymbol{x}_{19}$ (orange), and the measurements (green). It is obvious that the tuned state vector $\boldsymbol{x}_{19}$ significantly improves the estimation accuracy of pitch motion at the wave condition for Test 4510, which is also supported by the improved pitch RAO at $\beta_W = 150°$, as shown in Fig. 13. However, this may not help in the prediction of pitch motion for other wave conditions. The VERES-simulated pitch RAO at head sea $\beta_W = 0°$ after tuning for Test 4510 is illustrated in Fig. 14. In comparison with the pitch RAOs based on $\boldsymbol{x}^*$ and the measurements from the relevant test cases, the simulated RAO after tuning for Test 4510 deviates significantly, leading to increased prediction errors for head seas.

For the tuning of roll-related parameters, very little change in β'_{44} and its uncertainty is observed in Fig. 11b because the roll resonance period is approximately 15 s, where little wave energy exists for almost all the test cases. The damping term has a very limited effect on the responses outside the resonance. ZCG also changed less significantly due to its relatively small uncertainty. The uncertainty of ZCG even increased, as shown in Fig. 11d, indicating an initial underestimation of the uncertainty. A slightly deviating tuning of r_{44} is shown in Fig. 11e. As pointed out in Section 4.4, software-induced errors are most onerous in the roll motion estimation, and therefore, biased tuning for parameters related to roll motion is very challenging to handle. Indeed, a much more severe tuning bias of r_{44} can be obtained when the measurement space includes the derivatives and T_z of the roll angular displacement. It is therefore important to determine the measurement space and the noise matrix.

5.2. Case 2

Compared with Case 1, the measurement space was modified in Case 2, as shown in Table 6: (1) the noise variances of the pitch motion, velocity, and acceleration were reduced from 5% to 2% of the corresponding measured pitch responses for $\beta_W < 90°$; and (2) only the standard deviation of the pitch angular displacement was included in the measurement space with a noise variance of 5%. Fig. 15 illustrates the corresponding tuning results for the 6 uncertain vessel parameters. Compared with Case 1 (Fig. 11), the modification of the measurement space for pitch responses leads to a significant improvement in the tuning of r_{55} (Fig. 15f). Due to the reduction in $\boldsymbol{R}$ for pitch-related measurements for $\beta_W < 90°$ and the fact that the reference pitch RAO based on $\boldsymbol{x}^*$ matches very well with the measurements for $\beta_W < 90°$, faster tuning convergence of r_{55} was observed for Case 2. Furthermore, because the pitch motion derivatives and T_z were removed from the measurement space for $\beta_W \geq 90°$, the resulting tuned r_{55} value at $k = 24$ deviated much less from the true value, even though the system still intended to increase the value of r_{55}.

On the other hand, worse tuning of β'_{44} (Fig. 15b) and r_{44} (Fig. 15e) were observed, although the measurement space related to roll motion did not change compared with Case 1. This outcome was mainly due to the multimodal and nonlinear characteristics of the seakeeping model tuning problem. Multiple combinations of β'_{44}, ZCG, and r_{44} can possibly lead to the same standard deviation of the roll motion considered in the measurement space. Therefore, the weighted statistical linear regression [26] based on the deterministically selected sigma points may lead to different tuning directions, depending on the state mean, covariance matrix, and hyperparameters of the UKF model. For example, after the system propagation for $k = 7$ (Test 4120), a smaller ZCG and larger r_{44} than in Case 1 were predicted. Different sets of sigma points were therefore assessed between Case 1 and Case 2. A smaller r_{44} helps to reduce the roll resonance period and consequently increase the RAO amplitudes for periods less than the resonance period,

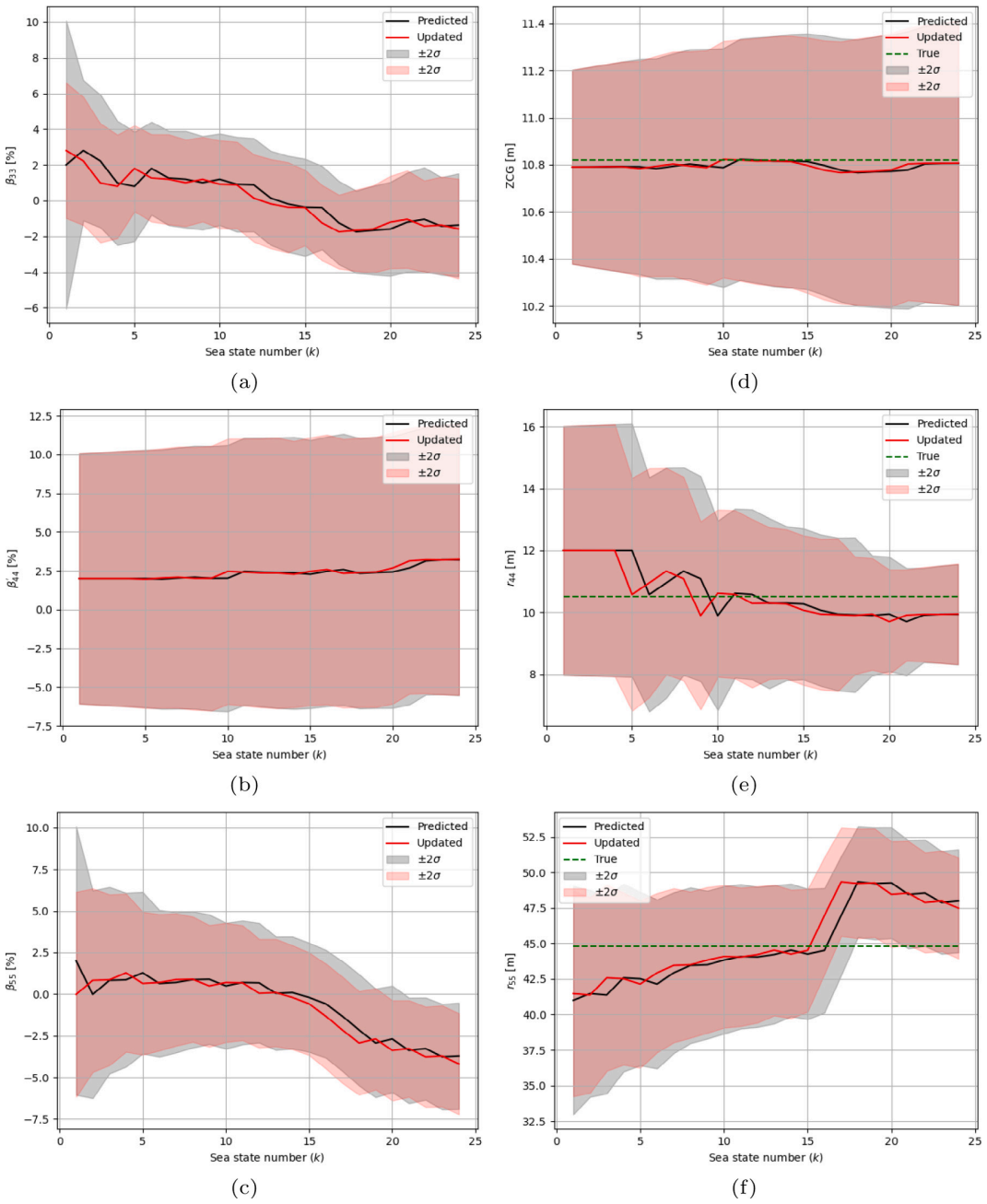

Fig. 11. The state estimation for Case 1 after system propagation ("Predicted") and measurement update ("Updated") for each model test case described in Table 1. Subplots illustrate the tuning of (a) β_{33}; (b) β'_{44}; (c) β_{55}; (d) ZCG; (e) r_{44}; (f) r_{55}. (For interpretation of the references to color in this figure legend, the reader is referred to the web version of this article.)

whereas a larger ZCG stretches the RAO towards larger periods, leading to an increased resonance period, larger RAO amplitudes for small periods (e.g., 3–6 s) before the cancellation effect (e.g., at approximately 8 s in Fig. 7), but smaller RAO amplitudes for larger periods (e.g., 8–14 s) on the lower side of the resonance period. These complicated influences on the roll motions cause the seakeeping parameter tuning to be nonlinear and multimodal, leading to the state-dependent tuning direction. In addition, as

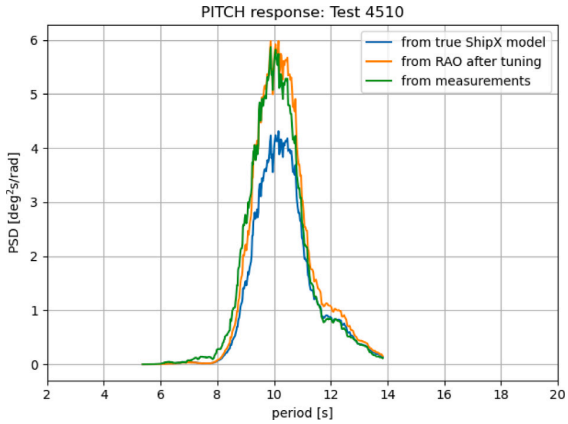

Fig. 12. The pitch motion spectra for the wave condition of Test 4510 ($k = 19$) for $\beta_W = 150°$. Blue: spectrum estimated from the simulated reference RAO based on $\boldsymbol{x}^*$; orange: spectrum estimated from the VERES-simulated RAO based on $\boldsymbol{x}_{19}$; green: spectrum estimated directly from the measurements. (For interpretation of the references to color in this figure legend, the reader is referred to the web version of this article.)

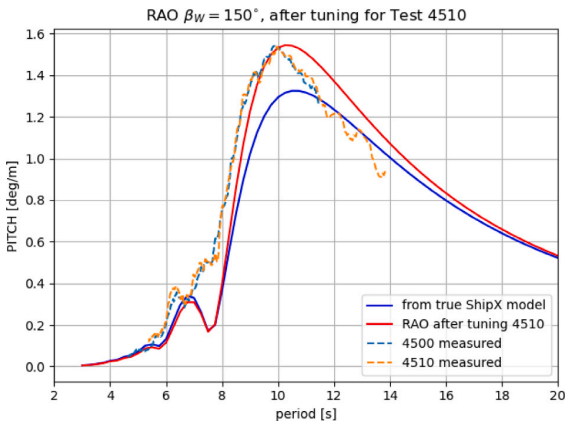

Fig. 13. The pitch RAOs for $\beta_W = 150°$. Blue: the simulated reference RAO based on $\boldsymbol{x}^*$; red: the VERES-simulated RAO based on $\boldsymbol{x}_{19}$, i.e., after tuning for Test 4510 ($k = 19$); dashed: RAOs estimated directly from the measurements for $\beta_W = 150°$. (For interpretation of the references to color in this figure legend, the reader is referred to the web version of this article.)

shown in Fig. 9, a much larger roll motion estimation error is expected for $\beta_W < 90°$ due to the moonpool effects. The high local peak of the roll RAO in Test 4210 (Fig. 9) before 10 s can never be simulated within the considered uncertainty ranges of the parameters and without considering the moonpool coupling effect in the seakeeping simulations. Therefore, reliable tuning of the roll-motion-related parameters cannot be expected for $\beta_W < 90°$.

Compared with Case 1, different tuning results for roll-motion-related parameters were observed for $\beta_W < 90°$ even though the roll-related measurement space is the same for both Case 1 and Case 2 (for $\beta_W < 90°$). This is believed to be due to the small influence of ZCG on the pitch motion as indicated in Table 3. Compared with Case 1, the reduced measurement uncertainty variances ($\boldsymbol{R}$) in Case 2 for pitch-related characteristics at $\beta_W < 90°$ may make the tuning of ZCG more dependent on the pitch measurements. Consequently, the tuning of other roll-motion-related parameters such as β'_{44} and r_{44} can be influenced by those differently tuned ZCG values.

5.3. Case 3

Compared with Case 2, Case 3 changes only the initial value of ZCG and increases the initial variance from 0.04 to 1.0 m^2. The tuning results illustrated in Fig. 16 indicate how the interaction between the tuning of ZCG and that of r_{44} leads to the increasingly biased tuning of r_{44}. Larger ZCG uncertainty allows the UKF model to vary more in terms of the ZCG value to help further reduce the measurement residual. Consequently, biased tuning of the seakeeping model parameters is more likely to occur when the measurement function has significant systematic errors.

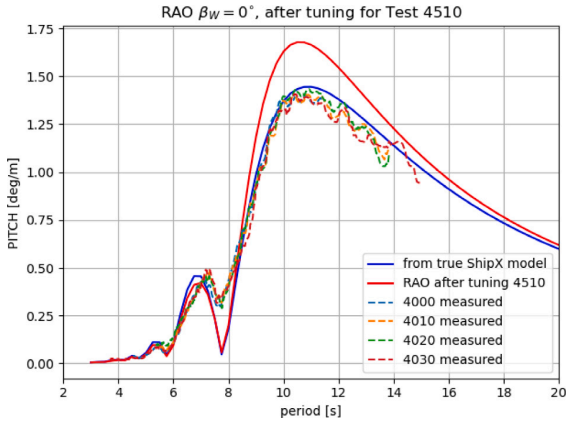

Fig. 14. The pitch RAOs for $\beta_W = 0°$. Blue: the simulated reference RAO based on $\boldsymbol{x}^*$; red: the VERES-simulated RAO based on $\boldsymbol{x}_{19}$, i.e., after tuning for Test 4510 ($k = 19$); dashed: RAOs estimated directly from the measurements for $\beta_W = 0°$. (For interpretation of the references to color in this figure legend, the reader is referred to the web version of this article.)

As shown in Fig. 17, the UKF model succeeded in reducing the residual of the roll motion standard deviation for Test 4420 ($k = 17$) by reducing ZCG (Fig. 16d). Reduced errors in the roll RAOs between those measured (dashed lines) and those simulated by ShipX (VERES) based on $\boldsymbol{x}_{17}$ (red) were also observed for periods less than the resonance period, as illustrated in Fig. 18, in comparison with the VERES-simulated RAO based on the true state $\boldsymbol{x}^*$ (blue). However, this updated roll RAO will lead to significant roll motion prediction errors for wave conditions with periods near or larger than the resonance period.

It is also noted that β'_{44} was slightly reduced. In fact, a further reduction in β'_{44} can help to increase the roll spectral density near the resonance (e.g., 13–17 s). However, the linear regression at the selected sigma points for $k = 17$ suggested that tuning ZCG was more efficient, mainly because most of the roll motion energy considered in the measurement space was outside the resonance period, implying a smaller contribution from β'_{44} to the roll motion for this sea state. When calculating the roll motion standard deviation for Test 4420, the spectrum was cut off at a period of 15 s as described in Section 4.1. It is believed that including responses larger than 15 s can help the UKF model realize the contribution of β'_{44} to the roll motion, though only if the second-order roll motion can be clearly removed before tuning. For Test 4420, it is possible that the response periods of the first-order and second-order roll motions overlap due to the broadband wave spectrum. The significant wave loads at 5 to 10 s may induce the second-order roll motions at 10 to 15 s, where significant first-order motions exist. The signal filtering described in Section 4.1 cannot deal with this overlap, leading to additional error sources between the predicted response versus the measured one.

5.4. Case 4

As shown in the previous case studies, biased tuning of r_{44} and r_{55} is due to the systematic errors of the measurement functions introduced by the simulated RAOs $|H_X(\omega, \beta_W|\boldsymbol{\mathcal{X}}_{k+1,i})|$ at the sigma points in Eq. (10). It is assumed in Case 4 that better prior knowledge about the uncertainties of the simulated RAOs can be included, i.e., better matches for (1) the simulated roll RAOs versus the measurement at $\beta_W \geq 90°$ and (2) the simulated pitch RAOs versus the measurement at $\beta_W < 90°$. Therefore, as summarized in Table 8, the measurement space of Case 4 did not consider roll motions for $\beta_W < 90°$ and pitch motions for $\beta_W \geq 90°$.

Fig. 19 illustrates improved tuning results for β_{55} (Fig. 19c), r_{44} (Fig. 19e), and r_{55} (Fig. 19f) compared with those in Case 2. Slightly biased tuning of ZCG is shown in Fig. 19d, mainly due to the significant systematic error in the simulated roll RAOs, even though this error was much less for $\beta_W \geq 90°$.

Comparing Figs. 15f and 19f, it is interesting to note the different tuning r_{55} for $\beta_W < 90°$, e.g., $k \in [6, 14]$, even though the initial state and the measurement space related to pitch motions are the same for Case 2 and Case 4 for $\beta_W < 90°$. In fact, the state covariance matrix $\boldsymbol{P}$ and the matrix square root calculation of $\left[\sqrt{(N+\lambda)\boldsymbol{P}_k}\right]_j$ in Eq. (1) were influenced by removing the roll motion from the measurement space for $\beta_W < 90°$. Consequently, the selection of sigma points and the weighted statistical linear regression were affected, which can easily lead to different tuning results involving nonlinear functions.

Moreover, r_{55} was actively tuned in Case 4 even for $\beta_W > 90°$, where the pitch motions were removed from the measurement space. In fact, the tuning of r_{55} was actually influenced by the heave measurements made at the OQUS camera location, where the heave motion was affected by the coupling effect from the pitch, as shown in Eq. (11). Thus, the pitch-related measurements were implicitly considered in the measurement space for $\beta_W \geq 90°$.

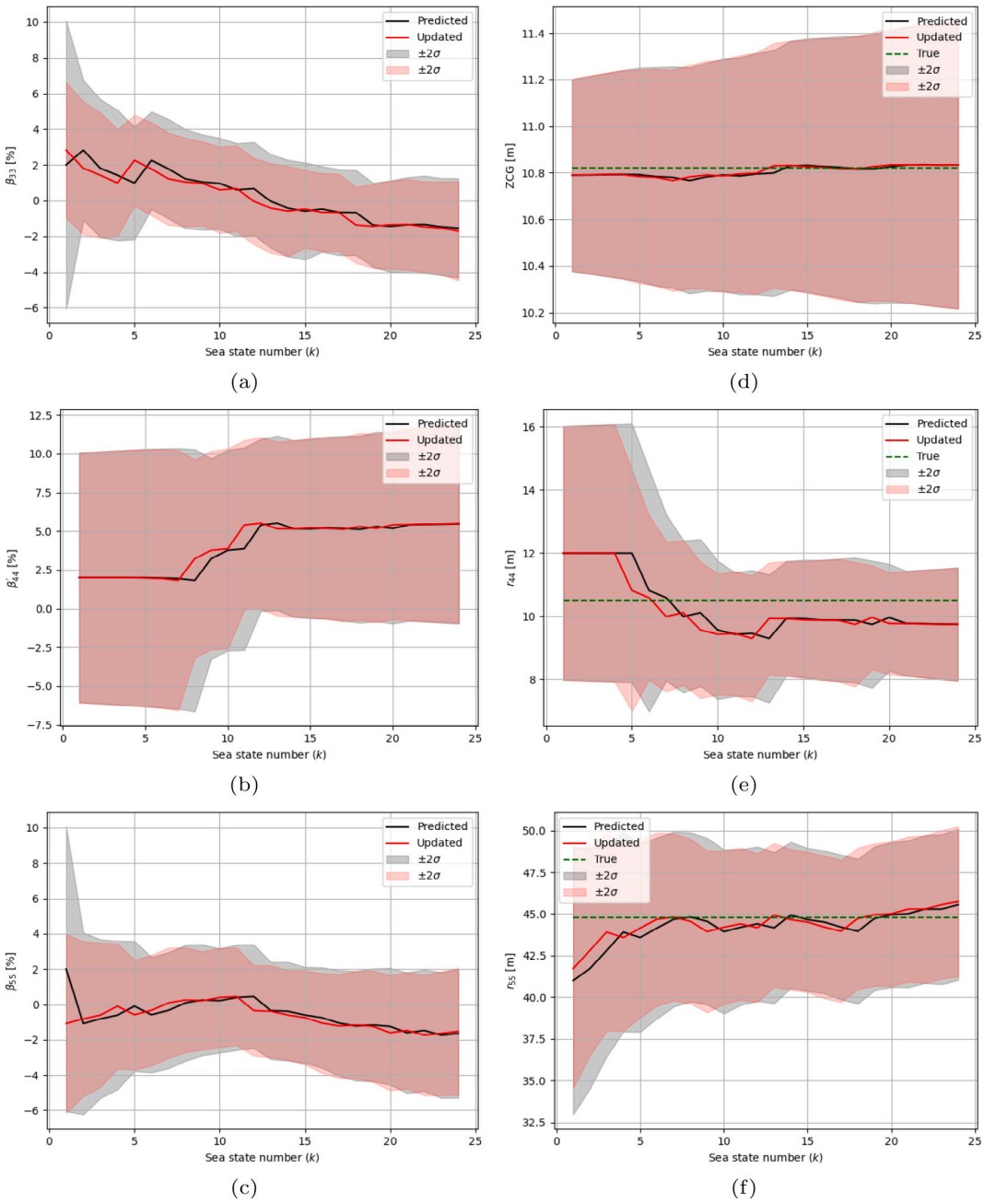

Fig. 15. The state estimation for Case 2 after system propagation ("Predicted") and measurement update ("Updated") for each model test case described in Table 1. Subplots illustrate the tuning of (a) β_{33}; (b) β'_{44}; (c) β_{55}; (d) ZCG; (e) r_{44}; (f) r_{55}. (For interpretation of the references to color in this figure legend, the reader is referred to the web version of this article.)

6. Conclusions and future work

The present paper demonstrated the application of the previously proposed algorithm in relation to the tuning of important uncertain vessel seakeeping parameters based on the unscented Kalman filter (UKF) [22] by using seakeeping (zero speed) model

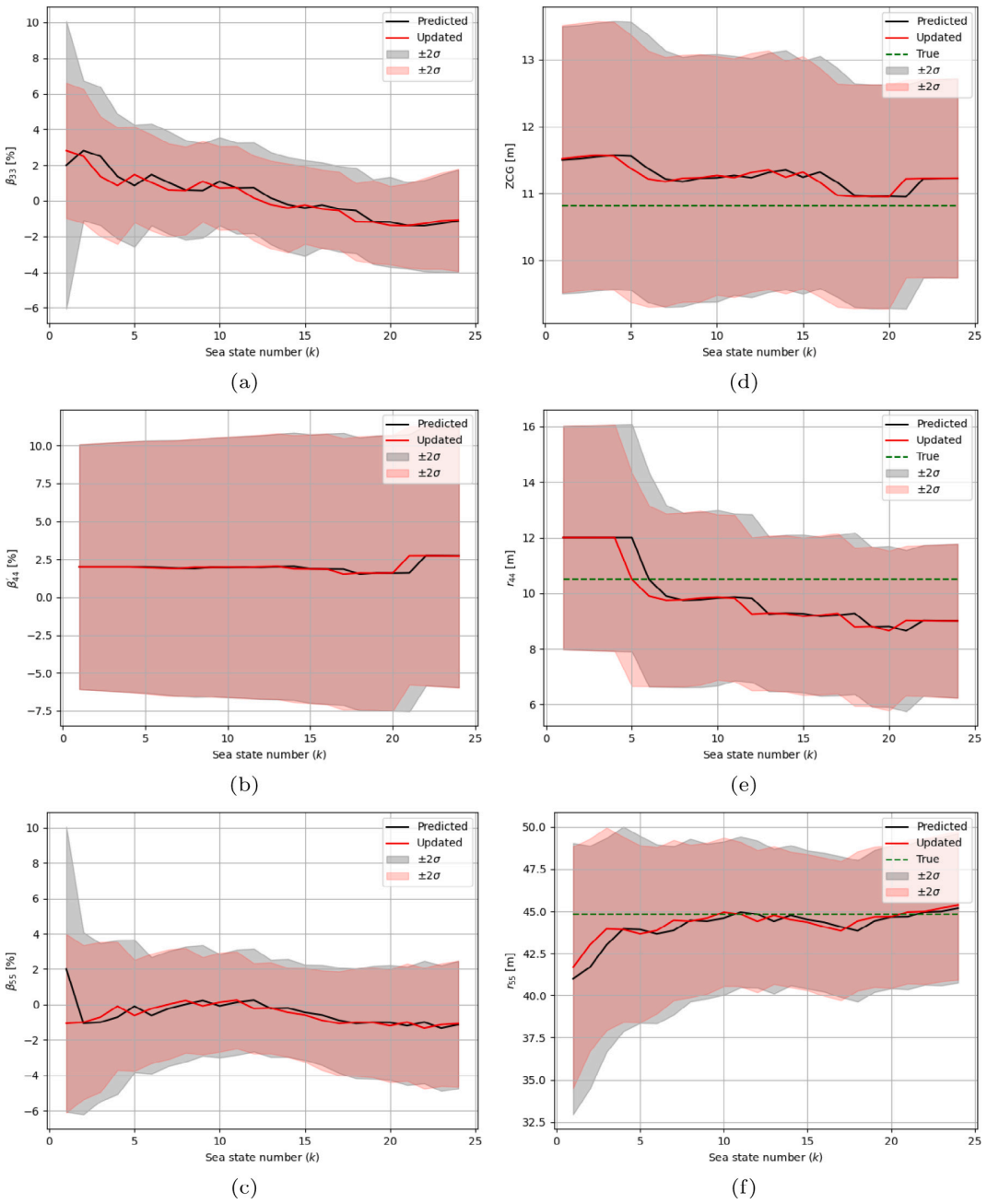

Fig. 16. The state estimation for Case 3 after system propagation ("Predicted") and measurement update ("Updated") for each model test case described in Table 1. Subplots illustrate the tuning of (a) β_{33}; (b) β'_{44}; (c) β_{55}; (d) ZCG; (e) r_{44}; (f) r_{55}. (For interpretation of the references to color in this figure legend, the reader is referred to the web version of this article.)

tests for an advanced offshore construction vessel. The uncertain vessel parameters (i.e., the state space) were selected based on parametric sensitivity studies. Rational tuning results were achieved by carefully designing the measurement space. The influences of the considered state space and measurement space on the tuning results were discussed in Section 5.

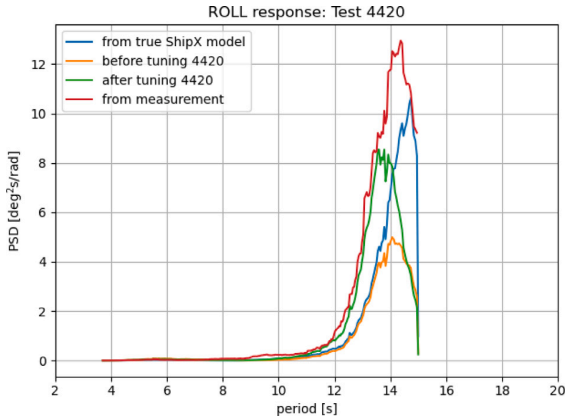

Fig. 17. The roll motion spectra for the wave condition of Test 4420 ($k = 17$). Blue: spectrum estimated from the VERES-simulated RAO based on $\boldsymbol{x}^*$; orange: spectrum estimated from the VERES-simulated RAO based on the state before tuning for Test 4420, i.e., $\boldsymbol{x}_{16}$; green: spectrum estimated from the VERES-simulated RAO based on the state after tuning for Test 4420, i.e., $\boldsymbol{x}_{17}$; red: spectrum estimated directly from the measurements for Test 4420. (For interpretation of the references to color in this figure legend, the reader is referred to the web version of this article.)

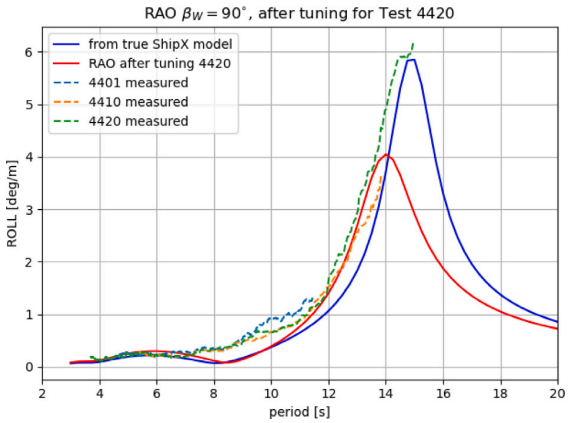

Fig. 18. The roll RAOs for $\beta_W = 90°$. Blue: the VERES-simulated RAO based on $\boldsymbol{x}^*$; red: the VERES-simulated RAO based on $\boldsymbol{x}_{17}$, i.e., after tuning for Test 4420 ($k = 17$); dashed: RAOs estimated directly from the measurements for $\beta_W = 90°$. (For interpretation of the references to color in this figure legend, the reader is referred to the web version of this article.)

The fundamental goal is to modify the important vessel parameters based on vessel motion measurements and the corresponding wave information for a limited number of sea states. Consequently, the accuracy of the calculated linear transfer functions can be improved across the whole range of wave frequencies, particularly at critical frequencies (e.g., around resonance) which may have not been observed. Hence, the most fundamental assumption (and the most critical limitation) is that the linear transfer functions simulated by the application of seakeeping analysis must be sufficiently representative with respect to the relevant vessel motions of interest at the wave frequencies. However, systematic errors are never expected to vanish.

Therefore, it is extremely important to determine the state space and measurement space for a successful tuning. Without inclusion of all the important and uncertain vessel parameters in the state space, the algorithm will try to tune some other influential parameters in the state space to reduce the residual, which will definitely lead to biased tuning results. Understanding the systematic errors from the measurement functions due to the applied simplifications and assumptions associated with the seakeeping simulations and the consequent motion estimation is the key to properly determining the measurement space and its uncertainties. When the systematic errors from seakeeping simulation are relatively small, more relevant measured response characteristics in the measurement space and reduced measurement noise variance can help accelerate the tuning towards the correct values, e.g., the tuning of r_{55} for $\beta_W < 90°$ in Case 2 (Section 5.2). Including characteristics of the response velocities and accelerations into the measurement space can enable tuning towards the true results because the motion PSDs are "weighted" differently at different frequencies. The measurement space is hence more informative.

However, it is advised not to design a too informative measurement space by including excessive measured response characteristics when the systematic errors from the measurement functions are large and especially if they are biased. For example as observed

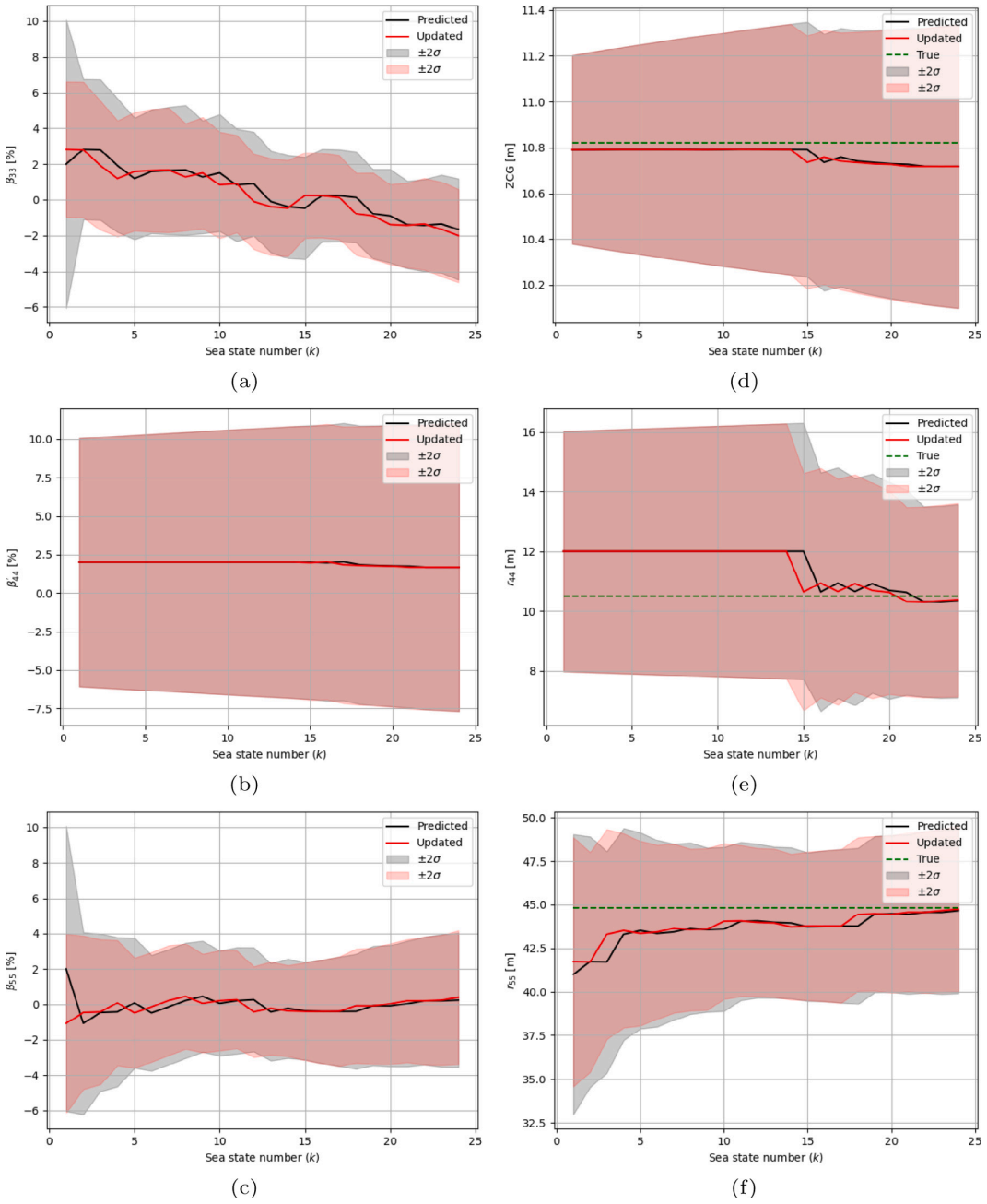

Fig. 19. The state estimation for Case 4 after system propagation ("Predicted") and measurement update ("Updated") for each model test case described in Table 1. Subplots illustrate the tuning of (a) β_{33}; (b) β'_{44}; (c) β_{55}; (d) ZCG; (e) r_{44}; (f) r_{55}. (For interpretation of the references to color in this figure legend, the reader is referred to the web version of this article.)

by a comparison of Figs. 11f and 15f, due to large systematic errors of the reference RAO for pitch with $\beta_W \geq 90°$, the excessive pitch-related measurement space in Case 1 leads to a significantly biased tuning of r_{55}. The existence of moonpools on the studied vessel leads to larger and biased errors of the simulated RAOs for some DOFs at some wave headings, as thoroughly discussed in Section 4.1. Thus, a flexible measurement space that can be modified according to the wave information and improved knowledge on the limitations of the applied seakeeping analysis can potentially improve the tuning results, e.g., as shown in Section 5.4.

All the four cases indicate insignificantly reduced uncertainties of roll-related parameters, i.e., β'_{44}, ZCG, and r_{44}. Even increased uncertainties of β'_{44} (Fig. 16d) and ZCG (Figs. 11d, 15d and 19d) were observed. These observed large uncertainties after tuning are mainly because:

(1) Relatively large measurement uncertainties were applied to the quantities related to roll motion (i.e., σ_{η_4} and $T_{z(\eta_4)}$), as specified in Table 4.
(2) Roll velocity and acceleration were not considered to be part of the measurement space. This less informative roll-related measurement space led to larger uncertainties after convergence.
(3) β'_{44} is basically little sensitive to roll motions for most of the tested sea states, due to the wave spectral peak periods located well away from the roll resonance period.

The increased uncertainty of ZCG for Case 1, Case 2, and Case 4 is believed to be due to its too small initial variance compared with the actual uncertainties from signals, measurement functions, and system propagation model, etc. The convergent variances of those roll-related parameters are actually affected in an interactive way. A less uncertain ZCG led to a less uncertain r_{44} (Figs. 11 and 15), and vice versa (Fig. 16). The resulting large variances of roll-related parameters after tuning are still believed to be very valuable, because:

(a) As long as the estimated uncertainty reflects reality, a model tuning algorithm which provides uncertainty quantification is usually better than parametric optimization algorithms that are based on minimization of a residual (i.e., cost function), which rather results in "deterministic" tuning results. Such deterministic results do not reveal the associated uncertainties and may therefore introduce large estimation errors without this being apparent.
(b) Uncertainty quantification of the important vessel parameters offers a unique opportunity to perform quantitative reliability or risk assessment for advanced onboard decision support systems, in applications related to marine operations, autonomous ships, etc.

Several parameters may influence the same vessel motion in a similar way, e.g., the effect of r_{44} and ZCG on roll motions. Due to the nonlinear and nonmonotonic relationship between the vessel parameters and the characteristics of the relevant measured vessel response, the present algorithm may lead to tuning of the parameters towards wrong values. This may still be acceptable with respect to vessel motion prediction for similar wave conditions but is unacceptable for very different wave conditions. Examples are illustrated in Figs. 14 and 18. Future research needs to clarify how to treat these challenges. The proposed algorithm will in any case try to tune the parameters to reduce the measurement residual, based on assessments at several deterministically selected sigma points around the state mean. Therefore, the tuning is sensitive to the state mean, the state covariance, and the hyperparameters of the UKF model (e.g., α). The algorithm should be further developed to improve its stability and robustness, especially when a critically large bias due to the measurement functions or the system propagation functions exists.

As explained in Section 5.3, the higher-order responses may not be easy to filter out due to the potential overlapping of the response frequency ranges with the first-order responses. Future research is hence required with respect to improving the higher-order response identification and filtering to improve the performance of the tuning algorithm.

In the present paper, the tuning algorithm was assessed only by model-scale measurements in a laboratory environment with minor uncertainties regarding the wave conditions. The tuning algorithm should be further validated by cases involving full-scale measurements, where the uncertainties of sea states are much more significant and therefore must be considered in a probabilistic way, e.g., as proposed by Han et al. [22]. In addition, larger variation in the wave conditions can be expected in real applications. Consequently, the UKF-based tuning algorithm must be modified to tune the sea-state-dependent parameters (e.g., β_{44}) and to use this tuned information in the present sea state to improve the vessel motion prediction accuracy for future unobserved wave conditions.

Declaration of competing interest

The authors declare that they have no known competing financial interests or personal relationships that could have appeared to influence the work reported in this paper.

Acknowledgments

This work was made possible through the Centre for Research based Innovation MOVE, financially supported by the Research Council of Norway, NFR project no. 237929, and the consortium partners (http://www.ntnu.edu/move). Special thanks are given to Salt Ship Design AS for the permission to use the relevant information, data, and numerical model from their seakeeping model tests. Thanks are also given to professor Trygve Kristiansen at NTNU, Martin Gutsch, Senthuran Ravinthrakumar, and Kjetil Berget at SINTEF Ocean AS for the valuable support and discussions regarding model testing, vessel hydrodynamics and moonpool coupling effects.

References

[1] DNVGL-ST-N001. Marine operations and marine warranty. Technical Report, DNV GL; 2016.
[2] WAMIT INC. WAMIT user manual, version 6.4. Technical Report, WAMIT, INC.; 2009.
[3] Fathi DE. ShipX Vessel Responses (VERES), User's manual. Technical Report, SINTEF Ocean AS; 2018.
[4] Gourlay T, von Graefe A, Shigunov V, Lataire E. Comparison of AQWA, GL rankine, MOSES, OCTOPUS, PDStrip and WAMIT with model test results for cargo ship wave-induced motions in shallow water. In: Proceedings of the ASME 2015 34th International Conference on Ocean, Offshore and Arctic Engineering, Vol. 11. St. John's, Newfoundland, Canada; 2015.
[5] Tellkamp J, Bruns A, Gosch T, Günther H, Hansen PF, Nielsen UD, Papanikolaou A, Spanos D, Papatzanakis G, Kassner S, Wittkuhn D, Tränkmann I, Ehrke K-C, Krüger S, Vorhoelter H, Kluwe F, Jaap Struijk JKN. ADOPT summary of experiences and needs for further development. Technical Report, FORCE Technology and Uniresearch; 2009.
[6] Dannenberg J, Hessner K, Naaijen P, van den Boom H, Reichert K. The on board wave and motion estimator OWME. In: Proceedings of the 20th International Offshore and Polar Engineering Conference. International Society of Offshore and Polar Engineers; 2010.
[7] Clauss GF, Kosleck S, Testa D. Critical situations of vessel operations in short crested seas - forecast and decision support system. J Offshore Mech Arct Eng 2012;134(3). http://dx.doi.org/10.1115/1.4004515.
[8] Connell BSH, Rudzinsky JP, Brundick CS, Milewski WM, Kusters JG, Farquharson G. Development of an environmental and ship motion forecasting system. In: International Conference on Offshore Mechanics and Arctic Engineering, Volume 11: Prof. Robert F. Beck Honoring Symposium on Marine Hydrodynamics, 2015, http://dx.doi.org/10.1115/OMAE2015-42422.
[9] Naaijen P, van Oosten K, Roozen K, van't Veer R. Validation of a deterministic wave and ship motion prediction system. In: International Conference on Offshore Mechanics and Arctic Engineering, 2018, http://dx.doi.org/10.1115/OMAE2018-78037.
[10] ECMWF. Part VII: ECMWF wave model. In: IFS Documentation CY41R2. IFS Documentation, (7). ECMWF; 2016, URL: https://www.ecmwf.int/node/16651.
[11] Chan H-S, Armaoglu E, Thomson M, Garner A, Parisotto A, Sovilla S. Response forecasts for a suspended wellbay module and flare tower during transit to shore. In: The 29th International Ocean and Polar Engineering Conference. Honolulu, Hawaii, USA; 2019.
[12] Hilmer T, Thornhill E. Deterministic wave predictions from the wamos II. In: OCEANS 2014 - TAIPEI. 2014, p. 1–8.
[13] Stredulinsky DC, Thornhill EM. Ship motion and wave radar data fusion for shipboard wave measurement. J Ship Res 2011;55:73–85.
[14] Nouguier F, Grilli ST, Guérin C. Nonlinear ocean wave reconstruction algorithms based on simulated spatiotemporal data acquired by a flash LIDAR camera. IEEE Trans Geosci Remote Sens 2014;52(3):1761–71. http://dx.doi.org/10.1109/TGRS.2013.2254494.
[15] Nielsen UD. A concise account of techniques available for shipboard sea state estimation. Ocean Eng 2017;129:352–62. http://dx.doi.org/10.1016/j.oceaneng.2016.11.035.
[16] Ren Z, Han X, Verma AS, Dirdal JA, Skjetne R. Sea state estimation based on vessel motion responses: Improved smoothness and robustness using Bézier surface and L1 optimization. Mar Struct 2021;76:102904. http://dx.doi.org/10.1016/j.marstruc.2020.102904.
[17] Xu H, Soares CG. Hydrodynamic coefficient estimation for ship manoeuvring in shallow water using an optimal truncated LS-SVM. Ocean Eng 2019;191:106488.
[18] Fossen T, Sagatun S, Sørensen A. Identification of dynamically positioned ships. Control Eng Pract 1996;4(3):369–76. http://dx.doi.org/10.1016/0967-0661(96)00014-7.
[19] Kaasen KE, Berget K, Lie H, Bjørkli R. Automatic tuning of vessel models offshore: A feasibility study using high-precision data from model test. In: Offshore Technology Conference, (OTC-30690-MS). Houston, Texas, USA; 2020.
[20] Han X, Leira BJ, Sævik S. Vessel hydrodynamic model tuning by discrete Bayesian updating using simulated onboard sensor data. Ocean Eng 2021;220. http://dx.doi.org/10.1016/j.oceaneng.2020.108407, URL: https://www.sciencedirect.com/science/article/pii/S0029801820313147.
[21] Gelman A, Carlin J, Stern H, Dunson D, Vehtari A, Rubin D. Bayesian Data Analysis. third ed.. 2013.
[22] Han X, Leira BJ, Sævik S, Ren Z. Onboard tuning of vessel seakeeping model parameters and sea state characteristics. Mar Struct 2021;78. http://dx.doi.org/10.1016/j.marstruc.2021.102998.
[23] Julier SJ, Uhlmann JK. A general method for approximating nonlinear transformations of probability distributions. 1996.
[24] Julier SJ. The scaled unscented transformation. In: Proceedings of the 2002 American Control Conference (IEEE Cat. No. CH37301), Vol. 6. IEEE; 2002, p. 4555–9.
[25] ITTC. Recommended procedures and Guidelines: Global Loads Seakeeping Procedure. Technical Report, International Towing Tank Conference; 2011.
[26] Van Der Merwe R, et al. Sigma-point Kalman filters for probabilistic inference in dynamic state-space models (Ph.D. thesis), OGI School of Science & Engineering at OHSU; 2004.
[27] Han X, Sævik S, Leira BJ. A sensitivity study of vessel hydrodynamic model parameters. In: Proceedings of the ASME 2020 39th International Conference on Ocean, Offshore and Arctic Engineering, Vol. 1. Virtual, Online; 2020.
[28] Virtanen P, Gommers R, Oliphant TE, Haberland M, Reddy T, Cournapeau D, Burovski E, Peterson P, Weckesser W, Bright J, van der Walt SJ, Brett M, Wilson J, Millman KJ, Mayorov N, Nelson ARJ, Jones E, Kern R, Larson E, Carey CJ, Polat I, Feng Y, Moore EW, VanderPlas J, Laxalde D, Perktold J, Cimrman R, Henriksen I, Quintero EA, Harris CR, Archibald AM, Ribeiro AH, Pedregosa F, van Mulbregt P, and SciPy 10 Contributors. SciPy 1.0: Fundamental algorithms for scientific computing in python. Nature Methods 2020;17:261–72. http://dx.doi.org/10.1038/s41592-019-0686-2.
[29] Fathi DE. ShipX Vessel Responses (VERES), User's manual. echnical Report, SINTEF Ocean AS; 2018.
[30] Ommani B, Kristiansen T, Berget K. Investigating a simplified model for moonpool piston mode response in irregular waves. In: Proceedings of the ASME 2018 37th International Conference on Ocean, Offshore and Arctic Engineering. Madrid, Spain; 2018.
[31] Ravinthrakumar S, Kristiansen T, Ommani B. On the Hydrodynamic Interaction Between Ship and Free-Surface Motions on Vessels With Moonpools, In: Proceedings of the ASME 2019 38th International Conference on Ocean, Offshore and Arctic Engineering, Glasgow, Scotland, UK; 2019:.
[32] Ravinthrakumar S, Kristiansen T, Molin B, Ommani B. Coupled vessel and moonpool responses in regular and irregular waves. Appl Ocean Res 2020;96.
[33] Faltinsen OM. Sea Loads on Ships and Offshore Structures. New York: Cambridge University Press Cambridge; 1990.
[34] ITTC. Recommended procedures and Guidelines: Numerical Estimation of Roll Damping. Technical Report, International Towing Tank Conference; 2011.
[35] Kaplan P. Lecture notes on nonlinear theory of ship roll motion in a random seaway. 1966.
[36] Han X, Sævik S, Leira BJ. Tuning of vessel parameters including sea state dependent roll damping. Ocean Eng 2021;233. http://dx.doi.org/10.1016/j.oceaneng.2021.109084.
[37] Fathi DE, Hoff JR. ShipX Vessel Responses (VERES), Theory manual. Technical Report, SINTEF Ocean AS; 2017.
[38] Ikeda Y. On roll damping force of ship - effect of friction of hull and normal force of bilge keels. Technical Report 00401, Osaka Prefecture University; 1978.
[39] Ikeda Y, Himeno Y, Tanaka N. On eddy making component of roll damping force on naked hull. Technical Report 00403, Osaka Prefecture University; 1978.
[40] Ikeda Y, Komatsu K, Tanaka N. On roll damping force of ship-effects of hull surface pressure created by bilge keels. Technical Report 00402, Osaka Prefecture University; 1979.
[41] Rezende FC, Chen XB, Ferreira MD. Second order roll motions for fpso's operating in severe environmental conditions. In: Offshore Technology Conference, Number OTC-18906-MS, Houston, Texas, USA; 2007, http://dx.doi.org/10.4043/18906-MS.
[42] Dhavalikar SS. Comparative study of seakeeping analysis results from various methods. In: Proceedings of the ASME 2011 30th International Conference on Ocean, Offshore and Arctic Engineering. Volume 1: Offshore Technology; Polar and Arctic Sciences and Technology, 2011, p. 217–23. http://dx.doi.org/10.1115/OMAE2011-49223.

Appendix B

List of Previous PhD Theses at the Department of Marine Technology

Previous PhD theses published at the Department of Marine Technology (earlier: Faculty of Marine Technology)
NORWEGIAN UNIVERSITY OF SCIENCE AND TECHNOLOGY

Report No.	Author	Title
	Kavlie, Dag	Optimization of Plane Elastic Grillages, 1967
	Hansen, Hans R.	Man-Machine Communication and Data-Storage Methods in Ship Structural Design, 1971
	Gisvold, Kaare M.	A Method for non-linear mixed -integer programming and its Application to Design Problems, 1971
	Lund, Sverre	Tanker Frame Optimalization by means of SUMT-Transformation and Behaviour Models, 1971
	Vinje, Tor	On Vibration of Spherical Shells Interacting with Fluid, 1972
	Lorentz, Jan D.	Tank Arrangement for Crude Oil Carriers in Accordance with the new Anti-Pollution Regulations, 1975
	Carlsen, Carl A.	Computer-Aided Design of Tanker Structures, 1975
	Larsen, Carl M.	Static and Dynamic Analysis of Offshore Pipelines during Installation, 1976
UR-79-01	Brigt Hatlestad, MK	The finite element method used in a fatigue evaluation of fixed offshore platforms. (Dr.Ing. Thesis)
UR-79-02	Erik Pettersen, MK	Analysis and design of cellular structures. (Dr.Ing. Thesis)
UR-79-03	Sverre Valsgård, MK	Finite difference and finite element methods applied to nonlinear analysis of plated structures. (Dr.Ing. Thesis)
UR-79-04	Nils T. Nordsve, MK	Finite element collapse analysis of structural members considering imperfections and stresses due to fabrication. (Dr.Ing. Thesis)
UR-79-05	Ivar J. Fylling, MK	Analysis of towline forces in ocean towing systems. (Dr.Ing. Thesis)
UR-80-06	Nils Sandsmark, MM	Analysis of Stationary and Transient Heat Conduction by the Use of the Finite Element Method. (Dr.Ing. Thesis)
UR-80-09	Sverre Haver, MK	Analysis of uncertainties related to the stochastic modeling of ocean waves. (Dr.Ing. Thesis)
UR-81-15	Odland, Jonas	On the Strength of welded Ring stiffened cylindrical Shells primarily subjected to axial Compression
UR-82-17	Engesvik, Knut	Analysis of Uncertainties in the fatigue Capacity of

		Welded Joints
UR-82-18	Rye, Henrik	Ocean wave groups
UR-83-30	Eide, Oddvar Inge	On Cumulative Fatigue Damage in Steel Welded Joints
UR-83-33	Mo, Olav	Stochastic Time Domain Analysis of Slender Offshore Structures
UR-83-34	Amdahl, Jørgen	Energy absorption in Ship-platform impacts
UR-84-37	Mørch, Morten	Motions and mooring forces of semi submersibles as determined by full-scale measurements and theoretical analysis
UR-84-38	Soares, C. Guedes	Probabilistic models for load effects in ship structures
UR-84-39	Aarsnes, Jan V.	Current forces on ships
UR-84-40	Czujko, Jerzy	Collapse Analysis of Plates subjected to Biaxial Compression and Lateral Load
UR-85-46	Alf G. Engseth, MK	Finite element collapse analysis of tubular steel offshore structures. (Dr.Ing. Thesis)
UR-86-47	Dengody Sheshappa, MP	A Computer Design Model for Optimizing Fishing Vessel Designs Based on Techno-Economic Analysis. (Dr.Ing. Thesis)
UR-86-48	Vidar Aanesland, MH	A Theoretical and Numerical Study of Ship Wave Resistance. (Dr.Ing. Thesis)
UR-86-49	Heinz-Joachim Wessel, MK	Fracture Mechanics Analysis of Crack Growth in Plate Girders. (Dr.Ing. Thesis)
UR-86-50	Jon Taby, MK	Ultimate and Post-ultimate Strength of Dented Tubular Members. (Dr.Ing. Thesis)
UR-86-51	Walter Lian, MH	A Numerical Study of Two-Dimensional Separated Flow Past Bluff Bodies at Moderate KC-Numbers. (Dr.Ing. Thesis)
UR-86-52	Bjørn Sortland, MH	Force Measurements in Oscillating Flow on Ship Sections and Circular Cylinders in a U-Tube Water Tank. (Dr.Ing. Thesis)
UR-86-53	Kurt Strand, MM	A System Dynamic Approach to One-dimensional Fluid Flow. (Dr.Ing. Thesis)
UR-86-54	Arne Edvin Løken, MH	Three Dimensional Second Order Hydrodynamic Effects on Ocean Structures in Waves. (Dr.Ing. Thesis)
UR-86-55	Sigurd Falch, MH	A Numerical Study of Slamming of Two-Dimensional Bodies. (Dr.Ing. Thesis)
UR-87-56	Arne Braathen, MH	Application of a Vortex Tracking Method to the Prediction of Roll Damping of a Two-Dimension Floating Body. (Dr.Ing. Thesis)

UR-87-57	Bernt Leira, MK	Gaussian Vector Processes for Reliability Analysis involving Wave-Induced Load Effects. (Dr.Ing. Thesis)
UR-87-58	Magnus Småvik, MM	Thermal Load and Process Characteristics in a Two-Stroke Diesel Engine with Thermal Barriers (in Norwegian). (Dr.Ing. Thesis)
MTA-88-59	Bernt Arild Bremdal, MP	An Investigation of Marine Installation Processes – A Knowledge - Based Planning Approach. (Dr.Ing. Thesis)
MTA-88-60	Xu Jun, MK	Non-linear Dynamic Analysis of Space-framed Offshore Structures. (Dr.Ing. Thesis)
MTA-89-61	Gang Miao, MH	Hydrodynamic Forces and Dynamic Responses of Circular Cylinders in Wave Zones. (Dr.Ing. Thesis)
MTA-89-62	Martin Greenhow, MH	Linear and Non-Linear Studies of Waves and Floating Bodies. Part I and Part II. (Dr.Techn. Thesis)
MTA-89-63	Chang Li, MH	Force Coefficients of Spheres and Cubes in Oscillatory Flow with and without Current. (Dr.Ing. Thesis
MTA-89-64	Hu Ying, MP	A Study of Marketing and Design in Development of Marine Transport Systems. (Dr.Ing. Thesis)
MTA-89-65	Arild Jæger, MH	Seakeeping, Dynamic Stability and Performance of a Wedge Shaped Planing Hull. (Dr.Ing. Thesis)
MTA-89-66	Chan Siu Hung, MM	The dynamic characteristics of tilting-pad bearings
MTA-89-67	Kim Wikstrøm, MP	Analysis av projekteringen for ett offshore projekt. (Licenciat-avhandling)
MTA-89-68	Jiao Guoyang, MK	Reliability Analysis of Crack Growth under Random Loading, considering Model Updating. (Dr.Ing. Thesis)
MTA-89-69	Arnt Olufsen, MK	Uncertainty and Reliability Analysis of Fixed Offshore Structures. (Dr.Ing. Thesis)
MTA-89-70	Wu Yu-Lin, MR	System Reliability Analyses of Offshore Structures using improved Truss and Beam Models. (Dr.Ing. Thesis)
MTA-90-71	Jan Roger Hoff, MH	Three-dimensional Green function of a vessel with forward speed in waves. (Dr.Ing. Thesis)
MTA-90-72	Rong Zhao, MH	Slow-Drift Motions of a Moored Two-Dimensional Body in Irregular Waves. (Dr.Ing. Thesis)
MTA-90-73	Atle Minsaas, MP	Economical Risk Analysis. (Dr.Ing. Thesis)
MTA-90-74	Knut-Aril Farnes, MK	Long-term Statistics of Response in Non-linear Marine Structures. (Dr.Ing. Thesis)
MTA-90-75	Torbjørn Sotberg, MK	Application of Reliability Methods for Safety Assessment of Submarine Pipelines. (Dr.Ing.

		Thesis)
MTA-90-76	Zeuthen, Steffen, MP	SEAMAID. A computational model of the design process in a constraint-based logic programming environment. An example from the offshore domain. (Dr.Ing. Thesis)
MTA-91-77	Haagensen, Sven, MM	Fuel Dependant Cyclic Variability in a Spark Ignition Engine - An Optical Approach. (Dr.Ing. Thesis)
MTA-91-78	Løland, Geir, MH	Current forces on and flow through fish farms. (Dr.Ing. Thesis)
MTA-91-79	Hoen, Christopher, MK	System Identification of Structures Excited by Stochastic Load Processes. (Dr.Ing. Thesis)
MTA-91-80	Haugen, Stein, MK	Probabilistic Evaluation of Frequency of Collision between Ships and Offshore Platforms. (Dr.Ing. Thesis)
MTA-91-81	Sødahl, Nils, MK	Methods for Design and Analysis of Flexible Risers. (Dr.Ing. Thesis)
MTA-91-82	Ormberg, Harald, MK	Non-linear Response Analysis of Floating Fish Farm Systems. (Dr.Ing. Thesis)
MTA-91-83	Marley, Mark J., MK	Time Variant Reliability under Fatigue Degradation. (Dr.Ing. Thesis)
MTA-91-84	Krokstad, Jørgen R., MH	Second-order Loads in Multidirectional Seas. (Dr.Ing. Thesis)
MTA-91-85	Molteberg, Gunnar A., MM	The Application of System Identification Techniques to Performance Monitoring of Four Stroke Turbocharged Diesel Engines. (Dr.Ing. Thesis)
MTA-92-86	Mørch, Hans Jørgen Bjelke, MH	Aspects of Hydrofoil Design: with Emphasis on Hydrofoil Interaction in Calm Water. (Dr.Ing. Thesis)
MTA-92-87	Chan Siu Hung, MM	Nonlinear Analysis of Rotordynamic Instabilities in Highspeed Turbomachinery. (Dr.Ing. Thesis)
MTA-92-88	Bessason, Bjarni, MK	Assessment of Earthquake Loading and Response of Seismically Isolated Bridges. (Dr.Ing. Thesis)
MTA-92-89	Langli, Geir, MP	Improving Operational Safety through exploitation of Design Knowledge - an investigation of offshore platform safety. (Dr.Ing. Thesis)
MTA-92-90	Sævik, Svein, MK	On Stresses and Fatigue in Flexible Pipes. (Dr.Ing. Thesis)
MTA-92-91	Ask, Tor Ø., MM	Ignition and Flame Growth in Lean Gas-Air Mixtures. An Experimental Study with a Schlieren System. (Dr.Ing. Thesis)
MTA-86-92	Hessen, Gunnar, MK	Fracture Mechanics Analysis of Stiffened Tubular Members. (Dr.Ing. Thesis)

MTA-93-93	Steinebach, Christian, MM	Knowledge Based Systems for Diagnosis of Rotating Machinery. (Dr.Ing. Thesis)
MTA-93-94	Dalane, Jan Inge, MK	System Reliability in Design and Maintenance of Fixed Offshore Structures. (Dr.Ing. Thesis)
MTA-93-95	Steen, Sverre, MH	Cobblestone Effect on SES. (Dr.Ing. Thesis)
MTA-93-96	Karunakaran, Daniel, MK	Nonlinear Dynamic Response and Reliability Analysis of Drag-dominated Offshore Platforms. (Dr.Ing. Thesis)
MTA-93-97	Hagen, Arnulf, MP	The Framework of a Design Process Language. (Dr.Ing. Thesis)
MTA-93-98	Nordrik, Rune, MM	Investigation of Spark Ignition and Autoignition in Methane and Air Using Computational Fluid Dynamics and Chemical Reaction Kinetics. A Numerical Study of Ignition Processes in Internal Combustion Engines. (Dr.Ing. Thesis)
MTA-94-99	Passano, Elizabeth, MK	Efficient Analysis of Nonlinear Slender Marine Structures. (Dr.Ing. Thesis)
MTA-94-100	Kvålsvold, Jan, MH	Hydroelastic Modelling of Wetdeck Slamming on Multihull Vessels. (Dr.Ing. Thesis)
MTA-94-102	Bech, Sidsel M., MK	Experimental and Numerical Determination of Stiffness and Strength of GRP/PVC Sandwich Structures. (Dr.Ing. Thesis)
MTA-95-103	Paulsen, Hallvard, MM	A Study of Transient Jet and Spray using a Schlieren Method and Digital Image Processing. (Dr.Ing. Thesis)
MTA-95-104	Hovde, Geir Olav, MK	Fatigue and Overload Reliability of Offshore Structural Systems, Considering the Effect of Inspection and Repair. (Dr.Ing. Thesis)
MTA-95-105	Wang, Xiaozhi, MK	Reliability Analysis of Production Ships with Emphasis on Load Combination and Ultimate Strength. (Dr.Ing. Thesis)
MTA-95-106	Ulstein, Tore, MH	Nonlinear Effects of a Flexible Stern Seal Bag on Cobblestone Oscillations of an SES. (Dr.Ing. Thesis)
MTA-95-107	Solaas, Frøydis, MH	Analytical and Numerical Studies of Sloshing in Tanks. (Dr.Ing. Thesis)
MTA-95-108	Hellan, Øyvind, MK	Nonlinear Pushover and Cyclic Analyses in Ultimate Limit State Design and Reassessment of Tubular Steel Offshore Structures. (Dr.Ing. Thesis)
MTA-95-109	Hermundstad, Ole A., MK	Theoretical and Experimental Hydroelastic Analysis of High Speed Vessels. (Dr.Ing. Thesis)
MTA-96-110	Bratland, Anne K., MH	Wave-Current Interaction Effects on Large-Volume Bodies in Water of Finite Depth. (Dr.Ing. Thesis)
MTA-96-111	Herfjord, Kjell, MH	A Study of Two-dimensional Separated Flow by a Combination of the Finite Element Method and

		Navier-Stokes Equations. (Dr.Ing. Thesis)
MTA-96-112	Æsøy, Vilmar, MM	Hot Surface Assisted Compression Ignition in a Direct Injection Natural Gas Engine. (Dr.Ing. Thesis)
MTA-96-113	Eknes, Monika L., MK	Escalation Scenarios Initiated by Gas Explosions on Offshore Installations. (Dr.Ing. Thesis)
MTA-96-114	Erikstad, Stein O., MP	A Decision Support Model for Preliminary Ship Design. (Dr.Ing. Thesis)
MTA-96-115	Pedersen, Egil, MH	A Nautical Study of Towed Marine Seismic Streamer Cable Configurations. (Dr.Ing. Thesis)
MTA-97-116	Moksnes, Paul O., MM	Modelling Two-Phase Thermo-Fluid Systems Using Bond Graphs. (Dr.Ing. Thesis)
MTA-97-117	Halse, Karl H., MK	On Vortex Shedding and Prediction of Vortex-Induced Vibrations of Circular Cylinders. (Dr.Ing. Thesis)
MTA-97-118	Igland, Ragnar T., MK	Reliability Analysis of Pipelines during Laying, considering Ultimate Strength under Combined Loads. (Dr.Ing. Thesis)
MTA-97-119	Pedersen, Hans-P., MP	Levendefiskteknologi for fiskefartøy. (Dr.Ing. Thesis)
MTA-98-120	Vikestad, Kyrre, MK	Multi-Frequency Response of a Cylinder Subjected to Vortex Shedding and Support Motions. (Dr.Ing. Thesis)
MTA-98-121	Azadi, Mohammad R. E., MK	Analysis of Static and Dynamic Pile-Soil-Jacket Behaviour. (Dr.Ing. Thesis)
MTA-98-122	Ulltang, Terje, MP	A Communication Model for Product Information. (Dr.Ing. Thesis)
MTA-98-123	Torbergsen, Erik, MM	Impeller/Diffuser Interaction Forces in Centrifugal Pumps. (Dr.Ing. Thesis)
MTA-98-124	Hansen, Edmond, MH	A Discrete Element Model to Study Marginal Ice Zone Dynamics and the Behaviour of Vessels Moored in Broken Ice. (Dr.Ing. Thesis)
MTA-98-125	Videiro, Paulo M., MK	Reliability Based Design of Marine Structures. (Dr.Ing. Thesis)
MTA-99-126	Mainçon, Philippe, MK	Fatigue Reliability of Long Welds Application to Titanium Risers. (Dr.Ing. Thesis)
MTA-99-127	Haugen, Elin M., MH	Hydroelastic Analysis of Slamming on Stiffened Plates with Application to Catamaran Wetdecks. (Dr.Ing. Thesis)
MTA-99-128	Langhelle, Nina K., MK	Experimental Validation and Calibration of Nonlinear Finite Element Models for Use in Design of Aluminium Structures Exposed to Fire. (Dr.Ing. Thesis)
MTA-99-	Berstad, Are J., MK	Calculation of Fatigue Damage in Ship Structures.

129		(Dr.Ing. Thesis)
MTA-99-130	Andersen, Trond M., MM	Short Term Maintenance Planning. (Dr.Ing. Thesis)
MTA-99-131	Tveiten, Bård Wathne, MK	Fatigue Assessment of Welded Aluminium Ship Details. (Dr.Ing. Thesis)
MTA-99-132	Søreide, Fredrik, MP	Applications of underwater technology in deep water archaeology. Principles and practice. (Dr.Ing. Thesis)
MTA-99-133	Tønnessen, Rune, MH	A Finite Element Method Applied to Unsteady Viscous Flow Around 2D Blunt Bodies With Sharp Corners. (Dr.Ing. Thesis)
MTA-99-134	Elvekrok, Dag R., MP	Engineering Integration in Field Development Projects in the Norwegian Oil and Gas Industry. The Supplier Management of Norne. (Dr.Ing. Thesis)
MTA-99-135	Fagerholt, Kjetil, MP	Optimeringsbaserte Metoder for Ruteplanlegging innen skipsfart. (Dr.Ing. Thesis)
MTA-99-136	Bysveen, Marie, MM	Visualization in Two Directions on a Dynamic Combustion Rig for Studies of Fuel Quality. (Dr.Ing. Thesis)
MTA-2000-137	Storteig, Eskild, MM	Dynamic characteristics and leakage performance of liquid annular seals in centrifugal pumps. (Dr.Ing. Thesis)
MTA-2000-138	Sagli, Gro, MK	Model uncertainty and simplified estimates of long term extremes of hull girder loads in ships. (Dr.Ing. Thesis)
MTA-2000-139	Tronstad, Harald, MK	Nonlinear analysis and design of cable net structures like fishing gear based on the finite element method. (Dr.Ing. Thesis)
MTA-2000-140	Kroneberg, André, MP	Innovation in shipping by using scenarios. (Dr.Ing. Thesis)
MTA-2000-141	Haslum, Herbjørn Alf, MH	Simplified methods applied to nonlinear motion of spar platforms. (Dr.Ing. Thesis)
MTA-2001-142	Samdal, Ole Johan, MM	Modelling of Degradation Mechanisms and Stressor Interaction on Static Mechanical Equipment Residual Lifetime. (Dr.Ing. Thesis)
MTA-2001-143	Baarholm, Rolf Jarle, MH	Theoretical and experimental studies of wave impact underneath decks of offshore platforms. (Dr.Ing. Thesis)
MTA-2001-144	Wang, Lihua, MK	Probabilistic Analysis of Nonlinear Wave-induced Loads on Ships. (Dr.Ing. Thesis)
MTA-2001-145	Kristensen, Odd H. Holt, MK	Ultimate Capacity of Aluminium Plates under Multiple Loads, Considering HAZ Properties. (Dr.Ing. Thesis)
MTA-2001-146	Greco, Marilena, MH	A Two-Dimensional Study of Green-Water

		Loading. (Dr.Ing. Thesis)
MTA-2001-147	Heggelund, Svein E., MK	Calculation of Global Design Loads and Load Effects in Large High Speed Catamarans. (Dr.Ing. Thesis)
MTA-2001-148	Babalola, Olusegun T., MK	Fatigue Strength of Titanium Risers – Defect Sensitivity. (Dr.Ing. Thesis)
MTA-2001-149	Mohammed, Abuu K., MK	Nonlinear Shell Finite Elements for Ultimate Strength and Collapse Analysis of Ship Structures. (Dr.Ing. Thesis)
MTA-2002-150	Holmedal, Lars E., MH	Wave-current interactions in the vicinity of the sea bed. (Dr.Ing. Thesis)
MTA-2002-151	Rognebakke, Olav F., MH	Sloshing in rectangular tanks and interaction with ship motions. (Dr.Ing. Thesis)
MTA-2002-152	Lader, Pål Furset, MH	Geometry and Kinematics of Breaking Waves. (Dr.Ing. Thesis)
MTA-2002-153	Yang, Qinzheng, MH	Wash and wave resistance of ships in finite water depth. (Dr.Ing. Thesis)
MTA-2002-154	Melhus, Øyvin, MM	Utilization of VOC in Diesel Engines. Ignition and combustion of VOC released by crude oil tankers. (Dr.Ing. Thesis)
MTA-2002-155	Ronæss, Marit, MH	Wave Induced Motions of Two Ships Advancing on Parallel Course. (Dr.Ing. Thesis)
MTA-2002-156	Økland, Ole D., MK	Numerical and experimental investigation of whipping in twin hull vessels exposed to severe wet deck slamming. (Dr.Ing. Thesis)
MTA-2002-157	Ge, Chunhua, MK	Global Hydroelastic Response of Catamarans due to Wet Deck Slamming. (Dr.Ing. Thesis)
MTA-2002-158	Byklum, Eirik, MK	Nonlinear Shell Finite Elements for Ultimate Strength and Collapse Analysis of Ship Structures. (Dr.Ing. Thesis)
IMT-2003-1	Chen, Haibo, MK	Probabilistic Evaluation of FPSO-Tanker Collision in Tandem Offloading Operation. (Dr.Ing. Thesis)
IMT-2003-2	Skaugset, Kjetil Bjørn, MK	On the Suppression of Vortex Induced Vibrations of Circular Cylinders by Radial Water Jets. (Dr.Ing. Thesis)
IMT-2003-3	Chezhian, Muthu	Three-Dimensional Analysis of Slamming. (Dr.Ing. Thesis)
IMT-2003-4	Buhaug, Øyvind	Deposit Formation on Cylinder Liner Surfaces in Medium Speed Engines. (Dr.Ing. Thesis)
IMT-2003-5	Tregde, Vidar	Aspects of Ship Design: Optimization of Aft Hull with Inverse Geometry Design. (Dr.Ing. Thesis)
IMT-	Wist, Hanne Therese	Statistical Properties of Successive Ocean Wave

2003-6		Parameters. (Dr.Ing. Thesis)
IMT-2004-7	Ransau, Samuel	Numerical Methods for Flows with Evolving Interfaces. (Dr.Ing. Thesis)
IMT-2004-8	Soma, Torkel	Blue-Chip or Sub-Standard. A data interrogation approach of identity safety characteristics of shipping organization. (Dr.Ing. Thesis)
IMT-2004-9	Ersdal, Svein	An experimental study of hydrodynamic forces on cylinders and cables in near axial flow. (Dr.Ing. Thesis)
IMT-2005-10	Brodtkorb, Per Andreas	The Probability of Occurrence of Dangerous Wave Situations at Sea. (Dr.Ing. Thesis)
IMT-2005-11	Yttervik, Rune	Ocean current variability in relation to offshore engineering. (Dr.Ing. Thesis)
IMT-2005-12	Fredheim, Arne	Current Forces on Net-Structures. (Dr.Ing. Thesis)
IMT-2005-13	Heggernes, Kjetil	Flow around marine structures. (Dr.Ing. Thesis
IMT-2005-14	Fouques, Sebastien	Lagrangian Modelling of Ocean Surface Waves and Synthetic Aperture Radar Wave Measurements. (Dr.Ing. Thesis)
IMT-2006-15	Holm, Håvard	Numerical calculation of viscous free surface flow around marine structures. (Dr.Ing. Thesis)
IMT-2006-16	Bjørheim, Lars G.	Failure Assessment of Long Through Thickness Fatigue Cracks in Ship Hulls. (Dr.Ing. Thesis)
IMT-2006-17	Hansson, Lisbeth	Safety Management for Prevention of Occupational Accidents. (Dr.Ing. Thesis)
IMT-2006-18	Zhu, Xinying	Application of the CIP Method to Strongly Nonlinear Wave-Body Interaction Problems. (Dr.Ing. Thesis)
IMT-2006-19	Reite, Karl Johan	Modelling and Control of Trawl Systems. (Dr.Ing. Thesis)
IMT-2006-20	Smogeli, Øyvind Notland	Control of Marine Propellers. From Normal to Extreme Conditions. (Dr.Ing. Thesis)
IMT-2007-21	Storhaug, Gaute	Experimental Investigation of Wave Induced Vibrations and Their Effect on the Fatigue Loading of Ships. (Dr.Ing. Thesis)
IMT-2007-22	Sun, Hui	A Boundary Element Method Applied to Strongly Nonlinear Wave-Body Interaction Problems. (PhD Thesis, CeSOS)
IMT-2007-23	Rustad, Anne Marthine	Modelling and Control of Top Tensioned Risers. (PhD Thesis, CeSOS)
IMT-2007-24	Johansen, Vegar	Modelling flexible slender system for real-time simulations and control applications
IMT-2007-25	Wroldsen, Anders Sunde	Modelling and control of tensegrity structures.

		(PhD Thesis, CeSOS)
IMT-2007-26	Aronsen, Kristoffer Høye	An experimental investigation of in-line and combined inline and cross flow vortex induced vibrations. (Dr. avhandling, IMT)
IMT-2007-27	Gao, Zhen	Stochastic Response Analysis of Mooring Systems with Emphasis on Frequency-domain Analysis of Fatigue due to Wide-band Response Processes (PhD Thesis, CeSOS)
IMT-2007-28	Thorstensen, Tom Anders	Lifetime Profit Modelling of Ageing Systems Utilizing Information about Technical Condition. (Dr.ing. thesis, IMT)
IMT-2008-29	Refsnes, Jon Erling Gorset	Nonlinear Model-Based Control of Slender Body AUVs (PhD Thesis, IMT)
IMT-2008-30	Berntsen, Per Ivar B.	Structural Reliability Based Position Mooring. (PhD-Thesis, IMT)
IMT-2008-31	Ye, Naiquan	Fatigue Assessment of Aluminium Welded Box-stiffener Joints in Ships (Dr.ing. thesis, IMT)
IMT-2008-32	Radan, Damir	Integrated Control of Marine Electrical Power Systems. (PhD-Thesis, IMT)
IMT-2008-33	Thomassen, Paul	Methods for Dynamic Response Analysis and Fatigue Life Estimation of Floating Fish Cages. (Dr.ing. thesis, IMT)
IMT-2008-34	Pákozdi, Csaba	A Smoothed Particle Hydrodynamics Study of Two-dimensional Nonlinear Sloshing in Rectangular Tanks. (Dr.ing.thesis, IMT/ CeSOS)
IMT-2007-35	Grytøyr, Guttorm	A Higher-Order Boundary Element Method and Applications to Marine Hydrodynamics. (Dr.ing.thesis, IMT)
IMT-2008-36	Drummen, Ingo	Experimental and Numerical Investigation of Nonlinear Wave-Induced Load Effects in Containerships considering Hydroelasticity. (PhD thesis, CeSOS)
IMT-2008-37	Skejic, Renato	Maneuvering and Seakeeping of a Singel Ship and of Two Ships in Interaction. (PhD-Thesis, CeSOS)
IMT-2008-38	Harlem, Alf	An Age-Based Replacement Model for Repairable Systems with Attention to High-Speed Marine Diesel Engines. (PhD-Thesis, IMT)
IMT-2008-39	Alsos, Hagbart S.	Ship Grounding. Analysis of Ductile Fracture, Bottom Damage and Hull Girder Response. (PhD-thesis, IMT)
IMT-2008-40	Graczyk, Mateusz	Experimental Investigation of Sloshing Loading and Load Effects in Membrane LNG Tanks Subjected to Random Excitation. (PhD-thesis, CeSOS)
IMT-2008-41	Taghipour, Reza	Efficient Prediction of Dynamic Response for Flexible amd Multi-body Marine Structures. (PhD-

		thesis, CeSOS)
IMT-2008-42	Ruth, Eivind	Propulsion control and thrust allocation on marine vessels. (PhD thesis, CeSOS)
IMT-2008-43	Nystad, Bent Helge	Technical Condition Indexes and Remaining Useful Life of Aggregated Systems. PhD thesis, IMT
IMT-2008-44	Soni, Prashant Kumar	Hydrodynamic Coefficients for Vortex Induced Vibrations of Flexible Beams, PhD thesis, CeSOS
IMT-2009-45	Amlashi, Hadi K.K.	Ultimate Strength and Reliability-based Design of Ship Hulls with Emphasis on Combined Global and Local Loads. PhD Thesis, IMT
IMT-2009-46	Pedersen, Tom Arne	Bond Graph Modelling of Marine Power Systems. PhD Thesis, IMT
IMT-2009-47	Kristiansen, Trygve	Two-Dimensional Numerical and Experimental Studies of Piston-Mode Resonance. PhD-Thesis, CeSOS
IMT-2009-48	Ong, Muk Chen	Applications of a Standard High Reynolds Number Model and a Stochastic Scour Prediction Model for Marine Structures. PhD-thesis, IMT
IMT-2009-49	Hong, Lin	Simplified Analysis and Design of Ships subjected to Collision and Grounding. PhD-thesis, IMT
IMT-2009-50	Koushan, Kamran	Vortex Induced Vibrations of Free Span Pipelines, PhD thesis, IMT
IMT-2009-51	Korsvik, Jarl Eirik	Heuristic Methods for Ship Routing and Scheduling. PhD-thesis, IMT
IMT-2009-52	Lee, Jihoon	Experimental Investigation and Numerical in Analyzing the Ocean Current Displacement of Longlines. Ph.d.-Thesis, IMT.
IMT-2009-53	Vestbøstad, Tone Gran	A Numerical Study of Wave-in-Deck Impact usin a Two-Dimensional Constrained Interpolation Profile Method, Ph.d.thesis, CeSOS.
IMT-2009-54	Bruun, Kristine	Bond Graph Modelling of Fuel Cells for Marine Power Plants. Ph.d.-thesis, IMT
IMT 2009-55	Holstad, Anders	Numerical Investigation of Turbulence in a Sekwed Three-Dimensional Channel Flow, Ph.d.-thesis, IMT.
IMT 2009-56	Ayala-Uraga, Efren	Reliability-Based Assessment of Deteriorating Ship-shaped Offshore Structures, Ph.d.-thesis, IMT
IMT 2009-57	Kong, Xiangjun	A Numerical Study of a Damaged Ship in Beam Sea Waves. Ph.d.-thesis, IMT/CeSOS.
IMT 2010-58	Kristiansen, David	Wave Induced Effects on Floaters of Aquaculture Plants, Ph.d.-thesis, CeSOS.

IMT 2010-59	Ludvigsen, Martin	An ROV-Toolbox for Optical and Acoustic Scientific Seabed Investigation. Ph.d.-thesis IMT.
IMT 2010-60	Hals, Jørgen	Modelling and Phase Control of Wave-Energy Converters. Ph.d.thesis, CeSOS.
IMT 2010- 61	Shu, Zhi	Uncertainty Assessment of Wave Loads and Ultimate Strength of Tankers and Bulk Carriers in a Reliability Framework. Ph.d. Thesis, IMT/ CeSOS
IMT 2010-62	Shao, Yanlin	Numerical Potential-Flow Studies on Weakly-Nonlinear Wave-Body Interactions with/without Small Forward Speed, Ph.d.thesis,CeSOS.
IMT 2010-63	Califano, Andrea	Dynamic Loads on Marine Propellers due to Intermittent Ventilation. Ph.d.thesis, IMT.
IMT 2010-64	El Khoury, George	Numerical Simulations of Massively Separated Turbulent Flows, Ph.d.-thesis, IMT
IMT 2010-65	Seim, Knut Sponheim	Mixing Process in Dense Overflows with Emphasis on the Faroe Bank Channel Overflow. Ph.d.thesis, IMT
IMT 2010-66	Jia, Huirong	Structural Analysis of Intect and Damaged Ships in a Collission Risk Analysis Perspective. Ph.d.thesis CeSoS.
IMT 2010-67	Jiao, Linlin	Wave-Induced Effects on a Pontoon-type Very Large Floating Structures (VLFS). Ph.D.-thesis, CeSOS.
IMT 2010-68	Abrahamsen, Bjørn Christian	Sloshing Induced Tank Roof with Entrapped Air Pocket. Ph.d.thesis, CeSOS.
IMT 2011-69	Karimirad, Madjid	Stochastic Dynamic Response Analysis of Spar-Type Wind Turbines with Catenary or Taut Mooring Systems. Ph.d.-thesis, CeSOS.
IMT - 2011-70	Erlend Meland	Condition Monitoring of Safety Critical Valves. Ph.d.-thesis, IMT.
IMT – 2011-71	Yang, Limin	Stochastic Dynamic System Analysis of Wave Energy Converter with Hydraulic Power Take-Off, with Particular Reference to Wear Damage Analysis, Ph.d. Thesis, CeSOS.
IMT – 2011-72	Visscher, Jan	Application of Particla Image Velocimetry on Turbulent Marine Flows, Ph.d.Thesis, IMT.
IMT – 2011-73	Su, Biao	Numerical Predictions of Global and Local Ice Loads on Ships. Ph.d.Thesis, CeSOS.
IMT – 2011-74	Liu, Zhenhui	Analytical and Numerical Analysis of Iceberg Collision with Ship Structures. Ph.d.Thesis, IMT.
IMT – 2011-75	Aarsæther, Karl Gunnar	Modeling and Analysis of Ship Traffic by Observation and Numerical Simulation. Ph.d.Thesis, IMT.

Imt – 2011-76	Wu, Jie	Hydrodynamic Force Identification from Stochastic Vortex Induced Vibration Experiments with Slender Beams. Ph.d.Thesis, IMT.
Imt – 2011-77	Amini, Hamid	Azimuth Propulsors in Off-design Conditions. Ph.d.Thesis, IMT.
IMT – 2011-78	Nguyen, Tan-Hoi	Toward a System of Real-Time Prediction and Monitoring of Bottom Damage Conditions During Ship Grounding. Ph.d.thesis, IMT.
IMT- 2011-79	Tavakoli, Mohammad T.	Assessment of Oil Spill in Ship Collision and Grounding, Ph.d.thesis, IMT.
IMT- 2011-80	Guo, Bingjie	Numerical and Experimental Investigation of Added Resistance in Waves. Ph.d.Thesis, IMT.
IMT- 2011-81	Chen, Qiaofeng	Ultimate Strength of Aluminium Panels, considering HAZ Effects, IMT
IMT- 2012-82	Kota, Ravikiran S.	Wave Loads on Decks of Offshore Structures in Random Seas, CeSOS.
IMT- 2012-83	Sten, Ronny	Dynamic Simulation of Deep Water Drilling Risers with Heave Compensating System, IMT.
IMT- 2012-84	Berle, Øyvind	Risk and resilience in global maritime supply chains, IMT.
IMT- 2012-85	Fang, Shaoji	Fault Tolerant Position Mooring Control Based on Structural Reliability, CeSOS.
IMT- 2012-86	You, Jikun	Numerical studies on wave forces and moored ship motions in intermediate and shallow water, CeSOS.
IMT- 2012-87	Xiang ,Xu	Maneuvering of two interacting ships in waves, CeSOS
IMT- 2012-88	Dong, Wenbin	Time-domain fatigue response and reliability analysis of offshore wind turbines with emphasis on welded tubular joints and gear components, CeSOS
IMT- 2012-89	Zhu, Suji	Investigation of Wave-Induced Nonlinear Load Effects in Open Ships considering Hull Girder Vibrations in Bending and Torsion, CeSOS
IMT- 2012-90	Zhou, Li	Numerical and Experimental Investigation of Station-keeping in Level Ice, CeSOS
IMT- 2012-91	Ushakov, Sergey	Particulate matter emission characteristics from diesel enignes operating on conventional and alternative marine fuels, IMT
IMT- 2013-1	Yin, Decao	Experimental and Numerical Analysis of Combined In-line and Cross-flow Vortex Induced Vibrations, CeSOS

IMT-2013-2	Kurniawan, Adi	Modelling and geometry optimisation of wave energy converters, CeSOS
IMT-2013-3	Al Ryati, Nabil	Technical condition indexes doe auxiliary marine diesel engines, IMT
IMT-2013-4	Firoozkoohi, Reza	Experimental, numerical and analytical investigation of the effect of screens on sloshing, CeSOS
IMT-2013-5	Ommani, Babak	Potential-Flow Predictions of a Semi-Displacement Vessel Including Applications to Calm Water Broaching, CeSOS
IMT-2013-6	Xing, Yihan	Modelling and analysis of the gearbox in a floating spar-type wind turbine, CeSOS
IMT-7-2013	Balland, Océane	Optimization models for reducing air emissions from ships, IMT
IMT-8-2013	Yang, Dan	Transitional wake flow behind an inclined flat plate-----Computation and analysis, IMT
IMT-9-2013	Abdillah, Suyuthi	Prediction of Extreme Loads and Fatigue Damage for a Ship Hull due to Ice Action, IMT
IMT-10-2013	Ramìrez, Pedro Agustìn Pèrez	Ageing management and life extension of technical systems- Concepts and methods applied to oil and gas facilities, IMT
IMT-11-2013	Chuang, Zhenju	Experimental and Numerical Investigation of Speed Loss due to Seakeeping and Maneuvering. IMT
IMT-12-2013	Etemaddar, Mahmoud	Load and Response Analysis of Wind Turbines under Atmospheric Icing and Controller System Faults with Emphasis on Spar Type Floating Wind Turbines, IMT
IMT-13-2013	Lindstad, Haakon	Strategies and measures for reducing maritime CO2 emissons, IMT
IMT-14-2013	Haris, Sabril	Damage interaction analysis of ship collisions, IMT
IMT-15-2013	Shainee, Mohamed	Conceptual Design, Numerical and Experimental Investigation of a SPM Cage Concept for Offshore Mariculture, IMT
IMT-16-2013	Gansel, Lars	Flow past porous cylinders and effects of biofouling and fish behavior on the flow in and around Atlantic salmon net cages, IMT
IMT-17-2013	Gaspar, Henrique	Handling Aspects of Complexity in Conceptual Ship Design, IMT
IMT-18-2013	Thys, Maxime	Theoretical and Experimental Investigation of a Free Running Fishing Vessel at Small Frequency of Encounter, CeSOS
IMT-19-2013	Aglen, Ida	VIV in Free Spanning Pipelines, CeSOS

IMT-1-2014	Song, An	Theoretical and experimental studies of wave diffraction and radiation loads on a horizontally submerged perforated plate, CeSOS
IMT-2-2014	Rogne, Øyvind Ygre	Numerical and Experimental Investigation of a Hinged 5-body Wave Energy Converter, CeSOS
IMT-3-2014	Dai, Lijuan	Safe and efficient operation and maintenance of offshore wind farms ,IMT
IMT-4-2014	Bachynski, Erin Elizabeth	Design and Dynamic Analysis of Tension Leg Platform Wind Turbines, CeSOS
IMT-5-2014	Wang, Jingbo	Water Entry of Freefall Wedged – Wedge motions and Cavity Dynamics, CeSOS
IMT-6-2014	Kim, Ekaterina	Experimental and numerical studies related to the coupled behavior of ice mass and steel structures during accidental collisions, IMT
IMT-7-2014	Tan, Xiang	Numerical investigation of ship's continuous- mode icebreaking in leverl ice, CeSOS
IMT-8-2014	Muliawan, Made Jaya	Design and Analysis of Combined Floating Wave and Wind Power Facilities, with Emphasis on Extreme Load Effects of the Mooring System, CeSOS
IMT-9-2014	Jiang, Zhiyu	Long-term response analysis of wind turbines with an emphasis on fault and shutdown conditions, IMT
IMT-10-2014	Dukan, Fredrik	ROV Motion Control Systems, IMT
IMT-11-2014	Grimsmo, Nils I.	Dynamic simulations of hydraulic cylinder for heave compensation of deep water drilling risers, IMT
IMT-12-2014	Kvittem, Marit I.	Modelling and response analysis for fatigue design of a semisubmersible wind turbine, CeSOS
IMT-13-2014	Akhtar, Juned	The Effects of Human Fatigue on Risk at Sea, IMT
IMT-14-2014	Syahroni, Nur	Fatigue Assessment of Welded Joints Taking into Account Effects of Residual Stress, IMT
IMT-1-2015	Bøckmann, Eirik	Wave Propulsion of ships, IMT
IMT-2-2015	Wang, Kai	Modelling and dynamic analysis of a semi-submersible floating vertical axis wind turbine, CeSOS
IMT-3-2015	Fredriksen, Arnt Gunvald	A numerical and experimental study of a two-dimensional body with moonpool in waves and current, CeSOS
IMT-4-2015	Jose Patricio Gallardo Canabes	Numerical studies of viscous flow around bluff bodies, IMT

IMT-5-2015	Vegard Longva	Formulation and application of finite element techniques for slender marine structures subjected to contact interactions, IMT
IMT-6-2015	Jacobus De Vaal	Aerodynamic modelling of floating wind turbines, CeSOS
IMT-7-2015	Fachri Nasution	Fatigue Performance of Copper Power Conductors, IMT
IMT-8-2015	Oleh I Karpa	Development of bivariate extreme value distributions for applications in marine technology,CeSOS
IMT-9-2015	Daniel de Almeida Fernandes	An output feedback motion control system for ROVs, AMOS
IMT-10-2015	Bo Zhao	Particle Filter for Fault Diagnosis: Application to Dynamic Positioning Vessel and Underwater Robotics, CeSOS
IMT-11-2015	Wenting Zhu	Impact of emission allocation in maritime transportation, IMT
IMT-12-2015	Amir Rasekhi Nejad	Dynamic Analysis and Design of Gearboxes in Offshore Wind Turbines in a Structural Reliability Perspective, CeSOS
IMT-13-2015	Arturo Jesùs Ortega Malca	Dynamic Response of Flexibles Risers due to Unsteady Slug Flow, CeSOS
IMT-14-2015	Dagfinn Husjord	Guidance and decision-support system for safe navigation of ships operating in close proximity, IMT
IMT-15-2015	Anirban Bhattacharyya	Ducted Propellers: Behaviour in Waves and Scale Effects, IMT
IMT-16-2015	Qin Zhang	Image Processing for Ice Parameter Identification in Ice Management, IMT
IMT-1-2016	Vincentius Rumawas	Human Factors in Ship Design and Operation: An Experiential Learning, IMT
IMT-2-2016	Martin Storheim	Structural response in ship-platform and ship-ice collisions, IMT
IMT-3-2016	Mia Abrahamsen Prsic	Numerical Simulations of the Flow around single and Tandem Circular Cylinders Close to a Plane Wall, IMT
IMT-4-2016	Tufan Arslan	Large-eddy simulations of cross-flow around ship sections, IMT

IMT-5-2016	Pierre Yves-Henry	Parametrisation of aquatic vegetation in hydraulic and coastal research,IMT
IMT-6-2016	Lin Li	Dynamic Analysis of the Instalation of Monopiles for Offshore Wind Turbines, CeSOS
IMT-7-2016	Øivind Kåre Kjerstad	Dynamic Positioning of Marine Vessels in Ice, IMT
IMT-8-2016	Xiaopeng Wu	Numerical Analysis of Anchor Handling and Fish Trawling Operations in a Safety Perspective, CeSOS
IMT-9-2016	Zhengshun Cheng	Integrated Dynamic Analysis of Floating Vertical Axis Wind Turbines, CeSOS
IMT-10-2016	Ling Wan	Experimental and Numerical Study of a Combined Offshore Wind and Wave Energy Converter Concept
IMT-11-2016	Wei Chai	Stochastic dynamic analysis and reliability evaluation of the roll motion for ships in random seas, CeSOS
IMT-12-2016	Øyvind Selnes Patricksson	Decision support for conceptual ship design with focus on a changing life cycle and future uncertainty, IMT
IMT-13-2016	Mats Jørgen Thorsen	Time domain analysis of vortex-induced vibrations, IMT
IMT-14-2016	Edgar McGuinness	Safety in the Norwegian Fishing Fleet – Analysis and measures for improvement, IMT
IMT-15-2016	Sepideh Jafarzadeh	Energy effiency and emission abatement in the fishing fleet, IMT
IMT-16-2016	Wilson Ivan Guachamin Acero	Assessment of marine operations for offshore wind turbine installation with emphasis on response-based operational limits, IMT
IMT-17-2016	Mauro Candeloro	Tools and Methods for Autonomous Operations on Seabed and Water Coumn using Underwater Vehicles, IMT
IMT-18-2016	Valentin Chabaud	Real-Time Hybrid Model Testing of Floating Wind Tubines, IMT
IMT-1-2017	Mohammad Saud Afzal	Three-dimensional streaming in a sea bed boundary layer
IMT-2-2017	Peng Li	A Theoretical and Experimental Study of Wave-induced Hydroelastic Response of a Circular Floating Collar
IMT-3-2017	Martin Bergström	A simulation-based design method for arctic maritime transport systems

IMT-4-2017	Bhushan Taskar	The effect of waves on marine propellers and propulsion
IMT-5-2017	Mohsen Bardestani	A two-dimensional numerical and experimental study of a floater with net and sinker tube in waves and current
IMT-6-2017	Fatemeh Hoseini Dadmarzi	Direct Numerical Simualtion of turbulent wakes behind different plate configurations
IMT-7-2017	Michel R. Miyazaki	Modeling and control of hybrid marine power plants
IMT-8-2017	Giri Rajasekhar Gunnu	Safety and effiency enhancement of anchor handling operations with particular emphasis on the stability of anchor handling vessels
IMT-9-2017	Kevin Koosup Yum	Transient Performance and Emissions of a Turbocharged Diesel Engine for Marine Power Plants
IMT-10-2017	Zhaolong Yu	Hydrodynamic and structural aspects of ship collisions
IMT-11-2017	Martin Hassel	Risk Analysis and Modelling of Allisions between Passing Vessels and Offshore Installations
IMT-12-2017	Astrid H. Brodtkorb	Hybrid Control of Marine Vessels – Dynamic Positioning in Varying Conditions
IMT-13-2017	Kjersti Bruserud	Simultaneous stochastic model of waves and current for prediction of structural design loads
IMT-14-2017	Finn-Idar Grøtta Giske	Long-Term Extreme Response Analysis of Marine Structures Using Inverse Reliability Methods
IMT-15-2017	Stian Skjong	Modeling and Simulation of Maritime Systems and Operations for Virtual Prototyping using co-Simulations
IMT-1-2018	Yingguang Chu	Virtual Prototyping for Marine Crane Design and Operations
IMT-2-2018	Sergey Gavrilin	Validation of ship manoeuvring simulation models
IMT-3-2018	Jeevith Hegde	Tools and methods to manage risk in autonomous subsea inspection,maintenance and repair operations
IMT-4-2018	Ida M. Strand	Sea Loads on Closed Flexible Fish Cages
IMT-5-2018	Erlend Kvinge Jørgensen	Navigation and Control of Underwater Robotic Vehicles

IMT-6-2018	Bård Stovner	Aided Intertial Navigation of Underwater Vehicles
IMT-7-2018	Erlend Liavåg Grotle	Thermodynamic Response Enhanced by Sloshing in Marine LNG Fuel Tanks
IMT-8-2018	Børge Rokseth	Safety and Verification of Advanced Maritime Vessels
IMT-9-2018	Jan Vidar Ulveseter	Advances in Semi-Empirical Time Domain Modelling of Vortex-Induced Vibrations
IMT-10-2018	Chenyu Luan	Design and analysis for a steel braceless semi-submersible hull for supporting a 5-MW horizontal axis wind turbine
IMT-11-2018	Carl Fredrik Rehn	Ship Design under Uncertainty
IMT-12-2018	Øyvind Ødegård	Towards Autonomous Operations and Systems in Marine Archaeology
IMT-13-2018	Stein Melvær Nornes	Guidance and Control of Marine Robotics for Ocean Mapping and Monitoring
IMT-14-2018	Petter Norgren	Autonomous Underwater Vehicles in Arctic Marine Operations: Arctic marine research and ice monitoring
IMT-15-2018	Minjoo Choi	Modular Adaptable Ship Design for Handling Uncertainty in the Future Operating Context
MT-16-2018	Ole Alexander Eidsvik	Dynamics of Remotely Operated Underwater Vehicle Systems
IMT-17-2018	Mahdi Ghane	Fault Diagnosis of Floating Wind Turbine Drivetrain- Methodologies and Applications
IMT-18-2018	Christoph Alexander Thieme	Risk Analysis and Modelling of Autonomous Marine Systems
IMT-19-2018	Yugao Shen	Operational limits for floating-collar fish farms in waves and current, without and with well-boat presence
IMT-20-2018	Tianjiao Dai	Investigations of Shear Interaction and Stresses in Flexible Pipes and Umbilicals
IMT-21-2018	Sigurd Solheim Pettersen	Resilience by Latent Capabilities in Marine Systems
IMT-22-2018	Thomas Sauder	Fidelity of Cyber-physical Empirical Methods. Application to the Active Truncation of Slender Marine Structures
IMT-23-2018	Jan-Tore Horn	Statistical and Modelling Uncertainties in the Design of Offshore Wind Turbines

IMT-24-2018	Anna Swider	Data Mining Methods for the Analysis of Power Systems of Vessels
IMT-1-2019	Zhao He	Hydrodynamic study of a moored fish farming cage with fish influence
IMT-2-2019	Isar Ghamari	Numerical and Experimental Study on the Ship Parametric Roll Resonance and the Effect of Anti-Roll Tank
IMT-3-2019	Håkon Strandenes	Turbulent Flow Simulations at Higher Reynolds Numbers
IMT-4-2019	Siri Mariane Holen	Safety in Norwegian Fish Farming – Concepts and Methods for Improvement
IMT-5-2019	Ping Fu	Reliability Analysis of Wake-Induced Riser Collision
IMT-6-2019	Vladimir Krivopolianskii	Experimental Investigation of Injection and Combustion Processes in Marine Gas Engines using Constant Volume Rig
IMT-7-2019	Anna Maria Kozlowska	Hydrodynamic Loads on Marine Propellers Subject to Ventilation and out of Water Condition.
IMT-8-2019	Hans-Martin Heyn	Motion Sensing on Vessels Operating in Sea Ice: A Local Ice Monitoring System for Transit and Stationkeeping Operations under the Influence of Sea Ice
IMT-9-2019	Stefan Vilsen	Method for Real-Time Hybrid Model Testing of Ocean Structures – Case on Slender Marine Systems
IMT-10-2019	Finn-Christian W. Hanssen	Non-Linear Wave-Body Interaction in Severe Waves
IMT-11-2019	Trygve Olav Fossum	Adaptive Sampling for Marine Robotics
IMT-12-2019	Jørgen Bremnes Nielsen	Modeling and Simulation for Design Evaluation
IMT-13-2019	Yuna Zhao	Numerical modelling and dyncamic analysis of offshore wind turbine blade installation
IMT-14-2019	Daniela Myland	Experimental and Theoretical Investigations on the Ship Resistance in Level Ice
IMT-15-2019	Zhengru Ren	Advanced control algorithms to support automated offshore wind turbine installation
IMT-16-2019	Drazen Polic	Ice-propeller impact analysis using an inverse propulsion machinery simulation approach
IMT-17-2019	Endre Sandvik	Sea passage scenario simulation for ship system performance evaluation

IMT-18-2019	Loup Suja-Thauvin	Response of Monopile Wind Turbines to Higher Order Wave Loads
IMT-19-2019	Emil Smilden	Structural control of offshore wind turbines – Increasing the role of control design in offshore wind farm development
IMT-20-2019	Aleksandar-Sasa Milakovic	On equivalent ice thickness and machine learning in ship ice transit simulations
IMT-1-2020	Amrit Shankar Verma	Modelling, Analysis and Response-based Operability Assessment of Offshore Wind Turbine Blade Installation with Emphasis on Impact Damages
IMT-2-2020	Bent Oddvar Arnesen Haugaløkken	Autonomous Technology for Inspection, Maintenance and Repair Operations in the Norwegian Aquaculture
IMT-3-2020	Seongpil Cho	Model-based fault detection and diagnosis of a blade pitch system in floating wind turbines
IMT-4-2020	Jose Jorge Garcia Agis	Effectiveness in Decision-Making in Ship Design under Uncertainty
IMT-5-2020	Thomas H. Viuff	Uncertainty Assessment of Wave-and Current-induced Global Response of Floating Bridges
IMT-6-2020	Fredrik Mentzoni	Hydrodynamic Loads on Complex Structures in the Wave Zone
IMT-7-2020	Senthuran Ravinthrakumar	Numerical and Experimental Studies of Resonant Flow in Moonpools in Operational Conditions
IMT-8-2020	Stian Skaalvik Sandøy	Acoustic-based Probabilistic Localization and Mapping using Unmanned Underwater Vehicles for Aquaculture Operations
IMT-9-2020	Kun Xu	Design and Analysis of Mooring System for Semi-submersible Floating Wind Turbine in Shallow Water
IMT-10-2020	Jianxun Zhu	Cavity Flows and Wake Behind an Elliptic Cylinder Translating Above the Wall
IMT-11-2020	Sandra Hogenboom	Decision-making within Dynamic Positioning Operations in the Offshore Industry – A Human Factors based Approach
IMT-12-2020	Woongshik Nam	Structural Resistance of Ship and Offshore Structures Exposed to the Risk of Brittle Failure
IMT-13-2020	Svenn Are Tutturen Værnø	Transient Performance in Dynamic Positioning of Ships: Investigation of Residual Load Models and Control Methods for Effective Compensation
IMT-14-2020	Mohd Atif Siddiqui	Experimental and Numerical Hydrodynamic Analysis of a Damaged Ship in Waves
IMT-15-2020	John Marius Hegseth	Efficient Modelling and Design Optimization of Large Floating Wind Turbines

IMT-16-2020	Asle Natskår	Reliability-based Assessment of Marine Operations with Emphasis on Sea Transport on Barges
IMT-17-2020	Shi Deng	Experimental and Numerical Study of Hydrodynamic Responses of a Twin-Tube Submerged Floating Tunnel Considering Vortex-Induced Vibration
IMT-18-2020	Jone Torsvik	Dynamic Analysis in Design and Operation of Large Floating Offshore Wind Turbine Drivetrains
IMT-1-2021	Ali Ebrahimi	Handling Complexity to Improve Ship Design Competitiveness
IMT-2-2021	Davide Proserpio	Isogeometric Phase-Field Methods for Modeling Fracture in Shell Structures
IMT-3-2021	Cai Tian	Numerical Studies of Viscous Flow Around Step Cylinders
IMT-4-2021	Farid Khazaeli Moghadam	Vibration-based Condition Monitoring of Large Offshore Wind Turbines in a Digital Twin Perspective
IMT-5-2021	Shuaishuai Wang	Design and Dynamic Analysis of a 10-MW Medium-Speed Drivetrain in Offshore Wind Turbines
IMT-6-2021	Sadi Tavakoli	Ship Propulsion Dynamics and Emissions
IMT-7-2021	Haoran Li	Nonlinear wave loads, and resulting global response statistics of a semi-submersible wind turbine platform with heave plates
IMT-8-2021	Einar Skiftestad Ueland	Load Control for Real-Time Hybrid Model Testing using Cable-Driven Parallel Robots
IMT-9-2021	Mengning Wu	Uncertainty of machine learning-based methods for wave forecast and its effect on installation of offshore wind turbines
IMT-10-2021	Xu Han	Onboard Tuning and Uncertainty Estimation of Vessel Seakeeping Model Parameters